

ROYAL HOLLOWAY UNIVERSITY OF
LONDON

DOCTORAL THESIS

**Emplacement and evolution of sills into shallow magma
chambers and hydrocarbon reservoirs**

Zöe Amanda Barnett

*A thesis in fulfilment of the requirements for the degree of Doctor of
Philosophy in the*
Earth Sciences Department

August 2014

Declaration of Authorship

I, Zoe Barnett hereby declare that this thesis and the other work presented in it is entirely my own. Where I have consulted the work of others, this is always clearly stated.

Signed: _____

Date: _____



“Rocks are records of events that took place at the time they formed. They are books. They have a different vocabulary, a different alphabet, but you learn how to read them.”

John McPhee

Abstract

Volcanism occurred 56Ma along the Vøring Margin, offshore Norway, during continental break-up. The focus of this thesis is on sills along this margin, particularly (1) on sill emplacement, (2) how they may evolve into a shallow magma chambers or (3) act as fractured reservoirs for hydrocarbons. Numerical models show that because of mechanical layering, dykes are commonly deflected into sills due to debonding, stress barriers, and elastic mismatch. Once emplaced a sill can take on a variety of geometries and begin to expand via elastic-plastic deformation of the strata. In order for a sill to evolve into a shallow magma chamber, a high magma injection rate is needed so that the sill remains at least partially molten. The molten sill creates a stress barrier causing subsequent dyke injections to be absorbed into the initial sill.

The majority of sills, however, do not evolve into shallow magma chambers, but may act as fractured hydrocarbon reservoirs, depending on (1) sill geometry, (2) sill thickness, and (3) sill margins. For sills to act as fractured reservoirs their lower margins must be ruptured, while the upper margins remain intact and form a seal, allowing the accumulation of hydrocarbons within the sills. By contrast, if the lower margins remain intact, forms a seal, the sill may trap hydrocarbons, particularly when in conjunction with sealing normal faults and dykes. While sill propagation may reactivate faults, and temporarily increase their permeability, subsequent geothermal fluid circulation (due to the sill) may contribute to ‘healing’ and ‘sealing’ of the fault, thereby reducing its permeability. Fluid transport in sills is primarily through fracture networks, most of the fractures being columnar joints, which favour transport particularly if (1) they have large apertures (through the cubic law and flow channelling) and (2) favourably orientated in relation to the local stress field.

Contents

Declaration of Authorship.....	2
Abstract	4
Contents	5
List of figures	10
List of tables.....	20
Acknowledgements	21
Chapter 1: Introduction	22
1.1 General introduction.....	22
1.2 Aims and objectives	22
1.3 Why is the research important?	24
1.4 Methods	24
1.5 Funding and supervision	24
1.6 Thesis outline	24
Chapter 2: Geological history of the Vøring Margin	26
2.1 Introduction to the northwest Atlantic Margin.....	26
2.2 Regional tectonics	27
2.2.1 Permian tectonics to pre-break-up	28
2.2.2 Tectonism after continental break-up.....	33
2.3 Vøring Margin and Basin	35
2.3.1 Sediment deposition in the Vøring Basin	41
2.4 Sills in the Vøring Basin and their importance	43
2.4.1 Paleocene-Eocene Thermal Maximum (PETM).....	47
2.5 Lower crustal body (LCB) and T-Reflection	48
2.6 Global examples of hydrocarbons and associated volcanic rocks.....	51
2.6.1 Thermal effects of sills.....	53
2.7 Concluding remarks on the Norwegian Margin	53
Chapter 3: Principles of fracture mechanics	55
3.1 Introduction	55
3.2 Stress	55
3.3 Displacement, deformation and strain.....	58
3.4 Elasticity.....	59
3.5 Modes of cracks.....	63
3.6 Hydrofractures.....	64
3.6.1 Dykes	64
3.6.2 Inclined sheets.....	66
3.6.3 Sills.....	67

3.6.4	Laccoliths	69
3.7	Overpressure, excess pressure and total pressure.....	70
Chapter 4:	Methods	72
4.1	Introduction	72
4.2	Modelling	72
4.2.1	Conceptual and scale models	72
4.2.2	Mathematical models	73
4.2.2.1	Finite element method	75
4.3	COMSOL	77
4.3.1	Solid Mechanics	78
4.3.1.1	Hydrofractures and fault zones.....	78
4.3.1.2	Weak contacts and fault zones	79
4.3.1.3	Boundary loading and topography	80
4.3.1.4	Mechanical properties	81
4.3.1.5	Stationary and time-dependent models	81
4.3.1.6	Output parameters	82
4.3.2	Fluid flow: laminar flow and particle tracing	83
4.3.2.1	Fracture networks	83
4.3.2.2	Fluid properties.....	83
4.3.2.3	Stationary and time-dependent models	84
4.3.2.4	Output parameters	84
4.4	Seismic line interpretation.....	84
4.5	Field and data processing	85
4.5.1	Field measurements.....	85
4.5.1.1	Whin Sill geological background	87
4.5.1.2	Stardalur sill cluster geological background	90
4.5.2	Data analysing.....	94
4.5.2.1	Rose diagrams and stereonet.....	94
4.5.2.2	Use of photographs.....	94
4.5.2.3	Graphical plots: Fracture orientation; Fracture apertures; Fracture spacing; Fracture frequency.....	95
Chapter 5:	Sill emplacement	96
5.1	Introduction	96
5.1.1	Dyke initiation and propagation.....	97
5.1.2	Dyke propagation at a weak contact	101
5.2	Sill formation hypotheses	102
5.2.1	Neutral buoyancy hypothesis	103

5.2.2	Stress rotation hypothesis.....	104
5.3	Numerical models.....	105
5.3.1	Young's modulus contrast between layers.....	105
5.3.2	Weak contacts	109
5.4	Discussion: Sill emplacement mechanisms.....	112
5.4.1	Cook-Gordon debonding.....	113
5.4.2	Stress barrier.....	114
5.4.3	Elastic mismatch	115
5.4.3.1	Dundurs elastic mismatch parameter	116
5.5	Conclusions	117
Chapter 6: Sill evolution into a shallow magma chamber		119
6.1	Introduction	119
6.2	Sill geometry	120
6.2.1	Volcano topography	124
6.3	Sill growth	131
6.3.1	Small sills.....	132
6.3.2	Large sills	139
6.4	Whin Sill.....	149
6.5	Shallow magma chamber formation.....	154
6.5.1	Sill evolution into a shallow magma chamber	155
6.5.2	Sill complexes	160
6.6	Discussion	165
6.6.1	Saucer-shaped sill emplacement mechanisms	165
6.6.2	Shallow magma chamber formation	166
6.7	Conclusions	169
Chapter 7: Faults - their permeability and relation to sills.....		171
7.1	Introduction	171
7.1.1	Fault core.....	172
7.1.2	Fault damage zone.....	173
7.1.3	Fault slip.....	174
7.1.4	Faults and hydrocarbon exploration.....	175
7.2	Sill interaction with grabens.....	176
7.3	Local stress field within a fault zone.....	181
7.4	Fluid flow within a fault zone	186
7.4.1	Non reactivated fault	186
7.4.2	Fault reactivation.....	187
7.5	Discussion	196

7.6	Conclusions	200
Chapter 8: Scaling exponents and entropies of sills, laccoliths and fracture lengths		202
8.1	Introduction	202
8.2	Power-laws	202
8.3	Entropy	203
8.4	Sill and laccolith thicknesses.....	204
8.4.1	Sills.....	205
8.4.2	Laccoliths	207
8.4.3	Tabular intrusions.....	209
8.5	Fracture lengths	212
8.6	Discussion	217
8.6.1	Test for power-laws.....	217
8.6.2	Entropy	220
8.6.3	Fracture growth	225
8.7	Conclusions	227
Chapter 9: Fracture networks in sills		231
9.1	Introduction	231
9.2	Fractures in the study area.....	234
9.3	Fracture orientation	234
9.3.1	Whin Sill	234
9.3.2	Stardalur sill cluster.....	236
9.4	Fracture spacing and fracture frequency	236
9.4.1	Whin Sill	238
9.4.2	Stardalur sill cluster.....	239
9.5	Fracture aperture.....	244
9.5.1	Whin Sill	244
9.5.2	Stardalur sill cluster.....	244
9.6	Fluid flow	247
9.6.1	Permeability and porosity	247
9.6.2	Fracture interconnectivity in fractured reservoirs	253
9.7	Discussion	258
9.7.1	Permeability and porosity: implications for reservoir quality.....	258
9.7.2	Vøring Margin.....	287
9.7.3	Flow channelling and the cubic law: implications for fluid transport within fractured reservoirs	288
9.8	Conclusions	291

Chapter 10: Sills as potential hydrocarbon fractured reservoirs	292
10.1 Introduction	292
10.2 Numerical models of solidified sills.....	296
10.2.1 Extensional tectonic regime	297
10.2.2 Compressional tectonic regime	297
10.3 Modelling of sills and faults in the Vøring Margin.....	301
10.3.1 Line MNR05-7397	305
10.3.2 Line MNR06-7365	309
10.4 Sills as seals for hydrocarbons	319
10.5 Fractured reservoirs associated with sill emplacement	320
10.5.1 The Utgard sills	327
10.6 Conclusions	329
Chapter 11: Discussion	332
11.1 Limitations and assumptions	332
11.2 Emplacement of sills	333
11.3 Shallow magma chambers.....	335
11.4 Faulting.....	339
11.5 Sills as fractured reservoirs	341
11.5.1 Seals, traps and fractured reservoirs.....	341
11.5.2 Fluid flow through sills	343
11.6 Further work	344
Chapter 12: Conclusions	347
References	349
Appendices.....	380
A. Simple solid mechanics model set-up in COMSOL	380
B. Fluid flow model set-up in COMSOL	386
C. Seismic lines MNR05-7397 and MNR06-7365	392
D. Barnett, Z., Gudmundsson, A., 2014. Numerical modelling of dykes deflected into sills to form a magma chamber	394

List of figures

Figures in Chapter 1

Figure 1.1: Depth converted profile of the Vøring Basin.....	23
--	----

Figures in Chapter 2

Figure 2.1: Map of offshore Norway.....	27
Figure 2.2: Tectonic event summary of regions adjacent to the Atlantic Margin post Carboniferous.....	28
Figure 2.3: Isochron maps illustrating regional depocentres.....	30
Figure 2.4: Map illustrating tectonic activity from Jurassic to Cretaceous.....	32
Figure 2.5: Inversion structures, mainly domes and reverse faults along the Atlantic Margin of intra-Cenozoic age.....	34
Figure 2.6: Map illustrating areas of Neogene uplift along the Atlantic Margin.....	36
Figure 2.7: Vøring Basin evolution.....	38
Figure 2.8: Sketch map of the mid-Norwegian Margin.....	40
Figure 2.9: Seismic interpretation of the Vøring Margin.....	42
Figure 2.10: Sill facies modified from Planke et al. (2005).....	45
Figure 2.11: Schematic illustration of a hydrothermal vent complex.....	46
Figure 2.12: Utgard well 6607/5-2 illustrating the sill intrusions and lithological units.....	48
Figure 2.13: Cross-section through the Vøring Margin illustrating the location of the T-Reflection.....	50
Figure 2.14: World map showing the geographical locations of hydrocarbons found in the regions of igneous complexes.....	52
Figure 2.15: Graph illustrating heat dissipation between 6 sills and the host rock in which they are emplaced over 20 ka.....	53

Figures in Chapter 3

Figure 3.1: An internal point can be represented by nine components of the stress tensor, which can be arranged as a matrix.....	57
Figure 3.2: Stress-strain curve for a linear elastic material.....	61
Figure 3.3: Schematic illustration of Poisson's ratio.....	62
Figure 3.4: Discontinuities loaded in both compression and extension.....	63

Figure 3.5: Fracture displacements are primarily denoted by mode I, mode II and mode III.....	64
Figure 3.6: Feeder dyke, Las Cañadas, Tenerife illustrating the directions of the principal stresses, the aperture and height of the dyke.....	66
Figure 3.7: Photograph of an inclined sheet.....	67
Figure 3.8: Regional dyke swarm, near Masca, Tenerife.....	68
Figure 3.9: Stepped sill intruded into a basaltic lava flow, SE Iceland.....	69
Figure 3.10: Pillow lavas, SW Iceland.....	70
Figure 3.11: Photograph of a laccolith.....	71

Figures in Chapter 4

Figure 4.1: Schematic comparison between the meshes of finite element method (FEM) and boundary element method (BEM).....	76
Figure 4.2: A mesh indicating the location of the elements and nodes.....	77
Figure 4.3: A schematic illustration of a sill in 2D and 3D.....	79
Figure 4.4: Seismic line demonstrating how sills were identified.....	86
Figure 4.5: Field measurements and equipment.....	87
Figure 4.6: Overview of the Whin Sill locations, NE England.....	89
Figure 4.7: Hand specimen and thin section analysis of Whin Sill.....	90
Figure 4.8: Google Earth images of profile lines where fracture measurements were taken.....	91
Figure 4.9: Hand specimen and thin section analysis of Stardalur sill.....	93
Figure 4.10: Google Earth image representing the location of the Stardalur sill cluster and locations of profile lines taken.....	93

Figures in Chapter 5

Figure 5.1: Photographs of arrested dykes and feeder dykes.....	100
Figure 5.2: Schematic illustration of scenarios for when a dyke meet a contact....	102
Figure 5.3: Magma transport is governed by magma density, ρ_m relative to the density of the host rock, ρ_r , and the excess pressure in the source chamber.....	104
Figure 5.4: Geometry of numerical models in Figures 5.6, 5.7 and 5.8.....	106
Figure 5.5: FEM model of a dyke propagating through interchanging soft, 5 GPa and stiff, 20 GPa layers showing contours of tensile stress.....	107

Figure 5.6: FEM models showing maximum principal stress trajectories for a dyke/inclined sheet meeting a strong contact.....	108
Figure 5.7: FEM models showing tensile stresses for a dyke/inclined sheet meeting a weak contact.....	110
Figure 5.8: FEM models showing maximum principal stress trajectories for a dyke/inclined sheet meeting a weak contact.....	111
Figure 5.9: FEM model illustrating the effects of a stress barrier.....	112
Figure 5.10: A conceptual model demonstrating the opening of a weak contact through Cook-Gordon debonding.....	114
Figure 5.11: Dundurs elastic mismatch parameter.....	118

Figures in Chapter 6

Figure 6.1: Six schematic illustrations of sill geometries.....	120
Figure 6.2: Photographs illustrating a variety of sill geometries.....	121
Figure 6.3: Seismic line MNR05-7397, illustrating the various relationships between sills.....	122
Figure 6.4: Model set up for Figures 6.5 and 6.6.....	123
Figure 6.5: FEM model of tensile stress illustrating the growth of the sill and maximum principal compressive stress trajectories illustrating the propagation path of the sill that is emplaced at a contact 4 km below the free surface.....	125
Figure 6.6: FEM model of tensile stress and the maximum principal compressive stress trajectories illustrating the propagation path of a sill emplaced at a contact 1 km below the free surface.....	126
Figure 6.7: Model set up for Figure 6.8.....	127
Figure 6.8: FEM models of tensile stress contours and maximum principal compressive stress trajectories illustrating the various sill geometries influenced by differing volcano topographies.....	129
Figure 6.9: FEM model representing tensile stresses associated with a sill that is emplaced 4 km below the surface.....	133
Figure 6.10: Schematic illustration of a small sill within a homogeneous medium.....	134
Figure 6.11: Numerical results illustrating the maximum displacement of the roof of a small sill.....	135

Figure 6.12: Schematic illustration of a small sill within a heterogeneous crust....	136
Figure 6.13: FEM models showing displacement of the sill roof in a heterogeneous crust at a stiff-soft host rock boundary.....	137
Figure 6.14: FEM models showing displacement of the sill roof in a heterogeneous crust at a soft-stiff host rock boundary.....	138
Figure 6.15: Schematic illustration of a large sill emplaced into a heterogeneous crust.....	141
Figure 6.16: Numerical representation of the maximum deflection of the large sill roof.....	141
Figure 6.17: 3D FEM model of tensile stresses and surface deformation relating to a large sill.....	142
Figure 6.18: Schematic illustration of a large sill into a single layered system.....	143
Figure 6.19: Schematic illustration of a large sill into a multilayered system.....	143
Figure 6.20: Graphical representation of sill roof and floor deflection for varying sill diameters of 4-10 km	144
Figure 6.21: Graphical representation of sill roof and floor deflection for varying sill diameters of 8-20 km.....	145
Figure 6.22: Graphical relationship between the underburden deflection and the overburden deflection.....	145
Figure 6.23: Graphical representation of sill roof and floor deflection for varying sill diameters of 4-10 km.....	146
Figure 6.24: Graphical representation of sill roof and floor deflection for varying sill diameters of 8-20 km.....	147
Figure 6.25: Graphical relationship between the underburden deflection and the overburden deflection.....	147
Figure 6.26: FEM model of tensile stress contours of a large sill, with a diameter of 4 km, emplaced at a depth of 1 km illustrating deformation to the overburden and surface.....	148
Figure 6.27: Schematic illustrations of sill growth.....	150
Figure 6.28: Photographs of Whin Sill hand specimens and columnar joint thickness.....	151
Figure 6.29: Ropy flow structures seen in the Whin Sill.....	152
Figure 6.30: Magma finger from the main Whin Sill.....	153
Figure 6.31: Photograph of impure marble, known as ‘sugar limestone’	153

Figure 6.32: Photographs to illustrate various contacts seen in the field, demonstrating an overall stepped geometry of the Whin Sill.....	156
Figure 6.33: FEM model showing maximum principal compressive stress trajectories, and their distribution following the emplacement of a sill.....	159
Figure 6.34: Schematic illustration of a penny-shaped sill that may inflate into an oblate shallow magma chamber.....	160
Figure 6.35: FEM models of tensile stress contours. Largest sill varies in location in the sill complex and overpressure within the sills varies throughout complex.....	163
Figure 6.36: 3D FEM models of tensile stress contours with deformation for a sill complex.....	164
Figure 6.37: Saucer-shaped sill emplacement based on a) Francis (1982), b) Chevallier and Woodford (1999) and c) Malthe-Sørenssen et al. (2004).....	167

Figures in Chapter 7

Figure 7.1: Schematic illustration of a fault zone.....	172
Figure 7.2: Fault zone in Howick Quarry, NW England.....	173
Figure 7.3: 3D block diagram of a graben and the associated horst structure.....	176
Figure 7.4: Schematic illustration of model set-up for Figure 7.5.....	177
Figure 7.5: FEM model of von Mises shear stresses of a graben inducing a stress barrier favouring sill emplacement.....	178
Figure 7.6: Graphical representation of fault slip.....	179
Figure 7.7: Schematic illustration of fault model set up in Figure 7.8.....	180
Figure 7.8: FEM model of von Mises shear stress for sill-fault interaction.....	182
Figure 7.9: Schematic illustration of two offset fault zones.....	183
Figure 7.10: FEM model representing von Mises shear stress contours of a fault zone.....	184
Figure 7.11: FEM model of von Mises shear stress across two normal faults.....	185
Figure 7.12: FEM model of tensile stresses about two offset normal faults.....	185
Figure 7.13: Model of fluid flow through a non-active fault.....	188
Figure 7.14: Model of fluid flow through an active fault.....	189
Figure 7.15: Schematic illustration to show the rotation of the stress field and the fault dip.....	190
Figure 7.16: Fluid flow across a fault with varying dip with a local stress field rotated anti-clockwise.....	191

Figure 7.17: Fluid flow across a fault with varying dip with a local stress field rotated clockwise.....	193
--	-----

Figures in Chapter 8

Figure 8.1: A cumulative frequency plot illustrating a power-law distribution for sill thicknesses across the globe.....	206
Figure 8.2: A bi-logarithmic plot of global sill thickness in Figure 8.1 illustrating the break in slope.....	206
Figure 8.3: A bi-logarithmic plot of global sill thickness representing two distinct populations based on Figure 8.2.....	207
Figure 8.4: Cumulative frequency plot showing a power-law distribution for laccolith thicknesses worldwide.....	208
Figure 8.5: Bi-logarithmic plot of laccolith thickness in Figure 8.4 showing a break in slope.....	208
Figure 8.6: Bi-logarithmic plot of laccolith thickness showing two distinct populations based on Figure 8.5.....	209
Figure 8.7: Power-law distribution for tabular intrusions.....	211
Figure 8.8: A cumulative frequency plot illustrating a power-law distribution for fracture lengths of the columnar joints in the Whin Sill, NE England.....	214
Figure 8.9: A bi-logarithmic plot of fracture lengths in Figure 8.8 illustrating the break in slope.....	214
Figure 8.10: A bi-logarithmic plot of fracture lengths representing two distinct populations from Figure 8.9.....	215
Figure 8.11: A cumulative frequency plot illustrating a power-law distribution for fracture lengths of the columnar joints in the Stardalur sill cluster, SW Iceland....	215
Figure 8.12: A bi-logarithmic plot of fracture lengths in Figure 8.11 illustrating the break in slope.....	216
Figure 8.13 : A bi-logarithmic plot of fracture lengths representing two distinct populations from Figure 8.12.....	216
Figure 8.14: Power-law distribution for fracture lengths.....	218
Figure 8.15: Significance tests for power-law fit for sills and laccoliths.....	219
Figure 8.16: Significance tests for power-law fit for fracture lengths in the Whin Sill and Stardalur sill cluster.....	220
Figure 8.17: Linear relationship between entropy and sill/laccolith thickness.....	221

Figure 8.18: Linear relationship between entropy and fracture length.....	222
Figure 8.19: Tabular intrusions with corresponding length, L, thickness, T, and lateral area, A, showing a ‘S’ shape representing the various emplacement styles.....	223
Figure 8.20: Rose diagrams for fracture orientations within the Whin Sill: Bamburgh-Holy Island fractures, Dunstanburgh fractures, Ward’s Hill Quarry fractures, Hadrian’s Wall fractures and Co. Durham fractures.....	228
Figure 8.21: Rose diagrams of fracture orientations in the Whin Sill: Holy Island sill, Alnwick sill and Hadrian’s Wall-Pennines sill.....	229
Figure 8.22: Rose diagrams of vertical fractures in the Stardalur sill cluster.....	230

Figures in Chapter 9

Figure 9.1: Columnar joint formation.....	232
Figure 9.2: Plumose structure indicating the fanning of hackles (yellow lines) from an apex.....	233
Figure 9.3: Fracture orientations within the Whin Sill.....	235
Figure 9.4: Fracture orientations within the Stardalur sill cluster.....	237
Figure 9.5: Fracture spacing of vertical/sub-vertical fractures and fracture frequency in the Whin Sill.....	240
Figure 9.6: Fracture spacing of vertical/sub-vertical fractures and fracture frequency in the Stardalur sill cluster.....	242
Figure 9.7: Plot of the fracture apertures measured in the Whin Sill.....	245
Figure 9.8: Plot of the fracture apertures measured in the Stardalur sill cluster.....	248
Figure 9.9: Tension fracture in Þingvellir, Southwest Iceland. Groundwater is able to flow along the fracture through the lava whose walls are fairly smooth although irregular.....	250
Figure 9.10: Photographs of open and closed fractures.....	251
Figure 9.11: Interbedded sandstones and shales, Cullernose Point, NE England illustrating fracture related permeability in a sedimentary rock.....	252
Figure 9.12: Fracture clustering in the Whin Sill at Castle Hill, Holy Island, NE England, illustrating fracture related permeability.....	252
Figure 9.13: Laminar flow between two vertical fractures.....	253
Figure 9.14: Fluid flow velocity through an orthogonal fracture system that have equal apertures.....	255

Figure 9.15: Fluid flow velocity through an orthogonal fracture system that have unequal apertures.....	256
Figure 9.16: Fracture map of Castle Point, near Dunstanburgh, Northumberland coast, NE England.....	258
Figure 9.17: Fracture map of Cullernose Point, near Dunstanburgh, Northumberland coast, NE England.....	259
Figure 9.18: Fracture map of Profile 1, Stardalur, SW Iceland.....	260
Figure 9.19: Fracture map of Falcon Clints, Co. Durham, NE England.....	261
Figure 9.20: Fracture map of Castle Hill, Holy Island, Northumberland, NE England.....	262
Figure 9.21: Fracture network from Castle Point, Whin Sill. The FEM stationary model represents the velocity of laminar flow for water.....	263
Figure 9.22: Water particle tracing for fluid flow in the Whin Sill fracture network at Castle Point.....	264
Figure 9.23: Fracture network from Castle Point, Whin Sill. FEM stationary model represents the velocity of laminar flow for crude oil.....	269
Figure 9.24: Crude oil particle tracing for fluid flow in the Whin Sill fracture network at Castle Point.....	270
Figure 9.25: Fracture network from Stardalur sill cluster, profile 1. The FEM model represents the velocity of laminar flow for water.....	275
Figure 9.26: Water particle tracing for fluid flow in the Stardalur fracture network.....	276
Figure 9.27: Fracture network from Stardalur sill cluster, profile 1. The FEM model represents the velocity of laminar flow for crude oil.....	280
Figure 9.28: Crude oil particle tracing for fluid flow in the Stardalur fracture network.....	281
Figure 9.29: Sub-vertical fracture aperture variation along three profiles: Profile 1, Stardalur sill cluster; Holy Island, Whin Sill; Harkess Rock, Whin Sill.....	285

Figures in Chapter 10

Figure 10.1: Photographs of contact metamorphism indicating the terms chilled selvage and baked margin.....	294
---	-----

Figure 10.2: Map illustrating depths of sills and their associated hydrothermal vents in the Vøring Basin, highlighting the location of seismic lines MNR05-7397 and MNR06-7365.....	296
Figure 10.3: Model set-up of sill 5.....	297
Figure 10.4: FEM model of tensile stress contours around a concave sill that is subject to extension.....	298
Figure 10.5: FEM model of tensile stress contours around a concave sill that is subject to extension.....	299
Figure 10.6: FEM model of sill 5 representing tensile stress contours.....	300
Figure 10.7: Schematic illustration offshore Norway showing the location of seismic lines MNR05-7397 and MNR06-7365 in the Vøring area.....	302
Figure 10.8: Schematic illustration of line MNR05-7397.....	303
Figure 10.9: Schematic illustration of line MNR06-7365.....	304
Figure 10.10: Line MNR05-7397. FEM models of tensile stresses from a time sequence of 56Ma to present.....	306
Figure 10.11: Line MNR05-7397. FEM models of shear stresses, von Mises, from a time sequence of 56Ma to present.....	310
Figure 10.12: Line MNR06-7365. FEM models of tensile stresses from a time sequence of 56Ma to present.....	313
Figure 10.13: Line MNR06-7365. FEM models of shear stresses, von Mises, from a time sequence of 56Ma to present.....	316
Figure 10.14: Schematic illustration of a sill as a seal and trap towards hydrocarbon accumulation.....	320
Figure 10.15: Kinematic model of forced fold above a saucer shaped sill.....	321
Figure 10.16: Schematic illustration of a sill functioning as a fractured reservoir.....	322
Figure 10.17: FEM model of tensile stress illustrating the increased permeability along a normal fault on line MNR05-7397.....	323
Figure 10.18: FEM model of tensile stress illustrating increased permeability along a normal fault on line MNR06-7365.....	324
Figure 10.19: FEM model of tensile stress contours illustrating possible hydrocarbon accumulation on line MNR05-7397.....	325
Figure 10.20: FEM model representing tensile stress contours illustrating a possible fractured reservoir on line MNR05-7397.....	326

Figure 10.21: FEM model representing tensile stress contours illustrating a possible fractured reservoir on line MNR06-7365.....	327
Figure 10.22: FEM model representing shear stress contours illustrating zones of shear fracture formation/reactivation on line MNR05-7397.....	328
Figure 10.23: FEM model representing tensile stress contours illustrating zones of tensile fracture formation/reactivation on line MNR06-7365.....	329
Figure 10.24: FEM model of tensile stresses in the Utgard sill (well 6607/5-2).....	330

Figures in Chapter 11

Figure 11.1: Schematic illustration showing the formation of a shallow magma chamber.....	337
Figure 11.2: Photograph illustrating the geometry of the Stardalur sills, which is then schematically illustrated.....	339
Figure 11.3: Slaufudalur Pluton, SE Iceland.....	340
Figure 11.4: Thin section of Stiflisdalsvatn sill. Implications for fluid flow paths.....	345

List of tables

Tables in Chapter 4

Table 4.1: Modelling parameters for time-dependent models of the Vøring Margin.....	82
---	----

Tables in Chapter 8

Table 8.1: Statistical analysis of tabular intrusions - sills and laccoliths worldwide.....	210
Table 8.2: Data of fracture length measurements from the Whin Sill, NE England and the Stardalur sill cluster, SW Iceland.....	213

Tables in Chapter 9

Table 9.1: Statistics for all fracture spacings measured along 18 profiles across the Whin Sill.....	241
Table 9.2: Statistics for all fracture spacings measured along 21 profiles across the Stardalur sill cluster.....	243
Table 9.3: Statistics for all apertures measured along 18 profiles across the Whin Sill.....	246
Table 9.4: Statistics for all apertures measured along 21 profiles of the Stardalur sill cluster.....	249

Acknowledgements

I would first like to thank my supervisor Professor Agust Gudmundsson for his helpful discussion and guidance. Also, John Browning for being a great field assistant in NE England and Iceland, whilst also providing discussion of newly developed ideas. Tectonor AS, E-ON Ruhrgas Norge, RWE Dea Norge and Repsol Exploration Norge for their support and permission for publishing papers and conference participation. Also, Rock Fractures and Fluid Flow research group for their helpful input into the project.

At Royal Holloway my thanks also go to Frank Lehane and Mark Longbottom for their IT support, Neil Holloway for thin section preparation and Kevin D'Souza for his help in the optics lab and with the preparation of some Tenerife field panoramas.

At Tectonor AS, I thank Ingrid Fjeldskaar Løtveit, Willy Fjeldskaar, Magnhild Sydnes and Ivar Grunnaleite for their kind hospitality at project meetings and informative discussion. I thank especially Ivar Grunnaleite for providing the 1-1 sill geometries, without which, numerical models could not be run accurately.

Thank you to Professor Sandy Cruden for providing data on sills and laccoliths for Chapter 8.

Thank you to Michelle Barnett and Ingrid Fjeldskaar Løtveit for their helpful feedback on first drafts of this thesis, which helped to improve the final version of my thesis.

Finally, thanks go to my friends and family for their support over these past three years. Most of all, my parents, Pamela and Adrian Barnett, and my sister, Michelle Barnett, who have been an inspiration and have always encouraged me to follow my dreams. This thesis is dedicated to you all, because with your support I will continue to succeed throughout my future in geology.

Chapter 1: Introduction

1.1 General introduction

The future of petroleum exploration will be partly related to volcanic margins, but to be successful, a good understanding of such volcanic margins must be attained. For this PhD thesis the Vøring Margin, offshore Norway is of particular interest, an area where petroleum exploration has been on-going since the 1990s (Fig. 1.1). The geological history of the Vøring Margin is complex, with several phases of extension, notably the North Atlantic break-up, and also phases of compression. This tectonic evolution has had a large impact on the regional and local stresses of the area in both time and space from the Late Mesozoic (Fjeldskaar *et al.*, 2009; Grunnaleite *et al.*, 2009). This tectonic history will have had a great impact on the sills in the Vøring Margin, especially as regards to the sills acting as potential fractured hydrocarbon reservoirs.

Evidence also suggests that some sills have the ability to evolve into shallow magma chambers, depending on certain conditions, where the largest chambers are thought to have formed from large sills or sill clusters. Thus, sill emplacement is important in the fields of petroleum and volcanotectonics.

1.2 Aims and objectives

This thesis is composed of two parts. The first part is a joint study with Tectonor AS and Sintef Petroleum entitled ‘The effect of magmatic sill emplacement on the petroleum systems in the Vøring Margin’. The project looks at how sills and dykes can contribute to the formation of a hydrocarbon reservoir, and how these dense igneous rocks can also act as seals for the migration of hydrocarbons. The main aims of this joint study are to investigate (1) thermal effects of sills, (2) effects of sill emplacement on hydrocarbon maturity, (3) diagenetic alteration of the sediments, (4) effects of sill emplacement on hydrocarbon migration, (5) how sills can act as seals, and (6) how sills can act as fractured reservoirs. My part of the project focuses on aims (4), (5) and (6). I make conceptual, analytical and numerical models on sill

emplacement, specifically on how a sill forms, grows and reaches its final geometry. Of particular importance to the project and the petroleum industry is to investigate how a sill itself and the junction between the sill and a fault (or a dyke) have the potential to act as fractured reservoirs, their mechanical interactions, and how a sill can act as a seal for hydrocarbons. The second part of the thesis is to look at all of these results in a volcanotectonic context to understand the mechanism of dyke and sill emplacement and the evolution of sills into shallow magma chambers.

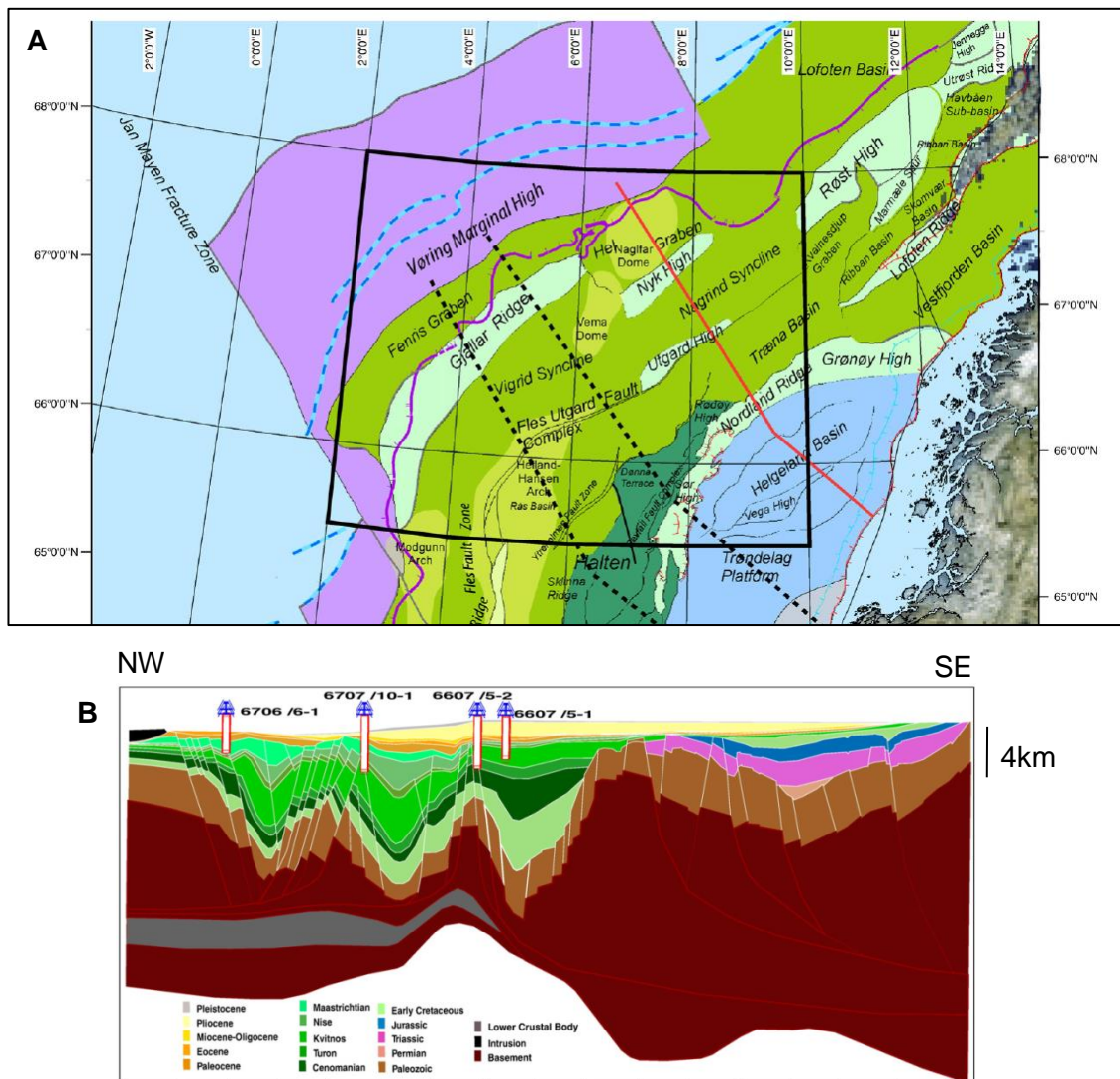


Figure 1.1: (A) Map of offshore Norway, indicating profile line in (B) with solid red line. (B) Depth converted profile of the Vøring Basin, highlighting well sites (Fjeldskaar *et al.*, 2009). A detailed description of the area is provided in Chapter 2.

1.3 Why is the research important?

This thesis will be of interest to the petroleum industry primarily because a significant part of its future explorations will be related to volcanic extrusions and intrusions along volcanic margins. In order for such explorations to be successful there must be a good understanding of volcanic provenances, especially their thermal and tectonic evolution and potential to form hydrocarbon reservoirs. From research it shows that many models need developing, especially models relating to dyke and sill emplacement. Thus, improved knowledge of igneous complexes within sedimentary basins yielding hydrocarbons is important.

1.4 Methods

Predominantly, the methods used in this thesis are field studies and numerical modelling, together with analytical modelling. Field work was carried out primarily to study the permeability and porosity of sills to act as good hydrocarbon reservoirs. Field work was conducted over two field seasons, in August 2012 in Iceland, and between June and August 2013 in NE England (for the Whin Sill) and in SW Iceland, to investigate fracture networks in sills.

1.5 Funding and supervision

Funding for this PhD was provided by Tectonor AS, with additional support from the Research Committee, Department of Earth Sciences, Royal Holloway University of London and the University of London Grants for PGR study costs. This project was supervised by Professor Agust Gudmundsson, Royal Holloway University of London.

The joint project with Tectonor AS and Sintef Petroleum, 'VøMag', was supported by three oil companies based in Norway: E.ON Ruhrgas Norge, RWE Dea Norge and Repsol Exploration Norge. Their support and permission for presenting at conferences and publishing papers is much appreciated.

1.6 Thesis outline

First, a geological overview is given of the Vøring Margin including a geological setting and associated geological background in Chapter 2. Then, in Chapters 3 and 4

important terminology is explained and methods used are described. Next, results are analysed and interpreted in Chapters 5-10. In Chapter 11, ideas and observations made from previous chapters are discussed, including the limitations and assumptions made in the models, what the results imply, and how this thesis can be advanced upon in the future. Lastly, the main conclusions are drawn in Chapter 12 to give an overview of the thesis.

Chapter 2: Geological history of the Vøring Margin

2.1 Introduction to the northwest Atlantic Margin

The Atlantic Margin is a passive margin extending from Great Britain to Norway, including Ireland and the Faroe Islands, and encompassing numerous sedimentary basins, including the Vøring Basin (Fig. 2.1). It extends from the western Barents Sea to the Rockall Trough, ~3000 km. Numerous lineaments occur along this passive margin, the three dominating trends being NE-SW, N-S and NW-SE, relating to extensional events in the Mesozoic and the Cenozoic. These events span approximately 350 Ma from the formation of the Caledonides owing to the closure of the Iapetus Ocean, followed by collapse and back-sliding of the orogeny to the opening of the NE Atlantic and associated continental break-up. The rifting of the NE Atlantic occurred in three phases (1) Permo-Triassic, (2) Jurassic-Cretaceous and (3) Cretaceous-Paleocene, where there was a shift in the rift axis from E-W (Jurassic) to NW-SE (Lower Cretaceous), resulting in overall offsets towards the site of subsequent continental break-up. These shifts are recognisable through the associated intense faulting and magmatism (Doré *et al.*, 1999).

A sector of the North Atlantic Margin is the continental margin off mainland Norway, a rifted volcanic margin (mid-Norwegian Margin). The coupled continental margins of Norway and Greenland and the Barents Sea form part of the North Atlantic Volcanic Province. This province is characterised by voluminous magmatic activity during continental break-up, leaving a valuable imprint of igneous extrusives and intrusions, for example sills, which are of significant importance for the petroleum industry. From north to south, the mid-Norwegian Margin (Fig. 2.1) hosts the Møre, Vøring and Lofoten-Vesterålen Margins, each separated by fracture zones, namely the East Jan Mayen Fracture Zone (EJMFZ) and the Bivrost Lineament (BL) (Eldhom *et al.*, 2002; Mjelde *et al.*, 2003; Faleide *et al.*, 2008).

2.2 Regional tectonics

The NW Atlantic Margin and the East Greenland Margin have a sustained geological history of intermittent extension phases and basin formation during the Devonian until the Late Cenozoic time (Fig. 2.2). After the Caledonian orogeny (Devonian), the extensional event initiated, resulting in the formation of sedimentary basins offshore Norway, East Greenland and offshore Britain. There have been three extensional and three compressional episodes along the Atlantic Margin (Bjørnseth *et al.*, 1997; Doré *et al.*, 1999; Skogseid *et al.*, 2000; van Wijk and Cloetingh, 2002; Eldholm *et al.*, 2002): (1) Permo-Triassic rifting, (2) Jurassic-Cretaceous rifting, (3) Upper Cretaceous compression, (4) Cretaceous-Paleocene rifting, (5) Lower Eocene compression, and (6) Middle Oligocene compression.

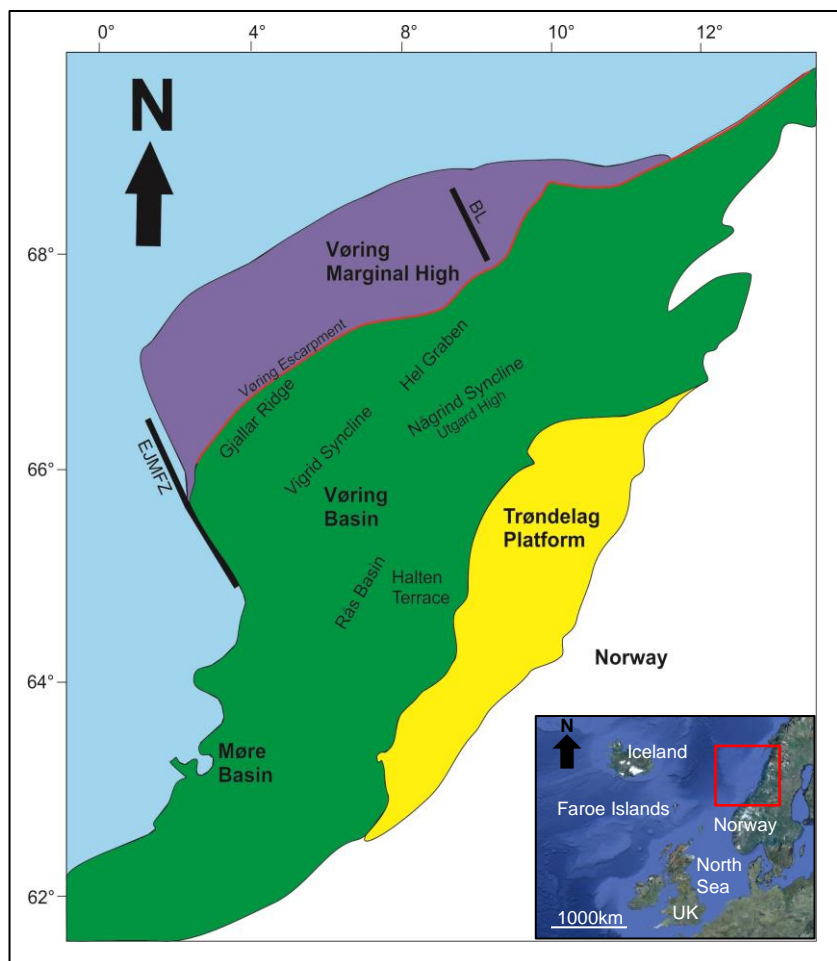


Figure 2.1: Map of offshore Norway, illustrating the location of the Vøring Basin bound to the south by the East Jan Mayen Fracture Zone (EJMFZ) and to the north by the Bivrost Lineament (BL). Also, indicating from NW-SE the location of the Vøring Marginal High, Vøring Escarpment, Gjallar Ridge, Hel Graben, Vigrid and Någrind Synclines, Rås Basin, Halten Terrace, and the Trøndelag Platform (redrawn from Fjeldskaar *et al.*, 2008).

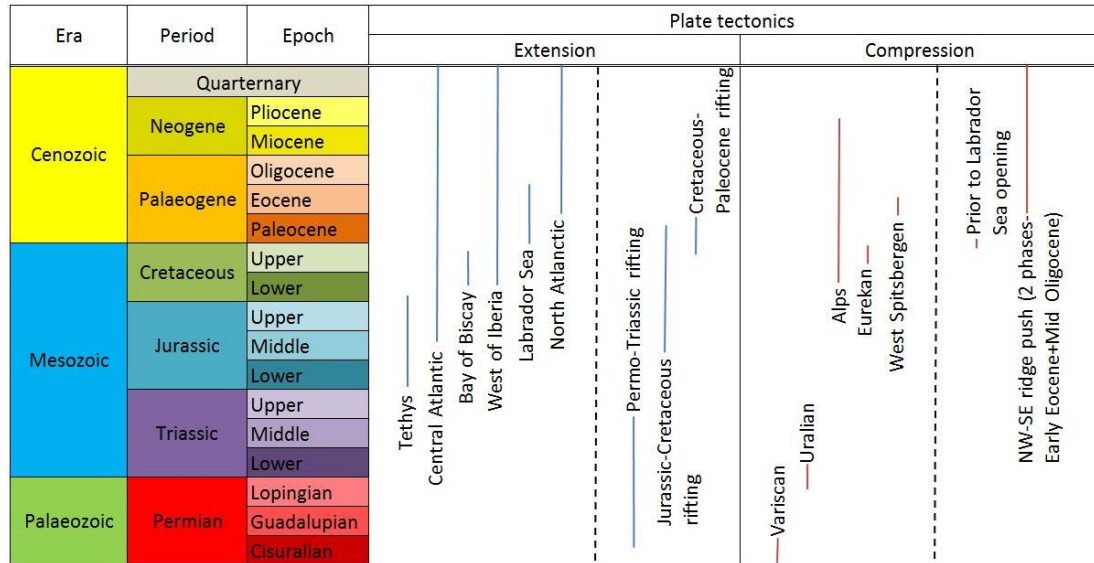


Figure 2.2: Tectonic event summary of regions adjacent to the Atlantic Margin post Carboniferous (modified from Doré *et al.*, 1999).

2.2.1 Permian tectonics to pre-break-up

1. Permo-Triassic rifting

The boundary between the Permian and the Triassic marks the transition from the Palaeozoic to the Mesozoic, a major extinction event and the formation of the supercontinent Pangea. Pangea was unstable, leading to continental break-up primarily along orogenic belts (Doré *et al.*, 1999). This extensional event is predominantly marked by half-grabens infilled by continental sediments of ~8 km thickness, which trend similar to that of the Caledonian mountain chain. The mid-Norwegian Margin is comprised of the Froan, Brønnøysund and Vestfjorden Basins exhibiting NE-trending half-grabens (Doré *et al.*, 1999).

This extensional event is poorly dated owing to overprinting with younger sediments and structures, and is best seen in East Greenland, where it is marked by normal faults in the Middle Permian and fault blocks of the Lower Jurassic. Selected areas along the Atlantic Margin, for example Northern North Sea, North Celtic Sea, also show two phases of extension. In relation to the petroleum industry, the Permo-Triassic rifting event has had little impact on hydrocarbon exploration along the Atlantic Margin due to uplift and erosion of sandstones relating to subsequent extensional events (Doré *et al.*, 1999).

2. Jurassic-Cretaceous rifting

Basins formed during the Permo-Triassic extension were flooded owing to sea level rise, and to sea floor spreading in the Tethys Ocean, and in the proto-Central Atlantic Ocean, there was a shift in the rift axis. Jurassic-Cretaceous rifting is often discussed in the literature as one episode, but Lundin and Doré (1997) argue that this is not the case. They propose that there were two phases of extension marked by a rotation of the minimum principal stress direction. The main phase of rifting occurred in the Mid-Upper Jurassic, forming E-W lineaments vastly different to the subsequent stress field leading to the unzipping of the NE Atlantic. By the Lower Cretaceous, sea floor spreading had ceased in the Tethys Ocean and the minimum principal compressive stress was rotated to a NE-SW orientation. Nonetheless, these two phases of extension are somewhat continuous through time, but not in space. It is during this period of extension that the current basins seen formed, for example the Møre and Vøring Basins (Skogseid *et al.*, 2000). As a result of this extensional phase there was major faulting, reactivation of older faults and rotation of fault blocks, followed by subsidence (Mjelde *et al.*, 2005). With respect to effects on hydrocarbons, the extension in the Lower Cretaceous buried Jurassic sediments, causing fast maturation of Jurassic organic material (source rocks) (Doré *et al.*, 1999). It is to be noted here that the base of the Cretaceous (BCU), in the centre and western parts of the Vøring Basin, has not yet been defined and interpretations vary by several kilometres (Eldholm *et al.*, 2002). This interpretation is important, as it will affect the maturation and migration of the hydrocarbons in the basin.

3. Upper Cretaceous, Maastrichtian compression

The Upper Cretaceous phase of compression saw a shift in the sediment deposition from the Rås Basin, which is situated northwest of the Vigrind Syncline in the Vøring Basin (Fig. 2.3). The compression also caused tightening of the syncline structures, for example the Vigrind and Någrind Synclines, and the formation of inversion structures in the Rås Basin. This episode coincided with a period of extension in the Labrador Sea, which may have set up a short period of compression along the Norwegian Margin before sea floor spreading occurred in the Labrador Sea to the west (Bjørnseth *et al.*, 1997).

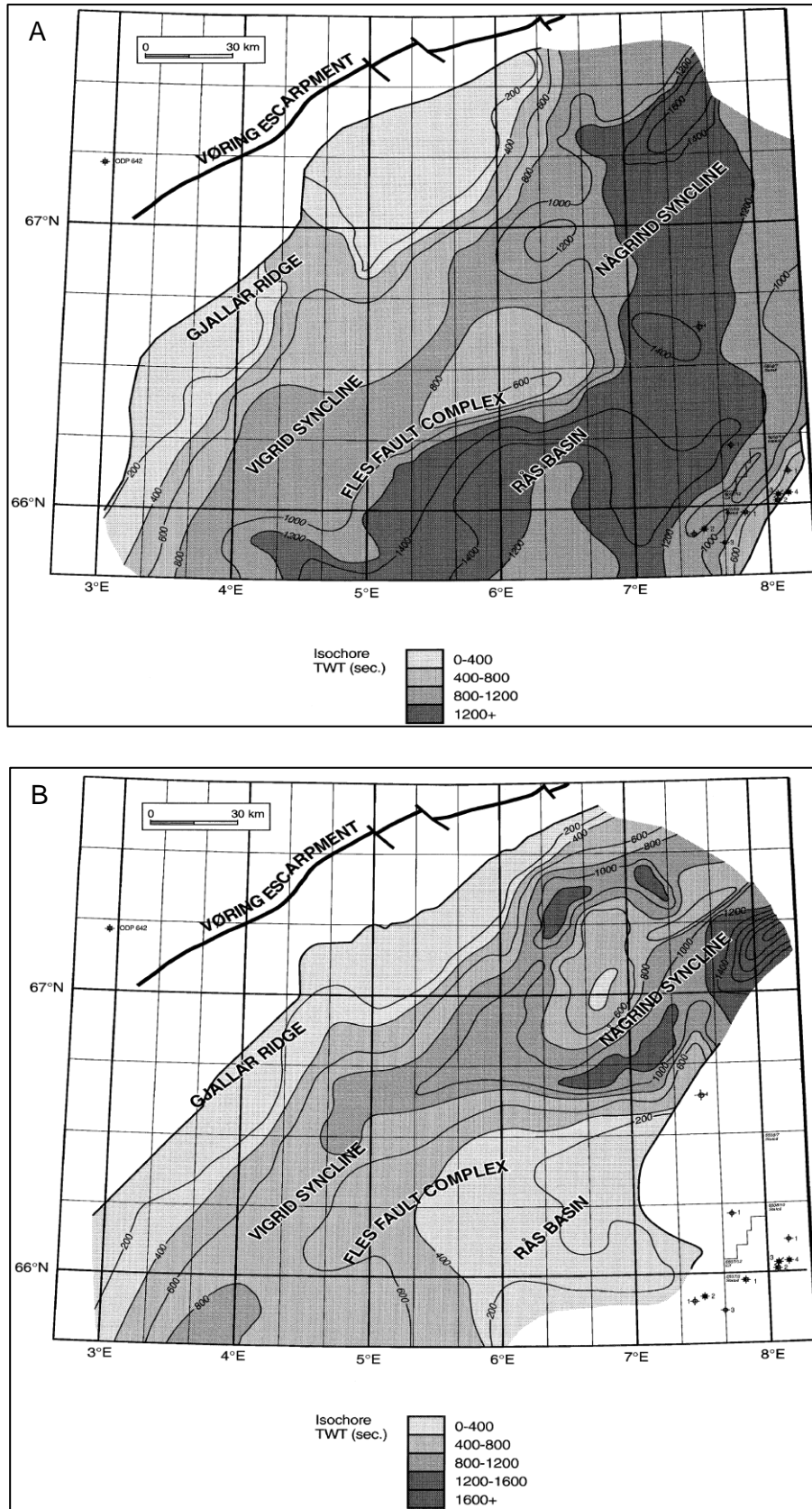


Figure 2.3: Isochron maps illustrating regional depocentres. (A) Early Cenomanian-Early Campanian, Rås Basin is regional depocentre, which shifts to (B) the Vigrid and Någrind Synclines in the Late Campanian-Maastrichtian (Bjørnseth *et al.*, 1997).

4. Cretaceous-Paleocene rifting

By the Early Cretaceous, sea floor spreading had almost ceased in the Tethys Ocean and rifting had ceased in Central Europe (Lundin and Doré, 1997). The Cretaceous-Paleocene rifting between Greenland and Norway lasted for 18-20 Ma (Skogseid *et al.*, 1992), causing shear (strike-slip) movements in the De Geer Zone (Norwegian-Greenland Sea) and the formation of pull-apart basins in the SW Barents Sea, NE Greenland and the Wandel Sea Basin (Faleide *et al.*, 2008). Many authors (e.g. Eldholm *et al.*, 2002; Faleide *et al.*, 2008) consider the Cretaceous-Paleocene extension to be a continuous event through to the opening of the NE Atlantic. However, Lundin and Doré (1997) suggest a phase of extension in the Vøring Basin of Cenomanian age approximately. This extensional phase suggested by Lundin and Doré (1997) is marked in the basin by the Gjallar Ridge, a sequence of extensional complexes, and Nyk High (angular unconformity in the outer parts of the Vøring Basin). This period of extension is associated with uplift in the Norwegian Sea, which caused an influx of sands, of early Upper Cretaceous age, into the flanks of the basin, and a major input of sands, of later Upper Cretaceous age, in the NW of the basin. Lundin and Doré (1997) explain these pulses of sands as a result of tectonic activity and not because of sea level change. This is due to the depocentre being located along the flanks of the basin, and not within the basin as expected during sea level rise.

Along the Utgard High and the Fles Fault Zone in the Vøring Basin, normal faulting and reactivation of a major Cretaceous fault occurred during the Paleocene. Beneath the Gjallar Ridge a domed crustal reflector has been detected and is thought to be associated with magmatic underplating. This underplating is believed to be a result of the migration of the Icelandic Plume towards the thinned ridge axis, which induced pressure leading to melt production and voluminous magmatism and the consequent opening of the Atlantic (Skogseid *et al.*, 1992; Eldholm *et al.*, 2002). The opening of the NE Atlantic was from the southwest and propagated on a northeast trajectory (axis), extending (NW-SE) through the Rockall Trough, the Faroe-Shetland Trough, the centre of the Møre Basin, the east of the Vøring Basin and the SW Barents Sea (Fig. 2.4; Lundin and Doré, 1997). This opening caused a change in the thermal regime in the lithosphere, and also in the rheology of the crust owing to ductile deformation instead of brittle deformation (Eldholm *et al.*, 2002). The igneous

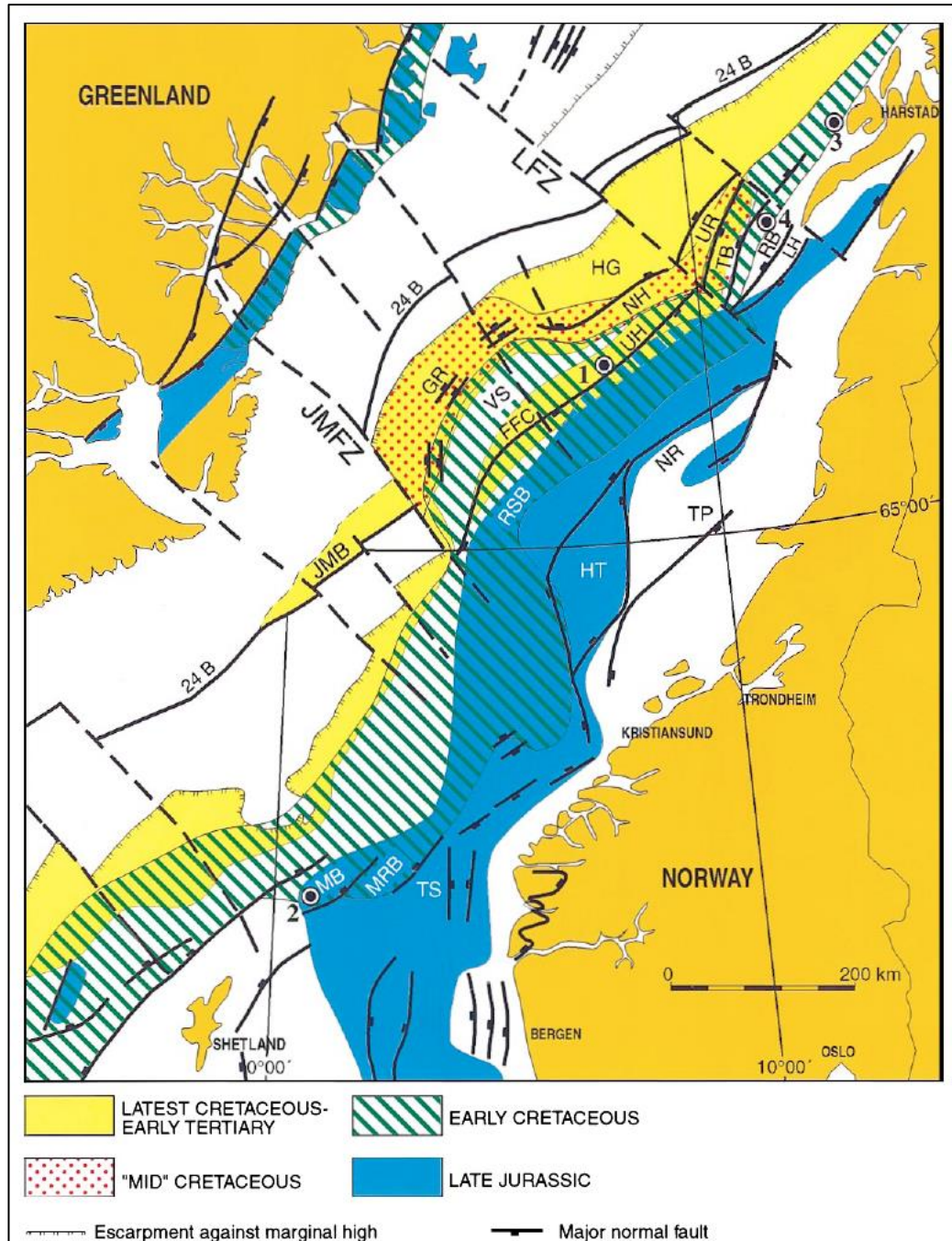


Figure 2.4: Map illustrating tectonic activity from Jurassic to Cretaceous. Abbreviations: FFC - Fles Fault Complex, GR - Gjeljar Ridge, HG - Hel Graben, HT - Halten Terrace, JMB - Jan Mayen Basin, JMFZ - Jan Mayen Fracture Zone, LH - Lofoten Horst, LFZ - Lofoten Fracture Zone, MB - Magnus Basin, MRB - Marulok Basin, NH - Nyk High, NR - Nordland Ridge, RB - Ribban Basin, RSB - Rås Basin, TB - Traena Basin, TP - Trøndelag Platform, TS - Tampen Spur, UH - Utgard High, UR - Utrøst Ridge, VS - Vigrid Syncline (Lundin and Doré, 1997).

activity relating to this rifting event is also seen in the Rockall Trough and the Faeroe-Shetland Basin, both of which yield extrusive magmatic complexes and extensive sill complexes (Thomson and Hutton, 2004; Rateau *et al.*, 2013; Egbeni *et*

al., 2014). The Paleocene also saw a clastic input with an eastern provenance into the Møre, Vøring, and Faroe-Shetland Basins and the Rockall Trough. These coarse sands were distributed according to the pre-existing basin structure and are an important target for petroleum exploration along the Atlantic Margin (Skogseid *et al.*, 1992; Doré *et al.*, 1999; Skogseid *et al.*, 2000).

2.2.2 Tectonism after continental break-up

Post continental break-up, the tectonic regime changed from NW-SE rifting to NW-SE compression because of a ridge push force from the Atlantic Ocean, which is still present today in the majority of NW Europe (Fejerskov and Lindholm, 2000; Fejerskov *et al.*, 2000; Hicks *et al.*, 2000; Lindholm *et al.*, 2000). Compression along the Atlantic Margin gave rise to inversion structures with NE-N trends, namely domes (the main feature) and reverse faulting (Fig. 2.5), for example Cretaceous normal faults were reversely reactivated by the Fles Fault Zone. The development of these structures can be correlated to the closure of the Tethys Ocean (Alpine orogeny) (Doré and Lundin, 1996). These inversion structures, however, only exhibit 1-2% crustal shortening and can be attributed mostly to ridge push as is also suggested by folds in East Greenland (Doré *et al.*, 1999). Ridge push compressive forces also have a clear NW-SE extension (Alpine) and exhibit this stress field at present (Müller *et al.*, 1992; Zoback, 1992; Heidbach *et al.*, 2010). Of interest to the petroleum industry are extensive dome structures that form good trapping mechanisms, whilst NW-SE faults (in alignment with the maximum horizontal stress) act as conduits for the migration of hydrocarbons because the minimum horizontal stress is perpendicular to the fault trend (Doré and Lundin, 1996).

The final phase of extension occurred on the northern part of the Atlantic Margin during the Oligocene-Miocene owing to reorientation of the plate movement from NW-SE to WNW-ESE. This extension phase culminated in the separation of the micro-continent Jan Mayen (Kolbeinsey Ridge) and termination of the Aegir Ridge and is recorded in various ways: faulting in East Greenland, rifting in the west Barents Sea, and the emplacement of sills at Hel Graben in the Vøring Basin (Doré *et al.*, 1999).

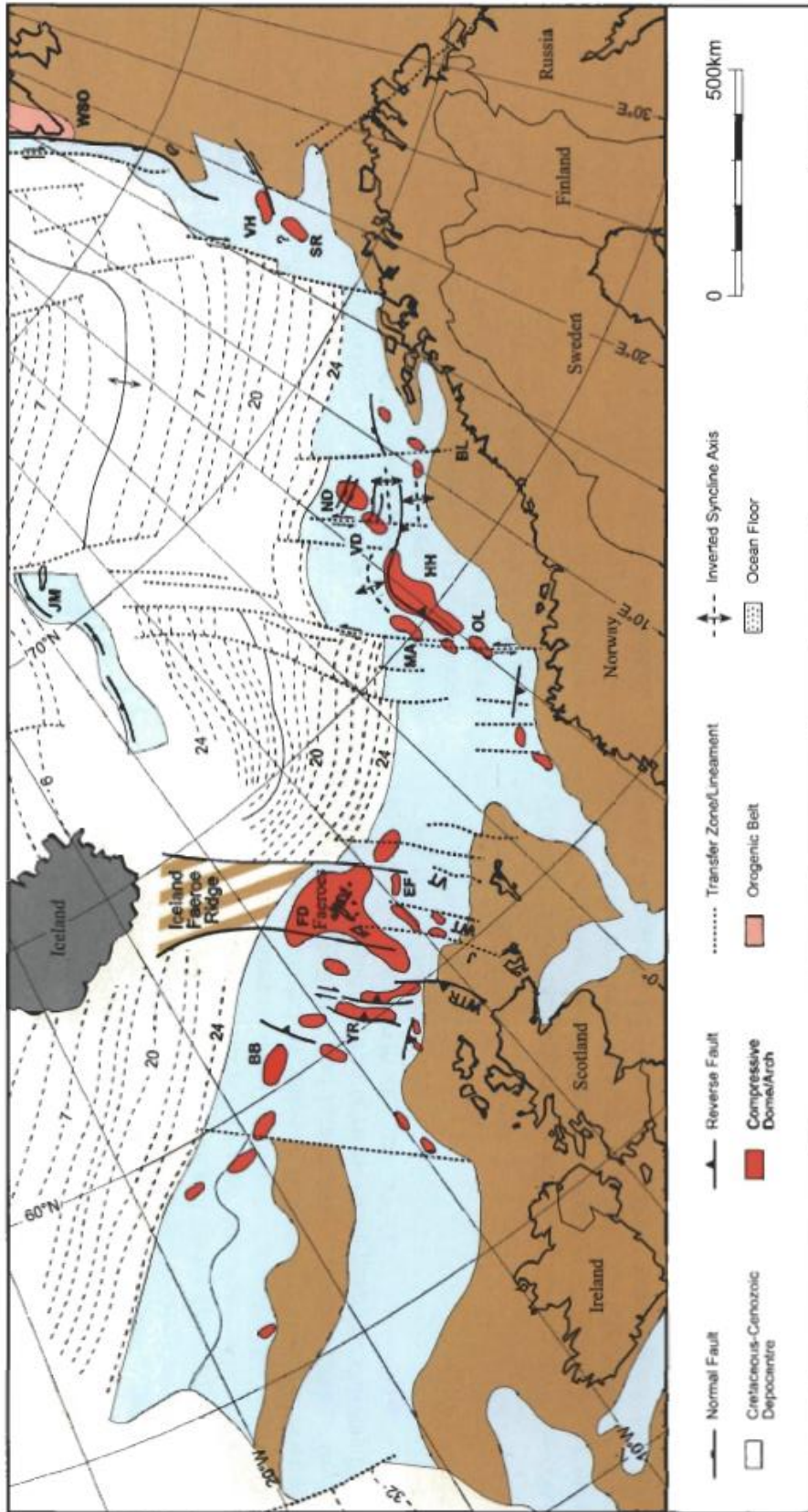


Figure 2.5: Inversion structures, mainly domes and reverse faults along the Atlantic Margin of intra-Cenozoic age. Abbreviations: BB – Brønnøysund Basin, EF – East Faroos High, FD – Faroos Dome, HH – Helland-Hansen Arch, JM – Jan Mayen, MA – Modgunn Arch, ND – Naglfar Dome, OL – Ormen Lange Dome, SR – Senja Ridge, VD – Vema Dome, VH – Veslemøy High, VT – Victory Transfer, WSO – West Spitsbergen Orogen, WT – Westray Transfer, WTR – Wyllie-Thompson Ridge, YR – Ymir Ridge (Doré *et al.*, 1999).

The final tectonic episode affecting the Atlantic Margin was a number of uplift events in the Neogene (Fig. 2.6), which helped shape the Norwegian coastline and sea masses that we see today. The initial uplift event is attributed to thermal uplift along the Atlantic suture and coincides with climate cooling. This cooling saw the nucleation of ice sheets on continents that had been previously uplifted, causing erosion during these glacial periods and uplift in the interglacials owing to isostatic rebound of the lithosphere. Late Cenozoic erosion and uplift had implications on hydrocarbon migration, as it caused tilting of the reservoirs and thus made it possible for hydrocarbons to escape from the trapping mechanisms (Doré *et al.*, 1999).

2.3 Vøring Margin and Basin

The Vøring Margin is a transform margin situated at 66-68°N off the west coast of Norway, and has three provinces, namely: the Trøndelag Platform in the southeast, and the Vøring Basin and the Vøring Marginal High, both in the northwest (Fig. 2.1). Beneath the Vøring Margin (also the Møre and Lofoten-Vesterålen Margins) there is a distinctive lower crustal body (LCB), known due to its high P-wave velocity of approximately 7.3-7.6 km/s (Mjelde *et al.*, 2005). The LCB is well developed and thought to have formed as a result of magmatic underplating (Mjelde *et al.*, 2005). However, alternative hypotheses have been put forward by Gernigon *et al.* (2004) and will be discussed later with respect to the T-Reflection.

The Trøndelag Platform is a ~160 km wide platform of Permo-Triassic age, located between the Vøring Basin and the Norwegian mainland. It contains Late Palaeozoic and Jurassic sediments, and has been relatively stable since the Jurassic. The Vøring Basin is a sedimentary basin formed during the Late Jurassic-Early Cretaceous owing to extension and thinning of the crust, and underwent extensive volcanism in relation to the rifting event. The basin is separated from the Vøring Marginal High by the Vøring Escarpment, which forms the Vøring Plateau. The Vøring Marginal High formed in the Early Cenozoic, Paleocene-Eocene, as a result of the continental break-up and extrusion of flood basalts. East of the Vøring Escarpment, volcanism led to a 10-40 km wide sill and lava flow complex (Skogseid *et al.*, 1992; van Wijk and Cloetingh, 2002).

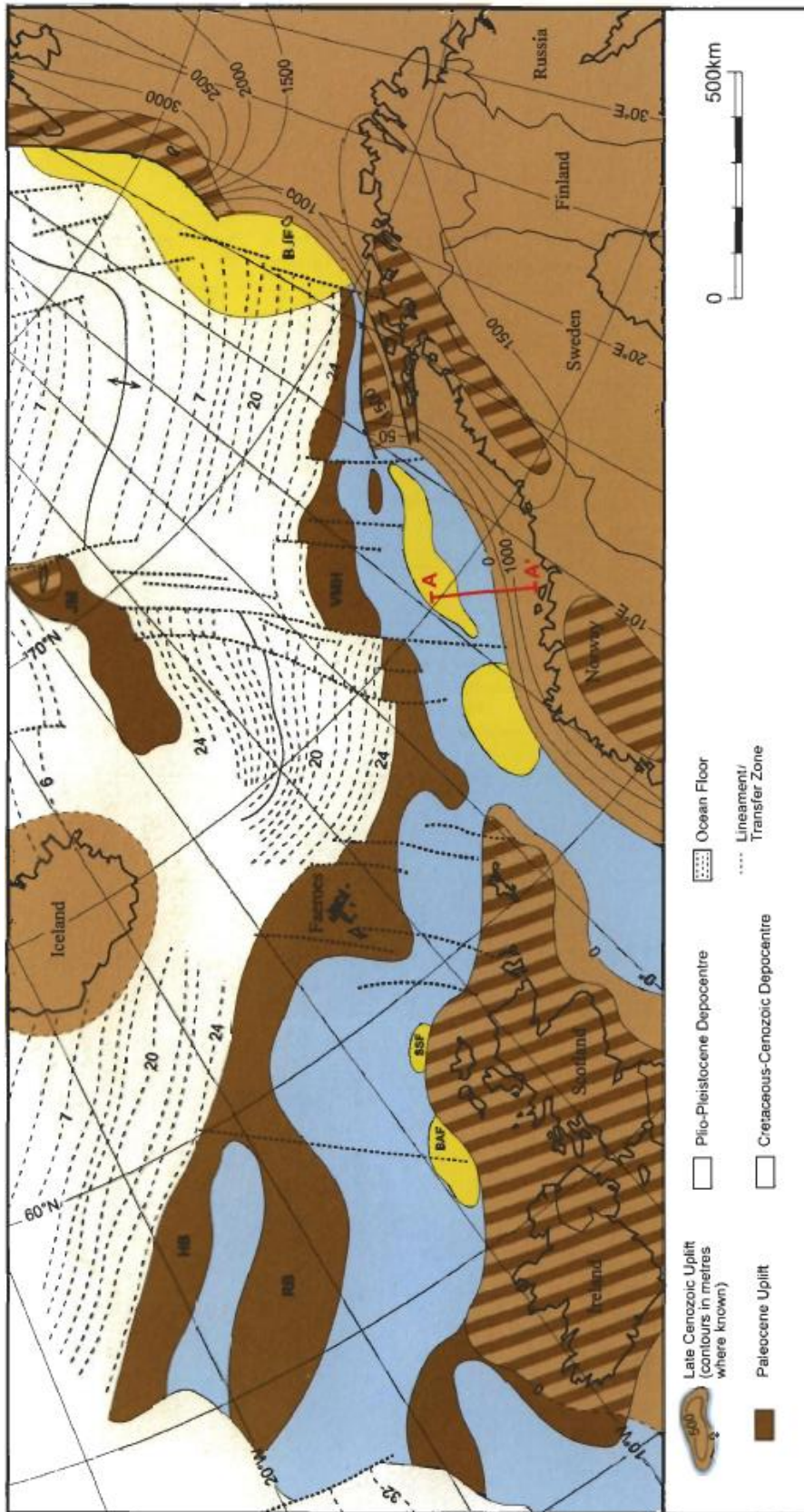


Figure 2.6: Map illustrating areas of Neogene uplift (light brown) along the Atlantic Margin. Abbreviations: BAF – Barra Fan, BJF – Bjørnøya Fan, HB – Hammerfest Basin, JM – Jan Mayen, RB – Røst Basin, SSF – Sula Sgeir Fan, VMH – Vøring Marginal High (Doré *et al.*, 1999).

The Vøring Margin was tectonically active from the Carboniferous to the Late Pliocene, with rifting events occurring approximately every 20-60 Ma, specifically in the Permo-Trias (290-235 Ma), the Mid Jurassic-Early Cretaceous (170-95 Ma) and the Late Cretaceous-Early Tertiary (75-57 Ma) (Fig. 2.7; Brekke, 2000; van Wijk and Cloetingh, 2002). The direction of extension was E-W to SE-NW, with each rift event relating to a shift in locus. These rifting events occurred where the lithosphere was weakest and led to the formation of sedimentary basins along the passive margin, located between the continent-ocean boundary and the mainland of Norway.

It is thought that the locus situated along the mid-Norwegian passive continental margin shifted to the west, from the Trøndelag Platform to the Vøring Margin (Fig. 2.8). The shift in locus could result in many extension phases. Therefore, the weak lithosphere of the first rifting event needed time to sufficiently cool before the next stretching event. Therefore, there must have been a long interval of tectonic quiescence between consequent rifting occurrences, thus, a low rate of lithospheric extension. When the lithosphere extended at higher rates, continental break-up occurred, that is, the unzipping of the North Atlantic Ocean. At this time crustal extension was initiated and rifting occurred because of the proto-Icelandic Plume causing uplift, which induced extension of the lithosphere that had already undergone tensional stresses. When the plume met the base of the lithosphere, melting occurred, which caused the lithosphere to be weakened along the NE Atlantic rift driving continental break-up (Skogseid *et al.*, 1992; Roberts *et al.*, 1997; van Wijk and Cloetingh, 2002; Gernigon *et al.*, 2003). When volcanism was terminated at the end of the Eocene, the Vøring Margin subsided due to thermal contraction and loading of sediment. The final rifting event along with the deterioration of climate in the Cenozoic determined the evolution of the Vøring Margin, especially towards the north (Hjelstuen *et al.*, 1999). During this final rifting event, deformation transitioned from brittle deformation at early rifting (~81-65 Ma) to ductile deformation and the late rifting phase (~65-55 Ma). This difference in deformation is possibly due to rift rheology because of the Iceland Plume (Ren *et al.*, 2003).

The rifting event (Fig. 2.8) that formed the Vøring Basin occurred as a result of continental break-up ~57.5 Ma, approximately 17.5 Ma after tectonic activity was initiated (Skogseid, 1994). Biostratigraphic data show that there was a change in

Era	Period	Epoch	Evolution of Vøring Basin/Margin	
Cenozoic	Quaternary		Major uplift	
	Neogene	Pliocene	NW-SE compression (minor rifting and volcanism)	
		Miocene		
	Palaeogene	Oligocene	Opening of NE Atlantic-Volcanism, rifting. Uplift and extensional faulting	
		Eocene		
paleocene				
Mesozoic	Cretaceous	Upper	Volcanism	
		Lower	Rifting, uplift, volcanism	
	Jurassic	Upper	Rifting at Halten Terrace	
		Middle		
	Triassic	Lower	Rifting at Halten Terrace	
		Upper		
		Middle		
	Palaeozoic	Permian	Lower	Rifting to form Brønnøysund, Froan and Vestfjorden Basins
			Lopingian	
		Carboniferous	Guadalupian	
Saurian				

Figure 2.7: Vøring Basin evolution indicating periods of compression, rifting, volcanism, uplift and subsidence post Carboniferous.

eustatic sea level in the Lower Cretaceous, from shallow marine to deep marine conditions. This led to an increase in accommodation for sediment infill (Faleide *et al.*, 2008). The first extensional event (within plate continental rifting) in the Vøring Basin is represented by a major onlap surface at Gjallar Ridge, possibly because of extensional faulting in the Early Cenomanian displayed by ramp and flat geometries to the SE of the fault. This led to the hanging wall syncline hypothesis, where the hanging wall is above the flat (Gjallar Ridge) and the syncline is above the ramp (Vigrud Syncline) (Bjørnseth *et al.*, 1997). A change in stress patterns in the basin was then seen in the Late Mesozoic, which can be summarised as follows: (1) Jurassic-Early Cretaceous was a period of extension followed by post-rift subsidence related to thermal subsidence in the Vøring Basin and the surrounding region. (2) Paleocene-Eocene saw the unzipping of the North Atlantic as the crust was weakened extensively in the Palaeozoic and Mesozoic, which caused the onset of volcanic activity forming the structural highs at the basin margins.

Ren *et al.* (2003) suggest that the onset of the second rifting episode was 81 Ma, with the main phase in the Campanian. This caused updoming of Cretaceous sediments owing to low-angled detachment structures. Within the basin there was Cretaceous thermal subsidence and post Cenomanian tectonically driven subsidence, which caused deformation, including normal faulting and folding. This extensional event (movement along the plate boundary) is seen by faulting in the Late Campanian with significant listric fault growth in Nyk High and the Fles Fault Complex. After this extensional event, a compressional event of Late Maastrichtian age followed. The third extensional event occurred soon after in the Late Paleocene, where Roberts *et al.* (1997) propose that the extension of the lower crust was greater than the extension of the upper crust, causing faulting approximately 20 Ma before continental break-up (Skogseid *et al.*, 2000). The onset of the continental break-up was in the Early Eocene between Greenland and Norway culminating in 3-6 Ma of igneous activity and the initiation of sea floor spreading-lithospheric thinning and subsidence. The lavas along the Vøring Margin form seaward dipping reflectors (SDR), characteristic of volcanic margins (Skogseid *et al.*, 1992; Skogseid, 1994). It was during this event that sills intruded into the Cretaceous organic rich sediments generating and releasing greenhouse gases (e.g. methane) into the oceans and atmosphere via hydrothermal vents (Stuevold *et al.*, 1992; Svensen *et al.*, 2004;

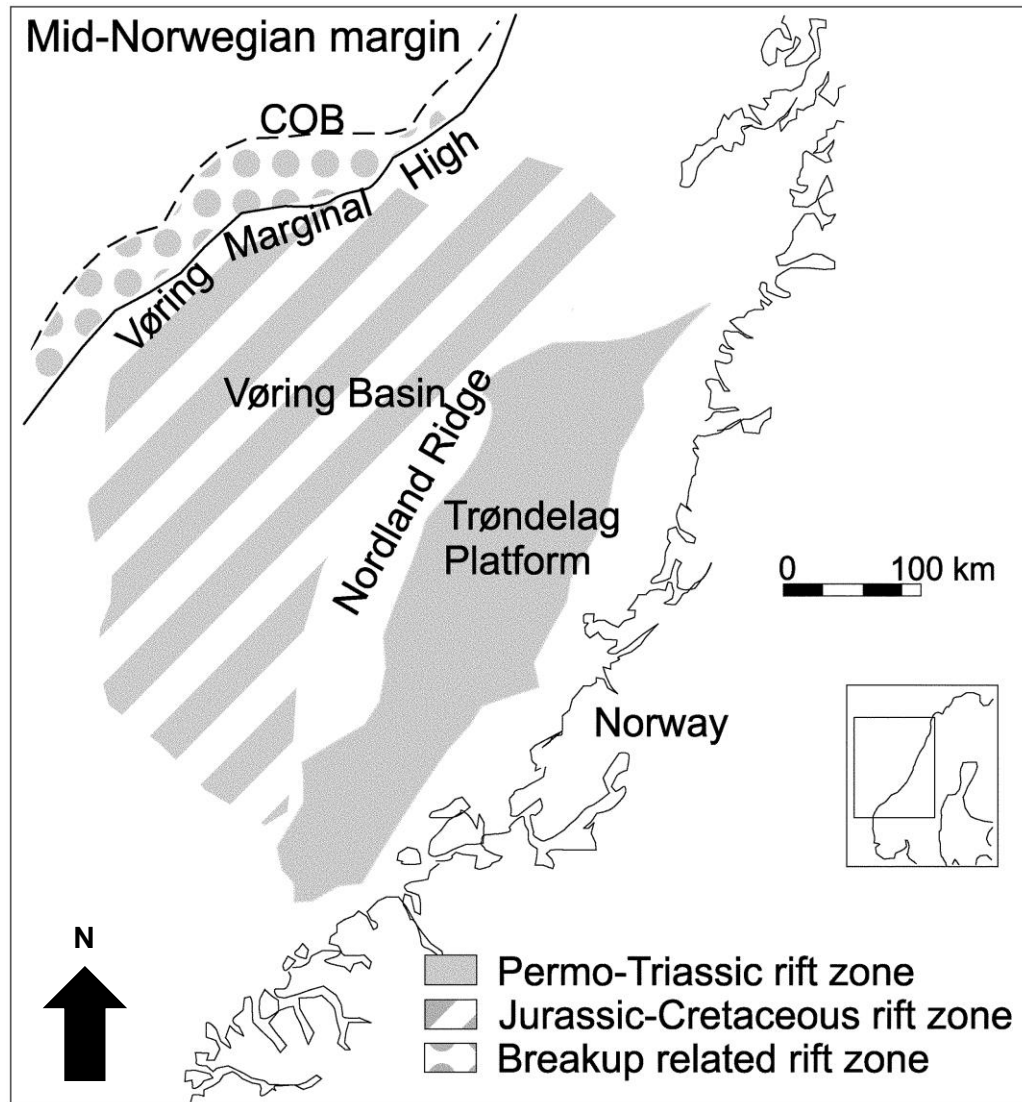


Figure 2.8: Sketch map of the mid-Norwegian Margin illustrating three rift zones (van Wijk and Cloetingh, 2002).

Planke *et al.*, 2005). It has been noted by Mjelde *et al.* (2005) that the Vøring Plateau has a thicker continental crust than the basin itself. They suggest that crustal thinning of the Cretaceous-Paleocene was not a result of pure shear, but of delamination, implying that the west of the Gjallar Ridge and the Nyk High was a lower plate boundary in the Upper Cretaceous/Paleocene and transferred into an upper plate boundary.

The Vøring Basin consists of sub-basins with grabens and structural highs formed during subsidence and segmentation prior to the continental rifting event. The basin is terminated by the Vøring Escarpment to the west and the Vøring Marginal High to

the east (Hjelstuen *et al.*, 1999; Fjeldskaar *et al.*, 2008; Faleide *et al.*, 2008). Mesozoic sediments that have been affected by faulting in the Paleocene-Eocene were intruded by sills and dykes landward of the continent-ocean boundary over an area of 100-200 km² (Fig. 2.9). These igneous intrusions had a large impact on the thermal regime of the sediments within the basin, which in turn had an effect on the hydrocarbon maturation of the source rocks. Features, in this basin, for example sedimentary, igneous and structural features are also seen on other NE Atlantic volcanic margins. Sill swarms and magmatic underplating under the western part of the basin caused thermal uplift as well as heating of the central and western part of the Vøring Basin, along with maximum subsidence landward of the continent-ocean boundary (Skogseid, 1994; Ren *et al.*, 2003; Fjeldskaar *et al.*, 2008).

The basin was active during the Tertiary, where there were phases of strike-slip compression that coincided with the Alpine orogeny (Brekke, 2000). Following continental break-up, the Vøring Margin developed into a passive rifted margin owing to subsidence on a regional scale and moderate sedimentation rates. The Vøring Basin then saw two final episodes of compression in the Early Eocene and Middle Oligocene (Bjørnseth *et al.*, 1997; Brekke, 2000). These phases are well documented within the basin by dome structures (anticlines), reverse faults and other inversion structures.

2.3.1 Sediment deposition in the Vøring Basin

The sediment in the Vøring Basin records the geological history along its passive margin pre-, during and post rifting. The structural relief of the Vøring Basin was covered during the Mid-Cretaceous, and fine grained clastic sediments of Upper Cretaceous age were deposited along with coarser sediments from East Greenland (Faleide *et al.*, 2008). Many sills in the Vøring Basin intruded into thick sediments of Upper Cretaceous age, indicating that the sills are of a Cenozoic age relating to the Paleocene-Eocene magmatic activity. The thick sediments are organic rich shales and mudstones with low permeability (Svensen *et al.*, 2004; Fjeldskaar *et al.*, 2008). As a result of the low permeability of the shales, cooling would be primarily through conduction. However, these low permeabilities do not prevent heat transport through

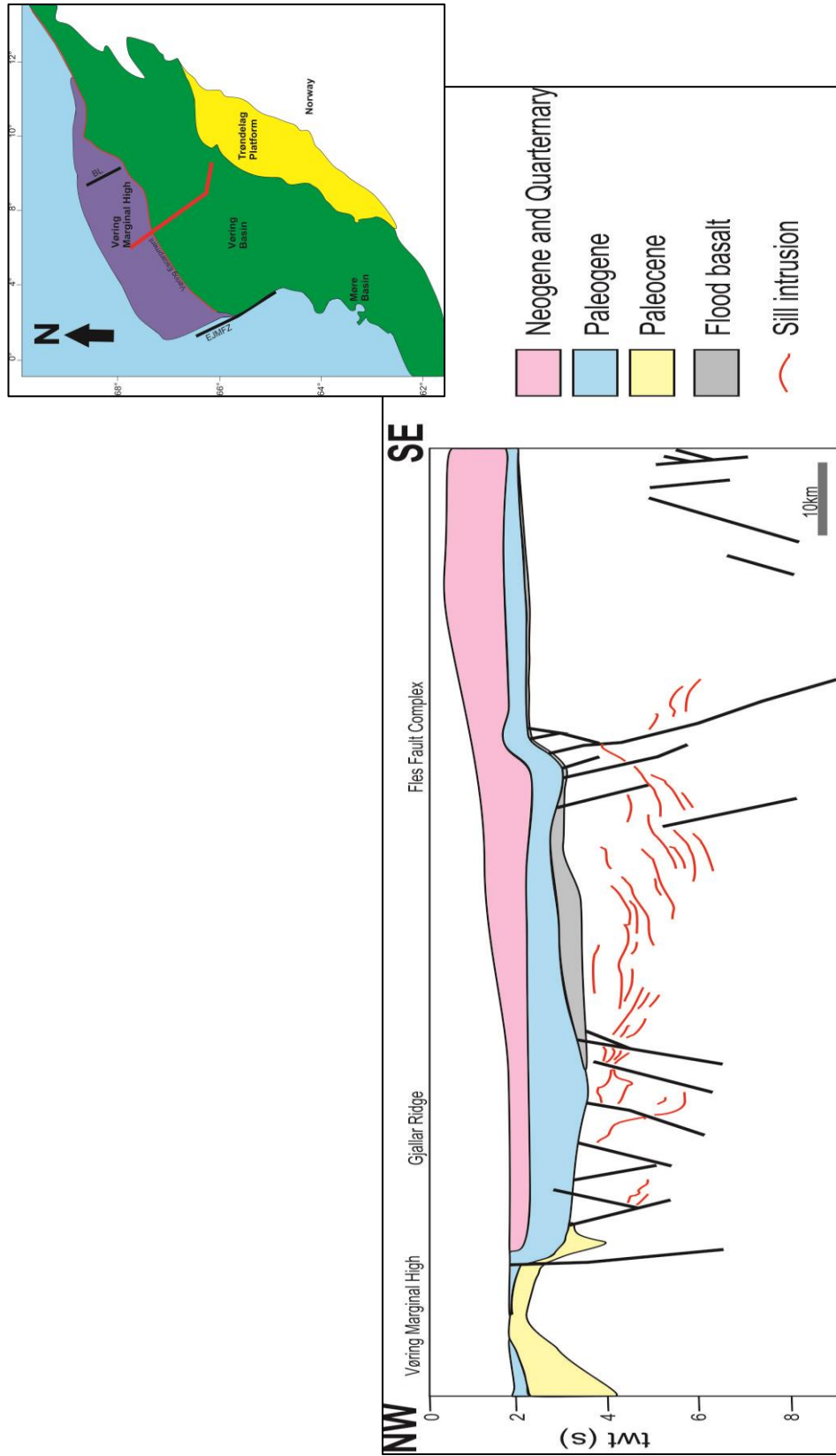


Figure 2.9: Seismic interpretation of the Vøring Margin (red profile line on inset map), illustrating the various levels of sill intrusions into sedimentary strata (redrawn from Eldholm *et al.*, 2002).

convection, because on heating, shales become dehydrated, leading to the formation of hydrofractures and fluid flow. Thus, heat transport can be by conduction and/or convection (Fjeldskaar *et al.*, 2008). Sediments in the western part of the basin imply that there was differential subsidence across the Vøring Basin, however the volcanic complex is still elevated. Along the continental shelf there is a distinctive unconformity marking the transition from moderate clastic sediment input, to rapid glacial sediment input from the glaciation of the Northern Hemisphere during the Pliocene (2.6 Ma). This extends to the eastern margins of the basin, building the continental shelf outwards to its current position (Skogseid, 1994; Eldholm *et al.*, 2002; Ren *et al.*, 2003).

2.4 Sills in the Vøring Basin and their importance

The sills in the Vøring Basin intruded into the lower crust. They have an average total thickness of ~100-300 m, and diameters of a few tens of kilometres, with sill complexes extending over at least 80,000 km² to the adjacent Møre Basin (Svensen *et al.*, 2004; Planke *et al.*, 2005). Sampling of the sills in the Utgard High suggests a micro-gabbroic mafic composition with little alteration (Ren *et al.*, 2003). Field data and seismic data show several levels of magmatic sill intrusions (Fig. 2.9). Their geometries vary with depth, with saucer-shaped sills being common at shallow-intermediate depths and layer-parallel intrusions being common at deeper depths within the basin. The sill geometries may be much influenced by the heterogeneities and structures present in the basin, for example faults, deformed strata and layering. The formation of a saucer-shaped sill is described by Malthe-Sørenssen *et al.* (2004), who conclude that when the host rock behaves as an elastic material, it has the ability to be uplifted as the sill transgresses when a critical size (lateral dimensions are at least two or three times greater than the thickness of the overburden) is reached. Deep seated sills are generally larger than shallow seated sills before they begin to transgress, as the critical size depends on depth as well as host rock characteristics. This is why deeper sills are most commonly planar. Also, it is important to note that the layer-parallel sills are found in unconsolidated sedimentary units, that is, they had no elasticity and would be emplaced similarly to a subsequent lava flow. Sill complexes, however, are intruded at progressively deeper depths towards the east in

the basin. In the centre of the basin they exhibit a stepping geometry in a SE direction. However, the sills along the Vøring Margin exhibit the same geometry in a NE direction (Planke *et al.*, 2005). It is suggested by seismic and field data that the major sill complexes were emplaced within a short period of time, with individual sills being emplaced within tens of years. Other studies, for example the Karoo Basin in South Africa, also show that there are many levels of volcanic intrusions within a sedimentary basin (e.g. Galerne *et al.*, 2008; Arnes *et al.*, 2011). However, sill complexes are not present in structural highs and in the western part of the Vøring Basin.

Planke *et al.* (2005) give a good account of the sill facies in the Vøring Basin. They identify several facies that have been categorised into saucer-shaped sills, layer-parallel sills, planar transgressive sills and fault block sills (Fig. 2.10). Within the two main categories of saucer-shaped sills and layer-parallel sills other characteristics are defined such as the size and smoothness of the sill, whether it is continuous and its depth below the palaeosurface.

Volcanic intrusions have a large impact on the geodynamics and structure of continental margins and their sedimentary basins. Hence, understanding the structural evolution of the Vøring Basin is the key to forecasting the presence of hydrocarbons within the basin and petroleum exploration at these sites. Sills are most likely emplaced along discontinuities, that is, weak contacts and fractures, where multiple discontinuities form a stack of thin sills. This is known as a sill complex, which generates a different cooling pattern than that of an individual sill. The emplacement of these sill complexes, along with dykes and other intrusive bodies would have had an effect on the thermal evolution of the basin and, hence, on its hydrocarbon maturation (Fjeldskaar *et al.*, 2008). This is because magmatic intrusions cause uplift and deformation, heating of the host rock and metamorphism, potentially accelerating hydrocarbon maturation in the source rock, and the baking of fluids in the host rock, which lead to the formation of hydrothermal vent systems. These are all short term effects. Long term effects include localised flow, compartmentalisation and metamorphism of the sediments, for example dolomitisation and compaction (Planke *et al.*, 2005). Hydrothermal vent systems form when a sill is emplaced within sedimentary rocks that have a high porosity and are mostly unconsolidated, causing fluidisation of sediment near the sill contacts and

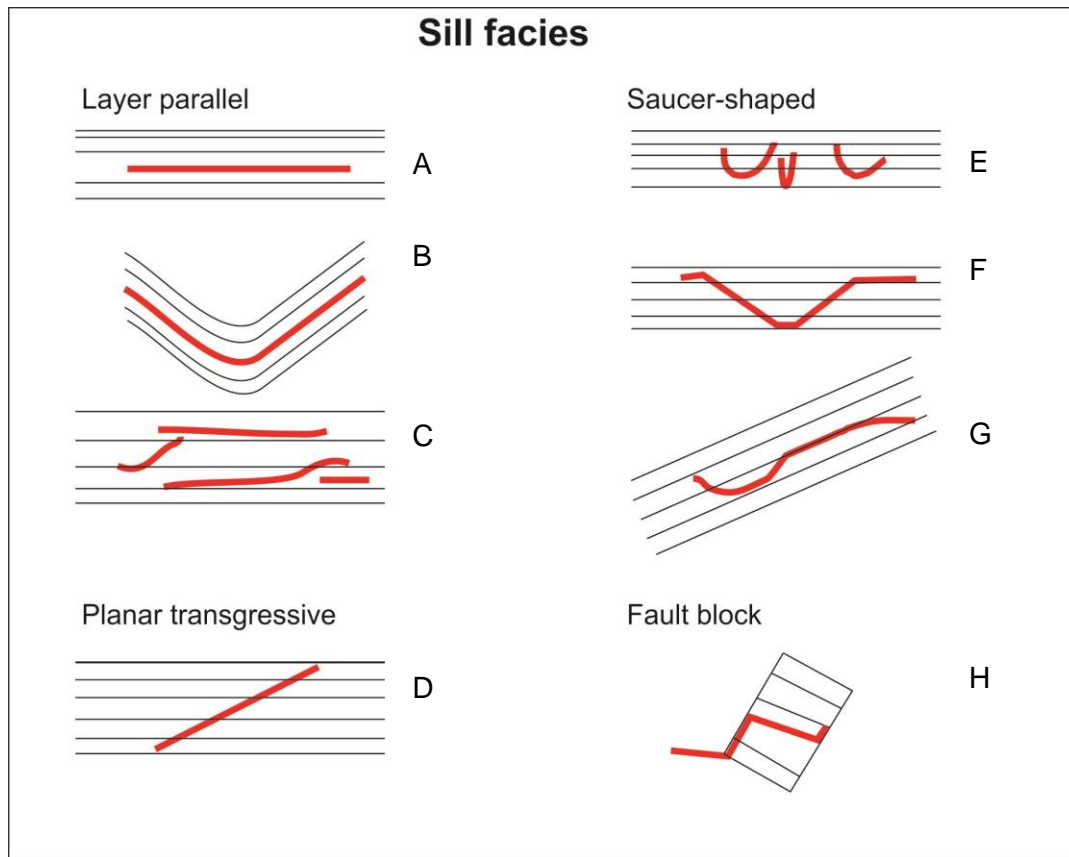


Figure 2.10: Sill facies modified from Planke *et al.* (2005). (A) Smooth layer-parallel, (B) basin parallel, (C) layer-parallel rough, (D) planar transgressive (E) saucer-shaped shallow intrusions, (F) saucer-shaped rough, (G) climbing saucer-shaped, (H) fault block. Rough describes an irregular seismic character, smooth describes a regular seismic character.

purging of porewaters towards the Earth's surface. The fluid pressure needed is to be larger than the hydrostatic pressure for a vent to form, and the pressure build up needs to be quicker than the pressure release. This may be because of an increase in pressure around individual sills owing to boiling of pore fluids in the host rock above the critical depth (i.e. shallow), and metamorphism, which generates gas. If the overburden is fractured, gas begins to rise towards the surface, and as the gas expands because of decompression there is fast fracturing of the overburden, which subsequently leads to explosive eruptions at the surface. In the Vøring Basin >50% of hydrothermal vents are formed above the sill tips or lateral ends (refer to Fig. 7 in Planke *et al.* (2005)). Therefore, hydrothermal vent formation is closely related to sill emplacement (Jamtveit *et al.*, 2004; Planke *et al.*, 2005). The hydrothermal vents in the basin are recognised on seismic due to the presence of vertical structures

originating at the sill tips and ending at the palaeosurface as eye-like structures (Fig. 2.11) (Planke *et al.*, 2003; Svensen *et al.*, 2003; Svensen *et al.*, 2004; Planke *et al.*, 2005). Similar characteristics are also recognised in the Karoo Basin (Jamtveit *et al.*, 2004). These hydrothermal vent characteristics have great implications for fluid migration in the basin.

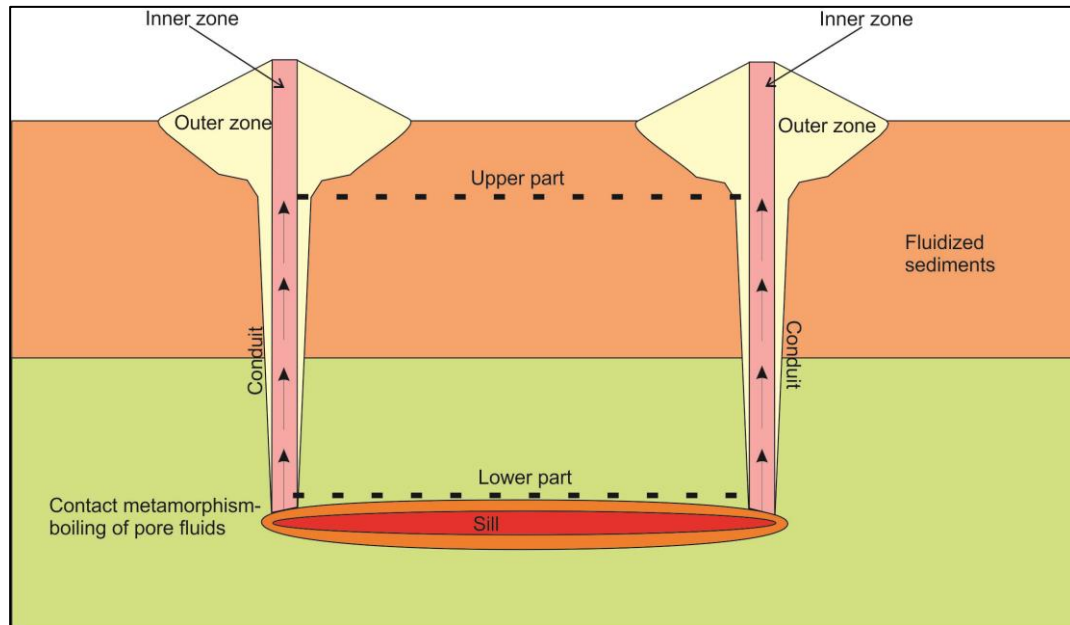


Figure 2.11: Schematic illustration of a hydrothermal vent complex consisting of an upper part (eye-like structure), a lower part and a conduit connecting the upper part with the sill (redrawn from Planke *et al.*, 2005).

Biostratigraphic dating of the hydrothermal vent complex shows that it formed 55-55.8 Ma due to the presence of *Apectodinium augustum* palynomorphs (Dinoflagellate) found 25 m above the eye-like structure of the hydrothermal centres. Some *in situ* mature *Apectodinium augustum* are thought to be related to the hydrothermal vent complex formation as their microfossils suggest local heating. A Paleocene horizon terminates the majority of hydrothermal vent complexes in the Vøring Basin, but has overlying extrusive 'Inner Flows' (subaqueous lava that flowed landward), as seen on seismic. This suggests that intrusive volcanism, that is, emplacement of sills and dykes occurred mostly before the extrusive volcanism, that is, flood basalts (Svensen *et al.*, 2004).

2.4.1 Paleocene-Eocene Thermal Maximum (PETM)

Svensen *et al.* (2004) put forward a hypothesis that the sill intrusions in the Vøring Basin induced contact metamorphism by baking the organic rich shales, which released carbon dioxide into the atmosphere triggering the Paleocene-Eocene thermal maximum (PETM). The PETM was a period when there was rapid global warming owing to a release of greenhouse gases (e.g. carbon dioxide and methane). The release of gases was via hydrothermal vent complexes from the contact aureoles located around the mafic sills (Svensen *et al.*, 2004; Planke *et al.*, 2005). This hypothesis is supported by the works of Planke *et al.* (2005), who recognised hydrothermal vent complexes on 2D seismic lines, and also the work of Storey *et al.* (2007), who dated the lavas and tuff layers in the area of the North Atlantic province. However, there were no radiometric dates for the sills in the Vøring Margin until Svensen *et al.* (2010), who published findings on zircons. They dated zircons found in the sills within the drill core from the Utgard structural high well 6607/5-2 using the $^{206}\text{Pb}/^{208}\text{U}$ dating system. The Utgard well 6607/5-2 (Fig. 2.12) cuts through three sills of a doleritic (micro-gabbroic) composition. The upper sill has a thickness of 2 m and is not seen on seismic lines as it is too thin. The middle sill has a thickness of 91 m and an age of 55.6 ± 0.3 Ma dated from 6 zircons. The lower sill is >50 m (the well terminates 50 m through the sill) with an age of 56.3 ± 0.4 Ma dated from 1 zircon. These dates for the middle and lower sill overlap within error margins and are in accordance with radiometric dates for igneous rocks in the North Atlantic Volcanic Province (Storey *et al.*, 2007). All of these sills were emplaced within Upper Cretaceous shales (Berndt *et al.*, 2000) and the middle and lower sills can be seen on seismic lines, especially the middle sill, which can be traced laterally for 100 km. From the mapping of the middle sill in the Utgard well, we know it is part of the sill complex in the Vøring Margin (Planke *et al.*, 2005) and from its dating we can determine that the sill complex was emplaced at the same time as the Utgard sills (Svensen *et al.*, 2010).

The PETM is dated at ~ 55.53 or ~ 55.93 Ma lasting approximately for 170 ka (Svensen *et al.*, 2010). The ages for this event overlap with the dating of the sills present in the Utgard borehole, therefore it can be said that there is a relationship between sill emplacement, methane gas generation and the PETM (Svensen *et al.*, 2010).

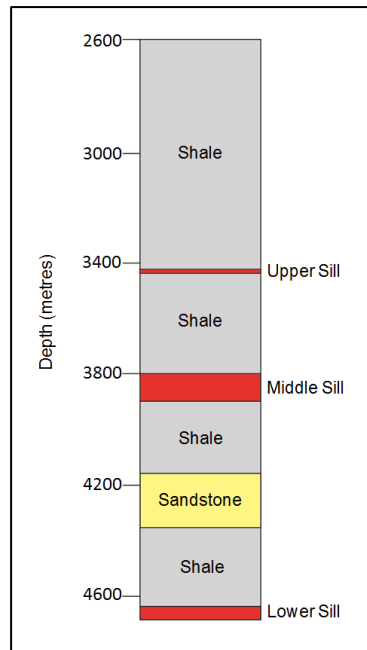


Figure 2.12: Utgard well 6607/5-2 illustrating the sill intrusions and lithological units. Areas above and below the middle and lower sill are zones of high temperature minerals metamorphosed from shale minerals. Methane is also given off in response to sill emplacement into the sedimentary basin (modified from Svensen *et al.*, 2010).

2.5 Lower crustal body (LCB) and T-Reflection

Passive margins are classified into either volcanic or non-volcanic. The Vøring Margin is a volcanic margin located in the North Atlantic Volcanic Province and is characterised (as are other volcanic margins) by (1) volcanic intrusions into sedimentary basins, (2) vent complexes above the tips of sills, (3) large volumes of magmatic material during rifting (SDRs), (4) little subsidence during and post rifting, and (5) a horizon with high P-wave velocities greater than 7.1 km/s in the lower crust (LCB) (Eldholm *et al.*, 2002; Gernigon *et al.*, 2004; Mjelde *et al.*, 2005; Gernigon *et al.*, 2006). These diagnostic features are thought to be because of enhanced lithospheric thinning and magmatic emplacement due to the Iceland Plume before the opening of the NE Atlantic (Skogseid *et al.*, 2000). However, this theory has been questioned by Gernigon *et al.* (2004) who reported the presence of a dome-shaped feature under the north Gjallar Ridge, which extends to the outer edge of the basin and the Fles Fault Complex (Fig. 2.13). This dome-shaped feature is referred to as the T-Reflection, a regional name. This T-Reflection is at the base of the

Tertiary horizon with dimensions of: width 20 km, top of the reflector at ~ 7.5 s (approximately 12.5 ± 2 km) and an overall round geometry that is well constrained at the north Gjallar Ridge. Also, gravity studies have revealed it to have a positive Bouguer anomaly, but there is no significant anomaly documented to be present in magnetic studies. This is due to a low magnetic reflectance, which could be explained by insufficient mafic minerals in the dome and/or the dome's high density. Seismic studies show that the T-Reflection coincides with the continental margin of the LCB forming a dome structure at mid-crust level, which is situated near lava flows that were emplaced during the break-up of the NE Atlantic (Gernigon *et al.*, 2004; Gernigon *et al.*, 2006).

There are three possible models proposed by Gernigon *et al.* (2004) to explain the presence of the dome (1) mafic/ultramafic model, (2) serpentinisation model and (3) retrograde, high-grade rocks model. The mafic/ultramafic model suggests a lower crustal body of picritic melts that underplated the lower crust during continental break-up. However, due to the high velocity of the LCB this could be a complex of sills. However, seismic, gravity and magnetic studies document that the T-Reflection marks the horizon between the overburden and underlying high density and velocity unit. Therefore, the dome does not represent sill intrusions. The serpentinisation model suggests that the dome exhibits high velocity and no magnetic anomalies. This may be explained by a serpentinised mantle that has high P-wave velocities in the range of 5-7.5 km/s, and high S-wave and P-wave ratios greater than 1.8, which is similar to the T-Reflection. However, a serpentinised mantle would suggest that magma emplacement was prior to the dome. These suite of rocks are related to extension in overly saturated hydrated environments, for example sea water seeping down fractures hydrating olivine into serpentine (Mjelde *et al.*, 2005). This is hard to explain as the top of the dome is 8-9 km beneath the north Gjallar Ridge, where sea water migration is not favoured because of large hydrostatic pressures (Gernigon *et al.*, 2004). Mjelde *et al.* (2005) also state that velocities for the Vøring Plateau do not favour the serpentinised mantle model. They interpret the lower crust to be magmatic underplating, which caused continental break-up. Finally, the retrograde, high-grade rocks model suggests that the T-Reflection could be explained by granulitic or eclogitic facies, which have been reported to exhibit high densities and high P-wave velocities. Studies presented in Gernigon *et al.* (2004) on the Møre Basin and North

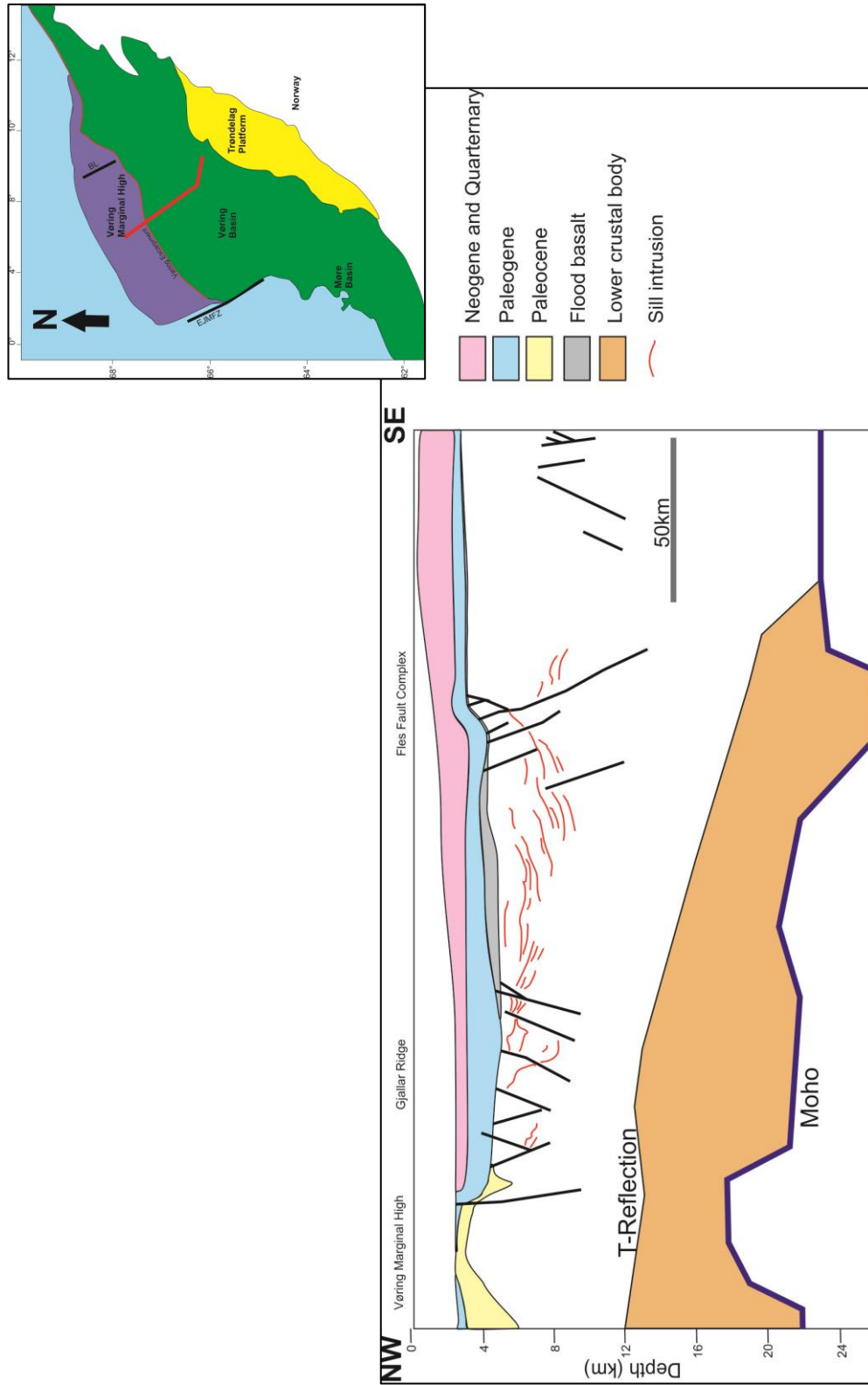


Figure 2.13: Cross-section through the Vøring Margin (red profile on inset map) illustrating the location of the T-Reflection which coincides with the upper margin of the LCB (modified from Eldholm *et al.*, 2002; Gernigon *et al.*, 2004).

Sea document high P-wave velocities ~ 8 km/s, which is akin to the lower crust velocities in the north Gjallar Ridge. Thus, the retrograde, ultra high pressure (granulitic/eclogite) rocks model is a coherent model for the T-Reflection representing the roof of a crystalline basement.

Furthermore, thermo-kinematic models presented by Gernigon *et al.* (2006) show that the magmatic underplating was located in the west of the Vøring Margin at a depth of 400-500 km. This sits in the same location as the LCB and also where the sills are within the basin. Their results also suggest that high temperatures are not necessarily needed for magmatic underplating. The LCB is thought to be magmatic, perhaps underplated, but this does not explain the low magnetic susceptibility. However, a non-magmatic interpretation is not viable owing to the magmatic emplacement along the Vøring Margin, and therefore yields major implications with regards to the thermal history of the basin (Gernigon *et al.*, 2009).

2.6 Global examples of hydrocarbons and associated volcanic rocks

Hydrocarbons have been reported globally (>100 countries) in the vicinity of igneous intrusions and lavas (Schutter, 2003b). Figure 2.14 shows the locations of known hydrocarbons that are associated with volcanic rocks, but it is to be noted that this is not a comprehensive list of sites (Chen *et al.*, 1999; Goodenough, 1999; references there in Schutter, 2003b; Parnell, 2004; Lee *et al.*, 2006; Zhu *et al.*, 2007; Cukur *et al.*, 2010; Gutmanis *et al.*, 2010; Hartley and Schofield, 2010; Wang *et al.*, 2011). Sedimentary basins that have a thermal history impacted due to igneous intrusions and yield productive hydrocarbons fields can be found at two locations: (1) subduction zones and (2) passive margins (Delpino and Bermúdez, 2009).

Sills and other igneous intrusions are often emplaced into sedimentary strata due to extensional tectonic forces. There are many examples worldwide: Vøring and Møre basins, offshore Norway, with sill complexes greater than $80,000 \text{ km}^2$ in lateral dimensions (Svensen *et al.*, 2004; Planke *et al.*, 2005). Karoo Basin, South Africa, has a sill and dyke complex $\sim 50,000 \text{ km}^3$, emplaced approximately 183 Ma over a period less than 1 Ma before the Gondwana continental break-up (Hughes, 1982; Duncan *et al.*, 1997). In the Theron Mountains, Antarctica, sills make up 30% within

the sedimentary strata, are commonly 1-50m thick, with the thickest sill, ‘Scarp-Capping Sill, at ~200 m. These sills are injected into terrestrial sediments of clastic mudstones and sandstones and give evidence for long distance magma transportation during the early stages of the Gondwana break-up (Leat *et al.*, 2006). Sverdrup Basin, Canadian Arctic Islands, has sills ~10-50 m thick emplaced into Mesozoic sediments in the Early Cretaceous to the Paleogene (Jones *et al.*, 2007). Wang *et al.* (2011) carried out numerical modelling on the production of hydrocarbons in the Bohai Bay Basin, East China. They show that for the two sills emplaced into the source rock, it took approximately 0.1 Ma for the sills to cool. Results also show that the organic material of an area ~100 m from the sill margins was transformed into hydrocarbons owing to heating of the sediment in the first 100 years. This however, was a much faster process of hydrocarbon production than normal. Hydrocarbon production is also located around the Auca Mahuida shield volcano in the Neuquén Basin, Argentina, especially from the basaltic sills themselves and also the near-by Tithonian black pelite source rocks (Rossello *et al.*, 2002). Finally, gas shows have been identified in three wells in relation with sills, namely wells 214/27-1, 214/28-1 and 205/10-2B in the Faroe-Shetland Basin. The gas is present within open fractures in the igneous bodies, which may have migrated from deeper sources into the sills (Rateau *et al.*, 2013). Generally, the sills in the Faroe-Shetland Basin may act as conduits and/or barriers towards hydrocarbon migration (Rateau *et al.*, 2013).

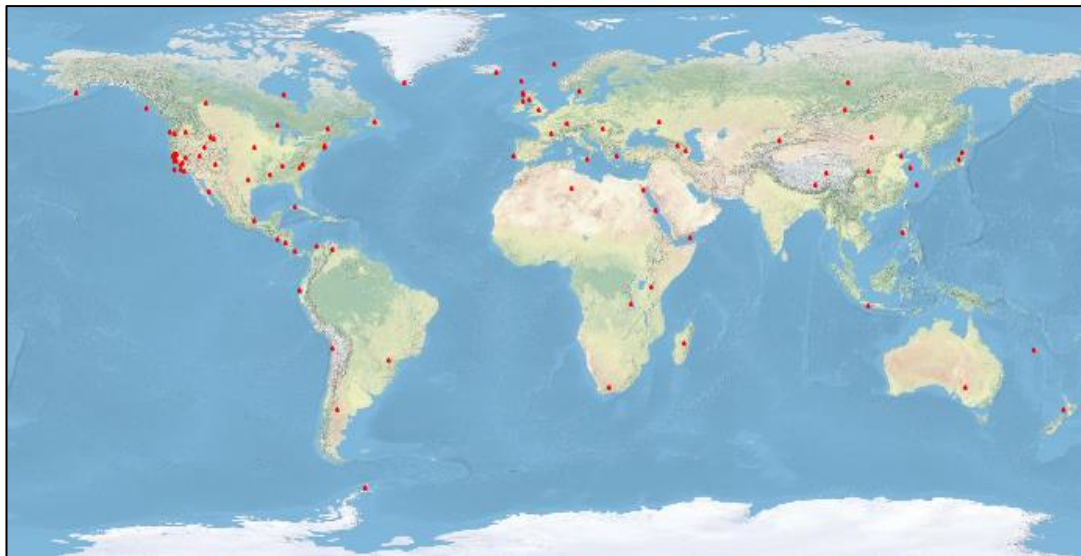


Figure 2.14: World map showing the geographical locations of hydrocarbons found in the regions of igneous complexes. Produced in ArcGIS, datum WGS 84.

2.6.1 Thermal effects of sills

Sills have a large impact on the thermal evolution of a sedimentary basin, particularly if the sills belong to a cluster or complex (Fig. 2.15; Galushkin, 1997; Lee *et al.*, 2006; Zhu *et al.*, 2007; Fjeldskaar *et al.*, 2008; Wang *et al.*, 2011). Also, the time of emplacement of the sill complexes will have significant effects on organic matter maturation and hence, the production potential of both oil and gas (Gudmundsson and Løtveit, 2012). Generally, the average thermal aureole for the maturity of organic matter is ~30-50% of the sill thickness (Galushkin, 1997). Berner *et al.* (2009) describe how the sill intrusions of the Beacon Supergroup, North Victoria Land, Antarctica caused abnormal thermal maturity of the sediments and that this thermal maturity decreased, as the distance away from the sills increased. This was also reported by Galushkin (1997) who show an exponential decay of vitrinite reflectance (a method to determine the maximum thermal history of organic matter in sedimentary basins) of black shale from the contact of the 15 m thick sill in the DSDP 41-368 well near Cape Verde Rise, East Atlantic.

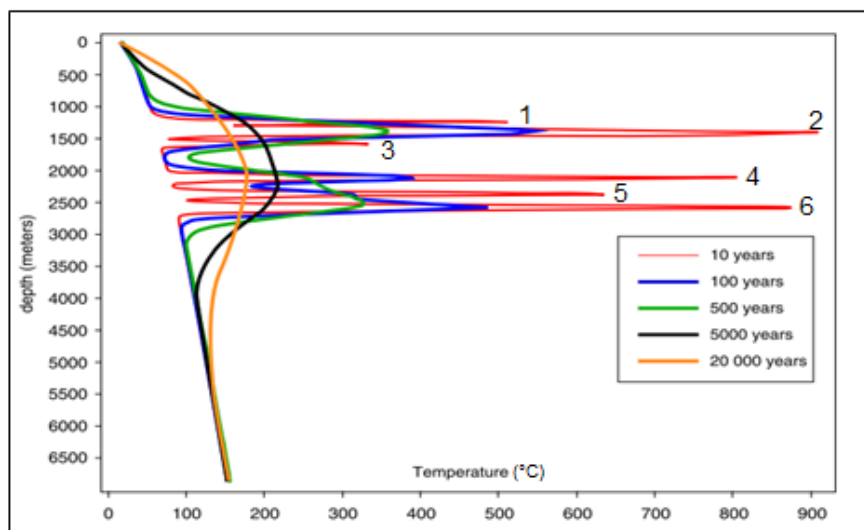


Figure 2.15: Graph illustrating heat dissipation between 6 sills and the host rock in which they are emplaced over 20 ka (after Fjeldskaar *et al.*, 2008).

2.7 Concluding remarks on the Norwegian Margin

The Atlantic passive margin has evolved through ~300-350 Ma (Doré and Lundin, 1996; Doré *et al.*, 1999) of geological time from the Late Palaeozoic until the

present, seeing several phases of extension and compression (Figs 2.2 and 2.7). The NE Atlantic Margin saw a lateral shift of the rift axis basinward towards the final break-up location, and is somewhat similar to the present day Red Sea-Gulf of Suez rift system (Lundin and Doré, 1997). The physiography (including tectonic and magmatic segmentation, crustal structure and sedimentation) that we see today is a response from sediment input and subsidence after the opening of the NE Atlantic Ocean and deepening of the associated Norwegian and Greenland Seas. With respect to the petroleum industry their interests have progressed from intra-continental rift zones, for example the North Sea, to the Atlantic passive margin and its associated basins. For this thesis we are interested in the Vøring Margin and its associated igneous intrusions.

Chapter 3: Principles of fracture mechanics

3.1 Introduction

This thesis is based on some principles of fracture mechanics as well as those of solid mechanics, structural geology and volcanotectonics. The volcanotectonic processes described here occur globally, and occupy a range of distances from a micro (mm) to macro scale (1000s km). In order to understand the methodologies, model results and discussions produced in this thesis it is important to understand the concepts behind them. Here I will introduce some basic ideas from linear elasticity, in particular those of stress, displacement, deformation and strain; modes of crack displacement; hydrofractures; and pressure.

3.2 Stress

Elasticity can be defined by the equations set out below. I start by introducing stress, σ , which is the average force per unit area acting within a deformable medium, namely:

$$\sigma = \frac{F}{A} \quad (3.1)$$

Stress is given the SI unit of the pascal (Pa, the same as for pressure), which is equivalent to one newton per square metre (N/m^2). Stress is thus defined by the force, F , in newtons and the area, A , in square metres on which the internal forces act within the deformable medium (Gudmundsson, 2011a). The internal forces are caused by external forces, either body forces or surface forces. Here, a body force is a gravitational force and surface forces are compressional or tensile forces (relating to compressional and extensional tectonic regimes). It is assumed that the internal forces are distributed evenly within the deformable medium. The medium is regarded as a continuous function of time and space, a continuum. The term σ denotes normal stress, which can either be tensile, a negative stress that acts normal

and away from the plane it operates on, or compressive, a positive stress that acts normal and towards the plane. Thus, for an extension fracture plane, tensile stress tends to open up the fracture whereas compressive stress tends to close the fracture. However, when a force acts parallel to the plane a shear stress, τ , is generated. By dividing the shear force, F , by the area, A , we can define shear stress as (Gudmundsson, 2011a):

$$\tau = \frac{F}{A} \quad (3.2)$$

Stress acting on a plane is a vector quantity as it has both magnitude and direction, known as a **stress vector**, and therefore, stress has three components, x, y and z. This is because the stress equation represents a reciprocal scalar quantity, where A is a scalar and F is a vector (\vec{F}), constituting to a vector quantity of $\vec{\sigma}$. Thus, Eq. 3.1 can be rewritten as:

$$\vec{\sigma} = \frac{\vec{F}}{A} \quad (3.3)$$

Stress at a given point, P, in a medium that acts as a continuum is given by nine components expressed as a second-rank tensor quantity, σ , with one normal stress and two tangential shear stresses, known as a **stress tensor** represented in Figure 3.1. If the stress tensor cube seen in Figure 3.1 is orientated at a certain angle then shear stresses are generated (Hudson and Harrison, 1997; Gudmundsson, 2011a; Gere and Goodno, 2012). Stress acting on a plane in a given direction is thus a vector, whereas stress at a point is a tensor.

Stress and pressure are generally very similar entities. However, they do have some differences and operate in different contexts. For example, the stress vector has both magnitude and direction, whereas pressure has only magnitude. Also, stress is used for materials with shear strength, within geology that is, rocks and sediments. By contrast, pressure is used for a hydrostatic stress field, where materials have no shear strength, such as liquids and gas (Fossen, 2010; Gudmundsson, 2011a).

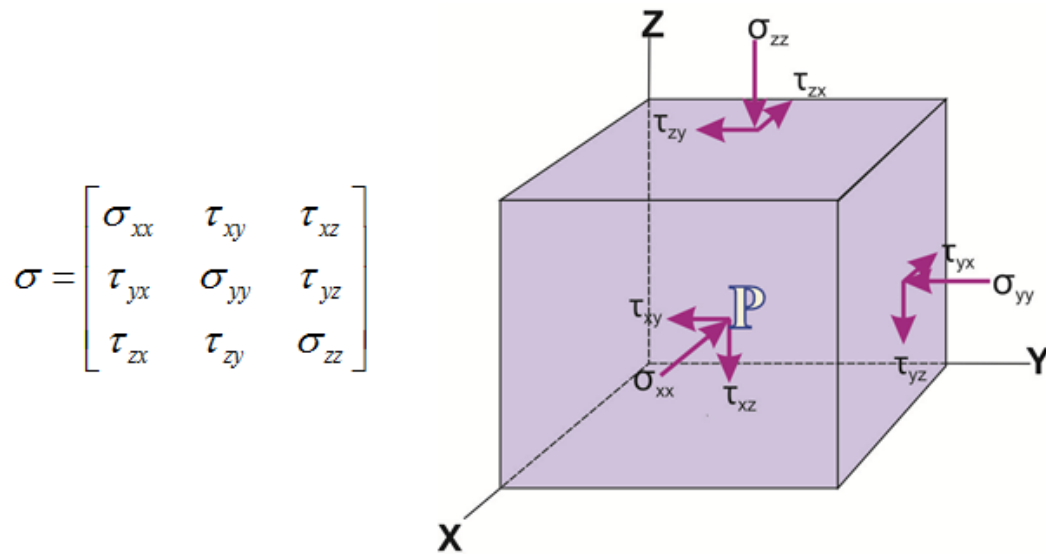


Figure 3.1: An internal point, P, within a medium aligned in the coordinate directions of x, y and z on a Cartesian axis can be represented by nine components of the stress tensor, which can be arranged as a matrix (modified from Fossen, 2010).

Principal stress is a normal stress that acts on a plane that is free of shear stress, more specifically the principal plane of stress. That is, for any given point, for example P in Figure 3.1, there are three planes of no shear stress, which are mutually perpendicular. Principal stresses are at 90° to each other (are orthogonal) and are denoted by σ_1 , the maximum principal compressive stress (minimum principal tensile stress), σ_2 , the intermediate principal compressive (tensile) stress and σ_3 , the minimum principal compressive stress (maximum principal tensile stress). These principal stresses can be defined algebraically as $\sigma_1 \geq \sigma_2 \geq \sigma_3$, but it is possible that two or more of the principal stresses are equal (Gudmundsson, 2011a; Gere and Googno, 2012). σ_1 is always positive in geology, σ_2 tends to be positive but can be negative, that is, tensile at shallow depths within the crust or at the surface, and σ_3 can be either positive (compressive) or negative (tensile).

Stresses measured at the Earth's surface or within the Earth's crust are primarily the principal stresses, which can then be related to the fault classification by Anderson (1951); normal, reverse and strike-slip faults. Simple stress analysis of the principal stresses within the Earth's crust assumes the crust being isotropic and homogenous, that is, with the same properties in all directions. When analysing many geological

structures and processes, particularly in relation to fractures, a two-dimensional analysis is sufficiently accurate. This follows partly because the intermediate principal stress commonly has little or no effect on the formation or development of the structures being analysed. The two of the principal stresses considered are then σ_1 , the maximum principal stress, and σ_3 , the minimum principal stress (σ_2 has no or little effect).

Stress fields define a region within a rock body where stress can be measured at every point and indicate how stress varies throughout the body. A stress field is a tensor field, a generalisation of a scalar or vector field which defines the state of stress at every point within a body (Jaeger *et al.*, 2007; Gudmundsson 2011a).

As the Earth's crust is layered with rocks of differing mechanical properties and has forces acting upon it, stress gradients are generated, that is, the stress tensor varies between different points (Jaeger *et al.*, 2007; Gudmundsson 2011a). Therefore, the Earth's crust is not strictly a continuum as rocks are fractured and have other cavities (collectively known as discontinuities). Hence, for certain analyses the rock bodies can be regarded as a discontinuum, where the internal stresses, that is, orientation and magnitude of principal stresses relate to the overall geometry of the crust. The sphere of influence of any discontinuity depends on its size, for example from weak contacts to tectonic faulting, which is known as a hierarchy (Hudson and Harrison, 1997). However, when dealing with sill emplacement at several kilometres depth the rock is best modelled as a continuum.

3.3 Displacement, deformation and strain

A particle of rock has a specific location that can be determined by the Cartesian coordinate system, which is the original state of the rock particle. When a load is applied to the rock, either tension or compression, the particle of rock is transformed to a new position (displaced). This is referred to as the displacement vector, a specific position of a particle of rock with reference to the original position of the particle defined as:

$$\vec{u} = \vec{P}_1 - \vec{P}_0 \quad (3.4)$$

where \vec{u} is the displacement field, \vec{P}_1 , the final placement vector, and \vec{P}_0 , the original placement vector, and can either be infinitesimal or finite (Jaeger *et al.*, 2007). When calculating the displacement vector at a point within a rock, the strain is needed to be known. Normal strain, ε , is closely related to displacement, and is defined as the ratio of change in length, ΔL , of the body to the original length, L , and most importantly describes the internal change of a rock body (Gudmundsson, 2011a).

$$\varepsilon = \frac{\Delta L}{L} \quad (3.5)$$

As Eq. 3.5 is a ratio, a geometric concept, strain is dimensionless and is therefore just a number, either a decimal or a percentage. Strain, in the same way as stress, can be presented as a strain tensor (Eq. 3.6) and can either be tensile or compressive (Gudmundsson, 2011a). Strain can be measured as elongation, where a load is applied, or by stretch, which is always negative.

$$\varepsilon = \begin{bmatrix} \varepsilon_{xx} & \varepsilon_{xy} & \varepsilon_{xz} \\ \varepsilon_{yx} & \varepsilon_{yy} & \varepsilon_{yz} \\ \varepsilon_{zx} & \varepsilon_{zy} & \varepsilon_{zz} \end{bmatrix} \quad (3.6)$$

Strain is also a description of deformation. A rock body can be deformed in two ways, either where there is no change in the internal configuration (translation - displacement vectors are equal, and rotation - displacement vectors are unequal) or where there is a change in the internal configuration, otherwise known as strain (dilation - a change in size, and distortion - a change in shape). Deformation of a rock tends to be heterogeneous, that is, strain is unequal at different parts within the rock because there are variations in the mechanical properties (Gudmundsson, 2011a).

3.4 Elasticity

Hooke's law of linear elasticity in solid mechanics states that the extension (strain) of a body is directly proportional to the force (stress) applied. Many materials obey

Hooke's law providing that the material does not exceed its elastic limit whereby, in the brittle field, a fracture occurs. Stresses are directly related to strains rather than to displacements. In elasticity, we normally do not use forces and displacements but rather stresses and strains (Jaeger *et al.*, 2007). The ratio between stress and strain is known as Young's modulus, E , and is given by:

$$E = \frac{\sigma}{\varepsilon} \quad (3.7)$$

Eq. (3.7) represents the one-dimensional Hooke's law (where the minus sign should be used in case of tensile stress, but is regarded as implied, and thus normally omitted in this thesis), Young's modulus has the same units as stress, Pa. From the stress-strain curve in Figure 3.2, Young's modulus can be determined from the gradient or slope of the line. Young's modulus itself describes the stiffness of a material, therefore a rock with a high Young's modulus is stiff and a rock with a low Young's modulus is soft or more correctly compliant. The toughness of a rock relates to the area under the stress-strain curve, where a tough rock has a large area under the stress-strain curve before it fails (accumulates large strain energy). Young's modulus of an *in situ* rock is normally lower than a laboratory sample because *in situ* rocks have many more pores and fractures, which tend to lower the stiffness of the rock body. Values used in this thesis lie within the range of *in situ* values for rift zone lithologies (Gudmundsson, 2004; Gudmundsson and Løtveit, 2005). In geology, a rock's Young's modulus depends on the pore spaces, fractures and other cavities, and *in situ* values are commonly in the order of giga-pascals, and often given as GPa (10^9 Pa) (Gudmundsson, 2011a). Young's modulus generally increases with depth and decreases with increasing porosity, temperature and water content (Gudmundsson, 2004).

Equation (3.7) carries certain assumptions. These include that the rock is homogenous, isotropic and a linear elastic material. To a first approximation, many solid rocks are roughly linear elastic, but commonly anisotropic and heterogeneous. In the numerical modelling the assumption of linear elastic material behaviour is used. In addition to Young's modulus, another elastic constant of proportionality,

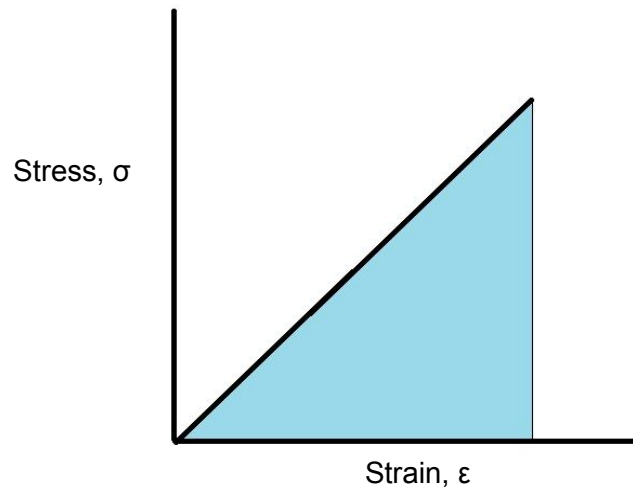


Figure 3.2: Stress-strain curve for a linear elastic material, where the slope of the line represents the Young's modulus of a rock, and the shaded blue area under the line is the strain energy per unit volume.

Poisson's ratio, is needed to specify the rock behaviour. This is when a body has an applied force, for example when a rock undergoes uniaxial extension, it is compressed in the lateral direction perpendicular to the axis of extension as seen in Figure 3.3. In rocks, lateral contraction is so small that it is not visible with the naked eye, but can be measured with sensitive measuring equipment.

Analytically, the lateral strain at a given point within a body is proportional to the axial strain at the same given point, providing that the body is isotropic. This defines Poisson's ratio, which is dimensionless denoted by the Greek letter ν (Gudmundsson, 2011a):

$$-\nu = \frac{\text{lateral strain}}{\text{axial strain}} \quad (3.8)$$

The values for Poisson's ratio are positive, commonly between 0.10 and 0.35 and typically being 0.25 (Gudmundsson, 2011a). Values are positive because Poisson's ratio is the negative of the ratio set out in Eq. (3.8), such that when a rock is under tension, axial strain is positive and lateral strain is negative. The vice versa happens for a rock under compression. This typical value was calculated by Siméon Denis

Poisson (1781-1840) for isotropic materials. It is assumed that the rock body is homogenous, isotropic and linearly elastic in order for the lateral strain to be kept constant throughout the body (Gudmundsson 2011a; Gere and Goodno 2012).

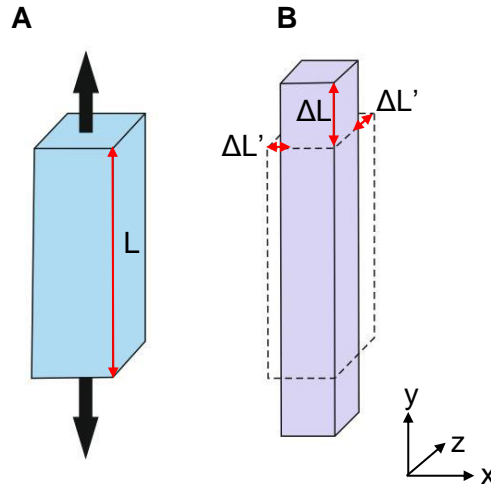


Figure 3.3: Schematic illustration of Poisson's ratio. (A) Body before loading, with black arrows representing the loading direction, (B) body after force has been applied, with the dotted line representing the original shape of the body before loading. Red arrows illustrate how the original body of length, L , is stretched in the y direction by ΔL (axial strain), and compressed in the x and z direction by $\Delta L'$ (lateral strain). In terms of Eq. (3.8), Poisson's ratio is equal to $\Delta L'$ divided by ΔL .

Although one-dimensional and two-dimensional Hooke's law have been of great importance for understanding geological phenomena, we must also sometimes consider what happens in three dimensions when a stress is applied to a sill or dyke (3D analysis). This is known as three dimensional Hooke's law, where lateral strains, which can be tensile or compressive, are applied in all directions perpendicular to the stress applied, which either increases or decreases a body's depth, strike dimension or thickness. The three dimensional Hooke's law can be regarded as principal strains in terms of principal stresses (biaxial stress) or as principal stresses in terms of principal strains (uniaxial stress) (Jaeger *et al.*, 2007; Gudmundsson 2011a; Gere and Goodno 2012).

The stiffness of rock is also determined by discontinuities that may be present within the body and also by the external surface forces. As illustrated in Figure 3.4, a compressional regime slowly pushes the two rock bodies together increasing the

stiffness, until eventually the discontinuity will become closed. Therefore, there is a limit to a stress-displacement curve. In an extensional regime however, there is no limit on a stress-displacement curve as the discontinuity opens up (Hudson and Harrison, 1997).

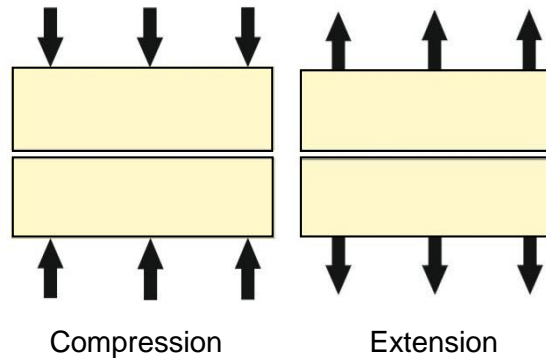


Figure 3.4: Discontinuities loaded in both compression and extension, otherwise known as a compressional and extensional regime.

3.5 Modes of cracks

Mode I, mode II and mode III are three primary displacement modes for cracks as illustrated in Figure 3.5. Mode I describes a displacement as an opening, where the walls of a crack move apart, that is, normal to the crack plane. Mode I cracks are otherwise known as tensile cracks, for example extension fractures. Mode II describes a displacement where the crack walls slide over each other in a direction perpendicular to the leading edge of the crack, that is, parallel to the crack plane and normal to the crack walls, for example dip slip faults. Mode III describes a displacement where the crack walls move relative to each other in a direction parallel to the leading edge of the crack, that is, parallel to the crack plane and walls, for example strike slip faults (Fossen, 2010; Gudmundsson, 2011a). These ideal modes of cracks are for pure extension and shear fractures because of the displacement that occurs across the plane of the fracture. With an extension fracture the displacement is perpendicular and beyond the plane, and for a shear fracture the displacement is parallel to the plane. However, many fractures (cracks) are mixed mode or hybrid, but there is always one dominant mode that can be used in modelling as a first calculation.

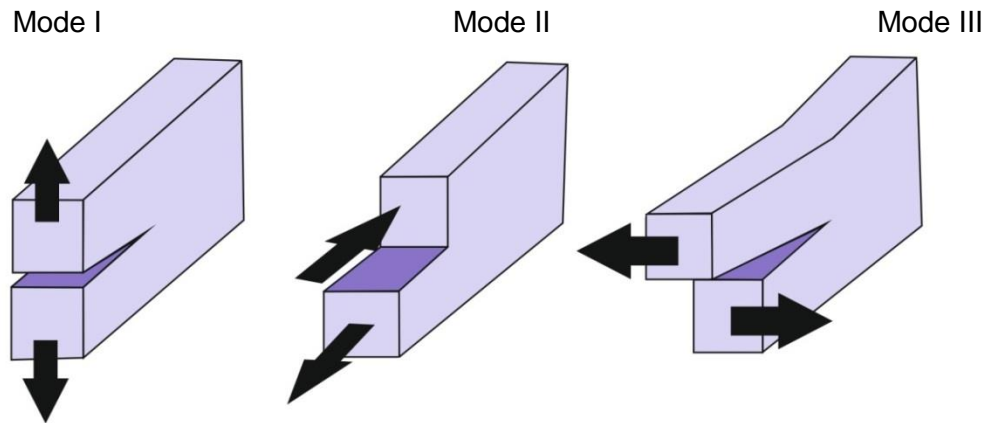


Figure 3.5: Fracture displacements are primarily denoted by mode I, mode II and mode III. Real life scenarios tend to be mixed mode fractures.

3.6 Hydrofractures

A hydrofracture is a fracture that is driven either wholly or partly by the overpressure of the fluid. Such fractures include: dykes, inclined sheets and sills, which are generated by magma; fractures generated by geothermal water or hydrocarbons and Man-made hydraulic fractures (Gudmundsson *et al.*, 2002a). Hydrofractures referred to in this thesis are dykes, sills, laccoliths and inclined sheets, which are opened up by magma and once they have fully developed the magma solidifies. Hydrofractures are common in the brittle crust and are classed as extension fractures (mode I cracks), where the normal stress on the plane of the hydrofracture is the minimum principal compressive stress. The fluid that drives the propagation of the hydrofracture is less dense than the host rock and therefore has positive buoyancy. However, most hydrofractures do not reach the surface, but become arrested at varying crustal levels despite their positive buoyancy (Gudmundsson and Brenner, 2001).

3.6.1 Dykes

A dyke can be regarded as a mode I Griffith crack, a pure extension fracture with no shear displacement, where the normal stress acting perpendicular on the dyke is the minimum compressive (maximum tensile) principal stress, hence why a dyke propagates vertically (Gudmundsson, 2003; 2011a; Gudmundsson and Løtveit,

2005). Dykes cut either planar structures, for example bedding in a sedimentary basin or massive formations, for example igneous intrusions discordantly (Fig. 3.6).

The term dyke refers to a sheet intrusion which is vertical or close to vertical with a small aspect ratio of length to thickness, that is, the thickness of a dyke is much smaller than its length, generally in the order of one thousand times smaller (Gudmundsson, 1984). They are parallel sided, tabular, sheet like intrusions ranging from centimetres to tens of metres or more in thickness (Fig. 3.6; Gudmundsson, 2011a). Thin dykes are formed from a single magma injection within hours (Gudmundsson, 1995), whereas thick dykes, that is, dykes thicker than that of the dyke swarms mode thickness, are formed in multiple injections over a period of months to thousands of years dependent on the magma supply and tectonic conditions (Gudmundsson, 1995). Magma injections can be represented by columnar joint rows, that is, one columnar row equals a single injection. Time also denotes this, as the magma is able to cool and solidify (Gudmundsson, 1995). Segmentation is characteristic of major dykes; this is because of the nature of the heterogeneous crust (Gudmundsson, 1995; 2002). As a dyke segment grows due to magma injection over time, it does so both vertically and laterally where segments may eventually link up.

Ideally, dyke geometry takes the form of a flat ellipse, which is controlled by the elasticity of the host rock. This ideal geometry is most likely observed in dykes where the host rock is close to homogeneous and isotropic. However, commonly the Earth's crust segments are composed of anisotropic and heterogeneous rocks because of mechanical layering, and dykes tend to become offset at sharp contacts or other discontinuities such as faults. Field studies also show dykes to be irregular or have a sinuous shape due to the magmatic overpressure, which depends on the local stress field (Gudmundsson, 2002; 2011a, b).

Most dykes form through multiple injections, accommodating themselves by pushing the host rock apart to form a path. They are considered as 'forceful' intrusions as they generate space by their magmatic overpressures, displacing the wall of the fracture causing the host rock to dilate but not deform (Hancock and Skinner, 2000).

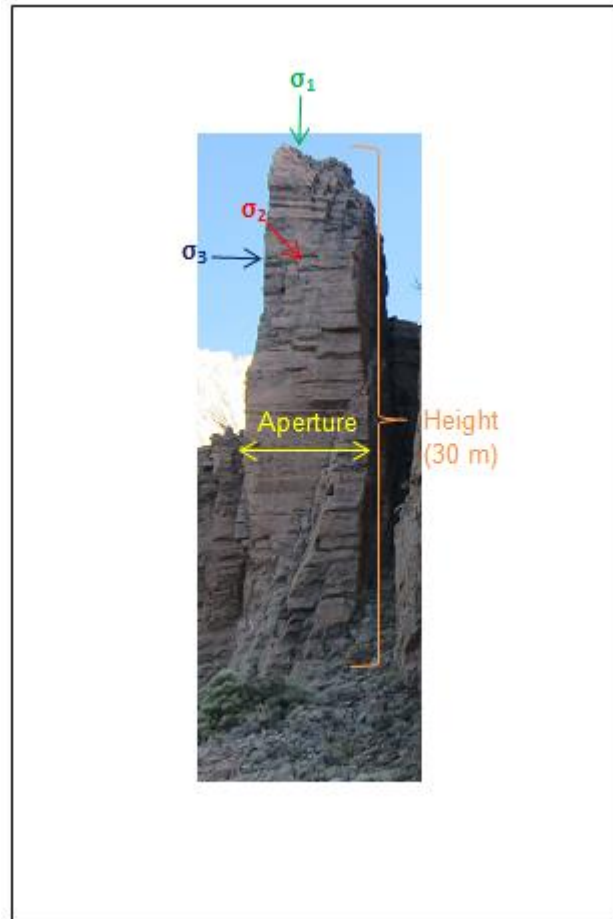


Figure 3.6: Feeder dyke, Las Cañadas, Tenerife illustrating the directions of the principal stresses, the aperture (thickness) and height of the dyke. View to the NE, dyke ~30 m high.

3.6.2 Inclined sheets

Inclined sheets are somewhat similar to dykes, that is, they are planar and discordant to the host rock and any other planar features (Fig. 3.7). The defining difference between dykes and inclined sheets is that inclined sheets are less steeply dipping (are inclined, 40-80° (Gudmundsson, 2002)) than dykes, and also are generally thinner. They are thinner primarily because their controlling dimensions are smaller since they come from shallow magma chambers where the height is small from the chamber towards the surface, in comparison to originating from a deeper reservoir (Gudmundsson, 2006). Inclined sheets tend to occur in swarms of inward dipping sheets. In comparison to dyke swarms, inclined sheet swarms have a higher intensity rate as they form in a fluctuating stress environment. This is because dyke swarms are injected from deep seated reservoirs where the local stress field is generated by

plate tectonics, more specifically plate pull, and is therefore stable. By contrast, inclined sheets are injected from a shallow magma chamber where the local stress field changes due to the varying geometry of the magma chamber. Therefore, we see cross cutting relationships, for example Tenerife, Canary Islands (Fig. 3.8) indicating that the inclined sheets are extension fractures, the same as dykes and sills (Gudmundsson, 2011a). This cross cutting relationship has been numerically modelled by Kühn and Dahm (2008), who show that dyke interaction depends on the stress field, that is, interaction is greatest when the horizontal tensile stresses are smaller than the over pressurised dyke tip.

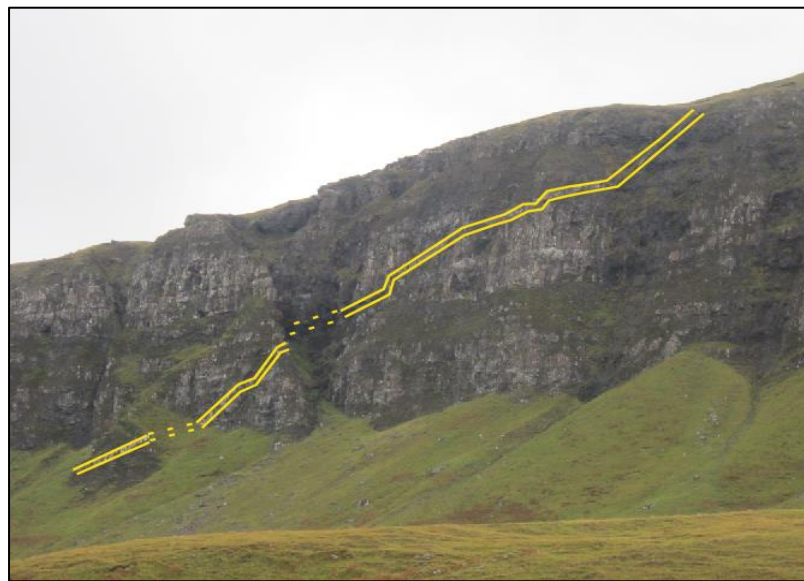


Figure 3.7: Photograph of an inclined sheet, ~3 m thick, depicted by the solid yellow line, displays a cross cutting relationship with the host rock, here a basaltic lava pile on the Isle of Mull, Scotland. The dashed line is the inferred path of the inclined sheet that has been covered by vegetation or has been highly eroded. View S (Barnett and Gudmundsson, 2014).

3.6.3 Sills

In contrast to dykes, sills do not normally cut through strata or beds or horizontal layers, but are concordant with them (Fig. 3.9). They are regarded to as a mode I Griffith crack with a circular cross section, that is, penny shaped interior crack or through the thickness crack (Gudmundsson, 1990). Sill-feeder relationships may vary, some sills are fed by dykes, others by interconnected sills that form sill complexes that supply magma to the surface (Thomson and Hutton, 2004; Cartwright

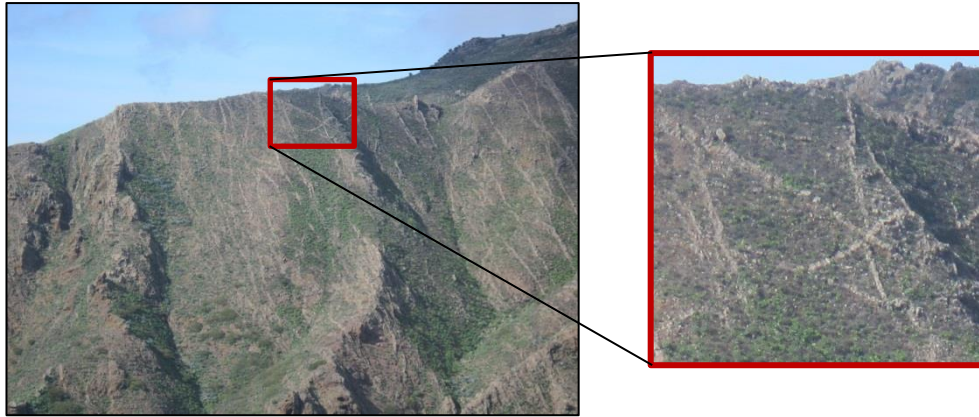


Figure 3.8: Regional dyke swarm, near Masca, Tenerife. In the red box is the cross-cutting relationship between dyke and inclined sheets to form a pentagonal shape. View W, sheets ~2-3 m thick.

and Hansen, 2006). As sills generally lie parallel to lava flows it is harder to distinguish between the two, unlike sheets and dykes, which cut lava flows. Several criteria can be used to distinguish between a sill and a lava flow (Gudmundsson, 2011a):

- Sills have a chilled selvage at its upper and lower contacts with the host rock. This is characterised by a glassy texture and gives rise to the common name of glassy margins. Whereas a lava flow only has a baked margin at its lower contact with the host rock.
- Columnar jointing is more common in sills than in lava flows. Columnar joints in sills occur as a result of slow cooling of the sill and are often well-developed because of this.
- Vesicles (formed when magmatic gases come out of solution due to a pressure decrease producing gas bubbles, preserving them as cavities in volcanic rocks) are densely populated in lava flows and are sparser in a sill.
- Scoria (breccia) is commonly found at the top and base of an a'ā lava flow (little scoria is associated with pahoehoe, and is less noticeable than a'ā lava), and is not normally associated with sills.
- A sill can be traced laterally and can be seen to cut strata or massive igneous bodies up or down the stratigraphy turning into a dyke or inclined sheet.

- Lava flows may have pillows (Fig. 3.10) if they were erupted under water or a weathered top surface if the eruption was subaerial.

To be able to distinguish between sills and lava flows in the field is important for several reasons, including palaeoenvironmental reconstructions, dating and stratigraphy. Isotopic analysis of lava flows can provide us with dates for part of a succession either igneous or sedimentary. However, sills are intrusive and date after the sediment was deposited in a sedimentary basin and are therefore important to determine a chronostratigraphy (Nichols, 1999).



Figure 3.9: Stepped sill intruded into a basaltic lava flow, SE Iceland. The horizontal sill lies concordant with the host rock, while the ‘step’, an inclined sheet cuts the lava. Sill is ~1 m thick, view N (Barnett and Gudmundsson, 2014).

3.6.4 Laccoliths

Laccoliths have similar emplacement mechanisms to sills as they are concordant intrusions that have a dome shape-flat roof and steep sides (Fig. 3.11; Cukur *et al.*, 2010). They tend to be emplaced at shallow depths within the crust generally < 3 km (Corry, 1988) and occur in a wide variety of tectonic settings, commonly associated with volcanic activity. Unlike sills, laccoliths grow predominantly in the vertical direction by up-bending of the overlying strata prior to initial emplacement (Pollard and Johnson, 1973).



Figure 3.10: Pillow lavas, SW Iceland, of a mafic composition with the characteristic ‘pillow’ morphology with radial fractures highlighted in red in the bottom right corner. Yellow note book (20 cm) for scale.

Over 50% of dykes, sills and other large, coarse grained plutons are solidified basalt that rose into the crust, but never erupted at the surface (Schmincke, 2004). For example, Gudmundsson (2002) stated that up to 90% of the Reykjadalur Central volcano in West Iceland was made up of arrested sheets. However, dykes are much more common than sills and other intrusive bodies because of the mechanics of their emplacement (Chapters 5 and 6).

3.7 Overpressure, excess pressure and total pressure

There are three types of pressure acting on or within a dyke or sill and also magma chambers. These are overpressure, excess pressure and total pressure. Overpressure, denoted by P_o , is the driving force that allows a dyke or sill to propagate further and can reach >10 MPa (Gudmundsson, 2011a) within the dyke or sill. This pressure is due to (1) the buoyancy of the magma, which results from a density contrast between the magma in the dyke or sill and the host rock in which the dyke or sill is propagating, and (2) the excess pressure in the magma chamber (Best, 2002; Gudmundsson, 2011a; Gudmundsson, 2012a). Excess pressure, denoted by P_e , is where the magma pressure is greater than the lithostatic pressure (the overburden



Figure 3.11: Laccolith of micro-gabbro composition, SW Iceland. View N, intrusion is ~15 m thick.

pressure or vertical stress, σ_v defined by $\sigma_v = \rho_r g z$, where ρ_r is the average density of crustal rock layers, g is gravity and z is the depth below the surface), and can be calculated as the total pressure minus the lithostatic pressure, with a value of 0.5-6 MPa (Gudmundsson, 2011a). For rupture to occur and a dyke to propagate, the excess pressure is usually equal to the tensile strength of the host rock (Gudmundsson, 2012a). Total pressure, denoted by P_t , is the lithostatic pressure in addition to the excess pressure (Best, 2002; Gudmundsson, 2011a; Gudmundsson, 2012a).

Chapter 4: Methods

4.1 Introduction

This chapter will describe the methods that were used in this thesis to investigate how sills are emplaced, how they interact with faults and how they may act as fractured reservoirs for hydrocarbons or as shallow magma chambers. Two types of investigations were undertaken: (1) numerical modelling and (2) fieldwork, and these are the methods described here. Not all the methods described in this chapter are used throughout the thesis and therefore, described in detail where necessary.

4.2 Modelling

Modelling is very important in structural geology, rock mechanics and volcanotectonics, as we can gain valuable knowledge and understanding of geological processes through modelling. We can use this knowledge and understanding to hypothesise and predict or forecast how geological processes interact with each other and form new structures, here through sill emplacement. To be able to understand these processes we must first understand the mechanical basics behind the formation of extension fractures in general. This is when a model, conceptual, analogue or mathematical (numerical, analytical) is set up (Middleton and Wilcock, 1994) based upon a hypothesis derived from observations, commonly from the field or geophysical data. Many models were made for each scenario tested. However, the numerical results that are displayed in this thesis are those that best fit field observations.

4.2.1 Conceptual and scale models

Conceptual models, which form a part of theoretical models, are basically ideas or illustrations; for example, in geological maps of structures or schematic illustrations of processes. Components within the model are based on observations or testable ideas or hypotheses. These models can be visualised by illustrations and schematic

diagrams to highlight particular aspects of the model, especially when conversing with other peers about an idea.

A scale model is a representation of a geological structure in nature, which maintains a relationship between all properties of the model. These scale models enable visualisation of geological structures without examining the physics of the structure in nature (Hubbert, 1937; Sanford, 1959). Scale models are generated by scaling the properties of a body from large-scale (e.g. kilometre) and long-time (e.g. thousands or millions of years) parameters to small-scale (e.g. centimetres) and short-time (e.g. minutes or hours). To choose the correct materials for the model, an understanding of continuum mechanics is needed in terms of mass, geometry, area and time, which are scaled proportionally using constitutive equations (Hubbert, 1937; Sanford, 1959; Middleton and Wilcock, 1994). However, not all factors can be scaled correctly and educated guesses must often be used for the interpretation of the model (Twiss and Moores, 2007).

Analogue models use scaling to demonstrate a theory or phenomenon using Man-made materials that are similar in the small-scale model to the real geological structures or processes (Hubbert, 1937). Thus, they are a representation of geological structures, for example calderas, intrusions and faults, and by reproducing such structures and applying loading conditions, it is possible to assess how certain fundamental processes occur. However, in many cases it is impossible for all of the parameters in the model to be scaled correctly, and therefore accuracy may be compromised (Mader *et al.*, 2004).

4.2.2 Mathematical models

Mathematical models include the subclasses of analytical and numerical models. Mathematical models use a set of constitutive equations that obey the conservation of physics (e.g. the conservation of mass) and physical constraints (e.g. boundary loads or displacements) that are applied to the model (Mader *et al.*, 2004). These differential equations are solved by integration to show the distribution in stress, strain and displacement throughout the body that is being deformed. The constitutive equations can be solved analytically or numerically (Twiss and Moores, 2007).

Analytical models can be solved without a modelling program, that is, they can be simply solved by hand, but they provide closed-form solutions. It can be argued that while analytical models may be aesthetically pleasing, they are generally fairly simple and cannot be used for the analysis of complex mechanical and geometrical systems, that is, analytical models are mostly used to provide solutions for simple geometries, homogenous and isotropic mediums and small strains. Thus, analytical models carry assumptions that may restrict application of these solutions to nature (Sanford, 1959). Therefore, analytical models are inappropriate for many realistic concepts involving mechanical contrasts within a multilayer, for example arrest of dykes in a heterogeneous and anisotropic crust, hence the use of numerical solutions (Twiss and Moores, 2007).

Numerical models are carried out using a computer program and provide approximate solutions for differential or integral equations. The solutions only relate to specific nodes or points in the structure being modelled. Numerical solutions complement the other models discussed, such as conceptual, analytical and analogue models. The numerical models presented here are mostly 2D, which is appropriate when producing numerical models of rock fractures, here, dykes, sills and faults (Logan, 2011). They can also simulate complex geometries, heterogeneous and anisotropic media and large strains (Logan, 2011; Twiss and Moores, 2007). The two common types of numerical modelling are finite element method (FEM) and boundary element method (BEM). FEM was developed in the 1940s originally by Hrennikoff (Hrennikoff, 1941) followed by McHenry (McHenry, 1943) and Courant (Courant, 1943). Studies until the 1960s only dealt with small displacements and strains in an elastic medium with static loading. This was then developed by Zienkiewicz *et al.* (1968) to include visco-elastic mediums, Wilson and Nickel (1966) to include heat conductivity, and Martin (1968) to include fluid flow. A more comprehensive history of FEM modelling is provided in Logan (2011). In the late 1970s with the development of computers came the use of the numerical technique BEM. However, the method was derived from mathematical theories from the 18th and 20th centuries, where a comprehensive history of this method is provided in Cheng and Cheng (2005).

The main differences between these two methods are in the calculations (differential or integral methods) and the different processes for discretisation of the numerical

problem. FEM uses a differential method (Zienkiewicz, 1977; Logan, 2011; Deb, 2006), that is, the numerical problem is discretised by a series of elements solved with differential equations (Fig. 4.1A and B). BEM on the other hand, uses an integral method (Brebbia and Dominguez, 1992), which is applied to the boundaries of the model, and therefore, the surface only needs to be discretised. This produces a smoother mesh in which the geometry can be followed precisely and not by a series of small elements (Fig. 4.1C and D). It can be said that BEM provides more accurate solutions around the boundary of a model, for example surface deformation, whereas FEM is more accurate at calculating stress concentrations around the tip of a fracture, for example propagating dykes. This thesis predominantly uses FEM modelling in the program COMSOL Multiphysics (COMSOL, 2012).

4.2.2.1 Finite element method

The finite element method (FEM) is a branch of numerical modelling used to analyse structural mechanics, fluid flow and heat transfer amongst other applications. The use of FEM models in volcanic studies started with two dimensional and axisymmetric models, for example the works of Dieterich and Decker (1975), Bianchi *et al.* (1984) and Yang *et al.* (1988). Nonetheless, FEM modelling has progressed over the years because of increased computational power, and models can now be produced in three dimensions (Ronchin *et al.*, 2013). FEM takes a continuum or a complicated body, which is divided into finite elements (small and manageable pieces) that can then be resolved in respect to each other. This process is known as meshing as illustrated in Figure 4.2, where the mesh is composed of elements. The more intricate the mesh, the smaller the elements. Normally, the small elements are used for those boundaries of the model where a more accurate solution needs to be calculated. Here, an assumption needs to be made for each element, based upon the analysis of the finite elements. Simultaneous equations can then be set up to describe each individual element with respect to its nodal points. These equations are then solved with global simultaneous equations once boundary and loading conditions are established. Solutions are then obtained and represent an approximation or prediction of the numerical model (Deb, 2006; Logan, 2011).

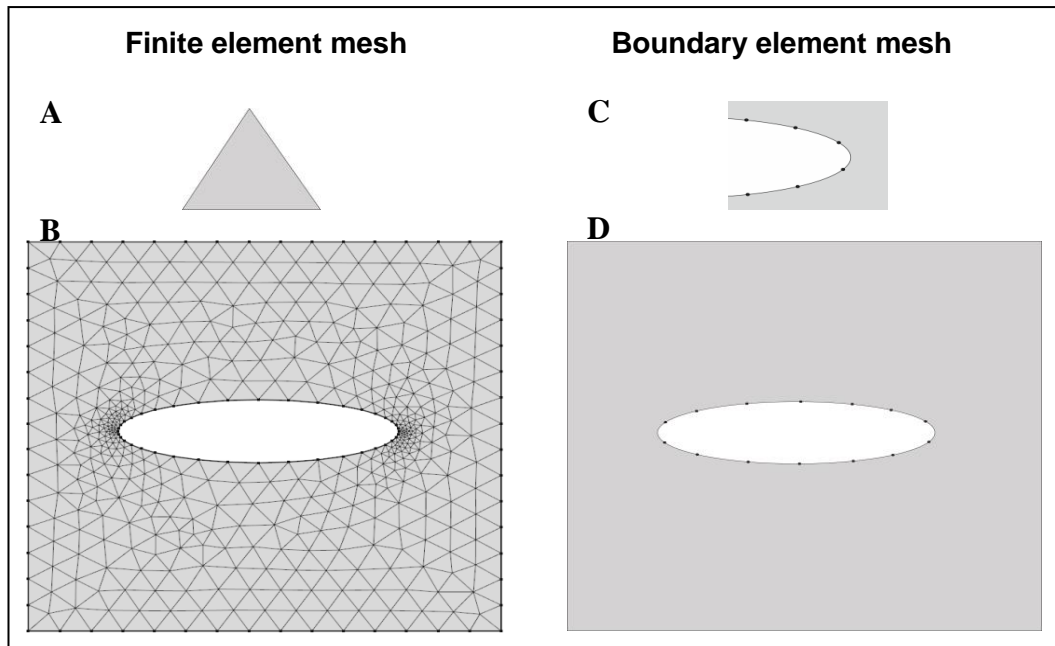


Figure 4.1: Schematic comparison between the meshes of finite element method (FEM) and boundary element method (BEM). (A) Triangular element and nodes on each vertex as shown in Figure 4.2. (B) FEM mesh, where the circular hole is made of individual small elements. (C) Line element united by nodes. (D) BEM mesh of a circular hole that can be traced exactly, the same geometry as B (modified from Brenner, 2003). FEM can be seen to subdivide the whole model into a triangular element network, whereas BEM can be seen to subdivide only the concerned boundary into linear elements.

There are both advantages and disadvantages to the finite element method. Advantages include FEM's adaptability allowing it to be applied to a wide variety of numerical problems that have irregular geometries, and varying boundary and load conditions. This is applicable to modelling produced for this thesis, in terms of analysing stresses along with associated deformations around geological geometries under a diverse range of loading conditions. As a result of improvements in technology, modelling now involves pre-processing and post-processing, which allows us to visualize the solution and interpret the model results efficiently and effectively. However, the main disadvantage of the finite element method, like any numerical methods, is that a closed-form solution cannot be provided, therefore in order to minimize error the number of elements needs to be increased, or model parameters need to be changed, as they cannot be extrapolated to various conditions (Deb, 2006; Logan, 2011). Lastly, any limitation that can occur may be due to the capacity of the computer's hard drive to be able to run a numerical model.

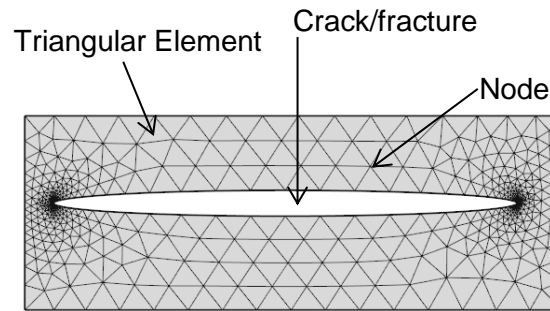


Figure 4.2: A mesh indicating the location of the elements and nodes. Elements are the small pieces and the nodes are the points at which each element meet. Note how the mesh becomes more finely detailed at the crack/fracture tips where an accurate solution would be applied.

4.3 COMSOL

Computer models have become increasingly more important for scientists and engineers. With computer models we must consider if the model outputs or results represent that of the real world to include all laws of physics. This is what COMSOL Multiphysics represents, a platform that can be easily transformed or adapted to various applications (www.comsol.com; COMSOL, 2012).

The numerical models produced using COMSOL Multiphysics versions 4.2 and 4.3 (COMSOL, 2012) represent stress fields or fluid velocities around inputted geometries. The process to producing these models can be split into three steps: (1) pre-processing, (2) analysis and (3) post-processing (Appendix A for step-by-step guide to a simple model). Models produced in COMSOL use two methods, solid mechanics and fluid flow. Stress modelling within the solid mechanics module was the dominant kind of numerical model produced in this thesis and in terms of the three steps named above are as follows: Pre-processing was the process of adding geometries to the model, here, hydrofractures and faults. The process of analysis was where mechanical properties were added to the model, specifically, Young's modulus, Poisson's ratio and densities of the rock units. Also, at this stage internal magmatic overpressure, thin elastic layer properties to contacts (known in the literature as an internal spring, e.g. Gudmundsson *et al.*, 2002) and external loading, either compression or tension were applied. The final stage of this process was to add a mesh, this was where the geological structures implemented in the model were divided (Fig. 4.2) and where stress calculations were carried out to provide an

accurate solution. The element size of each model varies and is noted with each model in terms of the minimum and maximum element size. The maximum element growth size is kept the same in all models at 1.1, as is the resolution of curvature at 0.2, and resolution of narrow regions at 1. Once the solution had been computed post-processing, a visualisation of stress fields that COMSOL had calculated, allowed for interpretation of the results.

4.3.1 Solid Mechanics

The solid mechanics module allowed for the performance of static and dynamic modelling in both 2D and 3D co-ordinate systems and to analyse stress fields associated with different aspects of structural and volcanological examples. This interface allowed for the modelling of a linear elastic material, to analyse stress outputs and also solved displacements in both stationary and time-dependent frames.

The main aim of the numerical models produced are to represent as accurately as possible what happens in nature, both today and in the past. A series of models were made with varying parameters (indicated for each model) and level of complexity to analyse scenarios studied within this thesis. The results displayed within this thesis best represent the scenario relating to geological structures and theories.

4.3.1.1 Hydrofractures and fault zones

Sills and dykes are classed as extension fractures that exhibit no displacement parallel with their walls. Displacement occurs only perpendicular to their walls, that is, the displacement is pure opening. Thus, extension fractures were modelled as mode I cracks that were driven by a given magmatic overpressure (Gudmundsson, 2003). Areas away from the dyke tip deform elastically because at a sufficient distance away from the tip, the strains are small. Hence, an intrusion can be modelled as a crack within a linear elastic body (Rubin, 1995). These hydrofractures along with faults (e.g. studies of faults in the Holocene rift zone of Iceland; Brenner and Gudmundsson, 2004) were modelled as elliptical cracks (2D) or cavities (3D) as their apertures varied roughly in accordance with an elliptical geometry. These elliptical cracks can be described in terms of their aperture, width and length as

illustrated in Figure 4.3. Lastly, fault zones were modelled as an elastic inclusion. They are named elastic because their elastic properties, that is, Young's modulus, are different from that of the host rock, and as inclusions because the fault, with a solid infill, is within a larger host body (Gudmundsson *et al.*, 2010).

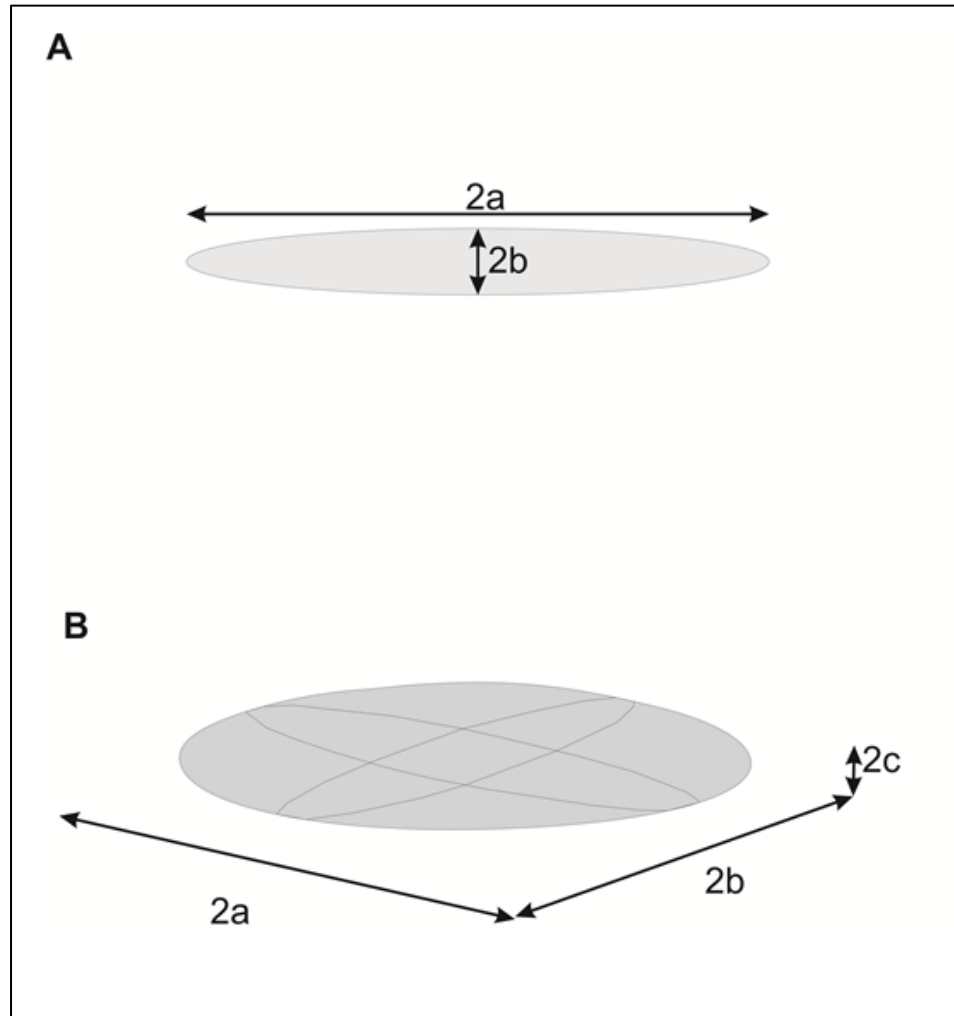


Figure 4.3: A schematic illustration of a sill in 2D and 3D. (A) Elliptical hole, representing a sill in 2D, showing the parameters a and b . $2a$ represents the largest length or major axis and $2b$ represents the aperture or the minor axis of the ellipse. σ_1 is the maximum stress that acts at the tips of the sills. (B) Penny-shaped crack, representing a sill in 3D, where $2a$ and $2b$ are the same as in (A) but $2c$ represents the depth of the sill.

4.3.1.2 Weak contacts and fault zones

A contact may have a finite strength of friction as described by the Coulomb criterion and therefore, the shear stress of the contact is limited, and sliding along the contact can occur (Zhang *et al.*, 2007). These contacts are best described as weak,

for example scoria layers relating to lava flows or shale or mudstone or clay in a sedimentary basin. These weak contacts were modelled as a ‘thin elastic layer’ commonly cited in the literature as an internal spring (e.g. Gudmundsson *et al.*, 2002a). The same type of model is used for some fault planes. However, for faults the shear strength is important, but less so for extension fractures. The weak contacts were modelled ahead of the propagating dyke or inclined sheet with a stiffness of 1 MPa/m. Also the weak contact was assumed to behave elastically, that is, the contact (or fault plane) had the ability to open up.

4.3.1.3 Boundary loading and topography

There are two types of boundary loads applied to the numerical models in this thesis (many more are possible in general, for example displacement, strain, heat flow, velocity, to name a few): (1) magmatic overpressure was taken at 10 MPa, a common value for a basic magma, estimated from field studies of numerous dykes (Kusumoto *et al.*, 2013). (2) Tectonic loading, taken to be 5 MPa (Andrew, 2008), unless otherwise stated.

All models produced in this thesis have at least one fixed edge to prevent rigid body rotation and translation. Where stated, two of the sides may have applied external loading, that is, extensional and compressional regimes and also a free surface. These regimes tend to apply to a tectonic history, especially in the case of modelling the Vøring sills offshore Norway, or to test hypotheses that are indicated with each model. A free surface describes the surface of the Earth, where a surface is in contact with fluid so that no shear stresses or forces are tolerated and the principal stresses must be perpendicular and parallel to the surface. A select few models have a topography added to illustrate topographic related stresses; the margins of the topography, that is, volcano geometry were once again modelled as a free surface.

Loading applied to the external boundaries had effects on the results produced in the model due to interference. This was minimised by making the boundaries of the model much larger than the structure (which was drawn to scale) being investigated, allowing for the production of more accurate and precise modelling of the magmatic overpressure and other internal forces.

4.3.1.4 Mechanical properties

Each model had a varying set of mechanical properties according to the different materials used. The mechanical properties applied include material density, Poisson's ratio and Young's modulus. Density of rocks and more importantly Young's modulus were taken from Appendix D and E in Gudmundsson (2011a), where Young's modulus is stated accordingly with each model. As hydrofracture propagation is much smaller than the velocity of seismic waves, static rather than dynamic Young's moduli were used (Brenner and Gudmundsson, 2004). Static Young's modulus may be as much as ten times lower than the dynamic modulus. All these mechanical values have been derived from laboratory experiments, which differ from field and *in situ* values due to rock heterogeneities and discontinuities, and are therefore an approximation to the true values. Young's modulus values used emphasise the great variations in stiffness in the crust - a variation by several orders of magnitude, whereas Poisson's ratio varies much less between lithologies (commonly by a factor of 1.5) and was therefore kept constant at 0.25.

4.3.1.5 Stationary and time-dependent models

The majority of models made were in a stationary framework and were therefore independent of time. This is the default solver within COMSOL and optimizes problems by constrained stationary partial differential equations (COMSOL, 2012). On the other hand, when modelling a tectonic history, time became an important factor. Here time-dependent modelling was used where the problem was constrained by time-dependent partial differential equations. This was the case for modelling the Vøring Margin (detailed geological history in Chapter 2; Table 4.1). Time dependency allowed the external loading conditions to be varied accordingly with the tectonic evolution of the Vøring Basin, in short, phases of extension and compression (e.g. Skogseid *et al.*, 1992; Roberts *et al.*, 1997; Brekke, 2000; van Wijk and Cloetingh, 2002; Gernigon *et al.*, 2003). The stiffness of the sills was kept constant at 40 GPa. This value was chosen because these sills are known to be of a micro-gabbroic composition (Svensen *et al.*, 2010). The value was kept constant because the sills would have cooled down in the first few thousand years (Fjeldskaar *et al.*, 2008) and therefore their stiffness would not alter significantly after this

period of time. These sills have been modelled within a shale host rock (known from Utgard well, Svensen *et al.*, 2010), which overtime would have undergone diagenesis and therefore with each time step became incrementally stiffer (1-20 GPa). It is important to note that time-dependent modelling means that the mechanical properties of rocks considered change over time, and that elasticity itself is not time-dependent.

Table 4.1: Modelling parameters for time-dependent models of the Vøring Margin (Gudmundsson, 2011a).

Time (Ma)	Shale, E (GPa)	Sill, E (GPa)	Tectonic regime
56 (Paleocene-Eocene)	1	40	Extension 5MPa
46 (Eocene)	4	40	Extension 5MPa
36 (Eocene)	8	40	Extension 5MPa
26 (Oligocene)	12	40	Compression 5MPa
16 (Miocene)	16	40	Compression 5MPa
0 (Holocene)	20	40	Compression 5MPa

4.3.1.6 Output parameters

There are three main outputs of models that were run: (1) stress (2D and 3D) - either normal stress or shear stress, (2) displacement (2D and 3D), and (3) 1D graphical to illustrate specific ideas. Results displayed within this thesis represent von Mises shear stress and the minimum compressive principal stress, σ_3 (the maximum principal tensile stress). Von Mises stress shows zones of high shear stress as it is characteristic of plastic flow, that is, the material does not return to its original shape. This shear stress is similar to the Coulomb criterion, which is standard for geology. On the other hand, the minimum compressive principal stress, σ_3 , shows zones of maximum tensile stress and is a normal stress, that is, the stress is applied perpendicular to the material surface. In addition, some models have trajectories displayed, representing (unless otherwise stated) the maximum principal compressive stress, σ_1 . This allows for further predictions into growth of both extension and shear fractures and opening displacements along contacts. In particular, extension fractures propagate parallel to σ_1 . Displacement results illustrated how a hydrofracture could inflate and also where weak contacts were most

likely to open up. Finally, 1D plots illustrated either stress magnitudes or displacement magnitudes, to quantify more accurately the 2D or 3D results displayed. These were processed using the statistical package SigmaPlot version 12.5.

4.3.2 Fluid flow: laminar flow and particle tracing

The fluid flow module allowed the generation of models to simulate the mechanics of laminar flow of an incompressible fluid. The Navier-Stokes equation was used to solve these models with respect to the velocity field of fluid transport and pressure gradients. The particle tracing allowed the modelling of particles (either macro- or microscopic) within a background fluid (Appendix B for a detailed model set-up).

4.3.2.1 Fracture networks

Fracture network maps that were traced from photographs to a high accuracy were inputted from CorelDRAW. The wall boundary condition was set at no slip and defines $u = 0$, where there is no fluid movement along the walls of the fractures. For particle tracing on the other hand, the wall condition was set to bounce because the particles were of microscopic scale and also, this reflects the particle from the fracture wall enabling the conservation of momentum. The primary particle condition was set as none and therefore, the bounce condition was always appreciated by the incident fluid particles (COMSOL, 2012). The wall condition for the outlets of the particle tracing was set to freeze, causing the particle to become frozen at the outlet wall allowing for visualization of the particles.

4.3.2.2 Fluid properties

Fluid properties are important when solving equations for momentum of the fluid. The two main fluids that were modelled here, were water (density = 1000 kg/m^3 , dynamic viscosity = $1.55 \times 10^{-3} \text{ Pa s}$), and crude oil (density = 900 kg/m^3 , dynamic viscosity = 0.05 Pa s), where the density and dynamic viscosity (relationship between shear stress and shear rate in the fluid) of the fluid were defined from Appendix E in Gudmundsson (2011a) and are noted accordingly with each model.

The inlet and outlet of fluid were then defined as a boundary condition for pressure, no viscous stress, here a pressure gradient was set at 6 Pa. This condition was used because it primarily controls the pressure along the entire fracture walls and is more robust for numerical simulations than normal stress boundary conditions.

The particle tracing module gave particle vectors, which used differential equations based on Newton's laws of motion and therefore, particle mass and forces acting upon the particle needed to be defined (COMSOL, 2012). The particle properties were as follows: particle density 900-1000 kg/m³ (dependent on fluid) and particle diameter 1x10⁻⁶ m. Finally drag force was selected abiding to Stokes law where the particles had a Reynolds number far less than one (COMSOL, 2012).

4.3.2.3 Stationary and time-dependent models

Laminar flow models were solved in the stationary domain, whilst particle tracing for fluid flow was solved in a time-dependent domain. Therefore, for particle tracing a number of particles per release could be inputted, usually $N = 100$ and were equally distributed throughout the fracture network (the edges of the model were divided into equal segments and the particle was placed in the centre of each segment) (COMSOL, 2012).

4.3.2.4 Output parameters

Results were plotted in a 2D frame work. Laminar flow presented results as a velocity field (m/s) and pressure (Pa), which was dependent on the location of the inlet and outlet of the fluid. The particle tracing outputted an animation in seconds, reflecting the velocity field respective of the laminar flow stationary results.

4.4 Seismic line interpretation

Igneous complexes were easily identified on seismic images (Fig. 4.4) because of the large acoustic impedance between the magmatic intrusion and the host rock, which gave a positive reflection. This is because the mafic intrusions have a larger density (2500-2600 kg/m³) than the sedimentary strata (~2300 kg/m³), and also a larger Young's modulus (Table 4.1). They have a high seismic velocity in the order of 5-7

km/s (Plank *et al.*, 1999; Bell and Butcher, 2002). Sills can be seen as high positive amplitude reflections that thin out against lower amplitude reflections of the sedimentary host rock. They can also be identified by their geometry, saucer-shaped or stacked, and their irregularity compared to the uniform sedimentary sequence. Finally, hydrothermal vents can sometimes be seen at the palaeosurface directly above the tips of the sill. Dykes however, although associated with sills, were hard to image due to their steep dip.

4.5 Field and data processing

4.5.1 Field measurements

Field measurements of fractures (both horizontal and vertical) in sills were made with over 70 fractures per profile or section, where some of the fractures belonged to sets, especially horizontal fractures. These were studied along a profile of 10-20 m, which was perpendicular to the overall trend of the dominant fractures (vertical or sub-vertical sets). Fractures identified were then projected to the profile line, that is, the tape measure, with measurements made as follows (Fig. 4.5):

- Length - where the fracture intersected the profile line.
- Orientation - strike and dip of the fracture.
- Displacement - the aperture of the fracture if open, closed or filled, measured with a feeler gauge (measured apertures as small as 0.05 ± 0.025 mm) or ruler for larger fractures (error of 0.5 mm).
- Type of fracture - extension fracture, shear fracture, mineral vein or joint.
- Infill of fracture - was the fracture infilled by minerals.
- Fracture spacing - a measure of the distance between one horizontal or vertical fracture and the next.
- Fracture frequency - a reciprocal of the fracture spacing, but was also measured as the number of fractures within a given area along the profile.

The basic geometry of the fractures could be described by their length and aperture, and could be measured with relative ease. The fracture length was the maximum dimension measured normal to the surface (horizontal fractures) or parallel to the

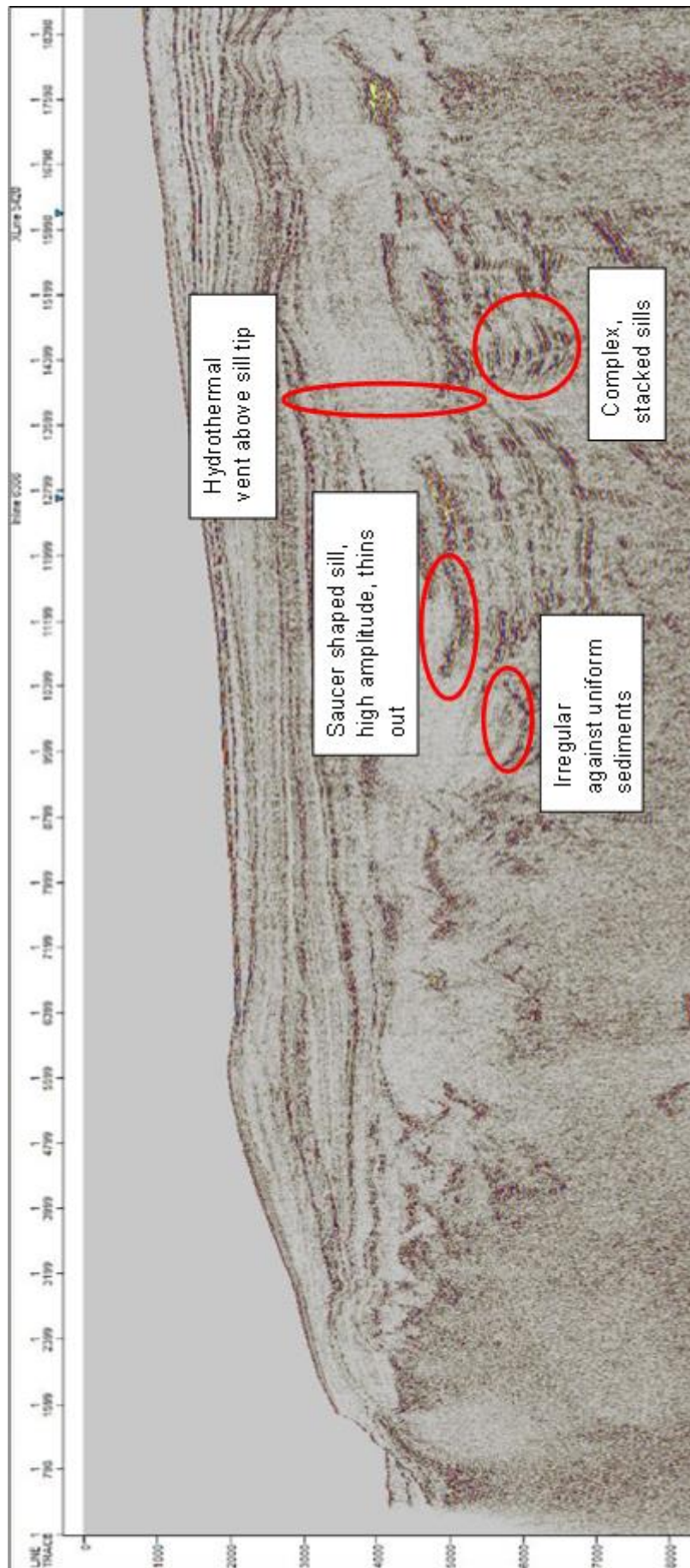


Figure 4.4: Seismic line demonstrating how sills were identified.

surface (vertical fractures). The aperture was measured as the lower bound, to be defined as the opening of the fracture measured perpendicular to the fracture walls. The fracture data was only collected from traces, that is, where the fracture intersected the surface of the sill outcrop. The final geometry of the fractures had been affected by post formation alteration in their apertures, for example weathering (chemical, physical and biological). Some fractures were infilled with minerals, either quartz or calcite, which is common at depth too, as seen from core samples. Mode I extension fractures that exhibited no shear displacement were measured, and during interpretation, apertures that had been weathered extensively were taken into account.

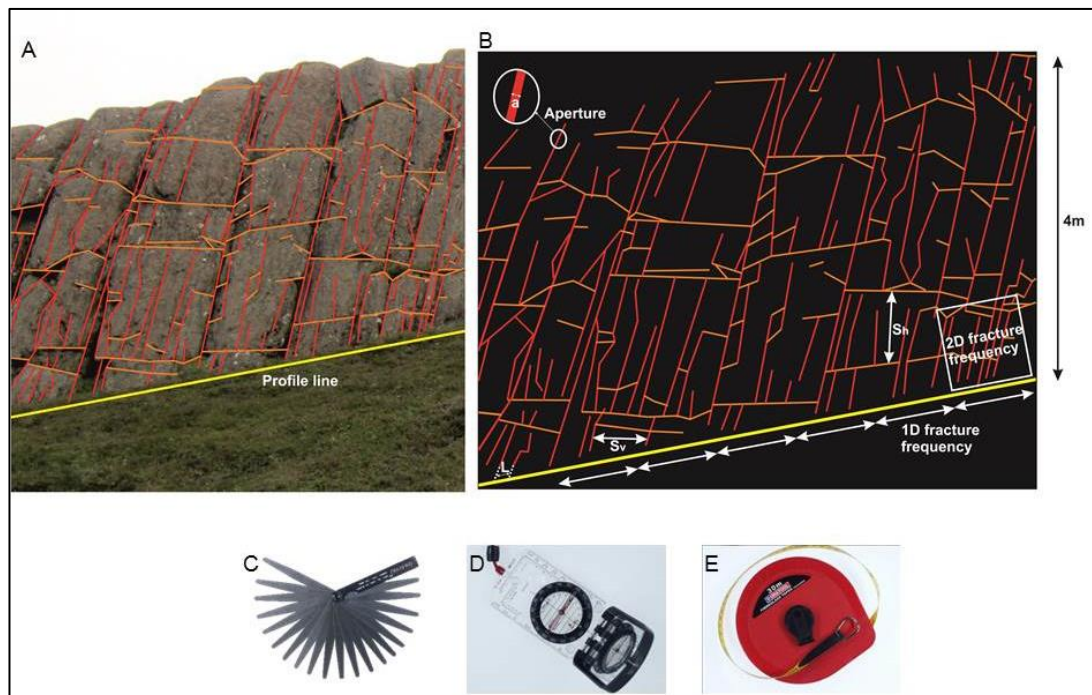


Figure 4.5: Field measurements and equipment. (A) Fracture network within Stardalur sill, SW Iceland, 4 m height, view NW: red = vertical/sub-vertical fractures, orange = horizontal/sub-horizontal fractures along a profile line (yellow) aligned parallel to the sill (perpendicular to main fracture sets). (B) Schematic illustration from (A) illustrating length = L , aperture = a , S_v = spacing between 2 vertical fractures, S_h = spacing between 2 horizontal fractures, 1D fracture frequency along profile line and 2D fracture frequency in a 1 m^2 transect. (C) Feeler gauge. (D) Silva compass clinometer. (E) 30 m long measuring tape.

4.5.1.1 Whin Sill geological background

The Whin Sill has been a prototype for the description of sills for many years: an igneous tabular sheet intruded concordantly into sedimentary units or lava flows,

studied by classic geologists such as Hutton (1832) and Sedgwick (1827). However, the Whin Sill is not a concordant sill as first described. Johnson and Dunham (2001) give a good account of how the Whin Sill complex transgresses through Carboniferous rocks along the east, south and north margins, while the west margin has been cut by the Pennine faults. Goultly (2005) on the other hand, gives a more detailed account of the emplacement mechanisms relating to the Whin Sill, especially the stepped transgressions (described in detail by Goultly *et al.* (2000) on Holy Island) rather than a circular saucer-shape.

The Whin Sill is an igneous complex that expands over Northumberland and County Durham (referred to as Co. Durham from here-in; Fig. 4.6). This complex is thought to have intruded in more than two events over 25 Ma from the Late Carboniferous to the Early Permian, approximately 295 ± 6 Ma (Liss *et al.*, 2004; Garcia *et al.*, 2006). The sill complex is thought to be emplaced at a palaeodepth of ~1-1.5 km (Francis, 1982) into Carboniferous sedimentary rocks, mainly limestones and shales (similar to that of the Vøring Margin), and expands over a sub-outcrop area of 5000 km² (Johnson and Dunham, 2001; Garcia *et al.*, 2006). The average thickness is in the order of 30 m, with the greatest thickness observed being 80 m (Liss *et al.*, 2004). The maximum thickness observed whilst undertaking my fieldwork was only ~30 m. The composition of the magma itself is of a tholeiitic quartz dolerite (Fig. 4.7A; Johnson and Dunham, 2001) - a good analogue for the Vøring sills with a micro-gabbro composition (Svensen *et al.*, 2010). Orthopyroxene, clinopyroxene and plagioclase are dominant phenocrysts, with clinopyroxene, plagioclase and magnetite forming the groundmass (Fig. 4.7B).

Palaeomagnetic data suggests that there are three discrete parts to the Whin Sill complex each with associated ENE-WSW trending feeder dykes: Holy Island Dyke that feeds the Holy Island Sill; High Green Dyke that feeds the Alnwick Sill; St. Oswald's Chapel Dyke that also feeds the Alnwick Sill; Hett Dyke that feeds the Hadrian's Wall-Pennines Sill (Liss *et al.*, 2004). However, whether these dykes feed the Whin Sill complex is controversial as there is no direct evidence to relate the dykes to the sill in the field (Johnson and Dunham, 2001).

Fieldwork was chosen to be carried out along the Whin Sill complex as it is very extensive and has some very good outcrops, with well-developed columnar jointing.

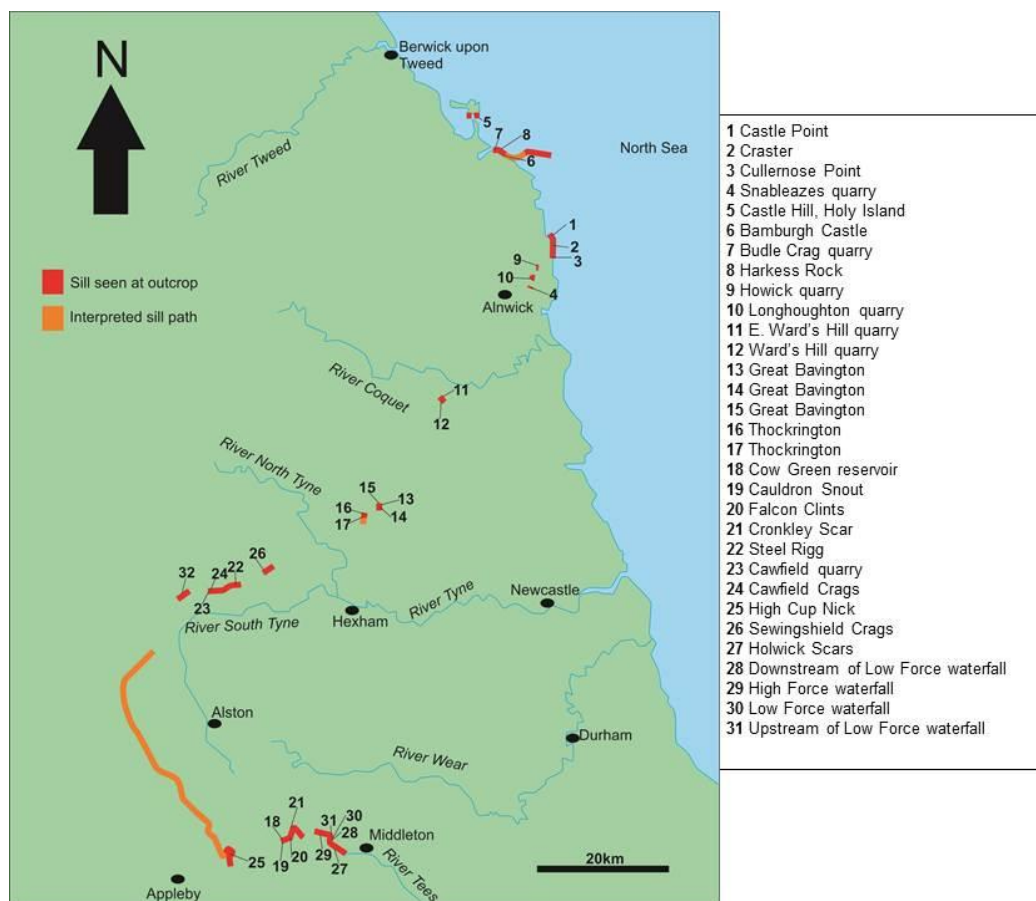


Figure 4.6: Top-Overview of the Whin Sill locations, NE England, please also refer to Figure 4.8. Bottom- Detailed overview of the Whin Sill outcropping across Northumberland and Co. Durham. Locations visited in red with associated locality number, and interpreted sill outcrop in orange as seen from a distance in the field (inaccessible) and also remote sensing from Google Earth.

The aims at this field location are to determine (1) sill thickness and lateral dimensions as far as possible, (2) conditions for sill emplacement, (3) contact metamorphism of the host rock and (4) the potential for the Whin Sill complex to act as a fractured hydrocarbon reservoir and why it did not develop into a shallow magma chamber. A total of 31 locations (Fig. 4.6) were visited to study the Whin Sill complex, where 17 profile lines (Fig. 4.8) were used to collect fracture orientations. Fracture orientations and apertures were plotted for all profiles, however only extensive profile lines that were longer than 10 m, were used to calculate fracture lengths, spacings and frequencies. Finally, although the Whin Sill is a complex, it will be referred to as the Whin Sill in this thesis.

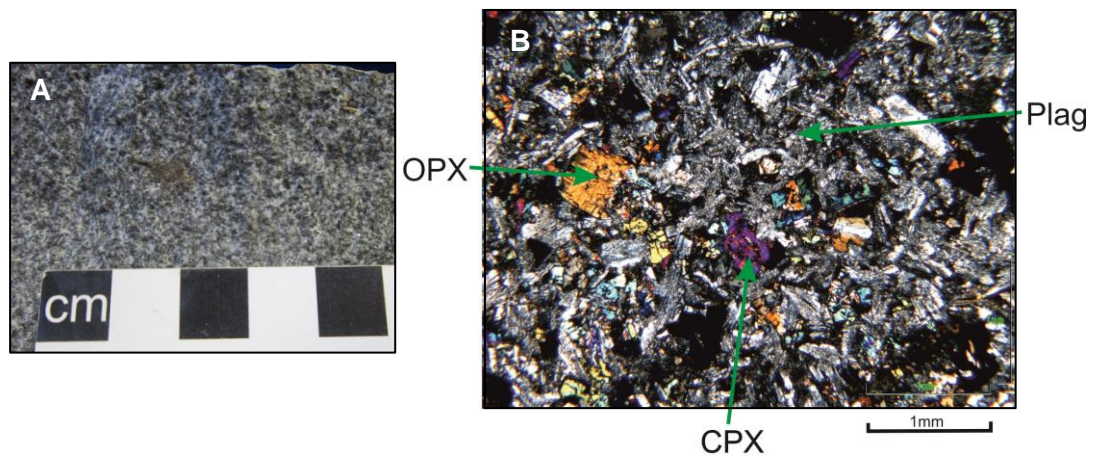
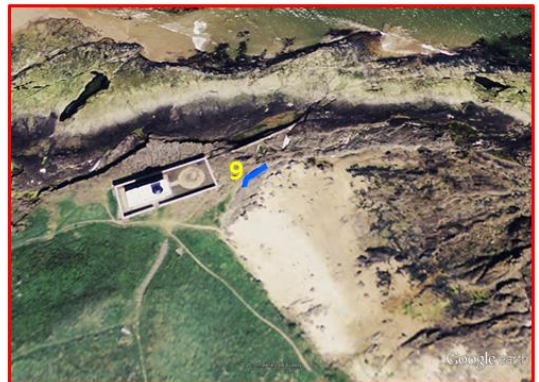
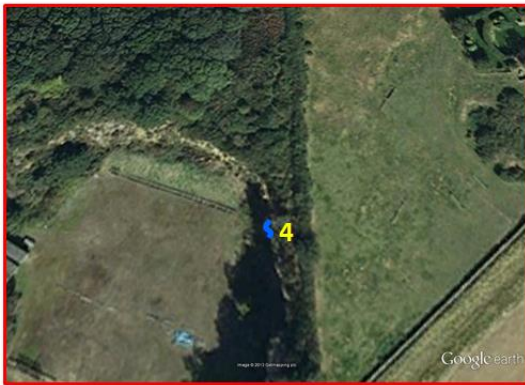


Figure 4.7: (A) Hand specimen of Whin Sill, illustrating a medium grained texture - hyperbyssal origin. (B) Thin section of Whin Sill, with scale bar of 1 mm, showing phenocrysts of orthopyroxene (OPX), plagioclase (Plag) and clinopyroxene (CPX) in groundmass dominantly formed of plagioclase, clinoproxene and magnetite.

4.5.1.2 Stardalur sill cluster geological background

The Stardalur sill cluster is part of the Stardalur volcanic system, which is situated in the Esja peninsula, SW Iceland. Lavas associated with this volcano were erupted ~1.7 Ma, followed by subsequent caldera collapse and glacial erosion exposing the sill cluster. The sills are emplaced within the Plio-Pleistocene Formation comprising of breccias, fine grained sediments, hyaloclastites and lavas (Fridleifsson, 1977; Pasquare` and Tibaldi, 2007). The sills have a micro-gabbroic composition (Fig. 4.9A; Pasquare` and Tibaldi, 2007) similar to that of the V`oring sills, and have well developed columnar jointing. Thin sections (Fig. 4.9B) show that the dominant



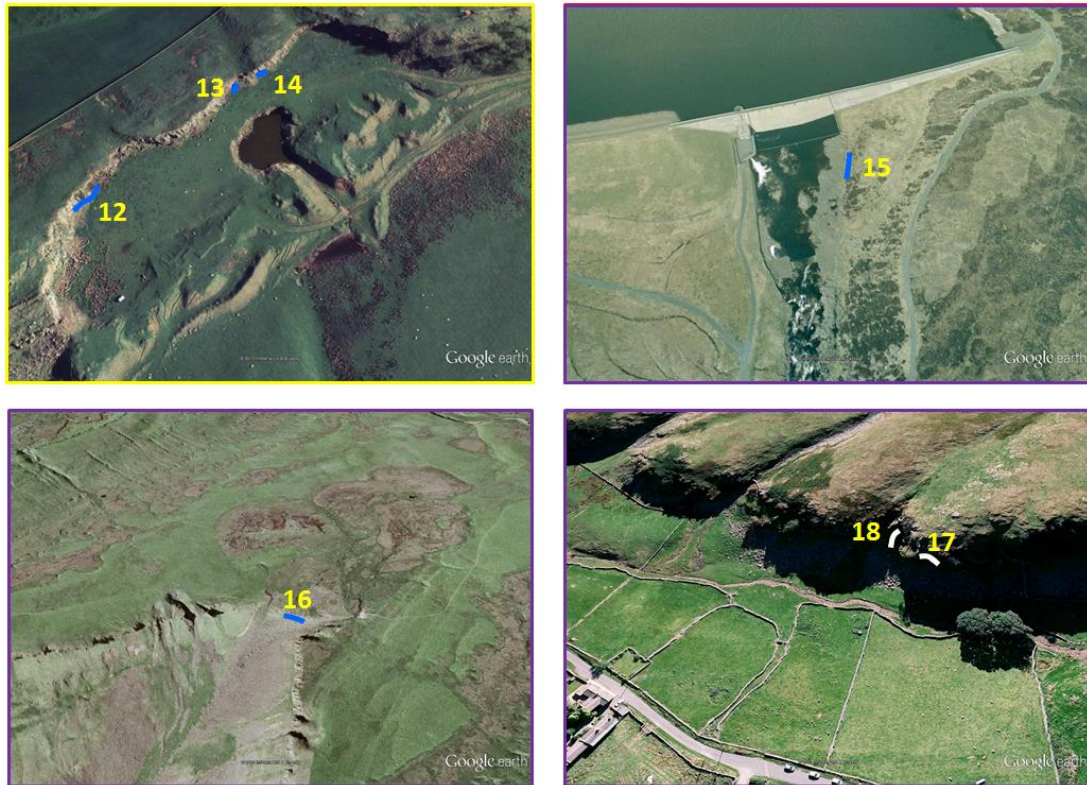


Figure 4.8: Google Earth images of profile lines (blue/white lines, also represent scale) where fracture measurements were taken. (1) Craster, view N, profile length 18 m, (2 and 3) Cullernose Point, view N, profile lengths 10 m, (4) Snableazes quarry, view N, profile length 5 m, (5 and 6) Holy Island, view N, profile lengths 10 m, (7 and 8) Bamburgh Castle, view N, profile lengths 2 m and 10 m respectively, (9) Harkess Rock, view N, profile length 10 m, (10) Ward's Hill quarry, view N, profile length 15 m, (11) Steel Rigg, view N, profile length 20 m, (12, 13 and 14) Walltown Crags, view S, profile lengths 16 m, 7 m and 8 m respectively, (15) Cow Green reservoir, view N, profile length 20 m, (16) High Cup Nick, view N, profile length 22 m, (17 and 18) Holwick Scars, view S, profile lengths 10 m and 12 m respectively. Image border colour relate to the top image in Figure 4.6 and specific parts of the sill complex.

phenocrysts are clinopyroxene, plagioclase and olivine with small opaque crystals in the ground mass. In hand specimen, the medium or coarse grained texture represents a shallow (hyperbyssal) depth of emplacement, and is also determined by the frequency of the columnar joints. The columns within the sills became rotated to having a more horizontal dip approaching the western part of the outcrop (e.g. profile 19-21).

The sills are stacked vertically and propagate from E-W, which relates to the extensional tectonic stress regime at the time of emplacement, where σ_3 trended N-S (Pasquarè ant Tibaldi, 2007) (Fig. 4.10). The field area was approximately 0.5 km²,

where 21 profiles were taken (Fig. 4.10). All fracture measurements and spacial variations were calculated from the 21 profiles, where sill thicknesses range from ~6-13 m. For a good comparison to the Whin Sill, a large data set was collected of approximately the same sample size, stated when interpreting results.

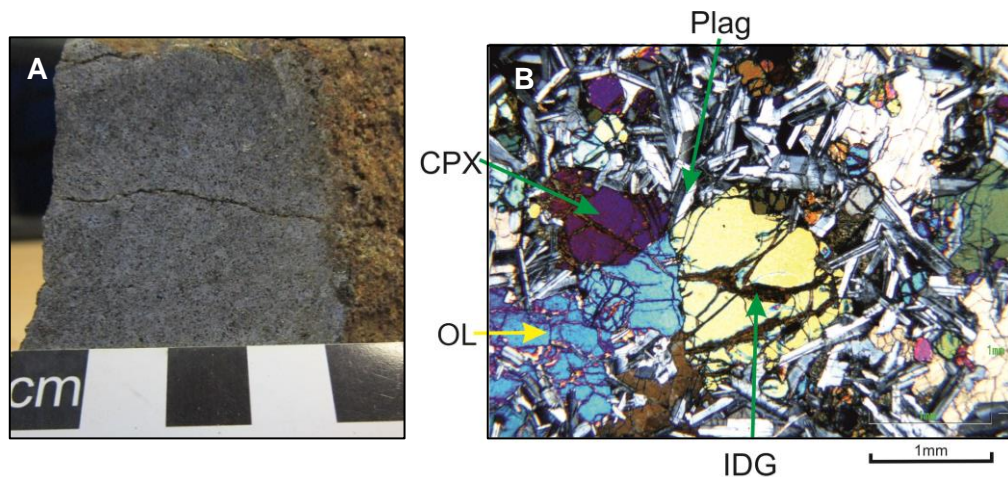


Figure 4.9: (A) Hand specimen of Stardalur sill, exhibiting a fine-medium grained texture of a hyperbyssal origin. (B) Thin section with large phenocrysts of olivine (OL), clinopyroxene (CPX), laths of plagioclase (Plag) and olivine altered to iddingsite (IDG), with 1 mm scale.

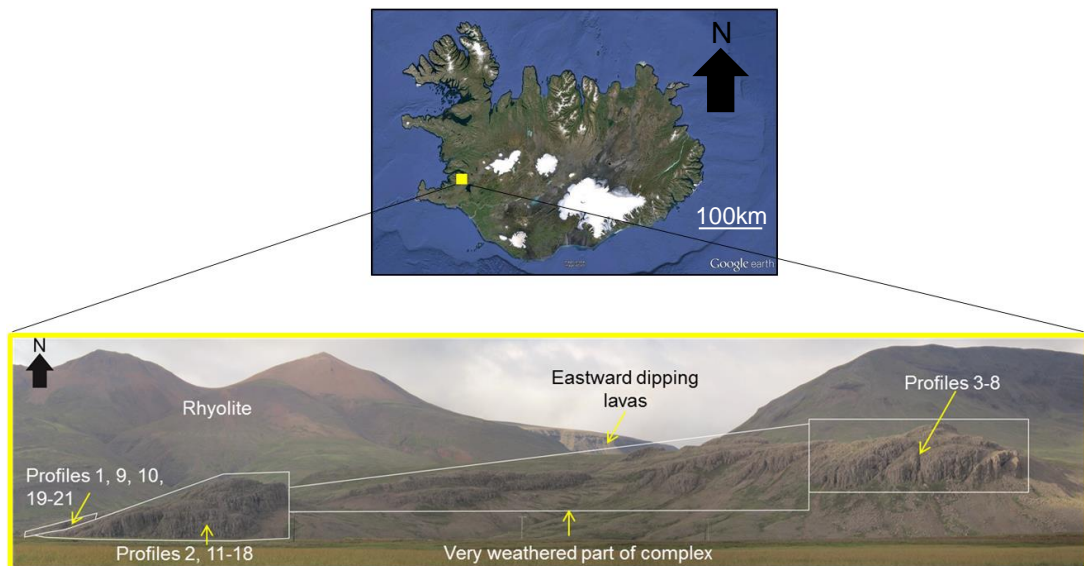


Figure 4.10: Google Earth image representing the location of the Stardalur sill cluster (yellow box), which is shown clearly by the photograph, illustrating the locations of profile lines taken across the cluster. Height of sill cluster in photograph is ~20 m.

4.5.2 Data analysing

4.5.2.1 *Rose diagrams and stereonets*

Orientations of fractures within the sills have been plotted on both rose diagrams and stereonets. This provides diagrams that presents the preferred orientation of the fractures irrespective of geographic location and variability across the field site (i.e. Whin Sill or Stardalur sill cluster).

Rose diagrams, a histogram where the orientation axis is about a circle, were plotted to show the direction in which the fractures were distributed. However, rose diagrams only display one aspect of the fracture attitude, here this was the strike. This was because only vertical, sub-vertical, horizontal and sub-horizontal fractures were plotted. Therefore, their dip was assumed to be kept constant to plot the rose diagram, and was of no limitation to the results. On the other hand, if the dip of the fracture was important then a stereonet was produced (Twiss and Moores, 2007).

Equatorial Equal-Area (Schmidt) stereonets were used as they presented no bias statistically and also plots could be compared, for example density distribution of the fractures. Poles to fracture planes were plotted rather than great circles and were represented as points on the plot. Generally, vertical fractures plotted around the perimeter of the stereonet projection, whereas horizontal fractures plotted across the diameter of the stereonet projection.

4.5.2.2 *Use of photographs*

Numerous photographs were taken in the field in order to calculate fracture frequencies and fracture lengths. These calculations were carried out using CorelDRAW X5, where each photograph was referenced to a scale included on the photograph (field assistant with a height of 1.8 m; head to waist of 1 m). With this scale, 1 m² area quadrats were drawn up and the fractures counted within. For fracture lengths, a line was traced along the fracture, which was then measured and calibrated to the given scale. However, this proved challenging in some cases, but estimating the uncertainty of the fracture measurements was harder because of the varying scales of the fractures.

4.5.2.3 Graphical plots: Fracture orientation; Fracture apertures; Fracture spacing; Fracture frequency

Graphical plots and statistical analysis was executed using SigmaPlot version 12.5 and Microsoft Excel 2010. Descriptive statistics mainly included arithmetic mean, median, range, standard deviation, but other statistics are mentioned in specific sections. Statistical tests, for example Pearson's correlation coefficient, were also conducted and are mentioned where necessary.

Chapter 5: Sill emplacement

5.1 Introduction

The principal mechanism for magma ascent through the crust is via dyke and sheet injection and propagation, at speeds of metres per second, and is well known throughout the literature (e.g. Lister and Kerr, 1991; Rubin, 1995). Dykes, both feeders and non-feeders, are an expression of an extending crust because they cause crustal dilation and, in addition, induce horizontal compressive stresses as a result of the magma overpressure (driving pressure). A feeder dyke is a dyke that brings magma to the surface to feed an eruption. Non-feeder dykes on the other hand, become arrested and never reach the surface. In the field there is normally no noticeable difference in these two dykes, but their geometries differ because of the effects of the free surface on the feeder dyke and also the over pressure, so that they differ close to the surface (Geshi *et al.*, 2010).

Geshi *et al.* (2010) carried out a study on Miyakejima Volcano, Japan of 165 dykes in the caldera walls. They observed that the non-feeder dykes tapered away within layers or were arrested bluntly at contacts in between layers. This is supported by Gudmundsson and Brenner (2005) who carried out thousands of measurements on arrested dykes and inclined sheets in Iceland and Tenerife, Canary Islands, where at a contact the dykes tended to either thin out and end abruptly, or became offset and propagated higher in the sequence. For example Figure 5.1A, which shows the dyke tip tapering away vertically. Geshi *et al.* (2010) also noted that feeder dykes are connected to spatter cones. This can be seen in Tenerife, where a feeder dyke reaches the surface, marked by a crater in the caldera walls of Las Cañadas (Fig. 5.1B). It can therefore be said that non-feeder geometries indicate an approximate overpressure within the dyke that controlled the mechanics of the dyke propagation, whilst feeders reflect conditions at the time of eruption.

Field studies and seismic imaging illustrate how the upper crust is layered, that is, it is heterogeneous and anisotropic. They show how dyke and sill complexes are not just injected into stratovolcanoes (Gudmundsson, 2011a, b; Gudmundsson, 2012b), but also into sedimentary basins, for example Vøring and Møre Basins, offshore

Norway (e.g. Skogseid, 1994; Brekke, 2000; Thomson and Hutton, 2004; Planke *et al.*, 2005; Hansen and Cartwright, 2006; Fjeldskaar *et al.*, 2008), and the Karoo Basin, South Africa (Chevallier and Woodford, 1999; Malthe-Sørenssen *et al.*, 2004; Galerne *et al.*, 2008; Polteau *et al.*, 2008a; Arnes *et al.*, 2011; Galerne *et al.*, 2011). These layers have different mechanical properties: (1) The modulus of elasticity, namely Young's modulus, which measures the stiffness of an elastic material. Stiffness of layers is a descriptive term for Young's modulus, and in relation to the heterogeneity of the Earth's crust describes soft (or compliant) and strong layers, that is, soft layers have a low Young's modulus, for example hyaloclastite has a Young's modulus of ~ 4 GPa, and strong layers have a high Young's modulus, for example gabbro has a Young's modulus of ~ 70 GPa. (2) Toughness of a rock is the area under the stress-strain curve (Fig. 3.2). In geology toughness is described by fracture toughness and material toughness. Fracture toughness is the critical stress intensity factor for a fracture to propagate, and material toughness is the critical energy release rate for a fracture to propagate. A fuller description of these terms is provided in Chapter 3.

Commonly rift zones and volcanic edifices are composed of lava flows (stiff) and pyroclastic flows (most, comparatively soft, except those that are welded). On the other hand, sedimentary basins have varying lithologies of sandstones (stiff) and shales (soft), for example. Furthermore, there are contacts between these alternating layers, which are either weak (that is to say, they are not welded and have the ability to open up, which is common at shallow depths), or have become strong as a result of welding. When a propagating dyke meets a weak contact it tends to be arrested or offset due to a contrast in mechanical properties (Fig. 5.1A), but when a propagating dyke meets a strong contact it tends to continue on its near vertical path.

5.1.1 Dyke initiation and propagation

A fundamental yet basic question is whether dykes propagate via existing weaknesses or fractures, or whether they produce a propagation path of their own irrespective of host rock weaknesses. The first scenario would produce variable dyke orientation, whereas the latter would favour a dyke with a near vertical path along the direction of the maximum principal compressive stress. We see both scenarios in

the field. Generally, dykes produce their own paths, but use existing weaknesses when suitable from an energy point of view, that is a path of least resistance.

For a dyke to transport magma it must originate from the source of the magma, either a deep reservoir or a shallow chamber. For a dyke to initiate from a magma chamber Eq. (5.1) below must be satisfied (Gudmundsson, 2012a):

$$P_t = \sigma_3 + T_0 \quad (5.1)$$

where P_t is total pressure, T_0 is the tensile strength of the host rock and σ_3 is the minimum principal compressive stress, which depends on the stress concentrations at the magma source (Jaeger *et al.*, 2007; Gudmundsson, 2012a). The propagation of a dyke is then dependent on the local stresses of the adjacent country rock, and most importantly the stress concentrations at the tip of the dyke, which would determine the path in which the dyke may follow.

Taking Eq. (5.1) into account, an equation for fracture formation can be formulated, which can be written as:

$$U_t = \Pi + W_s \quad (5.2)$$

where U_t is the total energy of the volcano, Π is the potential energy and W_s is the surface energy associated with dyke-fracture propagation (positive because it is the energy put into the system to generate the new surfaces for the propagating dyke) (Gudmundsson, 2012b). For a dyke or inclined sheet to form, the total energy present in the volcanic edifice must be kept constant or decrease. So, in order for the dyke to propagate, an area (dA) must be formed, where U_t is constant, so Eq. (5.2) can be rewritten as (Gudmundsson 2012b):

$$\frac{dU_t}{dA} = \frac{d\Pi}{dA} + \frac{dW_s}{dA} = 0 \quad (5.3)$$

where, the energy available (energy release rate, G) is denoted in Eq. (5.4) allowing for dyke propagation and extension due to the material toughness, G_c , of the host rock in Eq. (5.5) (Gudmundsson, 2012b):

$$G = -\frac{d\Pi}{dA} \quad (5.4)$$

$$G_c = \frac{dW_s}{dA} \quad (5.5)$$

As the dyke propagates the stored strain energy decreases (described by Eq. (5.4)), implying stable fracture propagation because of constant displacement boundary conditions (outer boundaries of the volcanic rift zone are fixed, that is, they do not move during dyke propagation). In contrast, constant load boundary conditions (stress, pressure and force are maintained during dyke propagation, that is, the boundaries of the volcanic rift zone are flexible during dyke propagation) implies unstable fracture propagation. This is because the strain energy of the volcano increases as the dyke propagates. Therefore, when a magma chamber inflates and the outer boundaries are flexible, more energy is available in the system to drive dyke propagation. Hence, G can increase, stay constant or decrease depending on the boundary conditions (Gudmundsson, 2012b). Potential stored energy is the main mechanism within a volcano that generates the formation of a feeder dyke and not just the thermal energy. The potential stored energy is within the layered strata when a volcanic edifice is loaded, for example inflation of the magma chamber (Mogi, 1958; Gudmundsson, 2012b).

Also, as a dyke is a type of extension fracture, it propagates primarily vertically as they are perpendicular to the minimum principal compressive stress irrespective of their geometry (i.e. field studies show that many dykes have an irregular or sinuous geometry) (Pinel and Jaupart, 2004). Numerical models show that at the lateral ends of a dyke there are large crack-tip tensile stresses generated by a large overpressure allowing the dyke to propagate further. This small area of large crack-tip tensile stresses can be described as a process zone at the tip of a propagating dyke, where

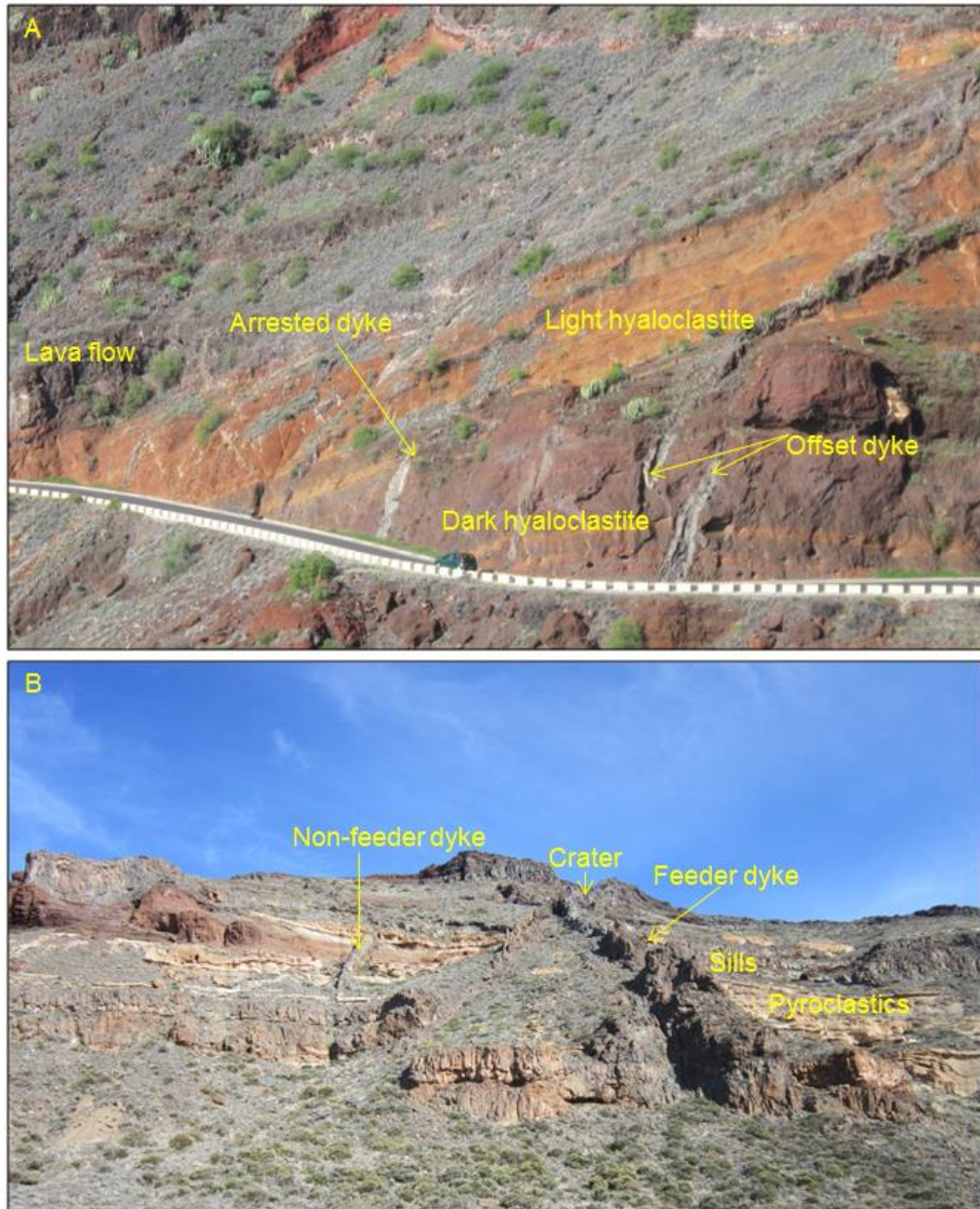


Figure 5.1: (A) Arrested and offset dyke tip in the road section along the Anaga peninsula, Tenerife, Canary Islands. These dykes cut through hyaloclastite rocks and are arrested either at the lighter hyaloclastite or at the overlying lava flow. View N, a car provides a scale with the dykes having a thickness of ~ 1.5 m. (B) Feeder dyke reaches surface transecting pyroclastic layers in the caldera walls of Las Cañadas, Tenerife, while a dyke to the left is arrested (non-feeder). View E, with this caldera wall face reaching heights of ~300 m.

microcracking and some plastic deformation occurs. Within this process zone fractures are formed and old ones reactivated allowing for further growth or propagation of the dyke. However, in a heterogeneous crust a dyke may be

temporarily arrested, until the overpressure increases filling the tip of the dyke (as the magma front lags behind dyke tip) and hence increases the tensile stress at the tip. When this is greater than the tensile strength of the host rock, the dyke can continue to propagate vertically (Gudmundsson and Brenner, 2001; Geshi *et al.*, 2012).

5.1.2 Dyke propagation at a weak contact

Field studies in Tenerife and Iceland along with works by Marinoni and Gudmundsson (2000), Gudmundsson (2002) and Geshi *et al.* (2010), show that the majority of dykes do not reach the surface, but are arrested at varying crustal levels. Dyke arrest can be explained on a regional and local scale. On a regional scale, (1) partly because of abrupt variations in Young's moduli across contacts, and (2) partly because of an overall lower Young's modulus, and hence less relative tensile stress concentration in the rift-zone layers at shallow than at great crustal depths (Gudmundsson and Brenner, 2004; Geshi *et al.*, 2010). On a local scale, for example volcanic edifices and sedimentary basins, dykes become arrested due to the local stress fields (stress barriers) and mechanical heterogeneity and anisotropy, which are irregular in comparison to a rift zone.

This chapter focuses on dyke propagation on a local scale. When a dyke meets a subhorizontal contact there are three possible outcomes (Fig. 5.2): (1) the dyke may become arrested (Fig. 5.2A), which is common when there is a large contrast in elastic properties, mainly the stiffness of the rocks, referred to as elastic mismatch. (2) The dyke may penetrate the contact (Fig. 5.2B), a necessary condition for a dyke to propagate to the surface. If the dyke penetrates the contact, it may become offset and vary in thickness between the different layers due to their varying stiffnesses. (3) The dyke may be deflected at the contact either in one direction (single deflection, Fig. 5.2C) or in two directions (double deflection, Fig. 5.2D), common in areas of extension. Generally, a dyke may penetrate the contact if the layers above and below the contact have the same stiffness, but is arrested or deflected if there is a large difference in stiffness between the enclosing layers. For a sill to form, the local horizontal compressive stress must be higher than the local vertical compressive stress (Anderson, 1951).

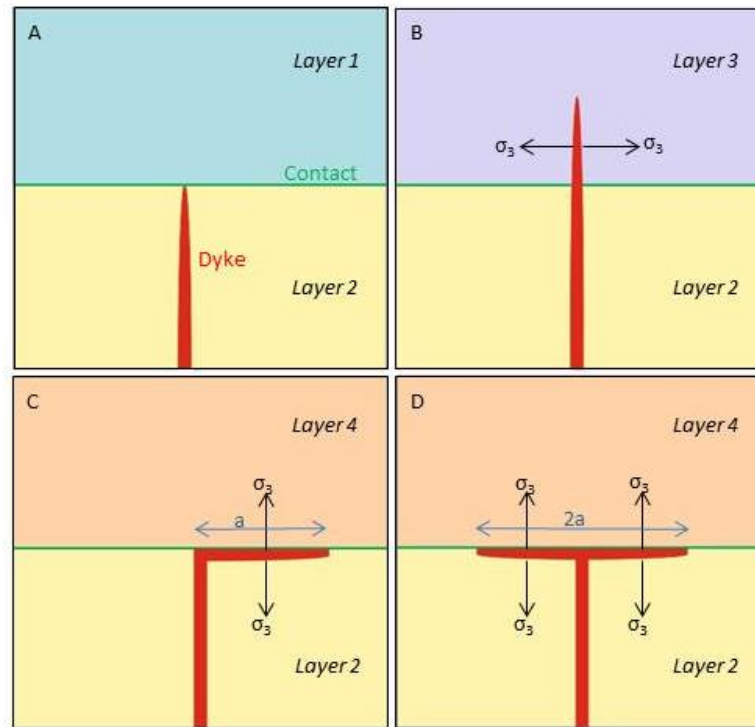


Figure 5.2: When a dyke meets a contact (discontinuity) it either may be (A) arrested, (B) penetrate the contact or become deflected either (C) singly or (D) doubly, where ‘a’ is the length of the sill. Layers 1 and 4 are stiffer than layer 2 providing a stress barrier due to elastic mismatch and layer 3 is the same stiffness as layer 2. σ_3 represents the minimum principal compressive stress allowing for sill emplacement (Barnett and Gudmundsson, 2014).

The aim of this chapter is to aid knowledge and understanding of the processes governing deflection of a dyke into a sill. This is because it is fundamental to understand the conditions for dyke arrest or propagation to the surface during periods of unrest as they can help assess the potential for volcanic eruptions (hazards and risks).

5.2 Sill formation hypotheses

Sills tend to be of a basic composition and therefore must be sourced from depths greater than that at which they are emplaced. Therefore, the majority of sills are fed by dykes or inclined sheets, so that the formation of a sill represents geometric rotation (Gretener, 1969). There are two main hypotheses for sill formation, either by neutral buoyancy (Corry, 1988) or by stress rotation (Roberts, 1970), also referred to

in the literature as the hydrostatic hypothesis and the tectonic hypothesis respectively.

5.2.1 Neutral buoyancy hypothesis

The hypothesis for neutral buoyancy is that the vertical ascent of magma through a dyke overshoots the level of neutral buoyancy and magma ascent stops due to tensile stresses (Francis, 1982; Corry, 1988; Ryan, 1993). However, the hypothesis for neutral buoyancy is contradicted by 3D seismic data and field studies (Cartwright and Hansen, 2006; Menand, 2008). This is because individual sills are seen to be emplaced at different levels within the stratigraphy, where some sills feed adjacent sills with magma. This was studied by Cartwright and Hansen (2006) who noticed stacked sills at different levels within the Earth's crust that are interconnected by sill junctions. They concluded that the vertical transport of magma could occur over a large lateral range (up to 10 km) through the upper crust, because sill complexes have the ability to develop continuous magma networks.

The level of neutral buoyancy alone is not sufficient to describe sill emplacement. However, in some cases the level of neutral buoyancy may arrest vertical dykes and deflect them laterally as seen in laboratory experiments, for example between crystalline basement rocks and overlying sediments (Fig. 5.3; Lister and Kerr, 1991; Pinel and Jaupart, 2004; Taisne and Jaupart, 2009). However, the role of buoyancy has been developed by Taisne and Jaupart (2009), who show that a dyke propagating through a low density layer can develop an overpressure favouring horizontal propagation as a sill, but this low density layer needs to have a thickness in the order of <700 m - 2 km. Such thicknesses are not commonly observed, even in sedimentary basins, thus sill emplacement cannot be explained by the level of neutral buoyancy alone.

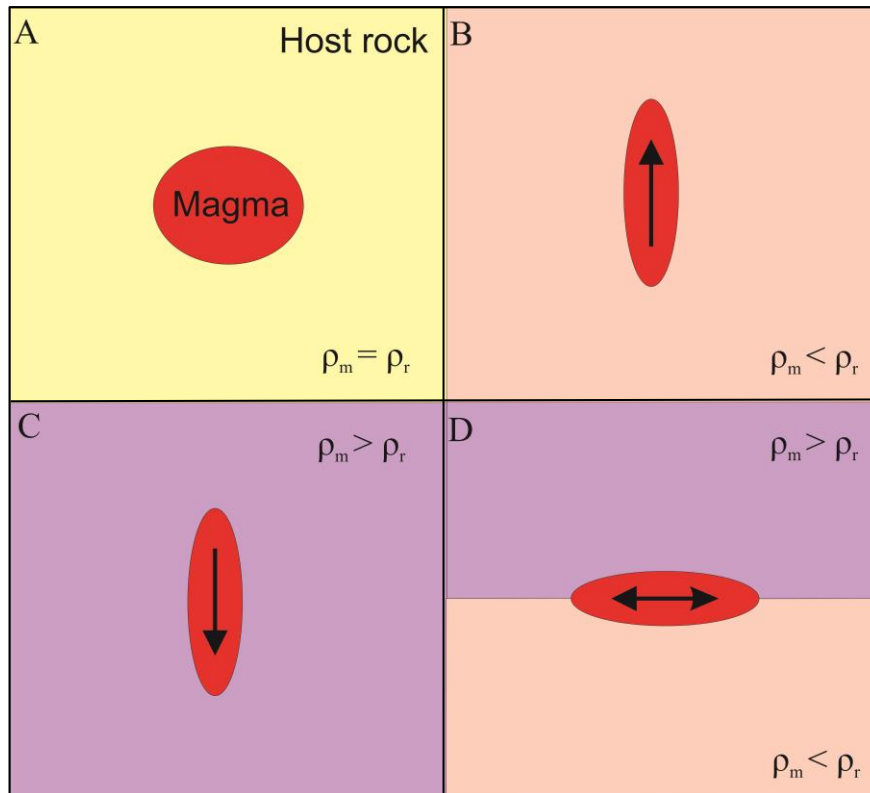


Figure 5.3: Magma transport is governed by magma density, ρ_m relative to the density of the host rock, ρ_r , and the excess pressure in the source chamber. (A) Magma is neutrally buoyant and will neither rise or fall; (B) magma is positively buoyant and will rise through the crust; (C) magma is negatively buoyant and will descend through the crust; (D) the magma is denser than the overlying strata and less dense than the underlying strata and will be transported laterally at the level of neutral buoyancy (modified from Lister and Kerr, 1991).

5.2.2 Stress rotation hypothesis

The hypothesis of stress rotation is as follows: for a sill to be fed by a dyke there must be a stress rotation from horizontal tension at deep levels to horizontal compression at shallower levels, that is, the minimum principal stress acting perpendicular to the dyke will become the maximum principal stress for sill emplacement, and the maximum principal stress acting parallel to the dyke will become the minimum principal stress (Anderson, 1951; Roberts, 1970). The theory of stress rotation by Roberts (1970) was not in agreement with Bradley's (1965) earlier hypothesis for sill emplacement in a sedimentary basin. This was due to gravitational processes where magma flowed beneath sedimentary strata because of the magma's larger density, governed by the principles of isostasy. Bradley (1965)

stated that to preserve equality in magmatic pressure and lithostatic pressure of the overlying strata, either (1) sheet intrusions were higher in the lithosphere due to surface depressions or (2) sheet intrusions were lower in the lithosphere due to surface elevations. However, Roberts (1970) contradicted this as a surface load would deform the local stress field due to gravitational forces acting upon the overlying strata. The deformation can be described using the maximum principal stress trajectories, which are deflected upwards due to surface elevations or deflected downwards due to surface depressions.

A well-known analogy for stress rotation, that is, sill formation, is hydraulic fracturing in the oil industry. Although the initiated fracture is Man-made it will align itself with the minimum principal stress exactly mirroring that of a natural fracture.

5.3 Numerical models

Based on field studies, numerical models are constructed to be able to test the idea set out in Figure 5.4, for when a dyke meets a weak contact. The question to be answered here is, 'when a dyke or inclined sheet approaches a weak contact, will the contact open up and potentially change a dyke into a sill or not?' To understand the interaction of a dyke with a contact, two scenarios are tested. Firstly, a strong contact (Figs. 5.5 and 5.6) and secondly, a weak contact (Figs. 5.7 and 5.8), to see the effects on the dyke propagation path at a contact with different properties. The element size of the mesh is kept constant with a maximum element size of 0.02 km, and minimum element size of 3.2×10^{-5} km. The model outputs will demonstrate: (1) the predicted path of the dyke according to the maximum principal compressive stress trajectories and (2) the local stress regime induced by the propagating dyke.

5.3.1 Young's modulus contrast between layers

It is well known that numerical modelling of the crust as homogenous and isotropic does not yield accurate results with regards to hydrofracture modelling, and that heterogeneity in the crust cannot be taken into account by analytical solutions, that

is, stress fields and layering. The first numerical model is set out to demonstrate how layering affects a propagating dyke where the contacts are strong and do not have the ability to open up. It is known that many dykes propagate parallel to the maximum compressive stress, and therefore, a favourably orientated local stress field is needed in order for the dyke to continue on a vertical or inclined path. It is also known that at shallow depths within the crust there is a large contrast in elastic properties due to mechanical layering. It is this vertical contrast in elastic properties that give rise to stiffness contrasts.

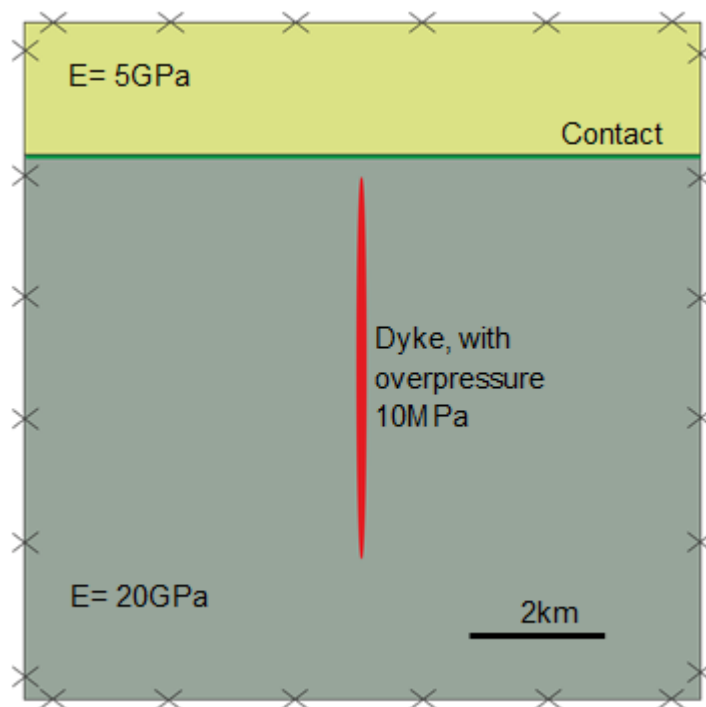


Figure 5.4: Geometry of numerical models produced in Figures 5.6; 5.7; 5.8 with a fixed dyke length. Edges of the model have been fixed represented by x's, but this is only a schematic illustration and the boundaries are much further away from the dyke in the model run in COMSOL as to avoid boundary effects (Barnett and Gudmundsson, 2014).

The first model analysed dyke ascent from alternating soft (low rigidity), and stiff (high rigidity) layers. It is composed of eleven layers where the dyke only propagates through eight of them. Each layer has an alternating Young's modulus (stiffness) from 5 GPa (soft; layer A) to 20 GPa (stiff; layer B) with a constant density and overpressure (Chapter 4; Gudmundsson, 2011a). The contacts are modelled as being

strong and therefore, do not have the ability to open up. The model was then fixed on all boundaries so that they were not allowed to move.

The main result from the model is the deformation applied to the dyke (the white area surrounding the dyke in Figure 5.5). When the dyke meets a contact it changes shape, and that shape relates to the stiffness of the layer. When the dyke propagates through a stiff layer the aperture thins or becomes concave, whereas when it propagates through a softer layer the aperture thickens or becomes convex. To be more specific, it can be seen that as the dyke approaches the contact small changes occur to the aperture. Then as the dyke propagates through the contact more significant changes in aperture occur, where we see thinning or thickening. The graph on the inset of Figure 5.5 represents the opening displacement of the dyke, that is, half of the dyke aperture, which illustrates the same conclusion - that the smallest aperture of the dyke is within the stiffer layer. It is to be noted here that the size of displacement is very small, on the order of millimetres, for a dyke on the order of a few metres long.

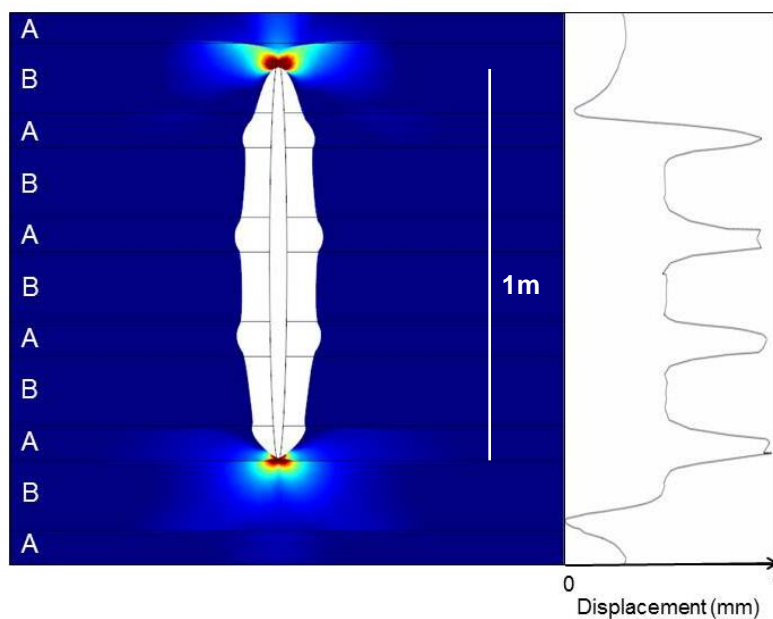


Figure 5.5: FEM model of a dyke (1 m) propagating through interchanging soft, 5 GPa (A) and stiff, 20 GPa (B) layers showing contours of tensile stress. The focus within this model is the white area surrounding the dyke representing the deformation of the dyke. Here we see that in the softer layers the dyke aperture is the greatest, that is, it has the largest deformation and that the stiff layers yield a smaller dyke aperture, that is, it has the smallest deformation. This is represented graphically (inset) showing the opening displacement of the dyke, with a constant overpressure of 10 MPa and shows again that the largest aperture of the dyke occurs in the softer layers ~1 mm.

Figure 5.6 considers the path of a dyke and inclined sheet on meeting a strong contact (does not have the ability to open up) between two adjacent layers of different Young's moduli (Fig. 5.4). Both Figure 5.6A and B show that there is little or no deviation of the hydrofracture path from its original vertical or inclined path as illustrated by the maximum principal compressive stress trajectories.

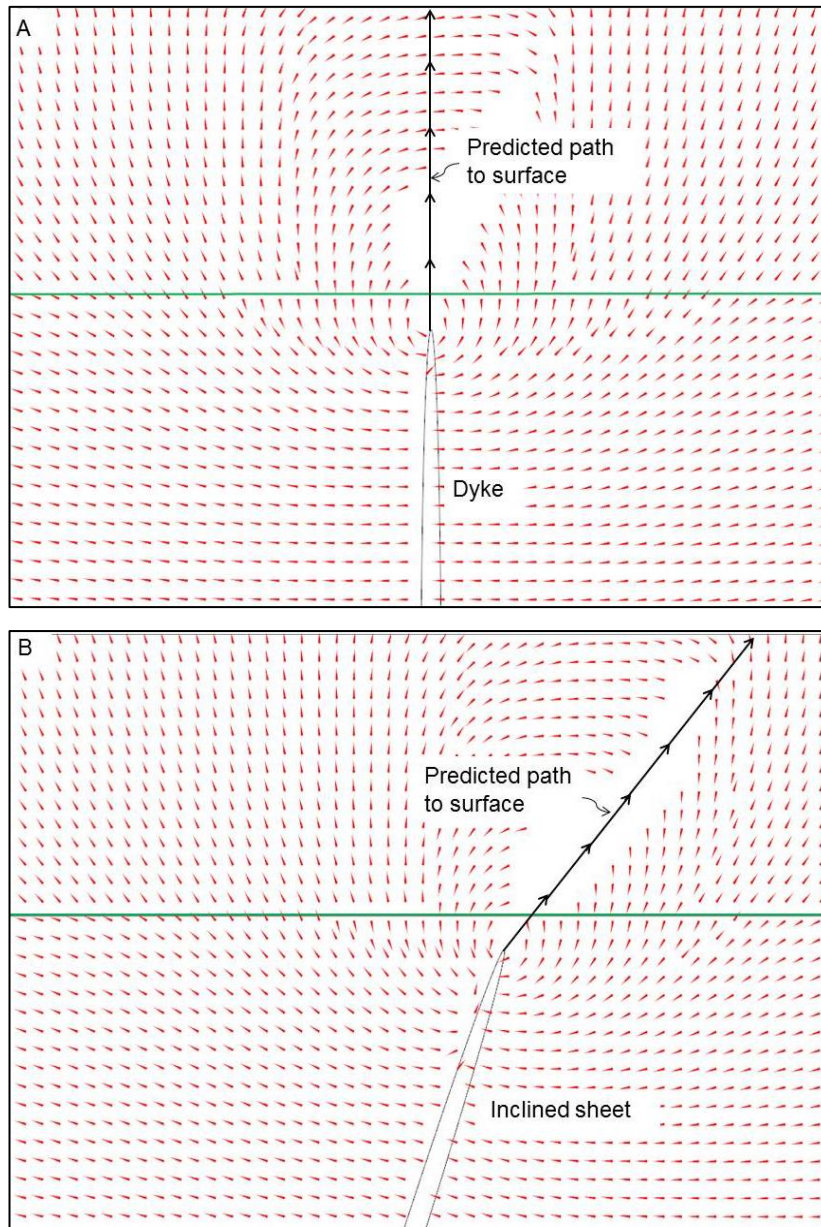


Figure 5.6: FEM models showing maximum principal stress trajectories and are modelled based on Figure 5.4. The trajectories (red ticks) are curved about the tip of (A) a vertical dyke and (B) an inclined sheet, allowing for further propagation towards the contact. The black arrows represent the predicted path of the dyke or inclined sheet towards the next layer or to the Earth's surface. Here, the contact does not have the ability to open up and the path of the propagating dyke or inclined sheet remains unaltered. The white areas are stress shadows.

5.3.2 Weak contacts

Sill emplacement has been known to follow planes of weaknesses or openings since the mid-20th Century (Mudge, 1968 and references there-in), thus in agreement with the stress rotation hypothesis. Therefore, it can be said that sill emplacement is encouraged when the contacts are weak and have the ability or potential to open up, otherwise regarded to as low fracture toughness. The second set of numerical models look at a weak contact where the mechanical properties of the layers are kept the same as in Figure 5.4. In Figure 5.7 the tensile stresses concentrate on the underside of the weak contact, but the distribution of these stresses is dependent on the angle at which the dyke or inclined sheet makes with the weak contact. Sheet interaction with the weak contact occurs a small distance away from the contact, and therefore opens up prior to sheet deflection. When the dyke approaches the contact perpendicularly (Fig. 5.7A), tensile stresses are equally distributed on either side of the propagating dyke, and above the dyke tip the contact begins to open up symmetrically (Cook and Gordon, 1964). Thus, allowing for the formation of a symmetrical sill (double deflected dyke). On the other hand, when an inclined sheet meets the contact at 45° (Fig. 5.7B), tensile stresses are concentrated to the right of the inclined sheet. It is in this region above the tip of the inclined sheet and to the right of it that the weak contact opens up.

Maximum compressive principal stress trajectories, σ_1 , are also analysed for the boundary conditions set in Figure 5.8, where a dyke or inclined sheet propagates towards a weak contact (layer above is soft, 5 GPa, and layer below is stiff, 20 GPa), where the dyke has a constant overpressure of 10 MPa. These trajectories show where extension occurs, in this case where the weak contact begins to open up (Cook and Gordon, 1964). Here, the σ_1 stress trajectories are perpendicular to the contact, where extension occurs allowing for sill emplacement.

A final model investigated the predicted path of a dyke through mechanically-layered crust. Here four layers with varying Young's moduli are modelled. The layer hosting the dyke is the stiffest with a value of 20 GPa followed by a softer layer of 2 GPa, with another adjacent stiffer layer of 5 GPa and 10 GPa. This mechanical layering has been chosen as it is known that the arrest or deflection of dykes and inclined sheets can occur at boundaries between stiff and overlying soft layers, and

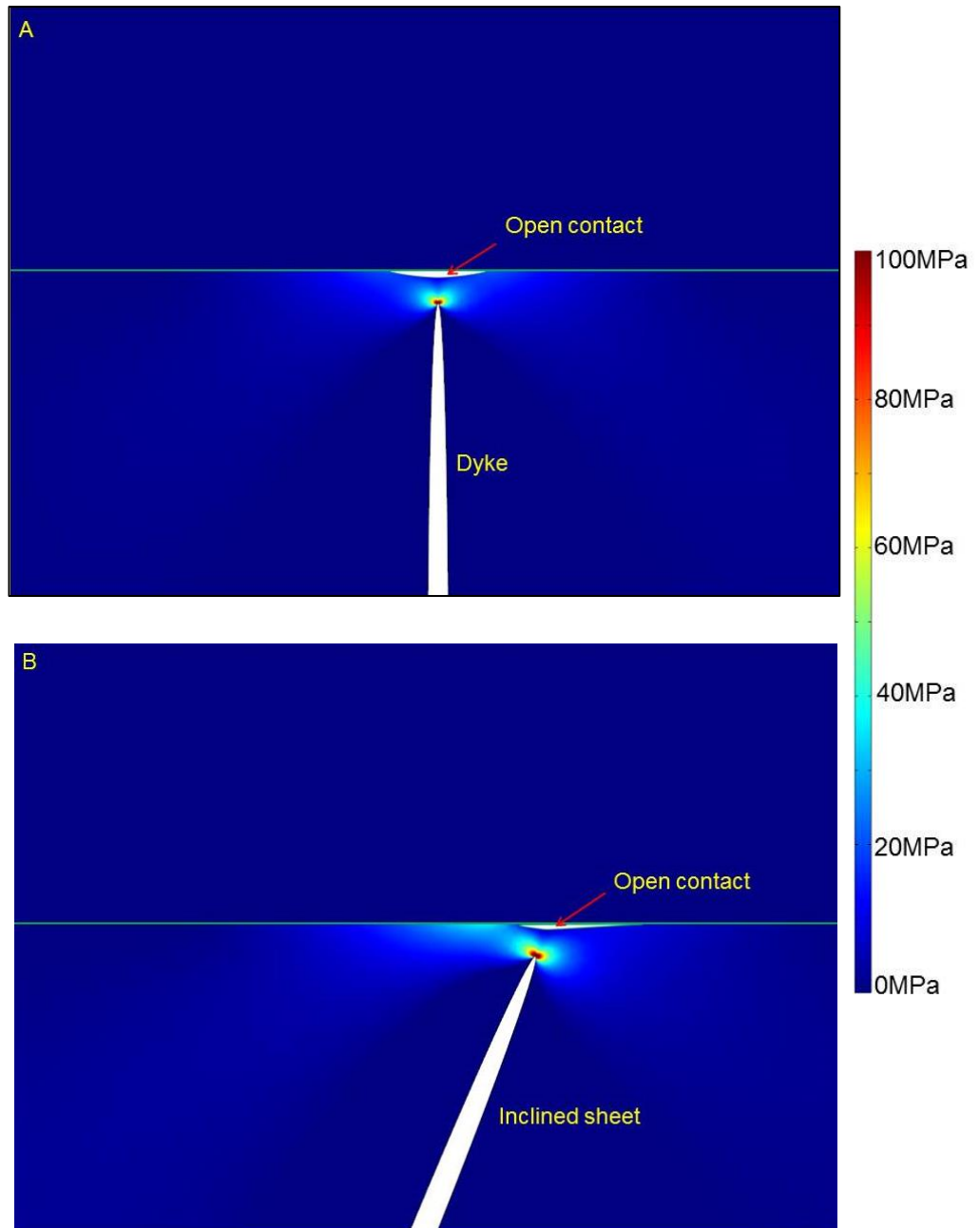


Figure 5.7: FEM models showing tensile stresses in mega pascals based on the schematic illustration in Figure 5.4. (A) Propagating dyke towards a weak contact induces large tensile stresses ahead of the dyke tip. This causes the contact to open up symmetrically for the double deflection of the dyke into a sill. (B) Propagating inclined sheet at 45° to the weak contact induces tensile stresses to the right of the sheet causing the contact to open up asymmetrically and the single deflection of the dyke into a sill (Barnett and Gudmundsson, 2014).

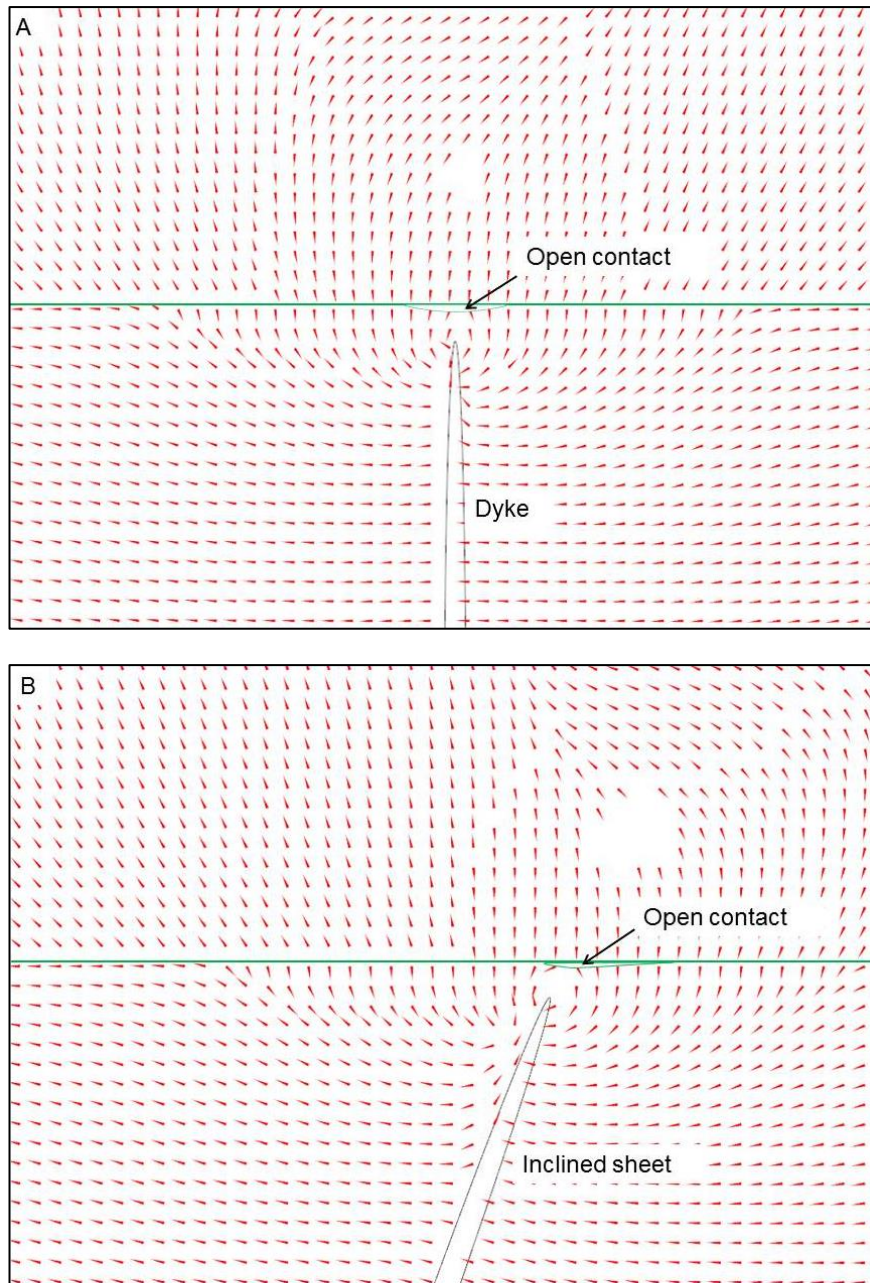


Figure 5.8: FEM models showing maximum principal stress trajectories. The trajectories are curved about the dyke/sheet tip allowing for further propagation towards the contact. (A) and (B) are the same model as shown in Figure 5.7. Here, illustrated the contact is opened up, in green, perpendicular to the propagating dyke/sheet allowing for the emplacement of a sill at the weak contact. The white areas are stress shadows (Barnett and Gudmundsson, 2014).

soft and overlying stiff layers (Gudmundsson and Brenner, 2001; Gudmundsson, 2011b; Geshi *et al.*, 2012). The uppermost boundary is not regarded as a free surface and is therefore fixed. Figure 5.9 illustrates the emplacement of a stepped sill; when

the dyke reaches the 2 GPa layer it continues on a vertical path and does not deviate away from its original path. However, when meeting a stiffer layer of 5 GPa the dyke is deflected into a symmetrical sill. The sill continues on this path along the weak contact for a short distance before deviating along an inclined path, which is more favourable. This inclined path is followed until the inclined sheet reaches the next layer (10 GPa) and once again is deflected into an asymmetric sill.

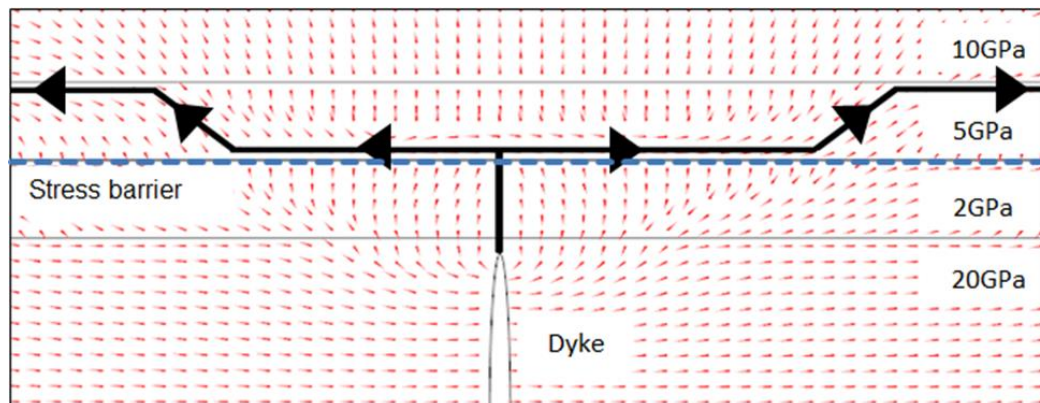


Figure 5.9: FEM model illustrating the effects of a stress barrier. The dyke can propagate through the softer layer, but when meeting the layer with a higher Young's modulus of 5 GPa the dyke is unable to propagate vertically as it meets a stress barrier. The dyke becomes deflected into a sill at this boundary as the maximum principal compressive stress has been rotated ninety degrees from being vertical to being horizontal. The interaction with the adjacent 10 GPa layer the sill follows an inclined path before being deflected once again as a sill due to a stiffer upper layer (Barnett and Gudmundsson, 2014).

5.4 Discussion: Sill emplacement mechanisms

Sill emplacement is controlled by several factors including the magmatic overpressure (and other magmatic driving forces, e.g. buoyancy), local stress field orientation, host rock mechanical properties (elasticity) and most importantly the strength of the contact between two differing horizons. Mechanical layering can cause a dyke to be deflected at a weak contact (interface) with reference to three mechanisms: (1) Cook-Gordon debonding (Cook and Gordon, 1964) (2) stress barriers (Anderson, 1951) and (3) elastic mismatch between layers in contact with each other (He *et al.*, 1994). All these mechanisms can act simultaneously, but any one may dominate. They depend on factors including the principal stresses being rotated at a contact, induced tensile stresses ahead of the propagating dyke tip

relating to the Cook-Gordon debonding mechanism, and finally the mechanical and material properties of the contact and surrounding host rock relating to material toughness and elastic mismatch.

5.4.1 Cook-Gordon debonding

In both scenarios presented, that is, a strong contact (Fig. 5.6) and a weak contact (Figs. 5.7 and 5.8) the crust is modelled as heterogeneous, with results illustrating the contact between two different layers. First, the contact is strong (Fig. 5.6) and does not have the ability to open up or be deformed. The model also shows that the dyke or inclined sheet do not deviate away from the vertical or inclined plane. However, this is not the case when modelling a weak contact (Figs. 5.7 and 5.8), which shows the predicted dyke or inclined sheet path to deviate towards the horizontal. Here it can be demonstrated that the contact opens up, and the dyke or inclined sheet has the ability to transform into a sill, depending also on the local stress field, that is, the rotation of the principal stresses (He *et al.*, 1994; Hutchinson, 1996). From these numerical results it can be interpreted that it is the large tensile stresses induced ahead of the dyke tip causing the opening of the contact that allows for the refraction of the dyke, referred to by Maccaferri *et al.* (2010) as the ‘refraction phenomenon’. This mechanism has also been supported by analogue models, for example Kavanagh *et al.* (2006).

The opening of the weak contact (Figs. 5.7 and 5.8) and the geometry of the opening is a consequence of the Cook-Gordon debonding mechanism leading to the cessation of propagating dykes or inclined sheets. For a homogenous rock, the induced tensile stress is approximately 20% of the dyke-perpendicular stress and located ahead of and parallel with the propagating dyke (Cook and Gordon, 1964; Gudmundsson, 2011b; Gudmundsson and Løtveit, 2012). This may allow the weak contact of varying attitudes to open up ahead of the dyke tip at varying distances (Fig. 5.10); a possible scenario for sill formation at shallow depths within the crust. Recent studies, for example Gudmundsson and Brenner (2001), Gudmundsson (2002) and Gudmundsson (2011b), illustrate that the Cook-Gordon debonding mechanism is important and that it is the tensile strength of the contact, which governs whether debonding will take place, that is, the tensile stresses of the contact are greater than their tensile strengths providing there is a favourably orientated contact. This

mechanism has also been illustrated via analogue modelling, for example Xu *et al.* (2003); Wang and Xu (2006).

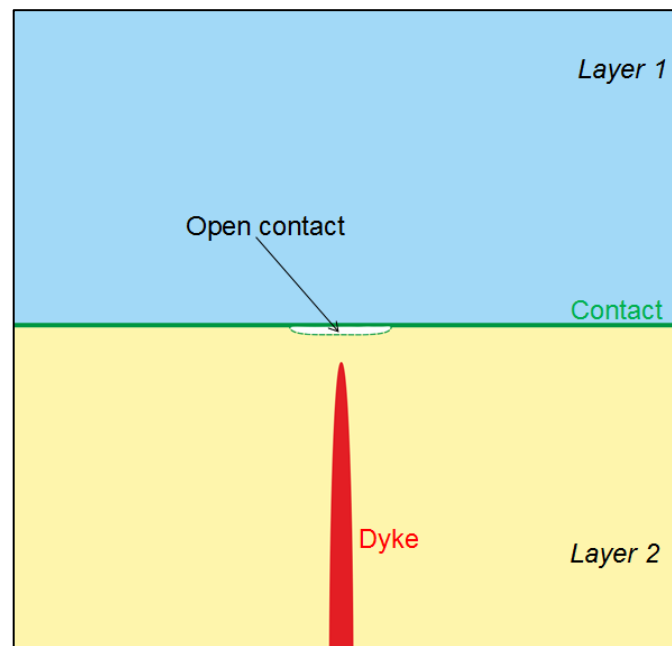


Figure 5.10: A conceptual model demonstrating the opening of a weak contact (green) through Cook-Gordon debonding between contrasting layers 1 (stiff) and 2 (soft) ahead of a dyke (red) (Barnett and Gudmundsson, 2014).

5.4.2 Stress barrier

The idea of a stress barrier has been known for many decades. For example, Anderson (1951) and Gretener (1969) both proposed that sills form under or in the lower part of a stress barrier. A stress barrier can be defined as a rock unit that yields an unfavourable stress field for dyke and inclined sheet propagation due to the adjacent layers having contrasting mechanical properties. There are two types of stress barriers: (1) stiffness of rocks increases with depth, for example at rift zones. This is due to hydrothermal alteration, which welds together contacts (heals and seals) making the heterogeneous layers more homogeneous. This process also increases the density, which has a positive correlation with Young's modulus (Jaeger and Cook, 1979). (2) Adjacent rock layers that have contrasting mechanical properties and are dependent on loading conditions. Here in Figure 5.9, there is a rotation of principal stresses in the layer above the contact into an unfavourable trend for vertical propagation. The maximum principal compressive stress, σ_1 , becomes

horizontal (parallel to σ_1) and the minimum principal compressive stress becomes vertical (perpendicular to σ_1). Thus, a rock layer with compressive stresses higher than the adjacent rock layers, for example in lava piles, can be produced by abrupt changes in Young's modulus between layers of soft and stiff rocks (Gudmundsson and Brenner, 2001; Gudmundsson, 2011b). A stress barrier may also develop when a dyke meets a stiff layer and may become arrested as it is unable to overcome the tensile strength of the host rock, possibly due to a low overpressure within the dyke (Geshi *et al.*, 2012). Stress barriers can form in both stiff and soft rocks; in a stiff layer there is a high stress field due to a high compressive stress, and the layer acts as a stress barrier to dyke propagation as a result of horizontal compression. However, horizontal extension leads to higher tension and low compressive stress in the stiff layers, and the soft layers act as a stress barrier suppressing the tensile stresses of the propagating dyke (Gudmundsson and Brenner, 2001; Gudmundsson, 2002). Stress barriers are the primary reason for sill emplacement in extinct rift zones, for example East Iceland (Gudmundsson, 1990).

5.4.3 Elastic mismatch

Elastic mismatch is related to the different properties of the adjacent host rock and the contact, primarily the material toughness and Young's modulus. This is demonstrated in Figure 5.6. The toughness of a material can be defined as the elastic or strain energy needed for a fracture (the dyke) to propagate through a material (the contact) and into the layer above. This can be associated with the one-dimensional Hooke's law (Fig. 3.2). These mechanisms have all been seen in the field, where sills have intruded into sedimentary basins. For example, because of elastic mismatch, a stress barrier has been formed arresting vertical propagation of a dyke and deflecting it along a boundary layer or weak contact.

The total energy release rate, G_{total} , must also be considered with regards to elastic mismatch, defined as:

$$G_{total} = G_I + G_{II} + G_{III} \quad (5.6)$$

For dykes and sills the energy release rate is denoted by G_I in Eq. (5.6). For the deflection of a dyke along a contact there tends to be more than one mode of loading (Fig. 3.5). Therefore, the total energy release rate can be regarded as a combination of G_I , G_{II} and G_{III} (where I, II and III represent the mode of loading), where $G_{\text{total}} = G_I + (G_{II} \text{ or } G_{III})$ (He and Hutchinson, 1989; Hutchinson, 1996; Gudmundsson, 2012b).

5.4.3.1 Dundurs elastic mismatch parameter

Dundurs (1969) elastic mismatch parameter, α , defined in Eq. (5.7) is a parameter that measures if a dyke will penetrate (G_p) or be deflected (G_d) along a contact, which is dependent on the strain energy release rate. In Eq. (5.7), E_1 is the Young's modulus of the layer above the contact, and E_2 is the Young's modulus of the layer with the dyke (Gudmundsson, 2011a).

$$\alpha = \frac{E_1 - E_2}{E_1 + E_2} \quad (5.7)$$

If a dyke penetrates a contact Eq. (5.8) must be satisfied, however, if a dyke is deflected along a contact Eq. (5.9) must be satisfied when there are mechanically dissimilar rocks in common scenarios.

$$\frac{G_d}{G_p} < \frac{\Gamma_D(\psi)}{\Gamma_L^I} \quad (5.8)$$

$$\frac{G_d}{G_p} \geq \frac{\Gamma_D(\psi)}{\Gamma_L^I} \quad (5.9)$$

Γ_D is the material toughness of the contact, Γ_L^I is the material toughness of the overlying rock and ψ is a measure of mode I to mode II proportionality (He and Hutchinson, 1989; Gudmundsson 2011a). The ratio of G_d/G_p is a function of α , which can be visualised in Figure 5.11, which shows that when the ratio G_d/G_p lies

below the curve then the dyke will become deflected along the contact (Fig. 5.11C and D inset). However, if the ratio of G_d/G_p lies above the curve then the dyke will penetrate the contact into the overlying layer (Fig. 5.11B inset). Dundurs (1969) shows that when α is equal to zero, dyke deflection along a contact can only take place if the material toughness of the contact itself is 26% (as G_d/G_p is 0.26) or less than that of the adjacent layer. When α is negative, that is, the stiffness of the layer above the contact is lower than the stiffness of the layer below the contact, the dyke will become arrested at the contact. However, if α is positive, that is the stiffness of the layer above is higher than the stiffness of the layer below the contact, the dyke is more likely to be deflected into a sill, especially when the mechanical properties of the two layers become more dissimilar. Whether the dyke becomes singly or double deflected has the same probability, as α remains roughly constant (Gudmundsson, 2011a; 2012b). This theoretical approach has been applied and justified by analogue models (Kavanagh *et al.*, 2006; Kavanagh *et al.*, 2013).

The results illustrated in Figures 5.7 and 5.6 can be justified by other works. Analogue models by Xu *et al.* (2003); Rivalta *et al.* (2005); Wang and Xu (2006); Kavanagh *et al.* (2006); Menand (2008); Kavanagh *et al.* (2013); analytical models by Gretener (1969); Bungler and Cruden (2011); numerical models including finite element and boundary element by Zhang *et al.* (2007); Maccaferri *et al.* (2010); Gudmundsson (2011b); Maccaferri *et al.* (2011).

5.5 Conclusions

When the crust is modelled as a homogeneous and isotropic medium, most dykes and inclined sheets should, theoretically, be able to reach the surface. However, it is well known that the crust is heterogeneous and anisotropic with numerous layers with various mechanical properties. It is because of this mechanical layering that the majority of dykes and inclined sheets never reach the surface, but are arrested at varying depths within the crust. The principal explanation for these arrests, as shown in the numerical models, is due to the presence of weak contacts between adjacent layers with differing mechanical properties, predominantly how soft or stiff the overlying layer is.

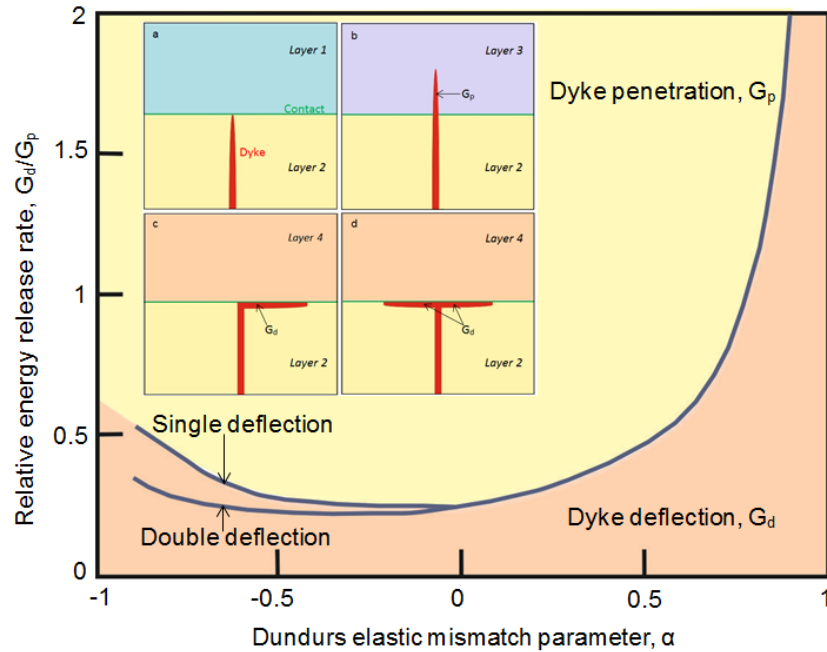


Figure 5.11: Dundurs elastic mismatch parameter, α , is a function of the relative energy release rate of the dyke penetration (G_p) to the relative release rate of dyke deflection into a sill (G_d). Dyke deflection tends to occur when α is positive, that is layer 1 above the contact has a higher Young's modulus, E , or stiffness than layer 2, the host rock. However, if α is negative there is a greater tendency that the dyke will become arrested at the contact, that is layer 1 has a lower E than layer 2 (Barnett and Gudmundsson, 2014 modified from He *et al.*, 1994). Inset: Modification of Figure 5.1 to define G_p in B and G_d in C and D.

Whether a dyke penetrates a contact or is deflected along it, depends on the properties of the contact and the stiffness of the overlying layer. When the contact is strong the dyke tends to continue on its vertical path. However, when the contact is weak, the dyke tends to be deflected into a sill as the contact has the ability to open up, known as Cook-Gordon debonding. Also, when the overlying layer is stiffer, then the dyke tends to be arrested or deflected due to unfavourable stress conditions, known as a stress barrier. Overall, the heterogeneity and anisotropy of the models favours sill emplacement due to elastic mismatch. Therefore, the mechanical boundaries within the crust may be regarded as traps for magma, where dykes become arrested and sills are emplaced.

Chapter 6: Sill evolution into a shallow magma chamber

6.1 Introduction

Dykes and sills play a major role in the accretion of the upper crust, and also are the fundamental building blocks of volcanoes, both active and extinct. A magma chamber is defined to be a body of partially or total molten rock located within the shallow depths of the crust and is fed by a deep seated magma reservoir. A shallow magma chamber can act as both a source and sink for magma, a source for dyke and inclined sheet magmatic injections, and a sink for magma from a deep seated reservoir. When a magma chamber is active it has different mechanical properties (Young's modulus for a fluid is zero) from those of the host rock. This is because of temperature and commonly, compositional differences that affect the size and shape of the chamber. This is particularly true for a pluton, a chamber that is no longer active and has solidified, as it may act as a stiff elastic inclusion within a softer host rock (Gudmundsson, 2012a).

Many shallow magma chambers are thought to develop from sills and maintain a sill-like geometry throughout their lifetime, for example at fast spreading ridges (Sinton and Detrick, 1992; Singh *et al.*, 2006; Kühn and Dahm, 2008). The concept of sill-like magma chambers has also been supported by geochemical and field observations in varying tectonic regions, for example Upton *et al.* (2005). The question is then: how can a sill evolve into a shallow magma chamber? As discussed in Chapter 5 sill formation is favoured by (1) mechanical contrast of host-rock layers, whereby a dyke is arrested due to contrasting stiff and soft layers, and (2) the presence of a weak contact so that tensile stresses generated by the approaching dyke open the contact deflecting the dyke into a sill. Development of these models in this chapter with regards to sill emplacement can address the question of how shallow magma chambers are formed. Thus, this chapter is split into two parts: (1) sill geometries and growth, and (2) shallow magma chamber formation.

6.2 Sill geometry

Sills exhibit a range of sizes and geometries, which are closely related to the host rock in which they are emplaced, whether it is igneous or sedimentary. Sills tend to have an aspect ratio (lateral dimension versus thickness) ranging on the order of 10^2 - 10^4 (Best, 2003). Some of the thickest sills are located in Antarctica (Leat *et al.*, 2006). The maximum thicknesses reach 150-433 m (Gunn, 1966) and can also be up to 600 m (Cruden and McCaffrey, 2006). Sills may also reach lateral dimensions on the order of tens of kilometres and areas up to hundreds to thousands of square kilometres (Kavanagh *et al.*, 2006; Hansen *et al.*, 2011). Sill geometries can be broadly classed into six groups as illustrated in Figures 6.1 and 6.2. These geometries relate to the elastic response of the host rock into which the sill is intruded. These are: straight sills, asymmetric or symmetric; sills concave up or down; and stepped sills, either stepped up or down. Concave down and stepped down sills are rarely observed and stepped up sills are commonly referred to as saucer-shaped sills.

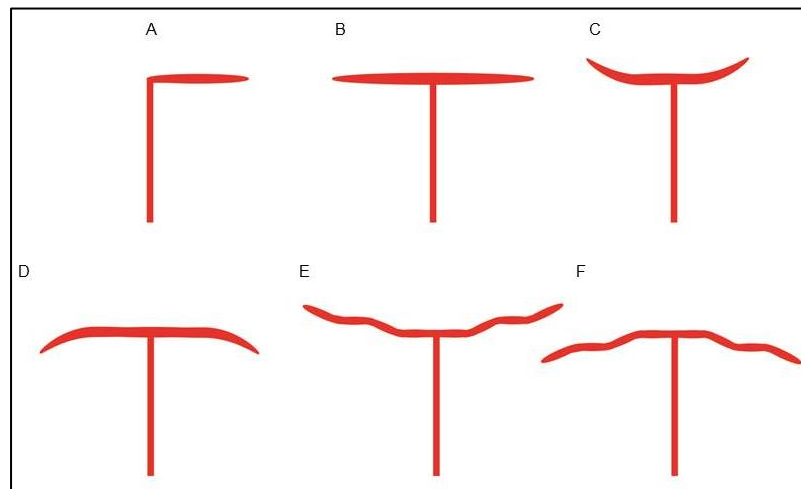


Figure 6.1: Six schematic illustrations of sill geometries: (A) asymmetric straight sill, (B) symmetric straight sill, (C) concave up sill, (D) concave down sill, (E) stepped up sill - saucer-shaped sill and (F) stepped down sill (Barnett and Gudmundsson, 2014).

Sills are well defined on seismic images due to the large contrast between the igneous intrusion and the sedimentary host rock. Hansen *et al.* (2004) classified three types of sill geometries in the Faroe-Shetland Basin: single sill, compound sill and sill complex. These types can also be identified in the Vøring Margin (Fig. 6.3). A

single sill has a continuous, smooth geometry, with concordant (concave) and discordant (inclined) components. A compound sill has a complex geometry with junctions that interconnect the concordant and discordant components. A sill complex is identified as an interconnected network of sills, both single and compound (Hansen *et al.*, 2004).

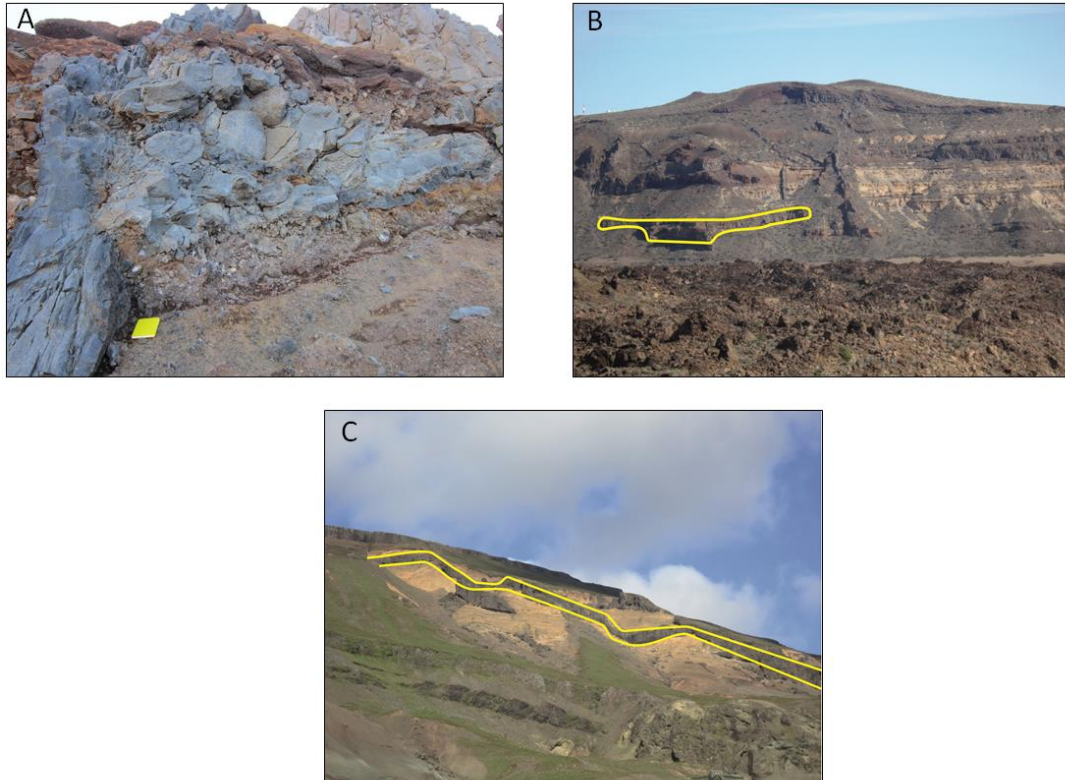


Figure 6.2: Photographs illustrating a variety of sill geometries: (A) asymmetric straight sill, Tenerife, view S and notebook for scale (B) concave sill, Las Cañadas, Tenerife, view E, caldera wall ~300 m (C) inclined stepped sill SW Iceland, view NE, ~2-3 m thick.

Along the Vøring Margin saucer-shaped sills are common. Malthe-Sørensen *et al.* (2004) and Polteau *et al.* (2008a) demonstrate how a saucer-shaped sill is an important geometry, with inclined limbs clearly cutting sub-horizontal strata. They drew key conclusions relating to the viscosity of the fluid, the nature of the host rock with regards to its tensile strength, doming of the host rock above the sill as it inflates, and development of an asymmetrical stress field at the tips of the sills. However, none of these fundamental conclusions took into account the temperature of the magma that would be injected to form the sill. Nevertheless, the physical

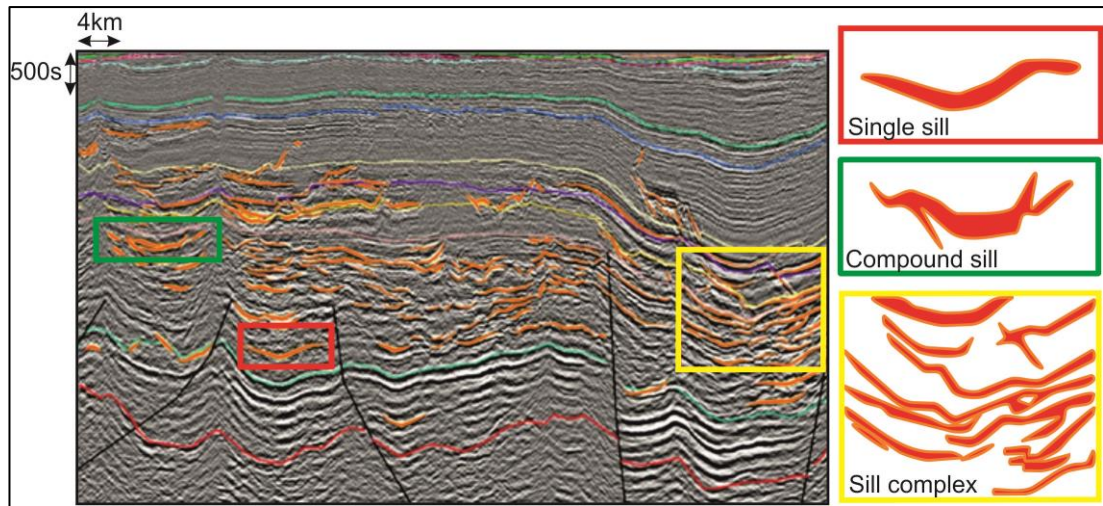


Figure 6.3: Seismic line MNR05-7397, illustrating the various relationships between sills (modified from Tector; www.tector.com), based on Hansen *et al.* (2004). NB. These sills are not on a 1:1 scale and are merely to show the sill geometries and junctions (interconnections).

processes that control the formation of a saucer-shaped sill remain the same although they form in differing host rocks with varying elastic properties. It is also noted from field studies that saucer-shaped sills form predominantly in sedimentary basins, for example the Vøring Margin (Thomson and Hutton, 2004; Hansen and Cartwright, 2006b, Polteau *et al.*, 2008a) and the Karoo Basin (Chevallier and Woodford, 1999; Malthe-Sørenssen *et al.*, 2004; Polteau *et al.*, 2008a; Galerne *et al.*, 2008, 2011), having important implications for the petroleum industry with regards to reservoirs, traps and hydrocarbon maturation. An in depth discussion of the mechanisms governing saucer-shaped sill emplacement is provided in Section 6.6.1 of this chapter.

Numerical models were made to better understand the emplacement mechanisms relating to different sill geometries that are seen in the Vøring Margin (Fig. 6.3). Asymmetric models were carried out in a heterogeneous medium, where the sill was emplaced along a contact at different depths (1 km and 4 km as this is where the majority of the Vøring sills are emplaced (Svensen *et al.*, 2010)) to investigate the effects the free surface may have on the sill geometry (Fig. 6.4). The stiffness of the layer above the contact was 5 GPa, and the underlying layer was 20 GPa, with an overpressure within the dyke and asymmetric sill of 10 MPa. The single deflection of the dyke was imposed as a starting condition in the model, where the starting lateral

dimensions of the sill was 500 m. The mesh was kept the same with a maximum element size of 0.02 km and a minimum element size of 3.2×10^{-5} km. Models were run in a series of steps to analyse the direction of the maximum principal compressive stress trajectories, thus there is no condition for halting the sill. The analysis of the trajectories determined the propagation path of the sill. For each set of models, a series of ten steps were solved, however, only the main four snapshots are illustrated here in Figures 6.5 and 6.6.

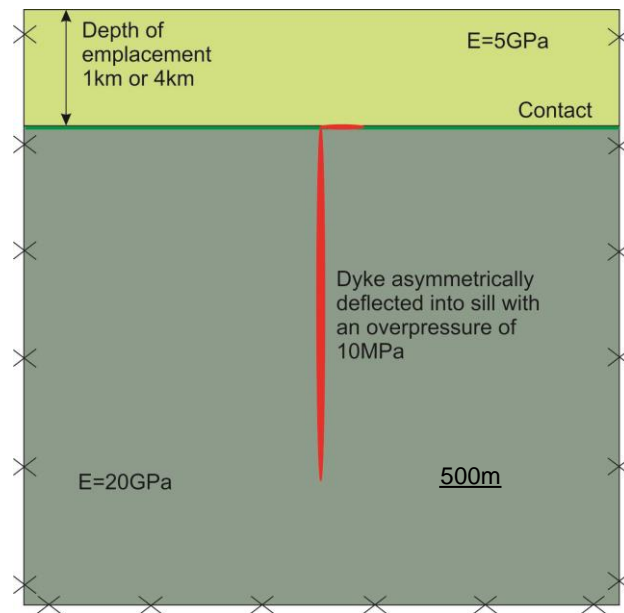


Figure 6.4: Model set up for Figures 6.5 and 6.6. Dyke is emplaced into a stiff rock with $E = 20$ GPa, and is singly deflected at a weak contact to form an asymmetric sill due to the overlying soft rock with $E = 5$ GPa. The overpressure is kept constant with the sill and dyke at 10 MPa, but emplacement depth was varied between 1 km and 4 km. The model is fixed at all sides, keeping the top side a free surface. Please note that this is only a schematic illustration for the model set up and the fixed boundaries are much larger in the numerical model so as to avoid boundary effects.

The effects of the Earth's free surface may be strong, but this depends on the emplacement depth of the sill with respect to its lateral dimensions. When the sill is emplaced at an interface at a depth of 4 km (Fig. 6.5), the surface effects are weak. Tensile stresses generated at the tip of the sill are <40 MPa, where the largest stress is at the tip of the sill, and decreases radially about the tip ~ 10 -20 MPa. The stress trajectories (white ticks) at the tip of the sill are inclined towards the surface, which become curved as the sill becomes longer. Following the inclination of the stress

trajectories, the sill follows a relatively straight path, which becomes inclined at a shallow angle of $<10^\circ$ as its lateral dimensions increase.

When the sill is emplaced at an interface located 1 km below the surface (Fig. 6.6), the surface effects are significantly stronger. These effects are seen both in the surface contour colours and the curvature of the stress trajectories. Figure 6.6B starts to show the effects of the free surface, where small stresses, <10 MPa, are generated. As the sill grows the zone of high stress, both about the tip of the sill and at the surface, increases to at least 20 MPa. These two zones begin to interact with each other, causing the stress trajectories to become curved, almost circular (Fig. 6.6C and D), where the overall geometry of the sill becomes concave.

The combination of both stress contours and trajectories indicate the location of a high stress zone at the tip of the sill. This zone is where new fractures are formed in the host rock and old fractures are reactivated. These fracture orientations are represented by the orientation of the stress trajectories, which are dependent on the effects of the free surface. At 4 km depth the sill follows a relatively straight path. However, when the sill is emplaced at an interface 1 km below the surface, the stress field and trajectory pattern differ considerably affecting the overall geometry of the sill. Shallow emplaced sills can also generate large stresses (40 GPa, this value is only theoretical as the tensile strength of rock is 2-4 MPa, thus in nature the host rock would break before such large tensile stresses were generated; Gudmundsson, 2011a) at the surface (Fig. 6.6), representing the formation of tension fractures (mode I) at the surface, and with increasing depth may form normal faults (mode II).

6.2.1 Volcano topography

Numerical models were next run to examine the loading effects of volcanoes on sill growth. In the case of a propagating dyke, gravity provides a vertical force. However, the propagation path is partly determined by the stress field exerted by the topographical load of the volcano (Muller *et al.*, 2001). This is because the vertical stress or overburden stress, σ_v , depends on gravity, g , depth of sill emplacement, z , and density of the overburden, ρ , such that $\sigma_v = \rho gz$.

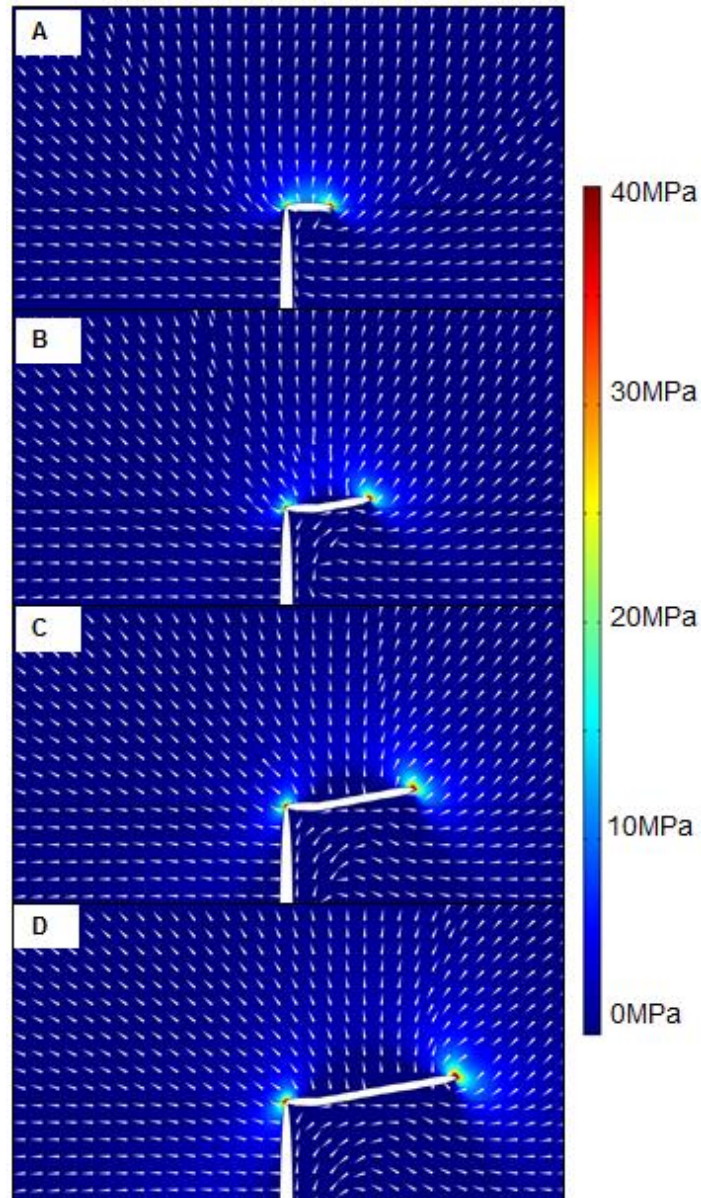


Figure 6.5: FEM model of tensile stress, shown as colour contours, illustrating the growth of the sill and maximum principal compressive stress trajectories (white ticks) illustrating the propagation path of the sill that is emplaced at a contact 4 km below the free surface.

In order to assess the loading effects of volcanoes many profiles were modelled. These volcano profiles are considered to be a good representation of shield and stratovolcanoes:

- Hekla, South Iceland, stratovolcano, elevation 1,488 m
- Snæfellsjökull, East Iceland, stratovolcano, elevation 1,446 m
- Mauna Kea, Hawaiian Islands, shield volcano, elevation 4,207 m (sea level)

- Mauna Loa, Hawaiian Islands, shield volcano, elevation 4,169 m (sea level)
- Mt. Fuji, Japan, stratovolcano, elevation 3,776 m
- Mt. Rainier, Washington, US, stratovolcano, elevation 4,392 m

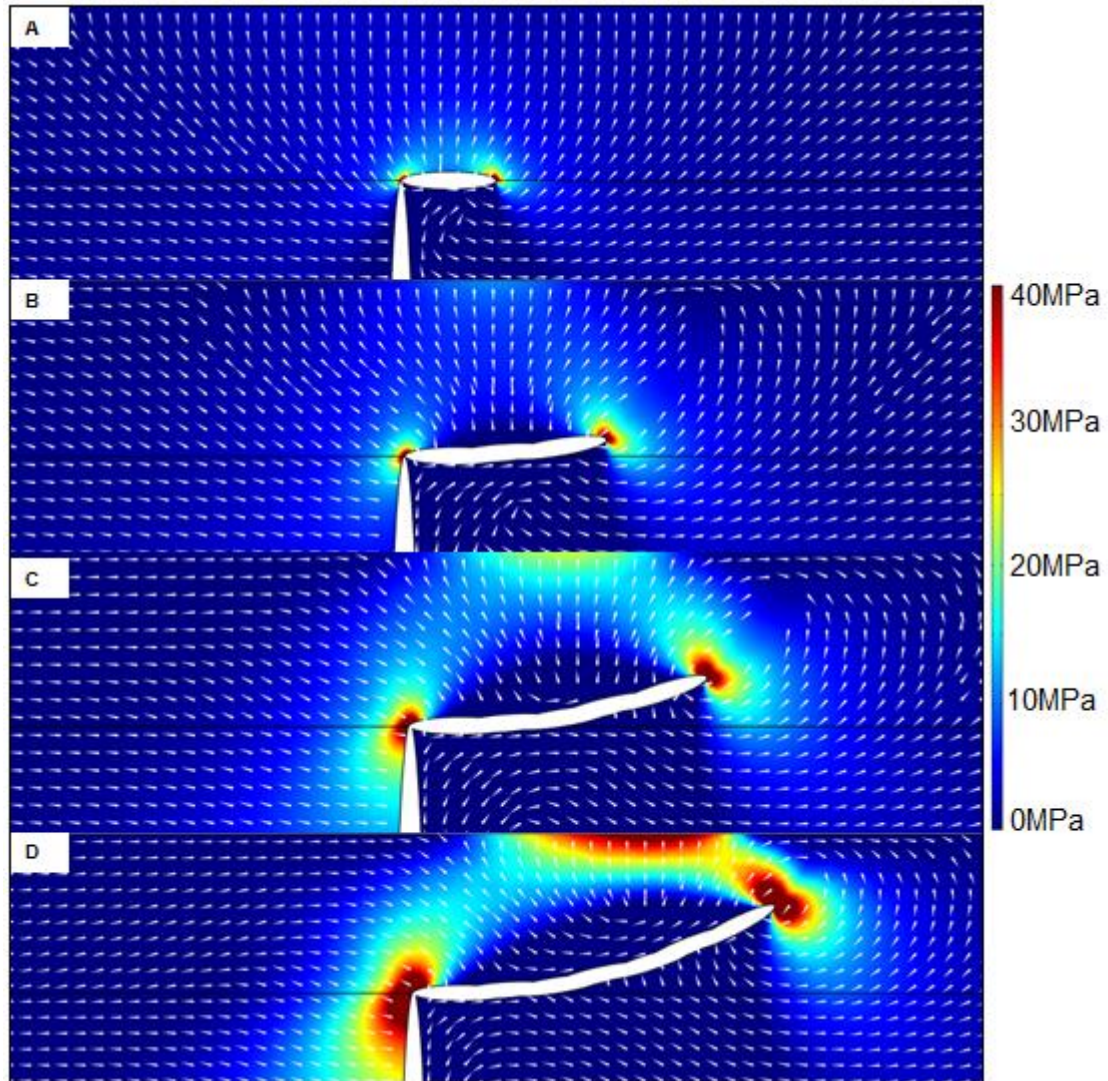


Figure 6.6: FEM model of tensile stress, shown as colour contours, and the maximum principal compressive stress trajectories (white ticks) illustrating the propagation path of a sill emplaced at a contact 1 km below the free surface.

Models were set-up as shown in Figure 6.7, where the volcano is modelled as homogeneous, with a Young's modulus of 5 GPa, and a sill is emplaced 2 km below the base of the volcano into a stiffer crust of 20 GPa (e.g. basaltic crust). The sill is set to have an overpressure of 10 MPa, the sides are fixed and the topography is a free surface. The mesh was the same for each volcano with a maximum element size of 0.02 km and a minimum element size of 3.2×10^{-5} km. Several models were

carried out in a series of steps to see the effects of topography on the stress trajectories and the propagation path of the sill. Thus, the initial length of the sill was the same (1 km) in each model and there was no halting condition for sill growth, that is, the final length of each sill was the same. Each volcano has a depression to its base due to the loading and gravitational effects of the volcano on the crust. This is because on a geological time frame, the lithosphere behaves elastically and therefore can bend beneath volcanoes.

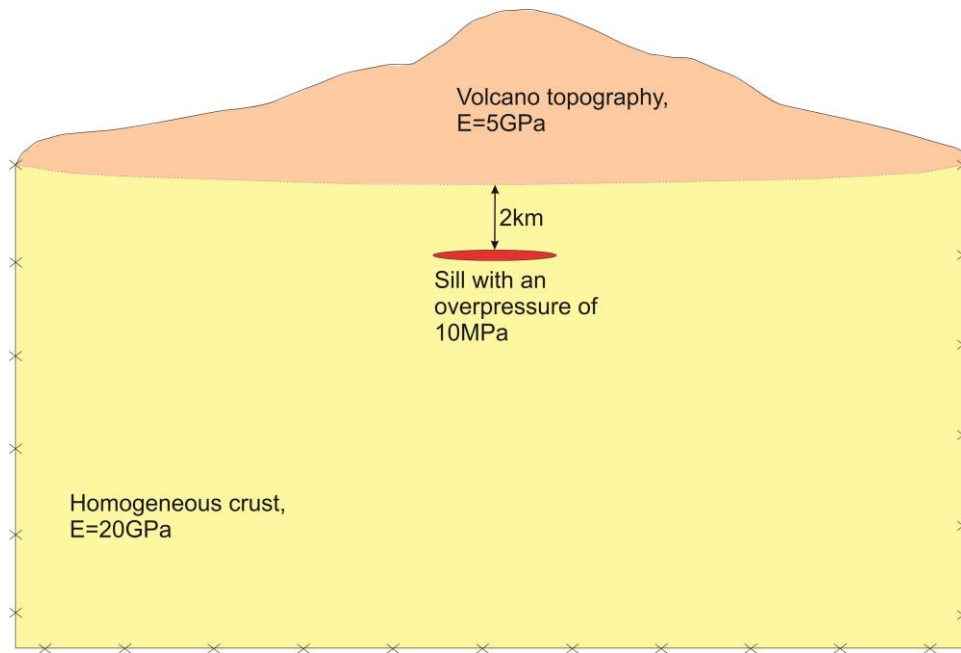


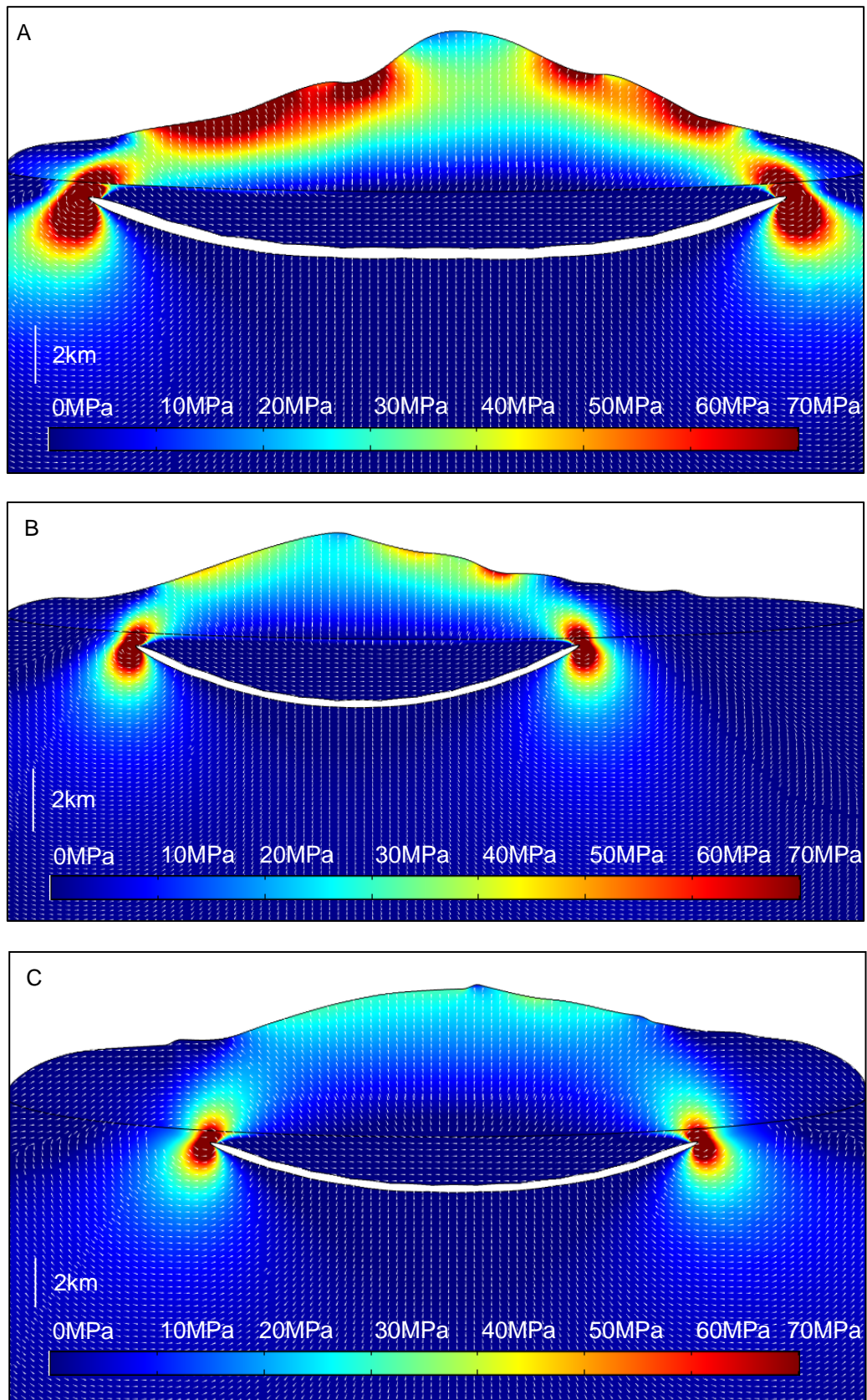
Figure 6.7: Model set up for Figure 6.8. A sill with an overpressure of 10 MPa, is emplaced at a depth of 2 km beneath the base of a volcano, where $E = 20$ GPa. Volcano topography varies, but E remains constant at 5 GPa, i.e. the volcano in general is softer than the upper crust. The model is fixed at the bottom and the edges of the upper crust, the topography of the volcano remains a free surface.

Models in Figure 6.8 have the same stress scale bars for each volcano to enable comparison and show the direct relationship between volcano topography and sill geometry. Generally, stratovolcanoes (Fig. 6.8A, B, E and F) have a larger surface effect than shield volcanoes (Fig. 6.8C and D) due to their large topographical gradients. Hekla (stratovolcano, elevation 1,488 m; Fig. 6.8A) has large tensile stresses concentrated on the flanks of the volcano, >70 MPa, which interact with the stresses generated by the sill tip of the same magnitude. This results in the overall sill geometry taking on the form of a broad concave sill, which is relatively flat at its

base under the peak of the volcano, and becomes more inclined towards the flanks of the volcano. Snæfellsjökull (stratovolcano, elevation 1,446 m; Fig. 6.8B) yields a smoother topography in comparison to Hekla, and this is reflected in the stresses generated at the flanks of the volcano being 30 MPa less. Similarly to Hekla, these surface stresses connect to a zone of tip stress (70 MPa), influencing the geometry of the sill. In the case of Snæfellsjökull, the sill has a smaller diameter resembling a concave shape. Mt. Fuji (stratovolcano, elevation 3,776 m; Fig. 6.8E) and Mt. Rainier (stratovolcano, elevation 4,392 m; Fig. 6.8F) also exhibit similar stress patterns on their flanks and are related to the sill tip stresses. Mt. Fuji, has large tensile stresses, similar in magnitude to Hekla, leading to a similar sill geometry. However, with respect to Mt. Fuji, there are large concentrations of tensile stresses along the upper sill margin. Mt. Rainier, on the other hand, yields similar stress patterns to Snæfellsjökull along its flanks, where tensile stresses are far less, in the order of 20-30 MPa. The sill geometry of Mt. Rainier is also similar to Snæfellsjökull, although slightly shallower by a few degrees. In the cases of the Hawaiian volcanoes, stresses generated by the volcanoes are much less due to the gentle flanks of the volcanoes. Mauna Kea (shield volcano, elevation 4,207 m; Fig. 6.8C) has tensile stresses <30 MPa, while Mauna Loa (shield volcano, elevation 4,169 m; Fig. 6.8D) has tensile stresses <10 MPa along the flanks of the volcano. Stresses are distributed symmetrically under the peak of the volcanoes due to the gentle dip of the flanks, unlike the stratovolcanoes. Sill geometries for these shield volcanoes are relatively flat at their centres and become slightly inclined towards their tips. Mauna Loa has the shallowest incline of $\sim 2^\circ$, while Mauna Kea is slightly steeper by a couple of degrees. Furthermore, Mauna Loa, similar to Mt. Fuji, has tensile stresses of ~ 40 MPa distributed across the sill roof, possibly due to the stresses concentrated about the peak of the volcano.

Vertical stresses for each volcano can be estimated according to $\sigma_v = \rho gz$. All these volcanoes have a basic to intermediate composition and therefore an average density of 2600 kg/m^3 (Gudmundsson, 2011a). The vertical stress is approximately 90-160 MPa for all volcanoes modelled and is irrespective of stratovolcano and shield volcano classification, that is, its inclination of its flanks, but rather their height above sea level. This vertical stress would also have an impact on the mechanical

ability of the sill to lift the adjacent host rock in order for the sill to inflate and evolve into a shallow magma chamber.



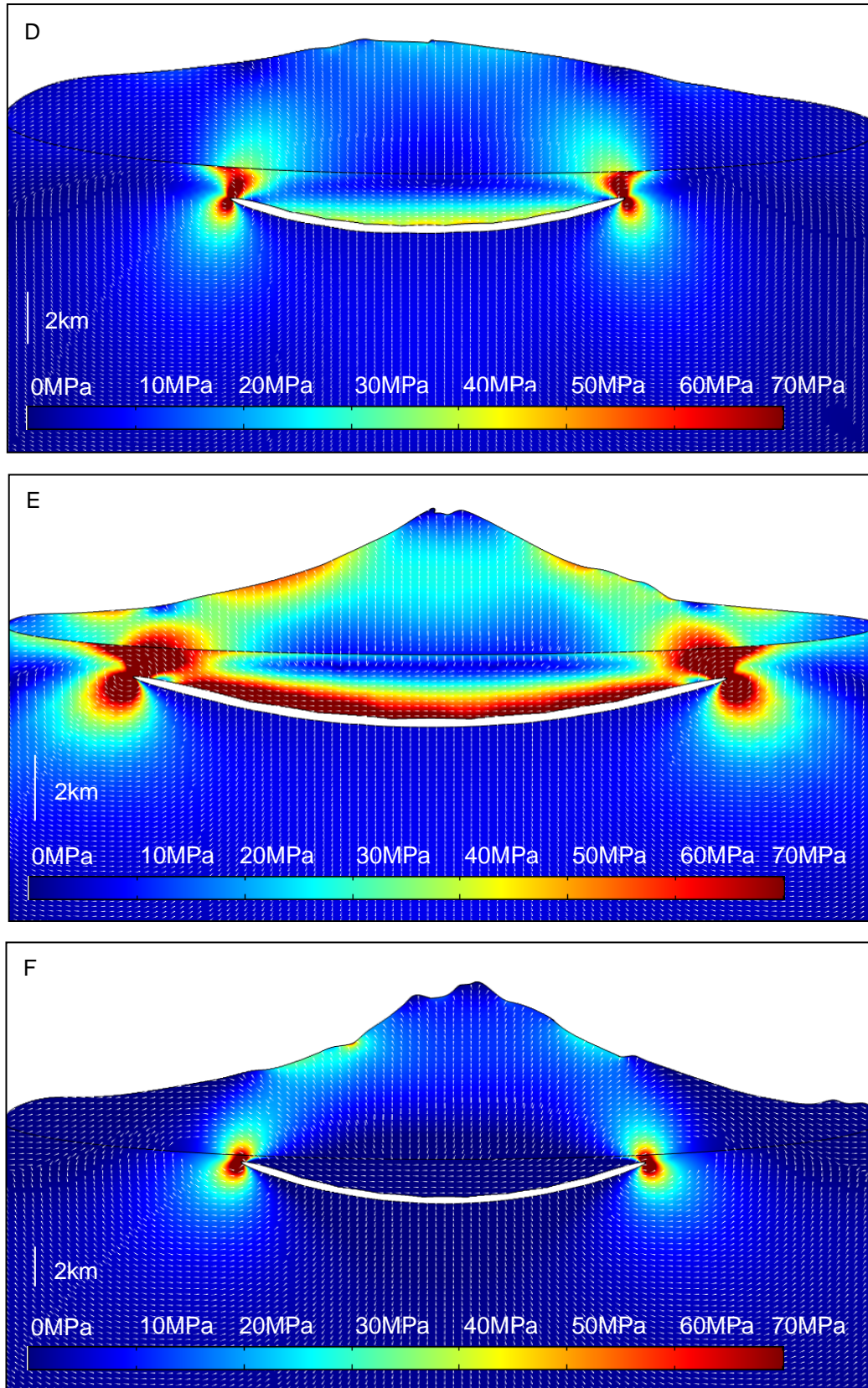


Figure 6.8: FEM models of tensile stress contours and maximum principal compressive stress trajectories (white ticks) illustrating the various sill geometries influenced by differing volcano topographies. (A) Hekla, (B) Snæfellsjökull, (C) Mauna Kea, (D) Mauna Loa, (E) Mt. Fuji and (F) Mt. Rainier. The base of the volcano is shown by the curved black trace.

6.3 Sill growth

Ideally a sill is emplaced within a homogenous, isotropic layer that is opened by a constant magmatic overpressure and over time exhibits an elliptical geometry whose aperture varies, that is, the largest aperture is at the centre of the sill and decreases towards the tips of the sill. However, emplacement into a completely homogenous layer is unlikely, owing to heterogeneities present within strata. As a result, the aperture of a sill generally varies from a smooth elliptical geometry.

Sills propagate further from their tips (lateral ends) because of the large tensile stresses generated by the narrower aperture of their tip. When these tip stresses are greater than the host rock's tensile strength in which the sill is emplaced, the sill can propagate further (Figs. 6.5 and 6.6). To apply an analytical solution, a sill can be regarded as a smooth elliptical hole with a constant overpressure. The maximum tensile stress at the sill tips is as follows:

$$\sigma_3 = -P_o \left[\frac{2a}{b} - 1 \right] \quad (6.1)$$

where σ_3 is the minimum principal stress, P_o is the magmatic overpressure, $2a$ is the major axis of the sill and b is half the minor axis of the sill (Gudmundsson, 2011a). The overpressure can be defined as

$$\Delta u_I = \frac{8P_o(1-\nu^2)a}{\pi E} \quad (6.2)$$

where Δu_I is the total thickness (aperture) of a mode I crack, here the sill, P_o is the magmatic overpressure, ν is Poisson's ratio (0.25), a is the radius of the sill, E is Young's modulus, and π is a constant (3.1416) (Gudmundsson, 2011a). This can be applied to the three areas of study in this thesis (Vøring sills, Whin Sill and Stordalur sill cluster).

The Vøring sills have a known thickness of 100 m in the Utgard well (Svensen *et al.*, 2010), lateral dimensions of approximately 30 km and are emplaced within shale units of 1 GPa stiffness (Table 4.1). From Eq. (6.2) an overpressure of 3 MPa is obtained. When substituted into Eq. (6.1), an average tip tensile stress of 1.8×10^3 MPa is calculated for the Vøring sills. The Whin Sill has an average thickness of 30 m and has lateral dimensions of approximately 80 km following a strike line of E-W (Liss *et al.*, 2004), dominantly emplaced within limestone of 20 GPa stiffness (Gudmundsson, 2011a; taking into account diagenesis at present, this could have been much lower at the time of emplacement). Therefore, an overpressure of 6 MPa can be obtained, with average tip tensile stress of 3×10^4 MPa. The Stardalur sill cluster however, has been significantly eroded due to glaciation. Nevertheless, it is known that this cluster is situated within a caldera that had a diameter of ~5 km and the cluster would have most likely extended across this diameter. The sills have been emplaced into the Plio-Pleistocene Formation (Chapter 4; Fridleifsson, 1977; Pasquare` and Tibaldi, 2007) with a stiffness of 4 GPa and each sill has a thickness of 10-30 m (Pasquare` and Tibaldi, 2007). From Eq. (6.2) an overpressure of ~13 MPa is obtained with an average tip tensile stress of $\sim 3.2 \times 10^3$ MPa from Eq. (6.1). However, these large tip stresses in the order of 10^3 - 10^4 are unrealistic in nature and are purely theoretical. This is because the *in situ* tensile strength of rock is 0.5-9 MPa, typically between 2-4 MPa, but in nature tensile stresses are smaller than tensile strength. Thus, the host rock would break before such large theoretical tip stresses are generated (Gudmundsson, 2011a).

6.3.1 Small sills

Small sills have lateral dimensions smaller than the depth below the surface at which they are emplaced. These small sills were modelled as described in Chapter 4. In Figure 6.9 a layered upper crust is modelled with alternating stiff layers of 30 GPa and soft layers of 5 GPa (Gudmundsson, 2011a), representing a typically stratified volcano, with a mesh that was the same as Figures 6.5, 6.6 and 6.8. The sill is emplaced at a depth of 4 km, and has a radius of 2 km, with each contact between the layers modelled as a thin elastic layer allowing for the occurrence of deformation. In Figure 6.9 tensile stresses of >100 MPa (theoretical value and unrealistic in nature owing to the tensile strength of rock being 2-4 MPa; Gudmundsson, 2011a) are

concentrated on the underside of the lower contact and also at the tips of the sill allowing for further growth. However, due to the small aspect ratio of the sill, the layers above the sill are hardly deflected. Thus, as there is no slip or deformation of the overlying layers in the crust, the displacement is the inflation of the sill itself (maximum deflection at the centre of 2.4 m).

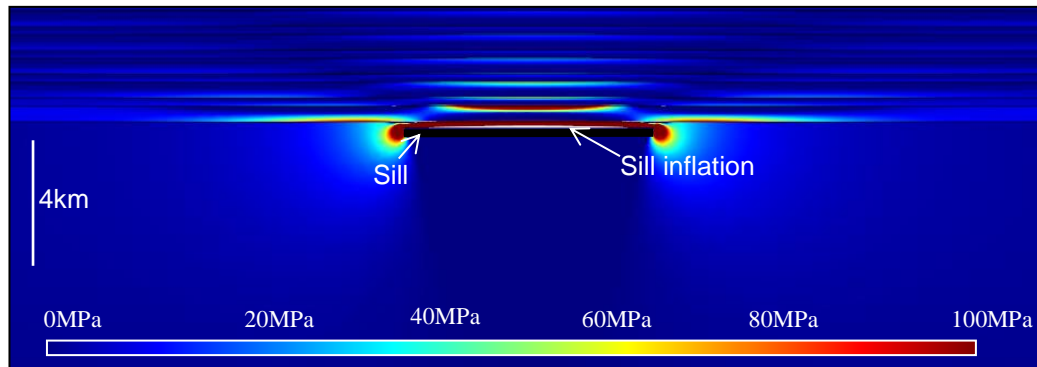


Figure 6.9: FEM model representing tensile stresses associated with a sill that is emplaced 4 km below the surface. Large tensile stresses, are located at the contacts between each layer. This sill is a small sill as it has a diameter smaller than the depth below the surface. Inflation is in the order of a couple of centimetres and therefore, would not act as a shallow magma chamber as it would solidify in a period of approximately 0.5 years (Barnett and Gudmundsson, 2014).

The next sets of models were set out to analyse the displacement or the opening of the sill in a 3D context. It is well known that a sill can be modelled as a penny-shaped crack, which has dimensions of a (half diameter in x direction), b (half diameter in y direction) and c (half the thickness in z direction) as shown in Figures 4.3 and 6.10. Analytical solutions follow (Sneddon and Lowengrub, 1969; Gudmundsson, 2011a):

$$w_{\max} = \frac{4P_o(1-\nu^2)a}{\pi E} \quad (6.3)$$

where w_{\max} is the deflection of the roof of the sill, P_o is the magmatic overpressure, ν is Poisson's ratio, a is the half diameter of the sill, π is a constant (3.1416) and E is Young's modulus in which the sill is emplaced. For a sill with a radius of 500 m, a

magmatic overpressure of 10 MPa emplaced into a body with a Young's modulus of 20 GPa, the deflection of the roof is calculated to be 0.30 m, where deflection describes the thickness if deformation starts with a discontinuity of zero thickness. This can be compared with numerical solutions from COMSOL (set up of the model shown in Fig. 6.10, where the mesh was the same as Figure 6.9, maximum element size of 0.02 km and a minimum element size of 3.2×10^{-5} km), which give the same value (Fig. 6.11). However, this analytical solution only applies to a sill that is emplaced into an infinite elastic medium, whereas sills are often emplaced at contacts between two dissimilar mechanical rocks.

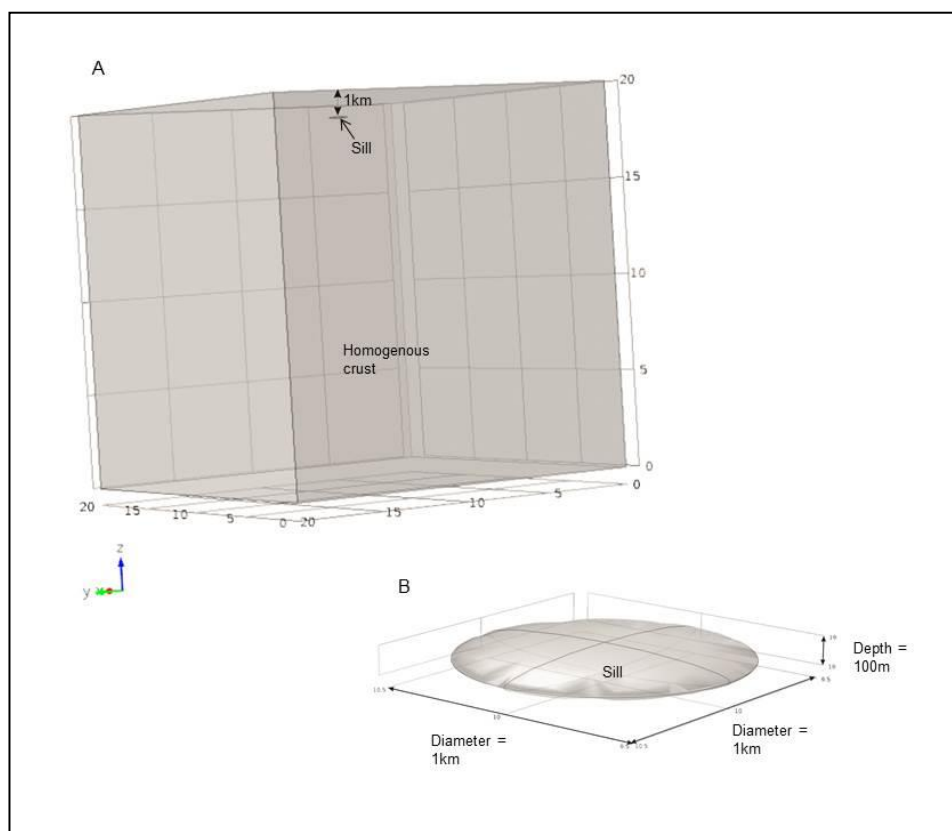


Figure 6.10: (A) Schematic illustration of a small sill whose diameter is 1 km and is situated at 1 km below the Earth's free surface into a homogeneous crust. (B) Close up illustration identifying parameters of a penny-shaped sill.

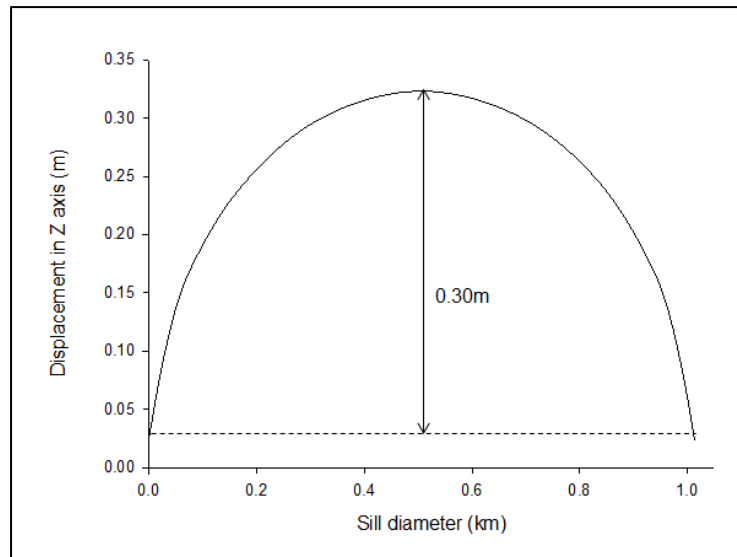


Figure 6.11: Numerical results illustrating the maximum displacement of the roof of a small sill.

A heterogeneous crust was next modelled as shown in Figure 6.12, where overpressure is kept constant at 10 MPa and layers alternate between 20 GPa, for example basalt, and 5 GPa, for example pyroclastic rock (Gudmundsson, 2011a). The results are presented in Figure 6.13 and are as follows: When the sill is emplaced at a contact with an overlying soft layer (5 GPa) and underlying stiff layer (20 GPa), the opening of the sill is 5.2 m. Large tensile stresses are concentrated around the margins of the sill, on the order of 9 MPa, allowing the sill to grow laterally and also vertically because the tensile strength of the host rock is assumed to be 0.5-9 MPa (Gudmundsson, 2011a). As the roof of the sill is emplaced within a soft rock, vertical growth of the sill is accommodated. However, the overlying stiffer layer induces a ‘barrier’ reducing the ability of the sill to inflate any further. This is also due to the aspect ratio of the sill, classified as a small sill, where there is the inability for the deformation of the overlying layers and thus, further sill growth.

For comparison, the model was made with different host rock Young’s moduli, such that the stiffer layers become soft, and the softer layers become stiff (Fig. 6.14). The sill is then emplaced at a contact with an overlying stiff layer and underlying soft layer, with a resultant maximum sill displacement of 2.7 m. Illustrated on the slices are the tensile stresses, which show the same distribution of stresses around the sill as in Figure 6.13, allowing for sill growth both laterally and vertically. However,

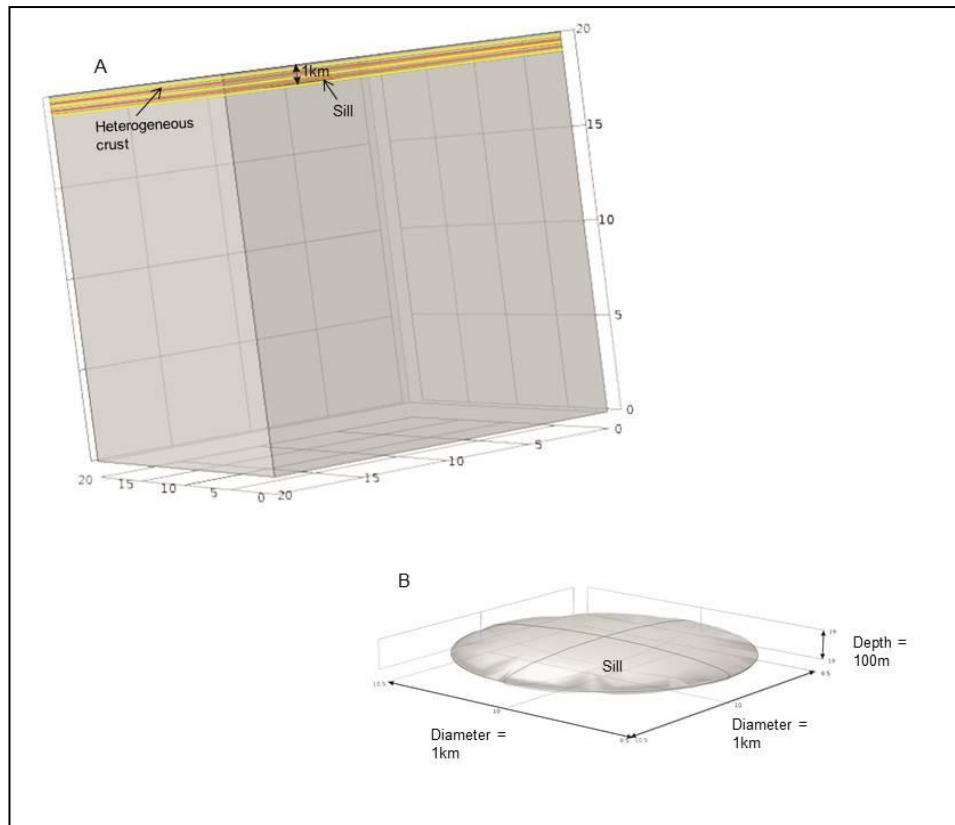


Figure 6.12: (A) Schematic illustration of a small sill whose diameter is 1 km and is situated at 1 km below the Earth's free surface within a heterogeneous crust (stiffness alternating between soft and stiff shown by bands of yellow and orange). (B) Close up illustration identifying parameters of a penny-shaped sill.

these stresses have been suppressed, with a maximum tensile stress of $\sim 7\text{--}8$ MPa (slice 1, Fig. 6.14) and the radial distribution of these stresses is much smaller than slice 1 in Figure 6.13. Thus, the ability for the sill to grow vertically or inflate depends on the overlying adjacent host rock. In comparison with 2D results (Fig. 6.9), the 3D results are justifiable with respect to small sills.

Small sills or thin sills lack the ability to act as shallow magma chambers because they would solidify in a short period of time. Jaeger (1957) calculated the time, t , in years, in which it takes for magma to cool and solidify within a sill with a deflection or half thickness, w , can be expressed as $t \approx 0.0825 \cdot w^2$. Hence, the sills represented in the 3D models (Figs. 6.10 and 6.11) that have a maximum roof deflection of 0.3 m in a homogeneous crust would solidify in ~ 0.007 years (2.5 days). For a heterogeneous crust where the sill roof is located within a soft layer with maximum

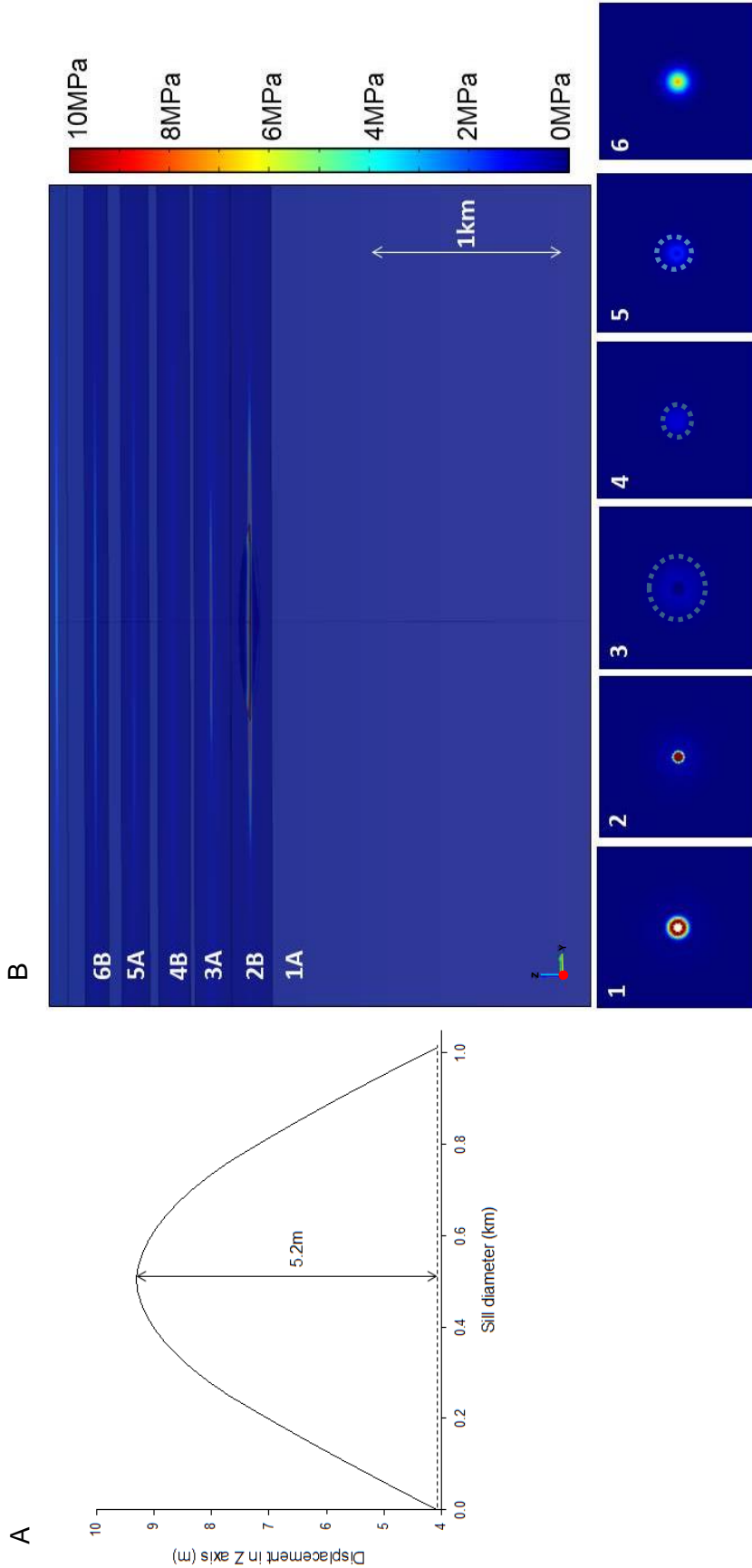


Figure 6.13: FEM models showing displacement of the sill roof (A) and tensile stresses indicated by the colour bar (B). A small sill with a radius of 500 m, emplaced 1 km below the surface into a heterogeneous crust, where layer **A** is a stiff rock with Young's modulus of 20 GPa (similar to a basalt) and layer **B** is a soft rock with Young's modulus of 5 GPa (similar to a pyroclastic rock). The overpressure within the sill is 10 MPa. (A) Shows the maximum displacement of the sill roof to be 5.2 m. (B) Shows the large tensile stresses to be distributed equally around the margins of the sill in cross section, where the slices (**1-6**) show the tensile stresses with each associated layer (**A** or **B**) in plan view. These slices show that the largest tensile stresses are around the sill (**1**), but with increasing distance from the sill these tensile stresses are relaxed, blue dotted line (**2-5**). However, in slice **6** we start to see the effects of the free surface inducing tensile stresses at the surface.

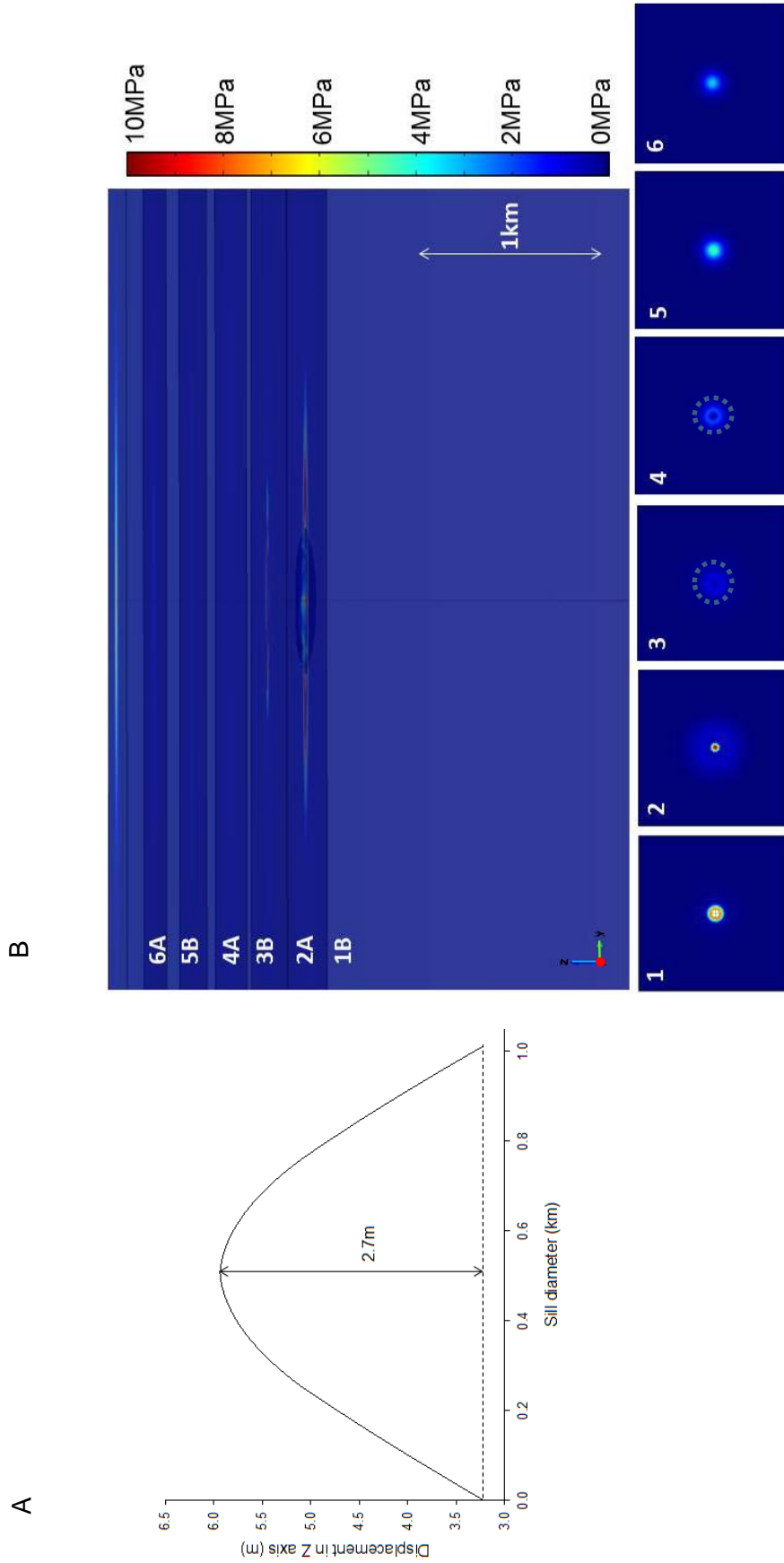


Figure 6.14: FEM models showing displacement of the sill roof (A) and tensile stresses indicated by the colour bar (B). A small sill with a radius of 500 m, emplaced 1 km below the surface into a heterogeneous crust, where layer **A** is a stiff rock with Young's modulus of 20 GPa and layer **B** is a soft rock with Young's modulus of 5 GPa. The overpressure within the sill is 10 MPa. (A) Shows the maximum displacement of the sill roof to be 2.7 m. (B) Shows the large tensile stresses to be distributed equally around the margins of the sill in cross section, where the slices (1-6) show the tensile stresses with each associated layer (A or B) in plan view. These slices show that the largest tensile stresses are around the sill (1), but with increasing distance from the sill these tensile stresses are relaxed, blue dotted line (2-4). However, in slices 5-6 we start to see the effects of the free surface inducing tensile stresses at surface.

deflection of 5.2 m (Fig. 6.13), solidification would occur at ~2.2 years. Whereas, if the sill was located in a stiffer layer where the maximum deflection is 2.7 m (Fig. 6.14), the sill would solidify at ~0.6 years.

6.3.2 Large sills

Large sills are such that their diameters are larger than the depth at which they are emplaced. Therefore, as the sill becomes thicker, the layers above the sill will start to be uplifted, mainly at the upper margin of the sill, but to some extent also down-bended under the sill. The ability of the layers to bend, gives rise to the potential for shallow magma chamber formation and in some locations even laccolith formation (Pollard and Johnson, 1973). Pollard and Johnson (1973) discussed how differing lithological layers significantly affect the elastic properties of these layers and therefore will act as a ‘stack’ of layers rather than as an individual layer. Thus, these mechanical layers have the ability to slide over one another, although there most likely will be friction between these layers to some degree. Analytical solutions (Ugural, 1981) allow for the calculation of the maximum deflection, w_{max} , of the sill roof given by

$$w_{max} = \frac{P_o a^4}{64D} \left(\frac{5 + \nu}{1 + \nu} + \frac{4d^2}{(1 - \nu^2)a^2} \right) \quad (6.4)$$

where P_o is the magmatic overpressure, ν is Poisson’s ratio, d is the depth below the surface at which the sill is emplaced, a is the radius of the sill and D is flexural rigidity. Flexural rigidity describes the ability of the weak contacts to slip as the sill starts to bend the overlying layers as it inflates, preserving the length of the layers and also, their thicknesses as slip is parallel to the layering. This parameter can be calculated as follows (Ugural, 1981):

$$D = \frac{Ed_e^3}{12(1 - \nu^2)} \quad (6.5)$$

where d_e is the effective thickness of the crust above the sill and has a value of $0.3d$ (Gudmundsson, 1990), E is Young's modulus of the layer in which the sill is emplaced and ν is Poisson's ratio. The effective thickness reduces the overall thickness of the overlying crust because the layers are able to slip at their contact, reducing the overall rigidity.

Petraske *et al.* (1978) discuss three sensitive factors for the deflection of the overburden. Firstly, they show how the radius of the sill is the most important factor affecting the maximum deflection of the sill roof, because the maximum deflection varies by the fourth power of the radius. Hence, by increasing the lateral dimensions of the sill, deformation of the overburden is more likely because of the magmatic overpressure. The second factor is the effective thickness of the overburden because it is a reciprocal of its third power. The third factor is that the deflection of the overlying strata is proportional to the magma overpressure.

Models were generated for a large sill emplaced at a depth of 1 km, with a radius of 2 km, into a layer with a Young's modulus of 5 GPa, something similar to a pyroclastic rock, which is driven open by a magmatic overpressure of 10 MPa, where the mesh was the same as for the small sills, with a maximum element size of 0.02 km and a minimum element size of 3.2×10^{-5} km. The maximum deflection of the sill roof is 30 m, as calculated from Eq. (6.4). This can be mirrored by numerical model results whose set-up is illustrated in Figure 6.15 with the same parameters as above. The graphical representation in Figure 6.16 from the numerical model shows the deflection of the sill roof also to be 30 m.

In general, Figure 6.17 shows that the maximum tensile stresses are at the periphery of the sill, while the maximum deformation is above the centre of the sill. Layer 1 is the horizon at which the sill is emplaced and layers 2-6 are above the sill. With increasing distance from the sill, the tensile stresses become relaxed around the margins of the sill from 30 MPa to 13 MPa. However, due to the effects of the free surface, tensile stresses increase above the centre of the sill and increase towards the surface (from layers 4-6) from approximately 16 MPa to at least 30 MPa. The deformation that is occurring above the sill is largest in the layer directly above the sill, ~50 m, and remains fairly constant in adjacent layers, ~35 m, with no enhanced effects from the free surface. Thus, the large tensile stresses generated above the

centre of the sill, towards the Earth's surface allow for the formation of tension fractures.

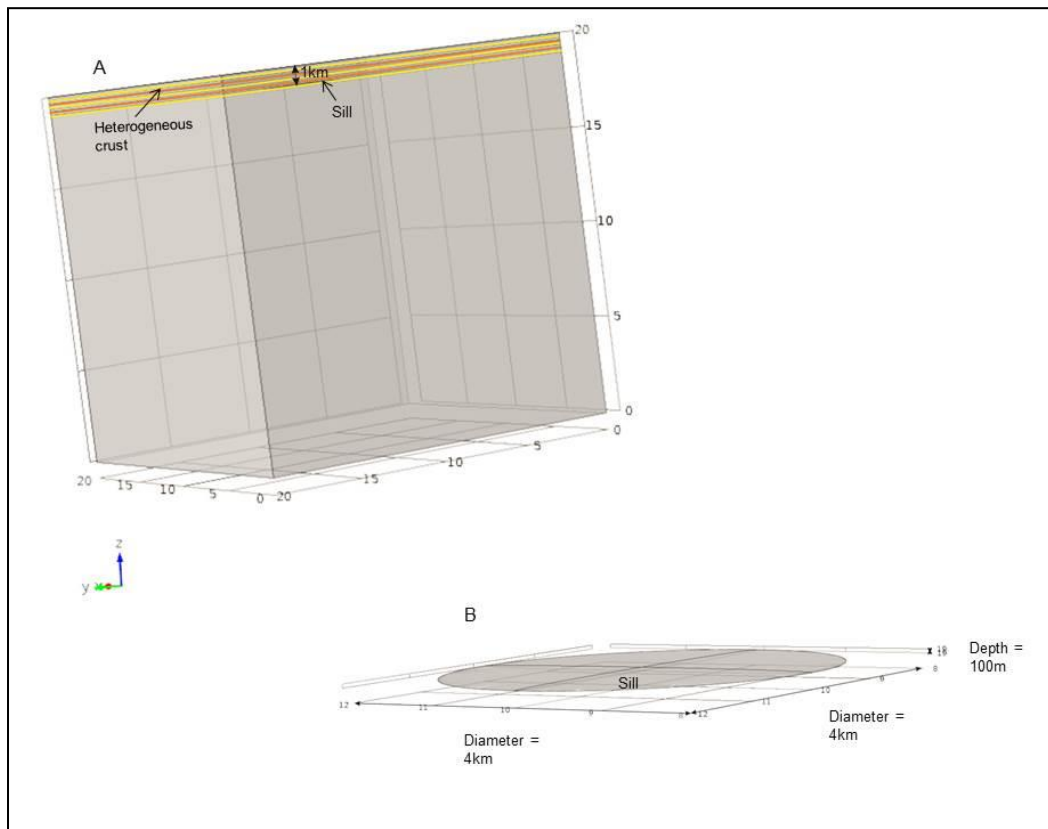


Figure 6.15: (A) Schematic illustration of a large sill emplaced into a heterogeneous crust 1 km below the surface. (B) Illustration of the sill parameters. The orange layers are soft pyroclastic layers of 5 GPa in comparison to the yellow stiffer basaltic layers of 20 GPa.

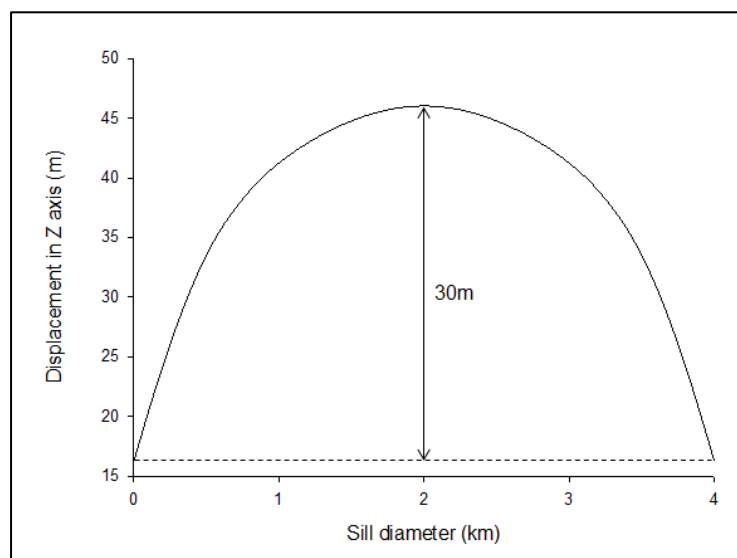


Figure 6.16: Numerical representation of the maximum deflection of the large sill roof at 30 m (the starting point is at 17 m with a maximum displacement of 47 m).

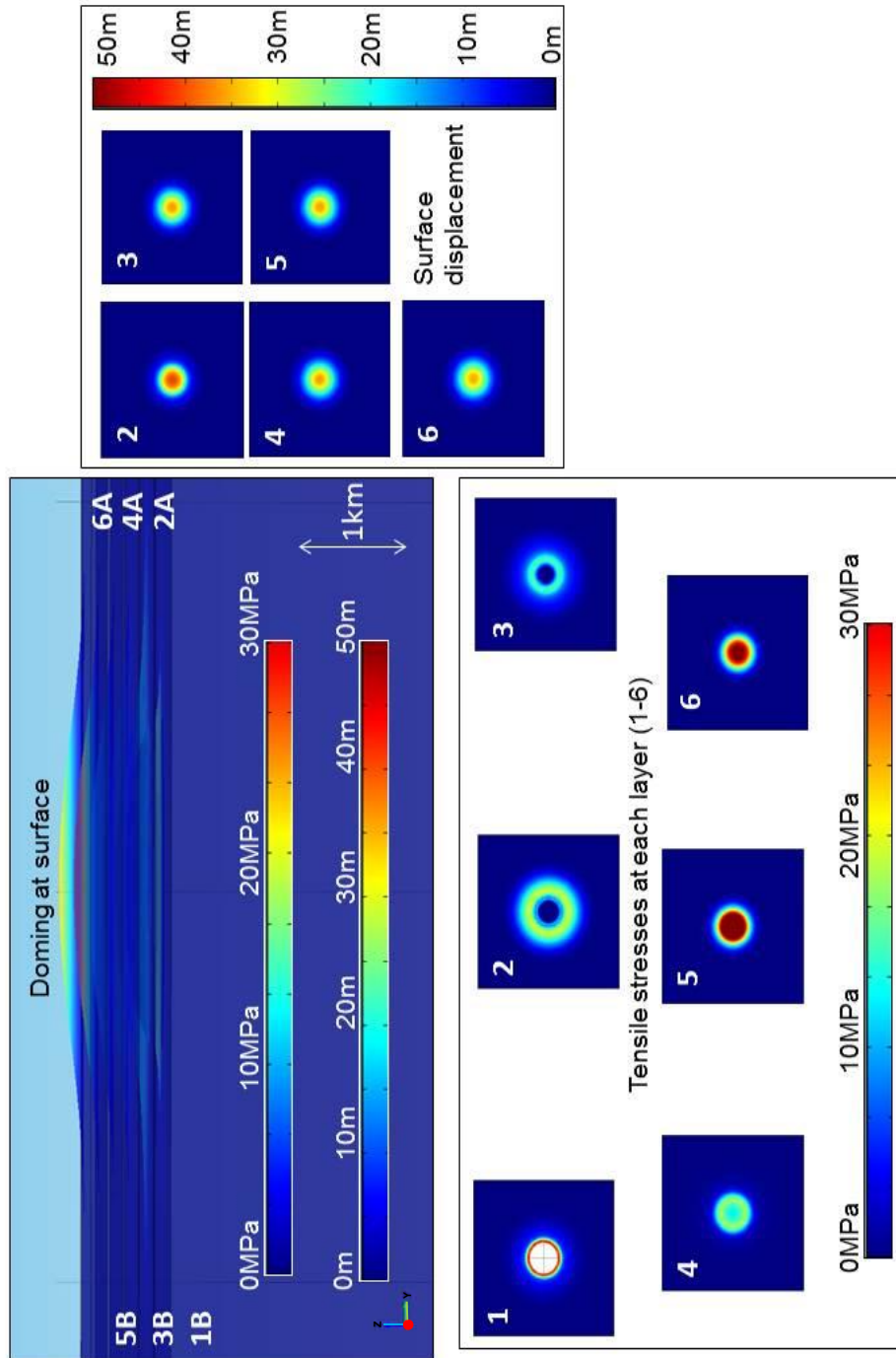


Figure 6.17: 3D FEM model of tensile stresses and surface deformation relating to a large sill. Right- shows the deformation of each layer above the sill, layer 2 being directly above the sill and layer 6 being the surface. Bottom- shows the tensile stress distribution around the sill (1) and distributed in the overlying layers (2-6).

The underburden deflection was also modelled, first in a one layered system (Fig. 6.18) and second in a multilayer system (Fig. 6.19). With both sets of systems, the sill is emplaced at an interface, with an overlying stiff layer, and an underlying soft layer. However, between the two systems the stiffness varies, by a factor of four in Figure 6.18 and a factor of three in Figure 6.19.

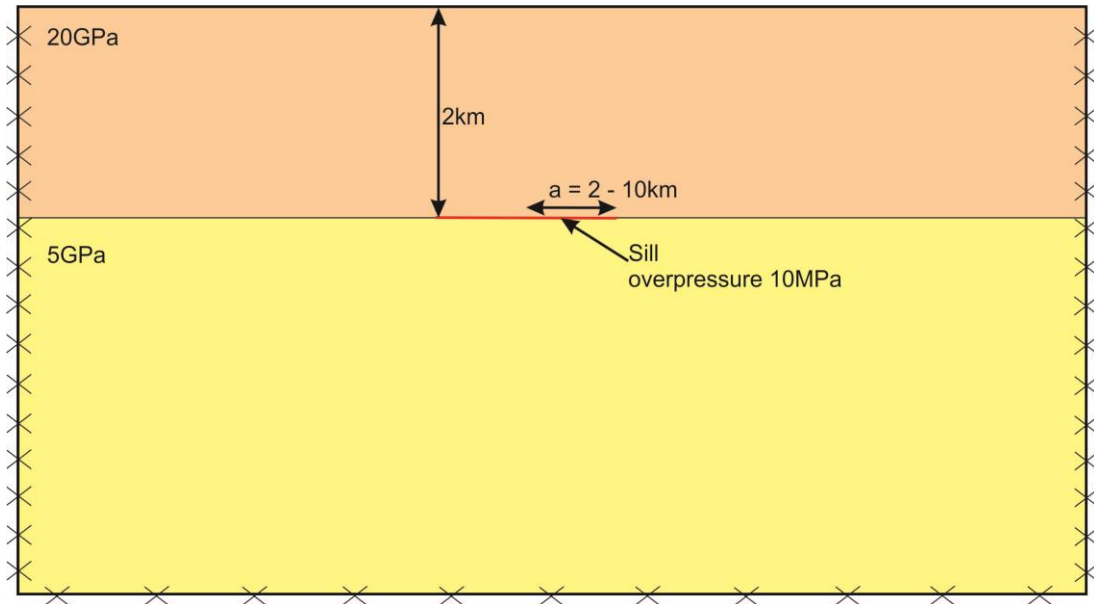


Figure 6.18: Schematic illustration of a large sill (radius, a , varies between 2 and 10 km) with a magmatic overpressure of 10 MPa, emplaced 2 km below the free surface into a single layered system. Orange layer is stiff, $E = 20$ GPa, and yellow layer is soft, $E = 10$ GPa.

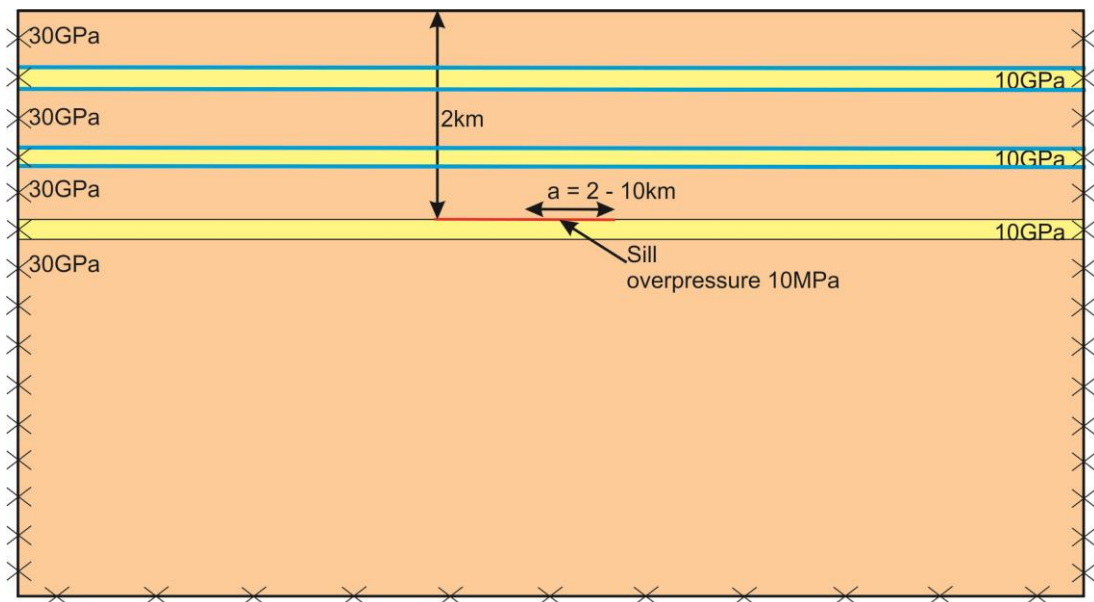


Figure 6.19: Schematic illustration of a large sill (radius, a , varies between 2 and 10 km) with a magmatic overpressure of 10 MPa, emplaced 2 km below the free surface into a multilayered system. Orange layers are stiff layers, $E = 30$ GPa, and yellow layers are soft layers $E = 10$ GPa, blue lines are weak contacts, with a spring constant of 1 MPa/m.

In Figure 6.20 the sill diameter varies between 4 km and 11 km and in Figure 6.21 the sill diameters are larger, from 8 km to 20 km. In general, as the sill diameter increases, so does the deflection of the roof and the floor of the sill. However, the deflection of the floor is far less than that of the roof. For example, a sill with a diameter of 4 km has a floor deflection of 5 m and a roof deflection of 9 m, which is almost double, but a sill with a diameter of 20 km has a floor deflection of 26 m and a roof deflection of 635 m, nearly twenty five times more. The relationship between the deflection of the floor and roof of the sill is portrayed in Figure 6.22, which shows a strong polynomial trend to both the floor ($R^2 = 0.997$) and the roof ($R^2 = 0.998$) deflection. These trends both have a degree of two, where the leading coefficient is -0.06 for the floor and 11.27 for the roof. Thus, with a degree of two there is one turning point. This turning point most likely relates to the mechanics of the layers, as it is harder for the sill floor to depress the underlying stiffer layer than it is for the roof to uplift a softer layer.

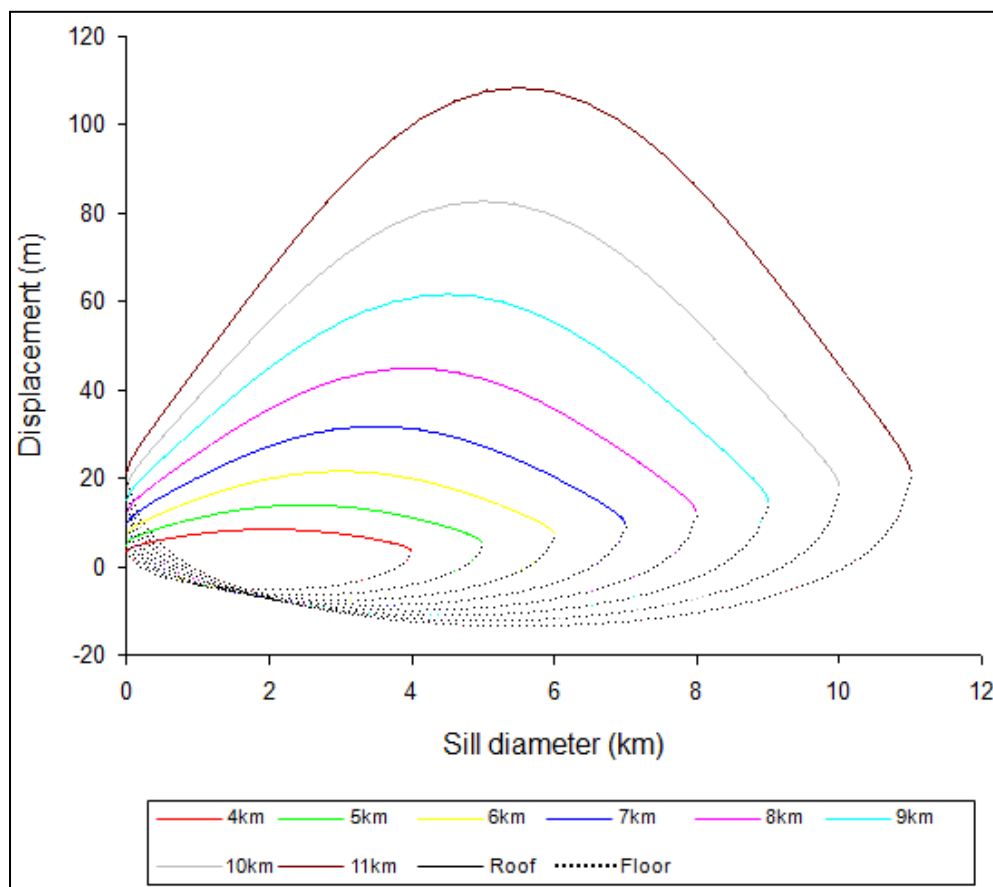


Figure 6.20: Graphical representation of sill roof (solid line) and floor (dashed line) deflection for varying sill diameters of 4-10 km based up on the model set-up in Figure 6.18.

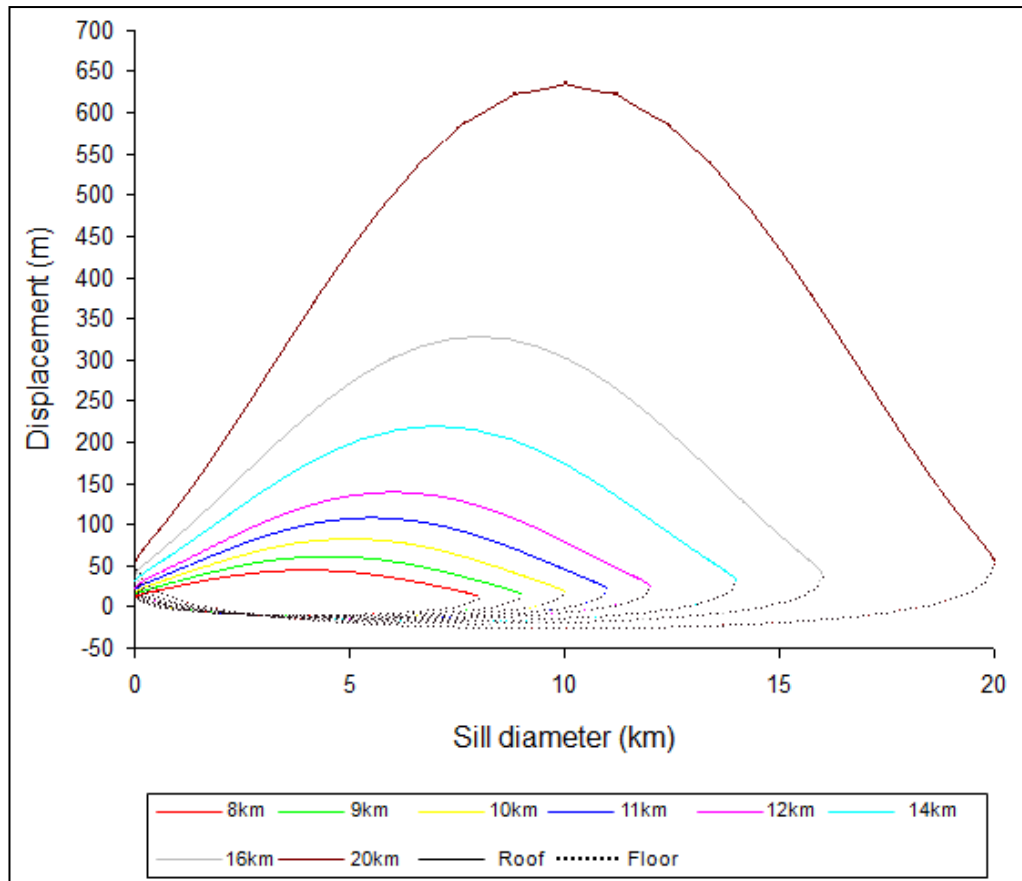


Figure 6.21: Graphical representation of sill roof (solid line) and floor (dashed line) deflection for varying sill diameters of 8-20 km based upon the model set-up in Figure 6.18.

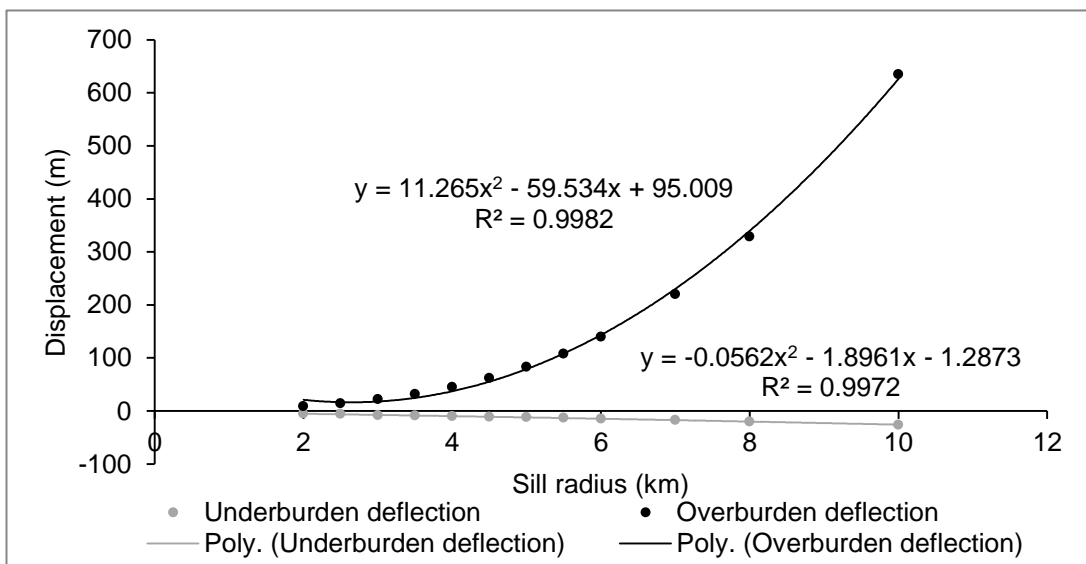


Figure 6.22: Graphical relationship between the underburden deflection (sill floor) and the overburden deflection (sill roof) illustrating a strong polynomial trend.

Similar results can be seen with a multilayer system, where the sill diameter varies from 4 km to 11 km (Fig. 6.23) and 8 km to 20 km (Fig. 6.24). However, the deflection of the sill floor is best described to be negligible in comparison to the sill roof. For example, the floor is deflected 1 m and the roof is deflected 52.5 m for a sill with a diameter of 4 km, but for a much larger sill of 20 km diameter, the floor is deflected 6.7 m while the roof is deflected 1.6 km. This relationship, which is strongly polynomial, is illustrated in Figure 6.25, and is similar to Figure 6.22, for the floor ($R^2 = 0.998$) and the roof ($R^2 = 0.999$). The polynomials have a degree of two, with a leading coefficient of 0.04 for the floor and 3.01 for the roof. Again, this degree of two is most likely related to the mechanics of the layers, but unlike the single layer system (Figs. 6.20-6.22) relates to the multiple layers above and below the sill. Lastly, the geometries of these curves (Figs. 6.20, 6.21, 6.23 and 6.24) represents the deformed sill body, and therefore, we can see that as the lateral dimensions of the original sill increase towards 20 km, inflation is similar to that of a laccolith (mushroom shaped).

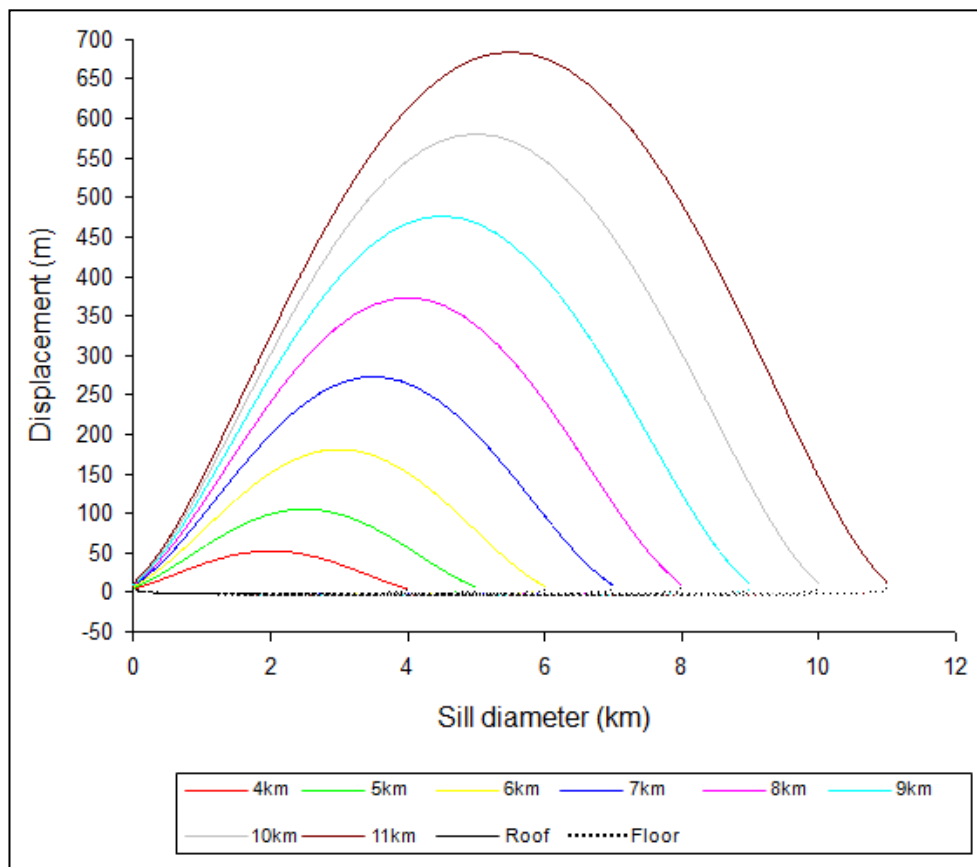


Figure 6.23: Graphical representation of sill roof (solid line) and floor (dashed line) deflection for varying sill diameters of 4-10 km based up on the model set-up in Figure 6.19.

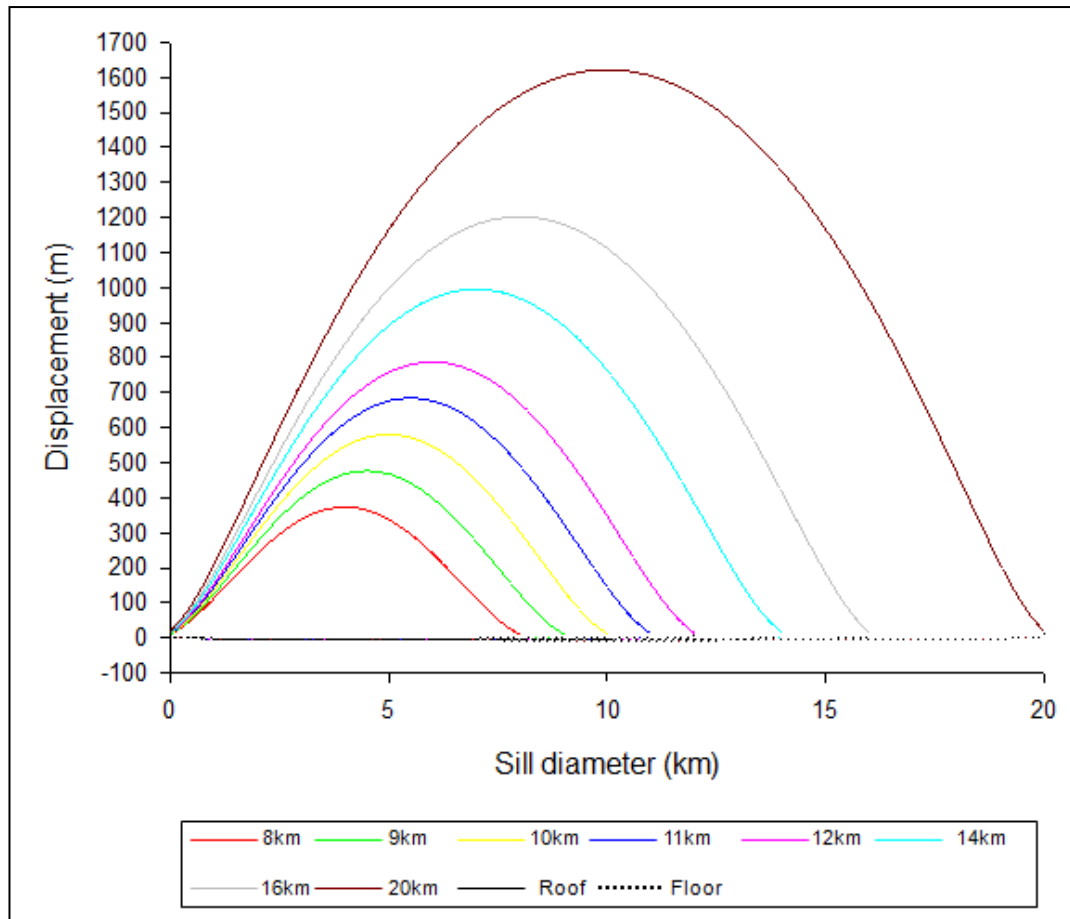


Figure 6.24: Graphical representation of sill roof (solid line) and floor (dashed line) deflection for varying sill diameters of 8-20 km based up on the model set-up in Figure 6.19.

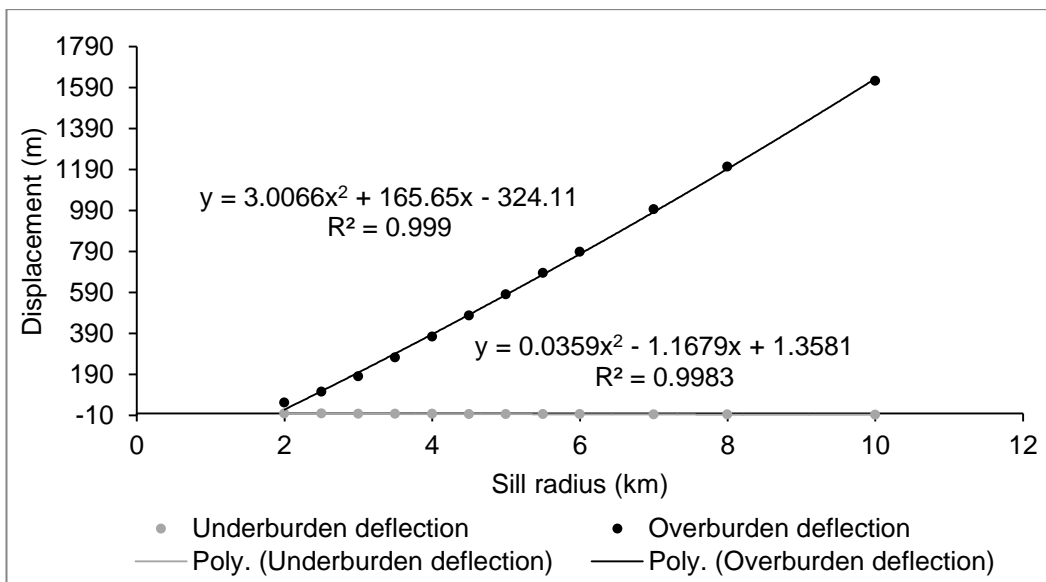


Figure 6.25: Graphical relationship between the underburden deflection (sill floor) and the overburden deflection (sill roof) illustrating a strong polynomial trend.

3D results in Figure 6.17 were compared with a 2D framework (Fig. 6.26). The sill is emplaced at a depth of 1 km into a host rock with a stiffness of 40 GPa. Above the sill there is a heterogeneous crust with ten layers, which alternate in stiffness between 10 GPa and 30 GPa. This model was set up for comparison with Figure 6.9 to show the effects of sill inflation, thus the mesh quality is the same. The tensile stresses at the tips of the sill are in the order of 100 MPa, illustrating a zone of high stress where the sill would grow laterally. However, these large tensile stresses are only theoretical and not realistic in nature. This is because the tensile strength of the host rock is approximately 2-4 MPa (Gudmundsson, 2011a), thus tensile stresses of 100 MPa cannot be maintained in nature as the host rock would fracture. The most prominent feature of this result is the deflection of the overburden accommodating sill inflation. This sill inflation would cause ground deformation and doming, inducing seismicity as new fractures form.

Large sills have the ability to function as shallow magma chambers because the time it would take for the magma to solidify is much longer than that of a small sill. Taking Jaeger's (1957) equation $t = 0.0825.w^2$, the time, t in years, it would take for a sill whose maximum deflection is 30 m to solidify would be just over 74 years. However, other parameters must be satisfied and are discussed in subsequent sections within this chapter.

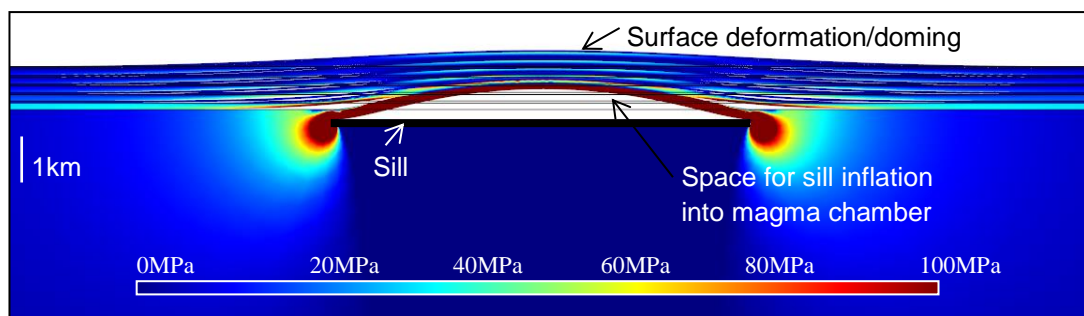


Figure 6.26: FEM model of tensile stress contours of a large sill, with a diameter of 4 km, emplaced at a depth of 1 km into a stiff, 40 GPa, layer. Above the sill there are alternating soft, 10 GPa, and stiff, 30 GPa, layers. The white area above the sill shows the deformation/upbending of the overburden to accommodate sill inflation. This deformation is also induced at the surface causing seismicity (Barnett and Gudmundsson, 2014).

In summary therefore, sills grow primarily from their tips as illustrated in Figure 6.27A and secondly via inflation as illustrated in Figure 6.27B. As shown in Figures 6.5 and 6.6, large concentrations of tensile (and shear) stresses exist about the sill tip. This can be inferred as a zone, specifically a process zone, where micro-cracking occurs. Micro-cracking may be the formation of new fractures or reactivation of old fractures, but these fractures determine the direction in which the sill advances. The magma then fills the tip of the sill, forming new tip stresses. Therefore, sill advancement can be described in three steps as illustrated in Figure 6.27A. Vertical sill growth or inflation depends on the lateral dimensions of the sill, the loading induced by the overburden, and whether the magmatic overpressure within the sill can overcome the tensile strength of the adjacent crustal layer. Generally, in order for deflection of the overburden to occur, a sill is described as being large, where the radius of the sill is equal to or larger than the depth at which the sill is emplaced (Figs. 6.17, 6.22, 6.25 and 6.27B).

6.4 Whin Sill

Fieldwork from the Whin Sill, NE England (Chapter 4 for detailed location map and geological history) has provided insights into the geometry of the sill complex, flow of magma within the sill and also, thermal relationships. Many of the outcrops yield very good columnar joints, and from the thickness of these columns the cooling of the sill can be determined qualitatively (Fig. 6.28). At the northern part of the complex, along the Northumberland coastline, the columns are relatively thin, approximately 0.1-0.2 m (Fig. 6.28A), whereas towards the southern part of the complex in Co. Durham, the columns are much thicker, approximately 0.4-0.5 m (Fig. 6.28C). The internal texture or grain size of the micro-gabbro is also an indicator of the magma cooling rate (Fig. 6.28B and C). Columnar joint morphology and magma cooling rates were investigated by Toramaru and Matsumoto (2004). They used analogue modelling to determine the relationship between the columnar joint thickness (modelled from a starch-water material) and the cooling rate (varying the distance from a lamp or heat source). They show that the cooling rate does not affect the mechanics of columnar joint formation, but the cross-sectional area of the columnar joint increases with increasing distance from the heat source. Thus, larger

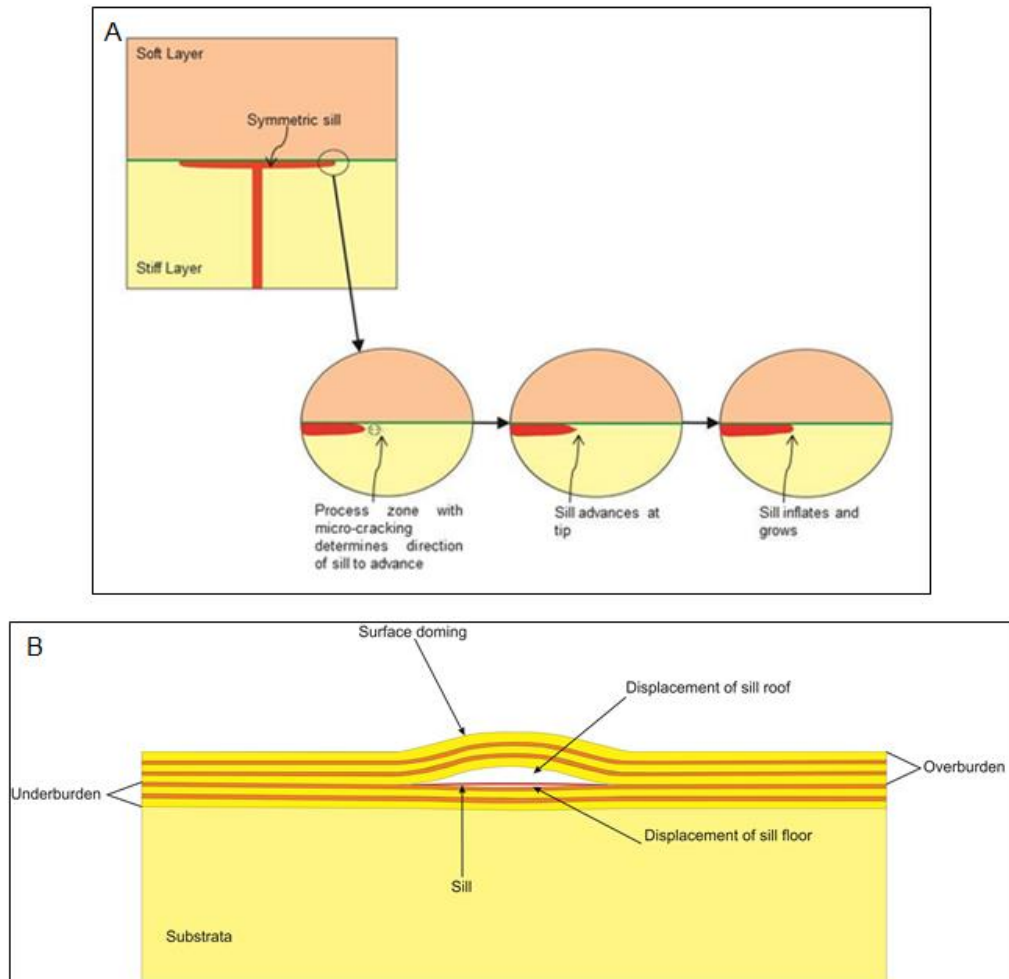


Figure 6.27: Schematic illustrations of sill growth. (A) Lateral sill growth and (B) vertical sill growth. Please see text for description.

columns are formed with a slower cooling rate because the cross-sectional area of the columns is inversely proportional to the cooling rate. Therefore, larger columns seen in Co. Durham reflect a slower rate of cooling, which is also reflected by the coarser grain of the micro-gabbro in the larger columns compared with the smaller columns and finer texture seen along the Northumberland coastline.

Flow structures were seen at two sites in Northumberland, Holy Island and Harkess Rock (Fig. 4.8). These flow structures have a ropey texture, similar to a pahoehoe lava flow. Liss *et al.* (2002) give an account of how these flow structures may have formed. They propose that the apex of the parabola structure, formed as a result of shearing by the magma flow, determines flow direction. When conducting fieldwork for this thesis, forty seven flow structures were identified (grid reference: NU17710

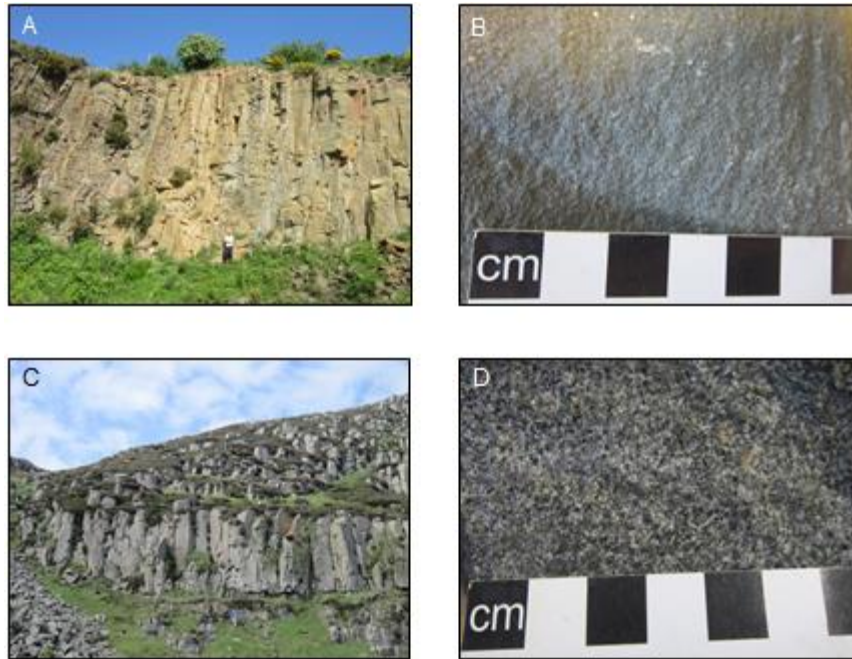


Figure 6.28: (A) Snableazes Quarry, view NE, columns have a small width, person for scale. (B) Fine grained texture to microgabbro from Snableazes Quarry. (C) Falcon Clints, view N, columns have a large width, person for scale. (D) Medium grained texture to microgabbro from Falcon Clints.

35652) and their dimensions and orientations were recorded. From Figure 6.29 an approximate flow direction to the southwest is illustrated, which is in agreement with Liss *et al.* (2002). Therefore, because these ropey flow structures represent a frozen record of the magma flow direction, it can be interpreted that the flow direction of the magma at the upper contact of the Whin Sill was in a south westerly direction.

At Snableazes Quarry (grid reference: NU22387 14028, Figs. 4.8 and 6.30) and at Cullernose Point (grid reference: NU25966 18692, Fig. 4.8) fingers of magma were identified that branched away from the main Whin Sill. Schofield *et al.* (2012) suggest that these fingers of magma represent non-brittle emplacement of magma into an unlithified or poorly consolidated host rock, which has the ability to act in a ductile behaviour, for example shale (Liss *et al.*, 2004; Thomson, 2007). The non-brittle emplacement of the magma implies that the host rock could flow in a viscous manner. Thus, the emplacement of these magma fingers is related to the rheology of the host rock as well as the dynamics of the magma.

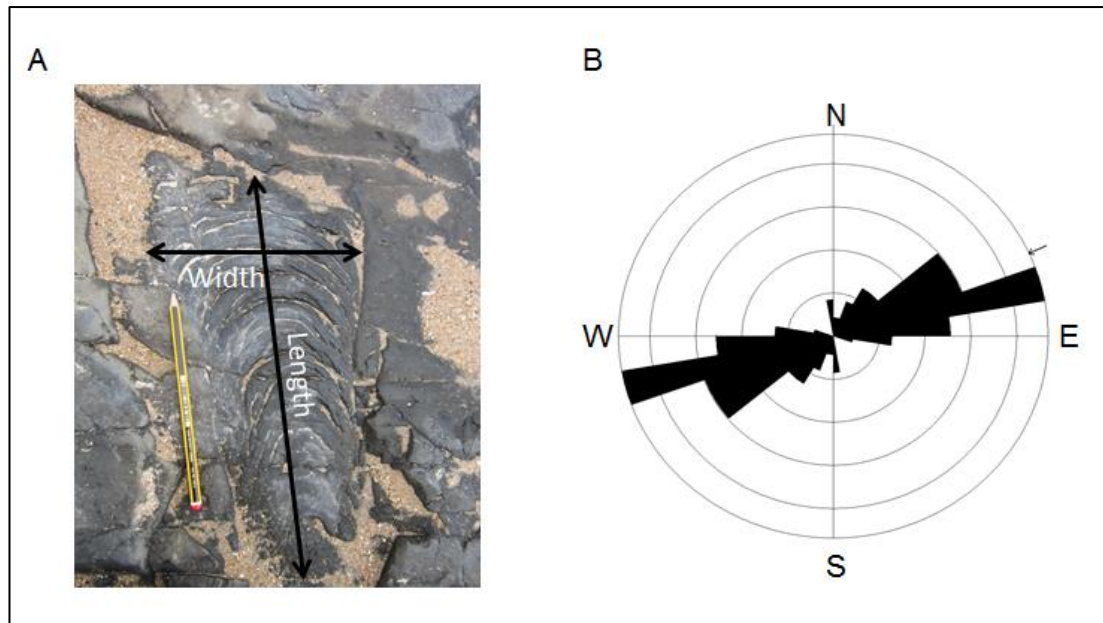


Figure 6.29: (A) Ropy flow structure, where the ropes can be defined by the infilling of sand grains. Flow direction towards the SW, where the apex of each parabola shaped rope closes. Length 39 cm, width 18 cm. (B) Rose diagram illustrating the direction of the 47 ropy flow structures towards the SW (circle interval 5%, sector angle 10°).

Study of the Whin Sill also gave the opportunity to investigate the effects of contact metamorphism. Contact metamorphism was identified both above and below the Whin Sill, but not necessarily at each location. The thickness of the contact metamorphosed zone varied between lithologies, where thicknesses of 40 m have been recorded by Johnson and Dunham (2001), although the outcrops visited exhibited metamorphosed zones a few metres thick. In the field, contact metamorphism was identified either by a change in colour or hardening of the lithology. This was particularly noticeable within the limestones, which had metamorphosed into marble, and therefore a sacroidal texture was plainly visible. This marble is colloquially known as ‘sugar limestone’ (Fig. 6.31). The thermal effects of sill emplacement, however, are beyond the scope of this thesis.

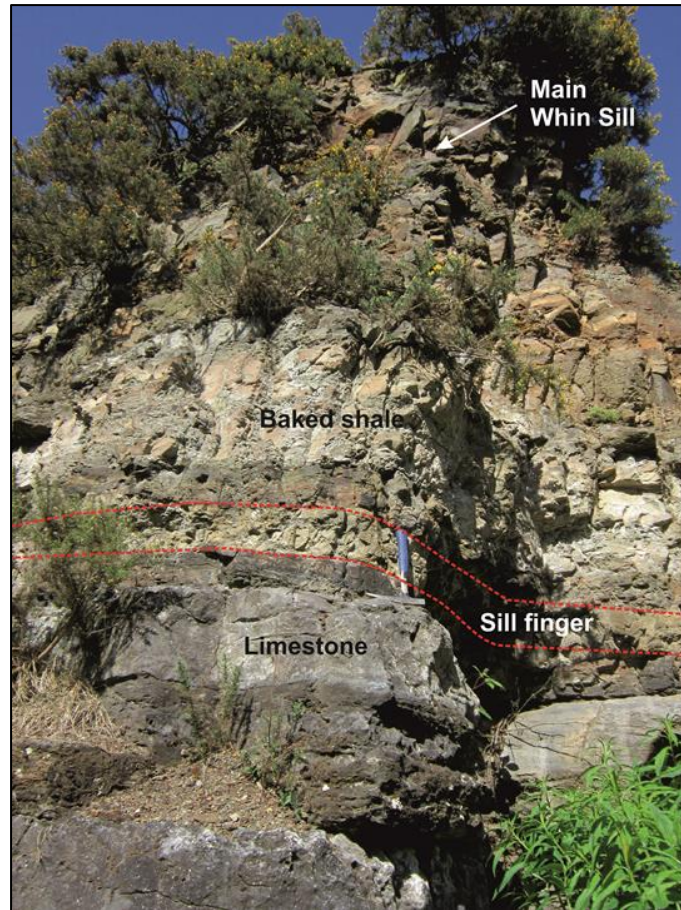


Figure 6.30: Magma finger from the main Whin Sill at Snableazes Quarry, view E, hammer for scale.



Figure 6.31: Photograph of impure marble, known as 'sugar limestone'. This sample was taken from a baked margin of limestone at Falcon Clints.

Following the contact of the Whin Sill at several localities gave an insight into its geometry, as the sill was seen to step or transgress through the stratigraphy (Fig. 6.32). These transgressions represent the brittle emplacement of the basic magma (Schofield *et al.*, 2012) and can be seen on a larger scale when examining the geological formations in which the Whin Sill intruded through. The locations of noticeable importance are at: Bamburgh Castle (grid reference: NU18176 35230; Fig. 6.32A), where the sill intruded a cross bedded sandstone of the Alston Formation; Snableazes Quarry (grid reference: NU22429 14003; Fig. 6.32B) above the sill contact there is sandstone and shale of the Alston Formation, and below the contact (grid reference: NU22408 14035) there is limestone from the Great Limestone Member; Howick Quarry (grid reference: NU23651 17645; Fig. 6.32C) where there is contact with limestone belonging to the Eelwell Limestone Member; Longhoughton Quarry (grid reference: NU22551 15137) where there is upper and lower contact seen with shale of the Strainmore Formation and limestone of the Great Limestone Formation; Ward's Hill Quarry (grid reference: NZ08201 96914, NZ07941 96663) where there is upper and lower contact with shale from the Strainmore Formation and limestone from the Great Limestone Member; Falcon Clints (grid reference: NY81723 28415; Fig. 6.32D) where there is lower contact of limestone seen belonging to the Lower Alston Group; High Cup Nick (grid reference: NY74564 26158) where there is lower contact with limestone and shale belonging to the Alston Formation; High Force (grid reference: NY87999 28369; Fig. 6.32E) where there is lower contact with limestone of the Alston Formation; and Low Force (grid reference: NY90473 27834; Fig. 6.32F) where there is lower contact with sandstone and shale metamorphosed into hornfels, also from the Alston Formation (British Geological Survey, April 2014).

6.5 Shallow magma chamber formation

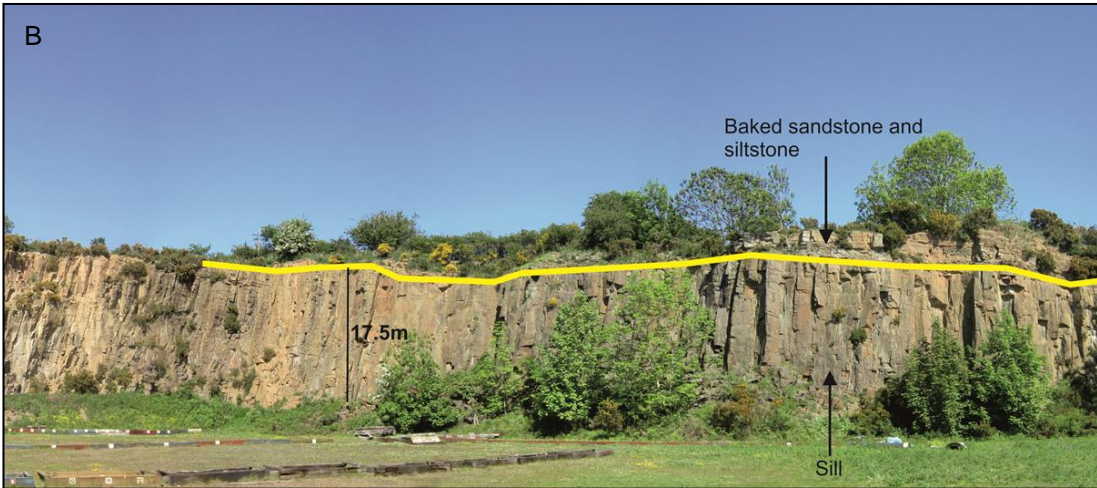
For many years, surface deformation generated by the inflation of a magma chamber has been explained in terms of the so-called 'Mogi model' or the nucleus-of-strain model (Anderson, 1936; Mogi, 1958). This is a simple analytical solution for an inflating spherical source (a magma chamber with a concentrated force with an infinitesimal volume) within a homogenous elastic half space, where there is a free

surface and four characterising parameters - the strength of the source and the three dimensional coordinates of the source centre. The nucleus-of-strain model produces stresses and displacement within a distance below an elastic half space. However, this is based on an assumption that the stresses and displacements produced by the nucleus-of-strain relates to stresses and displacements produced by the excess magmatic pressure. The ‘Mogi model’ also does not take into account that magma chambers are finite with varying sizes. Therefore, magma chambers are modelled as a cavity in three dimensions, in an elastic half space because the chamber behaves elastically during periods of unrest. Generally, the main problem with this model is that it assumes a homogeneous and isotropic crust, which is never the case for active volcanoes. Thus, layering, contacts, faults and fractures are ignored and often gives highly unreliable results. This model is generally used when there is an axial symmetry, little data or as a test before analysing a more realistic model (Mogi, 1958; Gudmundsson, 2006; Bonafede and Ferrari, 2009; Transatti *et al.*, 2011).

In the past decade the ‘Mogi model’ has been refined and developed (McTigue, 1987; Yang *et al.*, 1988; Fialko *et al.*, 2001; Bonafede and Ferrari, 2009). For example, Bonafede and Ferrari (2009) modelled a spherical magma chamber within a viscoelastic half space. They found the overpressure within the source to cause large scale deformation, dependent upon rheological parameters, and that inflation of the spherical source is due to the input of new magma from a large distance. Yet, many models do not take into account the heterogeneity of the crust, and this applies to the ‘Mogi model’. However, Masterlark (2007) and Amoroso *et al.* (2008) did take into account the layering of the upper crust and show that layering of the crust and the associated volcano has large effects on the estimated depth of the magma chamber.

6.5.1 Sill evolution into a shallow magma chamber

To investigate the effects the sill has on the local stress field, a simple model was made of a dyke that has been doubly deflected into a sill at a weak contact with an overlying soft layer and underlying stiff layer. The mesh quality was defined with a maximum element size of 0.02 km and a minimum element size of 3.2×10^{-5} km. The results in Figure 6.33 illustrate the alteration in the local stress field, where there





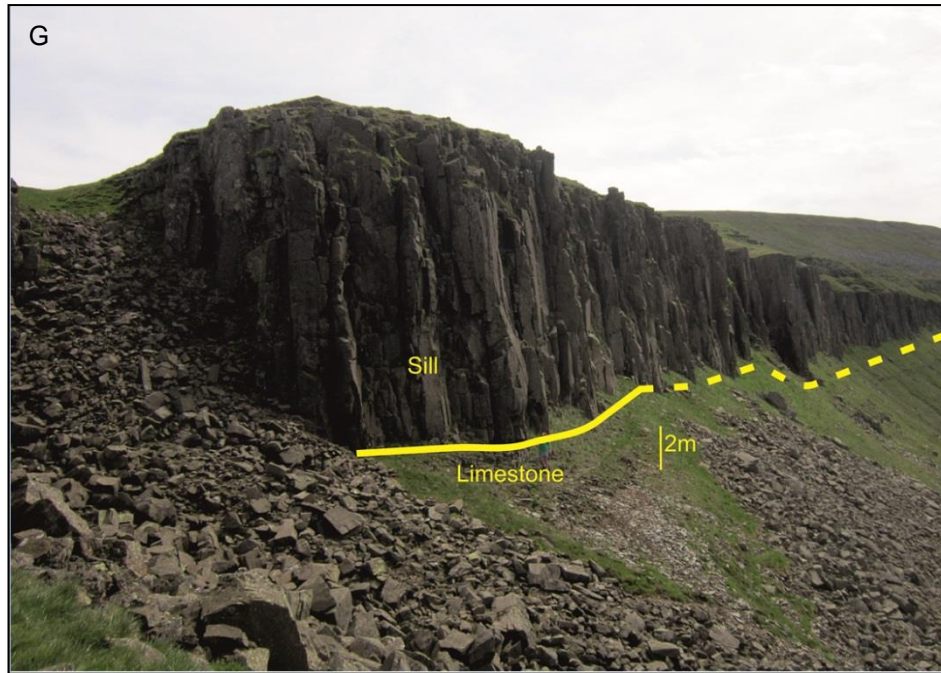


Figure 6.32: Photographs to illustrate various contacts seen in the field, demonstrating an overall stepped geometry of the Whin Sill. (A) Contact at Bamburgh Castle, view E; (B) Contact at Snableazes Quarry, view E; (C) Contact at Howick Quarry, view SW; (D) Contact at Falcon Clints, view NE; (E) Contact at High Force, view W; (F) Contact at Low Force, view SE; (G) Contact at High Cup Nick, view S.

is mainly a change in the vertical stress. This is because the sill grows primarily by upward bending of the overlying layers, so that the minimum principal compressive stress becomes the maximum principal compressive stress. The maximum principal compressive stress trajectories are inclined below the weak contact because of stress effects of the initial sill and its feeder dyke (Fig. 6.33A). As more dykes are injected into the system (Fig. 6.33B and C) they become deflected under the initial sill, because it is harder for later dykes to propagate through (partially) molten magma that resides in the initial sill. The magma transported by subsequent dykes can also be absorbed by the initial sill, and eventually expand into a shallow magma chamber, through under accretion.

As described in Section 6.3.2 a sill grows vertically by bending the adjacent layers (Figs. 6.17, 6.22, 6.25), mainly those above the sill, but to a smaller extent below the sill as well. The amount of deformation of the host rock depends on the dimensions

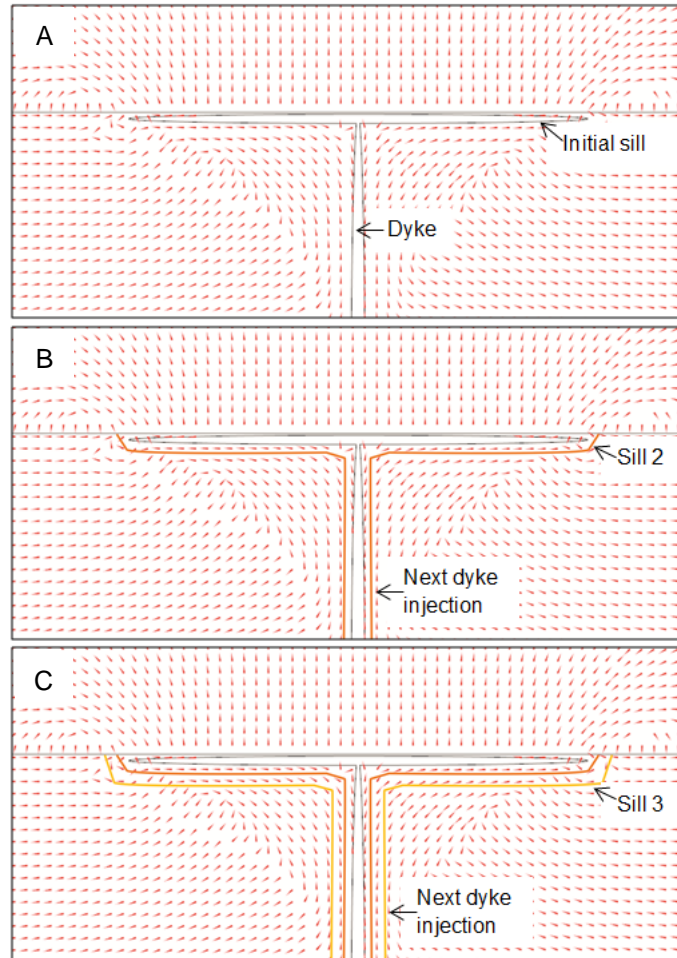


Figure 6.33: FEM model showing maximum principal compressive stress trajectories, red ticks and their distribution following the emplacement of a sill. Weak contact modelled as a thin elastic layer, with a stiffer, 20 GPa layer below the contact and a softer, 5 GPa layer above the contact, overpressure in the dyke/sill was 10 MPa. (A) Initial dyke was deflected at weak contact to form a symmetrical sill, (B) initial sill induces a stress barrier causing subsequent dyke injection to be deflected under the initial sill, this process is repeated in (C) to form a shallow magma chamber.

of the sill. To deform or bend the overlying layers, the sill must be classed as a large sill, where its radius is larger than the depth below the surface. In other words, the emplacement depth of the original sill determines flexural rigidity and the ability of the underlying layers to bend (Petraske *et al.*, 1978). Thus, for a magma chamber to develop, space must be created, which is normally generated via elastic deformation of the upper crust. The majority of magma chambers sustain an oblate ellipsoid geometry (Gudmundsson, 1990, 2012a), like that of a sill, until the magma chamber

becomes inactive (Fig 6.34; Gudmundsson, 1990, 2012a), for example at fast spreading ocean ridges (Macdonald, 1982).

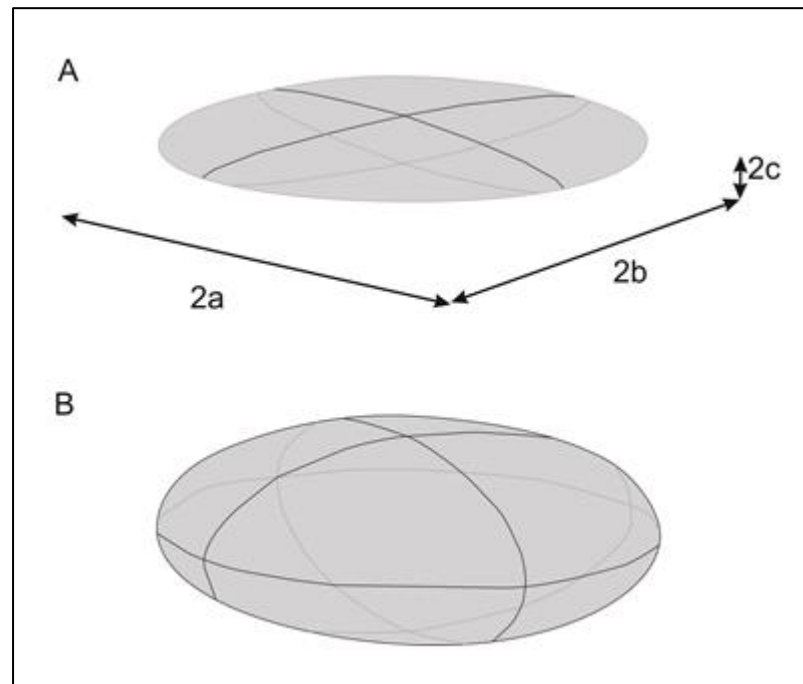


Figure 6.34: Schematic illustration of (A) penny-shaped sill that may inflate into (B) an oblate shallow magma chamber. $2A$ and $2B$ are the diameter of the sill; $2C$ is the depth of the sill.

6.5.2 Sill complexes

Previous works have been undertaken that focus on sill complexes, including magma chemistries and feeding mechanisms (e.g. Thomson and Hutton, 2004; Galerne *et al.*, 2008). A sill complex can be defined as a network of dykes and sills that are closely related to one another in the field or on seismic images. Sill complexes can develop continuous magma networks greater than 10 km in vertical height provided the stacked sills are interconnected by junctions – either sheets or dykes (Cartwright and Hansen, 2006). Sill complexes can also be laterally extensive, often referred to as compound sills (Hansen *et al.*, 2004). The feeding relationships of sill complexes have been studied in the field and on seismic lines, where Thomson and Hutton (2004) suggest that sill complexes in the North Rockall Trough could be nested, forming inter-feeding sill complexes. On the other hand, Galerne *et al.* (2011) illustrate 3D relationships between sills and their feeders from the Golden Valley sill complex, Karoo Basin in South Africa, where the feeders were most likely dykes and

not other sills. This interpretation has been supported by experimental modelling and geochemical analysis.

Sill complexes as seen in the caldera walls of Las Cañadas in Tenerife (Fig.5.1B), are emplaced in a relatively short period of geological time. The upper sill is often regarded as the oldest. This is because latter magma injections through dykes, would most likely be unable to propagate through the initial sill; firstly, because the initial sill is potentially still partially molten and secondly, the contact between the initial sill and the host rock will favour dyke deflection at this contact.

Numerical models in Figure 6.35 show how varying overpressure (10 MPa, 1 MPa and 0.2 MPa) and sill dimensions (7 km, 5 km and 3 km) can have an effect on whether the sill will rupture or not due to the accumulation of tensile stresses. The mesh is the same as for Figure 6.33. Figure 6.35A1 shows that the large sill (7 km), with the largest overpressure (10 MPa) dominates the local stress field and induces large stresses, ~35-40 MPa at the surface. Also, the upper margin of the middle sill (5 km) concentrates stresses of <35 MPa, and therefore magma could migrate upwards into the overlying small sill (3 km), which too is ruptured at its lower margin. Figure 6.35A2 illustrates that the small sill (3 km) with the largest overpressure (10 MPa) dominates the local stress field. The middle sill (5 km) becomes ruptured at the centre of its upper margin, with tensile stresses >40 MPa that relates to the zone of stresses from the tips of the upper sill (7 km). Figure 6.35A3 illustrates the stress distribution of varying sill sizes, while the overpressure remains constant (10 MPa) between them. This shows that the largest sill, similar to that of Figure 6.35A1 has a slightly wider radial zone of tensile stresses of 30-40 MPa. The tip stresses of each sill form a linear zone of stresses of 10-25 MPa, which induce a semi-circular zone of tensile stress of 40 MPa at the surface, where the greatest concentration is above the central axes of the sills.

Figure 6.35B1 illustrates that the large overpressure, 10 MPa, within the lower sill generates large tensile stresses, 40 MPa, which induces stresses of the same magnitude at the lower margin of the middle sill. Thus, magma could migrate from the lower sill into the middle sill. Figure 6.35B2 shows the vice versa of Figure 6.35B1, which illustrates the effects of the large overpressure in the upper sill that generates tensile stresses of 40 MPa at the tips and also at the upper margin of the

middle sill. This indicates that magma could migrate from the middle sill, as the upper margin is ruptured, into the upper sill, whose lower margins are ruptured. Figure 6.35B3 illustrates, as in Figure 6.35A3, that the larger sill generates large tip stresses, 40 MPa, which induces large surface stresses of the same magnitude.

Figure 6.35C1-C3 illustrates similar stress patterns as Figure 6.35B1-B3, but of a higher magnitude, as the location of the large sill is now at the top of the complex. In general, it can be concluded from the results that the sill with the largest dimensions, irrespective of its location within the complex, dominates the local stress field. Also, the largest sill induces stresses at the free surface and into the host rock, which may form interconnected fractures that could conduct magma either towards the surface or to the overlying sills. Furthermore, the overpressure has large effects on the local stress field and is also irrespective of the sill dimensions.

The rupture of these sills because of large tensile stress generation allows for the possible formation of a shallow magma chamber. This is because fractures form between the sills due to the large tensile stress field, and magma can be transported along these fractures interconnecting the individual sills into one possible magma chamber. These results are also seen in 3D models (Fig. 6.36). It is important to note that the large tensile stresses of 40 MPa are purely theoretical and are unrealistic in nature due to the tensile strength of rock being in the order of 2-4 MPa (Gudmundsson, 2011a). Thus, tensile stresses of 40 MPa are much larger than the tensile strength of rock in nature, and the host rock would have broken long before these model stresses can be achieved.

As shown in Section 6.3.2 in this chapter, sills can inflate vertically. Therefore, there is the possibility that individual sills within a complex could amalgamate through the inflation of each sill (Fig. 6.34), where inflation causes fracturing of the overburden and creates pathways for magma to be transported between each of the sills. Amalgamation, however, requires sills to be within a critical distance of each other, and depends also on sill radius and overpressure. This is portrayed in Figure 6.36, where models A and C show the sill deformation and the amalgamation of the sills into a possible shallow magma chamber. However, model B is unable to inflate sufficiently for the individual sills to amalgamate because the low overpressure of 0.2 MPa in the lower sill, and 1 MPa in the middle sill, is not large enough to overcome

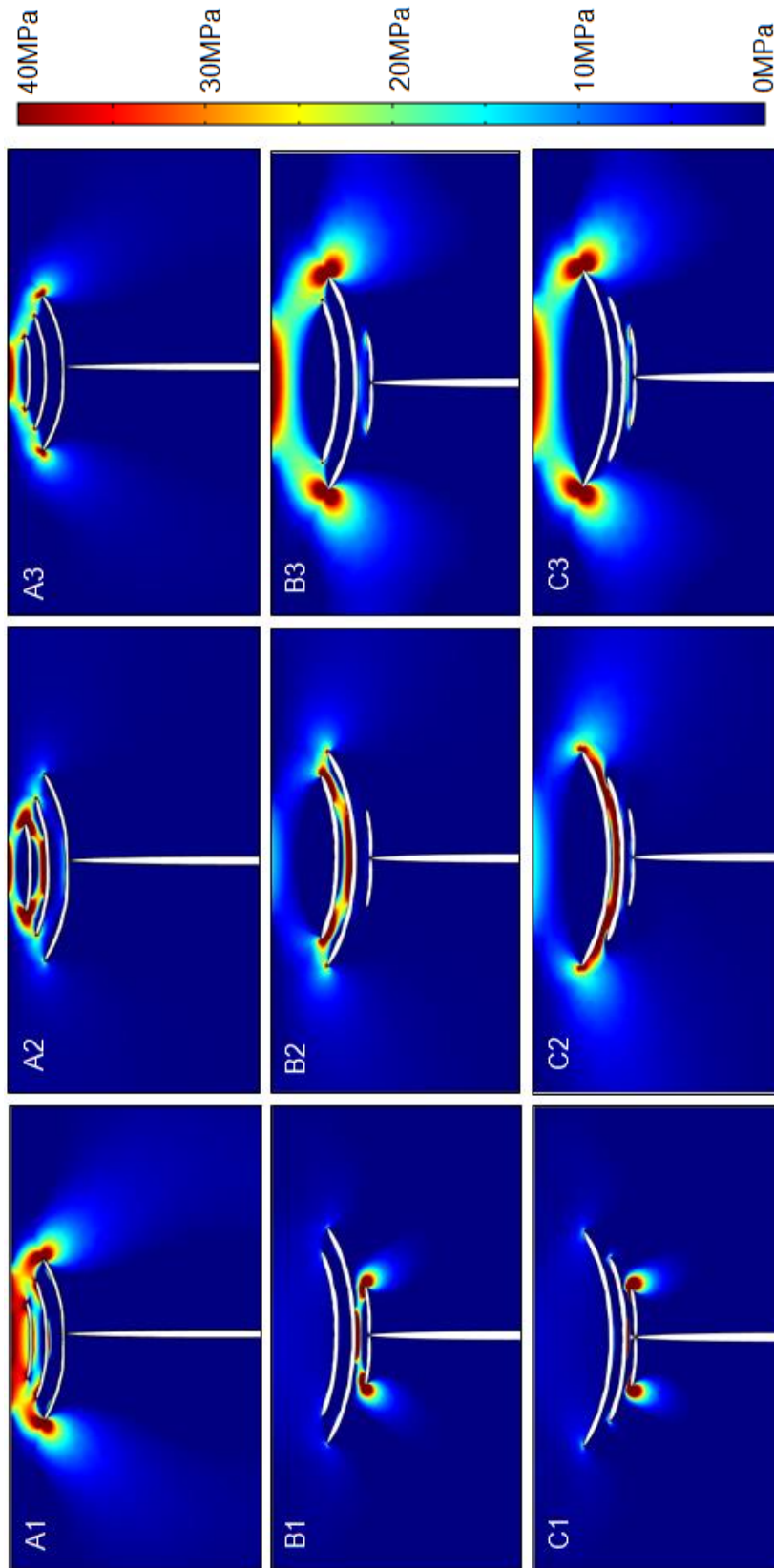


Figure 6.35: FEM models of tensile stress contours. (A-C) Largest sill varies in location in the sill complex and (1-3) overpressure within the sills varies throughout complex. Depth at which the dyke is deflected into the lower sill is 2.5 km below the Earth's free surface, where sides and bottom of the model are fixed. The host rock here is homogeneous, $E = 20$ GPa. (A) Largest sill is located at bottom of complex, (B) largest sill is located in centre of complex and (C) largest sill located at top of complex. (1) Overpressure of 10 MPa, in the bottom sill, 1 MPa in middle sill, and 0.2 MPa in upper sill, (2) overpressure of 0.2 MPa in lower sill, 1 MPa in middle sill and 10 MPa in upper sill, (3) all sills have the same overpressure, 10 MPa.

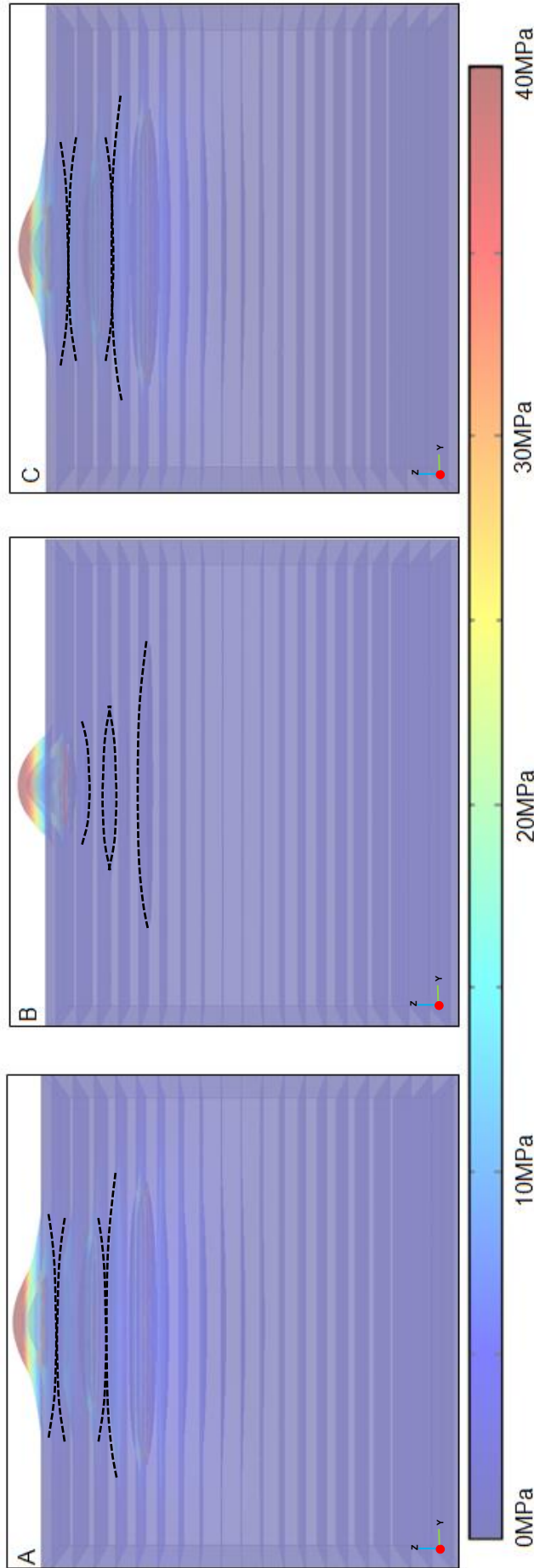


Figure 6.36: 3D FEM models of tensile stress contours with deformation for a sill complex. Sill ratio, a:b:c, where a is the sill radius in x-axis, b is the sill radius in the z-axis and c is the sill thickness in the y-axis, is as follows: large sill 1.5:1.5:0.015 km, middle sill 1:1:0.01 km, small sill 0.5:0.5:0.005 km. Depth of each model is 5 km beneath the Earth's free surface (three remaining sides are fixed) and the host rock has $E = 20$ GPa. (A) Large sill has the largest overpressure of 10 MPa, middle sill has an overpressure of 1 MPa and smallest sill has the smallest overpressure of 0.2 MPa. (B) Large sill has the smallest overpressure of 0.2 MPa, middle sill has an overpressure of 1 MPa, and the smallest sill has the largest overpressure of 10 MPa. (C) All three sills have the same overpressure of 10 MPa. (A) and (C) the three sills are seen to amalgamate into one (black dashed line), to form a shallow magma chamber, however this is not the case in (B) as the overpressure in the lower sills is not large enough to overcome the tensile strength of the host rock in order for the sills to inflate and amalgamate. Scale bar is faded, as the model is made up of a series of slices and is lit up with a screen light, enabling the visualisation of the deformation more clearly.

the tensile strength (maximum of 9 MPa; Gudmundsson, 2011a) of the host rock that has a Young's modulus of 20 GPa.

6.6 Discussion

6.6.1 Saucer-shaped sill emplacement mechanisms

There are three previous works that describe in detail the emplacement of saucer-shaped sills geometrically. These are illustrated in Figure 6.37. Francis (1982) states that magma with a constant pressure ascends through a dyke, where the density of the magma is greater than that of the host rock. At a contact, the dyke walls would collapse and the density contrast between magma and host rock would combine causing the magma to flow downwards towards the basin centre, below the level of buoyancy. Hydrostatic equilibrium would eventually be reached constraining magma accumulation to the basin floor. Hydrostatic equilibrium and the constant supply of magma from the dyke causes the magma to be forced updip on the opposite side of where the feeder dyke is emplaced within the basin. Francis's (1982) idea is based upon two sills, namely the Midland Valley Sill and the Whin Sill in the UK, and is represented in Figure 6.37A.

Chevalier and Woodford (1999) state that dykes feed inclined sheets causing the inclined sheet to propagate upwards to form a flat sill, which uplifts the overburden, this representing the outer sill. The overburden generates a force on the upper margin of the inclined sheet leading to further uplift, causing fractures to form adjacent to the inclined sheet at a lower level. This overtime forms the inner sill as the magma intrudes it. This hypothesis is based upon saucer-shaped sills in the Karoo Basin and is represented in Figure 6.37B.

Malthe-Sørensen *et al.* (2004) use numerical models where a low viscosity fluid is injected into an elastic medium at the level of neutral buoyancy. They state that a saucer-shaped sill forms as a result of relations between the overburden and the sill. A sill is emplaced into an originally isotropic stress field, but as the sill grows, anisotropy is induced into the stress field, in particular at the sill tips because the overburden is uplifted. This anisotropy impacts the geometry of the final sill and the formation of transgressive segments. First, the sill propagates linearly, but when the length of the sill is approximately equal to the overburden thickness, the sill begins

to propagate asymmetrically, inducing asymmetrical stresses at the sill tips. Second, asymmetry causes the sill to propagate upwards and uplifts the overburden, but because of pressure in the sill and the level of neutral buoyancy, the sill forms an outer sill at a lower angle close to horizontal. This hypothesis is based upon observations in sedimentary basins, for example the Karoo Basin, offshore Mid-Norway and NW Australian shelf and is illustrated in Figure 6.37C. Hansen and Cartwright (2006a) also support the work of Malthe-Sørensen *et al.* (2004), giving evidence that saucer-shaped sills are fed at the deepest point (although is not necessarily the central point) of the sill and propagate outwards to form the inner sill, upwards to form the inclined sheets and outwards again to form the outer sill. This model can be supported by back stripped data where the deepest part of the sill is the central part of the inner sill of the overall saucer-shaped geometry (Smallwood, 2009). Other seismic works and anomalies of magnetic susceptibility data (AMS), which provide information on the magma flow direction as magnetite orientates as a passive marker within the magma flow (e.g. Polteau *et al.*, 2008b; Galland *et al.*, 2009), show that a feeder at the shoulder of a saucer-shaped sill is not plausible (Hansen and Cartwright *et al.*, 2004; Thomson and Hutton, 2004; Polteau *et al.*, 2008b). This information supports the model by Malthe-Sørensen *et al.* (2004), where the feeder is located at the inner sill and the sill propagates upwards and outwards. Gouly and Schofield (2008) also support Malthe-Sørensen *et al.* (2004), as they use the theory of flexure to explain the emplacement of saucer-shaped sills, with results similar to what is observed in the Karoo Basin.

6.6.2 Shallow magma chamber formation

Formation of a shallow magma chamber could be best described as a process that is not continuous through space and time. A viable explanation for shallow magma chamber formation is by the incremental growth of sills or amalgamation of sill complexes. This then eliminates the ‘space’ problem if the shallow magma chamber is to grow just via inflation. Also, incremental growth could explain the formation of laccoliths as described by Cruden and McCaffrey (2006).

Doming of the overlying strata (Hansen and Cartwright, 2006a; Thomson, 2007) only

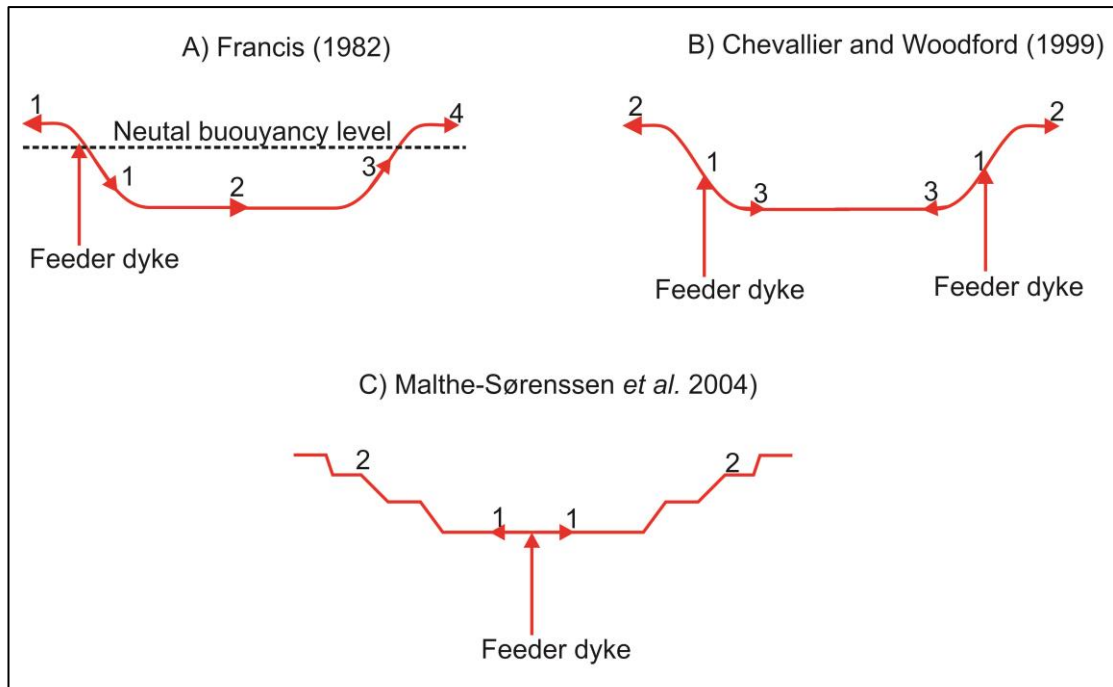


Figure 6.37: Saucer-shaped sill emplacement based on a) Francis (1982), b) Chevallier and Woodford (1999) and c) Malthe-Sørensen *et al.* (2004). The numbers on each model represent the steps in which the sill transgresses, and the arrows represent the flow of magma (modified from Polteau *et al.*, 2008a). Each of these models is discussed in greater detail above.

occurs at a certain depth as portrayed in Figures 6.17, 6.22 and 6.25. This is because of the flexural slip of the bedding, which requires a shallow depth where ductile deformation of the crust is dominant. This doming can firstly accommodate sill inflation, secondly allow for shallow magma chamber formation and thirdly can act as a trapping mechanism for other crustal fluids. Doming at the surface due to emplacement of intrusions has been studied for decades, for example Hawkes and Hawkes (1933), who studied the Sandfell laccolith, East Iceland, and Geyer and Gottsmann (2010), who studied the Rabaul uplift between 1971 and 1984. Hawkes and Hawkes (1933) provide field evidence that the host rock is upturned at approximately 60° to accommodate the Sandfell laccolith. In order to accommodate the laccolith, there would have been fracturing, flexing and differential displacement of the host rock above the roof of the laccolith. It is known that the doming of the host rock is due to the emplacement of magma, rather than due to an orogeny, as there is no folding of the local rocks. Hawkes and Hawkes (1933) concluded that space was 'created' via elastic bending in a NW-SE direction. Geyer and Gottsmann

(2010) use finite element modelling to analyse the effects of a layered crust with varying mechanical stiffnesses. They conclude from generic models that the surface deformation depends on the layered system, that is, the location of the soft and stiff layers with respect to the location of the shallow magma chamber. This result is also shown in Figures 6.13 and 6.14. On the other hand, at greater depths the overlying strata may have become faulted due to the dominance of brittle deformation (Thomson, 2007). This brittle deformation can also be seen on seismic traces due to brittle magma emplacement, which can be recognised by the stepped nature of saucer-shaped sills.

In order for a sill to evolve into a shallow magma chamber there must be a high supply of magma, that is, the dyke injection rate must be high in order for the magma in the initial sill to remain a fluid. Hardee (1982) determined that for magma chamber formation, there needs to be magmatic injections at a rate of approximately $10^{-3} \text{ km}^3/\text{year}$ or more, and could be less than ten injections in total. This dyke injection rate however, also depends on the thickness of the initial sill. If the initial sill is thick, at least several metres, then the magma will remain at least partially molten for a longer period of time than that of a thin sill. For a sill or newly formed shallow magma chamber to remain at least partially molten there must also be a fine balance heat ratio between the heat that is generated by the emplaced magma within a certain area of the crust, and the heat that is conducted away from this area. This is because over successive magmatic injections, the host rock begins to melt because heat is given off to the surroundings, away from the sill. Therefore, heat can accumulate between each magma injection within the host rock (walls of the conduit), melting more of the surrounding host rock and previously solidified magma batches to form a potential shallow magma chamber. Thus, providing this heat ratio remains balanced, there will be a significant mass of magma in the chamber that could fuel an eruption (Hardee, 1982; Glazner *et al.*, 2004).

Burchardt (2008) numerically modelled the Njardvik Sill, NE Iceland, producing similar results as Figure 6.33. Burchardt's (2008) results show that the initial sill causes a rotation in the local stress field and that subsequent dykes and inclined sheets are then deflected into sills to form a complex. Also, with each new sill emplacement, the older (previously emplaced) sills could be partially melted again due to heat accumulation, and therefore, the potential for sills to form shallow

magma chambers increases. This is especially the case with the amalgamation of the sill complex in Figure 6.36. If the sills do amalgamate, magma mixing will take place, forming a more evolved magma because of melting of the wall rock, stopping and fractional crystallisation.

Finally, volcano load along with systematic magma injections favours sill emplacement and evolution into a shallow magma chamber. Volcanoes are dynamic systems and grow with each eruption and intrusion (Kervyn *et al.*, 2009). Stratovolcanoes (e.g. Fig. 6.8A, B, E and F) can be referred to as composite volcanoes and have steep flanks, commonly 35-42° (Gudmundsson, 2009). This steep angle is caused by the high material toughness of the composite volcano, which is composed of multiple mechanical layers. These mechanical layers provide a higher resistance to dyke propagation, and therefore, more energy is needed to fail the host rock because of mechanisms such as Cook-Gordon debonding. Shield volcanoes (e.g. Fig. 6.8C and D) on the other hand, may be regarded as a basaltic edifice, which have gentle dipping flanks, commonly 2-12° (Gudmundsson, 2009). This is because the layers are mechanically similar and therefore, less energy is needed for a dyke to propagate towards the surface. Thus, eruptions are more frequent than for composite volcanoes.

6.7 Conclusions

There are many examples of dykes never reaching the surface to feed an eruption, but are commonly arrested (non-feeders) or deflected into sills (Marinoni and Gudmundsson, 2000; White *et al.*, 2011). Sills may then have the ability to evolve into shallow magma chambers or laccoliths (Gudmundsson, 1990, 2011b; Menand, 2011). Based upon the numerical and analytical models in this chapter, several conclusions can be made on sills evolving into shallow magma chambers.

Sills can take a variety of forms, including straight, concave and stepped (or saucer-shaped), and their final geometry is determined by the mechanical properties of the host rock in which they are emplaced and by the topographical load. Shallow magma chambers tend to evolve from straight, elliptical sills that have lateral dimensions greater than their depth below the surface. This is a critical factor, as it determines whether the overburden (and to some extent the underburden) can be deflected

upwards as the sill inflates in order to create space for the expanding sill. This inflation could possibly allow for a sill complex to amalgamate into a shallow magma chamber depending on the sill geometry and distance between vertically adjacent sills.

Chapter 7: Faults - their permeability and relation to sills

7.1 Introduction

A fault can be regarded as a discontinuity within the brittle crust, where there is a resultant displacement owing to fault slip. A fault is not simple, although often conceived as a lineament (plane) where there is no internal structure. In reality, this is not the case; a fault has an internal structure, is in fact a zone of certain, but variable, thickness and is therefore, termed as a fault zone. The structure of a fault zone depends on the depth at which the fault is formed, the host rock, fluid flow, magnitude of slip and the tectonic regime (Faulkner *et al.*, 2010). Fault zones consist of two structural units, namely a core and a damage zone. The core may also be regarded as a fault-slip zone, as this is where fault displacement occurs (high strain) and the damage zone may also be termed the transition zone (low strain) (Figs. 7.1 and 7.2). Typically the boundary between the fault core and damage zone is sharp, while the boundary between the damage zone and host rock is often more progressive, where fracture intensity decreases and permeability structures relating to faults become absent (Caine *et al.*, 1996; Gudmundsson, 2001). These structural units are not always present in each fault zone (Caine *et al.*, 1996). Faults initiate from the coalescence of discontinuities, for example tension fractures, which is well demonstrated in the field, for example Þingvellir, SW Iceland. This example shows tension joints developing into a normal fault, where the trace of the tension fractures at the tip of the fault is much smaller than the fault itself. When plotted on a graph to show trace lengths versus tension fractures and normal faults, a power-law size distribution would be seen, where there are many tension fractures, as they are small in length, and fewer normal faults with large trace lengths (Gudmundsson, 2005).

Fault zones commonly exhibit variation within a short distance either in the strike or dip dimension with respect to their mechanical properties and permeability structure. Thus, we need to understand fault zones as they are important for the transport of crustal fluids, for example oil and magma. More specifically, the permeability

evolution, which can be analysed by the faults internal structure, its mechanical properties and its associated stresses (Gudmundsson *et al.*, 2010).

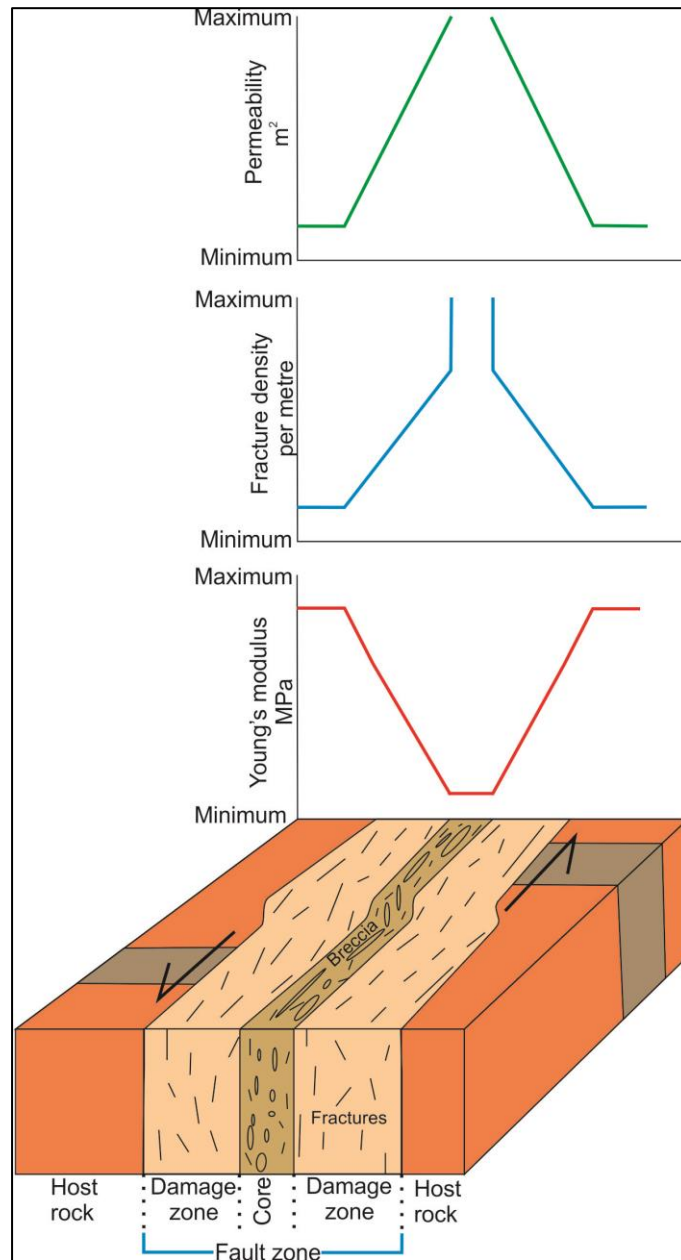


Figure 7.1: Schematic illustration of a fault zone. Young's modulus increases with distance from the core and the fracture density increases towards the core-damage zone boundary, thus permeability increases too towards this boundary (modified from Gudmundsson, 2011a; Meier *et al.*, 2013). This portrays that Young's modulus is inversely proportional to the fracture density.

7.1.1 Fault core

The core tends to be the thinnest part of the fault zone (Boutareaud *et al.*, 2008) and can reach tens of metres to a couple hundred metres (Bruhn *et al.*, 1994; Gray *et al.*,

1999), composed of fault breccias, gouge, cataclastic rocks and small scale fractures. These materials tend to form ellipsoidal units with an axis parallel to the fault trend (Fig. 7.1). The fault plane, where fault slip occurs may lie at the boundary of the core and damage zone or within the core itself. A fault plane can be defined as the trace of a fault along the surface and lies parallel to the fault zone. Fault slip or displacement occurs along this plane because it is a plane of weakness and is often composed of a few centimetres thick unconsolidated clay and gouge material. This is observed not only in outcrop, but also in drill cores and may be termed the ‘principal slip zone’, as this is where the fault often slips (Boutareaud *et al.*, 2008). As the majority of the fault slip occurs in the fault core, lithologies are crushed becoming a more ductile, softer material.

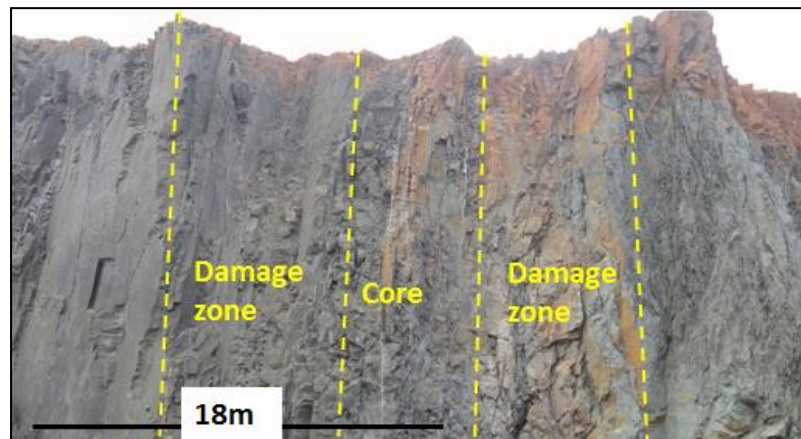


Figure 7.2: Fault zone in Howick Quarry, NW England (grid reference: NU23703 17470), cliff has a height of 18 m, view SW. This photograph illustrates the terms fault core, which yields many mineral veins, and damage zone.

7.1.2 Fault damage zone

The damage zone depends on the scale of the fault zone, for example in major faults the damage zone may reach a thickness of kilometres, and in general can be classed as the thickest part of the fault zone. This zone is located on either side of the core and consists of breccias too, but is much more densely fractured, normally lacking cataclasis zones. In general, the damage zone has a higher permeability than the core due to the presence of open fractures in the damage zone. These fractures present within the damage zone can vary from microfractures (grain size) to macrofractures

(Faulkner *et al.*, 2010). Young's modulus is higher in the damage zone too, and decreases towards the damage zone-core boundary until reaching a minimum within the core (Fig. 7.1; Agosta, 2008). Furthermore, the damage zone can be divided into sub-zones, with each individual sub-zone having different mechanical properties as a result of the variation in fracture clusters.

7.1.3 Fault slip

Over time a fault zone will evolve, where the core and damage zone both become thicker. Therefore, there is an increase in the permeability and changes to its mechanical properties, in particular, Young's modulus (Gudmundsson, 2000c; Gudmundsson, 2004; Gudmundsson *et al.*, 2009; Gudmundsson *et al.*, 2010). This is because of fault slip or displacement, which gradually increases the fault zone permeability. Hence, the area accommodated by fault breccia and fractures that surround the fault plane will become softer in contrast to the surrounding host rock, that is, the fault zone will have a lower Young's modulus over time. This can be reflected in a decrease in the L/U ratio in the following analytical solution:

$$\frac{L}{u} = \frac{E}{2\Delta\tau(1+\nu)} \quad (7.1)$$

where L is the strike dimension of a dip-slip fault, u is the displacement along the fault, E is Young's modulus, $\Delta\tau$ is the driving shear stress, and ν is Poisson's ratio (Gudmundsson, 2004). This shows that as a fault zone grows and evolves, u will become larger over time in relation to L (Gudmundsson, 2004; Gudmundsson, 2001a). Overall, because of fault slip, new fractures will form and old fractures will be reactivated, increasing the permeability of the damage zone by several orders of magnitude (Gudmundsson *et al.*, 2003).

7.1.4 Faults and hydrocarbon exploration

Normal faulting is well known in sedimentary basins and is of economic importance because they yield key components for hydrocarbon exploration since they can form traps and seals. However, if the faults become reactivated and the associated seal is breached and the trap loses its integrity, faults may be a high risk factor in hydrocarbon exploration as hydrocarbons leak towards the surface. There are known cases of breached seal and hydrocarbon leakage, for example in the North Sea caused by increased permeability of the fault (Faulkner *et al.*, 2010). Fault leakage has also been studied by Zhang *et al.* (2009), who showed that larger faults would have a higher tendency to leak hydrocarbons, because shorter faults would be buried by syntectonic sedimentation. They conclude that the spacing between adjacent faults is also important, where faults that are in close proximity to each other have a higher strain partitioning. Therefore, the strain can be distributed more evenly between the faults, reducing the fault displacement and thus preserving hydrocarbons. Hydrocarbon leakage associated with fault reactivation has also been documented in the Timor Sea (Zhang *et al.*, 2009). The main trapping mechanism was between extensional faults that were sealed by shales of Late Jurassic-Early Cretaceous age. However, these extensional faults were reactivated during the Late Tertiary causing the top seal to rupture and hydrocarbons to leak out. From Zhang *et al.*'s (2009) study it indicates that the displacement amount along the fault is crucial for the preservation of hydrocarbons.

Furthermore, Knipe *et al.* (1998) highlight the importance of scale (micro-macro) when analysing faults and their potential as seals. Factors identified are (1) sediment structure in 3D, (2) fault architecture including sub-zones, (3) petrophysical and mechanical properties of the fault and (4) fault evolution. Associated with these four factors is the geological history of the basin that is being analysed, as each factor is unique to each basin. Therefore, an in depth study is needed with respect to the faults within the Vøring Margin and not just the study of sill-fault interactions.

The aim of this chapter is to look at (1) sill interaction with normal faults and their effects on fault permeability, and (2) local stress fields in and around fault zones and the effects on fluid flow.

7.2 Sill interaction with grabens

A graben describes two normal faults that dip in towards each other. Slip along these normal faults is either on one or both sides, displacing crustal rocks into an elongate block (Fig. 7.3). Grabens are closely related to rift zones, which are a regional expression of graben structures.

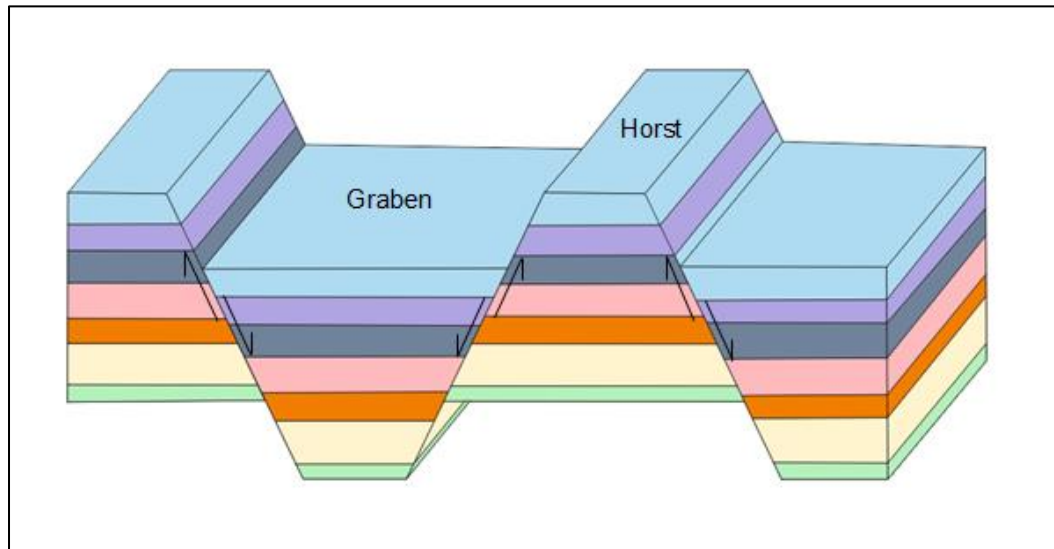


Figure 7.3: 3D block diagram of a graben and the associated horst structure. Arrows represent the direction of slip on the normal faults (boundary faults). Different colours represent differing lithologies, showing how they become offset owing to fault slip.

First, a model was set up of a dyke propagating towards an offset layer within a graben, representing that the graben had already undergone subsidence (Fig. 7.4). This is because field studies (Gudmundsson and Brenner, 2004) show that dyke tip stresses do not generate a graben, although some theoretical studies and geodetic studies (Rubin and Pollard, 1988) suggest this while others do not (Gudmundsson, 2003). If dykes did generate grabens, one would expect the dyke tip to come into contact with the graben, but this is not the case. However, such theoretical studies do not take into account the heterogeneity of the crust.

Each of the normal fault zones are modelled as elastic inclusions (for definition see Chapter 4), where the core is very soft or compliant with a Young's modulus of 0.1 GPa, while the damage zone is stiffer at 1 GPa (Gudmundsson *et al.*, 2010). The fault plane and weak contact are modelled as a 'thin elastic layer', 1 MPa/m, so that

the fault and contact have the ability to be displaced. The dyke propagates towards a stiffer layer of 20 GPa. The dip along the faults is 70° a common average dip for normal faults (Gudmundsson and Løtveit, 2005). All other parameters are as defined in Chapter 4, where the mesh quality is defined with a maximum element size of 0.02 m and a minimum element size of 3.2×10^{-5} m.

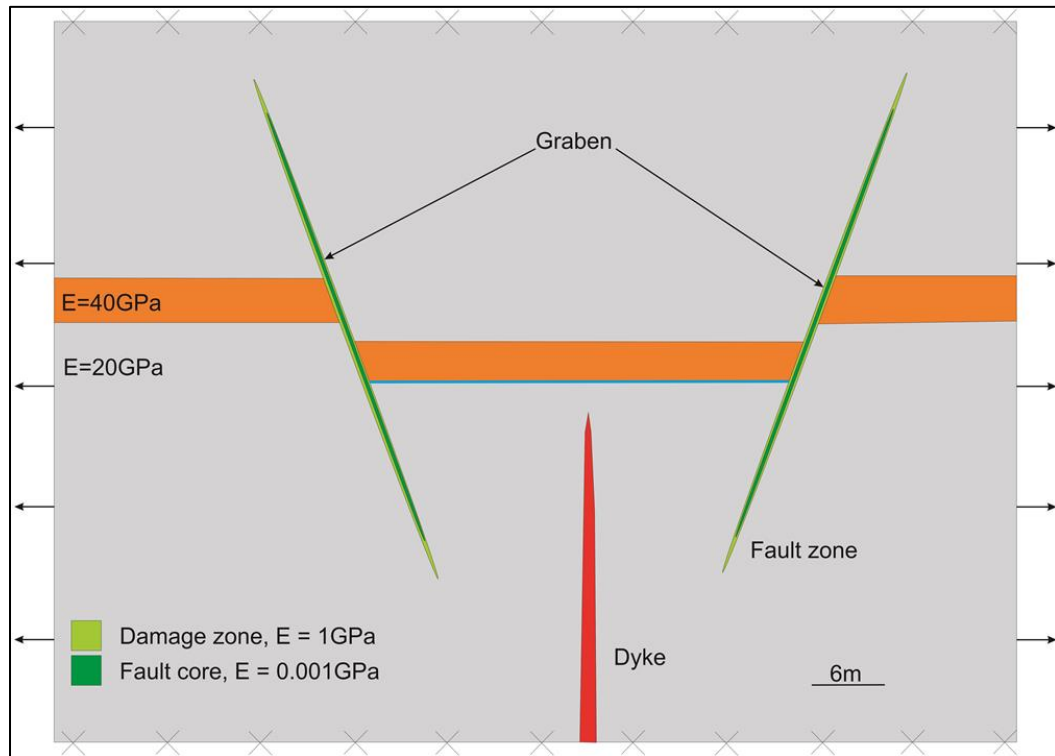


Figure 7.4: Schematic illustration of model set-up for Figure 7.5. A graben - two normal faults dipping towards each other, have a fault core with a stiffness of 0.1 GPa and a damage zone with a stiffness of 1 GPa. The host rock (grey) has a stiffness of 20GPa, with an adjacent layer (orange) that is stiffer at 40 GPa. The contact of this stiffer layer is modelled as a ‘thin elastic layer’ between the normal faults, as is the fault plane at 1 MPa/m (blue line). Extension was applied in the horizontal direction at 5 MPa (represented by outward facing arrows), while the top and bottom of the model was fixed (x’s).

The results in Figure 7.5 show a high distribution of shear stresses concentrated on the underside of the layer within the graben. As illustrated, the weak contact opens up ahead of the propagating dyke due to the Cook-Gordon debonding mechanism described in Chapter 5. Also, because of the subsidence that has occurred within the graben, there has been a change in the local stress field, where the maximum principal compressive stress is rotated 90° , from being horizontal to becoming

vertical. This rotation has induced a stress barrier favouring sill emplacement rather than dyke propagation (discussed earlier in Chapter 5).

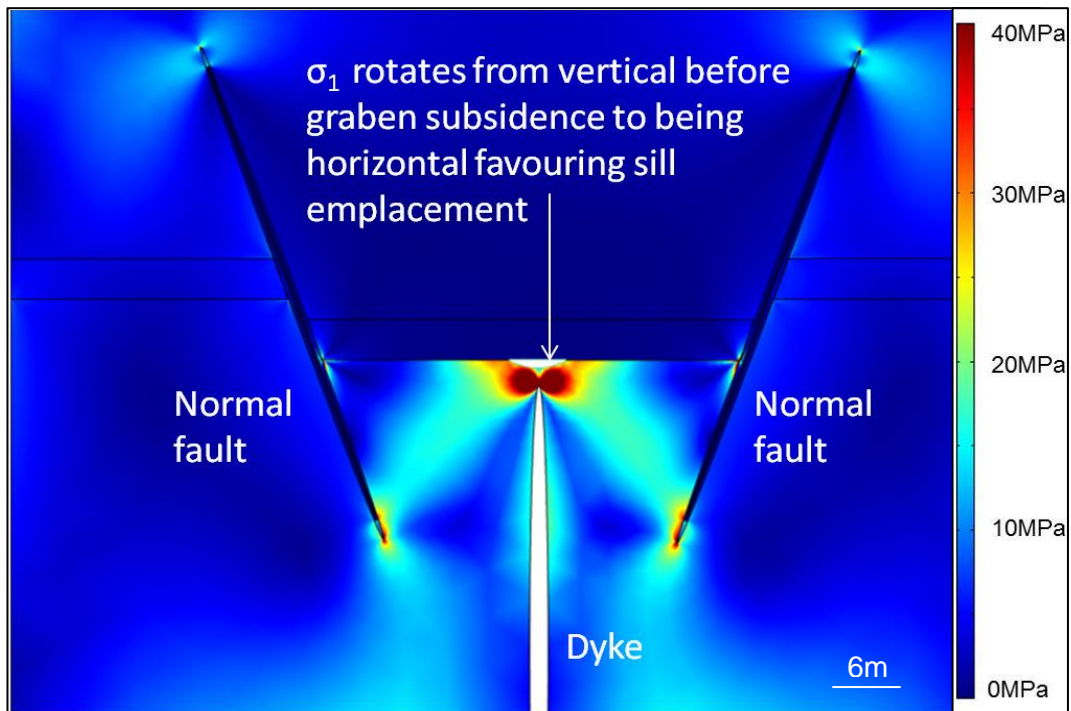


Figure 7.5: FEM model of shear stresses represented by colour contours. The graben (constituting of two normal faults) has induced a stress barrier into the local stress field, where the maximum principal compressive stress, σ_1 , has been rotated 90° from vertical to horizontal. Therefore, this induced stress field favours sill emplacement. Model set-up in Figure 7.4.

For the normal faults modelled in Figure 7.5 it is seen that the dip dimension is the controlling parameter. The faults did not extend from the free surface as they are buried, but they have a dip dimension, R , of 49 m within a seismogenic layer, T , of 116 m and are therefore, modelled as an interior crack. Hence, the displacement along this fault is a mode II crack, Δu_{II} (Gudmundsson, 2011a):

$$\Delta u_{II} = \frac{4\tau_d RV}{E} \tag{7.2}$$

where τ_d is the driving shear stress, commonly 3 MPa, E is Young's modulus and V is equal to $V = V(R/T)$, where $V(R/T)$ is as follows (Gudmundsson, 2011a):

$$V \frac{R}{T} = \frac{1.46 + 3.42 \left[1 - \cos \left(\frac{\pi R}{2T} \right) \right]}{\left[\cos \left(\frac{\pi R}{2T} \right) \right]^2} \quad (7.3)$$

From Eq. (7.2) and (7.3) a maximum slip at the centre of the fault plane can be obtained at a value of 4.3×10^{-2} m. This can be compared to the numerical solution on the graph in Figure 7.6.

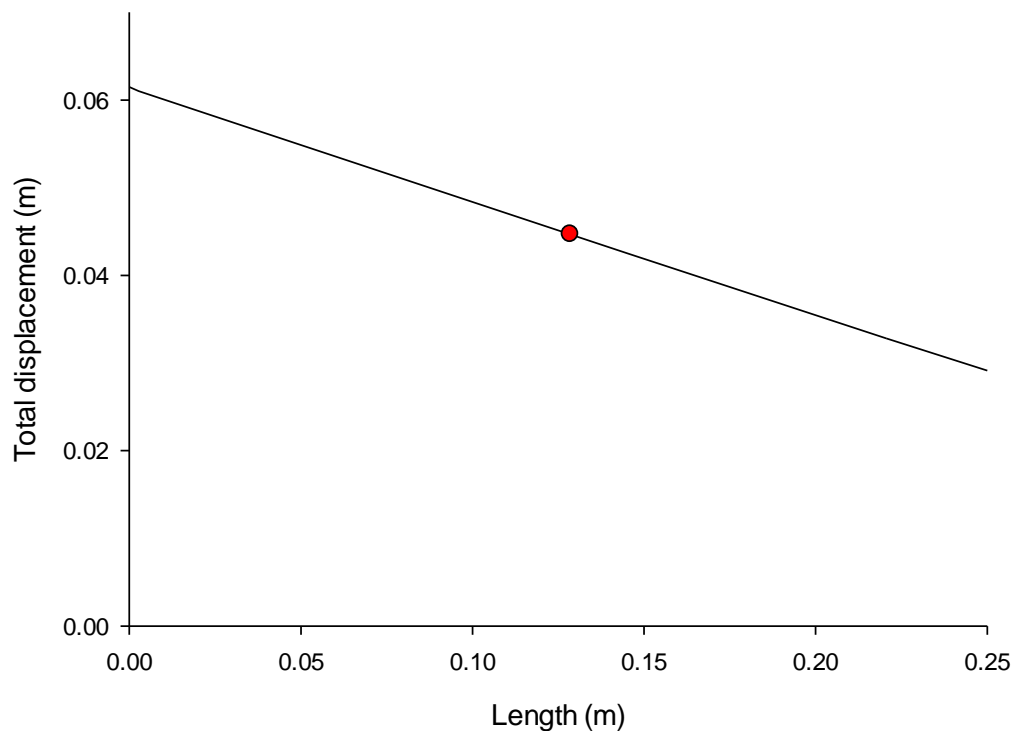


Figure 7.6: Graphical representation of fault slip. This is based upon 1D results from the normal fault in Figure 7.5, where the maximum displacement occurs at the centre of the fault plane, represented on the graph by the red dot at $\sim 4.3 \times 10^{-2}$ m.

Sills approaching faults are commonly seen within sedimentary basins (Fjeldskaar *et al.*, 2008; Gudmundsson, 2012a), where many sills are emplaced inside a graben. However, the properties of the fault determine whether the sill will be arrested at the fault or, alternatively become deflected up (and sometimes possibly down) along the

fault. Numerical models were set up to explore these scenarios. Figure 7.7 illustrates the set-up of the following models where the mechanical properties of the fault zones differ because of an increased number of sub-damage zones. Here the fault comprises of four zones: the fault plane with a spring constant of 1 MPa/m, the core with a Young's modulus of 0.5 GPa, inner damage zone (closest to the core) with a Young's modulus of 5 GPa and outer damage zone with a Young's modulus of 10 GPa (Gudmundsson *et al.*, 2010), with other parameters as set in Chapter 4, and the mesh the same as in Figure 7.5. Sub-damage zones are modelled, rather than one main damage zone, as it is well known (e.g. Ferrill *et al.*, 2008) that with each slip event the damage zone intensifies. The intensification depends on the fracturing within the damage zones and thus, the stiffness will vary.

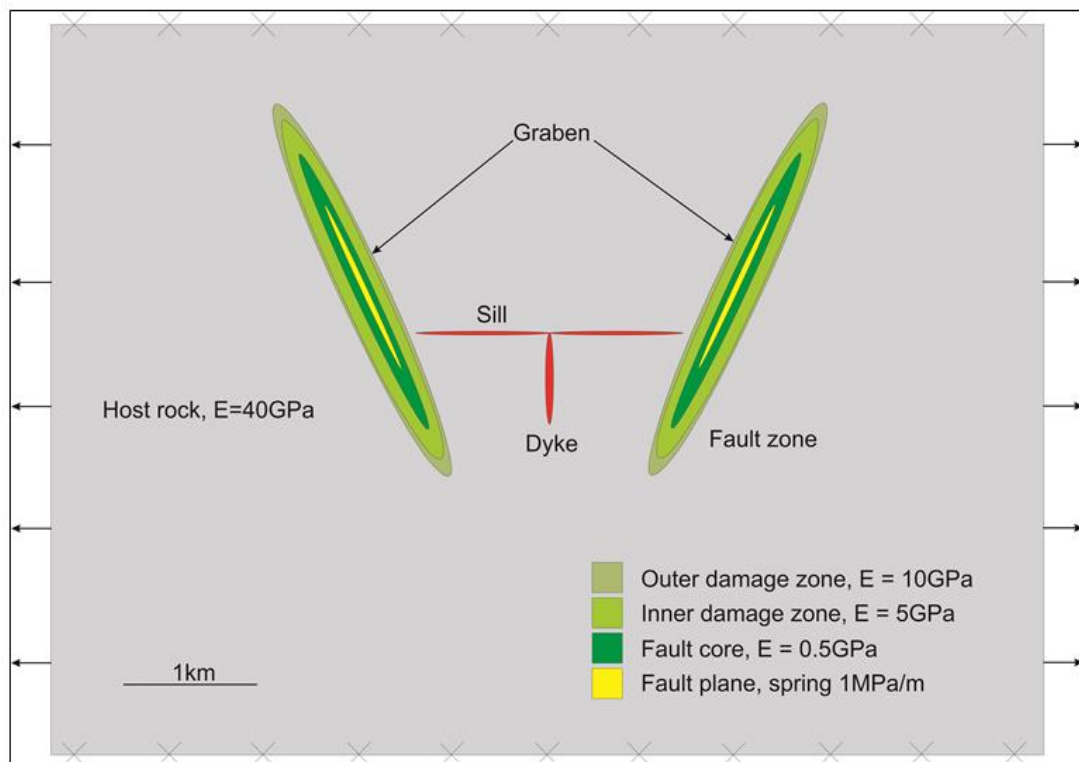


Figure 7.7: Schematic illustration of fault model set up in Figure 7.8. The varying green ellipses make up the fault zone with the fault plane in yellow and each shade of green representing the core (darkest green in the centre) with sub-damage zones (lighter greens around the core). The dyke and sill intrusions are drawn up in red, which both have a magmatic overpressure of 10 MPa. An extension of 5 MPa is applied in the horizontal plane (represented by outward facing arrows), and the top and bottom margins are fixed (x's).

The results are illustrated within Figure 7.8, where it is shown that when the sill approaches the normal faults it is arrested with high shear stresses being concentrated at the margins of the fault, which may induce possible fault reactivation. Figure 7.8A shows that when the sill approaches the fault zone there are a high concentration of shear stresses both at the tip of the sill and also, in the outer damage zone of the fault. Increases in shear stress generate the formation of new shear fractures and thereby increase the permeability of the fault, primarily in the dip-dimension. On the other hand, Figure 7.8B shows shear stresses at the tip of the sill, but no shear stresses concentrate within the fault zone itself. Around the fault plane there is a white area representing fault displacement or slip, where there would be an increase in the permeability along the fault. This increase in permeability would only be temporary after slip, because hydrothermal fluids and gases associated with sill emplacement would have the ability to migrate into the fault zone and help ‘heal’ and ‘seal’ the fault via secondary mineralisation. When a strong seal is formed, a trapping mechanism for hydrocarbons can be generated between the fault and sill tips (discussed in more detail in Chapter 10), which may last for a few million of years.

7.3 Local stress field within a fault zone

As discussed above, fault zones tend to consist of a core and damage zone, which have varying mechanical properties. As the fault evolves it may develop a number of sub-damage zones that also have varying stiffness's in accordance with their varying fracture densities. Thus, the local stress field between the core and damage zones, and the host rock will differ. To test this statement, numerical models were set-up in accordance with Figure 7.9. This figure illustrates schematically the difference between the varying mechanical units (the two damage zones, the core and fault plane) with no associated magmatic intrusion. The fault plane is modelled as a ‘thin elastic layer’ (Chapter 4), which is surrounded by the core with a stiffness of 1 GPa. This value is based upon *in situ* Young's modulus values for unconsolidated rocks (Gudmundsson *et al.*, 2010). In the model Young's modulus values are set at 5 GPa for the inner damage zone, closest to the core, 10 GPa for the outer damage zone (Gudmundsson *et al.*, 2010) and 40 GPa for the host rock. The mesh quality has a maximum element size of 0.05 m and a minimum element size of 1.15×10^{-4} m.

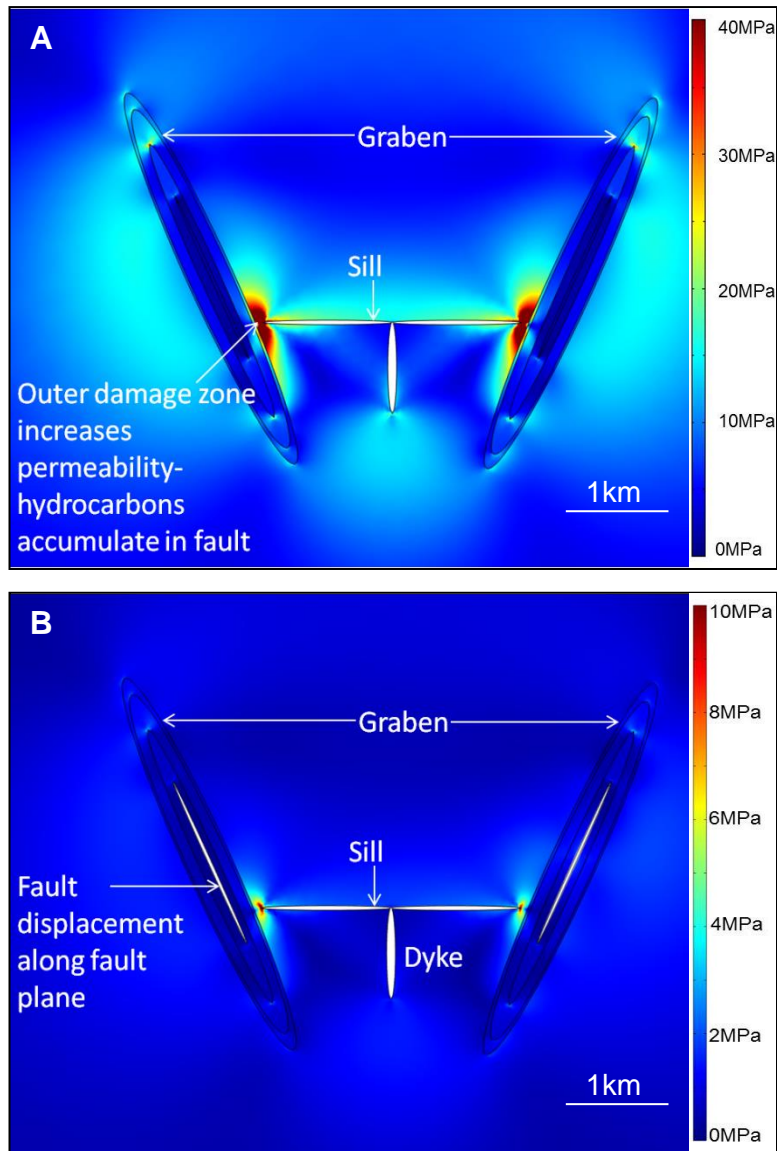


Figure 7.8: FEM model of shear stress colour contours for sill-fault interaction. On approach to the fault the shear stresses increase at the tips of the sill. (A) The shear stresses are concentrated in the outer sub-damage zone increasing its permeability. (B) The faults are reactivated as illustrated by the white area along the fault plane representing fault displacement. In both cases the sill is arrested at the fault.

Figure 7.10 shows that in general, due to the low Young's modulus of the fault zone causes the shear stresses to be much lower than that of the host rock. The lowest shear stresses, almost 0 MPa are around the fault plane, which indicates that the fault develops a stress shadow because of its low Young's modulus. Also, slip of the fault is confined to the fault plane, indicated by the white area. This is because, although there are a very small amount of shear stresses within the fault core, slip tends to

occur with the presence of a fault plane that is weak. Other factors driving fault slip include high fluid-pressure, a low friction coefficient and low normal stresses along the fault plane (Gudmundsson *et al.*, 2010). Shear stresses increase to approximately 3 MPa close to the tips of the fault zone, where the fault would propagate further. Larger shear stresses, >5 MPa, are present in the host rock because of its higher stiffness. These results indicate a change in the local stress field, not just within the fault zone, but also between the fault zone and the host rock in which it lies. With regards to permeability, the fault slip would temporarily increase the permeability of the core in the down-dip direction. However, over time diagenetic fluids, for example meteoric water or carbon dioxide rich groundwater (and geothermal fluids associated with sill emplacement), would help to ‘heal’ and ‘seal’ faults, reducing the overall permeability of the fault core during aseismic periods (Agosta, 2008).

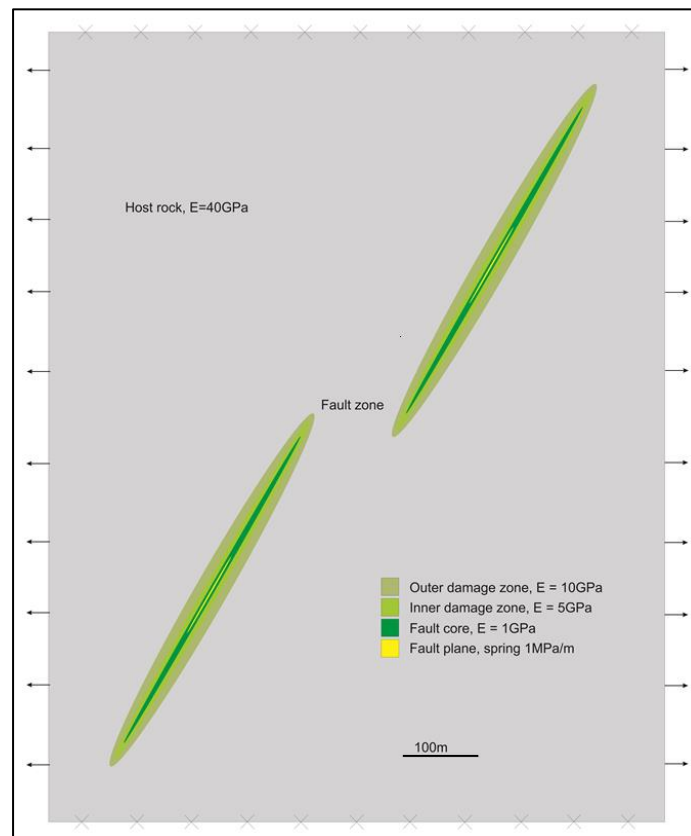


Figure 7.9: Schematic illustration of two offset fault zones (green). Each zone consists of a fault plane (yellow) with a spring constant of 1 MPa/m, a fault core with a stiffness of 1 GPa, an inner damage zone with a stiffness of 5 GPa and an outer damage zone with a stiffness of 10 GPa. This fault zone is an elastic inclusion, where the host rock is much stiffer than that of the fault zone at 40 GPa. Extension is applied in the horizontal direction with a magnitude of 5 MPa (represented by outward facing arrows), and the top and bottom of the model is fastened (x's).

The distribution of shear stresses (Fig.7.11) and tensile stresses (Fig.7.12) around two offset normal faults illustrate where micro-cracking would occur in the process zone at the fault tips (Gudmundsson, 2011a). This process zone would encourage the fault to grow by rupturing at the fault tip, as seen by high tip stresses. These tip stresses generally form a zone of stress concentration, especially where the fault zones overlap and interact with one another.

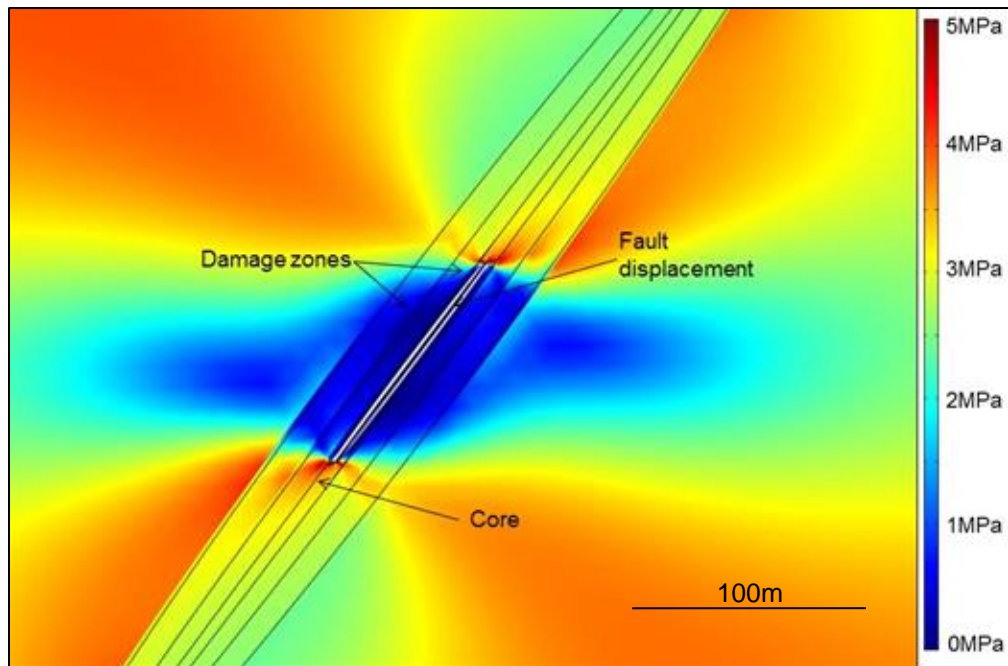


Figure 7.10: FEM model representing shear stress contours of a fault zone. The fault undergoes displacement as depicted by the white area surrounding the fault plane. The various shear stresses within the fault zone indicates how the fault can form its own local stress field, where the blue shows where a stress shadow developed because of its low stiffness.

The highest shear stresses (Fig. 7.11) are at the tips of the fault, but this concentration has an asymmetric distribution. Low stresses are concentrated around the central part of the fault zone, which is also asymmetrical. The tensile stresses (Fig. 7.12) reflect this same stress pattern, where the highest tensile stress coincides with the highest shear stress. However, on the whole, the tensile stresses are 2 MPa greater than that of the shear stresses. From the stress distribution patterns it can be seen that the width of the fault zone would remain relatively constant, but the fault would grow in the dip direction, with the fault plane taking the bulk of the displacement (Fig. 7.10). Over time, the growth of a fault in vertical section, would

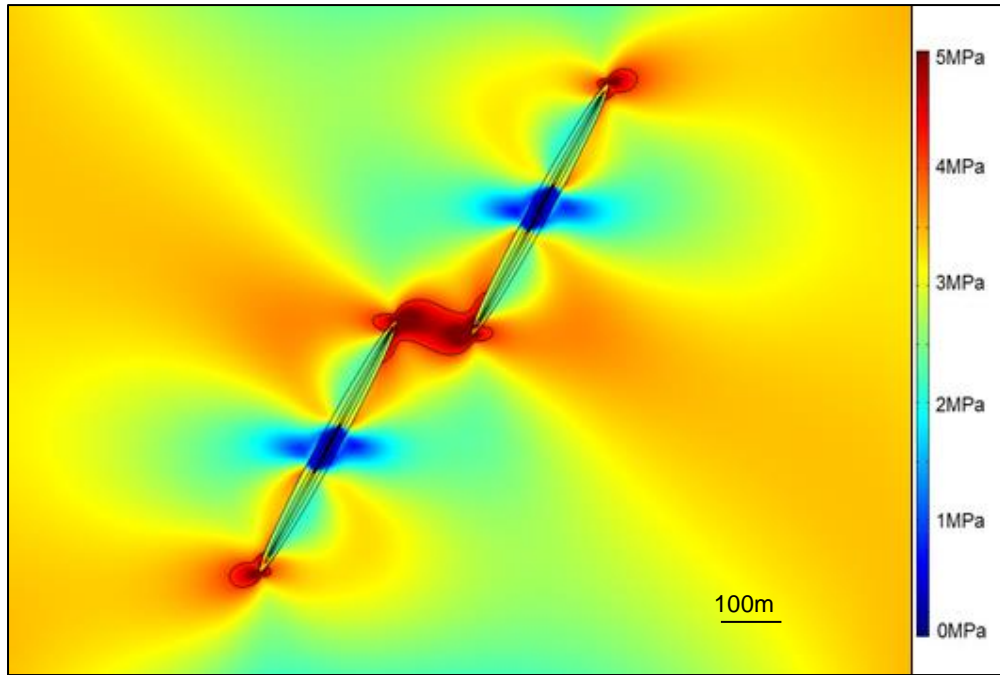


Figure 7.11: FEM model of shear stress colour contours across two normal faults. Shear stresses greater than 5 MPa are concentrated at the fault tips (area within black line) where shear fractures can be formed/old shear fractures reactivated within the process zone at the tip of the faults, and the blue represents a stress shadow caused by compliant fault rocks. Model set-up in Figure 7.9.

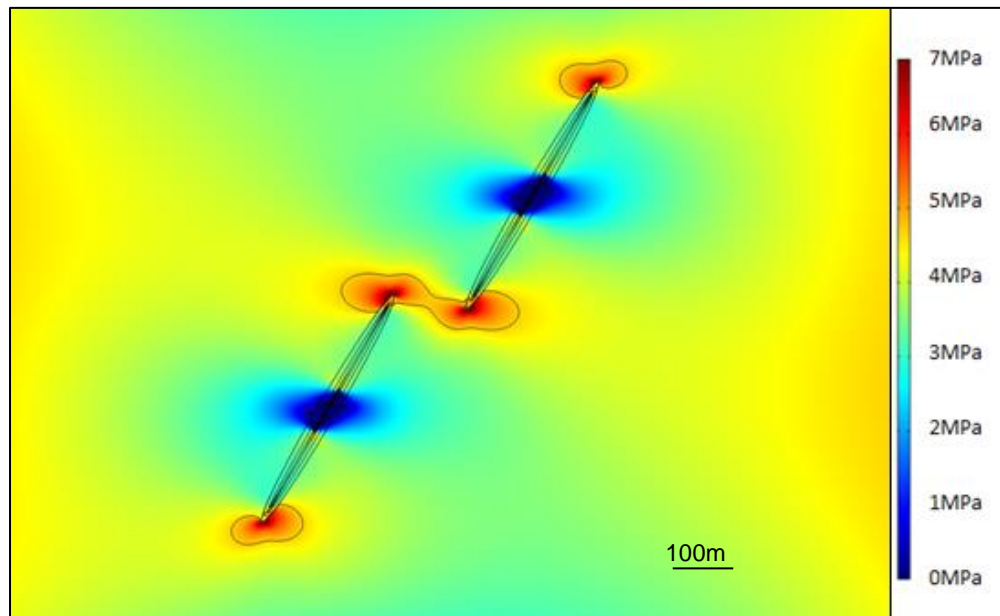


Figure 7.12: FEM model of tensile stresses colour contours about two offset normal faults. Tensile stresses are concentrated at the fault tips, generating a zone (area within black line) where tensile fracture formation/reactivation would occur within a process zone at the tips of the faults allowing for further fault propagation and perhaps eventual linkage. The blue areas represent a stress shadow as seen in Figures 7.10 and 7.11. Model set-up seen in Figure 7.9.

be via linkage of larger segments, which may be offset initially (as shown here) in the host rock, in the early evolution of the fault.

7.4 Fluid flow within a fault zone

To be able to understand fluid flow within a fault zone, the permeability structure must be first understood. This is because the mechanical structure of the fault with respect to the host rock, allows for analysis as to whether the fault will act as a barrier or conduit to fluid flow. However, fault permeability is more complex, due to the varying properties of a fault zone. In the field, palaeofluid flow can be identified by the presence of mineral veins. This was seen in Howick Quarry, NE England (grid reference: NU23703 17470; Fig. 7.2), where numerous mineral veins were present in the fault core, illustrating that once the core was permeable and transmitting fluids.

Fluid flow within a fault zone depends on its architecture and its permeability. Generally, the permeability of the core is very low during periods of no slip and therefore, fluid flow is not conducted through the core. However, when there are active periods of fault slip, the permeability of the core temporarily increases. The damage zone on the other hand, is more permeable overall because of the heterogeneities present, for example fractures. This is supported by laboratory experiments (e.g. Evans *et al.*, 1997) that indicate the damage zone may have a permeability several orders of magnitude larger than the core and the host rock.

To predict permeability of the fault zone, it is critical to understand the rocks making up a fault zone and how they respond to stress changes. The stresses within a fault do not only depend on their magnitudes (colour contours), but also on their trajectories. Thus, a series of models were set up to analyse fluid flow based upon the orientation of the maximum principal compressive stress trajectories, σ_1 , where the mechanical properties of the fault are as shown in Figure 7.9.

7.4.1 Non reactivated fault

Modelled first is an inactive fault, and thus the fault plane is not modelled as a ‘thin elastic layer’. The stiffness of the core is 1 GPa, while the damage zone is stiffer at

10 GPa (Gudmundsson *et al.*, 2010), within a host rock that has a stiffness of 40 GPa. The stress trajectories here are the minimum compressive stress, σ_3 , as this better illustrates the change in the trajectory orientation between the host rock, damage zone and core. Thus, fluid flow is perpendicular to the minimum compressive stress trajectories, that is, fluid flow is parallel with the maximum principal compressive stress trajectories. The orientation of the σ_3 trajectories is highlighted by the blue streamlines to visualise the vector magnitude (Fig. 7.13A). Figure 7.13B shows that the permeability of the core is low during inter-seismic periods and any fluid migration (blue streamlines) would not be conducted through the fault core, but through the damage zone, which has a higher permeability caused by the presence of fracture networks. This model illustrates that the core became ‘healed’ and ‘sealed’ and therefore, a barrier to flow. In the case of an old fault, the fault zone would become similar to the host rock in terms of the hydromechanical properties. Therefore, the effects of an old fault zone on fluid flow are very small.

7.4.2 Fault reactivation

Models were next set up to see the effects of fault slip on the transport of fluids, and therefore, the fault plane is modelled as a ‘thin elastic layer’ as described in Chapter 4. Figure 7.14 gives an overview of the orientation of the minimum principal compressive stress trajectories, σ_3 , highlighted by the blue streamlines. These streamlines clearly are deflected around the fault plane, however, as fluid flow is perpendicular to these vectors, it can be seen that the core became permeable during periods of fault activity. Once again, this illustrates the variation in the local stress field between the fault zone units and the host rock.

A more extensive investigation was next carried out to see the effects of the dip of the fault, and also the rotation of the local stress field. The fault zone stiffnesses are the same as above (Fig. 7.9), with a length of 500 m, dip varying between 40°-80°, and the local stress field with a magnitude of 5 MPa being rotated through 90° both in a clockwise and anti-clockwise direction (Fig. 7.15). The mesh quality is the same as for Figures 7.10, 7.11 and 7.13. Results presented here are for a fault dip of 40°, 60° and 80°, with extension rotated every 20° to illustrate and highlight the differences in fluid transport through a fault zone.

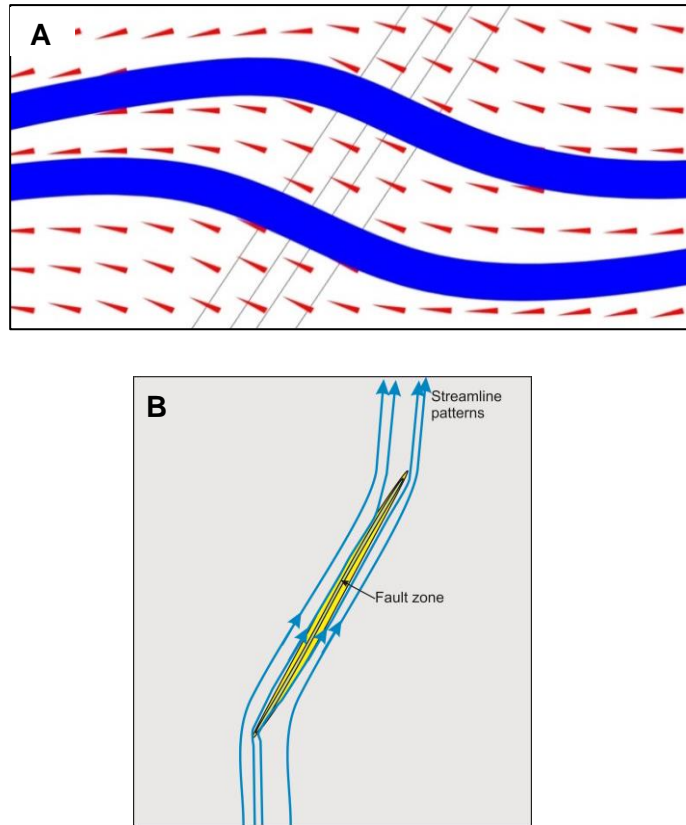


Figure 7.13: Model of fluid flow through a non-active fault. (A) FEM model representing minimum principal compressive stress trajectories, σ_3 , marked by the red ticks. Fault modelled as an elastic inclusion with a stiffness of 1 GPa in the core and 10 GPa in the damage zone, within a host rock that is much stiffer at 40 GPa. The stress trajectories change direction at the contact between the fault zone and the host rock indicated by the blue line. (B) Fluid flow is perpendicular to the σ_3 trajectories (and thus parallel to σ_1 trajectories) and has been schematically illustrated here. The fault zone is more permeable than the host rock, having a great effect on the transport of fluids as the streamlines (blue arrow lines) become diverted towards and into the fault itself. Scale is the same as in Figure 7.10.

Results in Figures 7.16 and 7.17 shows that the fault zone is permeable and the streamlines (fluid migration paths) became deflected because of (1) the varying mechanical properties of the fault zone, (2) the dip of the fault and (3) the orientation of the local stress field. The loading, oblique to the fault, along with the angle of dip of the fault and its mechanical properties of each unit, cause the principal stresses to become rotated, which determine the flow direction.

Generally, Figures 7.16 and 7.17 show the higher the dip of the fault, the closer together the streamlines, which is most likely a result of the smaller surface area in which the fault occupies with respect to the loading conditions. Thus, the local stress

field generated by the fault zone attracts fluid migration and is more efficient through a steeper dipping fault. The largest deflection of fluid through the fault zone is around the fault plane, because of its elastic behaviour and slip that occurs. Unlike an inactive fault (Fig. 7.13), fluid is transported through the core, which becomes temporarily permeable as pore spaces and fractures become interconnected. Other major deflections relate to the local stress field (loading conditions) that effect the vector of the streamlines, especially towards the edge of the model, causing them to become curved away.

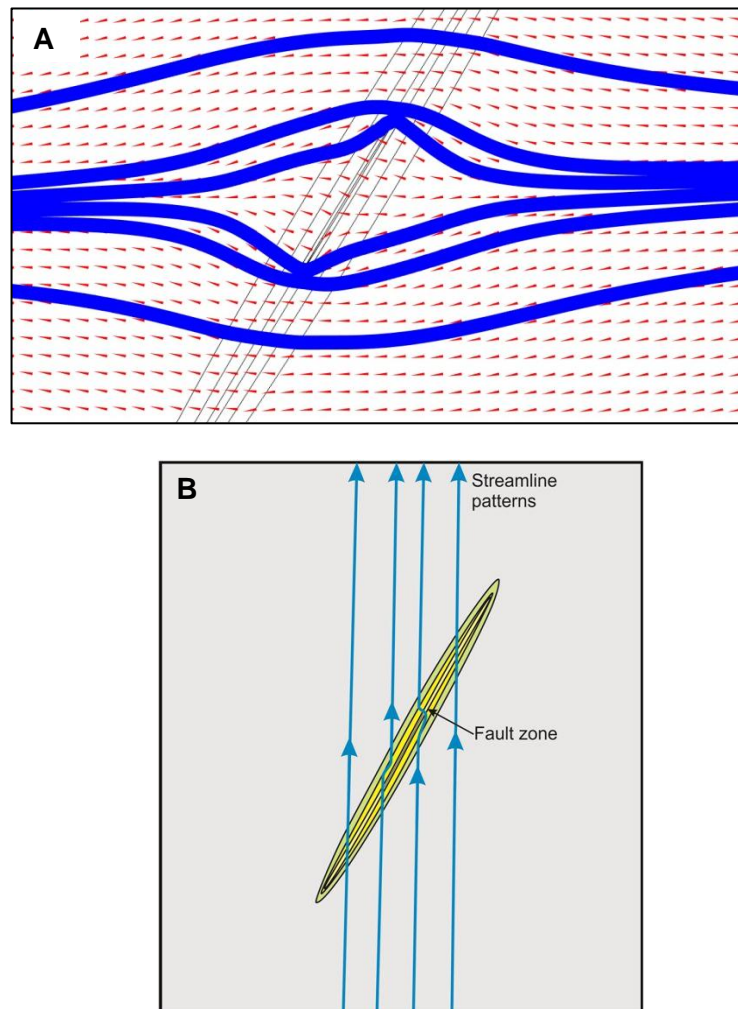


Figure 7.14: Model of fluid flow through an active fault. (A) FEM model representing minimum principal compressive stress trajectories, σ_3 , marked by the red ticks. The stress trajectories change direction not only at the contact between the fault zone and the host rock but also between the different units within the fault, marked by the blue lines. (B) Fluid flow is perpendicular to the σ_3 trajectories in (A) and has been schematically illustrated here. The fault core is less permeable than the damage zone and the host rock causing the fluid flow (streamlines) to curve around the fault core. Scale is the same as in Figure 7.10.

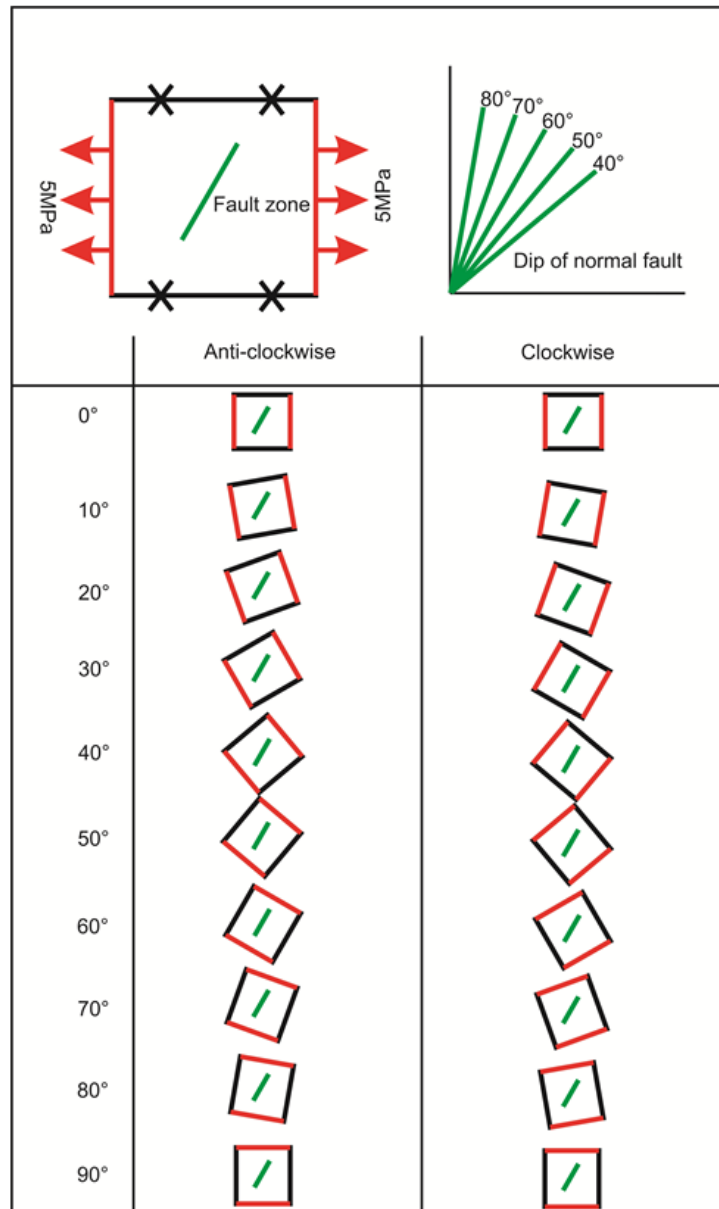
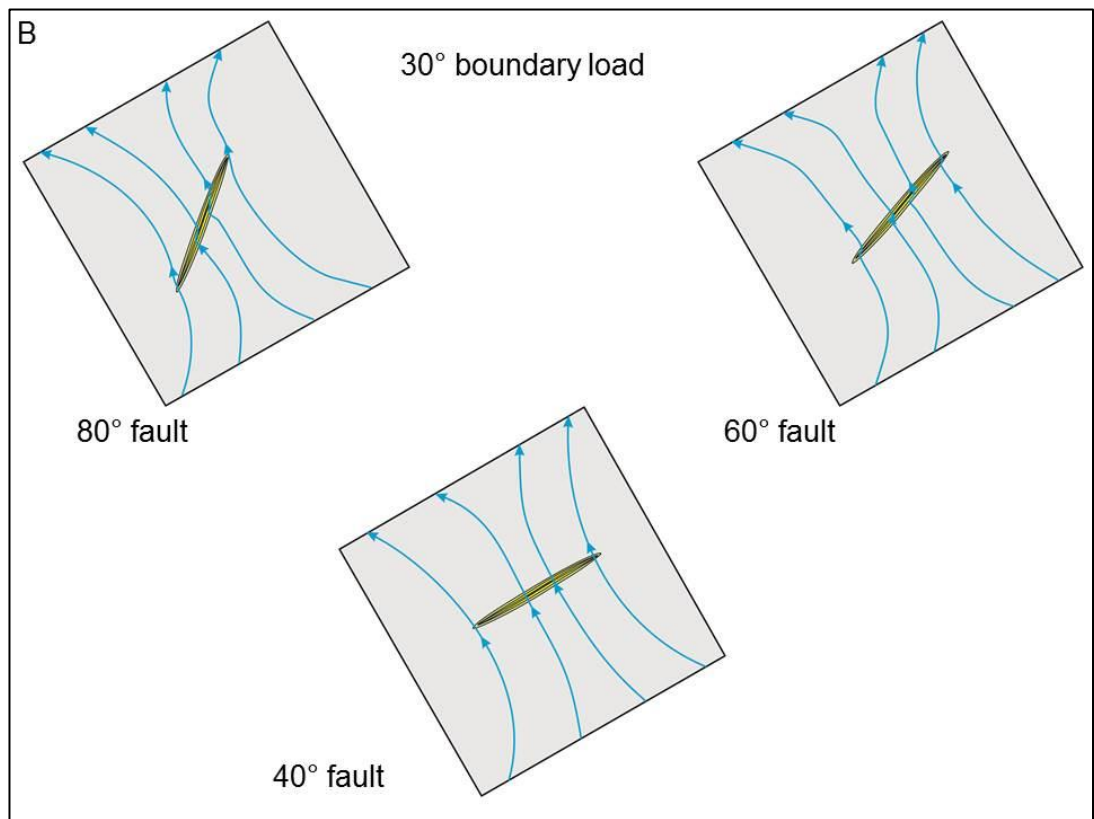
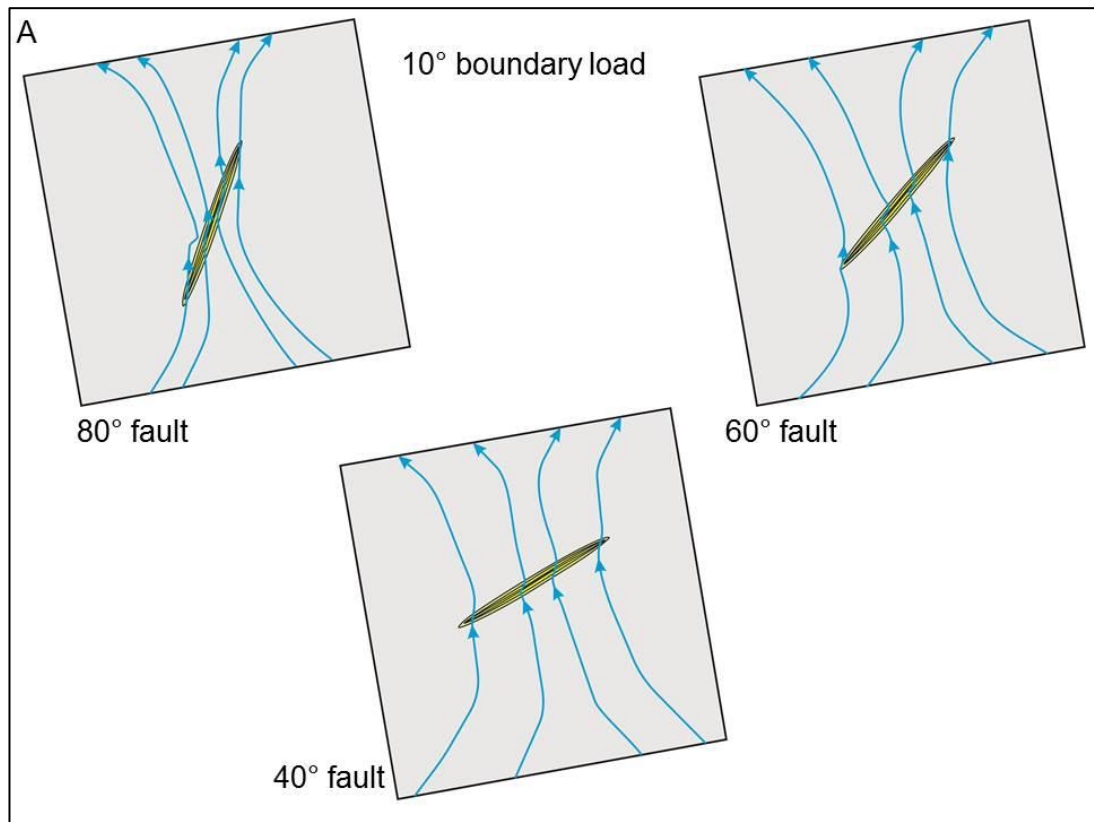
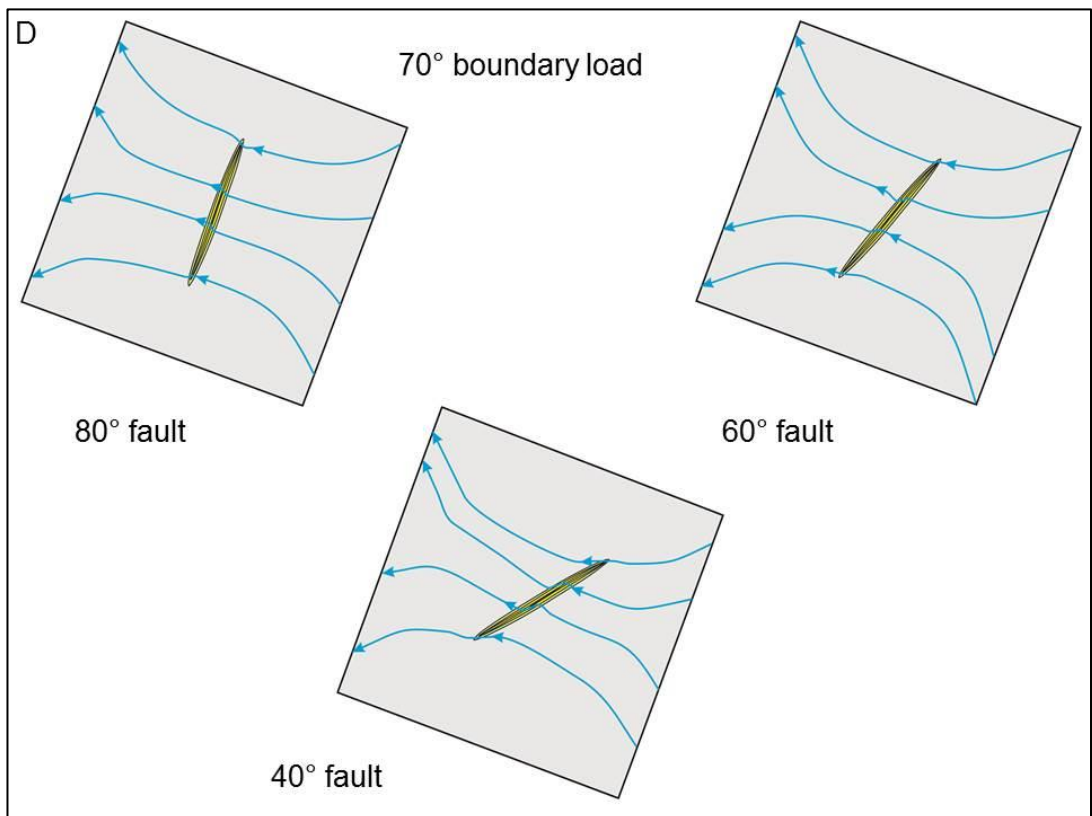
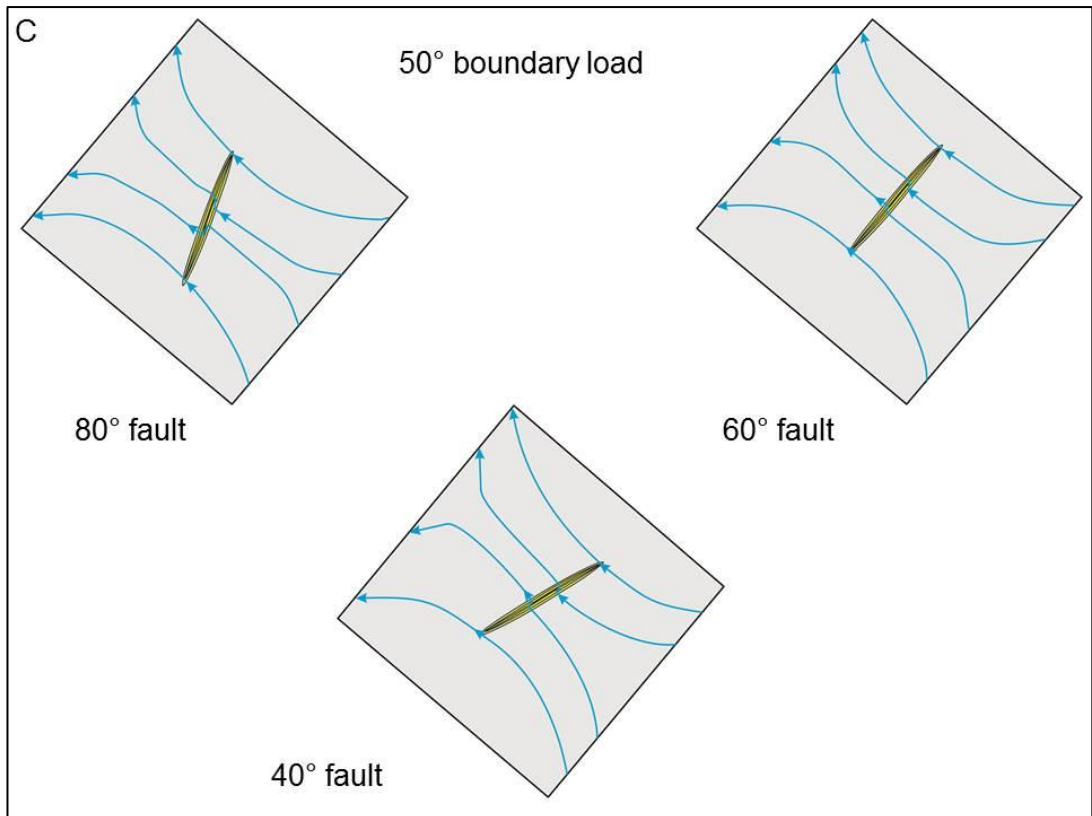


Figure 7.15: Schematic illustration to show the rotation of the stress field and the fault dip. Green line is the fault zone (properties same as Figure 7.9), red line is the 5 MPa extension applied, and the black lines are the fixed edges. These models are to explore the effects of the angle of the local stress field with the dip of the fault. Length of each fault is 500 m.

When loading is rotated anti-clockwise (Fig. 7.16), the flow direction is crudely perpendicular to the fault, showing how the fault is a conduit towards flow after fault slip. On the other hand, when loading is rotated clockwise (Fig. 7.17), the flow direction is more parallel to the fault, rather than cross-cutting. For example, Figure 7.17D shows an increased permeability of the core, where fluid is transported

parallel to the orientation of the core. This is due to the favourable orientation of the stress field (60° clockwise) and the dip of the fault (80° and 40°).





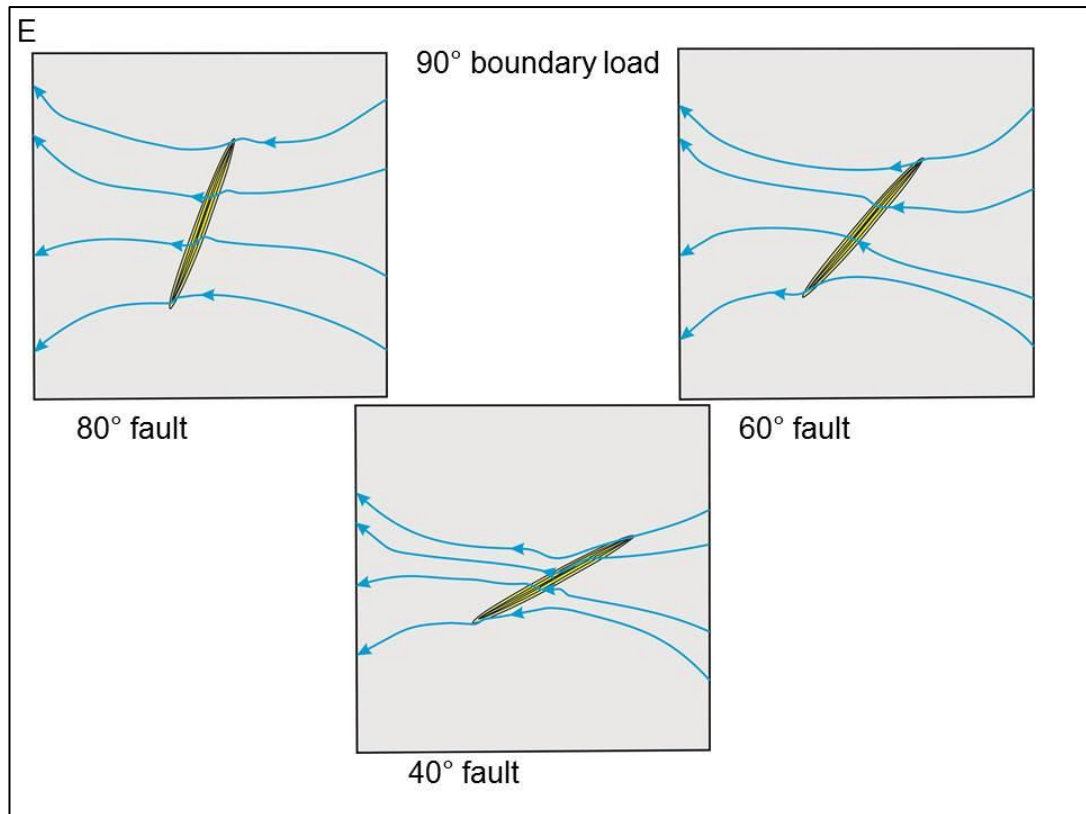
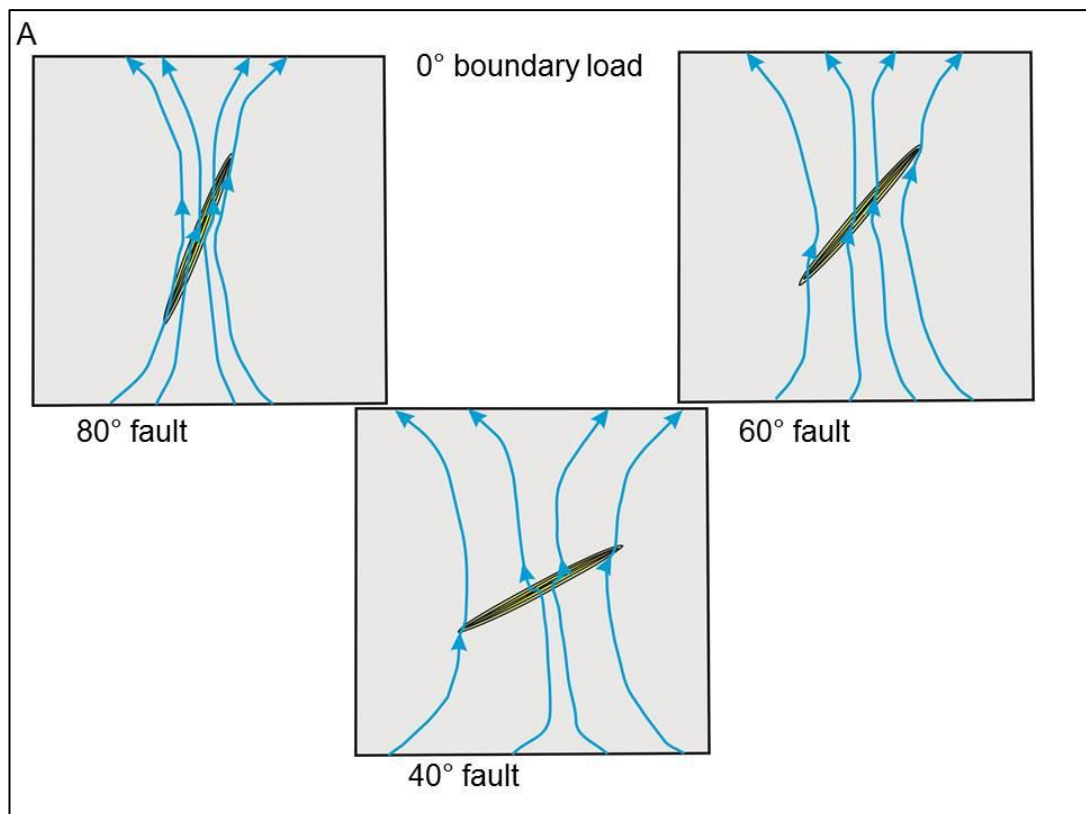
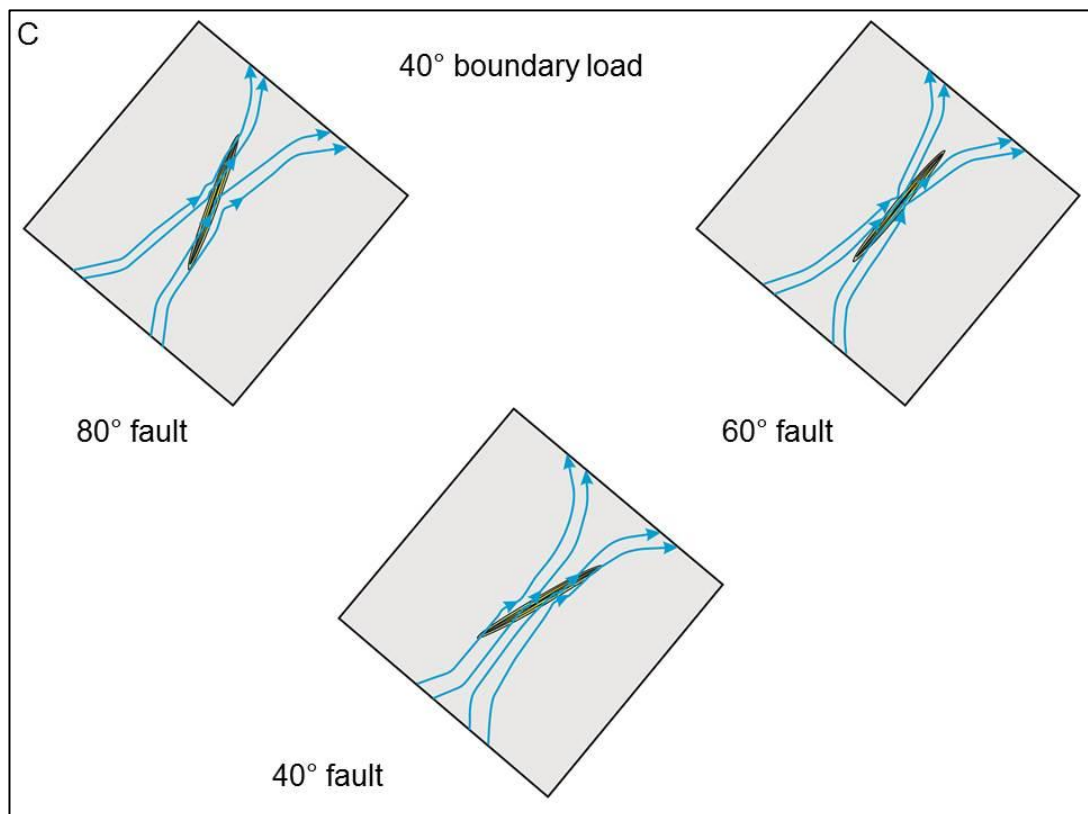
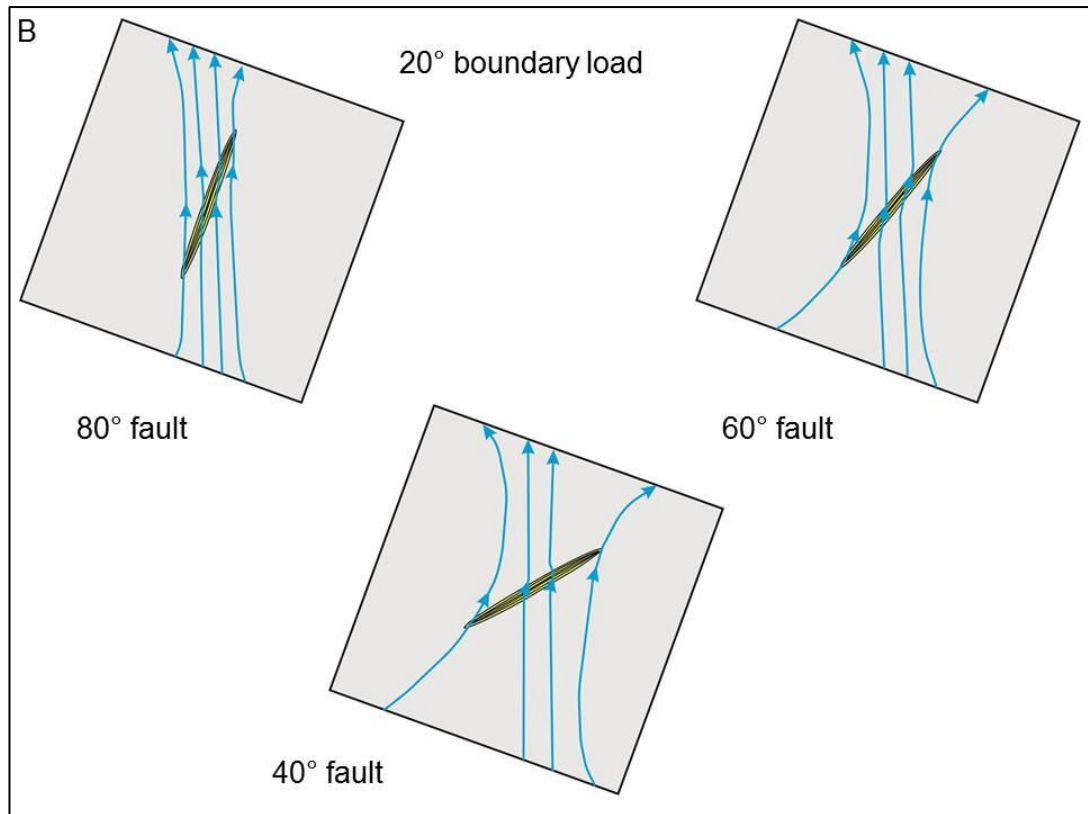


Figure 7.16: Fluid flow is perpendicular to the σ_3 trajectories and has been schematically illustrated here. Fault zone dips at 40°, 60° and 80°, where the stress field has been rotated anti-clockwise from 10°- 90°. Length of each fault is 500 m. Please refer to text for details.





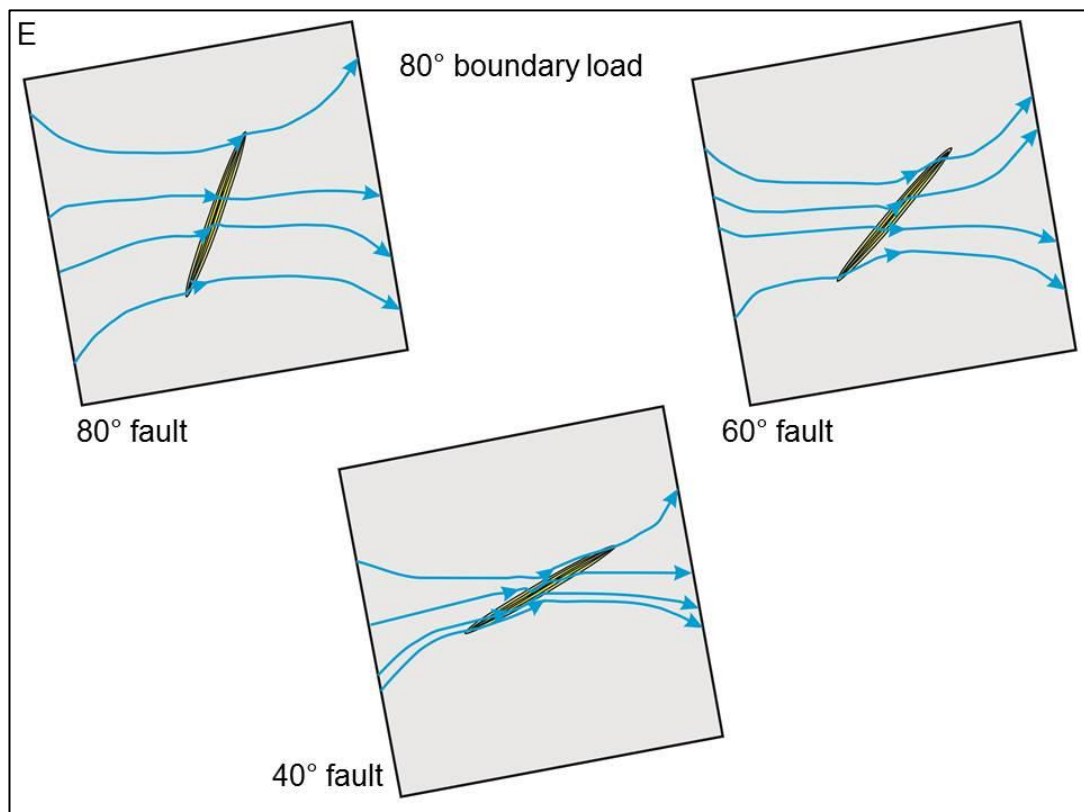
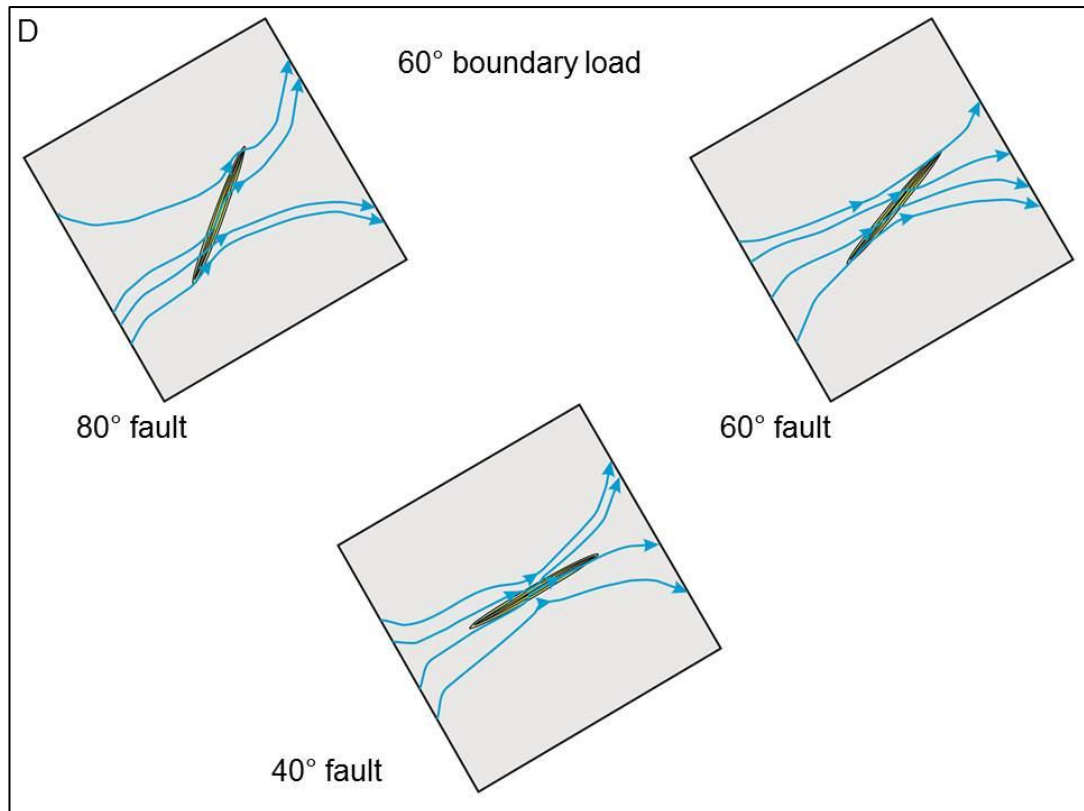


Figure 7.17: Fluid flow is perpendicular to the σ_3 trajectories and has been schematically illustrated here. Fault zone dips between 40°, 60° and 80°, where the stress field has been rotated clockwise from 0°- 80°. Length of each fault is 500 m. Please refer to text for details.

7.5 Discussion

Faults are dynamic systems and cannot be regarded to as a discrete surface. They have an internal structure, which is a primary factor influencing the mechanical properties of a fault, and also the fluid flow within the fault. The mechanical anisotropy controls both the evolution of the fault and the bulk fluid flow (as well as seismicity; Boncio, 2008). The size of the fault core and the presence of cataclastic rocks controls friction and fault slip and thus, the hydrodynamics of the fault, especially the permeability structure.

Fluid flow via faults and shear zones is important both for environmental reasons and economic reasons (e.g. petroleum industry, mining, and geothermal energy), an account of which is provided by McCraig (1989). McCraig's (1989) account included descriptions of how radon gas was escaping along the Brookneal fault zone, West Virginia, due to underlying uranium rich granite, a major environmental problem. Also, how faults are ubiquitous in the upper crust and are prime locations for gold exploration due to structural controls along faults and shear zones.

Results in Figure 7.5 are in agreement with models produced in Gudmundsson (2003), who also shows that grabens may cause dyke arrest because the minimum principal compressive stress that was originally horizontal, rotated to become vertical. This induced a stress barrier, especially within the stiff layers, causing eventual dyke arrest. If the dyke is deflected into a sill (Fig. 7.8), the intrusions can together create barriers and conductors to fluid flow. This would be dependent on the angle of these intrusions to the hydraulic gradient and the fracture network within. Also, the pre-existing normal faults may have an influence on magma pathways. For example, pre-existing fractures within the damage zone, which are favourably orientated and that have been reactivated, have the ability to act as magma conduits (Magee *et al.*, 2013).

The damage zone evolves along the length of the fault, where the main damage occurs closest to the fault plane. This is because of fault propagation, which occurs from the tips of the fault, where the highest shear stresses and tensile stresses are (Figs. 7.11 and 7.12). Generally, fault slip most often occurs over several seismic slip events. Thus, the first deformation event occurs close to and along the fault plane, allowing the fault to grow, and development of the (sub) damage zone(s).

However, the scale of faults is independent of fault failure and stress distributions (Zhang *et al.*, 2008). With respect to enhanced permeability, numerical models produced as shown in Figures 7.11, 7.12, 7.16 and 7.17 are coherent with previous studies. For example, Zhang *et al.* (2008) conclude that the permeability enhancement was simulated due to tensile failure of the fault. This tended to be at the tips of the fault or zones between adjacent faults, known as dilatant jogs. Thus, fluids could be transported to such sites even via rocks that are relatively impermeable. Over time, minerals (e.g. gold) may be precipitated due to fluid flow and chemical reactions. Also, the formation and/or reactivation of tensile and shear fractures can increase the hydraulic conductivity of the host rock in the region of the process zone. It is important to note that the hydraulic structure of a fault will vary in time as it evolves, for example the process zone at the fault tip, where microcracking occurs will form part of the damage zone over time (Evans *et al.*, 1997; Gudmundsson, 2011a). Therefore, to determine fluid flow three factors must be understood first. These are: the evolution of the local structural area, the mechanical growth of the fault, and the fault setting with respect to crustal fluids.

For fluid flow within a fault the interconnectivity of individual small fractures is very important (discussed further in Chapter 9). In general, the degree of fracture connectivity increases towards the fault core because of the damage zone evolution. Micarelli *et al.* (2006) classified the degree of interconnectivity: type 1: isolated fractures, type 2: simple connected fractures and type 3: multiple connected fractures. This study also analysed the porosity of faults in the Hyblean Plateau, Sicily, indicating that the porosity decreased adjacent to the fault plane irrespective of fault slip. This porosity reduction also coincided with a decrease in permeability. Overall, Micarelli *et al.* (2006) concluded that the fault plane acted as a barrier to fluid flow relative to the densely fractured damage zone that enhanced fluid flow. This conduit-barrier behaviour increased with fault displacement because (1) fractures within the damage zone grew and became further interconnected, and (2) the core became sealed over time due to cementation and cataclasis.

Laboratory tests provide quantitative and qualitative relationships between permeabilities of the host rock, damage zone and fault core. In general, the damage zone has a higher permeability than the host rock and fault core, where fluid flow may be enhanced in the damage zone as a result of interconnected fracture pathways

(Evans *et al.*, 1997; Micarelli *et al.*, 2006; Agosta, 2008; Lunn *et al.*, 2008). Permeability values for the damage zone are in the order of 10^{-15} - 10^{-17} m², for the fault core in the order of 10^{-17} - 10^{-21} m², and for the host rock in the order of 10^{-16} - 10^{-18} m² (Boutareaud *et al.*, 2008). These permeability values are dependent on clay content, the size and distribution of clasts, infilling of fractures and the orientation in which the sample is cut for measurement (perpendicular to or parallel to foliation - permeability could vary by up to three orders of magnitude) (Evans *et al.*, 1997). It can be determined from such tests and borehole measurements (Sibson, 2000) that the damage zone tends to have the highest hydraulic conductivity, especially when fractures within the damage zone are favourably orientated in the direction of the prevalent stress field.

Fluid flow modelling through fault zones has improved in the past few years (Faulkner *et al.*, 2010). It can be determined that factors controlling fluid flow are intrinsic, for example the fault lithology, fault slip, fault zone geometry (especially in 3D), conditions in which deformation occurs, fluid or rock interaction, and temporal and spatial variations on these factors (Caine *et al.*, 1996). On the other hand, extrinsic controls on fluid flow are dependent on the local stress field. For example, post glacial uplift can lead to generation and reactivation of tensile and shear fractures at a fault tip, for example Fennoscandia (Gudmundsson, 1999). This is because crustal rocks are weaker under tensile stresses (postglacial) rather than compressive stresses (glacial). Thus, pre-existing fractures may link-up, increasing the hydraulic conductivity of the host rock.

The numerical models for fluid flow in fault zones (Figs. 7.13, 7.14, 7.16 and 7.17) do not take into account (1) the scale of fractures in the damage zone, which may enhance fluid flow, and (2) the variability of the permeability in the fault core owing to fault slip. However, it can be seen that faults can act as conduits to flow, or barriers, or a combination of both, which is supported by the works of Caine *et al.* (1996), Evans *et al.* (1997), Lunn *et al.* (2008) and Wibberley *et al.* (2008). These mechanisms can act on a variety of scales, for example, Lunn *et al.* (2008) illustrate how the micro scale properties of a fault zone are critical to fluid flow and thus, fluid flow through fault zones is variable and heterogeneous through space and time.

In general, the fault core has a low permeability and therefore, forms a barrier (Fig. 7.13) to fluid flow, but this may not always be the case, particularly during and post fault slip (Fig. 7.16 and 7.17). This can be justified by many field studies, for example:

1. Babiker and Gudmundsson (2004) and references there-in, show that faults tend to conduct fluid flow during and post (short term) fault reactivation because of a large increase in fault core permeability.
2. Caine *et al.* (1996) state how the Dixie Valley fault, Nevada, acted as a conduit to flow after deformation, and sealed rapidly to form a barrier to flow.
3. Agosta (2008) based a study on normal faults in the Fucino Basin, Italy, who show that the fault core has low porosity and permeability values and acts as a barrier towards fluid flow. The damage zone, which has high porosity and permeability values, acts as a conduit towards fluid flow.

From these numerical models (Figs. 7.14, 7.16 and 7.17) it is clear that the permeability of the fault increases during fault reactivation. This is because reactivation could cause significant displacement and therefore, enhance fluid transport through the upper crust through these shear zones. Otherwise, faults can be described as being comparatively impermeable (Fig. 7.13). However, these numerical results only illustrate the migration paths of crustal fluids through a fault zone, but not the rate at which these fluids travel. This can be calculated analytically, where volumetric flow rate, Q , is as follows:

$$Q = \frac{b^3 W}{12 \mu_f} \left[(\rho_r - \rho_f) g \sin \alpha - \frac{\delta p_e}{\delta L} \right] \quad (7.4)$$

where b is the aperture of the dip-slip fault, W is the width of the plate perpendicular to fluid flow, μ_f is the dynamic viscosity of the fluid, ρ_r is the density of the host rock, ρ_f is the density of the fluid, g is the gravitational constant, α is the dip of the fault, δp_e is the excess pressure in the fluid source (equal to tensile strength of host rock) and δL is the flow along the length of the dip-slip fault (Gudmundsson, 2011a). It is the hydraulic gradient that has a significant effect on volumetric flow rate. This

has been reported by Babiker and Gudmundsson (2004), who show that if the fault trends perpendicular to the hydraulic gradient, then fluid flow is minimal. Contrastingly, if the fault trends parallel to the hydraulic gradient, then the fluid flow would reach a maximum and would be highly efficient. Such an effect is also presented by Gudmundsson (2001) who shows how fluid flow is favoured along vertical fractures rather than inclined fractures, and how strike-slip faults are more efficient at transporting fluid through the crust rather than dip-slip faults. For example, Husavik-Flatey Fault, Iceland, a strike-slip fault, conducts most of the fluid flow via fracture networks (Gudmundsson *et al.*, 2001). The results here of normal faults (Figs. 7.13, 7.14, 7.16 and 7.17) can also be attributed to strike-slip faults.

7.6 Conclusions

Fault zone permeability is critical to understand for crustal fluid movement, for example magma emplacement and hydrocarbon migration. Faults are dynamic features that have a complex structure, which can be simply described by two mechanical units, the core and damage zone. The main conclusion is that the fault zone develops its own stress field, which controls its permeability, as well as fault slip. The local stresses vary between each unit that form the fault zone, thus there is little uniform stress over the fault itself.

Normal faults are distinctive features within sedimentary basins, both in the field and on seismic lines, with the ability to transmit crustal fluids. They can have an effect on dyke and sill propagation too, especially within a graben. This is because graben subsidence induces a stress barrier favouring sill emplacement and dyke arrest. In a petroleum system faults have the ability to act as a trap (along with sills) providing that they are not reactivated. Otherwise, crustal fluids will migrate towards the surface as their permeability is temporarily increased. Nevertheless, even if fault reactivation does occur, the fault can act as a trap once ‘healed’ and ‘sealed’ by secondary mineralisation decreasing the overall permeability of the fault zone.

Lastly, faults can also generate efficient and effective paths for the migration of crustal fluids. This is because of the enhancement of permeability and formation of dilation zones owing to tensile failure of the fault. This allows for fluids to migrate

through otherwise impermeable rocks. In general though, the damage zone is the most economically significant of a fault zone as it conducts fluid flow.

Chapter 8: Scaling exponents and entropies of sills, laccoliths and fracture lengths

8.1 Introduction

Fractures in the Earth's crust partly control the probability of volcanic eruptions and associated volcano-tectonic seismicity, especially in relation to dykes, inclined sheets, sills and laccoliths, where sills can form networks or sill complexes. While fracture networks within these solidified intrusions control the permeability and porosity of fractured reservoirs. Thus, the understanding of sills and laccoliths as well as fracture networks is of fundamental importance, especially in the fields of volcanotectonics, hydrogeology and petroleum geology.

In the past decades power-law size frequency distributions have become a topic of interest in structural geology, for example Hatton *et al.* (2004), Yang *et al.* (2004) and Bungler and Cruden (2011), who explored power-law distributions. However, they have no established ideas relating the power-law size distributions to the principles of rock mechanics. Within this chapter power-law distributions are analysed on two different scales. Firstly, sill and laccolith thickness, that is, their growth in the vertical direction and secondly, fracture lengths within sills, that is the vertical and sub-vertical fractures that form within sills on cooling (columnar joints) and tectonic fractures. Therefore, the aim of this chapter is to explore these power-law relationships and relate them to the understanding of concordant intrusion (sills and laccoliths) growth and fracture growth within sills.

8.2 Power-laws

The distribution of fracture measurements, namely the concordant intrusions and fracture lengths follow a power-law relationship according to (Newman, 2005):

$$P(\geq x) = Cx^{-\gamma} \quad (8.1)$$

where $P(\geq x)$ is the number of intrusions or fractures that have a thickness or length larger than x , C defines a constant of proportionality and γ represents the scaling exponent (Newman, 2005). A power-law distribution implies that there are a larger number of small scale events or objects or processes with a smaller number of large scale events or objects or processes of a specific kind.

To determine whether a data set shows a power-law size distribution as portrayed in Eq. (8.1), the data is first organised and analysed using given bins, so that all intrusions or fractures within the data set are larger than the thickness or length x . Therefore, if we take for example, a bin of 10 m all intrusions or fractures that are greater than 0 m fall in the first bin, intrusions or fractures greater than 10 m fall in the second bin, intrusions or fractures greater than 20 m fall in the third bin, intrusions or fractures greater than 30 m fall in the third bin *et cetera*. These are referred to as cumulative frequency plots. Power-law relationships are determined by a straight line on a bi-logarithmic plot, that is, the logarithm is taken of both the x-axis and y-axis. The gradient of the line is equal to γ , the scaling exponent, which is negative because there are larger numbers of small intrusions or fractures than there are bigger intrusions or fractures.

To test the significance of these results and to determine the strength of the power-law, R^2 values are calculated to show the correlation within the data, where 1 is perfect correlation and 0 is no correlation. This is known as linear regression, which is calculated for each point on the scatter plot. Linear regression is calculated as the distance of a particular point from the regression line. However, on these bi-logarithmic plots there are deviations from the linear trend and two linear trends better fit the data. This is known as a double-scaling law and is commonly recognised with many power-law distributions (Hatton *et al.*, 1994; Micarelli *et al.*, 2006; Putz-Perrier and Sanderson, 2008; Mohajeri and Gudmundsson, 2012).

8.3 Entropy

Entropy is described in thermodynamics as a measure of disorder, however in relation to fracture mechanics is a measure of unavailable or useless energy within a system, for example fracture networks. The application of entropy to a system can be

related to probability, and can be presented using the Boltzmann equation (Sentha, 2006; Kardar, 2007; Blundell and Blundell, 2010):

$$S = k \ln W \quad (8.2)$$

where S is entropy, k is the Boltzmann constant with a value of $1.38065 \times 10^{-23} \text{ J K}^{-1}$, and W is the number of ways in which a system can arrange itself. The following equation describes a general probability distribution and can be expressed using Gibbs' entropy (Volkenstein, 2009):

$$S = -k \sum_{i=1}^t p_i \ln p_i \quad (8.3)$$

where k is Boltzmann's constant with a value of $1.38065 \times 10^{-23} \text{ J K}^{-1}$, t is the number of bins that have a frequency greater than 1, p_i is the cumulative frequency as a function of the total number of intrusions or fractures, such that cumulative frequency of intrusions or fractures within a given bin is divided by the total number of intrusions or fractures (Mohajeri and Gudmundsson, 2012).

On a power-law distribution entropy describes probability, and therefore, gives an indication of the spread of the data. Thus, intrusion thickness or fracture length is also a measure of entropy. To analyse the variation in entropy, Equation (8.3) is used to quantify the entropies of the intrusion thicknesses and fracture lengths, and to infer energy and how energy was used in a system.

8.4 Sill and laccolith thicknesses

Sill and laccolith thicknesses were obtained from the literature and field work (Jaeger, 1957; Corry, 1988; Goodenough, 1999; Johnson and Dunham, 2001; Hansen *et al.*, 2004; Liss *et al.*, 2004; Gudmundsson and Løtveit, 2005; Planke *et al.*, 2005; Cruden and McCaffrey, 2006; Gudmundsson, 2006; Leat *et al.*, 2006; Burchardt, 2008; Fjeldskaar *et al.*, 2008; Menand, 2008; Berner *et al.*, 2009; Cukur *et al.*, 2010; Svensen *et al.*, 2010; Bungler and Cruden, 2011; Gudmundsson, 2011b; Hansen *et al.*, 2011; Wang *et al.*, 2011; Bédard *et al.*, 2012; Gudmundsson, 2012a; Gudmundsson and Løtveit, 2012). For sill inflation and propagation it follows that

the tensile stress must be equal to the tensile strength of the host rock in which the sill is emplaced (Gudmundsson and Mohajeri, 2013). The range of sill thicknesses is from 0.3 to 600 m (Bunger and Cruden, 2011), which can be explained by the varying mechanics. The range of laccolith thicknesses is 15-2500 m (Bunger and Cruden, 2011). For these lateral intrusions their lengths range in approximately four orders of magnitude.

8.4.1 Sills

A cumulative frequency plot of the number of sills versus the sill thickness in metres (Fig. 8.1) displays a straight line on a bi-logarithmic plot, which indicates a power-law size relation. The scaling exponent is the gradient of the straight line on the bi-logarithmic plot calculated at 1.26, while R^2 is calculated as 0.85 and is statistically significant (McKillup and Darby Dyar, 2010). From Eq. (8.3) the entropy is calculated to be 2.13.

The bi-logarithmic plot (Fig. 8.2) displays a distinct straight line relationship, however this only holds for a restricted thickness of the sills. Therefore, the data is better represented by having two regression lines where the break occurs at approximately 240 m, illustrating two discreet sill populations (Fig. 8.3). Therefore, scaling exponents and entropies are calculated for these two populations. The R^2 value for population 1 of sills is 0.96 with a scaling exponent of 1.02, and for population 2, the R^2 value is 0.89 with a scaling exponent of 4.37. Entropies for these two populations are 2.15 and 2.10 respectively. As entropy changes as a consequence of inflation, the energy needed to inflate the sills in population 1 is approximately the same as the energy needed to inflate the sills in population 2. This shows the importance of dividing the data into populations in order to obtain better relationships, as here we show very strong correlation values that are more statistically significant.

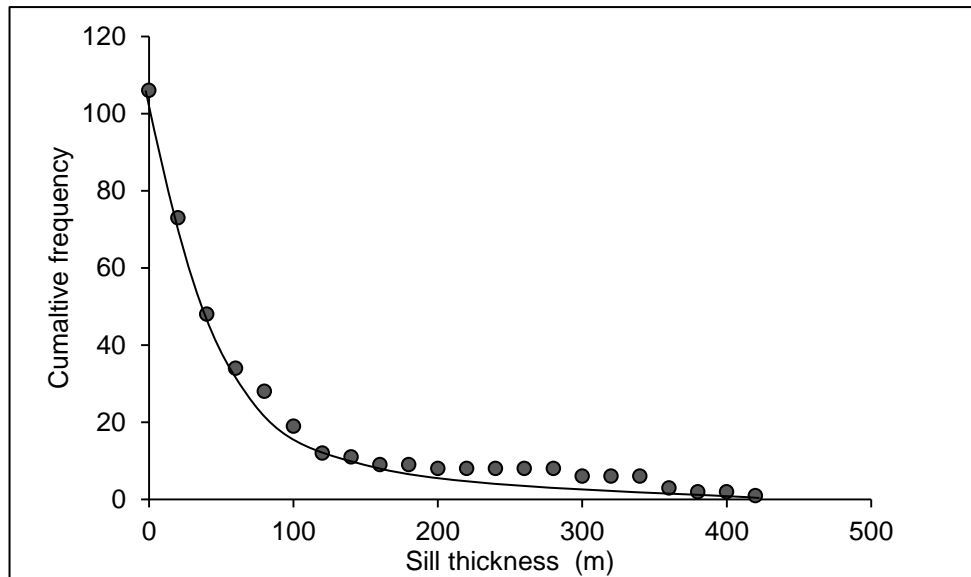


Figure 8.1: A cumulative frequency plot illustrating a power-law distribution for sill thicknesses across the globe, $N = 106$.

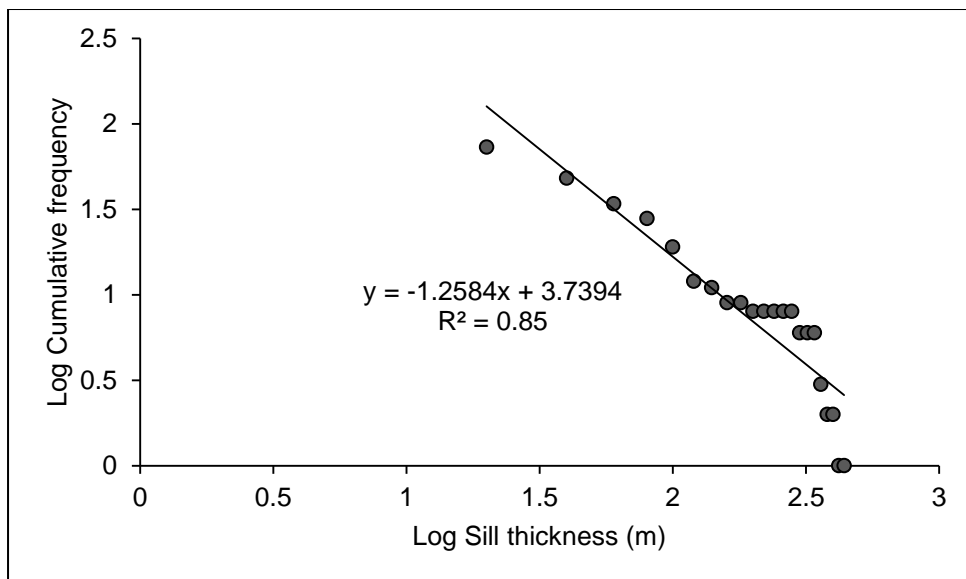


Figure 8.2: A bi-logarithmic plot of global sill thickness in Figure 8.1 illustrating the break in slope. The linear regression line shows the R^2 value and equation where the gradient determines the scaling exponent, γ .

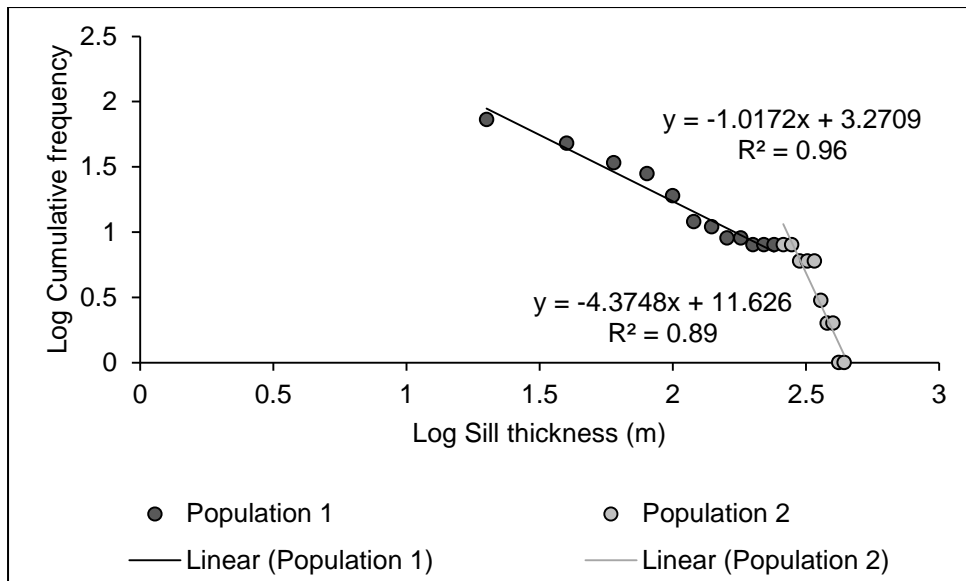


Figure 8.3: A bi-logarithmic plot of global sill thickness representing two distinct populations based on Figure 8.2. The population divide was decided as a midpoint because best fit lines either for all population 1 or all population 2 did not have an effect on the results. The linear regression line shows the R^2 value and equation where the gradient determines the scaling exponent, γ .

8.4.2 Laccoliths

Power-law trends are also obtained from the size-frequency distribution of laccoliths. These are displayed by the cumulative frequency plot (Fig. 8.4) and also the strong correlation of the linear trend on the bi-logarithmic plot (Fig. 8.5) with an R^2 value of 0.96. Entropy for this single power-law is calculated at 2.58, with a scaling exponent of 1.42. However, there was divergence from this single line power-law at thicknesses of about 300 m and, when the data are plotted as two sub-populations (Fig. 8.6), distinctively better fits are obtained with a R^2 value of 0.99 (almost a perfect fit) for population 1 (≤ 300 m) and a value of 0.98 for population 2 (> 300 m). Entropies and scaling exponents are recalculated for these two sub-populations, where population 1 has an entropy of 1.36 and scaling exponent of 0.45, and population 2 has an entropy of 2.48 and scaling exponent of 1.68. From these entropy calculations we can infer that almost two times the amount of energy is needed to form the laccoliths in population 2 than in population 1.

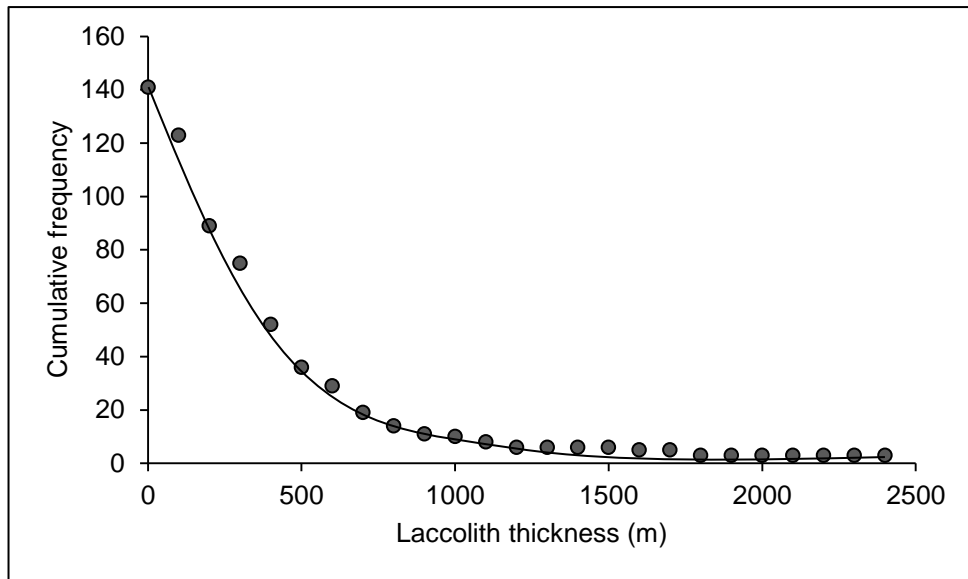


Figure 8.4: Cumulative frequency plot showing a power-law distribution for laccolith thicknesses worldwide, $N = 141$.

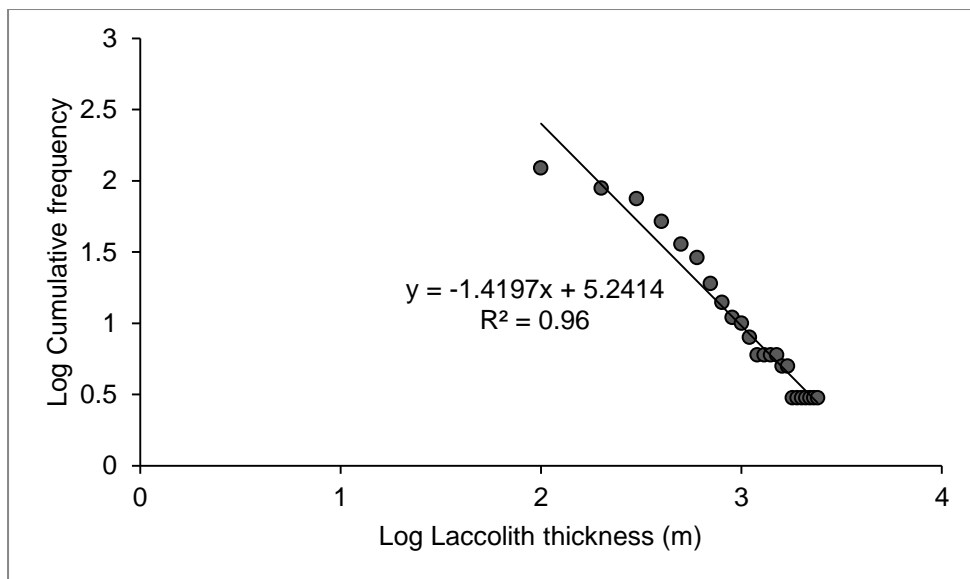


Figure 8.5: Bi-logarithmic plot of laccolith thickness in Figure 8.4 showing a break in slope. The linear regression line shows the R^2 value and equation.

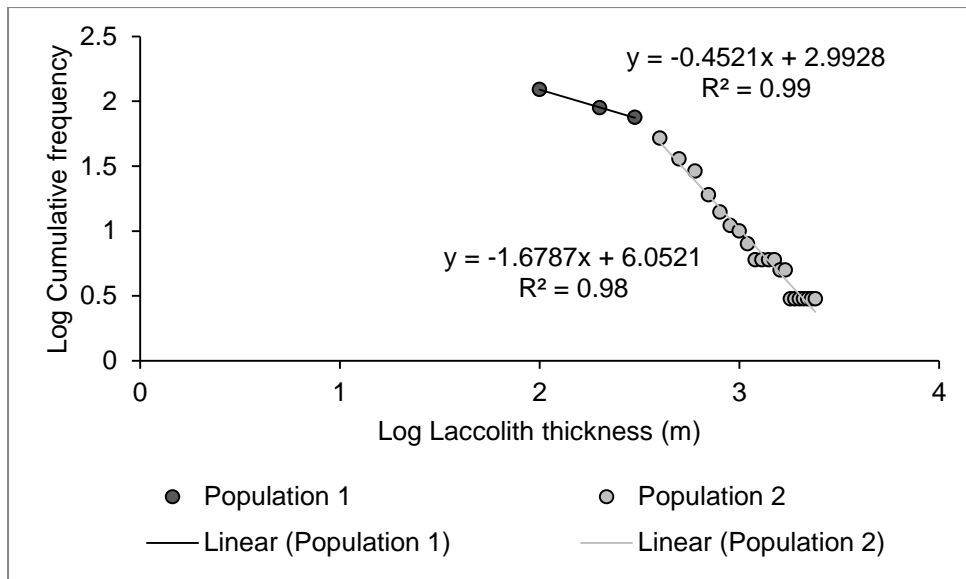


Figure 8.6: Bi-logarithmic plot of laccolith thickness showing two distinct populations based on Figure 8.5. Each linear regression line has an R^2 value and equation.

8.4.3 Tabular intrusions

Tabular intrusions (here only sills and laccoliths) are plotted together with statistical analysis for each (sub) population presented in Table 8.1. Plotting all the sill and laccolith data together (Fig. 8.7) illustrates a long tail to the cumulative frequency plot, where there are few thick intrusions in comparison to thin intrusions. This also demonstrates that more energy is needed to form these intrusions that lie along the tail of the distribution. A single line power-law shows a strong correlation with $R^2 = 0.90$, scaling exponent of 1.73 and entropy of 3.03. However, as the same for all single line power-laws presented here, there is a break in slope where some data deviates away from the single linear trend and two sub-populations can be distinguished. Population 1 has a R^2 value of 0.94, scaling exponent of 0.39 and entropy of 1.56, while population 2 has a stronger correlation with $R^2 = 0.99$, scaling exponent of 1.90 and entropy of 3. Furthermore, the possible artefacts that may have limited the data were considered. The division between the two populations in Figure 8.7C was decided upon as a midpoint that occurred where the data flattened. This is because all of this flattened region belonging to either population 1 or 2 did not have an effect on the results.

Table 8.1: Statistical analysis of tabular intrusions - sills and laccoliths worldwide. Thickness range, scaling exponent and entropy have been divided into sub-populations to give a better overview of the intrusion thickness distributions.

Population	N thickness	Mean thickness (m)	Median thickness (m)	Standard deviation	Variance	Thickness range (m)	Scaling exponent, γ	Entropy, S
Sills	106	83	40.00	116.66	1.36×10^4	0.3-600	1.26	2.13
Population 1						0.3-240	1.02	2.15
Population 2						240-600	4.37	2.10
Laccoliths	141	435.21	320.00	429.19	1.84×10^5	14.79-2500	1.30	2.58
Population 1						14.79-300	0.45	1.36
Population 2						300-2500	1.47	2.48
All data	247	283.97	160.00	375.75	1.41×10^5	0.3-2500	1.51	3.03
Population 1						0.3-200	0.37	1.56
Population 2						200-2500	1.75	3.00

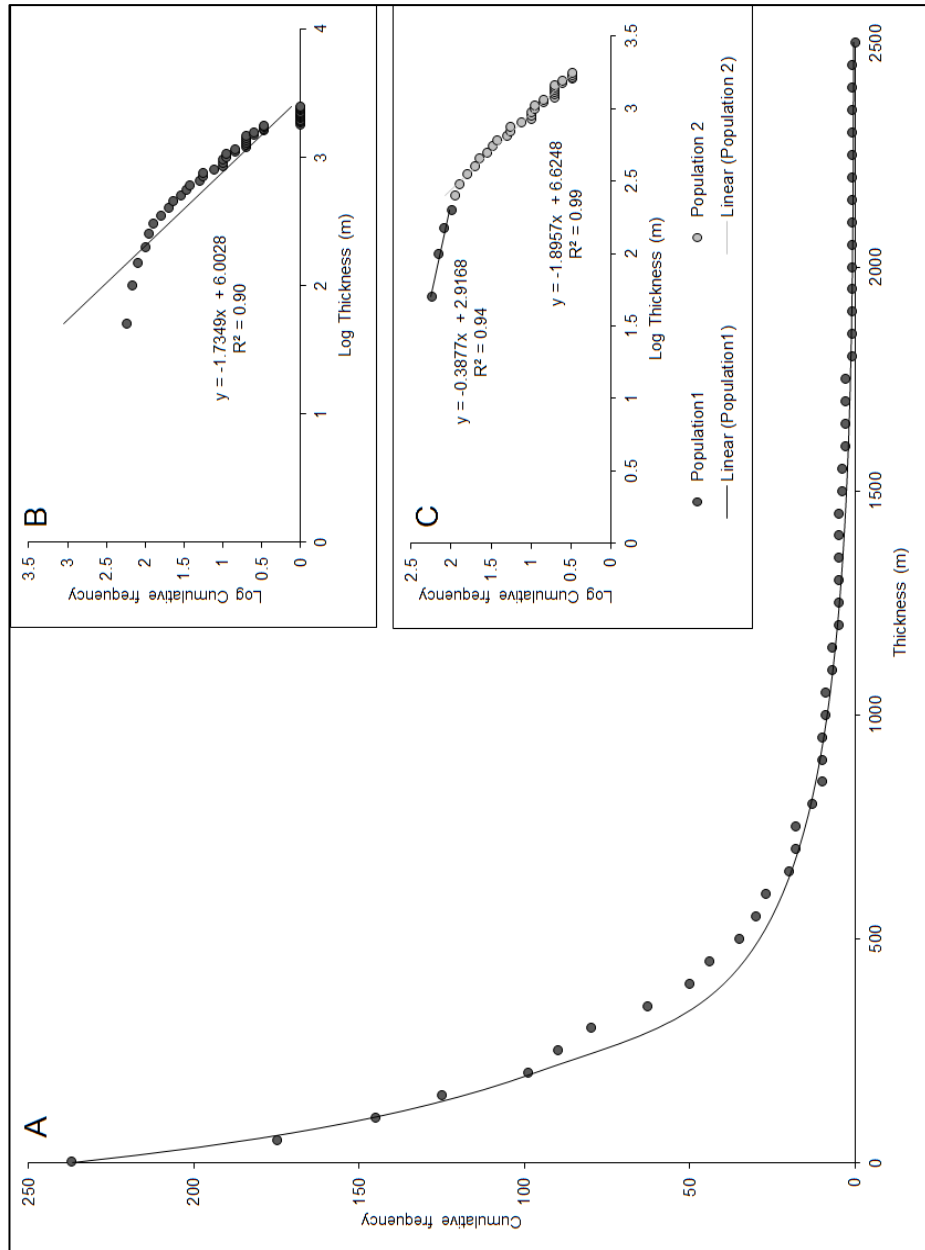


Figure 8.7: Power-law distribution for tabular intrusions. (A) Cumulative frequency plot illustrating a power-law distribution for thickness of sills and laccoliths. (B) Bi-logarithmic plot of intrusion thickness portraying the break in slope. (C) Bi-logarithmic plot of intrusion thickness representing two distinct populations. This was decided upon by taking a midpoint between the two populations because best fit lines for all of population 1 or all of population 2 did not have an effect on the results. The linear regression line shows the R^2 value and equation where the gradient determines the scaling exponent, γ , $N = 247$.

8.5 Fracture lengths

Fracture lengths were measured from the Whin Sill, NE England and also the Stardalur sill cluster, SW Iceland. The length of a fracture is defined as a straight line from end to end of the fracture using a tape measure in the field or a measuring tool in CorelDRAW for photographs (Chapter 4). The variation in fracture orientation is represented on rose diagrams illustrating a symmetrical pattern, trending perpendicular to the maximum principal tensile stress when the fractures formed. The fracture lengths measured from the Whin Sill and the Stardalur sill cluster have a range of 0.4-20 m, close to two orders of magnitude (Table 8.2). The shorter fractures are predominant in the Stardalur sill cluster as each individual sill has a thickness that is less than that of the Whin Sill. Each sill cluster or complex is first analysed individually.

The Whin Sill shows a good power-law as illustrated in Figure 8.8. On a bi-logarithmic plot (Fig. 8.9) there is a good correlation, with a R^2 value of 0.89. The gradient of the line, representing the scaling exponent, is 2.45 with entropy calculated as 1.62. There is a small break in the data at approximately 10 m, and is re-plotted as two populations (Fig. 8.10) of fractures where population 1 has a stronger correlation, R^2 of 0.91, than population 2, R^2 of 0.94. Population 1 has a scaling exponent of 1.48 and entropy of 1.49, whilst population 2 has a scaling exponent of 5.02 and entropy of 1.31. The entropy difference was 0.18 and is therefore very small between the two populations and the mechanisms in which the fractures grow.

The Stardalur sill cluster on the other hand shows a stronger power-law relationship of the fracture network within the sills (Fig. 8.11). On the bi-logarithmic plot in Figure 8.12 an R^2 value is calculated at 0.97 demonstrating a very strong correlation within the data, with a scaling exponent of 2.33 and calculated entropy of 1.4. On closer inspection of the data, a small break in the data can be identified at approximately 10 m to identify two populations in fracture lengths (Fig. 8.13). In Figure 8.13 population 1 has a stronger correlation, with a R^2 value of 0.97, than population 2, with a R^2 value of 0.88. Scaling exponents represented by the gradient of the regression line is 2.09 for population 1 and 3.57 for population 2. Entropies are re-calculated and give a value of 1.28 for population 1 and 1.43 for population 2.

Table 8.2: Data of fracture length measurements from the Whin Sill, NE England and the Stardalur sill cluster, SW Iceland. There are three fracture networks analysed: Whin Sill, Stardalur sill cluster and all the fracture measurements combined. Length, scaling exponent and entropy have been divided into sub-populations to give a better overview of the fracture length distributions.

Population	N lengths	Mean length (m)	Median length (m)	Standard deviation	Variance	Length range (m)	Scaling exponent, γ	Entropy, S
Whin Sill	416	4.75	4.00	3.36	11.30	0.47-20	2.45	1.62
Population 1						0.47-10	1.48	1.49
Population 2						10-20	5.02	1.31
Stardalur Sills	254	3.52	2.98	2.28	5.21	0.38-16.71	2.33	1.40
Population 1						0.38-10	2.09	1.28
Population 2						10-16.71	3.57	1.43
All data	670	4.29	3.52	3.06	9.34	0.38-20	2.49	1.55
Population 1						0.38-10	1.65	1.43
Population 2						10-20	3.87	1.34

Again, as the same for the Whin Sill, this entropy difference between the two fracture populations is small at 0.15.

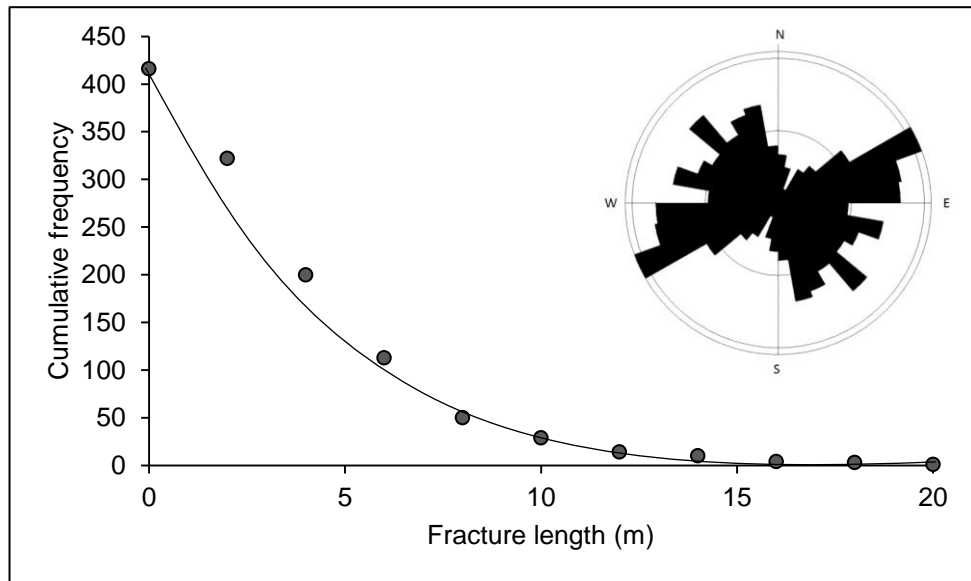


Figure 8.8: A cumulative frequency plot illustrating a power-law distribution for fracture lengths of the columnar joints in the Whin Sill, NE England. Rose diagram (inset) representing the strike distribution of the vertical fractures in the Whin Sill (circle interval 5%, sector angle 10°), N = 416.

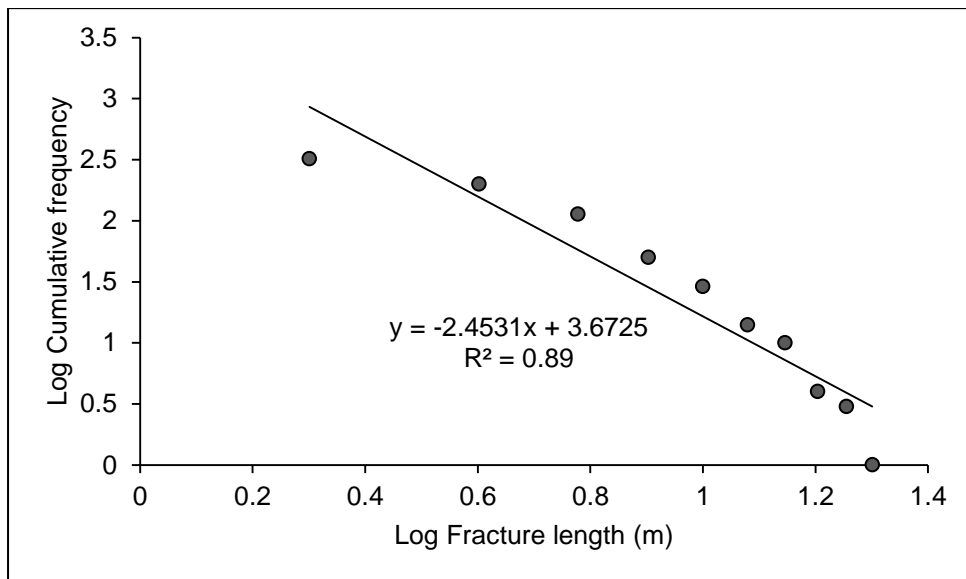


Figure 8.9: A bi-logarithmic plot of fracture lengths in Figure 8.8 illustrating the break in slope. The linear regression line shows the R^2 value and equation, where the gradient determines the scaling exponent, γ .

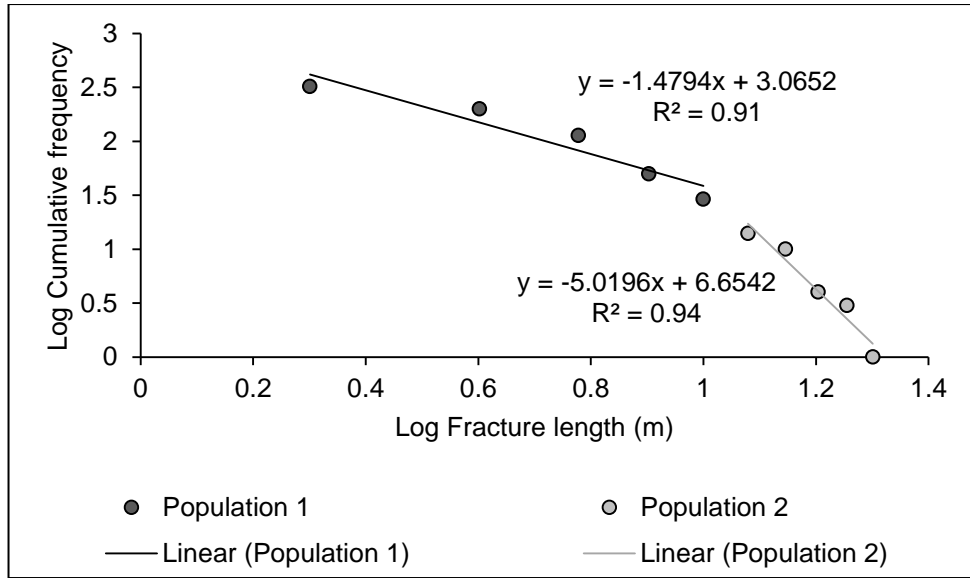


Figure 8.10: A bi-logarithmic plot of fracture lengths representing two distinct populations from Figure 8.9. The linear regression line shows the R^2 value and equation, where the gradient determines the scaling exponent, γ .

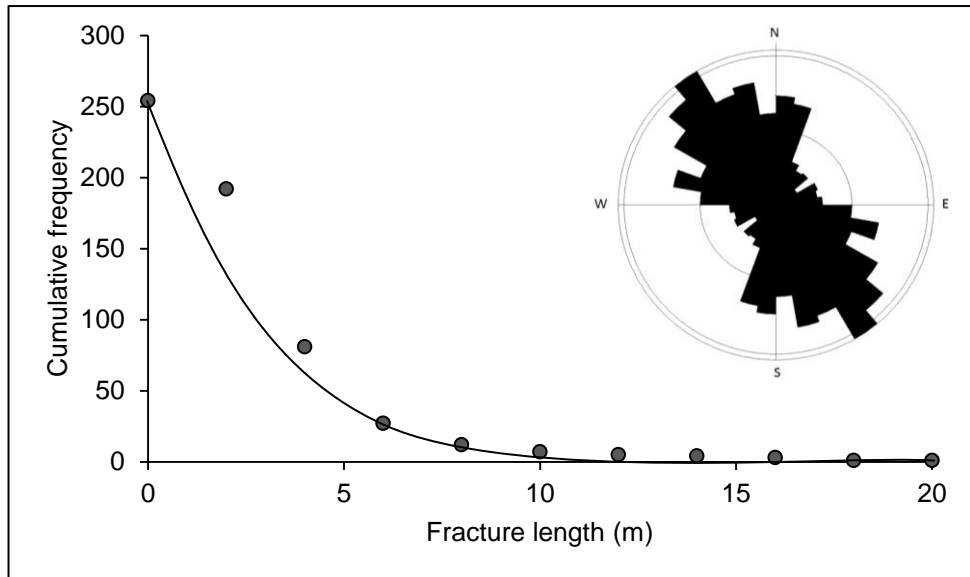


Figure 8.11: A cumulative frequency plot illustrating a power-law distribution for fracture lengths of the columnar joints in the Stardalur sill cluster, SW Iceland. Rose diagram (inset) of the vertical fracture orientation in the Stardalur sill cluster (circle interval 5%, sector angle 10°), $N = 254$.

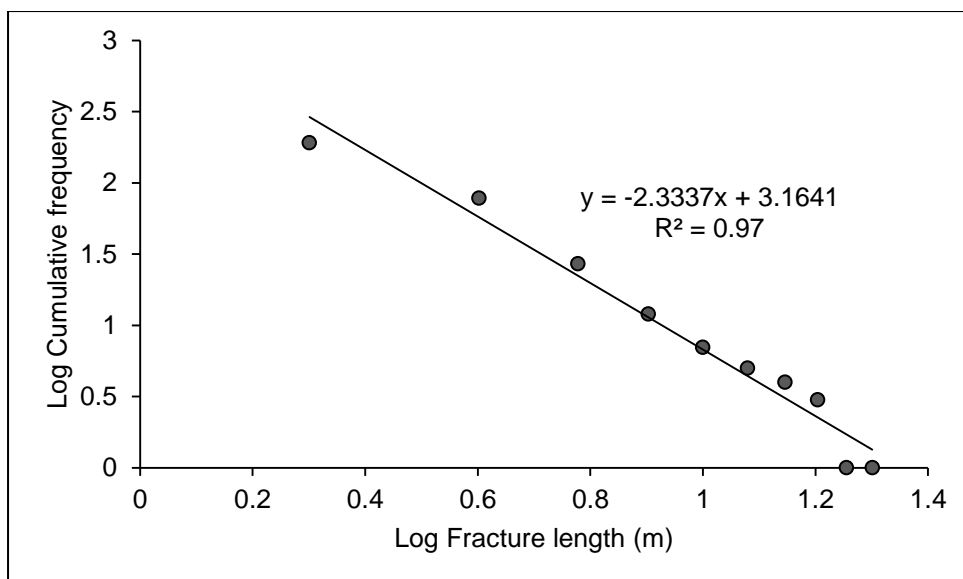


Figure 8.12: A bi-logarithmic plot of fracture lengths in Figure 8.11 illustrating the break in slope. The linear regression line shows the R^2 value and equation, where the gradient determines the scaling exponent, γ .

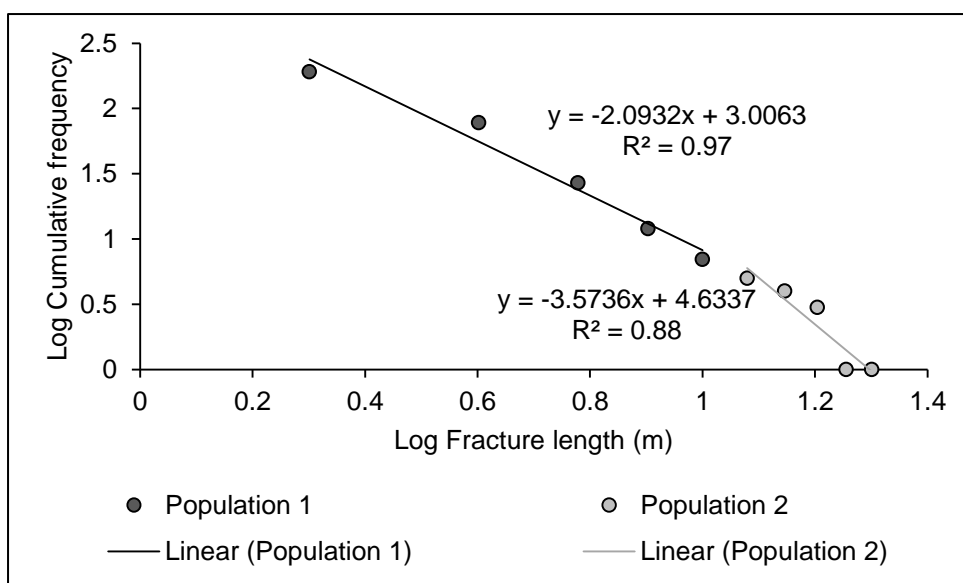


Figure 8.13: A bi-logarithmic plot of fracture lengths representing two distinct populations from Figure 8.12. The linear regression line shows the R^2 value and equation, where the gradient determines the scaling exponent, γ .

In Figures 8.9 and 8.12 each location (main population) is divided into two sub-populations (Figs. 8.10 and 8.13), which is determined by the break in slope of the regression line in the main population bi-logarithmic plots. For each population (including sub-populations) scaling exponents, γ , and entropies are calculated, giving

a total of 9 populations (Table 8.2). The data as a collective is plotted in Figure 8.14, which shows a strong correlation, with a R^2 value of 0.89, and a scaling exponent of 2.50. For the main population (a combination of the Whin Sill and Stardalur sill cluster) entropy is calculated at 1.55. When this main population is split into two smaller populations an even stronger correlation is seen, with an R^2 value of 0.94 for population 1 and 0.99 for population 2. Scaling exponents are determined by the gradient of the regression line for population 1 and population 2 at 1.65 and 3.87, with entropies of 1.43 and 1.34 respectively. Although the scaling exponent is significant with a difference of 2.22, this is not true for the entropy, which is very small, with a difference of 0.09. Error on these measurements is negligible and therefore omitted from the statistical plots.

8.6 Discussion

8.6.1 Test for power-laws

Power-law frequency distributions are determined by straight lines on a log-log plot of intrusion thickness or fracture length against cumulative frequency. The significance of these power-laws tests can be tested using a standard least-squares linear regression, which determines how well a linear trend describes the data where: $residuals = observed Y - predicted Y$. For this test to be significant certain criteria must be met: (1) the scatter should be random and show random distribution, (2) the residuals should be relatively small, (3) have a distribution that is aligned around 0 on the horizontal axis, and (4) the mean of the residuals must equal zero. Results for residuals of the sills and laccolith power-laws are shown in Figure 8.15 with a mean of the residuals for the sills -1.17×10^{-15} and -1×10^{-16} for the laccoliths. Therefore, the power-law relationships in Figure 8.15 are a good fit for the data ($R^2 = 0.85$ for sills and 0.96 for laccoliths). A parabolic function, also fits the data well ($R^2 = 0.90$ for sills and 0.98 for laccoliths). These parabolic functions are significant with respect to statistical analysis, but the R^2 values are not sufficiently different from the linear fits for the power-laws to be disregarded. This was also noted by Mohajeri and Gudmundsson (2012).

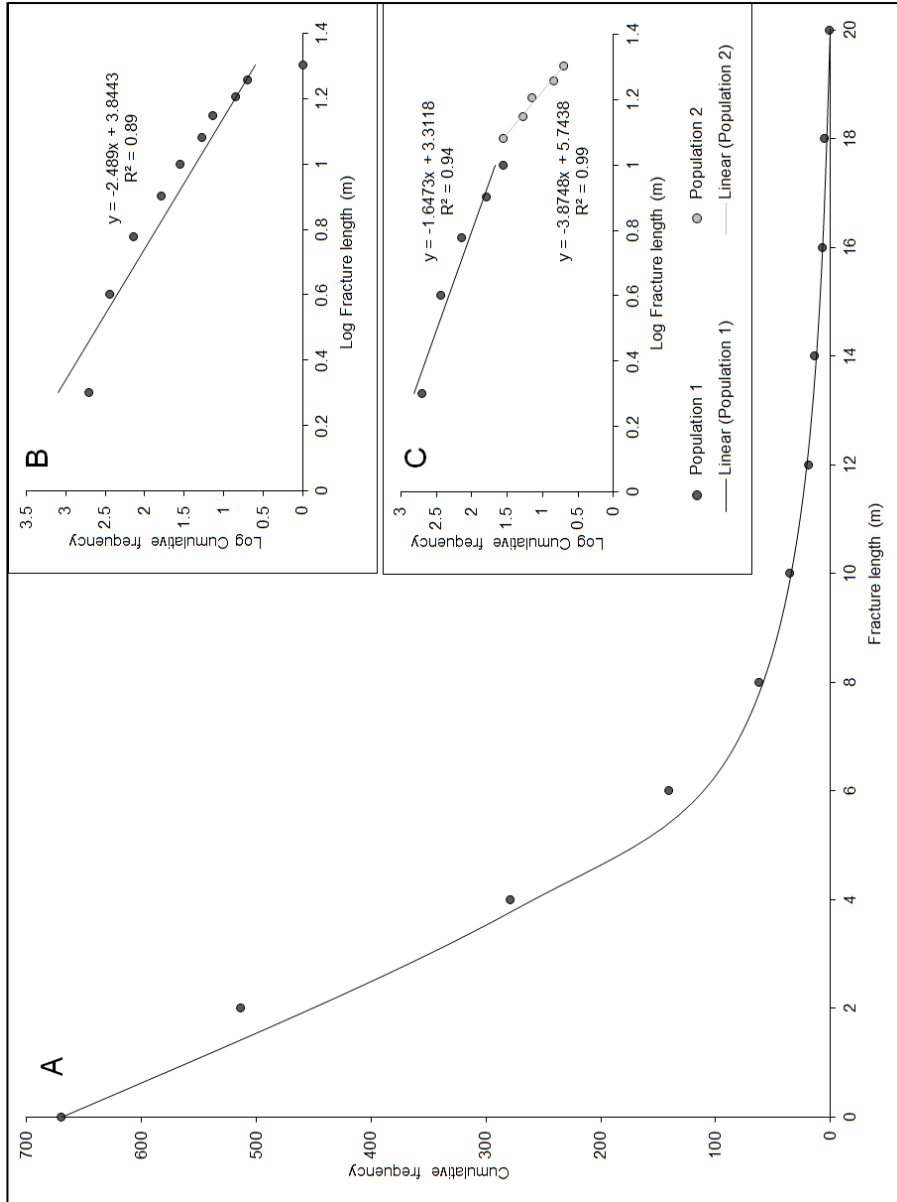


Figure 8.14: Power-law distribution for fracture lengths. (A) Cumulative frequency plot illustrating a power-law distribution for fracture lengths of the columnar joints in the Whin Sill and the Stardalur sill cluster. (B) A bi-logarithmic plot of fracture lengths illustrating the break in slope. (C) A bi-logarithmic plot of fracture lengths representing two distinct populations. The linear regression line shows the R^2 value and equation, where the gradient determines the scaling exponent, γ , $N = 670$.

Applied to fracture lengths (Fig. 8.16) linear regression yields a mean of the residuals of 2×10^{-16} . The power-law function has an R^2 value of 0.94 and is a good fit. For comparison a parabolic function is also plotted with a R^2 of 0.99 and is almost a perfect fit for statistical analysis. Again these R^2 values for the two functions (power-law and parabolic) are similar and therefore a power-law function is still acceptable.

Two best fit lines as shown in Figures 8.3, 8.6, 8.7C, 8.10, 8.13 and 8.14C are not an artefact of an incomplete data set, but represent a break in the slope and a phase change. This break is most likely related to the mechanism of formation of the sills and laccoliths. Although a parabola trend is a better fit (Figs. 8.15 C and 8.16C) than the single power-law trend (Figs. 8.15B and 8.16B), it cannot be explained by any laws of physics in terms of one continuous process, whereas a break in slope (two linear lines in Figures 8.3, 8.6, 8.7C, 8.10, 8.13 and 8.14C) can in terms of a phase change in emplacement as discussed in Section 8.6.2.

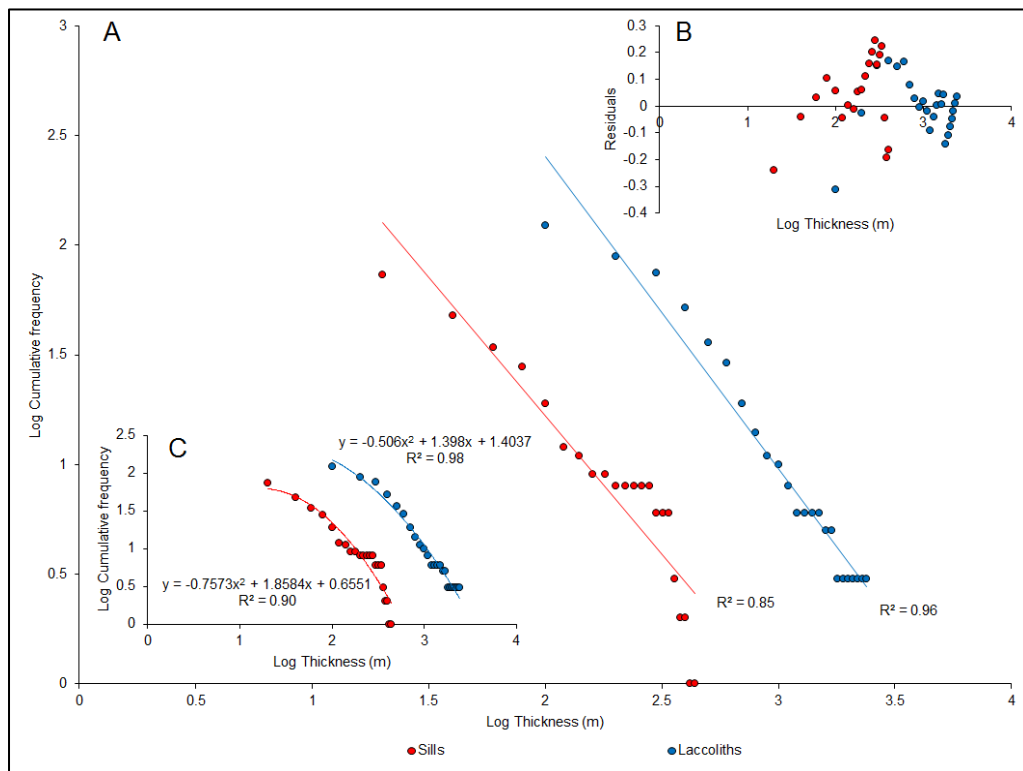


Figure 8.15: Significance tests for power-law fit for sills and laccoliths. (A) Single line power-laws, (B) residuals for the plot in (A), (C) parabola fit for sills and laccoliths for comparison.

8.6.2 Entropy

The tail of a power-law determines the dispersal of a data set, with a long, uniform tail suggesting that there is a large dispersal of the power-law distribution, that is, more energy is required, thus a high entropy (e.g. Fig. 8.7). Therefore, entropy must increase as the thickness of the sill or laccolith or the length of the fracture increases. Also, as standard deviation and variance are a measure of spread in data, and hence entropy, the tail of a power-law shows increased variability in the data. This is portrayed for the sills and laccoliths in Figure 8.17, where there is a strong correlation of thickness range and entropy between the sub-populations of sills and laccoliths yielding a linear correlation with an R^2 value of 0.67 and test statistic r , of 0.82. This can be tested to see if the linear correlation is significant using the Pearson correlation coefficient, r , using a significance level of 0.01. From the table of critical values, r is 0.798 when N is 9 and is statistically significant. For fracture lengths R^2 is 0.44 (Fig. 8.18) and test statistic r , is 0.66. The critical value r , using a significance level of 0.1 is 0.582 when N is 9, and therefore there is a linear correlation, as the test statistic is larger than the critical value.

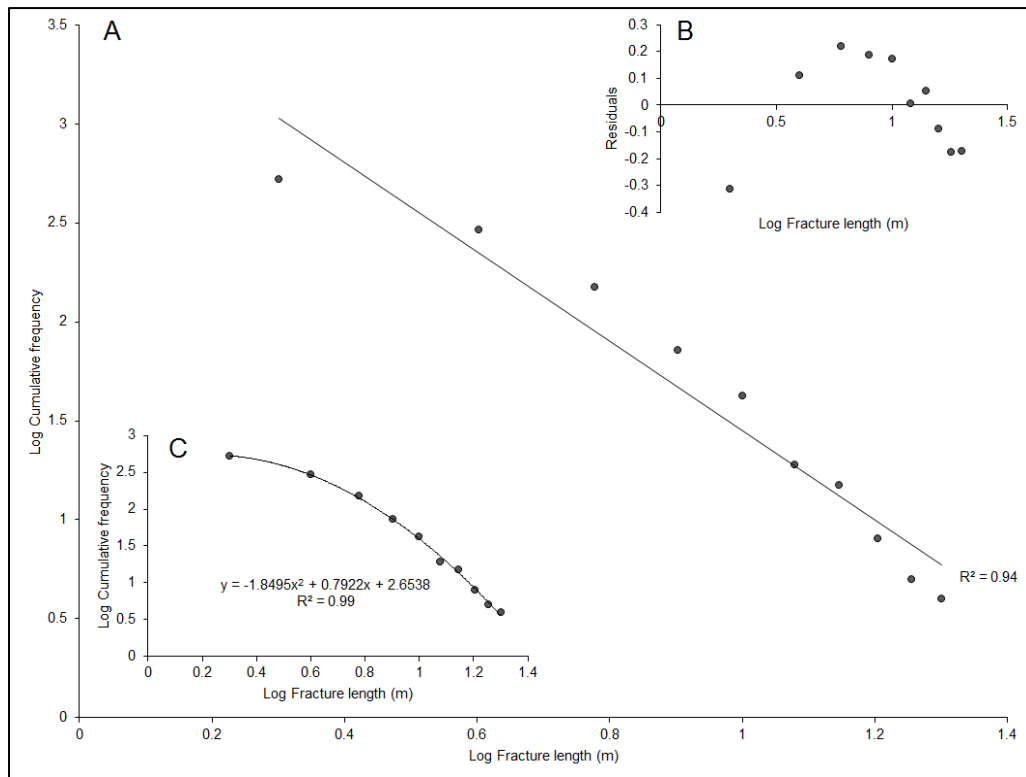


Figure 8.16: Significance tests for power-law fit for fracture lengths in the Whin Sill and Stardalur sill cluster. (A) Single line power-laws, (B) residuals for the plot in (A), (C) parabola fit for comparison.

Confidence levels, at both 95% and 99%, are determined using SigmaPlot, and are displayed in Figures 8.17 and 8.18. In Figure 8.17, although there is a strong correlation, one data point lies outside of the 95% confidence level, but is still within the 99% confidence level. In Figure 8.18 on the other hand, there is a weaker correlation, but the majority of the data still lies within the 95% confidence level. However, the Stardalur fracture populations mainly lie within the 99% confidence limit.

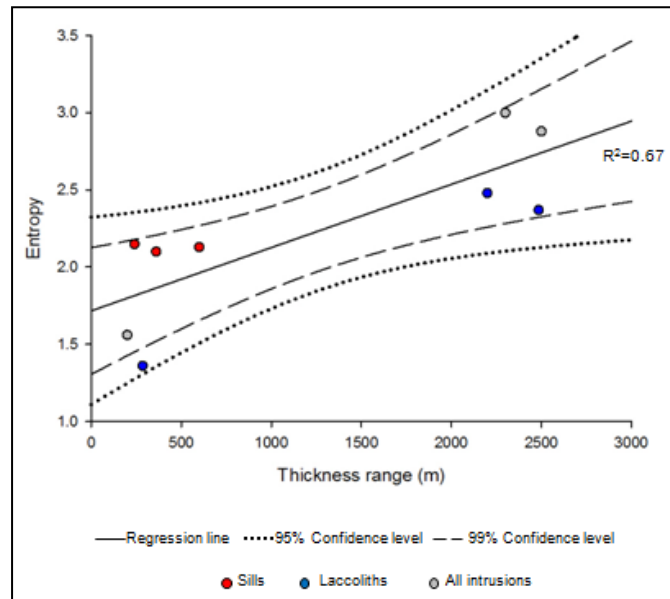


Figure 8.17: Linear relationship between entropy and sill/laccolith thickness from 9 lateral intrusion (sub) populations as shown in Table 8.1, with corresponding R^2 value and confidence levels (performed in SigmaPlot).

To compare the data on fracture lengths, bins are kept constant, with each bin representing an entropy level, where the bin width and entropy level are related through Eq. (8.3). This is because the probability of randomly selecting a fracture from a specific bin is a measure of chance, where the specific bin is affected by the calculated entropies in Eq. (8.3). However, bins cannot be kept constant for the intrusion data because of the difference in thickness measurements between the sills and laccoliths. Furthermore, as energy can be inferred from entropy, the bins in which each set of intrusions or fractures belong to, within the power-law plots, measure the energy levels within each bin. Therefore, in order for the sill to inflate or the fractures to propagate, that is, for them to fall within the next bin of the data,

more energy is needed. Thus, as shown on the power-law plots (Figs. 8.7 and 8.14), as we move towards the tail of the distribution there are fewer intrusions or fractures that sit within the given bin width.

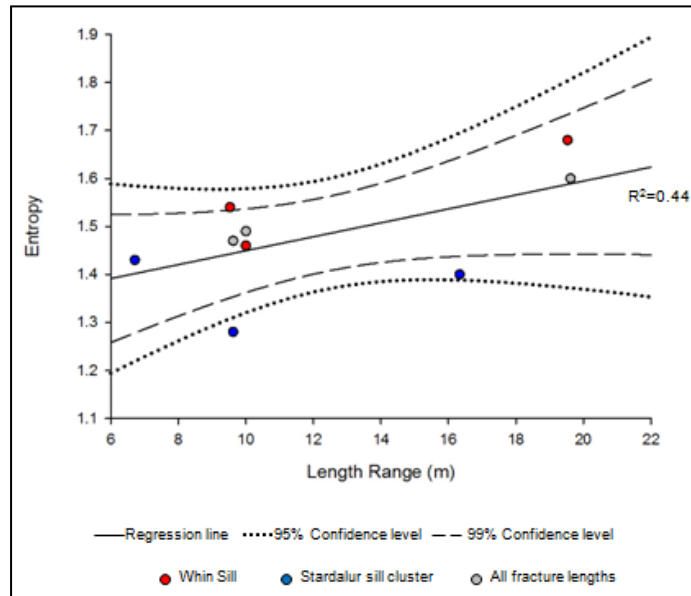


Figure 8.18: Linear relationship between entropy and fracture length from 9 lateral intrusion (sub) populations as shown in Table 8.2, with corresponding R^2 value. Confidence levels show the data to be still significant (performed in SigmaPlot).

Power-law trends are also better models as the data can be divided into sub-populations based upon their scaling exponents (gradients of the linear trends). The break in slope for the sills and laccoliths is most likely a result of the mechanics relating to their emplacement. The break in slope in Figure 8.3 may be attributed to the lateral dimensions of the sills and the depth below the free surface at which they are emplaced. For example, large sills (diameter of the sill is larger than the depth of emplacement) inflate by upbending the layers above (and to some extent down bending of the layers below). However, small sills (diameter of the sill is smaller than the depth of emplacement) do not have the ability to deflect the overlying layers, thus vertical growth is limited (Chapter 6). In the case of laccoliths they grow preferentially in the vertical direction (inflation), thus more energy is needed to overcome the tensile strength of the overlying strata (Figs. 8.6 and 8.7). This is reflected in the energy difference (Table 8.1) between sills, large sills and laccoliths, where more energy is needed to inflate these larger intrusions in order to overcome

the overburden stress. This energy difference also holds true for larger plutons that have larger dimensions and their ability to uplift the overburden or downbend the underburden (Fig. 8.19; McCaffrey and Petford, 1997; Cruden and McCaffrey, 2002; 2006).

Other factors may also contribute to the break in slope for sills and laccoliths, which may relate to the geometry of the sill, for example simple straight sills or complex stepped sills, or extrinsic and/or intrinsic controls, including emplacement depth, magma viscosity, magma composition, magma temperature and local tectonic regime. For example, laccoliths tend to be emplaced at shallow depths holding relatively high viscous magmas.

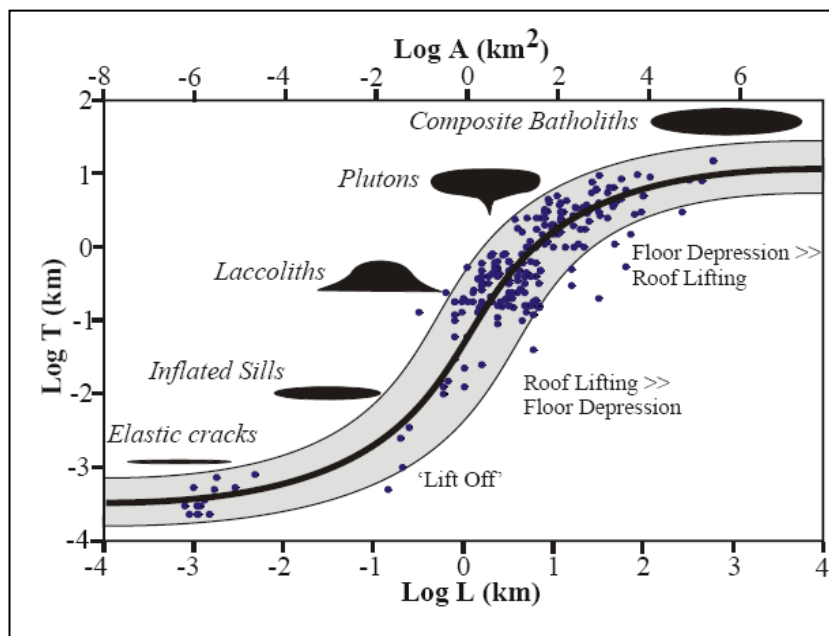


Figure 8.19: Tabular intrusions with corresponding length, L, thickness, T, and lateral area, A, showing a 'S' shape representing the various emplacement styles (Cruden and McCaffrey, 2002).

The break in slope (scaling exponent) and the calculated entropy values for fracture lengths may be explained by factors such as:

1. Fractures form from existing columnar joints. On expansion of the fracture network, the damage zone of the host rock increases with more tectonic fractures forming (post columnar joint formation). As these fractures grow they may interconnect reaching the percolation threshold (Berkowitz, 1995). Therefore, the scaling exponent increases as will entropy. As fractures

become interconnected and become larger and the associated damage zone increases, a through-the-thickness fracture forms (Xie, 1993).

2. The fracture lengths within the sills may be considered to be bound by the thickness of the sill. Therefore, the power-law distribution will have an upper and lower limit (dependent on the sill thickness) in which the power-law is invalid (Odling, 1997; Berkowitz *et al.*, 2000). By definition the only scale limit of a power-law is the size of the system measured (Bour and Davy, 1997). Therefore, fracture length and degree of interconnectivity will impact the rate of fluid flow especially when increasing the scale of the system.
3. Temperature contrast between the host rock and the magma within the sill. The larger the thermal gradient, the greater the thermal stresses and more well developed columnar joint formation. Therefore, on a power-law size distribution (Fig. 8.14) well developed columnar joints may lie in population 2 and less well developed may lie in population 1.

A break in slope to form sub-populations can be regarded as non-universal, because they may be caused by different mechanisms. This was discussed by Hatton *et al.* (1994) with relation to fracture lengths and their associated apertures. They concluded that the length of the fractures varied over approximately four orders of magnitude and the apertures varied by five orders of magnitude. Thus, a scaling behaviour was significant as the study of these fractures was carried out in a homogeneous area in NE Iceland. Break in slope, hence a change in scaling exponent, has also been demonstrated by other studies. For example, tension fractures and normal faults (Bour and Davy, 1997; Gudmundsson, 2005; Ferrill *et al.*, 2008; Mohajeri and Gudmundsson, 2012; Gudmundsson and Mohajeri, 2013), fault damage zone width and fault displacement (Micarelli *et al.*, 2006), frequency of extension (veins) and shear (faults) fractures in Kimmeridge Bay (Putz-Perrier and Sanderson, 2008), crack growth (Yang *et al.*, 2004), growth of sills and laccoliths (McCaffrey and Petford, 1997; Cruden and McCaffrey, 2002; Cruden and McCaffrey, 2006; Bungler and Cruden, 2011), permeability and interconnectivity of fractures (Long and Witherspoon, 1985; Berkowitz *et al.*, 2000), and monogenetic volcano size distribution (Pérez-López *et al.*, 2011).

8.6.3 Fracture growth

Fracture growth is described by Griffith's theory (Griffith, 1920): for equilibrium to be achieved then the potential elastic energy (including strain) is required to be at a minimum. If applied to a brittle body then the conditions needed for equilibrium can describe the advancement of a crack. When external loading is applied to a brittle body, stress concentrates within the body where there are weaknesses, for example microcracks that grow to form fractures (Xie, 1993). As the external loading increases the fractures begin to propagate, especially the larger fractures, until a through-going failure within the brittle body occurs (Gudmundsson, 2011a). In order for this process to occur Eq. (8.4) needs to be satisfied where the total energy in the system, U_t , must be larger than the threshold energy, G_c :

$$U_t = \Pi + W_s \quad (8.4)$$

where Π is the potential energy in the system, a combination of surface energy or work done to form a fracture surface, W_s , and the internal strain energy, U_o , stored pre-fracture formation (Gudmundsson, 2011a). If the total energy within the system is constant or decreases, an energy release rate, G , available for fracture propagation by differentiating can be determined from Eq. (8.4), thus (Gudmundsson, 2011a):

$$G = -\frac{d\Pi}{dA} \quad (8.5)$$

In order for the fracture to propagate, G_c , then Eq. (8.6) must be satisfied (Gudmundsson, 2011a):

$$G_c = \frac{dW_s}{dA} \quad (8.6)$$

However, Equations (8.5 and 8.6) relate to a fracture surface and can be re-written with respect to the fracture length. For mode I cracks, that is, extension fractures, the plain strain energy release rate, G_I , is as follows:

$$G_I = \frac{\sigma^2(1-\nu^2)\pi a}{E} \quad (8.7)$$

where σ is the applied tensile stress, ν is Poisson's ratio, π is a constant (3.1416), a is the half length of the fracture and E is the Young's modulus of the host rock that the fracture is propagating within (Gudmundsson, 2011a). Therefore, for the sill to inflate or the fractures within the solidifying sill to grow, a potential energy is required, which increases as the sill or laccolith or fracture grows.

For the columnar joints and tectonic fractures, additionally, they must be orientated favourably within the local stress field. The rose diagrams in Figure 8.20 show a wide distribution in the orientation of the fractures measured along the Whin Sill. However, they show that for the northern (Bamburgh, Holy Island and Dunstanburgh areas) and the southern parts of the complex (Co. Durham and Hadrian's Wall area), fractures are predominantly orientated along an approximate N-S trend. However, for the central part of the complex (Ward's Hill Quarry area) most fractures are aligned along an E-W trend. The difference in fracture orientation may be due to the different ages of the Whin Sill (complex). Liss *et al.* (2004) reported palaeomagnetic results for the Whin Sill identifying three main parts (Fig. 8.21). They show that the northern part of the complex (Holy Island Sill; Fig. 8.21A) has a similar intrusive age to the southern part of the complex (Hadrian's Wall-Pennines Sill; Fig. 8.21C), approximately 295 Ma and their geomagnetic poles cannot be distinguished. The middle part of the complex (Alnwick Sill; Fig. 8.21B) has a different virtual geomagnetic pole exhibiting an Early Permian age. However, it is not just the age of the sill that is a factor but also the orientation in which the sill was emplaced. For example, the Holy Island Sill (Fig. 8.21A) has a dominant fracture orientation of N-S and therefore lateral propagation was E-W, whereas the Alnwick Sill (Fig. 8.21B) has a dominant fracture orientation of E-W with lateral propagation along a N-S line, and the Hadrian's Wall-Pennines Sill (Fig. 8.21C) has a dominant fracture pattern NW-SE and a second pattern NE-SW representing the horse-shoe lateral propagation. These lateral propagations map that of the sill in Figure 4.6. All minor orientations on these rose diagrams most likely represent tectonic events after the columnar joints had formed.

The fracture orientation is also noted in the Stardalur sill cluster, which varies between each sill of the cluster. The Stardalur sill cluster was emplaced over a relatively short geological time period. The most western part of the cluster (profiles 1, 9, 10, 19-21; Fig. 8.22A) has a dominant fracture orientation of NE-SW, with a

minor orientation of E-W due to possible fracture growth during post-tectonic deformation. The second sill cluster (profiles 2, 11-18; Fig. 8.22B) is possibly the youngest sill. This is because a sill cluster forms because of mechanical barriers, that is, the overlying sills would most likely be still at least partially molten and the subsequent sills would be unable to propagate through (Chapter 6). This second sill cluster has a dominant NW-SE fracture orientation. The most eastern part of the sill cluster (profiles 3-8; Fig. 8.22C) has a dominant fracture orientation of E-W, with minor fracture orientations trending more towards the NW-SE, which may be due to post tectonic events.

It is important to note that with all these fracture orientations it is difficult to determine a palaeostress orientation for the sills. This is because columnar joints form perpendicular to the cooling surface, which will be concordant with bedding or other discontinuities illustrating that the maximum principal compressive stress was parallel to the bedding or discontinuity. However, tectonic extension and shear fractures can help identify a palaeostress orientation, as these fractures form in response to tectonic deformation following sill emplacement.

8.7 Conclusions

Each population, intrusion thickness or fracture length follows a power-law distribution, where each main population can be sub-divided into sub-populations based upon break in slope on a single line bi-logarithmic plot. These power-laws can also help to understand the mechanics behind sill and laccolith emplacement and also fracture growth within sills because of their strong correlations with entropies, scaling exponents and thickness or length ranges.

For sill or laccolith growth, a break of slope (scaling exponent) was determined, dividing the data into two populations, where each population relates to the mechanisms of formation. This mechanism can be described as the ability of a sill or laccolith to displace the overlying layers enabling vertical growth or inflation of the sill or laccolith. This inflation reflects the energy required to displace the overburden, which is inferred from the entropy calculations, where entropy is a measure of probability. A break of slope was also determined for the fracture

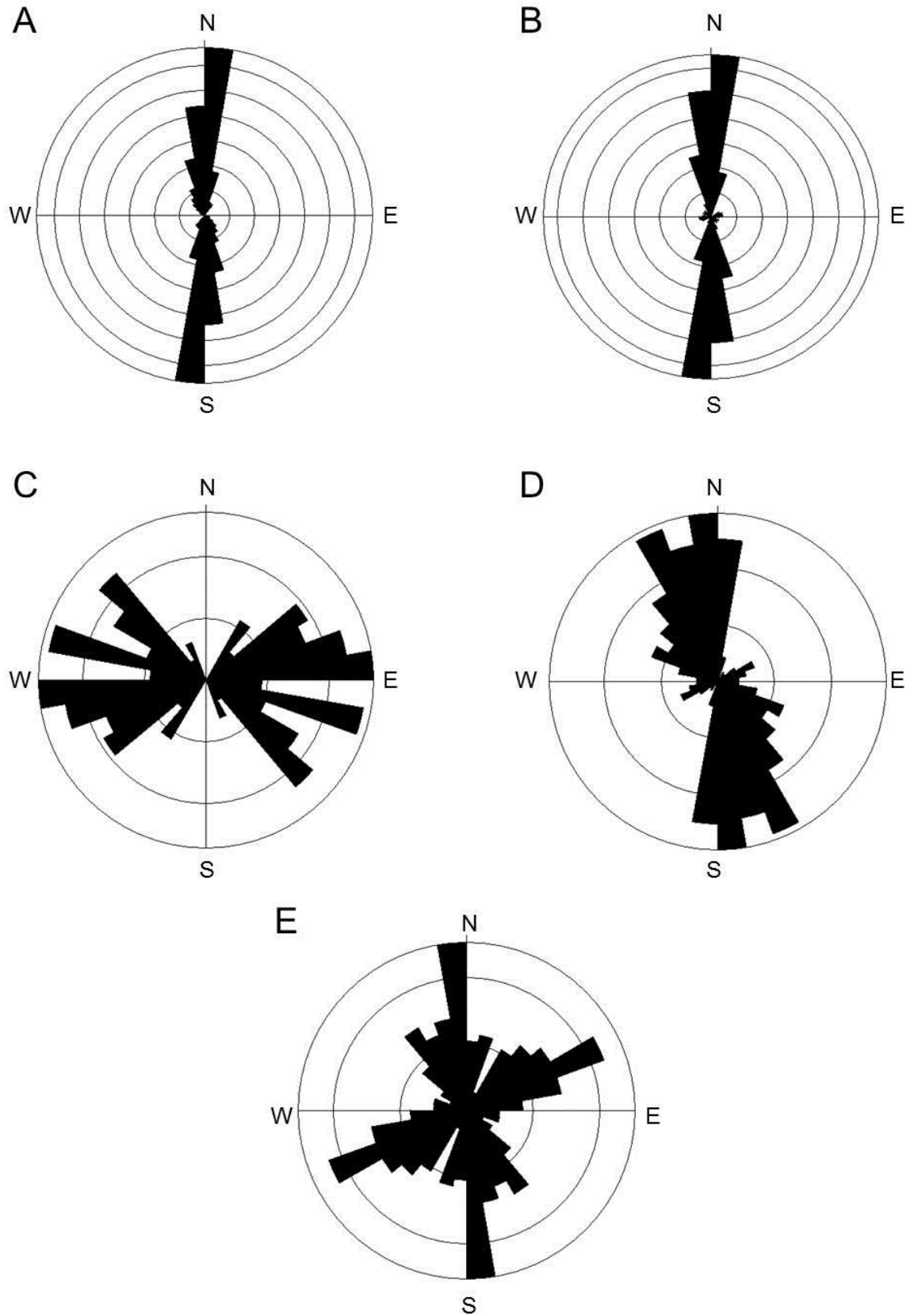


Figure 8.20: Rose diagrams for fracture orientations within the Whin Sill. (A) Bamburgh-Holy Island fractures, (B) Dunstanburgh fractures, (C) Ward's Hill Quarry fractures, (D) Hadrian's Wall fractures and (E) Co. Durham fractures (circle interval 5%, sector angle 10°), total N = 416.

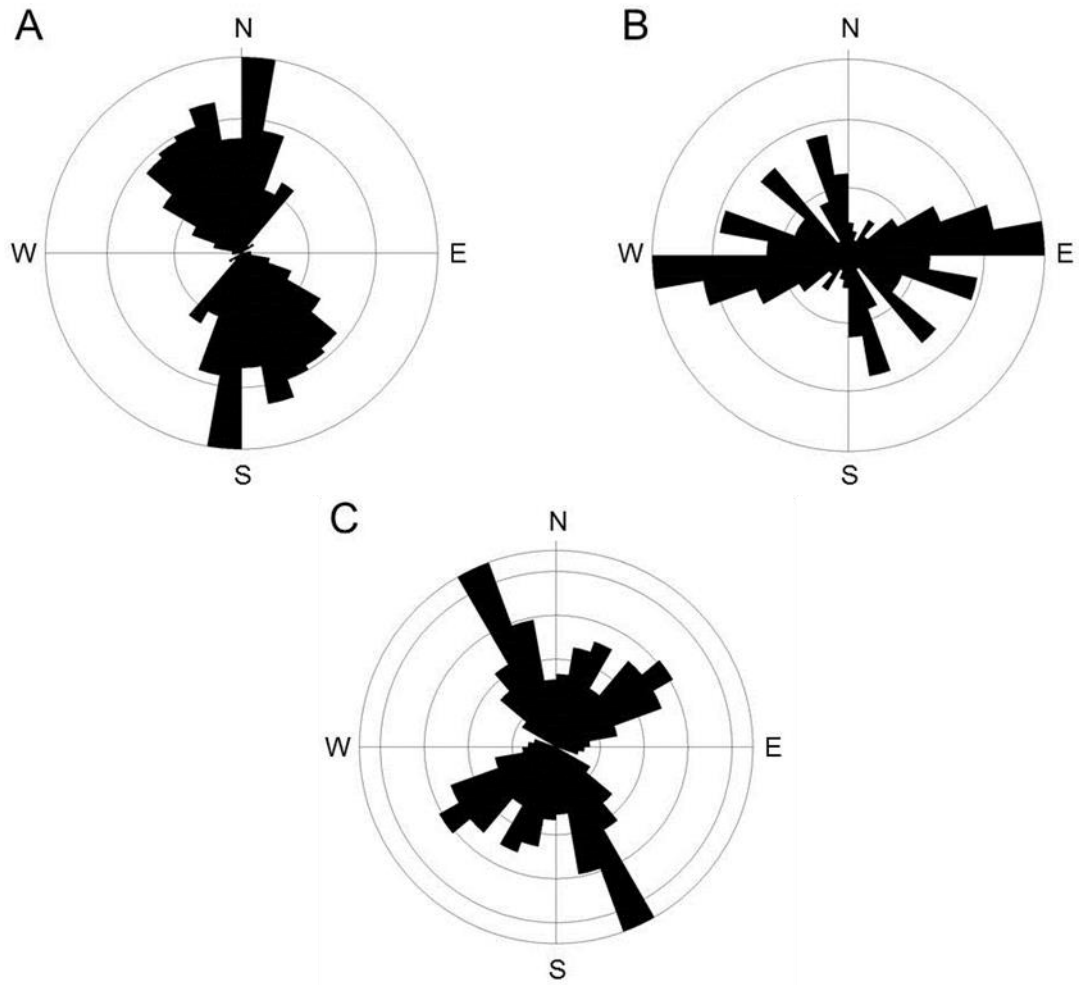


Figure 8.21: Rose diagrams of fracture orientations in the Whin Sill. (A) Holy Island Sill, (B) Alnwick Sill and (C) Hadrian's Wall-Pennines Sill (circle interval 5%, sector angle 10°), total N = 416. Classification of the sill into these three parts is based on Liss *et al.* (2004).

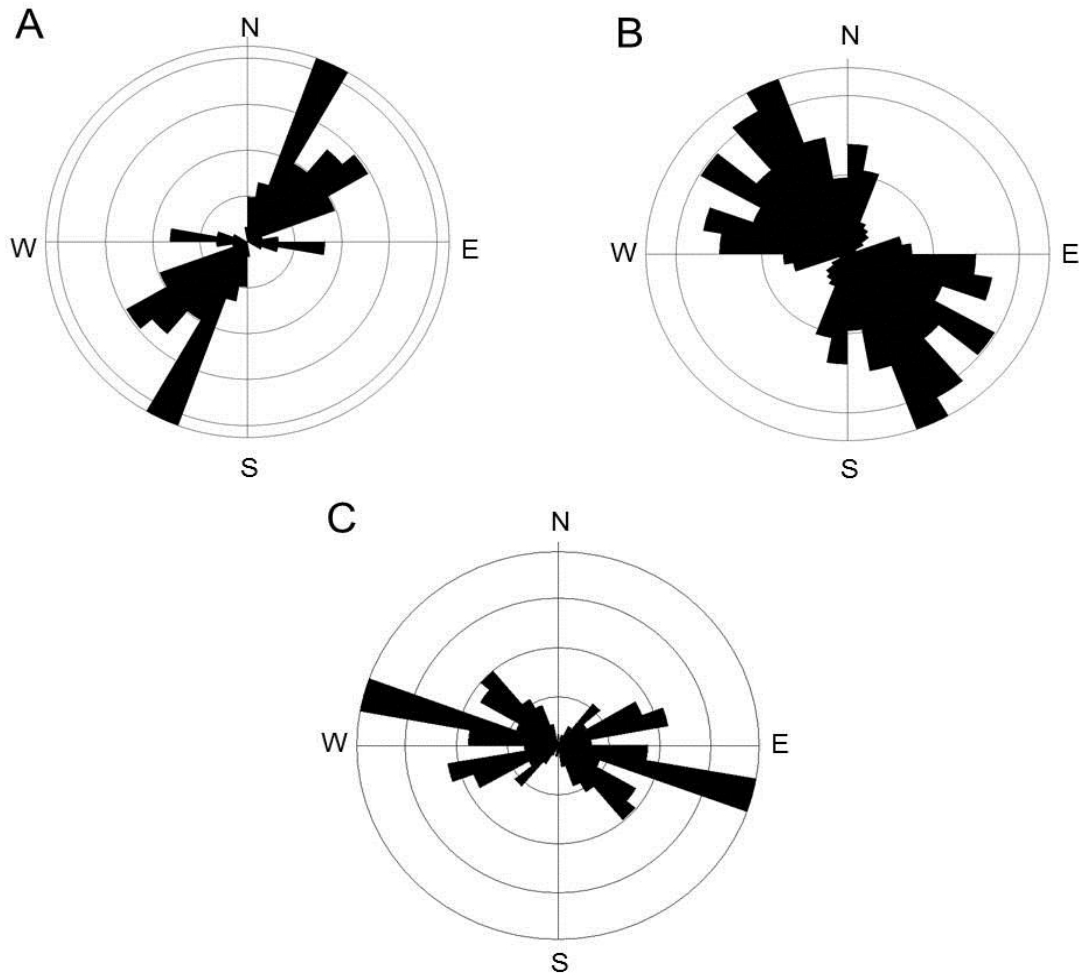


Figure 8.22: Rose diagrams of vertical fractures in the Stardalur sill cluster. (A) Profiles 1, 9, 10, 19-21, (B) profiles 2, 11-18, (C) profiles 3-8 (circle interval 5%, sector angle 10°), total $N = 254$.

networks, dividing the data into two populations. This break in slope along with calculated entropies reflect the conditions for fracture growth, that is, as the fractures grow to form a network, the scaling exponent and entropy will increase, where entropy is used to infer energy and how the energy is used within the network.

Chapter 9: Fracture networks in sills

9.1 Introduction

Until the late 1990s fracture networks and their effects on fluid flow were poorly understood (Odling *et al.*, 1999). The permeability of fractured reservoirs is primarily controlled by the configurations of their fracture networks; the attitudes, the apertures, and the lengths of the fractures that constitute the networks. *In situ* studies of fracture networks in carbonate reservoirs are necessarily limited (as here for the Vøring Margin) so that studies of analogues (here Iceland and NE England) are important for understanding their fracture permeability. The study of fractures and fracture networks also has applications for the mining industry, because of mineral infilling of fractures, engineering, because fractures affect the overall strength of rocks, and hydrogeology, because of their effects on storage capacity and the flow of fluids.

Two types of fractures are present in sills, and are especially noticeable in the Whin Sill: (1) columnar joints that control primary permeability and fracture porosity and (2) tectonic fractures that contribute to secondary permeability and porosity. Columnar joints form when the sill cools to 60% of its original temperature in degrees Celsius (e.g. for a mafic magma at 1300 °C, columnar joints would begin to form at ~800 °C), and are defined in the literature as cooling joints (Gudmundsson, 1990). For mafic sills, convecting fluids, typically water vapour, act to cool down the sill (Cathles *et al.*, 1997; Gudmundsson, 2011a). These columnar joints form predominantly perpendicular to the cooling surface due to thermal stresses and their growth is incremental (in stages), from the margins of the sill to its centre. First, cooling stresses increase at the sill margin to form the tip of a columnar joint. Second, the columnar joint begins to extend for a short distance until it meets ductile, hot magma, when the joint propagation temporarily stops (is arrested) (DeGraff and Aydin, 1987). This forms a cycle, causing the columnar joints to form an irregular path as shown in Figure 9.1A. Columnar joints are essentially fractures that divide a sill into columns with a hexagonal or pentagonal cross section (Fig.

9.1). These columns provide a well-established 3D fracture network, provided that they remain open and therefore increase vertical (and to some extent horizontal) permeability (Delpino and Bermúdez, 2009). The Stiflisdalsvatn Sill, SW Iceland, exhibits spectacular columnar jointing, showing the dominance of vertical fractures with few horizontal fractures (Fig. 9.1C).

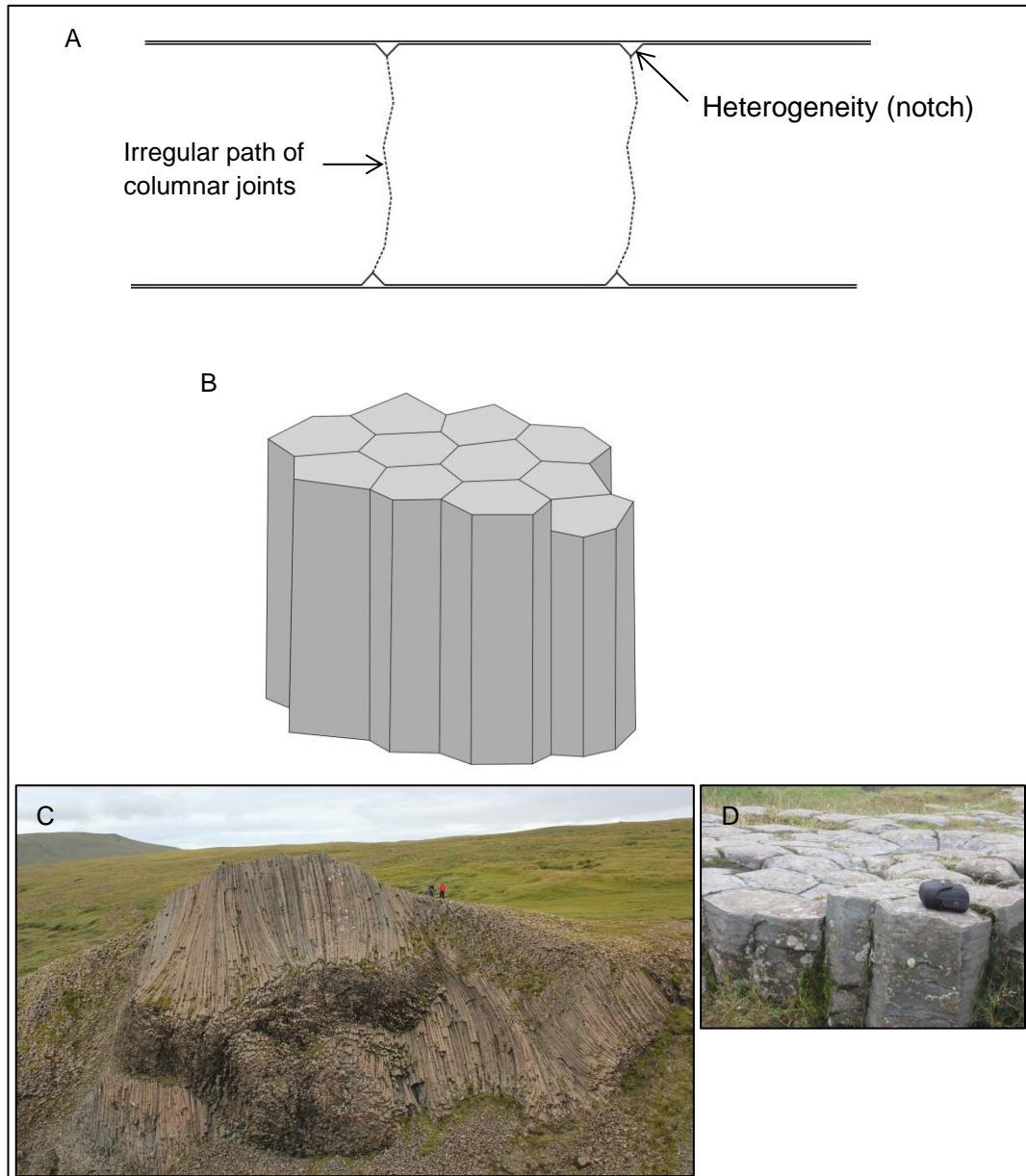


Figure 9.1: (A) Schematic illustration of columnar joint formation. (B) Detailed illustration of the notch at the sill margin in (A). (C) Stiflisdalsvatn Sill, SW Iceland, view NW. This sill is emplaced within Quaternary lavas and hyaloclastites. The sill is ~33m thick. (D) Geometry of columnar joints exhibiting a mostly hexagonal (in parts pentagonal) cross section, with a diameter of approximately 30cm, S Iceland.

The columnar joints (primary fractures), form a weakness in the sill from which tectonic fractures may develop. The growth of tectonic fractures is mainly controlled by the mechanical interaction between each individual fracture. As the fractures interact with each other, via crack-crack interaction, new fractures form in the vicinity (Barnett, 2011). This affects fracture spacing, which is dependent on the fracture-driving stress distribution (Fischer *et al.*, 1995). There are two dominant types of tectonic fractures: tension fractures, where displacement is perpendicular to the fracture plane and shear fractures, where displacement is parallel to the fracture plane.

The growth of an extension fracture was seen in an outcrop at Craster, near Dunstanburgh, NE England and shows a text book example of a plumose structure. This is illustrated in Figure 9.2 showing a hackle (yellow lines) fanning out from an axis where the fracture originated from, that is, where the tensile stress was largest. The velocity of the crack decreases towards the surface as indicated by the splaying of the hackles (DeGraff and Aydin, 1987).



Figure 9.2: Plumose structure indicating the fanning of hackles (yellow lines) from an apex. Notebook for scale, Craster, NE England.

The aim of this chapter is to analyse fracture networks from the Whin Sill, NE England and Stardalur sill cluster, SW Iceland, both analytically and numerically, to

investigate fluid flow through sills, and where possible apply this gained knowledge to the Vøring sills.

9.2 Fractures in the study area

Fractures measured in both the Whin Sill and the Stardalur sill cluster were predominantly extension fractures, for example joints, but a few shear fractures were also measured. The fracture attitude, aperture and spacings were measured for all profile lines for the Whin Sill (18 profiles – Fig. 4.8; 1037 fractures) and Stardalur sill cluster (21 profiles – Fig. 4.10; 909 fractures) as described in Chapter 4. The majority of fractures are cooling joints and therefore, the number of joints and fractures within the Whin Sill and Stardalur sill cluster was dependent on the contrast in temperature (thermal gradient) between the magma and host rock. Also, the well-defined cooling joints (larger columns) were formed due to a large thermal gradient, hence higher thermal stresses, which therefore implied that these sills were emplaced at shallow depths within the crust. Some of the fractures seen in outcrop were closed (did not have an aperture) because of ‘healing’ and ‘sealing’. This was due to the circulation of geothermal fluids post sill solidification, where, as a result, some of the fractures were infilled with secondary minerals, for example quartz or calcite. Also, primary cooling joints could have been reworked by post tectonic events and commonly impacted by the effects of weathering, modifying the fracture aperture and enhancing fluid transitivity. Therefore, the overall permeability and porosity of the sills most likely varied over time and also depend on the dimensions of the sill.

9.3 Fracture orientation

Fracture orientations were measured for all the vertical (sub-vertical) fractures that intersected the profile line and a few horizontal (sub-horizontal) fractures that were representative along the profile line.

9.3.1 Whin Sill

A total of 1037 fracture orientations were measured (both strike and dip) on the vertical face of the sill, where 666 fractures were measured along profiles greater

than 10 m (Fig. 9.3). The rose diagrams (Figs. 9.3A and B) show the dominating trend for the vertical and sub-vertical fractures is orthogonal, ENE and NW, in comparison to the horizontal and sub-horizontal fractures, which has a dominant trend of ENE. Based on the histogram (and stereonet; Figs. 9.3C and D) there are two main groups of fractures based upon their dip: vertical and sub-vertical fractures with dips in the range of 40-90° and horizontal and sub-horizontal fractures with dips in the range of 0-40°.

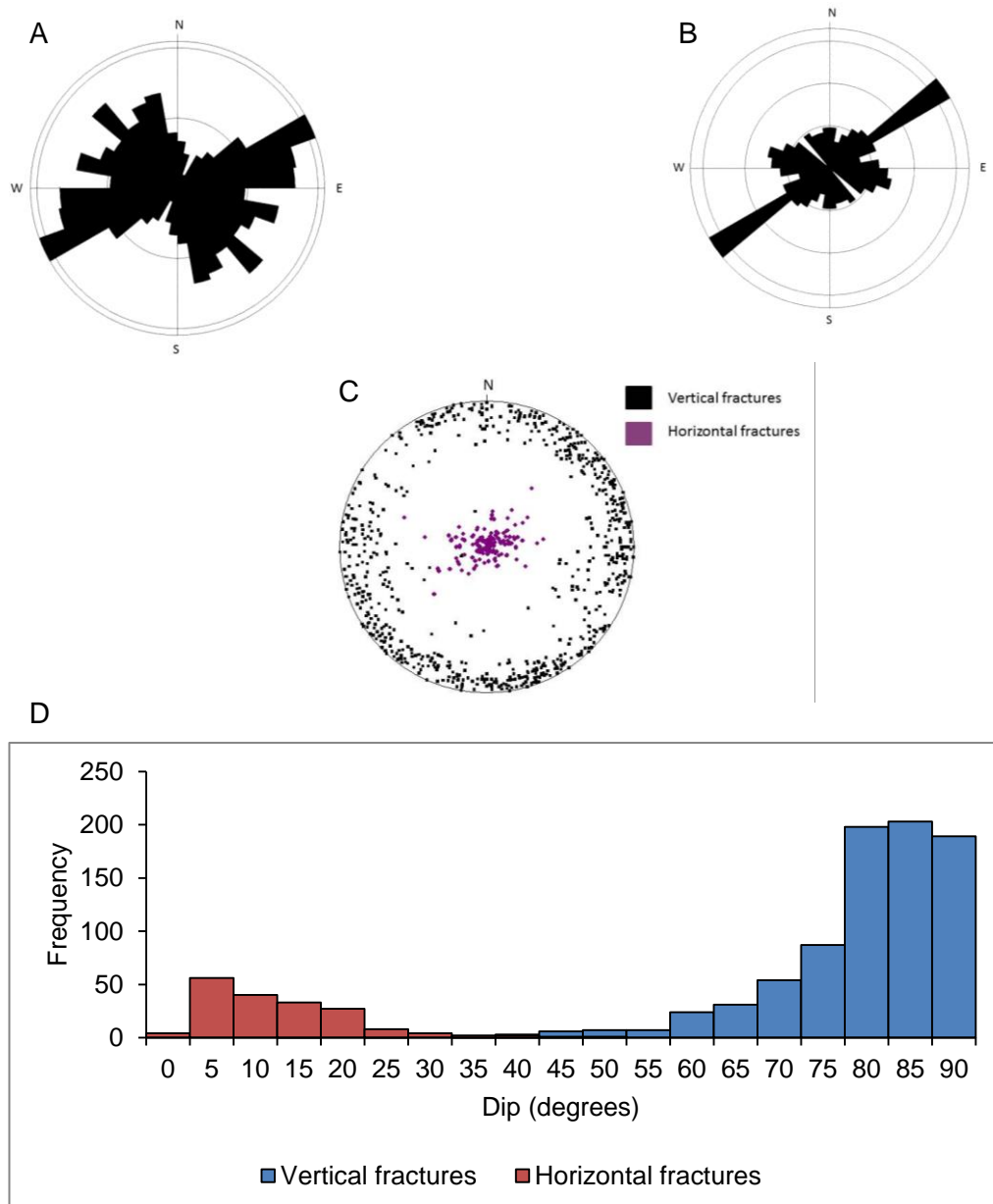


Figure 9.3: (A) Rose diagram of vertical fractures, N = 478. (B) Rose diagram of horizontal fractures, N = 188. Both rose diagrams have a circle interval of 5% and a sector angle of 10°. (C) Stereonet of all fractures, N = 666. (D) Histogram representing dip of both vertical and horizontal fractures.

9.3.2 Stardalur sill cluster

A total of 915 fracture orientations were measured (Fig. 9.4). The rose diagrams (Figs. 9.4 A and B) illustrate that the dominant orientation of the vertical fractures is NW, this trend is also seen in the horizontal fractures, which also has a second peak to the NE. The histogram (and stereonet; Figs. 9.4C and D) display a similar dip classification of vertical and sub-vertical fractures and horizontal and sub-horizontal fractures to the Whin Sill. The vertical and sub-vertical fractures have a range in dip from 40-90° and the horizontal and sub-horizontal fractures range from 0-55°. There is an overlap in the classification between these two sets of fracture dips because the fractures became rotated towards the tips of each sill within the cluster due to the sill's geometry.

9.4 Fracture spacing and fracture frequency

Fracture frequency (or intensity) and fracture spacing are a measure of the abundance of fractures in a given area. Fracture frequency (F) can be calculated in 1D, 2D or 3D, but only 1D and 2D calculations are performed as the top of the sills are rarely seen. This is defined as a ratio between the number of fractures measured along a profile (N) to the length of the profile (L) (Ortega *et al.*, 2006):

$$F = \frac{N}{L} \quad (9.1)$$

The spacing (S) is a measure between two parallel (or sub parallel) fractures along the profile line, and can be defined also as the reciprocal of the fracture frequency (Ortega *et al.*, 2006):

$$\bar{S} = \frac{1}{N} \sum_{i=1}^N S_i = \frac{L}{N} = \frac{1}{F} \quad (9.2)$$

The fracture spacings within the Whin Sill and the Stardalur sills have an impact on the mechanical properties of the sills and their permeabilities. The spacing between two (sub) parallel fractures is dependent on the initiation of each fracture and their propagation paths, including as to where they become arrested. This fracture spacing affects the permeability of the sills and their potential as fractured hydrocarbon

reservoirs. The main factors governing tectonic fracture initiation and propagation is the local stress field and the mechanical properties of the host rock, which determine the formation of fracture networks, thus permeability of the sills.

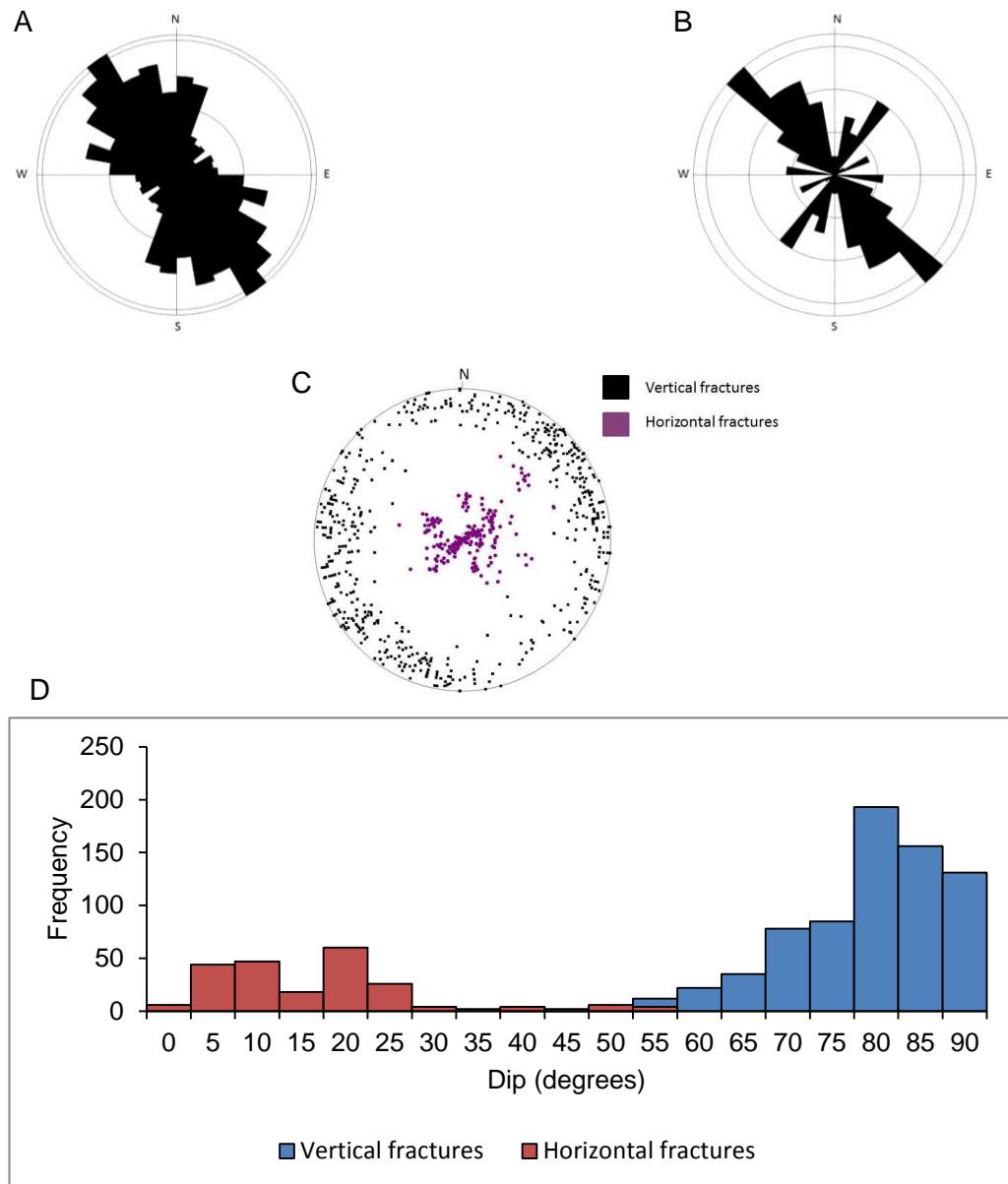


Figure 9.4: (A) Rose diagram of vertical fractures, N = 684. (B) Rose diagram of horizontal fractures, N = 231. Both rose diagrams have a circle interval of 5% and a sector angle of 10°. (C) Stereonet of all fractures, N = 915. (D) Histogram representing dip of both vertical and horizontal fractures.

Descriptive statistics, including arithmetic mean, median, standard deviation and range were calculated along with the coefficient of variation (C_v) describing the

clustering of fractures along each profile. C_v was calculated as standard deviation divided by the arithmetic mean and clustering can be described as follows (Larsen *et al.*, 2010):

$C_v = 1$ = random fracture spacing

$C_v > 1$ = clustered fractures

$C_v < 1$ = even spaced fractures

$C_v = 0$ = perfect even spacing

Oliveira and Brito (1998) quantitatively classify fracture density (average spacing) from high to low as follows:

<5 cm = high fracture density (H)

5-30 cm = dense fracture density (D)

30-100 cm = regular fracture density (R)

100-300 cm = low fracture density (L)

>300 cm = very low fracture density (VL)

Fracture frequency was also presented in histograms, where fractures were counted within a one metre squared area (Chapter 4). These fractures were those visible to the naked eye, and can be described as macro-fractures (studies have shown that the scale of observation has a large effect on fracture frequency calculations, e.g. Ortega *et al.*, 2006). Micro-fractures were those that reached the transect boundaries or fractures that were prominent in outcrop.

9.4.1 Whin Sill

A total of 1191 fracture spacing measurements were made along 18 profiles and were presented in histograms in Figure 9.5, which display a general log-normal distribution. The statistics for each profile line can be seen in Table 9.1. The mean spacing is 0.32 m, the median is 0.25 m, the mode is 0.1-0.2 m, the range is 1.56 m, the variance is 0.09 m, and the standard deviation is 0.30 m. The measures of variability, for example range, variance and standard deviation display a spread in

the data, although only small. C_v is between 0.70 and 1.41, indicating that the fractures are generally clustered, where some of the fracture clusters are more evenly spaced than others (Larsen *et al.*, 2010). Fracture frequency has a range of 1.72-9.09 per metre, with the fracture density, based upon Oliveira and Brito's (1998) classification, being dense to regular fracture density, which is in agreement with the C_v values calculated. Fracture frequency displays a log-normal distribution (Fig. 9.5), where the modal fracture frequency differs between 1D (4 fractures per metre) and 2D (6 fractures per metre), and would be expected to increase if this was carried out in a 3D space. Furthermore, the 2D fracture frequency range up to 52 fractures per metre, significantly larger than 1D fracture frequency that range up to 22 fractures per metre.

9.4.2 Stardalur sill cluster

Fewer fracture spacings were measured for the Stardalur sill cluster than the Whin Sill, at 1073 along a total of 21 profiles. These fracture spacings are graphically displayed in Figure 9.6A and B, which illustrate a log-normal distribution. Statistical analysis is presented in Table 9.2, where the mean is 0.53 m, the median is 0.41 m, the mode is 0.2 m, the range is 2.5 m, the variance is 0.26 m, and the standard deviation is 0.51 m. The variability in data indicates a small spread in the data. However, this spread is larger than that of the Whin Sill. C_v exhibits a range of 0.55-1.55 showing that the fractures are mostly clustered (Larsen *et al.*, 2010), although in comparison to the Whin Sill clustering has a greater distribution. Fracture frequency averages 0.55-6.25 per metre, with a classification of low density (e.g. profile 8) to a more regular pattern and even in some cases dense fracture frequencies (Oliveira and Brito 1998). This again is in agreement with the C_v values and portrays how the Stardalur sill cluster does not have a high clustering of fractures. With respect to the histogram in Figure 9.6, a log-normal distribution is portrayed, illustrating simpler relationships to that of the Whin Sill. 1D fracture frequency has a modal value of 2 fractures per metre, whereas 2D fracture frequency has a mode of 6 fractures per metre (though this peak is not as distinctive as 1D). The range for the 2D fracture frequency is larger at 33 fractures per metre, than the 1D fracture frequency at 17 fractures per metre and can be attributed to the greater area in which the fractures were counted.

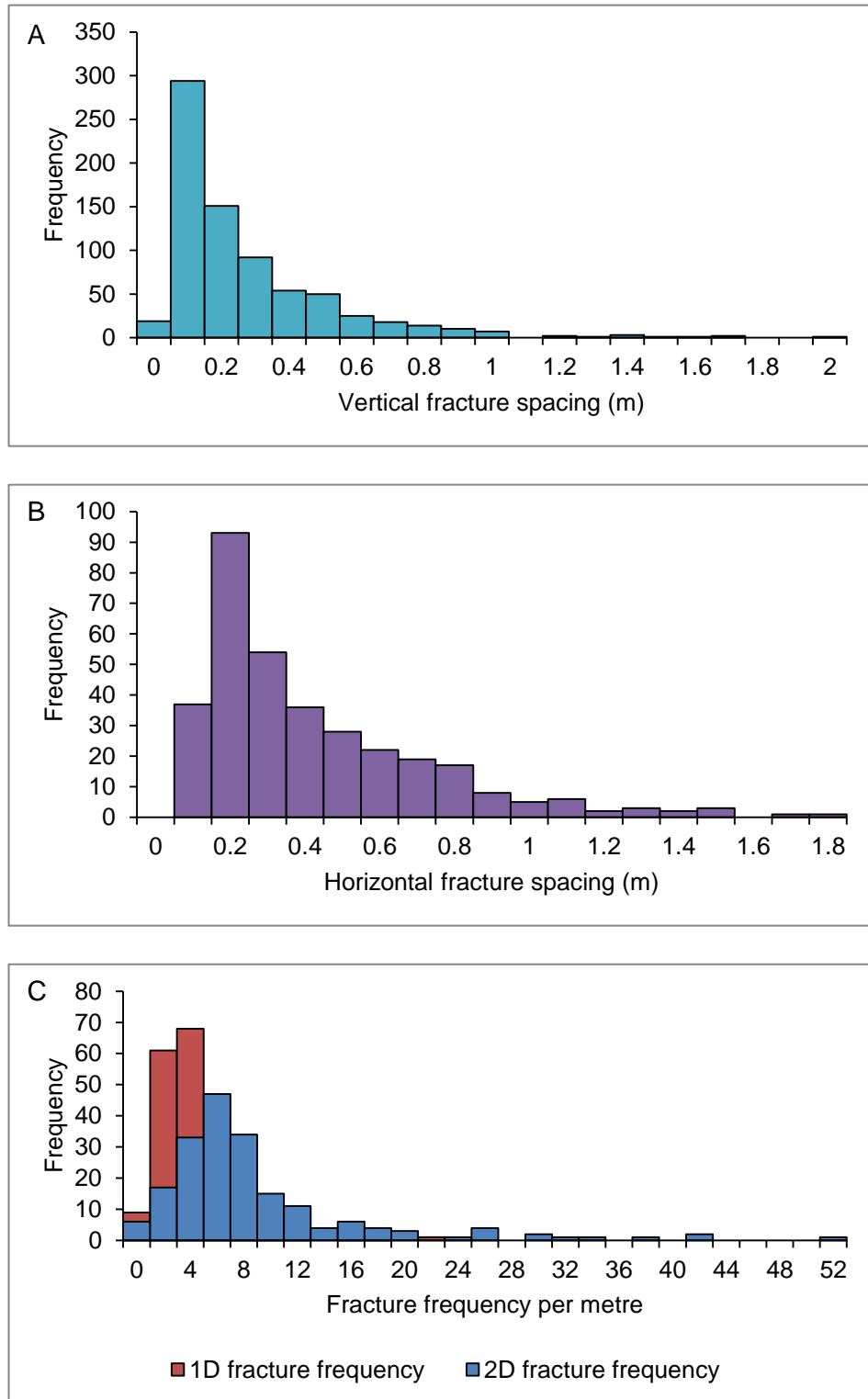


Figure 9.5: (A) Fracture spacing of vertical/sub-vertical fractures and (B) horizontal/sub-horizontal fractures displaying log-normal distribution. (C) Fracture frequency along profiles (1D) and a one metre squared area (2D) showing a log-normal distribution.

Table 9.1: Statistics for all fracture spacings measured along 18 profiles across the Whin Sill.

Profile line	Profile line orientation	N of spacings	Profile line length	Mean spacing	Median spacing	Standard deviation	Spacing range	C _v	Fracture density	Fracture frequency
1	074/04NE	147	18m	0.27m	0.18m	0.28m	1.40m	1.04	D	3.70/m
2	076/12E	65	10m	0.27m	0.20m	0.23m	1.05m	0.83	D	3.70/m
3	057/26E	76	10m	0.19m	0.12m	0.23m	1.51m	1.20	D	5.26/m
4	160/06S	36	5m	0.23m	0.15m	0.32m	1.80m	1.38	D	4.35/m
5	102/02E	159	10m	0.11m	0.08m	0.11m	0.50m	0.98	D	9.09/m
6	260/06E	47	10m	0.22m	0.20m	0.16m	0.69m	0.71	D	4.55/m
7	302/03S	10	2m	0.21m	0.22m	0.15m	0.47m	0.70	D	4.76/m
8	232/10E	28	10m	0.58m	0.46m	0.42m	1.75m	0.73	R	1.72/m
9	048/18W	104	10m	0.19m	0.12m	0.20m	1.02m	1.02	D	5.26/m
10	340/14S	91	15m	0.24m	0.20m	0.20m	0.85m	0.84	D	4.17/m
11	273/12W	70	20m	0.40m	0.31m	0.38m	1.80m	0.94	R	2.50/m
12	172/06N	54	16m	0.42m	0.37m	0.40m	2.10m	0.95	R	2.39/m
13	230/10S	15	8m	0.48m	0.40m	0.34m	1.29m	0.70	R	2.08/m
14	180/04N	37	7m	0.32m	0.23m	0.30m	1.10m	0.94	R	3.13/m
15	185/02N	98	20m	0.31m	0.20m	0.32m	2.00m	1.02	R	3.23/m
16	131/02W	86	11m	0.44m	0.31m	0.62m	5.41m	1.41	R	2.27/m
17	300/12NW	35	10m	0.46m	0.42m	0.37m	1.69m	0.80	R	2.17/m
18	025/40NE	33	12m	0.48m	0.35m	0.45m	1.60m	0.94	R	2.08/m

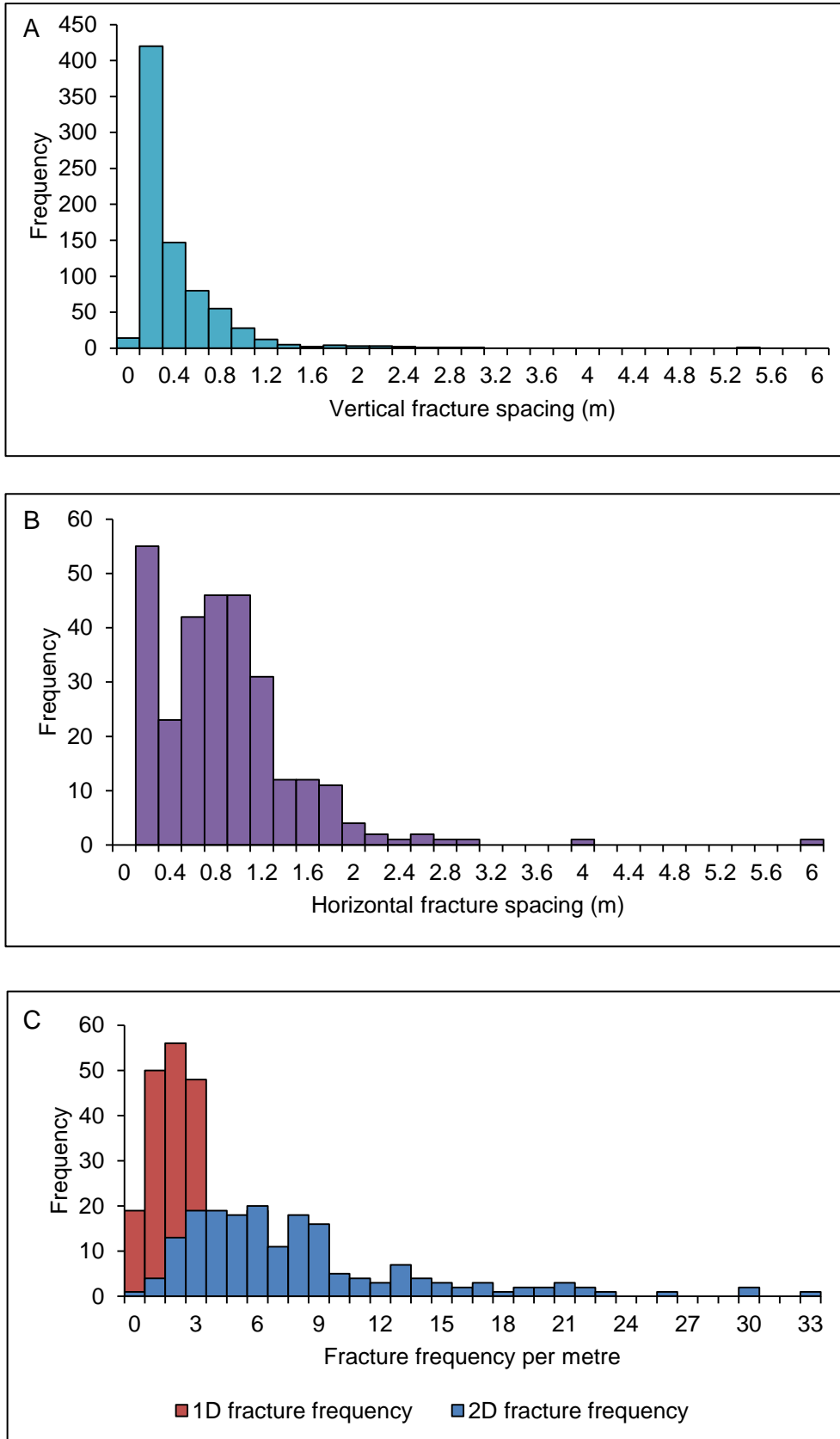


Figure 9.6: (A) Fracture spacing of vertical/sub-vertical fractures and (B) horizontal/sub-horizontal fractures displaying log-normal distribution. (C) Fracture frequency along profiles (1D) and a one metre squared area (2D) showing a log-normal distribution.

Table 9.2: Statistics for all fracture spacings measured along 21 profiles across the Stardalur sill cluster.

Profile line	Profile line orientation	N of spacing	Profile line length	Mean spacing	Median spacing	Standard deviation	Spacing range	C _v	Fracture density	Fracture frequency
1	238/20SW	85	20m	0.62m	0.42m	0.58m	2.84m	0.94	R	1.61/m
2	069/05N	52	20m	0.73m	0.61m	0.93m	5.98m	1.28	R	1.37/m
3	130/04E	25	14m	0.66m	0.44m	0.55m	1.88m	0.83	R	1.52/m
4	150/20E	41	15m	0.88m	0.75m	0.70m	2.98m	0.80	R	1.14/m
5	100/06N	18	12m	0.83m	0.63m	1.17m	5.34m	1.40	R	1.20/m
6	080/30SW	33	17.5m	0.93m	0.80m	0.72m	2.65m	0.77	R	1.08/m
7	092/08SW	19	14m	0.86m	0.60m	0.93m	2.90m	1.07	R	1.16/m
8	085/06SW	33	12m	1.01m	1.00m	0.56m	2.30m	0.55	L	0.99/m
9	062/20SW	46	20m	0.75m	0.71m	0.52m	2.05m	0.69	R	1.33/m
10	070/18SW	40	11m	0.45m	0.31m	0.41m	1.48m	0.92	R	0.55/m
11	050/12W	45	9m	0.41m	0.30m	0.39m	1.65m	0.94	R	2.44/m
12	060/04W	42	10m	0.23m	0.09m	0.30m	1.27m	1.32	D	4.35/m
13	244/08W	61	10m	0.18m	0.09m	0.20m	0.76m	1.07	D	5.56/m
14	065/14W	48	7m	0.16m	0.10m	0.20m	1.09m	1.19	D	6.25/m
15	055/28S	30	9m	0.50m	0.44m	0.37m	1.75m	0.75	R	2.00/m
16	021/20S	112	20m	0.29m	0.14m	0.41m	2.75m	1.44	D	3.45/m
17	160/16N	31	8m	0.36m	0.30m	0.29m	1.00m	0.81	R	2.78/m
18	057/28SW	48	9m	0.37m	0.20m	0.36m	1.14m	0.97	R	2.70/m
19	060/26SW	37	6m	0.51m	0.50m	0.38m	1.72m	0.74	R	1.96/m
20	058/20SW	100	11.5m	0.21m	0.10m	0.30m	1.67m	1.38	D	4.76/m
21	352/10SW	127	11m	0.23m	0.10m	0.36m	2.00m	1.55	D	4.35/m

9.5 Fracture aperture

Fracture aperture is the distance between two parallel walls that define a fracture. Ideally, a fracture would have smooth walls, however in nature this is not the case as they are often irregular. Therefore, fracture aperture is not constant but an average and is referred to in the literature (e.g. Larsen *et al.*, 2010) as kinematic aperture, defined as the width of the fracture including infilling of minerals.

9.5.1 Whin Sill

A total of 1037 fracture apertures were measured, where a minority were infilled with quartz or calcite. The majority of horizontal fracture apertures were closed, but for those that were open, the largest aperture was 40 mm with a modal aperture of 1 mm. On the other hand, the majority of vertical fracture apertures were open, and had a larger range from closed to 115 mm. Although, the modal value for the vertical fracture apertures is the same as for the horizontal fracture apertures at 1 mm (Fig. 9.7). Variability calculations were performed (Table 9.3) to show the spread in data with a mean of 3.03 mm, a standard deviation of 9.25 mm and a variance of 85.56 mm, indicating that the aperture data collected for the Whin Sill has a large variability, with a C_v of 1.6. This large range is illustrated in the histogram and cumulative frequency plot in Figure 9.7. The cumulative frequency plot also provides information with regards to fluid flow within the sill, as does the bi-logarithmic plot illustrating a distinctive power-law (Chapter 8). This power-law has an R^2 value of 0.98, indicating a strong correlation, which portrays the presence of many more small apertures (<10 mm) than larger apertures (>10 mm). However, these larger apertures (tail of the cumulative frequency plot), have most likely been affected by freeze-thaw weathering and erosion, especially those fractures that have apertures between 30 and 40 mm. Therefore, due to the effects of weathering and erosion, the median of 2.98 mm represents best the common aperture size.

9.5.2 Stardalur sill cluster

A total of 909 fracture apertures were measured along the 21 profiles carried out across the Stardalur sills. Some of these apertures were infilled, particularly to the west of the sill cluster. The vertical fractures have a range of 0-70 mm, while the

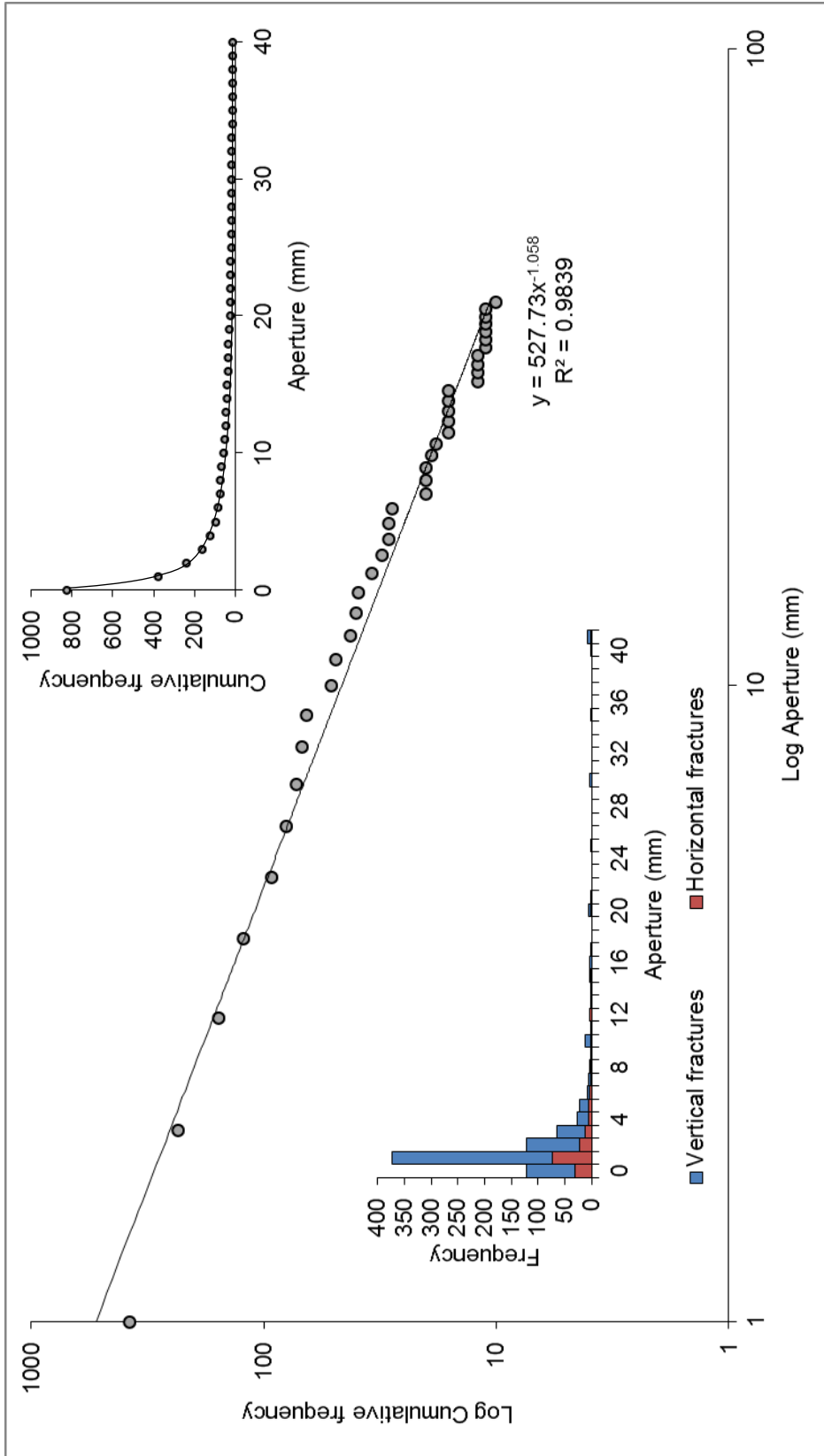


Figure 9.7: Plot of the fracture apertures measured in the Whin Sill, NE England. Bottom left inset illustrates the distribution of both the vertical and horizontal apertures on a histogram. Top right inset shows the cumulative frequency, which has been plotted as a log-log plot to display a clear power-law size distribution of the apertures with a R^2 value of 0.98. The dominant fractures have an aperture < 5 mm on the frequency plot with larger apertures channelling most of the fluid.

Table 9.3: Statistics for all apertures measured along 18 profiles across the Whin Sill.

Profile line	Profile line orientation	N of apertures	Profile line length	Mean aperture	Median aperture	Standard deviation	Aperture range	C _v
1	074/04NE	104	18m	7.26mm	3.00mm	12.55mm	89.85mm	1.73
2	076/12E	41	10m	5.31mm	3.00mm	16.25mm	104.50mm	3.06
3	057/26E	73	10m	1.39mm	1.00mm	1.79mm	10mm	1.28
4	160/06S	27	5m	1.76mm	1.50mm	1.91mm	7.00mm	1.08
5	102/02E	143	10m	0.73mm	0.15mm	1.20mm	8.00mm	1.63
6	260/06E	51	10m	11.00mm	3.00mm	19.13mm	100.00mm	1.74
7	302/03S	12	2m	0.51mm	0.35mm	0.42mm	1.50mm	0.83
8	232/10E	26	10m	2.08mm	1.00mm	3.80mm	20.00mm	1.83
9	048/18W	95	10m	0.88mm	0.15mm	1.28mm	6.00mm	1.45
10	340/14S	90	15m	1.70mm	1.00mm	2.69mm	20.00mm	1.58
11	273/12W	64	20m	0.78mm	0.25mm	1.31mm	8.00mm	1.68
12	172/06N	51	16m	2.01mm	1.00mm	0.94mm	20.00mm	0.47
13	230/10S	15	8m	3.73mm	3.00mm	2.99mm	10.00mm	0.80
14	180/04N	31	7m	2.15mm	1.00mm	3.56mm	17.00mm	1.66
15	185/02N	80	20m	1.01mm	0.18mm	2.93mm	25.00mm	2.90
16	131/02W	70	11m	7.13mm	1.50mm	19.22mm	115.00mm	2.69
17	300/12NW	32	10m	1.18mm	1.00mm	1.33mm	6.00mm	1.13
18	025/40NE	32	12m	2.09mm	1.00mm	2.44mm	10.00mm	1.17

horizontal fractures have a much smaller range of 0-10 mm, where most of them were closed. The modal aperture of all fractures is <1 mm, with a mean of 2.02 mm, a standard deviation of 6.59 mm and a variance of 43.39 mm indicating a large spread in the data, with a C_v value of 2.48 (Fig. 9.8; Table 9.4). In comparison with the Whin Sill the spread and variability of the data is smaller. The median of 0.26 mm better represents the common aperture of the total fractures measured because of the effects of weathering and erosion. The aperture sizes are also plotted on a cumulative frequency plot showing a distinctive power-law that is justified on the bi-logarithmic plot (Fig. 9.8) with a strong correlation, $R^2 = 0.96$. This correlation is very similar to that of the Whin Sill, where the dominant apertures are small but, the larger apertures conduct fluid flow.

9.6 Fluid flow

9.6.1 Permeability and porosity

Permeability and primary porosity have a positive correlation in unconsolidated sedimentary rocks (sediments). However, in consolidated strata this is not true because of diagenesis, which reduces porosity. Most fluid flow in consolidated sedimentary rocks and igneous rocks is through fractures that contribute to secondary porosity. The permeability of a sill depends wholly on fracture networks whose formation depends on the mechanical properties of the sill itself (Brenner and Gudmundsson, 2002). Fluid flow is controlled by fracture systems, here columnar joints and tectonic fractures present in a sill, and are very important for the migration of possible hydrocarbons and other crustal fluids (Fig. 9.9).

Sills can develop both primary and secondary porosity similar to sedimentary rocks. Primary porosity, for example, is where fractures formed during emplacement and cooling, whereas secondary porosity, for example, is where fractures formed post cooling. These fractures allow for the entrapment of hydrocarbons, an important igneous trap. Sills most likely will undergo weathering, affecting the overall porosity because cavities may form as a result of weathering effects, and could be filled by water and other diagenetic materials owing to burial. As most of these infills are water soluble, they are removed easily by late stage fluids causing an enlargement of the cavities forming reservoir spaces (Cukur *et al.*, 2010).

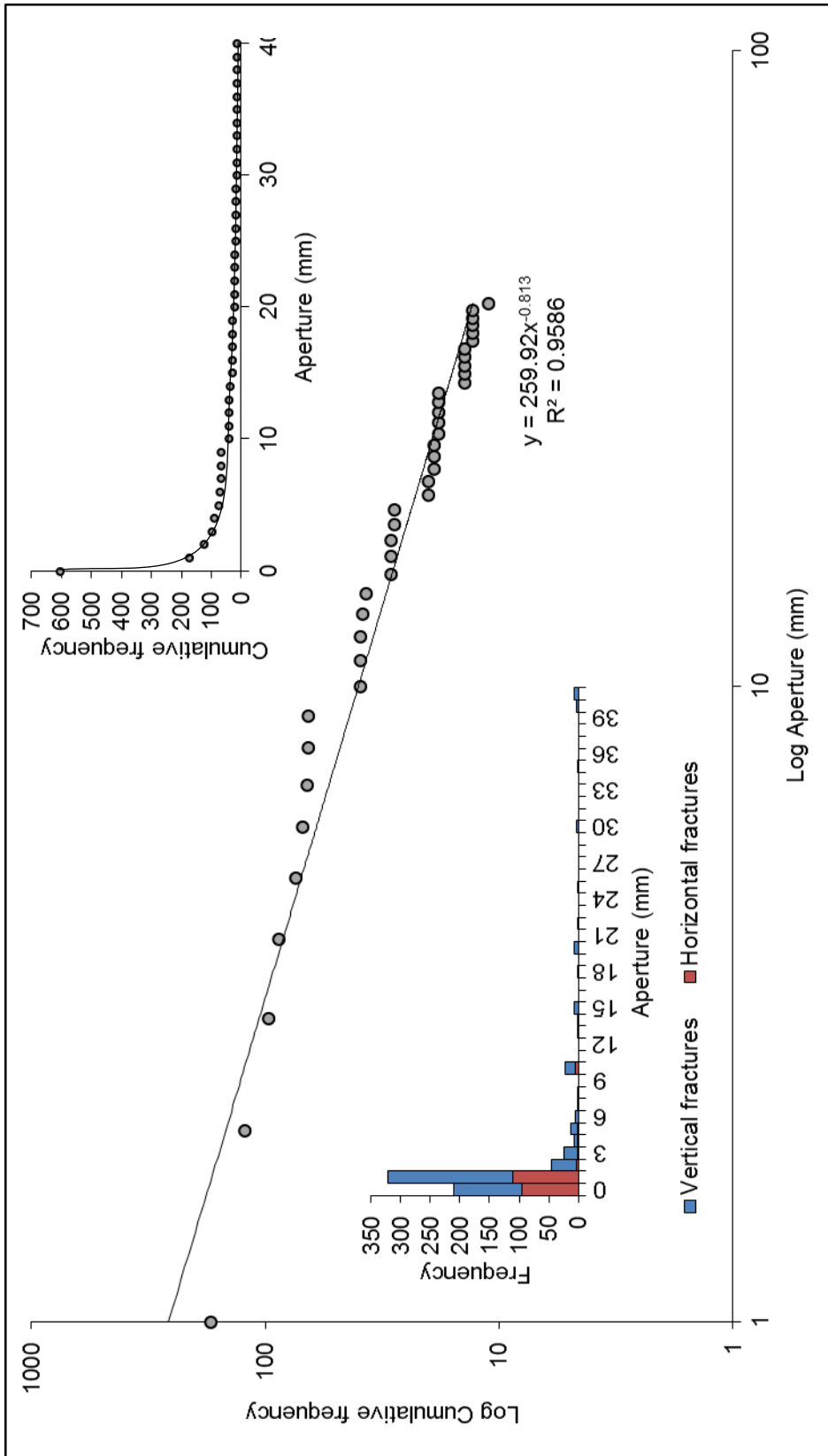


Figure 9.8: Plot of the fracture apertures measured in the Stardalur sill cluster, SW Iceland. Bottom left inset illustrates the distribution of both the vertical and horizontal apertures on a histogram. Top right inset shows the cumulative frequency, which has been plotted as a log-log plot to display a clear power-law size distribution of the apertures with a R^2 value of 0.96. The dominant fractures have a relatively small aperture <3 mm on the frequency plot with the larger apertures channelling most of the fluid.

Table 9.4: Statistics for all apertures measured along 21 profiles of the Stardalur sill cluster.

Profile line	Profile line orientation	N of apertures	Profile line length	Mean aperture	Median aperture	Standard deviation	Aperture range	C_v
1	238/20SW	69	20m	7.55mm	0.90mm	14.91mm	60mm	1.98
2	069/05N	40	20m	1.65mm	0.25mm	3.45mm	20mm	2.09
3	130/04E	27	14m	4.44mm	0.50mm	8.02mm	40mm	1.81
4	150/20E	26	15m	1.29mm	1.00mm	2.15mm	10mm	1.66
5	100/06N	20	12m	3.50mm	0.08mm	6.45mm	25mm	1.85
6	080/30SW	25	17.5m	2.80mm	0.20mm	4.50mm	15mm	1.61
7	092/08SW	23	14m	5.31mm	0.50mm	9.56mm	35mm	1.80
8	085/06SW	24	12m	4.43mm	0.28mm	9.29mm	40mm	2.10
9	062/20SW	32	20m	2.50mm	0.30mm	9.10mm	50mm	3.64
10	070/18SW	40	11m	1.71mm	0.50mm	3.94mm	20mm	2.30
11	050/12W	41	9m	0.50mm	0.01mm	1.58mm	10mm	3.20
12	060/04W	47	10m	0.28mm	0.01mm	0.87mm	5mm	3.14
13	244/08W	50	10m	1.94mm	0.15mm	9.88mm	70mm	5.09
14	065/14W	39	7m	1.81mm	0.50mm	3.51mm	15mm	1.94
15	055/28S	31	9m	1.32mm	0.05mm	2.04mm	10mm	1.80
16	021/20S	88	20m	0.44mm	0.08mm	0.73mm	3mm	1.68
17	160/16N	34	8m	2.42mm	0.01mm	6.36mm	30mm	2.63
18	057/28SW	48	9m	1.19mm	0.03mm	3.21mm	20mm	2.69
19	060/26SW	36	6m	2.40mm	0.03mm	7.61mm	40mm	3.17
20	058/20SW	82	11.5m	0.68mm	0.01mm	2.36mm	15mm	3.47
21	352/10SW	87	11m	0.22mm	0.01mm	0.55mm	4mm	2.50

The fracture permeability within a sill depends on the geometry of the fracture, whether the fracture is open or closed (Fig. 9.10), and if the fracture is closed, is it because of infilling of minerals. If the fracture is open the porosity will not be significantly altered, however the permeability will be significantly changed. This is because of the cubic law, where volumetric flow rate is proportional to the cube of the aperture of the fracture (Gudmundsson, 2011a). Therefore, any small changes in the fracture aperture will have a significant effect on the volumetric flow rate. Open fractures seen in the field can often be associated with the transport of groundwater, which can be seen on a variety of scales, from water falls to red oxidation staining where there is a trickle of water over a given period of time. Closed fractures, and fractures infilled by secondary minerals such as gypsum, calcite or quartz, are barriers to fluid flow.

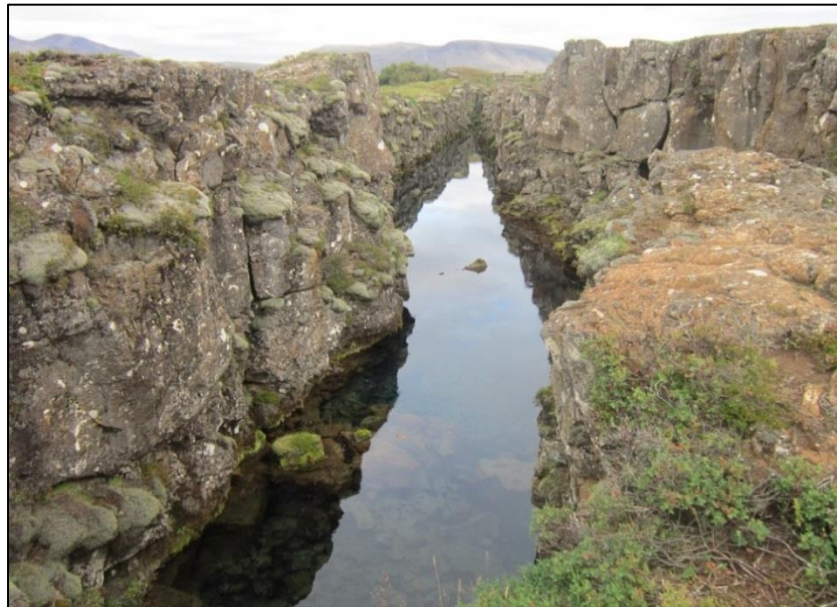


Figure 9.9: Tension fracture in Þingvellir, SW Iceland. Here, groundwater is able to flow along the fracture through the lava whose walls are fairly smooth although irregular. View NE, aperture is approximately 4 m.

Permeability structure differs between sedimentary strata and sills due to the difference in fracture networks. In sedimentary rocks, the main fracture surface or discontinuity is the bedding planes that tend to be horizontal with vertical joints that connect these surfaces. Therefore, the permeability can be described as anisotropic (Fig. 9.11) where permeability dominates along the vertical joints. In contrast, the fracture networks within sills tend not to be structured or ordered, and instead form

fracture clustering (Fig. 9.12). Permeability will vary because of the presence of clustering, where dense clustering results in a high permeability and sparse clustering and evenly spaced fractures results in a low permeability (Gudmundsson, 2011a).

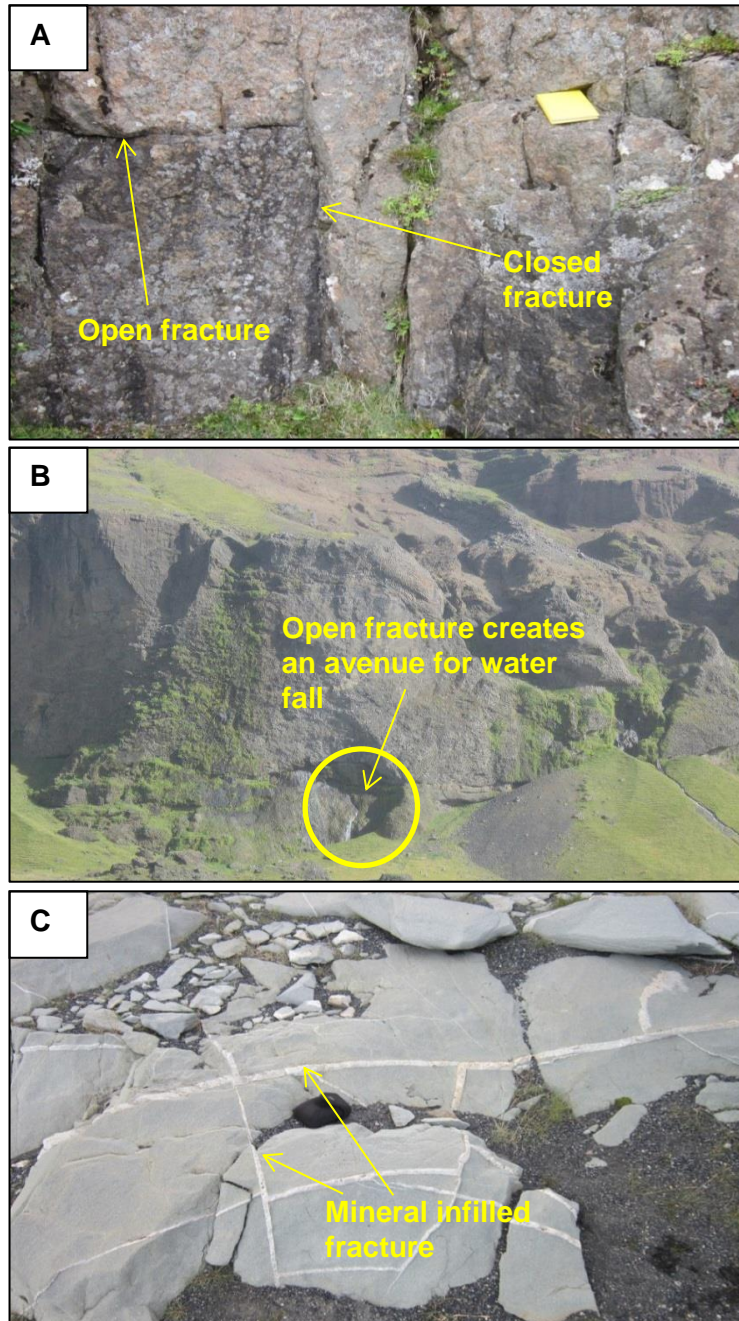


Figure 9.10: A) Stardalur sill, SW Iceland, open fractures, <1 cm, and closed fractures, with yellow notebook for scale. B) Open fracture in ~50 m sill, S Iceland, transporting water to create a small water fall. C) Mineral vein net complex, S Iceland, closed fractures infilled by quartz, with camera case for scale.

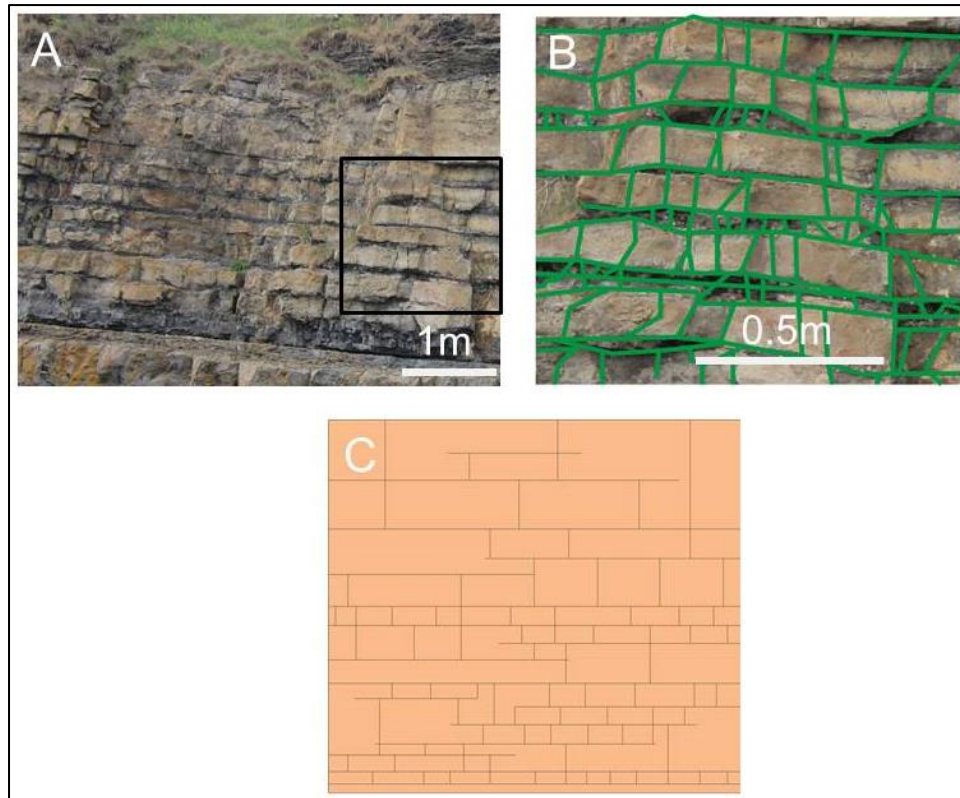


Figure 9.11: (A) Photograph of interbedded sandstones and shales, Cullernose Point, NE England, view W. (B) Typical sedimentary sequence where vertical fractures link up between the horizontal layering highlighted in green (based on black outlined area in (A)). (C) This is then schematically illustrated to show the fracture related permeability in a sedimentary rock.

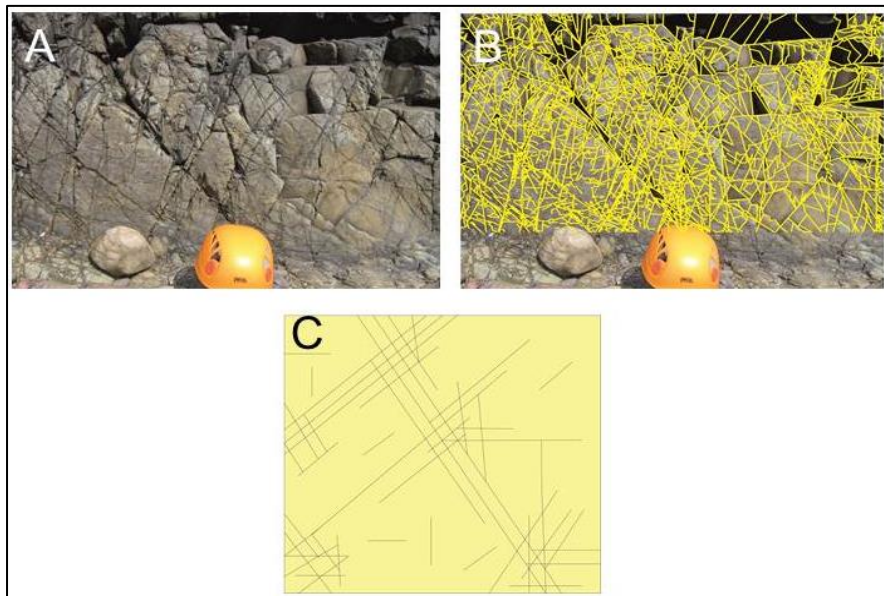


Figure 9.12: (A) Photograph of fracture clustering in the Whin Sill at Castle Hill, Holy Island, NE England, view N. (B) Fracture trace in yellow to highlight the clustering of the fractures due to the various orientations. (C) These fracture maps can be then schematically illustrated to show the clustering of fractures and the fracture related permeability in a sill.

9.6.2 Fracture interconnectivity in fractured reservoirs

It is well known about fluid flow through pores, described by Darcy's law, yet fluid flow can occur through fractures too (Fig. 9.13), or both pores and fractures. Fluid flow within fractures depends on their orientation, but more importantly the aperture or opening of each fracture. The variations in these apertures, whether closed or open, determine the fluid flow. Flow is dominant along large fractures, which are few (power-law distribution; Figs. 9.7 and 9.8) and in some systems may be less than 10% (Gudmundsson, 2011a).

To model fluid flow within a fractured body, the Navier-stokes equation can be used, which assumes that flow is laminar, that is, the particles within the fluid, for example oil or water, are transported in a straight trajectory parallel to the fracture walls. This is expressed by the cubic law as follows:

$$Q = \frac{\rho_f g W b^3}{12 \mu_f} \quad (9.3)$$

where Q is the volumetric flow rate, ρ_f is the density of the fluid, g is acceleration due to gravity, W is the width of the fracture perpendicular to fluid flow, b is the aperture of the fracture and μ_f is the viscosity of the fluid (Gudmundsson, 2011a).

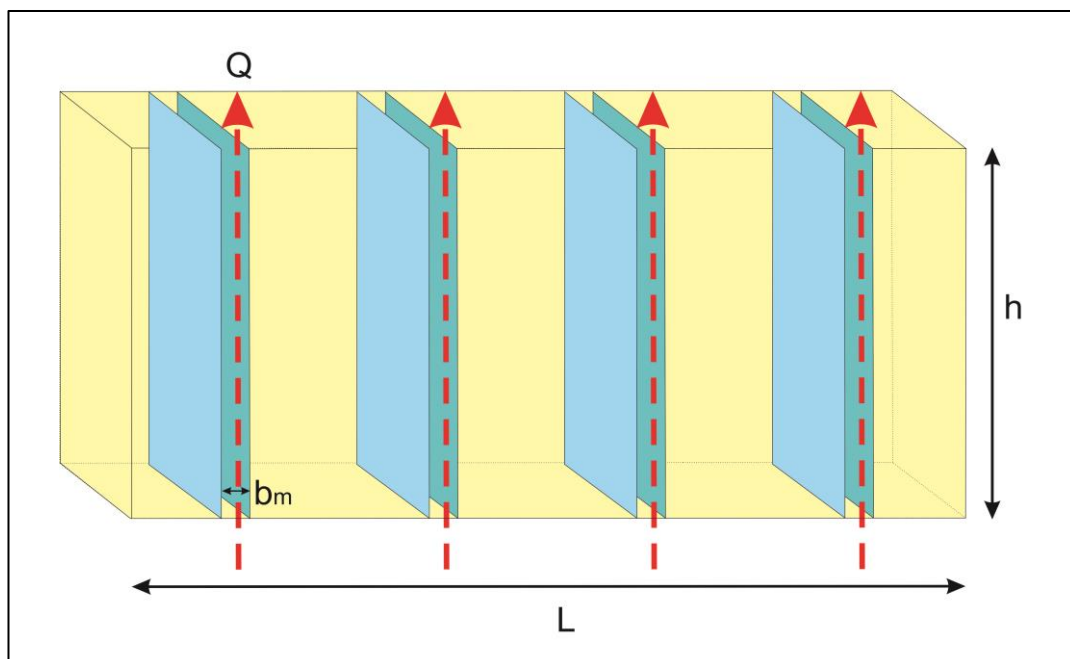


Figure 9.13: Laminar flow between two vertical fractures, with a profile line, L , and height of fractures, h , each fracture having an aperture of b_m (modified from Gudmundsson, 2011a).

First modelled is a set of orthogonal fractures with water flowing through the fractures. The boundary conditions of the walls were set to no slip in a stationary framework, with a pressure gradient of 6 Pa either in a vertical or horizontal direction (detailed method described in Chapter 4). Two sets of models were carried out: (1) equal aperture fractures and (2) unequal aperture fractures. These models are measured in unit length and are simply idealistic models that are not realistic of fracture systems in sills, but may be plausible in a sedimentary sequence. The mesh has a maximum element size of 0.2 unit length and a minimum element size of 0.001 unit length. These models were computed twice, first to show fluid flow velocity from bottom to top (vertical flow) and second to show fluid flow velocity from left to right (horizontal flow).

Figure 9.14 shows that irrespective of the pressure gradient, the velocity of the flow is constant along the pressure gradient. The velocity of the flow perpendicular to the pressure gradient is ~ 0.06 m/s, but where there is an intersection or T-junction the particles speed up perpendicular to the pressure gradient and slow down parallel to the pressure gradient. The velocity of the particles also slow down along the fracture walls due to friction and resistance to flow, therefore the highest velocity of the flow is in the centre of the fractures. In Figure 9.15 the most prominent change in the velocity is related to the aperture of the fracture; the larger the aperture the greater the flow velocity because this is the path of least resistance. As a result of this aperture variation the velocity of the flow varies throughout the fracture network.

Next, 2D maps of fracture traces were generated, both vertical and horizontal fractures (Figs. 9.16-9.20). The fractures found in outcrop are mainly tension fractures, that is, they had no shear displacement, with the majority of fractures being terminated against other favourably oriented fractures to form a fracture network. Fractures within sills may be considered as stratabound as they are restricted to the intrusion itself and therefore, the range in fracture length is limited. The two sites chosen for numerical modelling are Castle Point, Dunstanburgh (grid reference: NU25569 22036) for the Whin Sill and profile 1 (grid reference: 64.21334°N 021.52490°W) for the Stardalur sill cluster. Fluid flow modelling is only in the vertical direction because the columnar joints are dominant and these form the main fluid pathways. The mesh quality varies between the two sites due to the variation in apertures. The Whin Sill has a maximum element size of 0.05 m and a minimum

element size of 0.001 m, whereas the Stardalur sill cluster has a maximum element size of 0.2 m and a minimum element size of 7×10^{-4} m. Modelling is also compared between water and crude oil.

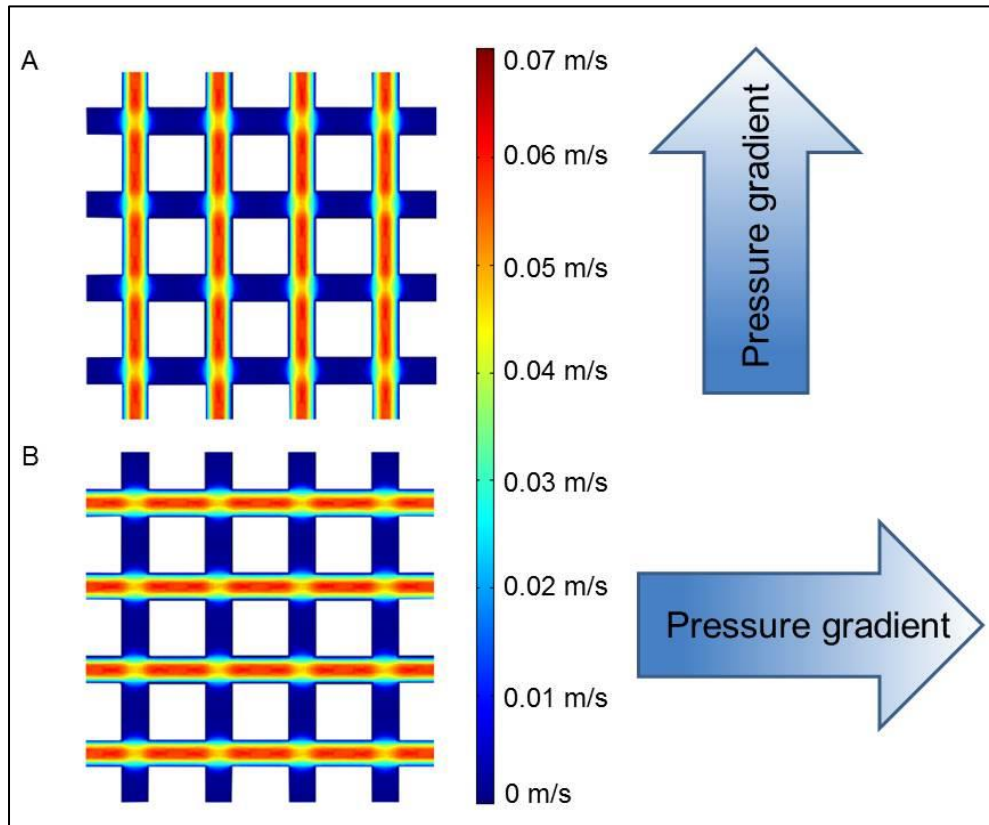


Figure 9.14: Fluid flow velocity through an orthogonal fracture system that have equal apertures. (A) Inlet of fluid (water) from the bottom of the fracture set to the outlet at the top following the pressure gradient. (B) Inlet of fluid from the left to the outlet on the right following the pressure gradient. The scale of these fracture networks is in unit length, thus, purely idealistic to investigate fluid flow in an orthogonal fracture system with equal fracture apertures.

On first inspection of the fracture maps (Figs. 9.21-9.28) it is seen that the vertical fractures are dominant, but the interconnectivity and fracture apertures between the two sites vary considerably. These fracture maps only take into account fractures that are open, that is to say there is displacement between the two fracture walls. Overall, the Whin Sill has a mean aperture of 2.93 mm, whereas the Stardalur sill cluster has a mean aperture, slightly larger, at 2.30 mm. However, at the two specific sites chosen for fluid flow modelling, the Stardalur sill apertures are considerably larger than that of the Whin Sill. This can be attributed to weathering and the effects of

deglaciation on the Stardalur sill cluster in comparison to the coastal section of the Whin Sill. This variation in fracture apertures is reflected in the fluid flow models (Figs. 9.21-9.28).

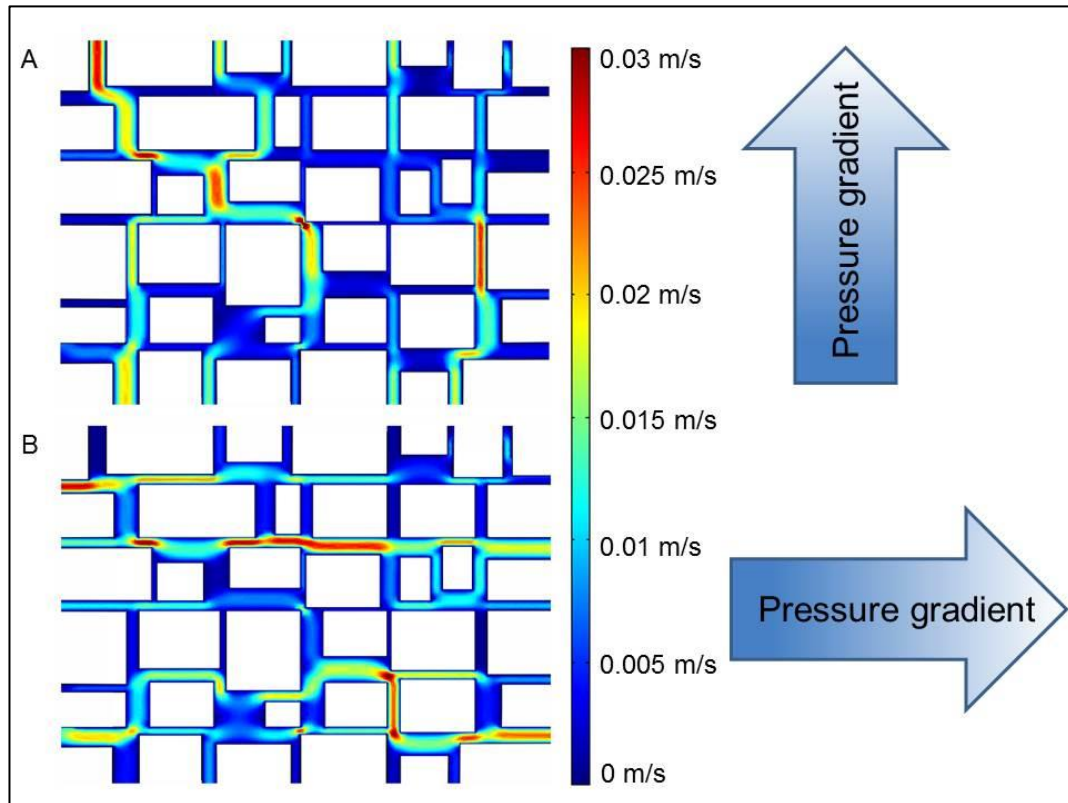


Figure 9.15: Fluid flow velocity through an orthogonal fracture system that have unequal apertures. (A) Inlet of fluid (water) from the bottom of the fracture set to the outlet at the top following the pressure gradient. (B) Inlet of fluid from the left to the outlet on the right following the pressure gradient. The scale of this model is in unit length and is an idealistic model to investigate fluid flow through an orthogonal fracture system with unequal apertures.

Numerical models in a stationary framework show that the permeability of the Whin Sill (Figs. 9.21 and 9.23) and the Stardalur sill cluster (Figs. 9.25 and 9.27) is higher parallel to the cooling surface rather than perpendicular to it. The dominant path of fluid flow is mostly via vertical and sub-vertical fractures, although the horizontal and sub-horizontal fractures form bridges between the vertical fractures, allowing some flow to be conducted. Fluid flow is also enhanced by the pressure gradient from the inlet (6 Pa) to the outlet (0 Pa), and if the fractures are not orientated favourably to this gradient, then flow is conducted along fractures with the greater aperture.

Figure 9.22 shows particle tracing of water particles at Castle Point, NE England. There is a minimal variation in fracture aperture in this section of fracture map. The fracture network is predominantly filled with water, although, those fractures that are not favourably orientated towards fluid flow remain empty. In general, the fractures that are almost vertical, contain water particles with the fastest velocity of ~ 0.06 m/s, whereas fractures that are at a low to horizontal angle yield particles with a near minimum particle velocity of $< 1 \times 10^{-4}$ m/s. In total, it takes 3.5 days for the fracture network to be filled with water. As the aperture variation is negligible here, the results cannot be explained in terms of fluid flow channelling, but rather by fracture orientation favourable to fluid flow. Figure 9.24 shows particle tracing of oil particles at Castle Point. The same pattern is seen in fluid migration paths but, the time (92.6 days to fill fracture network) it takes for the fluid to migrate is much slower, approximately three months more, compared to water. This is because the dynamic viscosity of crude oil is greater than water. Therefore, the force required to overcome the internal friction of crude oil is greater than that of water, and is shown by the slower particle velocity of $< 1 \times 10^{-5}$ m/s.

Figure 9.25 shows the particle tracing of water at Stardalur profile 1, SW Iceland. The water first fills the largest and sub-vertical fractures, at a speed of 0.04 m/s. However, along narrower sub-vertical and also sub-horizontal fractures the speed of the particles is much slower, less than 0.01 m/s. This is reflected in the time (Fig. 9.26) in which the water is transported along the fracture network. The larger fractures are filled within the first six time frames at 1 hour and it takes approximately 8 hours for the entire fracture network to be filled. As the Stardalur fracture network has larger fracture apertures than those at Castle Point, the particles along the fracture walls can be seen. Along the fracture walls there is no fluid flow, that is, the velocity is zero (Fig. 2.5A). The time-dependent models (Fig. 9.26) demonstrate fluid pathways and that not all fractures are favourably orientated towards fluid flow. Unlike the fracture network at Castle Point, flow channelling is effectively demonstrated along the Stardalur fracture network, both by the time it takes for fluid to fill the various apertures, but also by the speed of the particles. With regards to crude oil (Fig. 9.28), similar results are displayed with respect to fracture orientation and aperture controlling the fluid flow path. The major difference is the time it takes for the crude oil to fill the fracture network. For oil to fill the

fracture network it takes approximately three times longer because despite the migration path of the oil being exactly the same as that of water, the velocity of oil particles is slower, with a maximum velocity of only 0.01 m/s.

Fracture apertures can ideally be described as being elliptical or penny-shaped, but in reality they are irregular. In general, Figure 9.29 shows abrupt changes in aperture width within a short distance (<20 m). Figure 9.29A shows that the maximum aperture is 60 mm for the fractures along Profile 1, Stardalur sill cluster. In comparison with the Whin Sill (Figs. 9.29B and C), the apertures are much smaller, measuring less than 8 mm at both sites. Thus, variation in fracture apertures (Fig. 9.21-9.29) is important to understand, especially with respect to fluid flow.

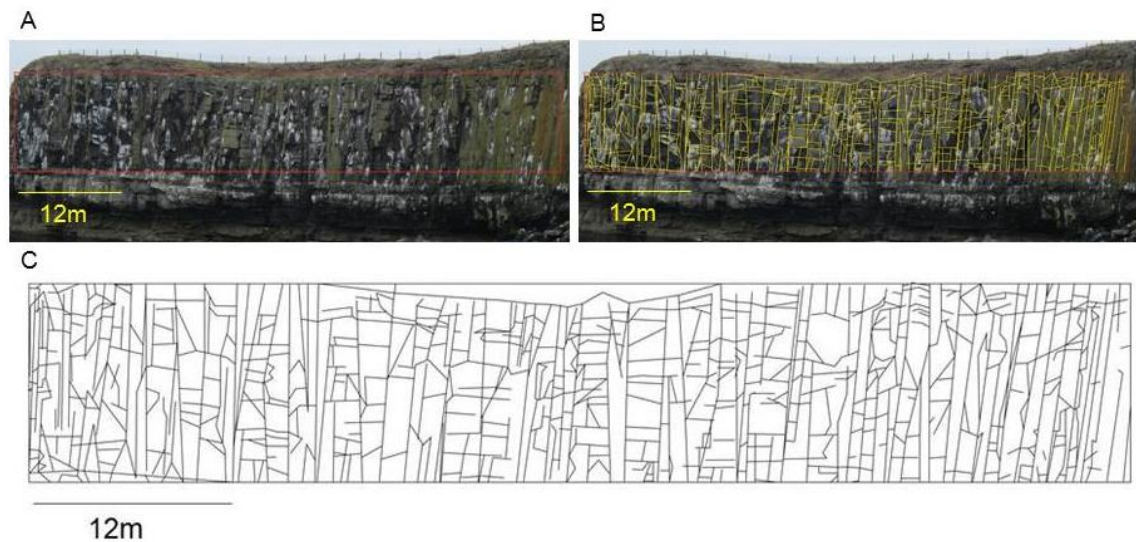


Figure 9.16: Fracture map of Castle Point, near Dunstanburgh, Northumberland coast, NE England, view E. (A) Fracture map location within red box, (B) fracture map overlain onto photograph, and (C) fracture map as shown in (B). Large scale of 12 m illustrates the dominance of the vertical fractures in the Whin Sill.

9.7 Discussion

9.7.1 Permeability and porosity: implications for reservoir quality

The number of fractures per unit length (fracture frequency) along a profile line is an important attribute to fracture networks. This is because the fracture frequency may

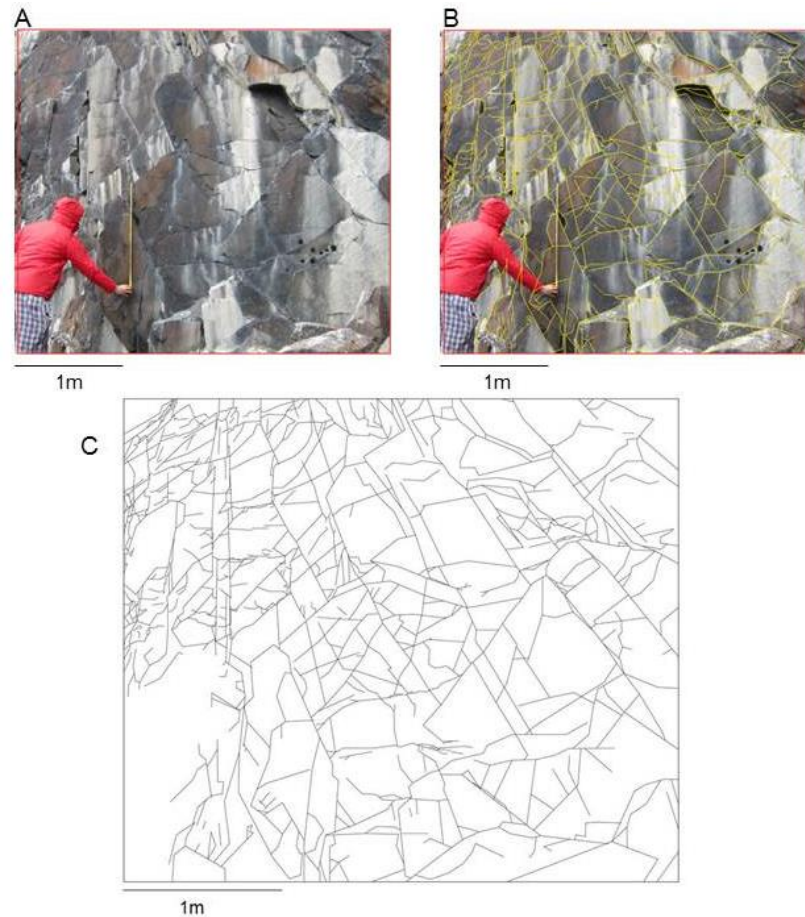


Figure 9.17: Fracture map of Cullernose Point, near Dunstanburgh, Northumberland coast, NE England, view N. (A) Fracture map location within red box, (B) fracture map overlain onto photograph, and (C) fracture map as shown in (B). Scale of 1 m illustrates the common clustering of fractures in the Whin Sill.

be a limiting factor for hydrocarbon exploration, as the frequency describes the abundance of tension fractures that are productive towards fluid flow. Thus, the overall probability of meeting such fractures when exploiting the fractures via boreholes and wells is variable.

The permeability of a fractured reservoir within a sill depends on fracture system connectivity (fracture orientation, spacing and offset), the stress field (controls fracture orientation and propagation) and the overpressure of the fluid (controls fracture aperture) (Gudmundsson, 2000b). The specific form of a fracture network also depends on the host rock. Within an igneous sill, the networks are columnar joints, which form perpendicular to the cooling surface. The majority of the joints

that form are therefore vertical and sub-vertical, with a minority of horizontal and sub-horizontal joints. As these two sets of joints become interconnected the

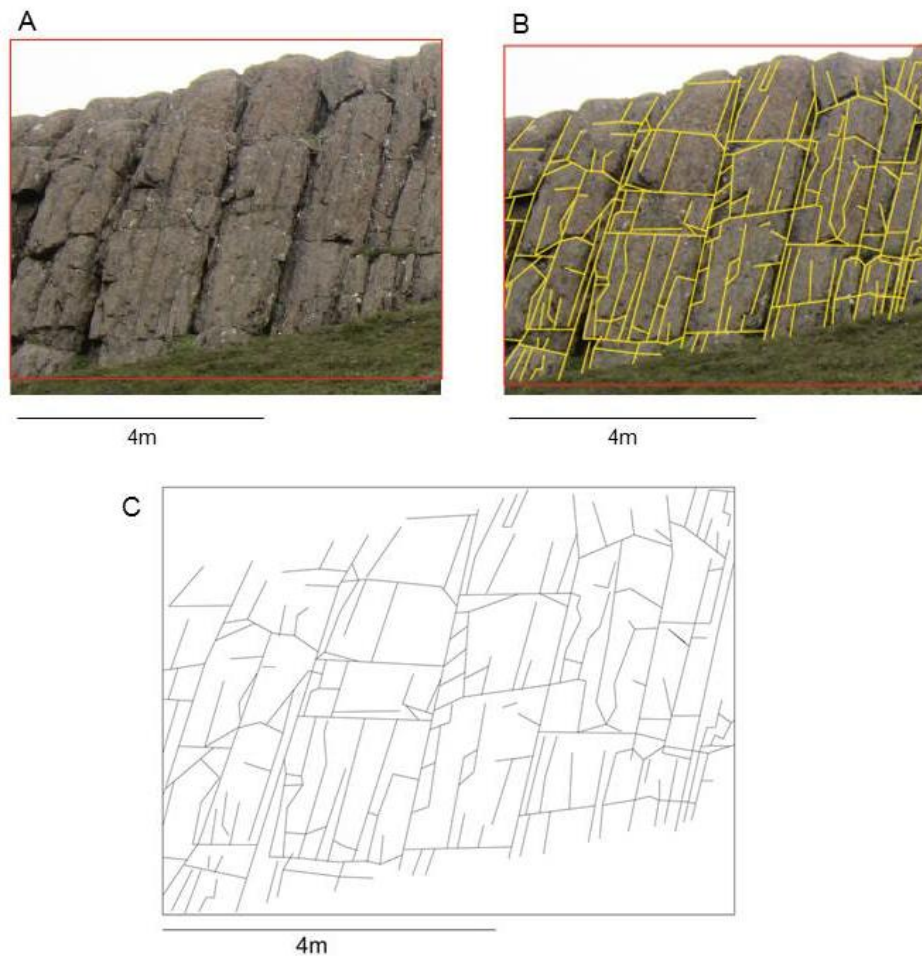


Figure 9.18: Fracture map of Profile 1, Stardalur, SW Iceland, view NW. Scale of 4 m illustrates the very high fracture frequency of vertical fractures in the Stardalur sill cluster. (A) Fracture map location within red box, (B) fracture map overlain onto photograph, and (C) fracture map as shown in (B). This map is representative for the fracture frequency of the Stardalur sill cluster overall.

permeability of the sill increases, even though the porosity remains very poor in a dense igneous rock. Igneous rocks generally have low-to-intermediate porosities <30% and permeabilities $<10 \times 10^{-3} \mu\text{m}^2$ (Huang *et al.*, 2009).

From the aperture data collected, permeabilities and porosities can be calculated for both the Whin Sill and the Stardalur sill cluster. Hydraulic conductivity, K_f , is the coefficient of permeability relating to Darcy's law and is primarily used for water and, hence for describing permeability in hydrogeology. Hydraulic conductivity has

the units of m/s, where flow is transported down a pressure gradient, that is, the outlet has a lower pressure than the inlet, and is as follows:

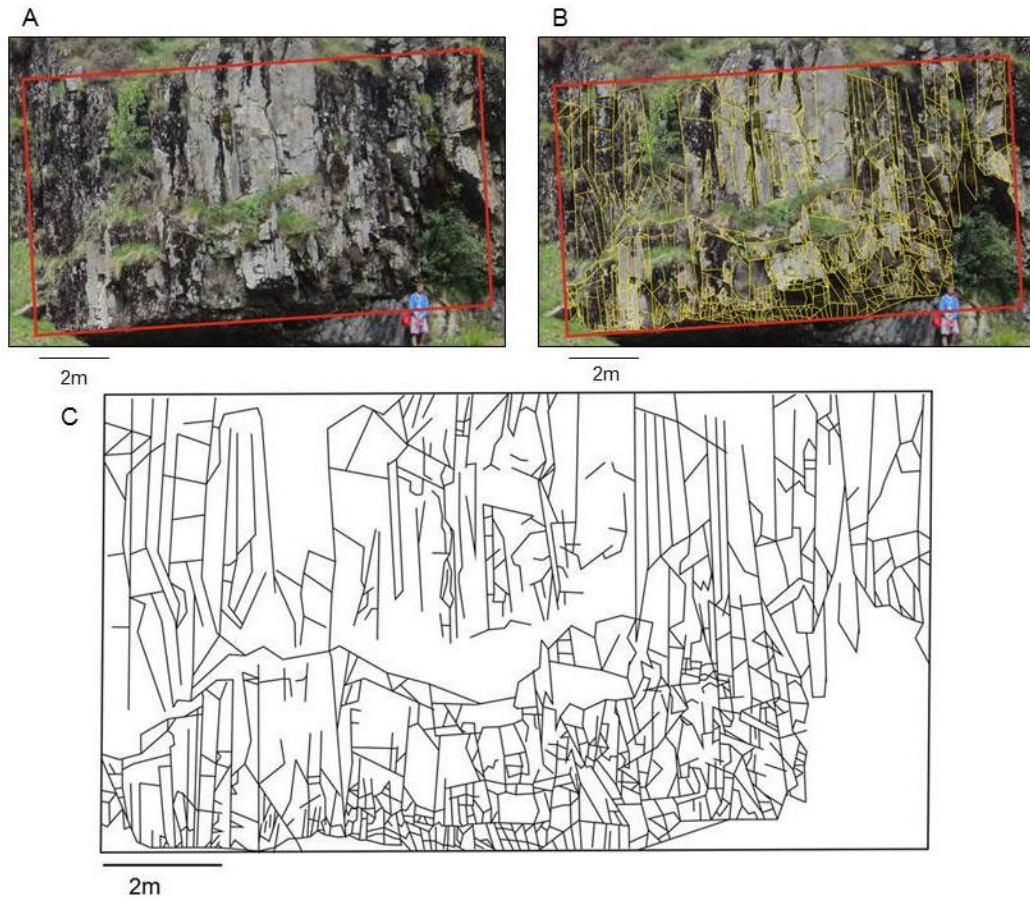


Figure 9.19: Fracture map of Falcon Clints, Co. Durham, NE England, view NE. (A) Fracture map location within red box, (B) fracture map overlain onto photograph, and (C) fracture map as shown in (B). Scale of 2 m shows the high fracture density at the margins (base) of the Whin Sill.

$$K_f = \frac{\rho_f g}{12\mu_f L} \left(\sum_{i=1}^m b_i^3 \right) \quad (9.4)$$

where ρ_f is the density of the fluid, g is acceleration due to gravity, μ_f is the dynamic viscosity of the fluid (water: 1.55×10^{-3} Pa s, crude oil: 0.05 Pa s), L is the profile length, m is the number of fractures that are parallel to each other, and b is the fracture aperture (Gudmundsson, 2011a). Intrinsic permeability, k_f , is used to describe the permeability in relation to any type of fluid, with units of m^2 : it is the common permeability measure in petroleum reservoir studies (Gudmundsson, 2011a):

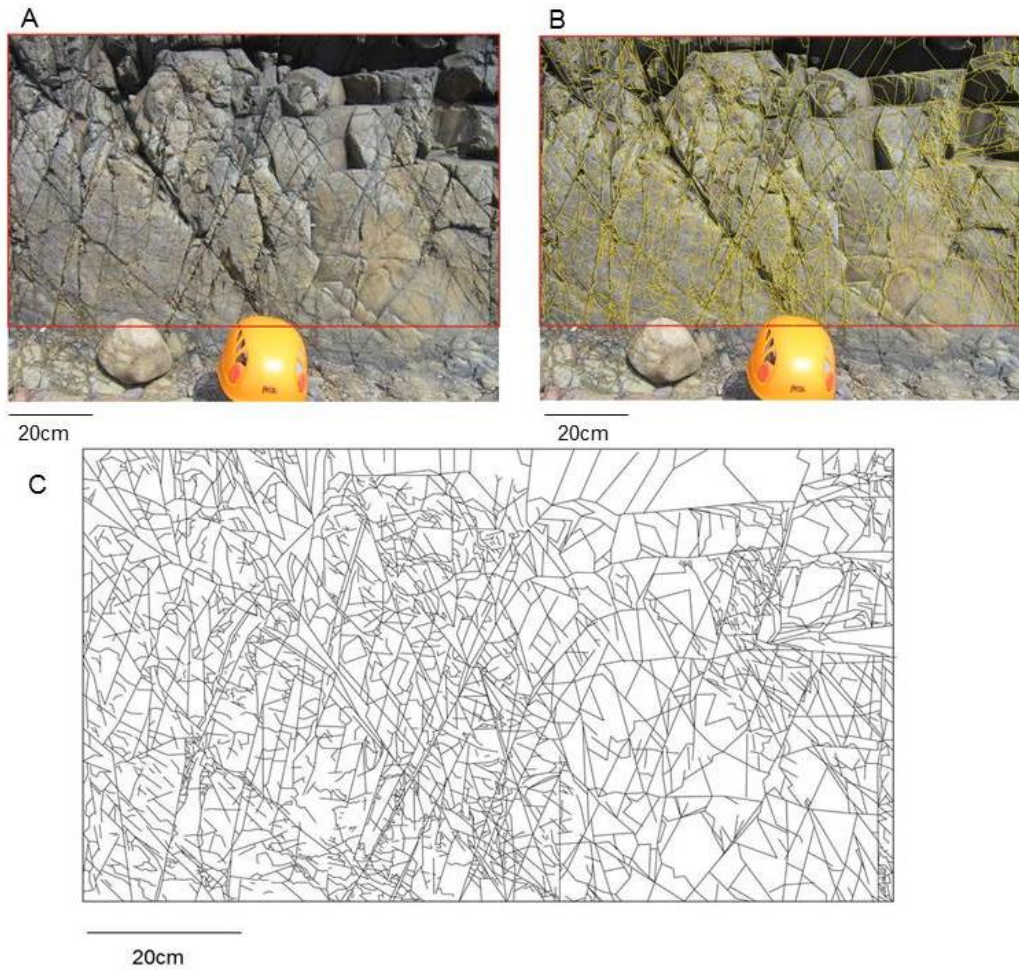


Figure 9.20: Fracture map of Castle Hill, Holy Island, Northumberland, NE England, view N. (A) Fracture map location within red box, (B) fracture map overlain onto photograph, and (C) fracture map as shown in (B). Scale of 20 cm illustrates the very high fracture frequency in the Whin Sill.

$$K_f = \frac{k_f \rho_f g}{\mu_f} \quad (9.5)$$

The permeability describes the ability of a fluid to flow with relative ease within the fractures, hence the fracture interconnectivity. Porosity, ϕ_f , on the other hand describes the space available within the sill that can yield hydrocarbons. This is given as a percentage and is defined as (Gudmundsson, 2011a):

$$\phi_f = \left(\sum_{i=1}^m b_i \right) L^{-1} \quad (9.6)$$

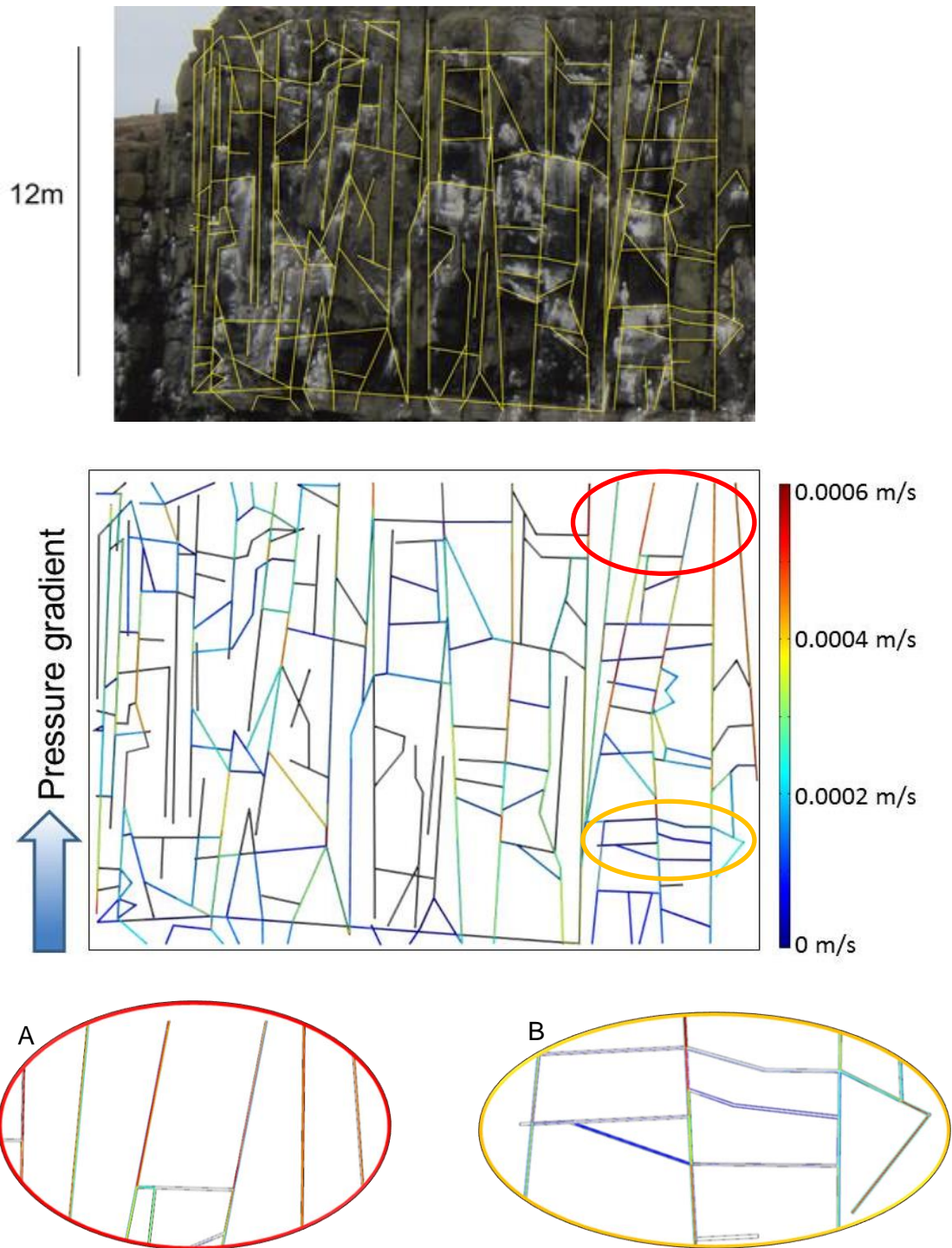
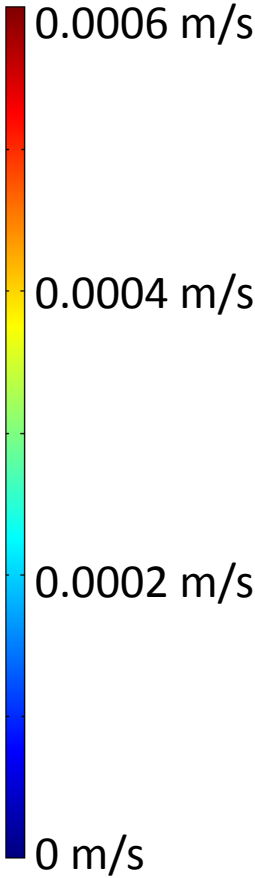
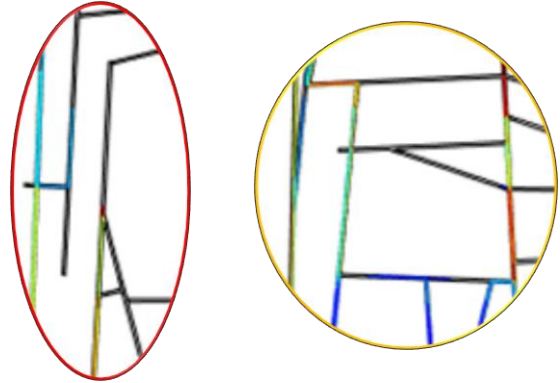
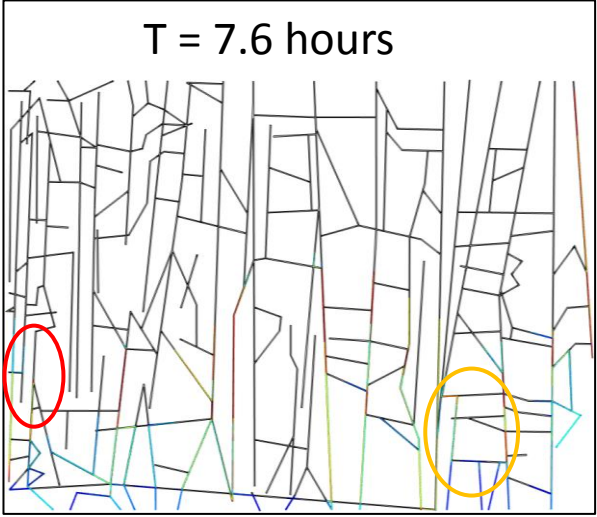
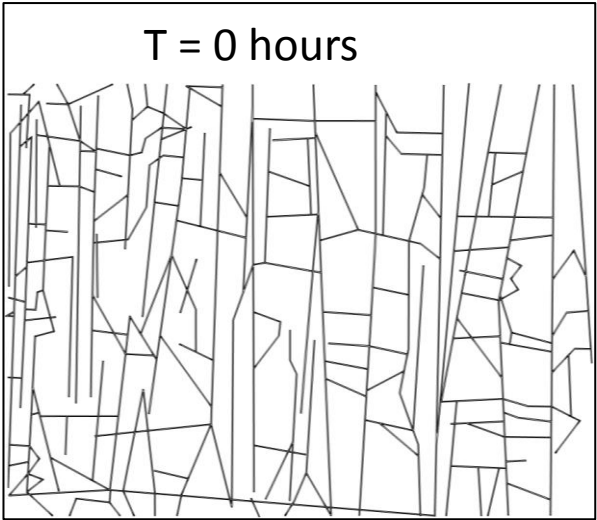
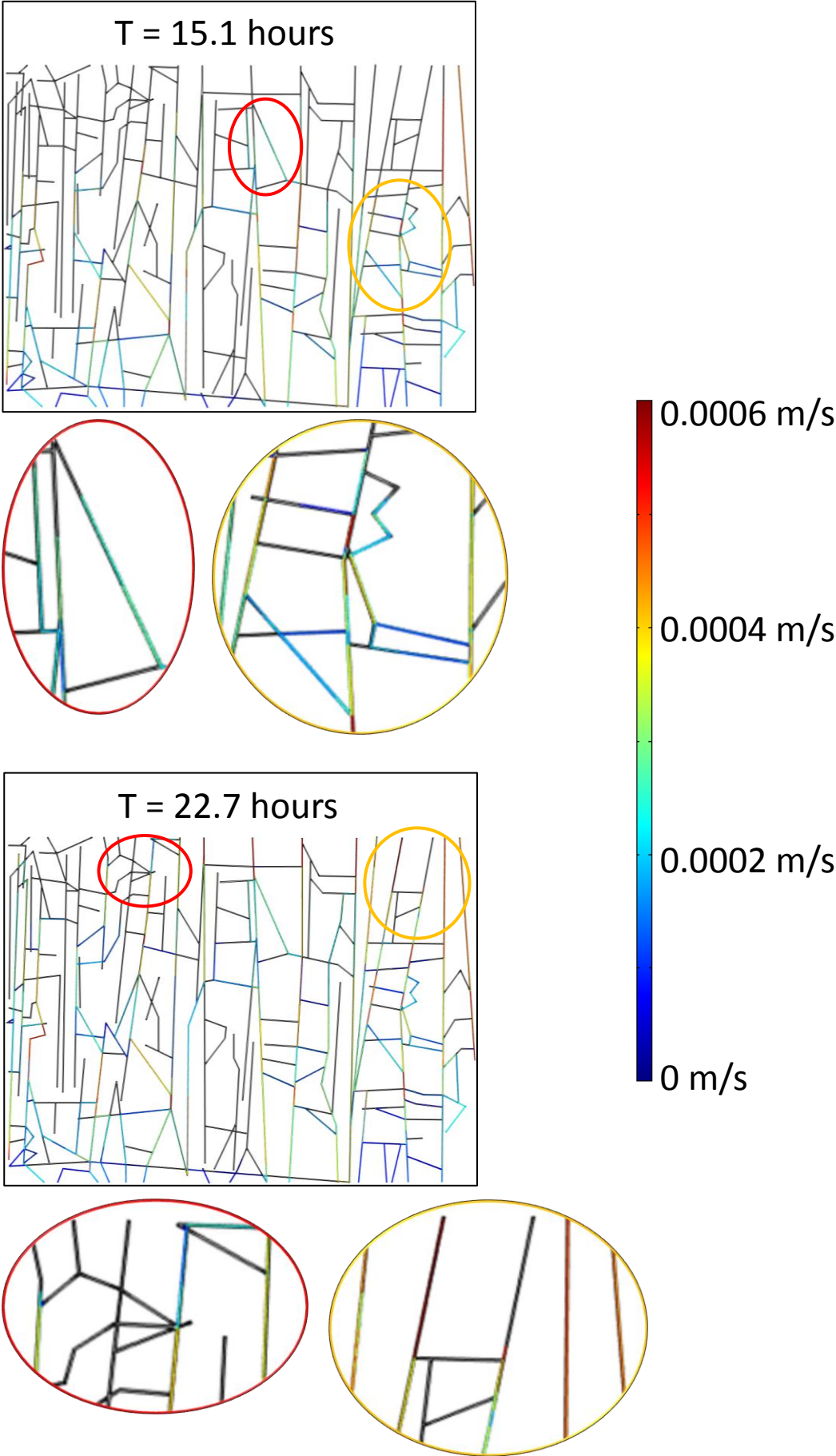
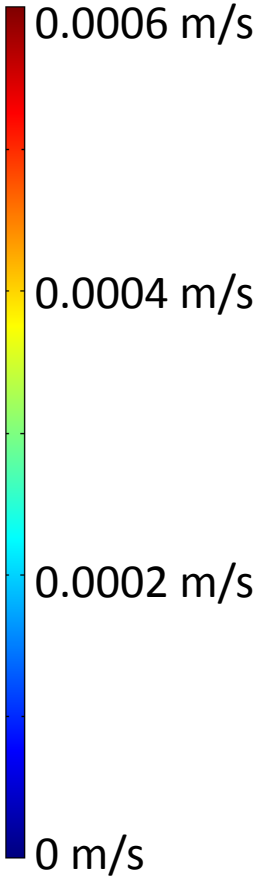
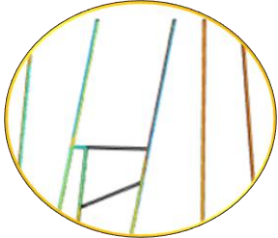
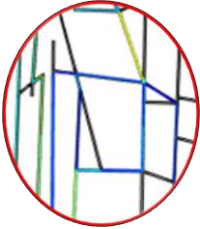
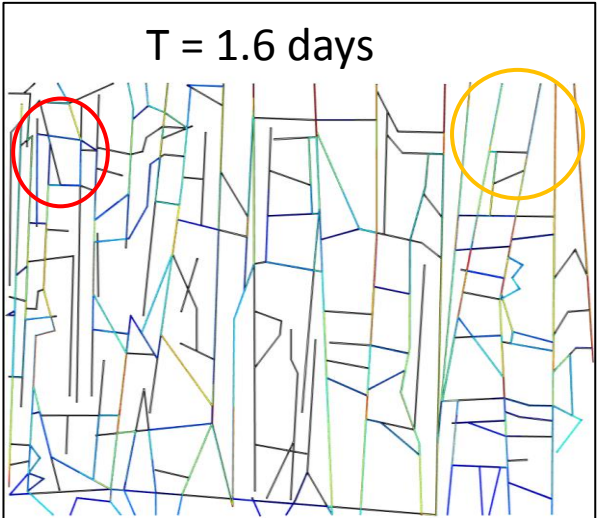
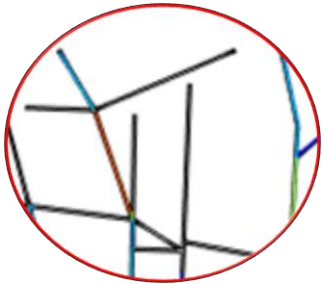
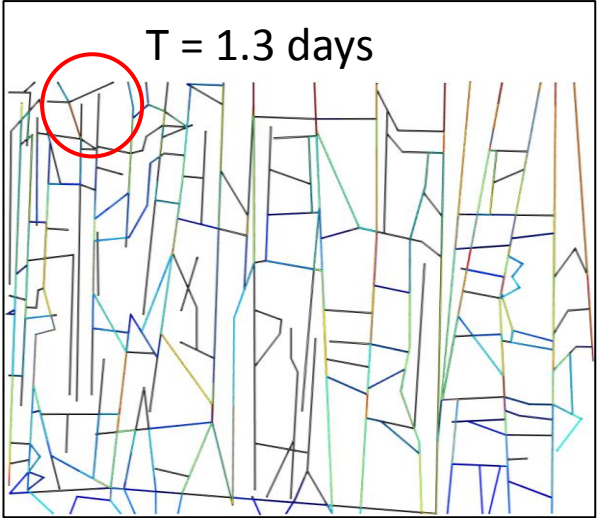
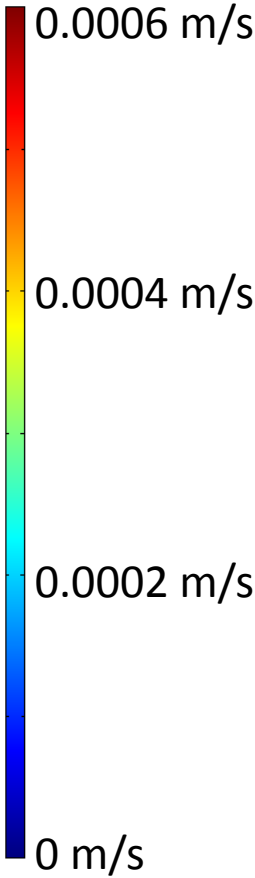
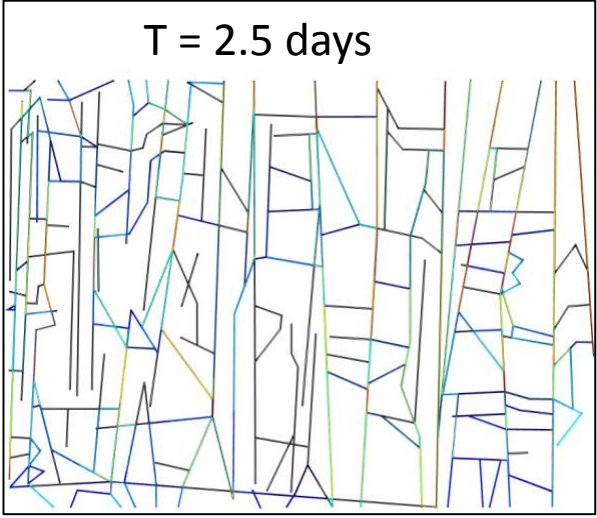
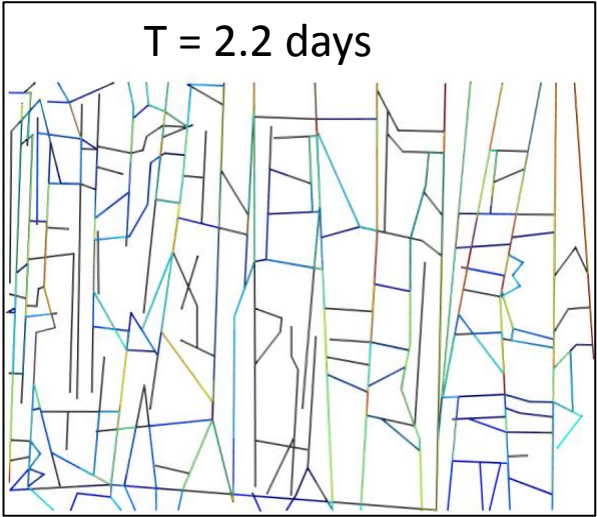
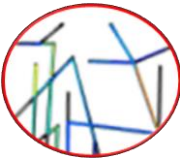
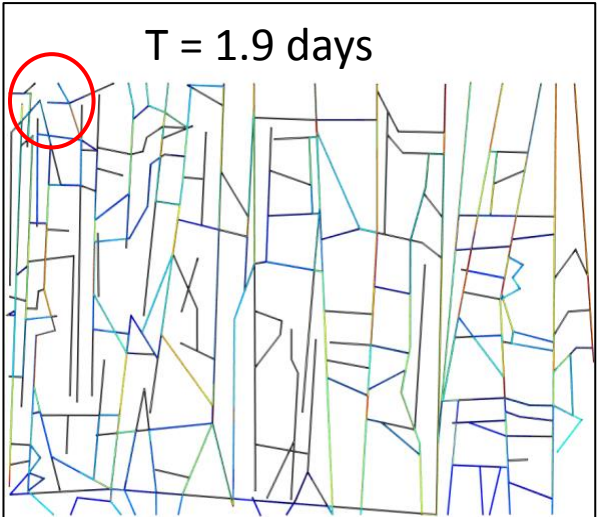


Figure 9.21: Fracture network from Castle Point, Whin Sill, approximately 144 m². The FEM stationary model (height 12 m, same as photograph) represents the velocity of laminar flow for water, where the pressure gradient is vertical from 6 Pa to 0 Pa. (A) Zoomed in section of red circle highlighting location of high fluid flow in vertical and sub-vertical fractures. (B) Zoomed in section of orange circle highlighting location of low or no fluid flow in horizontal and sub-horizontal fractures.









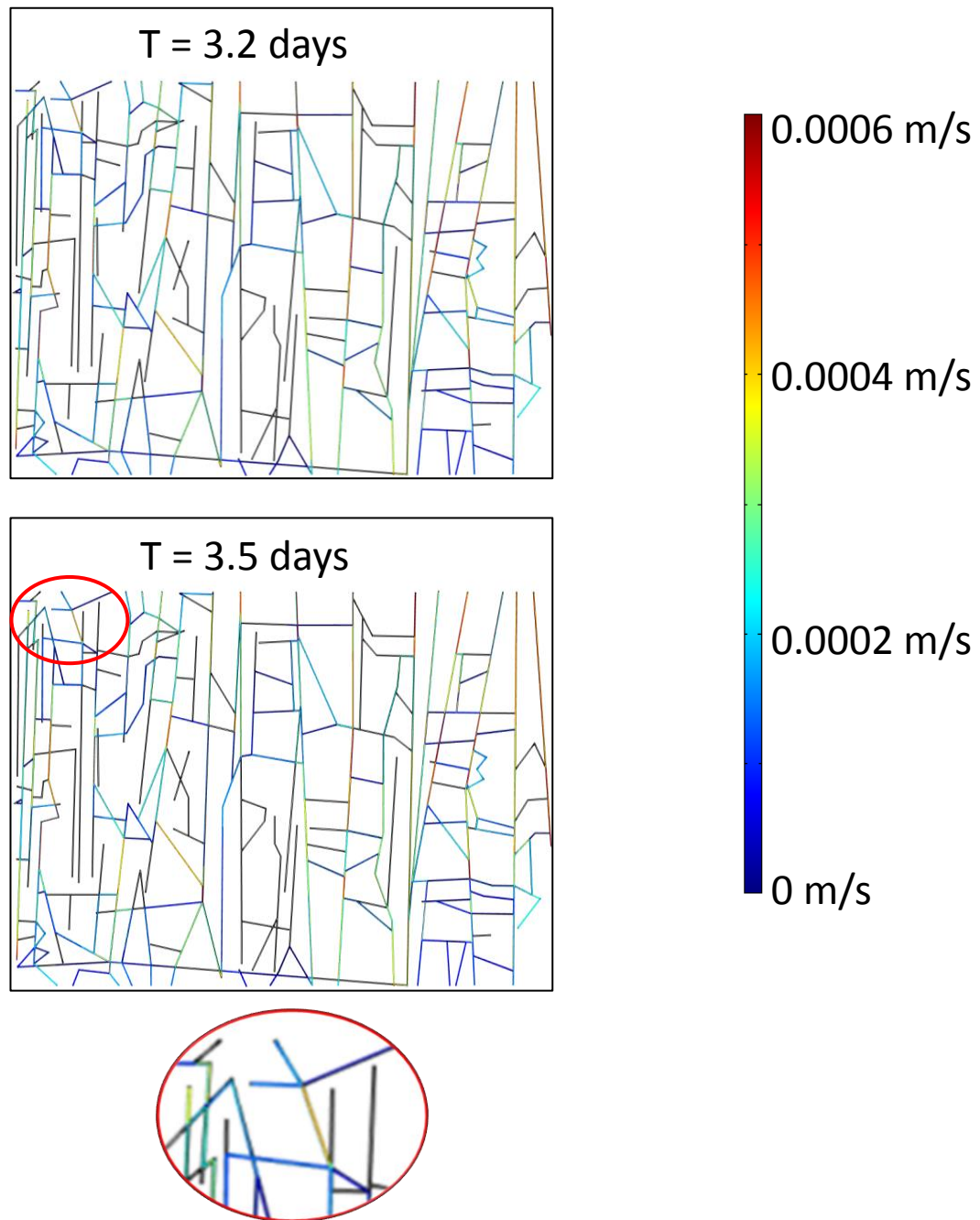


Figure 9.22: Water particle tracing for fluid flow in the Whin Sill fracture network at Castle Point, colour contours represents the time-dependent particle velocity in m/s and also the particle position. This represents 11 time frames where solutions were applied every 100 s. Note that the time scale is not in equal fractions illustrating that slower particles fill the sub-horizontal fractures. Model set up based on Figure 9.21, where height of model is 12m. Red and orange circles are zoomed in areas marked on each model to show key areas of interest of fluid flow within the fracture network. When $T = 0$ hours the fracture network is not filled with fluid. The zoom on the 3.6 days model represents the last fracture set to be filled with fluid completely.

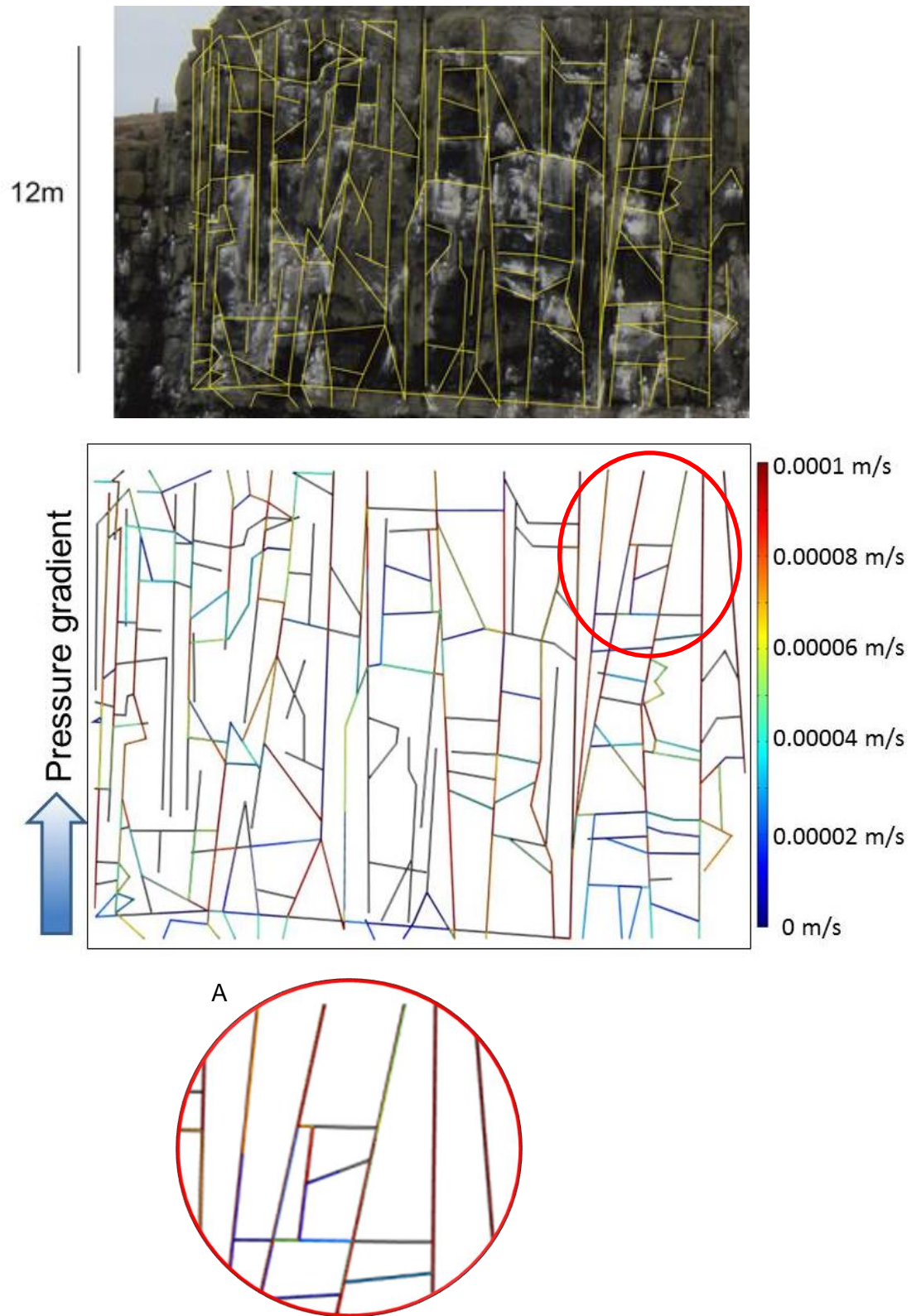
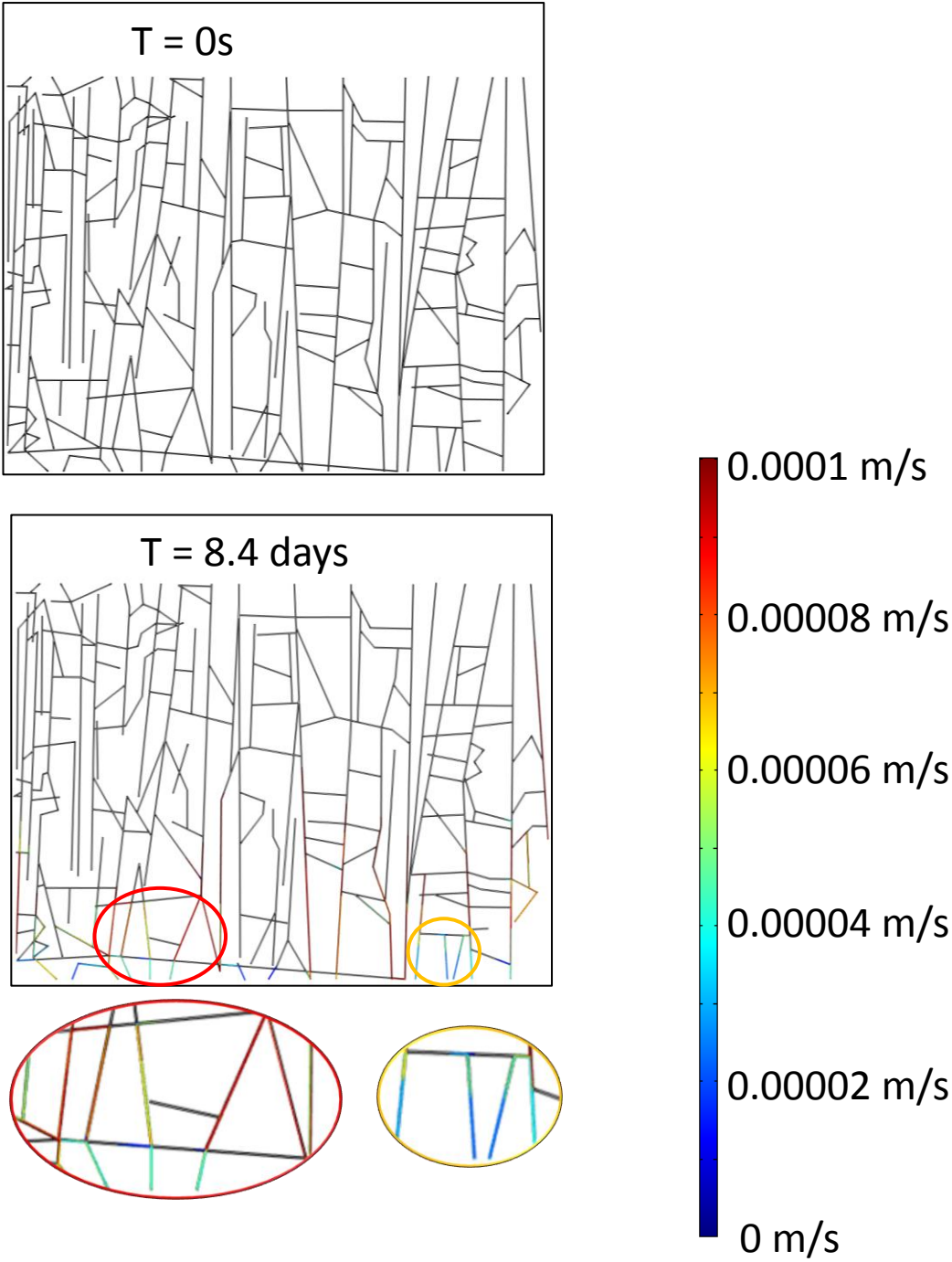
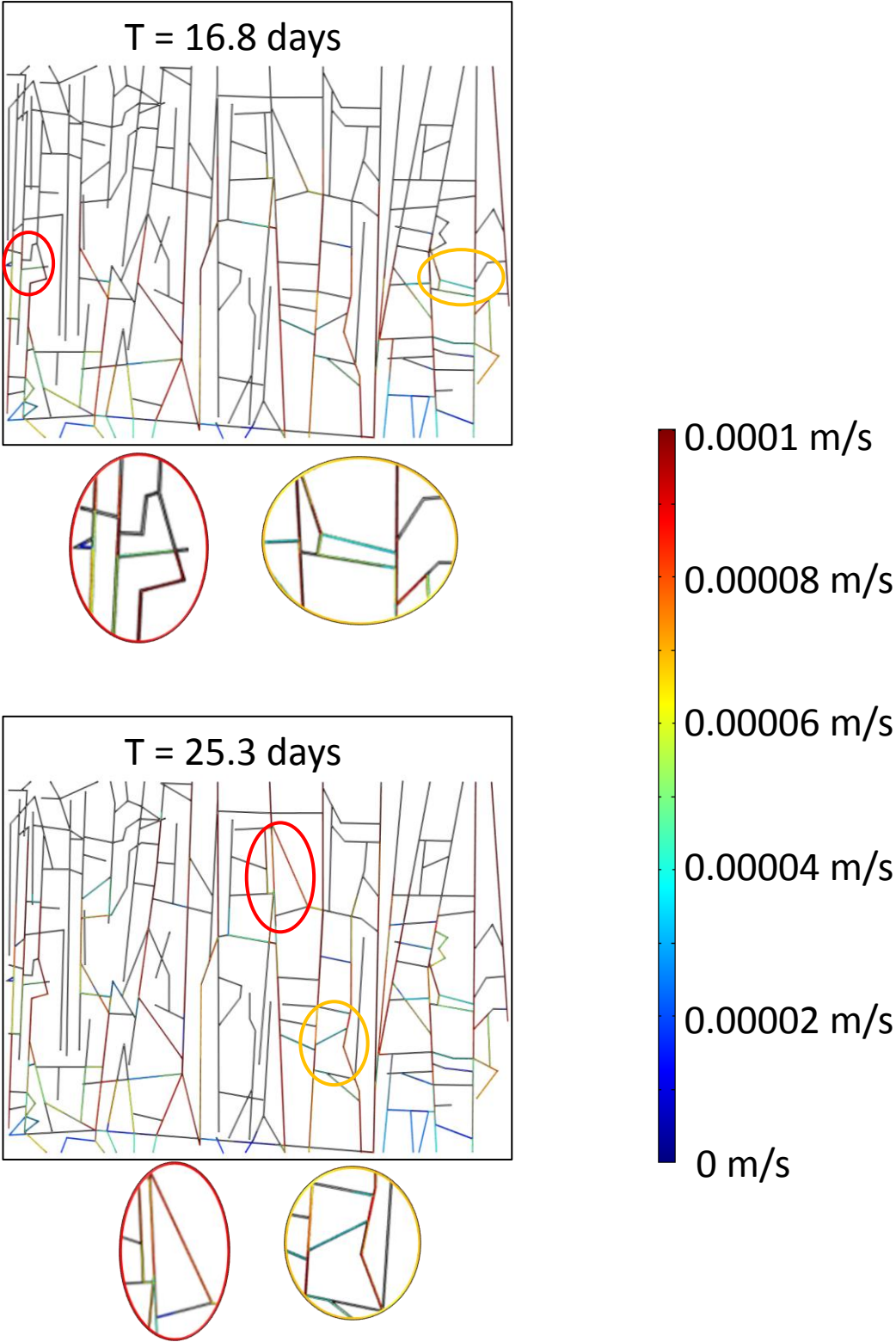
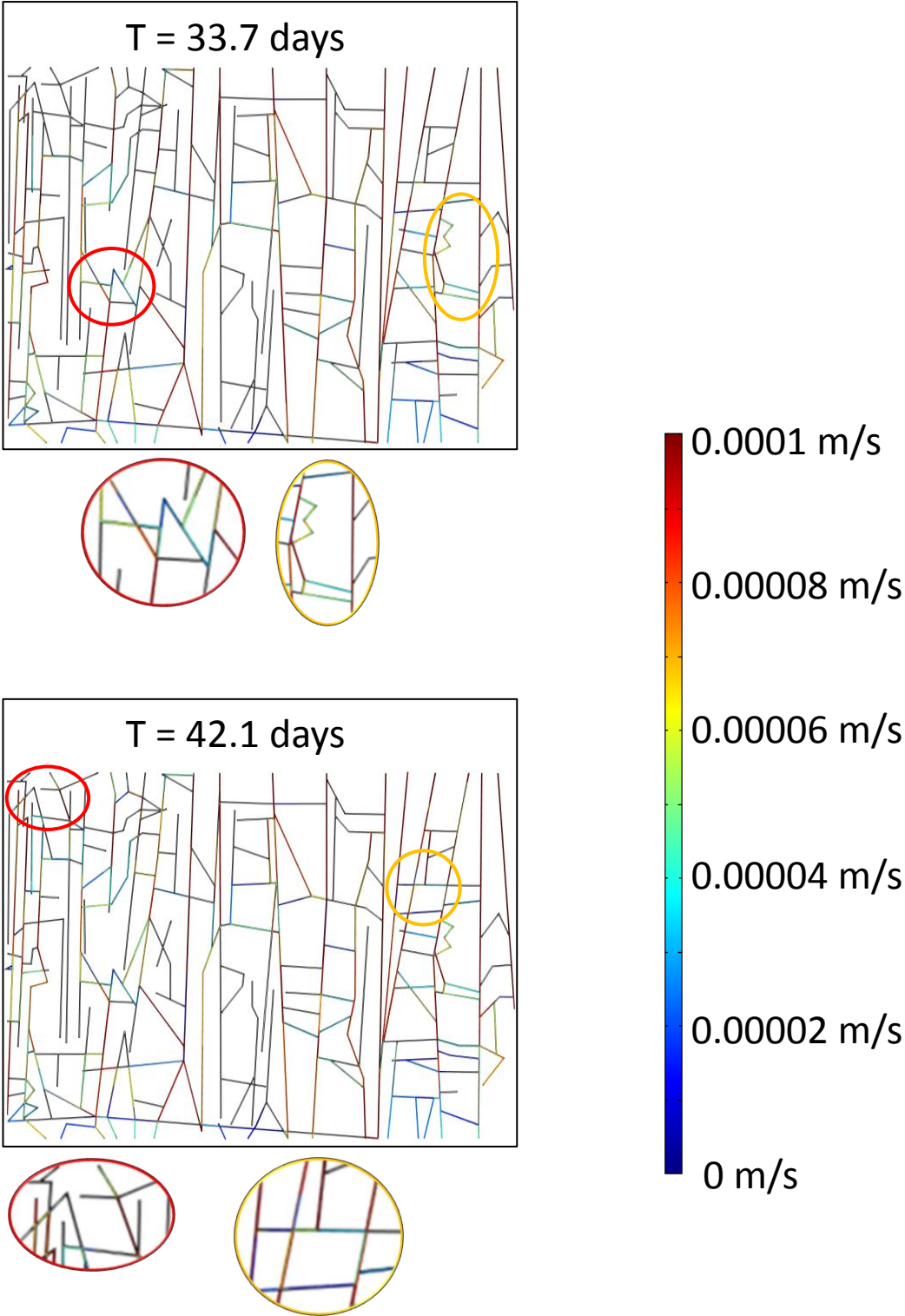
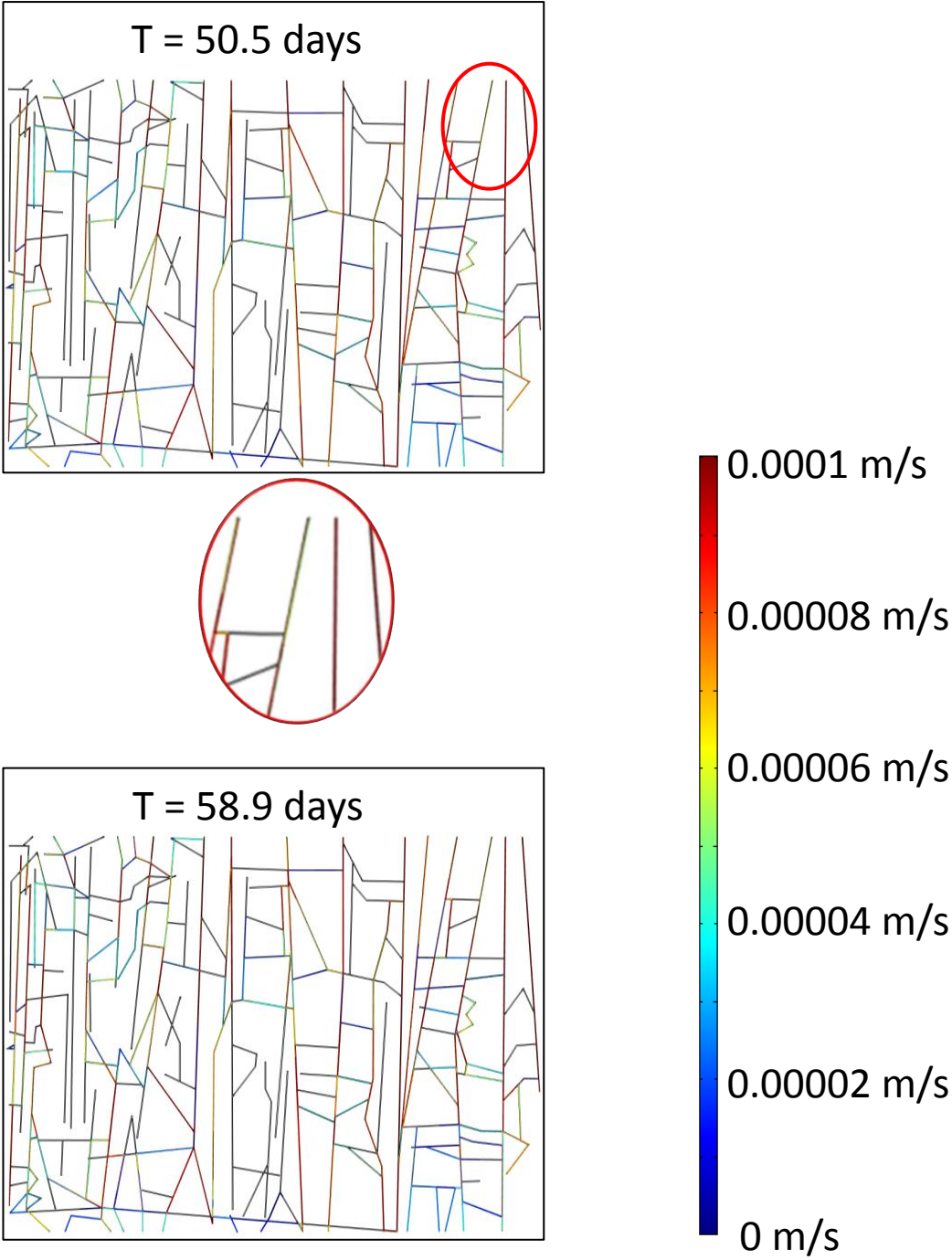


Figure 9.23: Fracture network from Castle Point, Whin Sill. FEM stationary model (height 12 m, same as photograph) represents the velocity of laminar flow for crude oil, where the pressure gradient is vertical from 6 Pa to 0 Pa in the direction of the arrow. (A) Zoomed in section of red circle highlighting location of high fluid flow in vertical and sub-vertical fractures (red colours) and low fluid flow on horizontal and sub-horizontal fractures (blue colours).









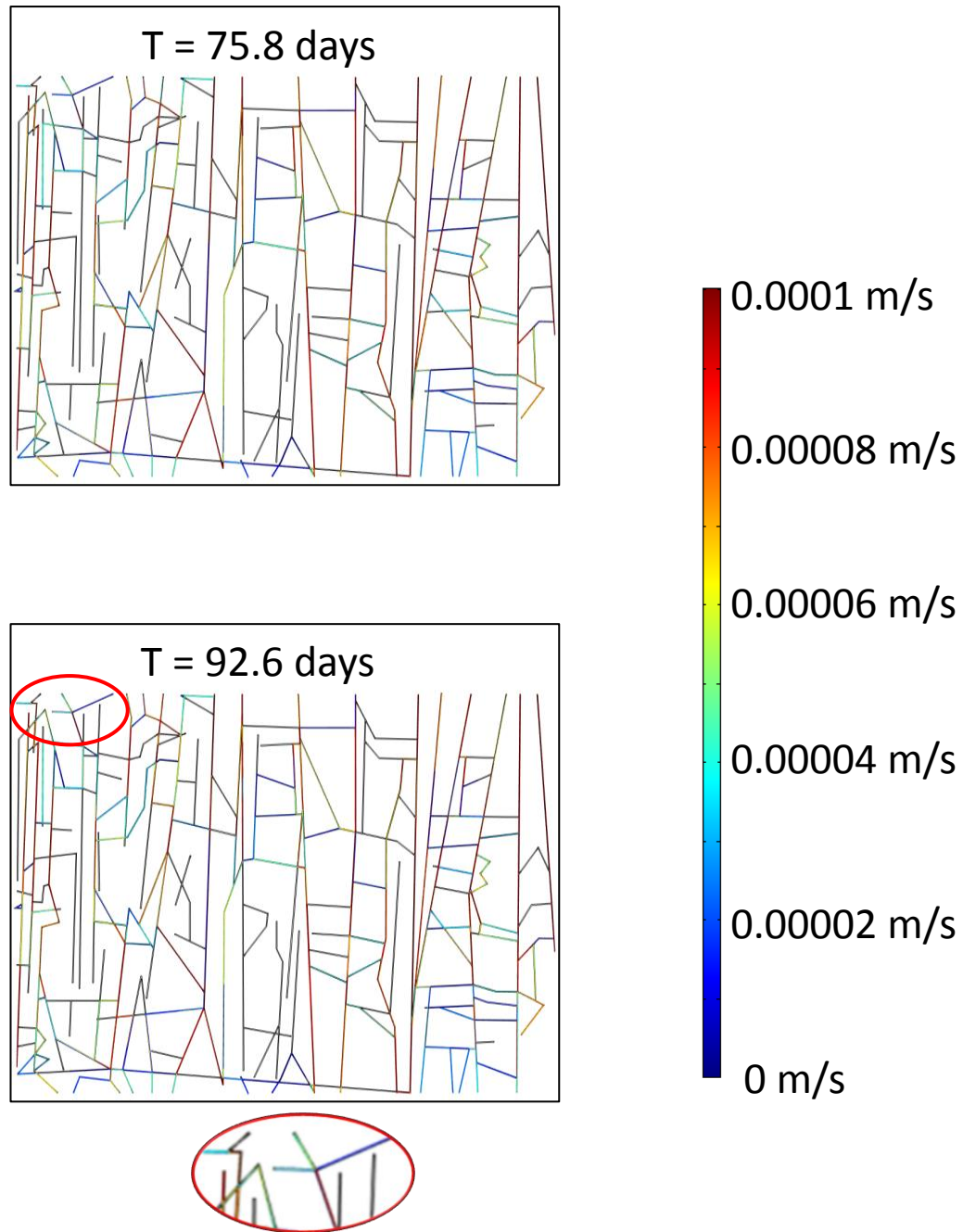


Figure 9.24: Crude oil particle tracing for fluid flow in the Whin Sill fracture network at Castle Point, colour contours represents the time-dependent particle velocity in m/s and also the particle position. This represents 10 time frames where solutions were applied every 1×10^4 s. Note that the time scale is not in equal fractions illustrating that slower particles fill the sub-horizontal fractures. Model set up based on Figure 9.23, height of model is 12 m. Red and orange circles are zoomed in areas marked on each model to show key areas of interest of fluid flow within the fracture network. When $T = 0$ hours the fracture network is not filled with fluid. The zoom on the 92.6 days model represents the last fracture set to be filled with fluid completely.

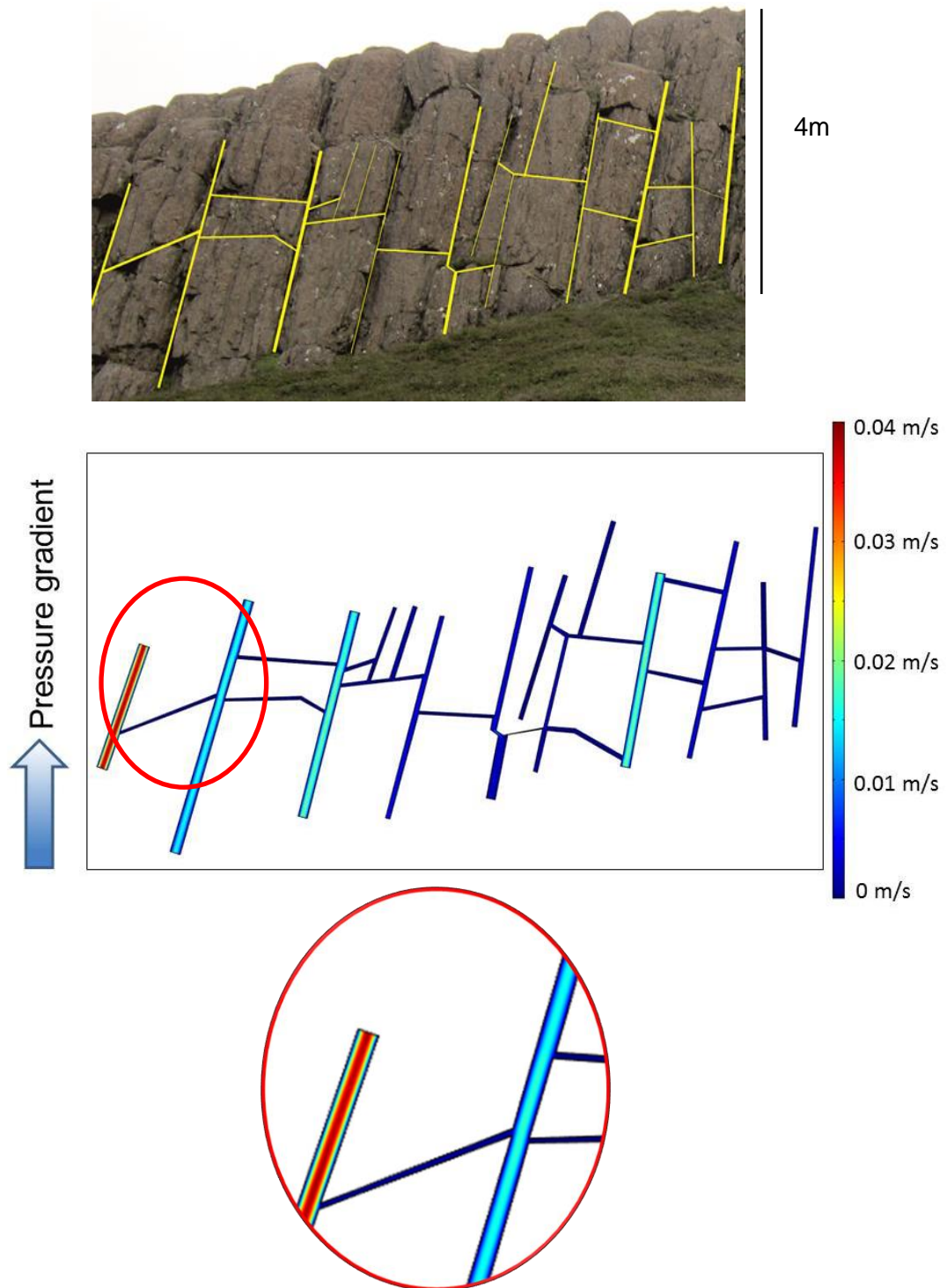
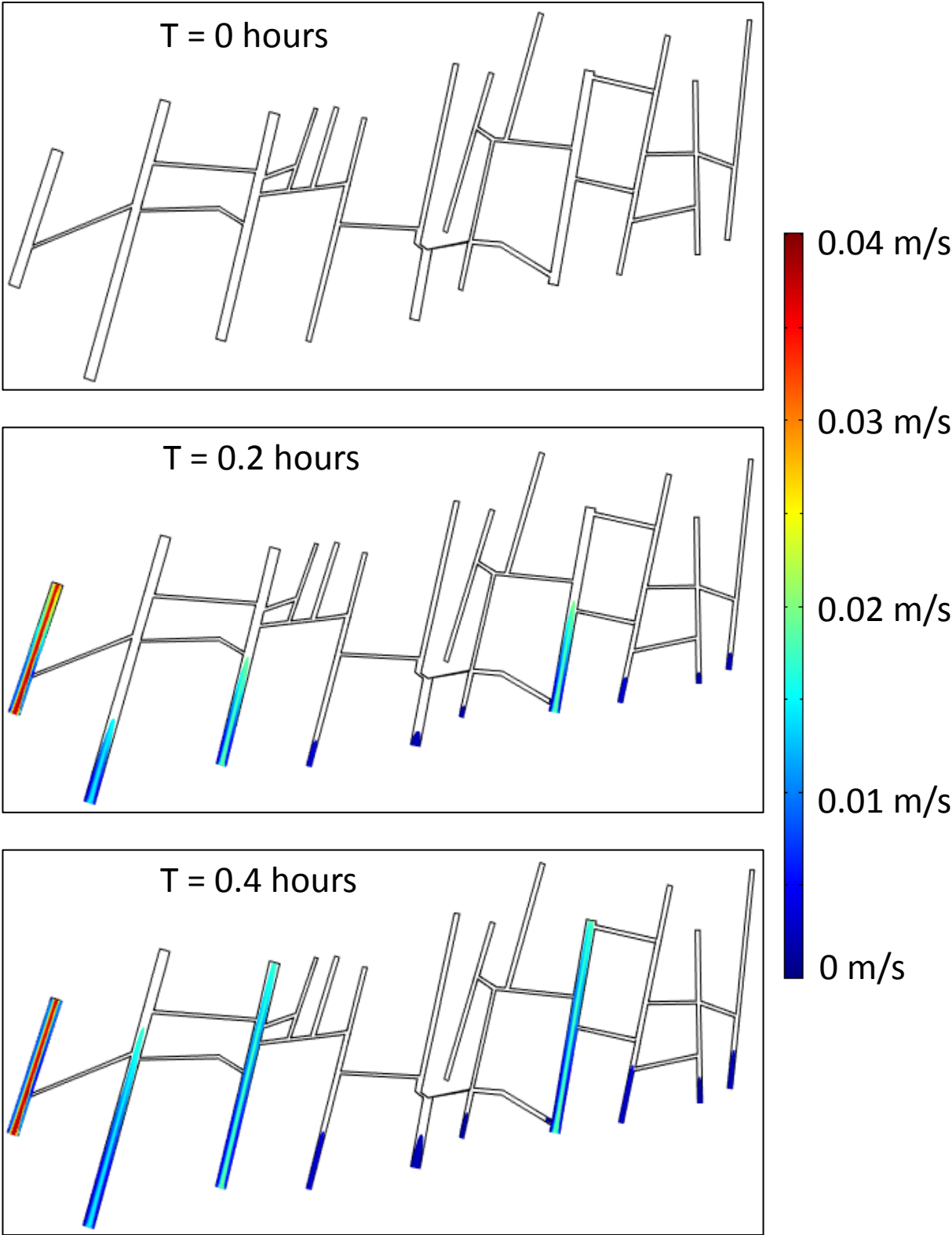
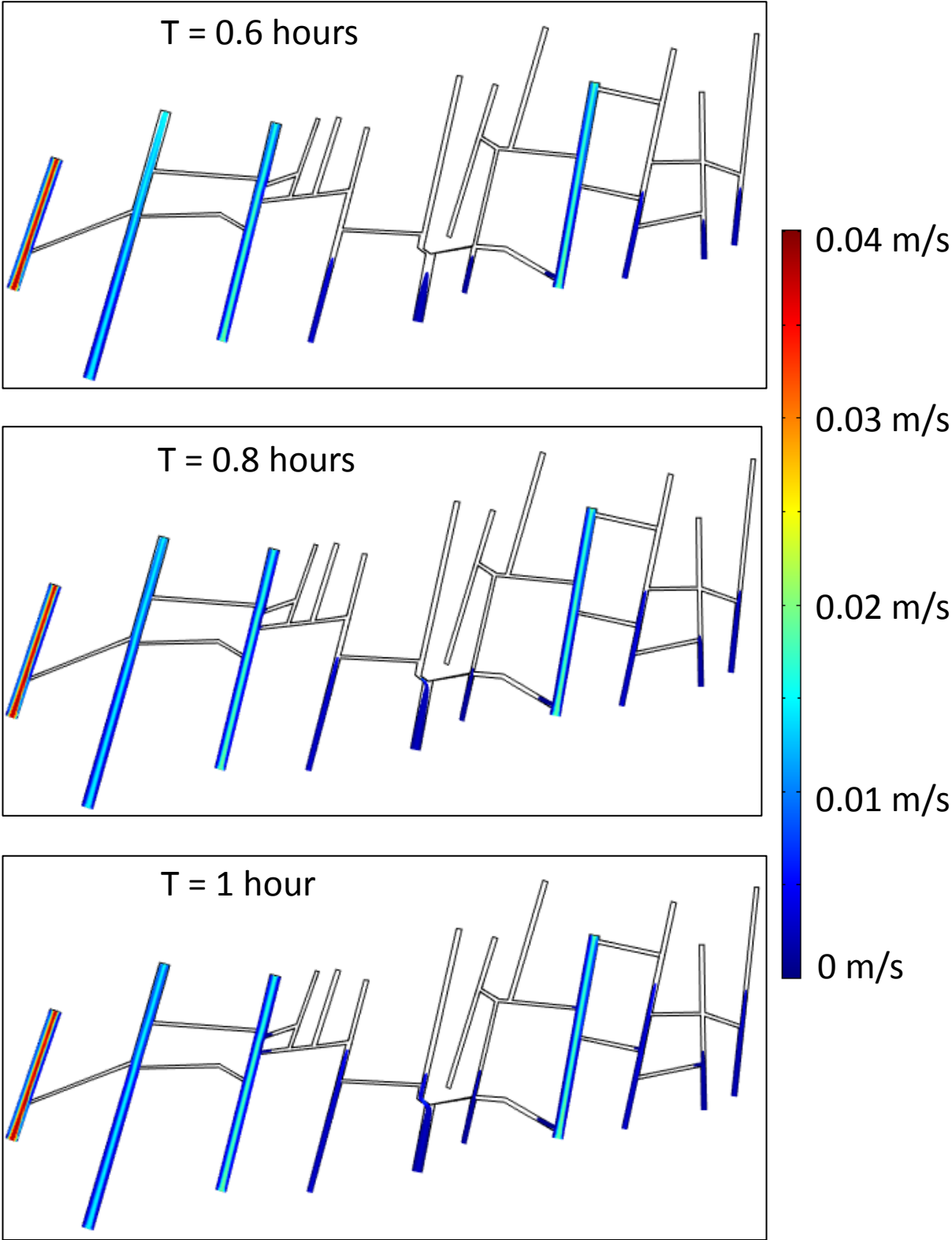
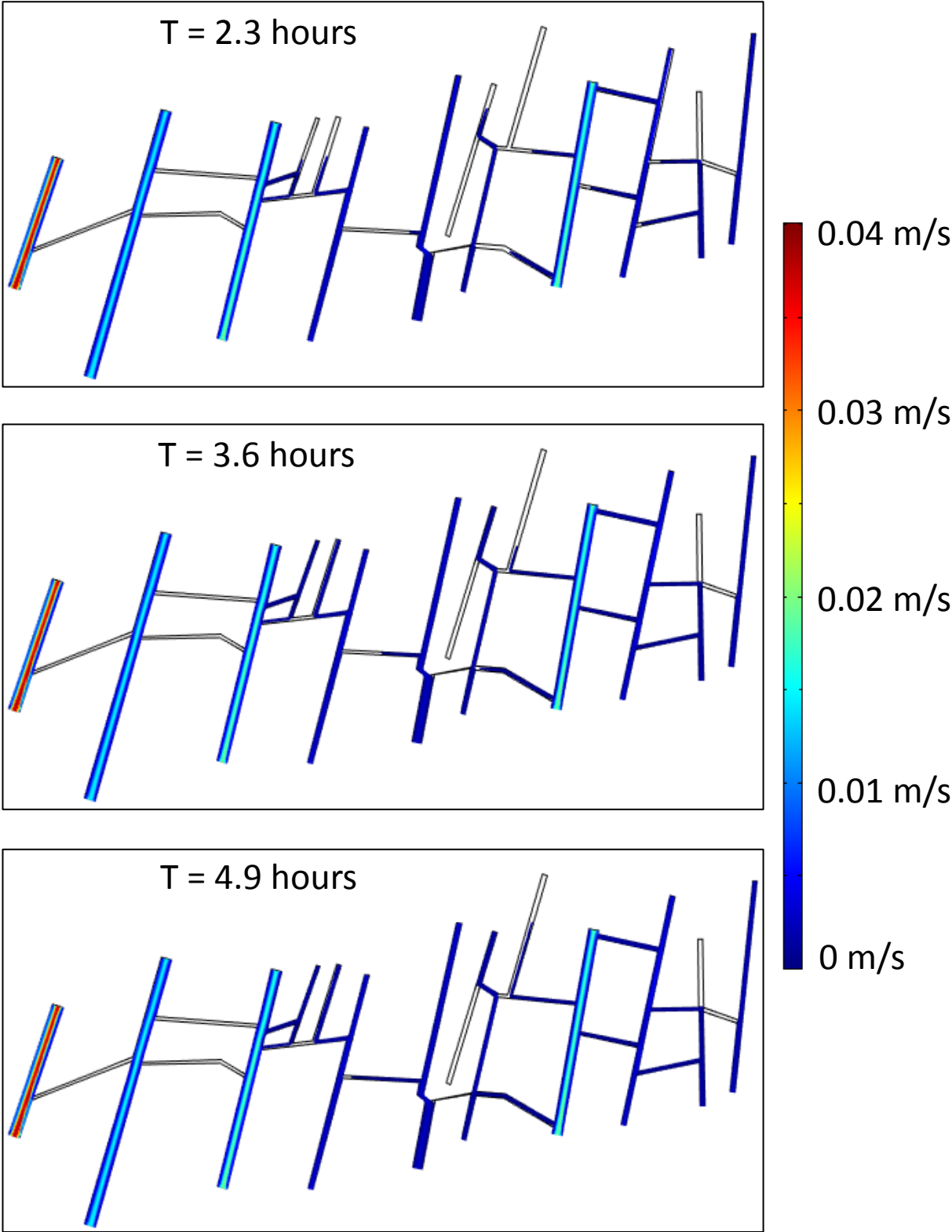


Figure 9.25: Fracture network from Stardalur sill cluster, profile 1. The FEM model (height 4 m, same as photograph) represents the velocity of laminar flow for water, where the pressure gradient is vertical, i.e. the inlet of water is from the base of the fractures to the outlet at the top of the fractures. The fastest flow is along the sub-vertical fractures (light blue and red colours) and the slowest flow is predominantly along horizontal and sub-horizontal fractures (dark blue colour). (A) Zoomed area of red circle illustrating that there is no fluid flow along the fracture walls themselves and only in the centre of the fractures.







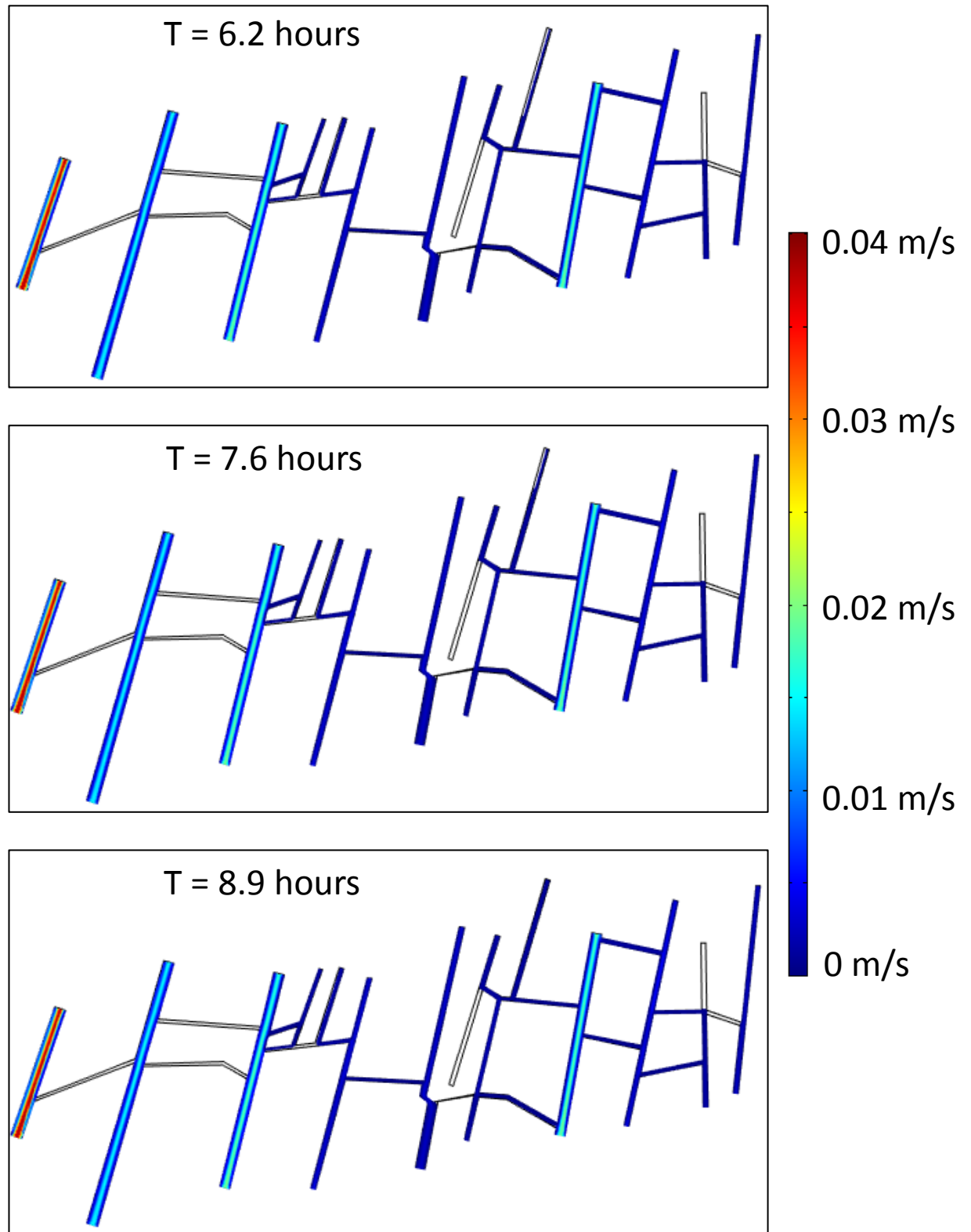


Figure 9.26: Water particle tracing for fluid flow in the Stardalur fracture network, where the colour contours represents the particle velocity in m/s and also the particle position. Note that the time scale is not in equal fractions illustrating that slower particles fill the narrower fractures. This Figure represents 12 time frames where solutions were applied every 100 s. Model set up based on Figure 9.25, where height of model is 4 m.

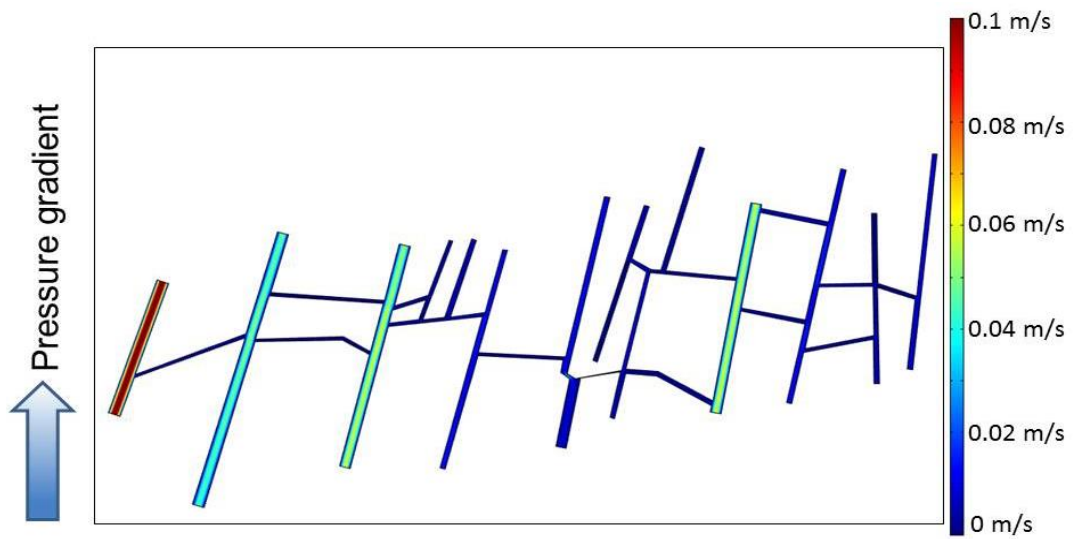
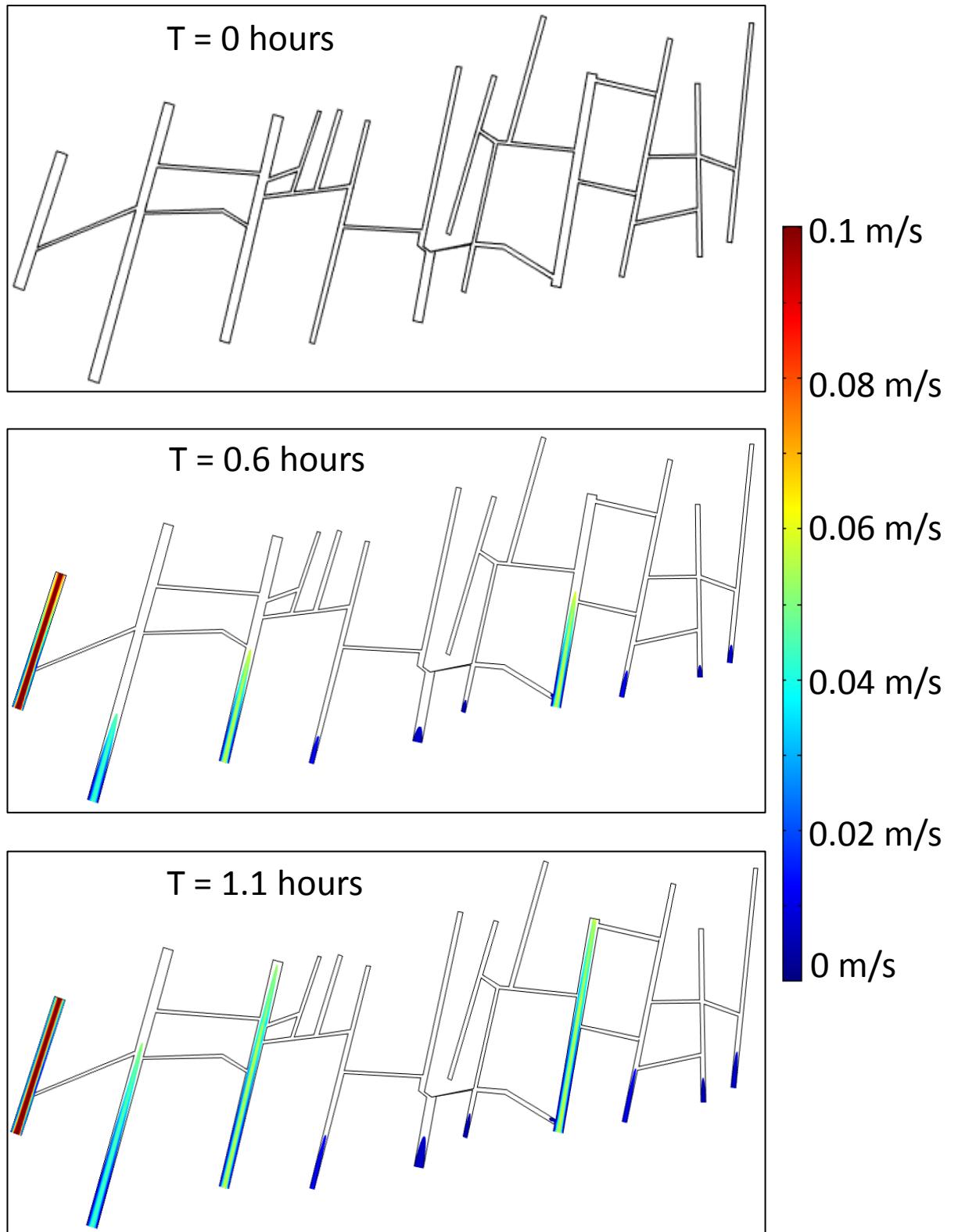
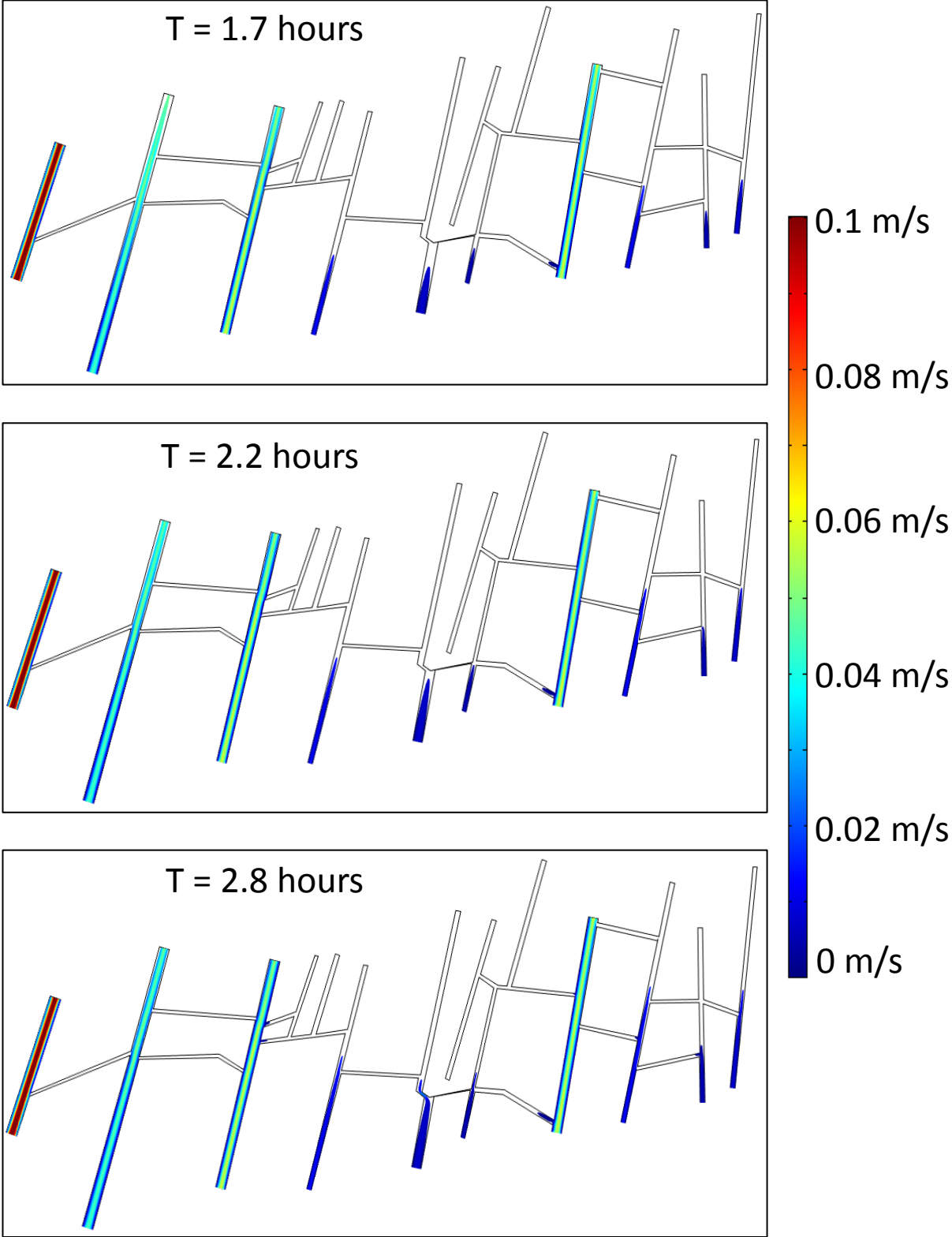
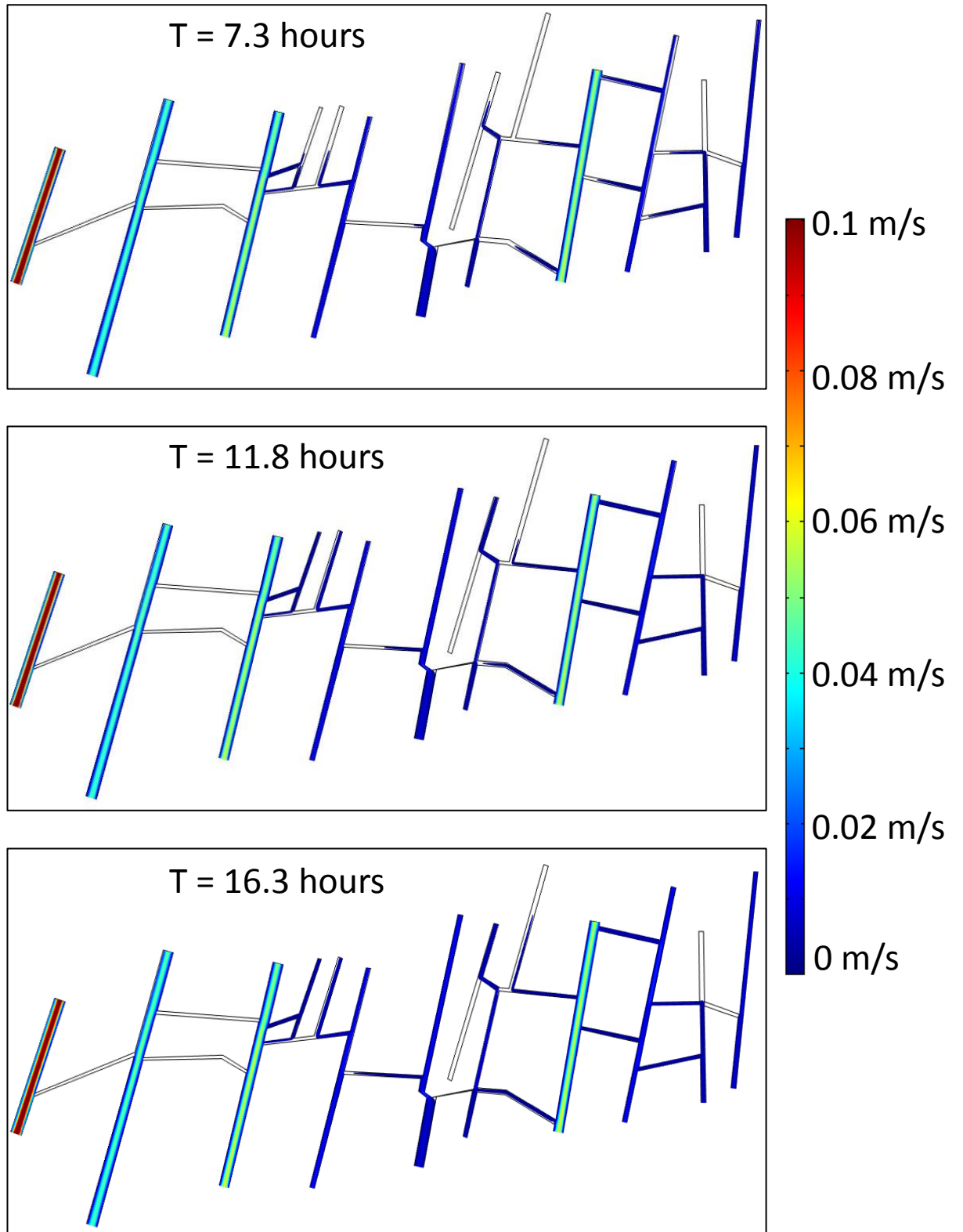


Figure 9.27: Fracture network from Stardalur sill cluster, profile 1. The FEM model (height 4 m, same as photograph) represents the velocity of laminar flow for crude oil, where the pressure gradient is vertical, i.e. the inlet of water is from the base of the fractures to the outlet at the top of the fractures. The fastest flow is along the sub-vertical fractures (red, yellow, green and light blue colours), while the slowest flow is along the horizontal and sub-horizontal fractures (dark blue colours).







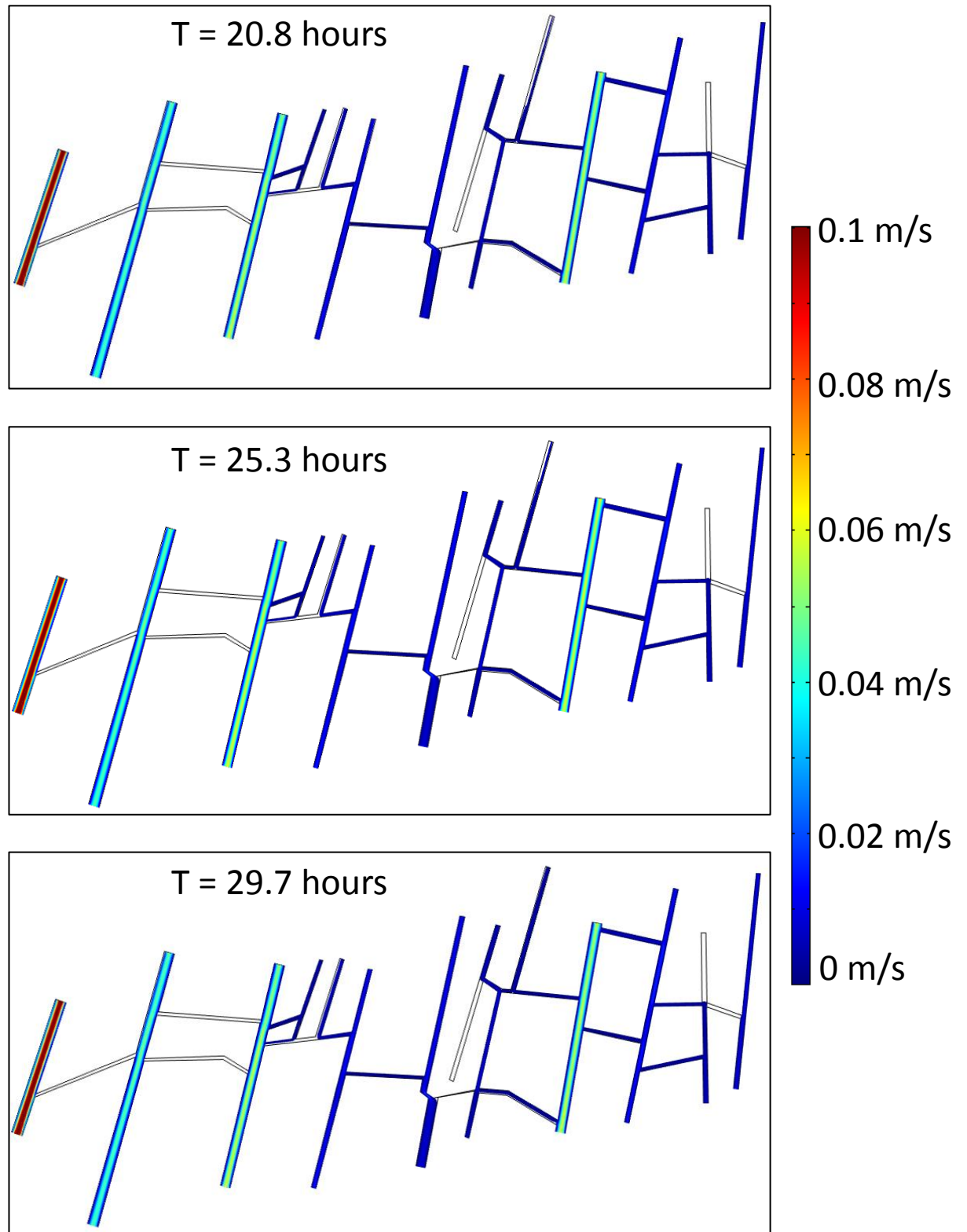


Figure 9.28: Crude oil particle tracing for fluid flow in the Stardalur fracture network, colour contours represents the particle velocity in m/s and also the particle position. Note that the time scale is not in equal fractions illustrating the slower particle fill in the narrower fractures. 12 time frames are shown where solutions were applied every 100 s. Model set up based on Figure 9.27, where height of model is 4 m.

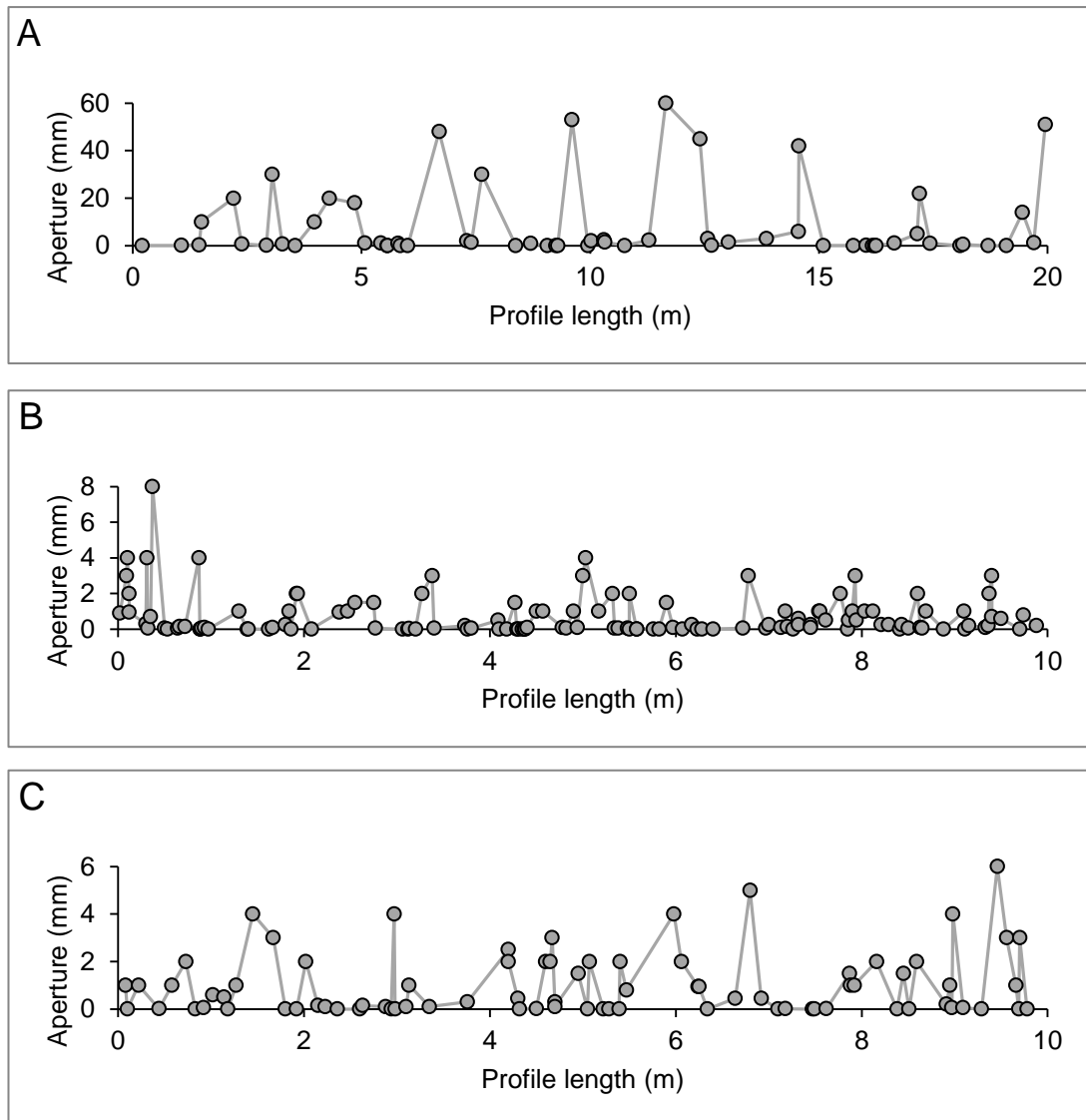


Figure 9.29: Sub-vertical fracture aperture variation along three profiles: (A) Profile 1, Stardalur sill cluster, (B) Holy Island, Whin Sill and (C) Harkess Rock, Whin Sill. Fluid flow is represented by the peaks on the scatter plots, illustrating the effects of flow channelling along the larger aperture fractures.

From Equations (9.5) and (9.6) intrinsic permeabilities and porosities were calculated as follows (the large apertures that had been clearly affected by weathering and erosion were removed): The Whin Sill has an average permeability of $0.59 \times 10^{-6} \text{ m}^2$ and average porosity of 1.89%; these values are relatively high and are most likely the result of weathering and erosion. Furthermore, along the top surface of the sill at Harkess Rock (grid reference: NU17662 35734), a large number of vesicles could be seen and gave a unique chance to study the porosity of the Whin Sill at this location with respect to a vesicle count. Vesicles within a transect area of

8 cm² were counted, to give an average void of 0.75 cm² and, a porosity of 0.11%. For comparison, the Stardalur sill cluster was calculated to have an average intrinsic permeability of 0.62×10^{-6} m² and average porosity of 0.68%.

Interconnection of fractures is dependent on the angle of the fractures. For a good network to form, the fractures must be at significant angles to each other, whereas, if the fractures are approximately parallel to each other there would be a unidirectional flow of crustal fluids. The majority of the fractures within both the Whin Sill and Stardalur sill cluster were vertical and sub-vertical exhibiting a range of strikes from 0 to 180°. The rose diagrams (Figs. 9.3 and 9.4) illustrate the dominant strike pattern. Therefore, there is an increased probability of the fractures intersecting with one another. This fracture interconnectivity is justified by the coefficient of variation (C_v) >1 for both the Whin Sill and the Stardalur sill cluster. Results of the numerical models in Figures 9.21-9.28 illustrate the importance of interconnectivity of fractures. Without connected fractures, the overall permeability of the reservoir would be dependent on the porosity of the groundmass, which for a micro-gabbro is very low. This conclusion has also been drawn by Brenner and Gudmundsson (2004) who studied permeability in layered reservoirs.

Reservoir quality can be compared between the Whin Sill and the Stardalur sill cluster in terms of the fracture spacing and frequency. The Whin Sill displays higher fracture interconnectivity, with a fracture spacing of 0-2 cm, than the Stardalur sill cluster, with a fracture spacing of 0-6 cm. This fracture interconnectivity is also reflected in the fracture frequencies. The Whin Sill has a mode of 4-6 fractures per metre, whereas the Stardalur sill cluster has a mode of 6 fractures per metre. Therefore, with respect to their fracture frequencies these two field areas are almost identical. On closer inspection, the Whin Sill has a larger fracture frequency of <52 /m², compared to the Stardalur sill cluster that has a fracture frequency of <33 /m². Overall, it can be determined that the Whin Sill has a higher reservoir quality and higher storage capacity than the Stardalur sill cluster based upon these statistics.

Permeability and porosity for the Stiflisdalsvatn Sill (Fig. 9.1C) have also been calculated because this sill shows outstanding columnar jointing and therefore offers a good comparison. This sill is approximately 33 m thick and calculations were performed based upon photographs and correlation to field measurements. The

permeability calculated is $2.6 \times 10^{-12} \text{ m}^2$ and porosity is 0.033%, with a common distance between fractures of 0.3 m. These calculations reflect the reservoir quality of the sill, which is very good as the storage capacity is high. Overall, the Stiflisdalsvatn Sill would yield a higher reservoir potential than the Whin Sill and Stardalur sill cluster, not just because of the high storage capacity but also because it is thicker.

9.7.2 Vøring Margin

When considering the reservoir quality of the sills in the Vøring Margin we must take into account the depth at which they are located, as this will affect the permeabilities (and porosities) of the sills. There are two explanations for this: (1) fracture aperture at depth is approximately 1/100 of those fracture apertures at the surface (Lee and Farmer, 1993) and (2) fracture frequency decreases in the top few hundred metres of the crust. As a result the permeability decreases with depth, especially in the top few tens of metres of the crust (Gudmundsson, 2011a).

The macroscopic cooling joints control the major component of porosity in sills and these are modified by post emplacement tectonic deformation, enhancing storage capacity and fluid flow through the fracture networks within the sills (Petford, 2003). Tectonic loading affects the aperture of the fractures, but this depends on whether the loading is extensional or compressional. Under extension, tensile stresses are concentrated within the sills and therefore the apertures of the fractures become greater. Under compression, compressive stresses are concentrated and the apertures of the fractures would decrease and fluid flow would therefore be reduced. This however, depends on the orientation of the fracture in relation to the extensional or compressive stresses (Fischer *et al.*, 1995; Brenner and Gudmundsson, 2004). Also, unloading of the overburden would have had an effect on the aperture of the fractures by further opening; this would most likely have occurred after the Neogene glaciation. Furthermore, igneous rocks are more resilient to diagenesis than sedimentary rocks and therefore, their permeability and porosity would have been better preserved (Schutter, 2003a, b).

The majority of the sills generate hydrothermal systems, as determined from the seismic sections (Svensen *et al.*, 2010). The life time of these systems depends on

the mass and temperature of the sills, for example a larger sill will maintain a hydrothermal system longer than a small sill. Therefore, sills located at shallow depths cool faster than sills located at great depths as they are unable to maintain a hydrothermal system (Cathles *et al.*, 1997). In turn, the cooling rate has an effect on the size of the columnar joints, where slower cooling forms larger columns and vice versa, which will have an impact on the permeability of the sills.

In summary, sills originally have no or very low permeability (and porosity) in their matrix, but after cooling the permeability of the sills will increase. This increase can be related to several parameters, including: (1) opening of fractures as a result of post tectonic deformation, (2) hydrothermal alteration and (3) diagenesis. On a basin scale these parameters will have a large impact on sill permeability, such that, some sills may remain impermeable while others become permeable.

9.7.3 Flow channelling and the cubic law: implications for fluid transport within fractured reservoirs

The bi-logarithmic plots (Figs. 9.7 and 9.8) for the Whin Sill and Stardalur sill cluster show very strong power-laws, which can be explained by the cubic law and flow channelling. Firstly, the cubic law states that the fluid flow through fractures is proportional to the cube of their apertures. Secondly, flow channelling defines the preferred path for fluid flow. This path will have the least resistance to the flow, that is, where the fracture walls are smooth and have little irregularity. With these two principles it can be determined that the majority of fluid will flow along smooth fractures with larger apertures, corresponding to the tail of the cumulative frequency plot.

The log-normal distribution displayed in Figures 9.5 and 9.6 have also been described by other authors (e.g. Odling, 1997; Larsen *et al.*, 2010 and references there in). Power-law distributions are also commonly cited in the literature (e.g. Vermilye and Scholz, 1995; Hillis, 1998; Marrett *et al.*, 1999; Berkowitz *et al.*, 2000; Gudmundsson *et al.*, 2002a; Ortega *et al.*, 2006; Klimczak *et al.*, 2010; Larsen *et al.*, 2010). It should be noted that the data presented on apertures have a low resolution towards the lower range of the data due to the inability of the feeler gauge

to measure below 0.05 mm. Therefore, there is a small bias in the variance of the data where the majority of the data lies.

One important factor to consider for fluid flow in fractures is the percolation threshold. In order for fluid flow to occur, a particular threshold must be met, and this is determined by fracture networks. This implies that there is only flow between fractures if they are interconnected (may be defined to behave mechanically or hydraulically as one fracture (Gudmundsson *et al.*, 2003)), where fracture clusters are formed of differing sizes and shapes (Figs. 9.16-9.20). Therefore, the numerical models produced are only of interest for fracture networks that are above the percolation threshold. Also, larger the profile lines on which these fracture networks were based, have a higher probability (approaching one) containing well-interconnected or clusters of fractures. This probability relates to a power-law for fracture connectivity of individual sets of fractures in both 2D and 3D space (Berkowitz, 1995). For fluid to be transmitted through a fractured body the fractures must be open (Fig. 9.29) and interconnected. Thus, the hydraulic conductivity of the sills can be related to the number of fractures that trend favourably to fluid flow. However, as the sill groundmasses are fairly impermeable, the fracture network will have a number of ‘dead-ends’ that will inhibit fluid flow within the sill (Odling, 1992; 1997).

The volumetric flow rate can also be solved analytically for both vertical, Q_z (Eq. 9.7), and horizontal flow, Q_x (Eq. 9.8):

$$Q_z = \frac{b^3 W}{12\mu_f} \left[(\rho_r - \rho_f)g - \frac{\delta P_e}{\delta z} \right] \quad (9.7)$$

$$Q_x = -\frac{b^3 W}{12\mu_f} \frac{\delta P_e}{\delta x} \quad (9.8)$$

where b is the aperture of the fracture, W is the width of an area perpendicular to the direction of the flow, μ_f is the dynamic viscosity of the fluid, ρ_r is the density of the host rock, ρ_f is the density of the fluid, g is the gravitational constant, $\delta P_e/\delta z$ is the pressure gradient in the direction of vertical flow through a fracture in an elastic

medium, and $\delta P_e/\delta x$ is the pressure gradient in the direction of horizontal flow (Gudmundsson, 2011a). Eq. 9.7 takes into account buoyancy, which has been shown by Gudmundsson *et al.* (2001) to have an effect on the volumetric flow rate. Using examples from field work the common profile lengths taken were ~ 10 m and can be taken to substitute for W . The arithmetic mean for the apertures of the vertical fractures are as follows:

- Whin Sill = 2.9 mm
- Stardalur sill cluster = 2.5 mm
- Vøring sills ~ 0.03 mm (calculation based on averages from field work and that aperture decreases with depth by 1/100 (Lee and Farmer, 1993)).

And for the horizontal apertures:

- Whin sill = 3.4 mm
- Stardalur sill cluster = 0.4 mm
- Vøring sills = 0.02 mm

Note here that all apertures are taken into account and are not adjusted for weathering. Calculations were produced based on water with a dynamic viscosity of 1.5×10^{-3} Pa s and density 1000 kg/m^3 , and also crude oil with a dynamic viscosity of 0.05 Pa s and density 900 kg/m^3 (Gudmundsson, 2011a). The temperature of the water was taken at 5°C , which is similar to temperatures of cold springs in Iceland (Gudmundsson *et al.*, 2001). The density of the host rock was taken at 2600 kg/m^3 , pressure gradient was 5 Pa/m and the gravity constant was 9.81 m/s . Substituting these values into Eq. (9.7) and Eq. (9.8), we obtain vertical volumetric flow rates as follows:

- Whin Sill water: $0.22 \text{ m}^3/\text{s}$, oil: $7.06 \times 10^{-3} \text{ m}^3/\text{s}$
- Stardalur sill cluster water: $0.14 \text{ m}^3/\text{s}$, oil: $4.45 \times 10^{-3} \text{ m}^3/\text{s}$
- Vøring sills water: $1.77 \times 10^{-7} \text{ m}^3/\text{s}$, oil: $5.65 \times 10^{-9} \text{ m}^3/\text{s}$

And horizontal volumetric flow rate:

- Whin Sill water: $1.12 \times 10^{-4} \text{ m}^3/\text{s}$, oil: $3.36 \times 10^{-6} \text{ m}^3/\text{s}$

- Stardalur sill cluster water: $2.21 \times 10^{-7} \text{ m}^3/\text{s}$, oil: $6.63 \times 10^{-9} \text{ m}^3/\text{s}$
- Vøring sills water: $2.00 \times 10^{-11} \text{ m}^3/\text{s}$, oil: $6.00 \times 10^{-13} \text{ m}^3/\text{s}$

These calculations show that the flow rate increases with the apertures of the fractures, and is approximately one thousand times greater in vertical fractures. They also show that the volumetric flow rate between water and crude oil differs significantly, with crude oil's volumetric flow rate being thirty two times slower than that of cold water. This time difference between water and crude oil is portrayed in Figures 9.21-9.28.

9.8 Conclusions

The fractures that were measured within the Whin Sill and the Stardalur sill cluster can be classified as stratabound because the fractures were confined within the sills. The permeability and porosity of the sills depend on these stratabound fractures - a combination of tectonic fractures and columnar joints. The majority of fractures yield a vertical or sub-vertical orientation, which are interconnected by horizontal or sub-horizontal fractures. This is illustrated on maps of the fracture networks. Graphically, fracture measurements yield two types of distribution: a log-normal distribution for fracture spacings and frequency, and a power-law size distribution for fracture apertures.

Fracture aperture plots along with numerical models demonstrate the cubic law, which shows that the larger apertures conduct the majority of the fluid through the sills and relate directly to flow channelling. For successful fluid movement and storage capacity through the sills, the fractures must be interconnected. This is portrayed in the fracture spacing and frequency histograms. Fracture connectivity also depends on the fracture orientation and size, as well as spatial correlation of the fracture spacing and frequency. Therefore, how these fracture networks grow determines the effectiveness of fluid flow. This growth is dependent on the local stress field at the time of formation, for example tensile stresses would have increased owing to postglacial uplift along the Vøring Margin (Gudmundsson *et al.*, 2002b). To conclude, the connectivity of fractures within otherwise impermeable sills is critical for fluid flow as the fractures provide major conduits for the transport of crustal fluids, including groundwater, geothermal fluids, and hydrocarbons.

Chapter 10: Sills as potential hydrocarbon fractured reservoirs

10.1 Introduction

Four conditions must be satisfied for a petroleum reservoir to form: (1) there must be a suitable source rock in which the hydrocarbons originate, (2) hydrocarbons must be able to migrate out of the source rock and upwards into (3) a reservoir where the hydrocarbons are (4) trapped due to a seal. Of great importance is the quality of the reservoir and the seal. The reservoir quality primarily depends on the permeability and porosity of the reservoir rock, as discussed in Chapter 9 in connection with sills as reservoirs. This is because a reservoir is defined to be a rock body that has the ability to hold and channel hydrocarbons, and thus must have sufficient permeability and porosity.

All types of reservoirs, whether they are sedimentary or igneous or metamorphic, are heterogeneous to some degree. Heterogeneities can be subdivided into primary heterogeneity, secondary heterogeneity and mechanical heterogeneity. Primary heterogeneity is the small-scale difference within a particular lithology, for example minerals present and grain-size variations. Secondary heterogeneity is because of changes within the lithology that relates to diagenesis and tectonic effects. Mechanical heterogeneity is related to variations in pore spaces within the lithology, as well as layering, faults or fractures being present; these heterogeneities can vary on a variety of scales, for example grain size, mineral size and pore spaces to columnar joints, weak contacts and normal faults (Brenner, 2003). It is the mechanical heterogeneities that affect the propagation of hydrofractures, here dykes that become deflected into sills, which have been focused upon in Chapter 5; these include Cook-Gordon debonding, stress barriers and elastic mismatch.

For any seal or reservoir to be apparent there must be a petroleum (or other fluid) source, which tends to be an organic rich horizon, most likely a black shale, as is the case in the Vøring Margin. For hydrocarbons to accumulate within a fractured reservoir a seal is required above the reservoir (in the roof of the reservoir) so that the hydrocarbons cannot migrate out of the reservoir and towards the surface. A

petroleum reservoir within a sill is termed a fractured reservoir, one where the dominant permeability of the reservoir is conducted by horizontal and vertical fractures collectively known as a fracture network (Aguilera, 1995). Huang *et al.* (2009) states that many fractured reservoirs have a fairly high productivity at the start, which gradually decreases thereafter. Here, fractured reservoirs can be classified as: (1) within the sill and (2) within the host rock. To note there are many other types of fractured reservoirs, but only sills and their host rocks are considered here.

A petroleum trap can be defined as a body of rock that arrests the migration of hydrocarbons, which can then accumulate, forming a reservoir that may be exploited. There are two main traps known within the petroleum industry, which are termed a stratigraphic trap and a structural trap. Stratigraphic traps occur where there is a change in permeability and porosity or a change in lithology; these stratigraphic variations are what control the extent of the reservoir. A structural trap is one where there is commonly a concave structure, for example an anticline, which forms due to small scale deformation, and defines the extent of the reservoir. Additionally, a structural trap can be a fault that forms a barrier to the migration of hydrocarbons because of the fault's low permeability after it has been 'healed' and 'sealed' after fault slip (Jahn *et al.*, 2008). As well as a trap there must also be a seal to stop the hydrocarbons from further migration. Seals have a low permeability, and within sedimentary basins they tend to be either a shale or evaporite. An igneous seal tends to have a high density and be unfractured, but due to the geometry of an igneous seal, for example sometimes concave up, there needs to be another barrier, perhaps a normal fault, which has sealed pore spaces by secondary minerals.

Seals naturally develop at the margins of sills and dykes. They exhibit two forms, a chilled selvage and a baked margin (Fig. 10.1). The chilled selvage forms when the magma, with a temperature of ~1100-1300 °C (basic magma), comes into contact with cold host rock in which it is intruded. The magma cools rapidly at the contact, forming a very fine grained margin, also known as a glassy margin. A baked margin refers to a zone where contact (thermal) metamorphism occurs in the host rock, mostly close to the sill contact. Often this margin can be distinguished in the field because of a change in colour and texture of the host rock (secondary mineralisation). Together, these two margins contribute to a zone of low

permeability around the sill, thus these margins can act as good seals and traps for hydrocarbons.

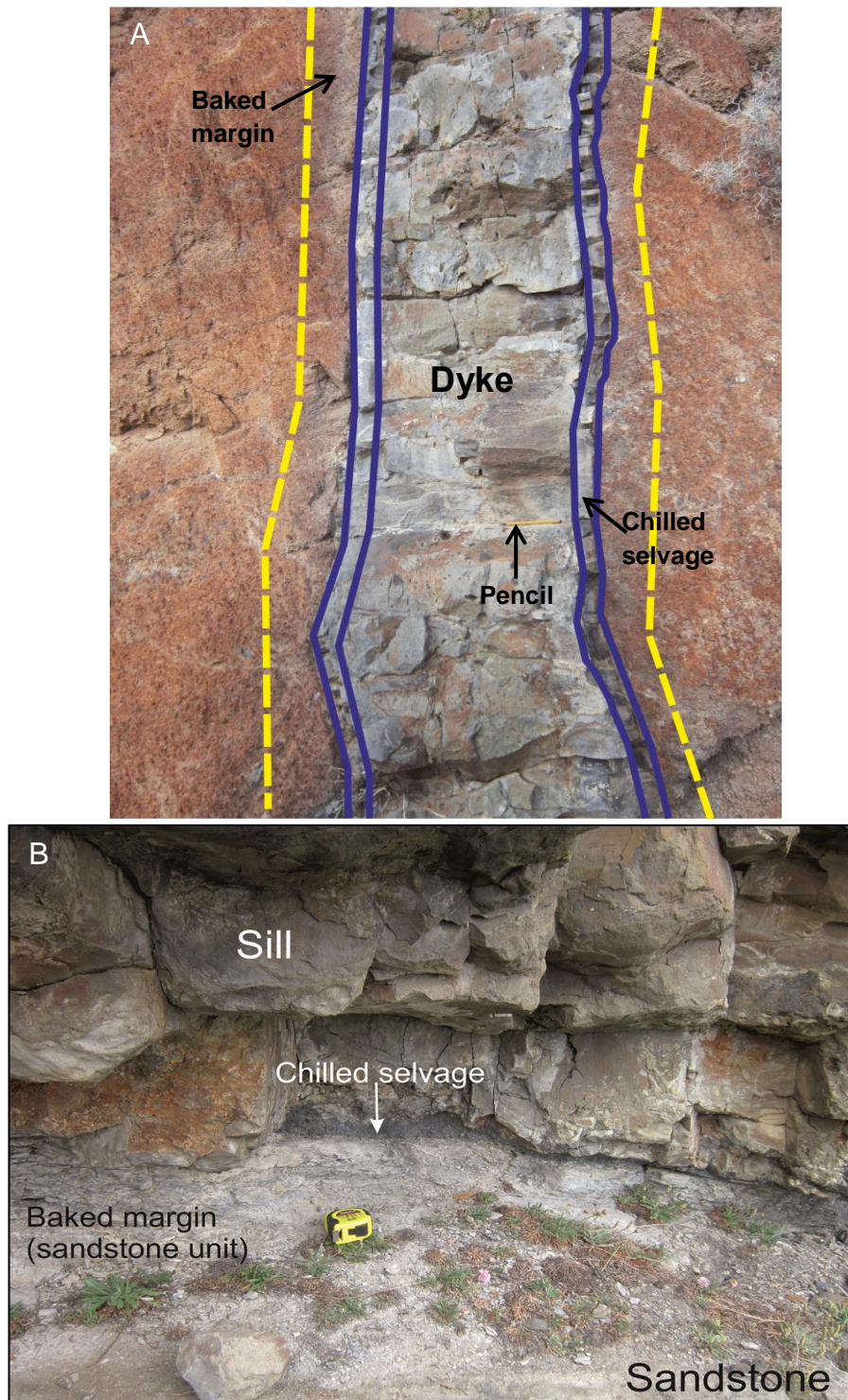


Figure 10.1: Photographs of contact metamorphism indicating the terms chilled selvage and baked margin (A) of a dyke emplaced into hyaloclastite, Anaga Peninsula, Tenerife, Pencil (15cm) for scale, view NE, and (B) underneath the Whin Sill, Cullernose Point, NE England. Tape measure (10cm) for scale, view N.

The maturation and migration of hydrocarbons in sedimentary basins is strongly influenced by petrophysical and thermal perturbations generated by igneous complexes. The heat transfer depends on the temperature and size of the magmatic intrusion and whether the cooling is convective or conductive (Lee *et al.*, 2006). Sill intrusions have significant implications for organic material maturation and hydrocarbon migration, aquifers for groundwater, and climate change because of the release of greenhouse gases from metamorphic aureoles around sills. Overall, sills increase the potential for forming hydrocarbons in sedimentary basins (Schutter, 2003a, b; Menand, 2008; Galland *et al.*, 2009). The thickness, lateral dimensions and temperature of the sill govern the area of hydrocarbon production and not just the regional geothermal gradient (Cukur *et al.*, 2010). Furthermore, volcanism can affect hydrocarbon migration as groundwater is converted to a supercritical state, which is a good solvent for hydrocarbons (Schutter, 2003a; Lee *et al.*, 2006).

Reservoirs associated with igneous rocks are known as unconventional reservoirs and have received little attention in the literature, but are becoming increasingly more important (e.g. Schutter 2003a, b; Wang *et al.*, 2011). Delpino and Bermúdez, (2009) review two different types of unconventional hydrocarbon systems relating to igneous activity: Type I when the igneous intrusion has been emplaced into the source rock, for example carbonate lithologies or black shales, and Type II when the igneous intrusion has been emplaced within another unit of sedimentary strata, in other terms is not the source rock. In the case of the sills in the Vøring Margin (Fig. 10.2), deep seated sills are Type I, emplaced into Lower Cretaceous units, with shallower sills seated above the source rock and possibly acting as Type II. Whether Type I or Type II systems, they can be referred to as being dynamic because they constantly evolve through time and space.

The aim of this chapter is to model the Vøring sills and associated faults in order to investigate the potential for hydrocarbon reservoirs, traps and seals. In Chapters 5 and 6, the mechanics and dynamics of sill emplacement are discussed, and are important to understand as sills yield potential petroleum prospectives within sedimentary basins.

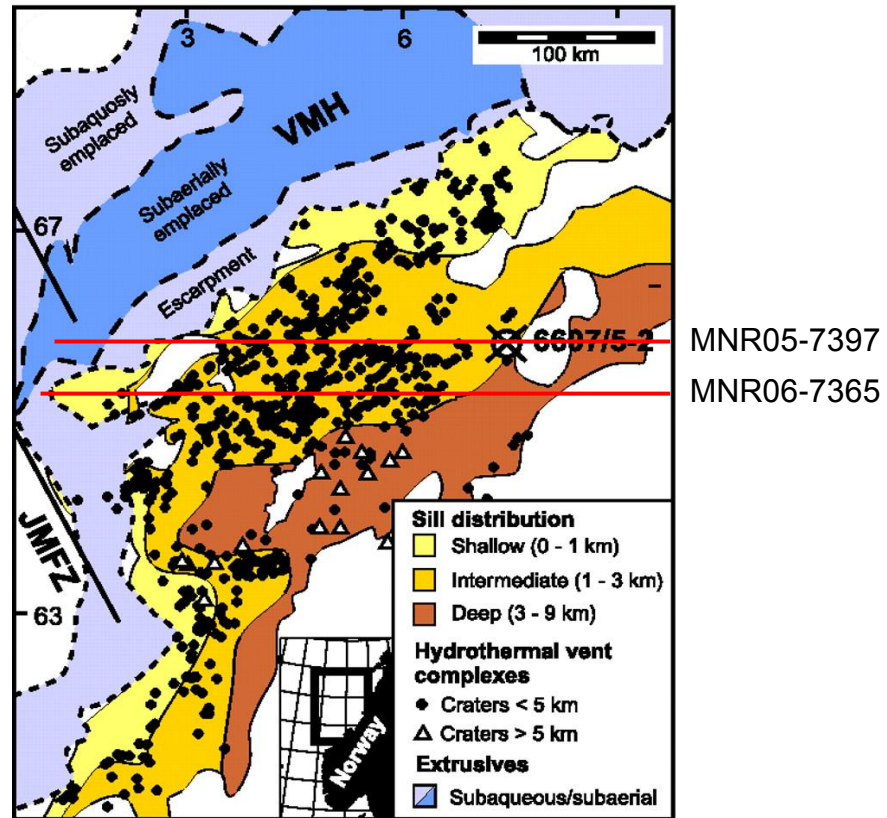


Figure 10.2: Map illustrating depths of sills and their associated hydrothermal vents in the Vøring Basin, highlighting the location of seismic lines MNR05-7397 and MNR06-7365. Brown colour for Type I system and Yellow/orange colours for Type II system (Svensen *et al.*, 2010).

10.2 Numerical models of solidified sills

Several simple models were applied to explore the conditions for seal rupture. First a concave up sill geometry was used, as this is a common geometry exhibited in the Vøring Margin, emplaced at 4 km depth. Then a more complex geometry was taken of sill 5 from the 3D cube, NH0202 (Fig. 10.3). The set-up of these models were kept the same: the sill is modelled to be much stiffer at 20 GPa, than that of the shale host rock at 0.01 GPa (young and soft shale; Gudmundsson, 2011a) and was run in a stationary framework: (1) extensional regime, 5 MPa and (2) compressional regime, 5 MPa (Fig. 10.3). The mesh quality for each of the models was the same with a maximum element size of 0.5 km and a minimum element size of 100 m.

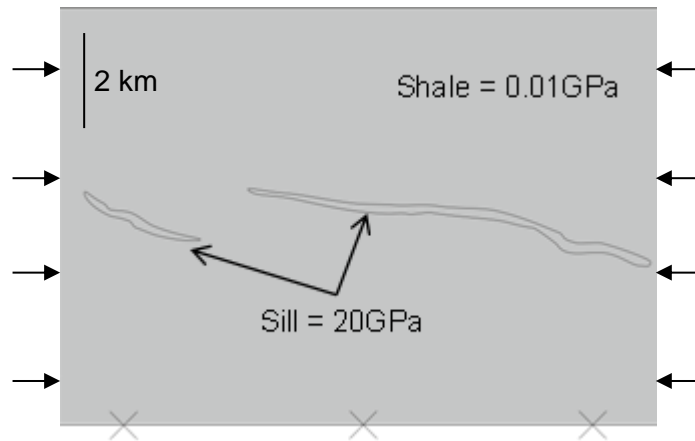


Figure 10.3: Model set-up of sill 5. The sill has a Young's modulus of 20 GPa and density 2600 kg/m^3 , emplaced within a soft host rock, shale with Young's modulus of 0.01 GPa and density 2300 kg/m^3 . External loading (arrows along model sides) is applied parallel to the model at 5 MPa in a compressional regime, while the bottom of the model is fixed (x's) and the top of the model a free surface (the sea bottom). This set-up is also true of the concave up sill models with an additional external loading of 5 MPa in extension (arrows are rotated 180°).

10.2.1 Extensional tectonic regime

Under an extensional tectonic regime (Fig. 10.4), tensile stresses are concentrated within the sill. Figure 10.4 shows that the tensile stresses are concentrated at the upper margin of the sill. This indicates that the upper margin is subject to rupture, while the lower margin remains intact. In this scenario the base of the sill would act as a seal towards upward migrating hydrocarbons. However, due to the concave upward geometry of this sill a secondary barrier would be needed, for example a dyke or a tight fault that has been 'healed' and 'sealed' and is not subject to reactivation. This barrier would need to be located at the tips of the sill in order to prevent the hydrocarbons continuing on a vertical migration path to shallower depths within the crust. The concave upward geometry of the sill itself though, may act as a trap, for example a straight or concave downward sill and will be illustrated in the next sub-section.

10.2.2 Compressional tectonic regime

When the sill is subject to a compressional tectonic regime (parallel with the lateral dimensions of the sill, Fig. 10.5), tensile stresses are concentrated around the margins of the sill. Figure 10.5 shows that the most likely location of fracturing is

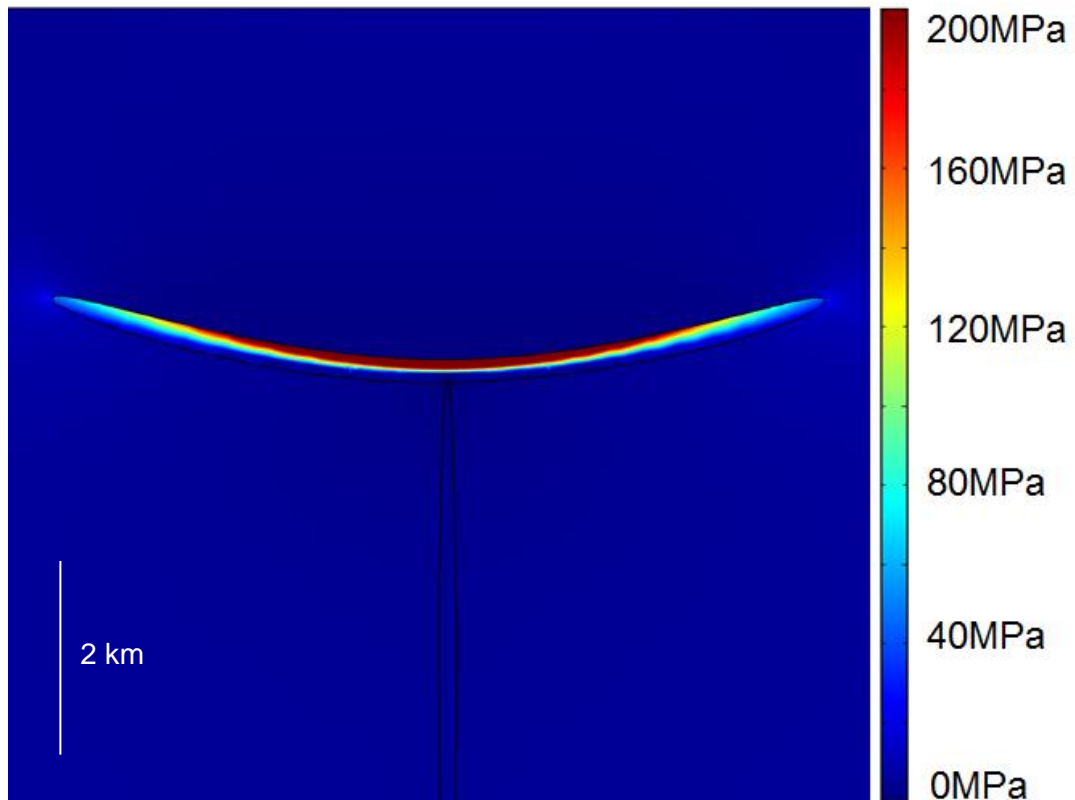


Figure 10.4: FEM model of tensile stress contours around a concave up sill that is subject to extension. Dyke is assumed to be at the centre of the sill. High tensile stresses (red) on the upper margin show where the sill is likely rupture, while the low tensile stresses (dark blue) along the lower margin show that the sill margin will remain intact.

along the lower boundary (because of the high tensile stress concentrating there) allowing the upward migrating hydrocarbons to accumulate within the sill. In this scenario the sill may act as a potential fractured reservoir because the upper margin remains intact to form a seal. Also, in this model there is a small area of tensile stresses, 20-40 MPa, within the dyke, highlighting possible tension fracture formation.

Sill 5 was also run in a compressive stress owing to ridge-push present offshore Norway today (Fejerskov and Lindholm, 2000; Fejerskov *et al.*, 2000; Hicks *et al.*, 2000; Lindholm *et al.*, 2000). The results in Figure 10.6 can be analysed in terms of the lower sill and the upper sill. The lower sill ruptures along its lower margins. Therefore, hydrocarbons could accumulate within the sill allowing it to function as a possible fractured reservoir, because the upper margin remains intact to form a seal. The upper sill on the other hand, has a more complex geometry, and on first

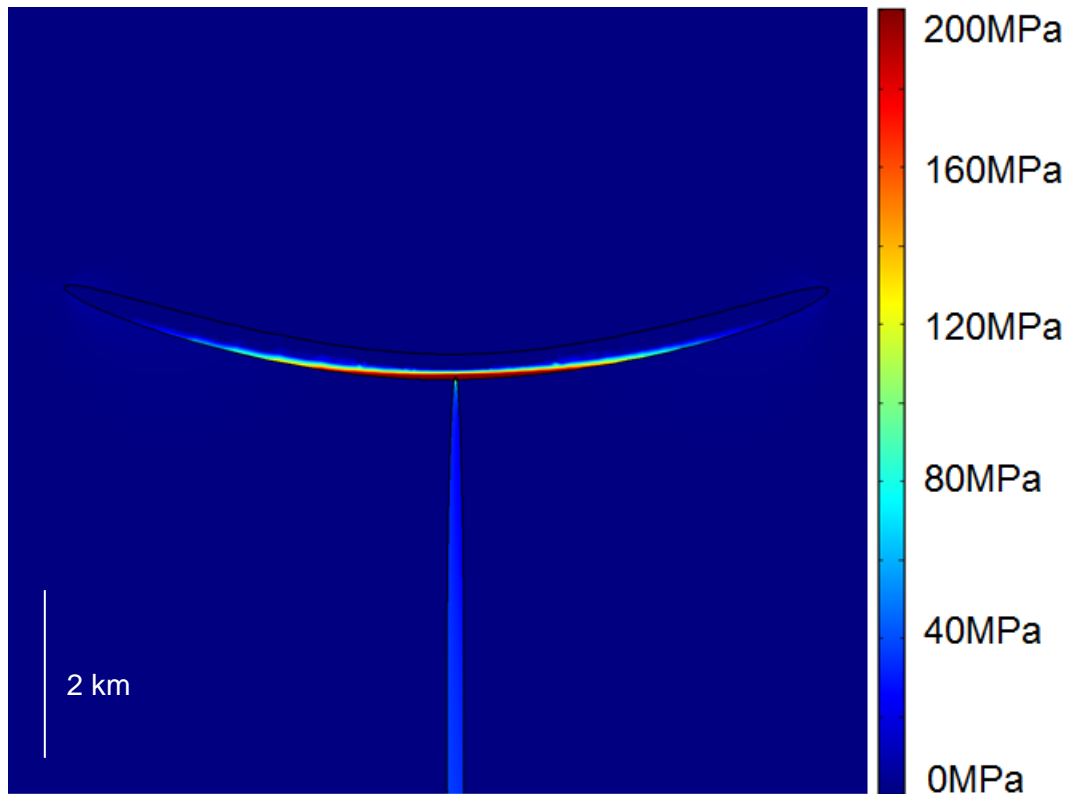


Figure 10.5: FEM model of tensile stress contours around a concave up sill that is subject to extension. Dyke is assumed to be located at the centre of the sill. High tensile stresses (red) along the lower margin shows where the sill is likely to rupture, while the low tensile stresses (dark blue) along the upper margin show that the sill margin will remain intact.

inspection would act neither as a seal or trap or fractured reservoir as both the upper and lower margins are ruptured at certain localities. However, the addition of secondary barriers that may be a dyke, for example (not seen on seismic lines) can aid in interpreting the location of reservoirs. With these secondary barriers, parts of the sill could act as a possible fractured reservoir, while other parts function as a seal and trap mechanism. Between the two barriers a hydrocarbon reservoir may form in the host rock, trapped by the concave down geometry at this point along the sill, and the impermeable nature of the barrier. The part of the sill closest to the lower sill may function as a fractured reservoir because the lower margin of the sill is ruptured allowing the hydrocarbons to migrate within. The effects of buoyancy would cause the hydrocarbons to migrate up towards the tip of the sill and accumulate, because the upper margin of the sill remains a seal. On the other hand, the other tip (towards the right hand side of the model) of this upper sill would allow hydrocarbons to migrate in as the lower margin is ruptured. However, because of buoyancy,

hydrocarbons would continue on an upward trajectory and out of the sill (above the secondary barriers) as a result of the rupture of the upper margin causing it to no longer function as a seal. This result is only an interpretation and has not been verified by field results.

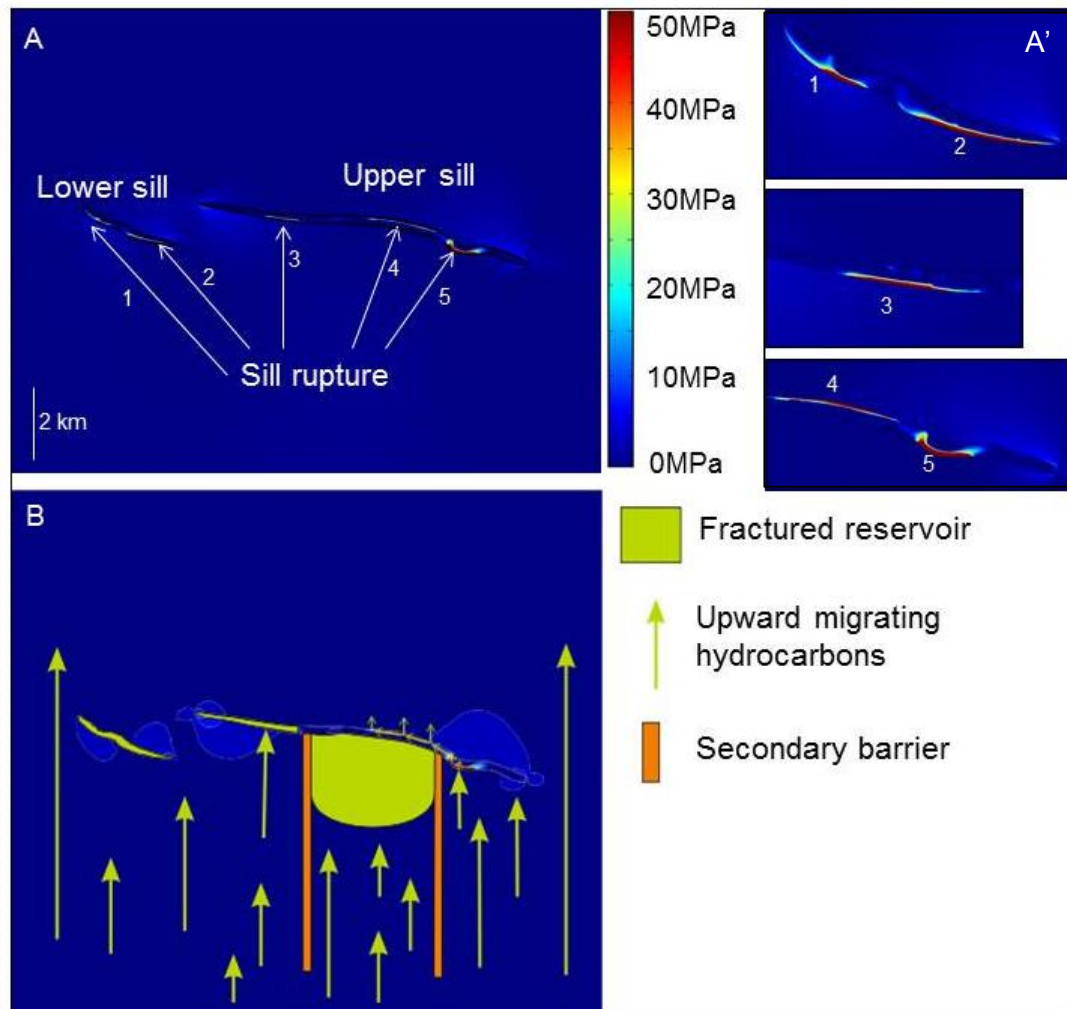


Figure 10.6: (A) FEM model of sill 5 representing tensile stress contours. Indicated are zones of rupture. (B) Schematic illustration based on the numerical results in (A) highlighting areas of hydrocarbon accumulation. Refer to text for description. Numbers 1-5 on the arrows in (A) represent areas of zoom in (A').

Figure 10.6 is run in a homogeneous medium, but results and interpretations of fractured reservoirs may be enhanced in a heterogeneous medium. We know from well data in the Vøring Basin (Svensen *et al.*, 2010) of the presence of a sandstone layer, which may act as a fractured reservoir itself or as a seal depending on its

permeability. This relies on the cementation of quartz and authogenic clays. The well data will be discussed later on in this chapter.

10.3 Modelling of sills and faults in the Vøring Margin

The modelling of sills and faults in this section is based on the interpretation of two seismic lines (MNR05-7397 and MNR06-7365), with locations shown in Figure 10.7. Each of the lines was divided to give an accurate overview of the sill and fault geometries (Figs. 10.8 and 10.9). Information was provided on interpreted horizons from these seismic lines, but was unable to be modelled as these horizons comprised of many lithological units that were undetermined. However, from the Utgard well 6607/5-2 (Svensen *et al.*, 2010) these lithological units of sandstones and shales are recognised. The well shows that the sills are emplaced in shale units only, and therefore the sills are modelled within a homogenous medium of shale.

As illustrated in the above section, the effects of the local stress field and varying mechanical properties of the host rock determine whether or not sills act as fractured reservoirs or as seals and traps. Here, different types of tectonic loading versus varying mechanical properties (Young's modulus) were added into a time-dependent model providing quasi-static models. The various types of loading are likely to have a cumulative effect on the rupture of the sill margins and hence need to be taken into account. The outline of the numerical models is set out in Figures 10.8 and 10.9, where the base of the model is fixed, the top (the sea bottom) remains a free surface and tectonic loading is applied in the horizontal direction. The parameters for these models are set out in Table 4.1, with the faults having a constant Young's modulus of 1 GPa. The mesh for each of these seismic lines is the same with a maximum element size of 0.01 km and a minimum element size of 1×10^{-4} km. From comparing lines MNR05-7397 (Fig. 10.8) and MNR06-7365 (Fig. 10.9), it can be seen that there are larger, more extensive sill complexes in MNR05-7397. Therefore, line MNR05-7397 offers a higher possibility for these sills to act as seals or fractured reservoirs.

Perhaps the most important factor as to whether the sill complexes in the Vøring Margin would act as fractured reservoirs or as seals and traps is the timing of the hydrocarbon migration. In order for the sill complexes to act as seals and traps they

must have been emplaced and solidified prior to hydrocarbon migration. However, determining the time of migration is rather complex. The age of the sills in the Vøring area are approximately 55-56 Ma (Svensen *et al.*, 2010), and would have cooled in less than one thousand years (in accordance with $t \approx 0.0825.w^2$ (Jaeger, 1957), where w is approximately 100 m, taken from well data (Svensen *et al.*, 2010) and t is in years).

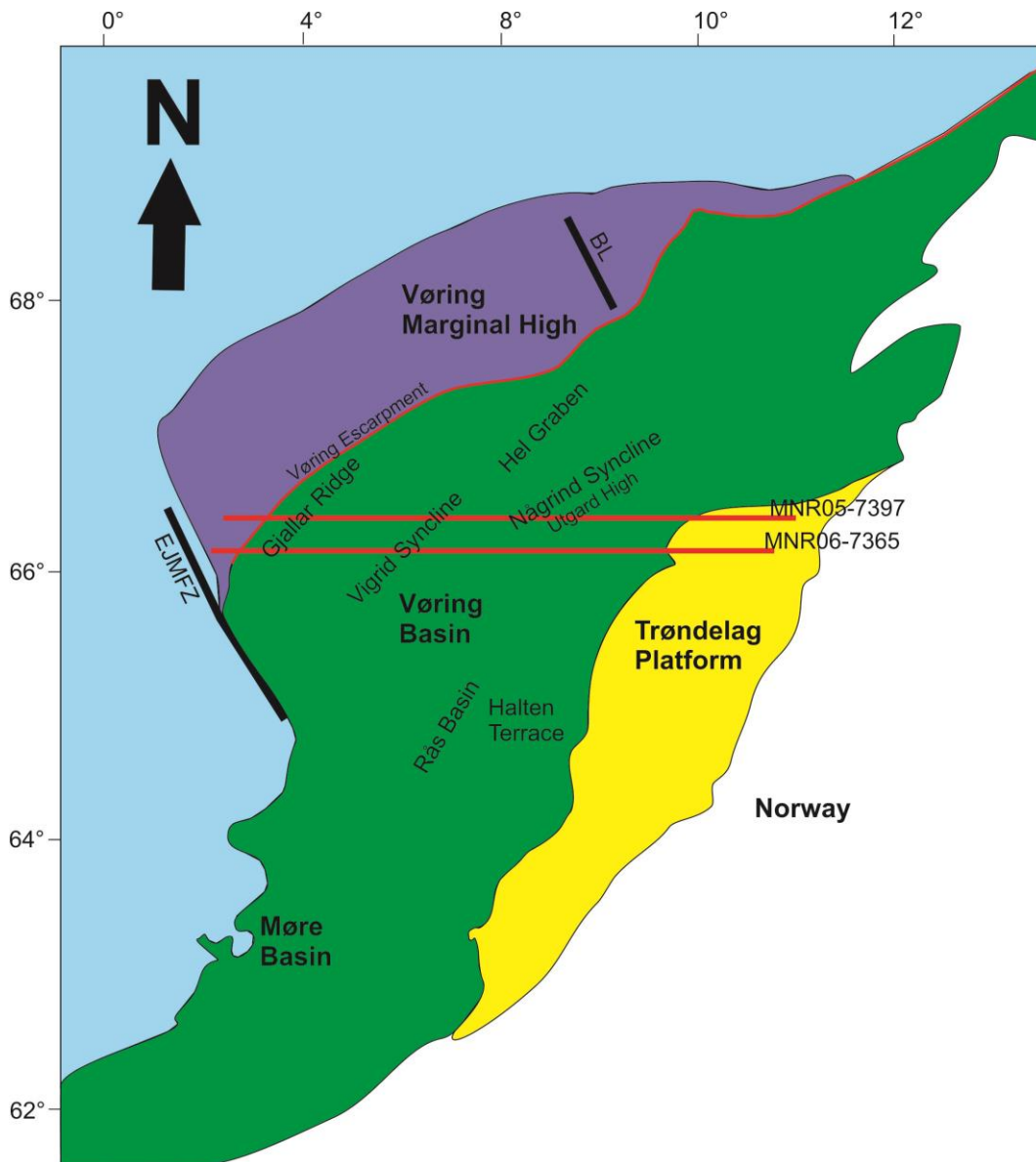


Figure 10.7: Schematic illustration offshore Norway showing the location of seismic lines MNR05-7397 to the north, and MNR06-7365 to the south in the Vøring area (redrawn from Fjeldskaar *et al.*, 2008).

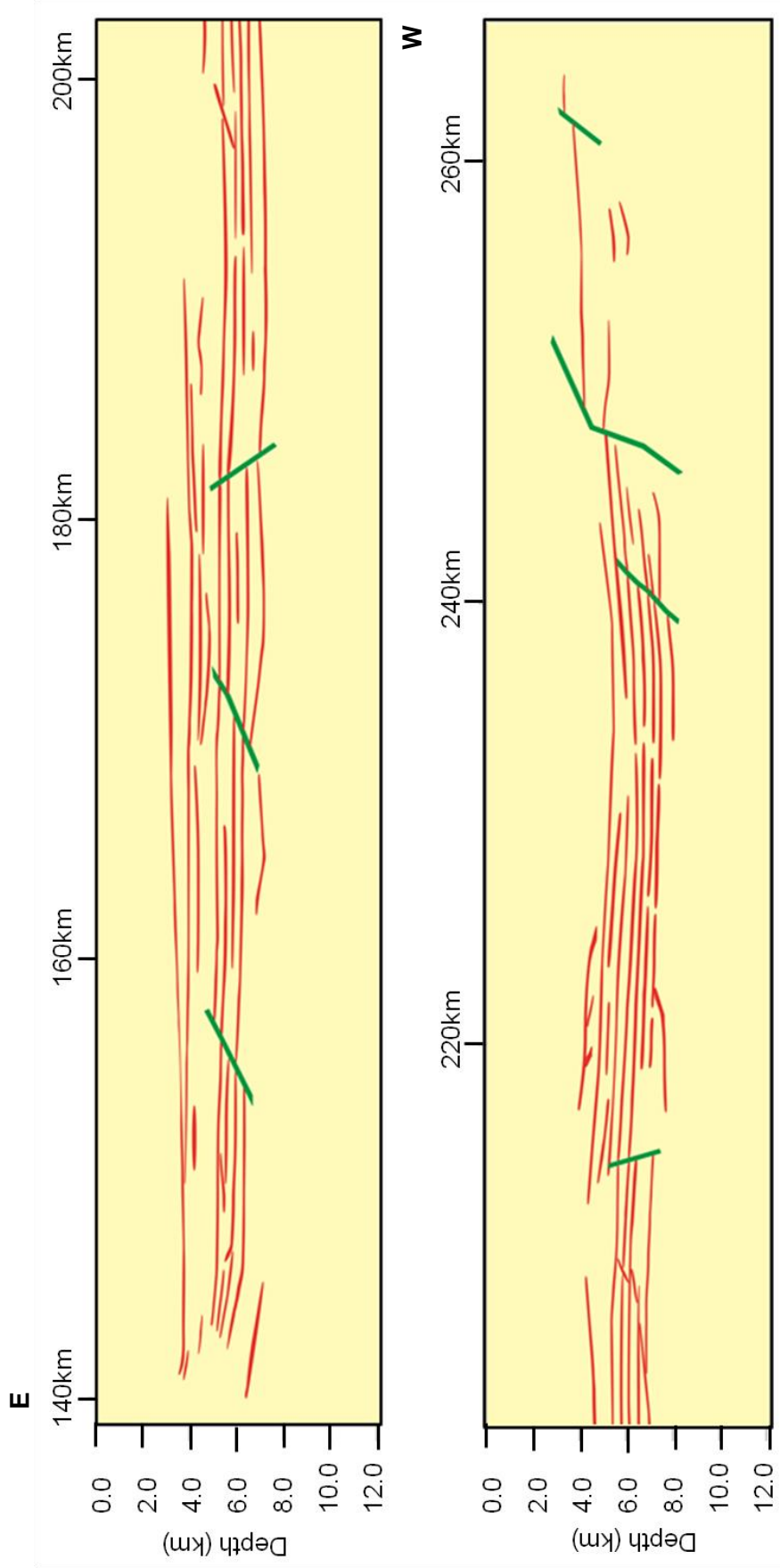


Figure 10.8: Schematic illustration of line MNR05-7397 where sills are mapped out in red and faults in green, in a shale host rock. Location of cross section in Figure 10.7. The orientation of this cross section is east, at 140km, to west, at ~270km.

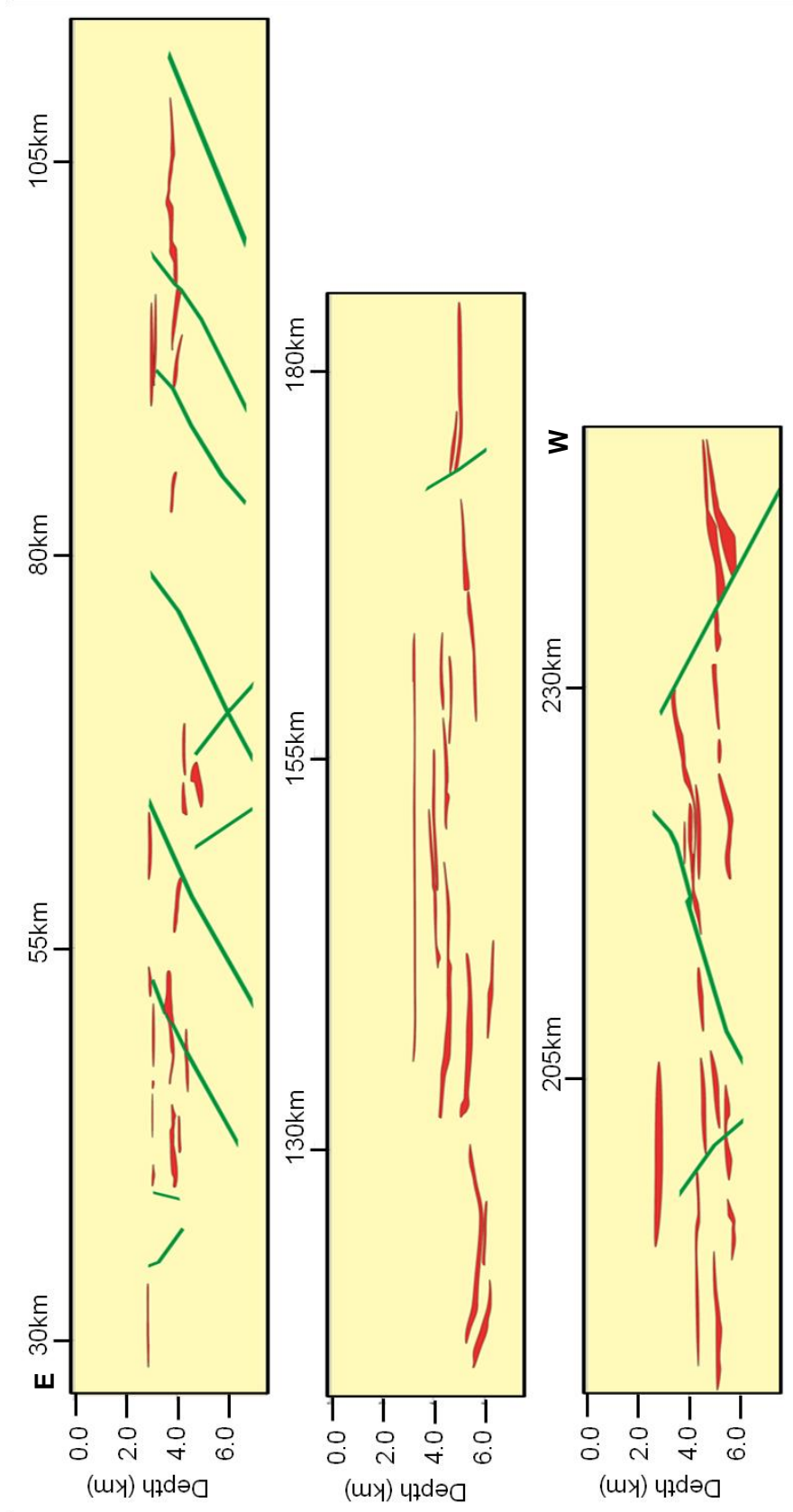


Figure 10.9: Schematic illustration of line MNR06-7365 where sills are mapped out in red and faults in green within a homogeneous shale host rock. Location of cross section in Figure 10.7. The orientation of this cross section is east, at ~25km, to west, at ~140km.

The numerical results show both the tensile stress and shear stress. To best represent these stresses, there are different scale bars that are dependent on each time frame, because in certain time frames stresses are very low (e.g. <1 MPa), and in others much larger (e.g. <50 MPa). Sills worldwide are subject to stress changes as a result of loading during and post emplacement relating to tectonic stresses. Here, the aim of the time-dependent modelling is to see the stress effects in and around sills during different tectonic loading events after emplacement.

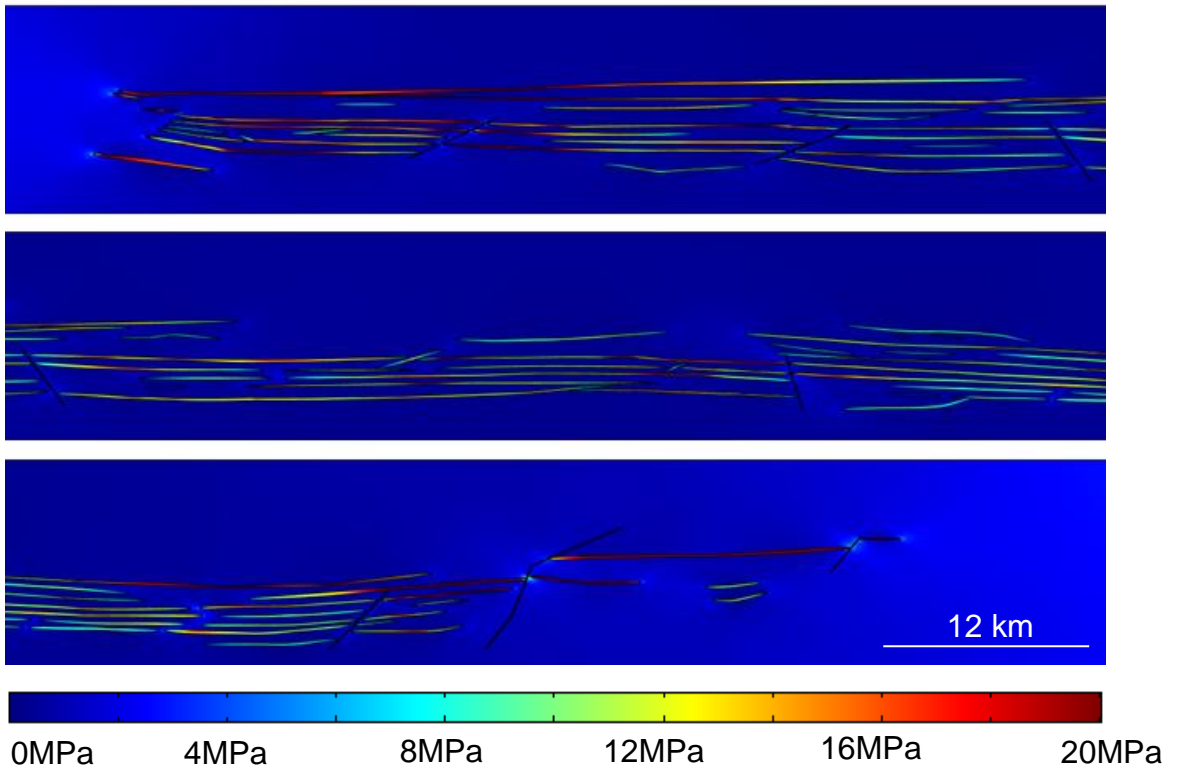
From first inspection of the mechanical properties shown in Table 4.1 it can be seen that the sills in the Vøring Margin are stiffer than the shale host rock. Consequently, tensile stresses would concentrate around and within the sills themselves, and the geometry of the sills would largely influence the location of these stresses.

10.3.1 Line MNR05-7397

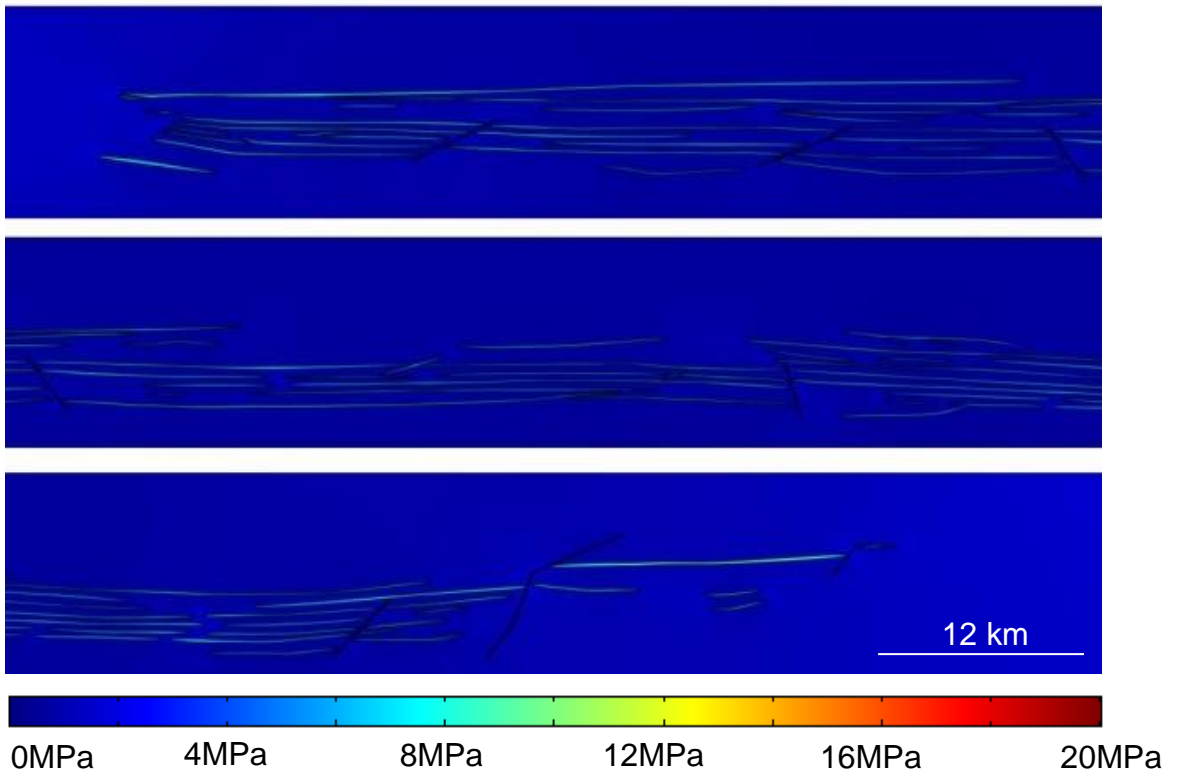
Two differing stress patterns can be seen in Figure 10.10: (1) concentration of tensile stresses within the sills at 56 Ma and 46 Ma and contrastingly, (2) concentration of tensile stresses around the margins of the sills from 36 Ma to present. At 56 Ma, tensile stresses range between 8 MPa and 20 MPa, which indicate the formation of tectonic fractures. These stresses relax at 46 Ma to <4 MPa, as at this time the shale is stiffer, thus there is a smaller contrast in stiffness between the sills and the host rock.

The sills situated along this line are extensive, with lateral dimensions greater than tens of kilometres, and have large mechanical interactions as illustrated by the high tensile stresses when $T = 36$ Ma to present (Fig. 10.10). The compressive stresses are concentrated about the tips of the sills, <0.1 MPa, and also on interaction with the faults. The concentration of stresses with regards to faults, for example, can be seen at $T = 36$ Ma where tensile stresses in the order of 20 MPa are distributed inside the fault, and at $T = 16$ Ma where tensile stresses in the order 1 MPa are concentrated around the fault. There is no concentration of tensile stresses around the lower margins of the sills and therefore, the sill would not function as a fractured reservoir. Hydrocarbons could migrate however, towards the tips of the sills where there are an increased number of tension fractures (formed by an increase in tensile stress) and

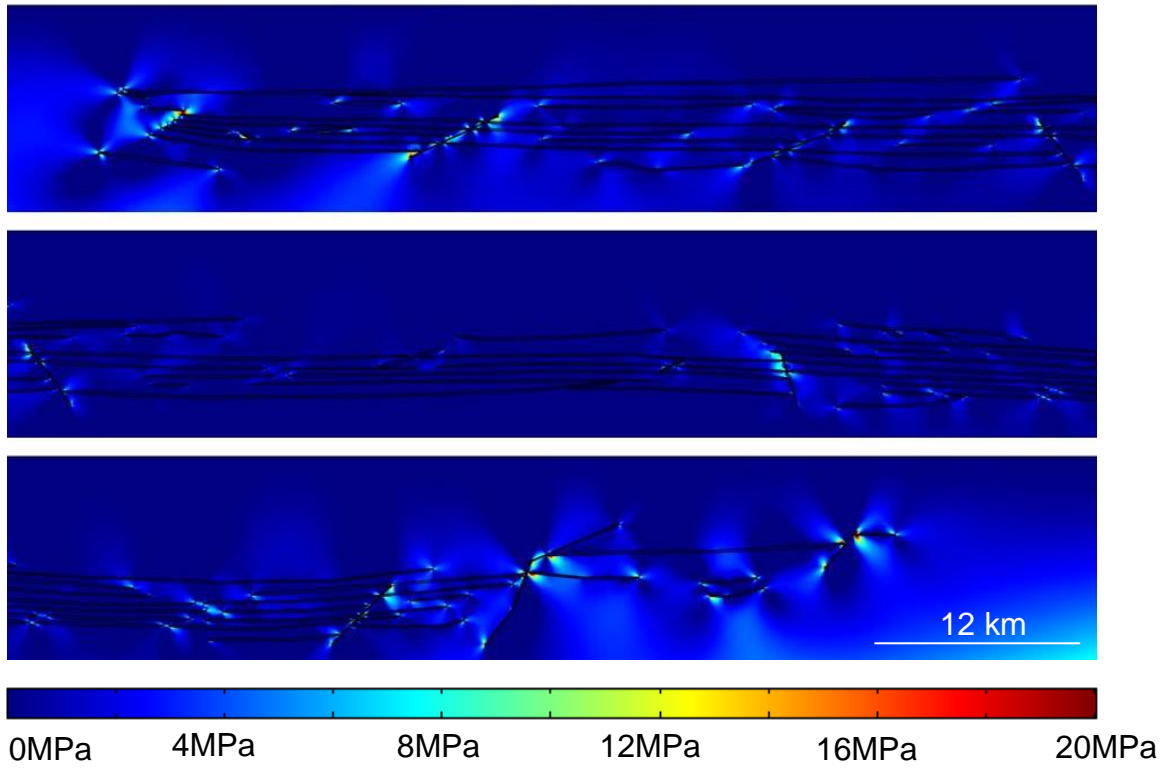
T=56Ma



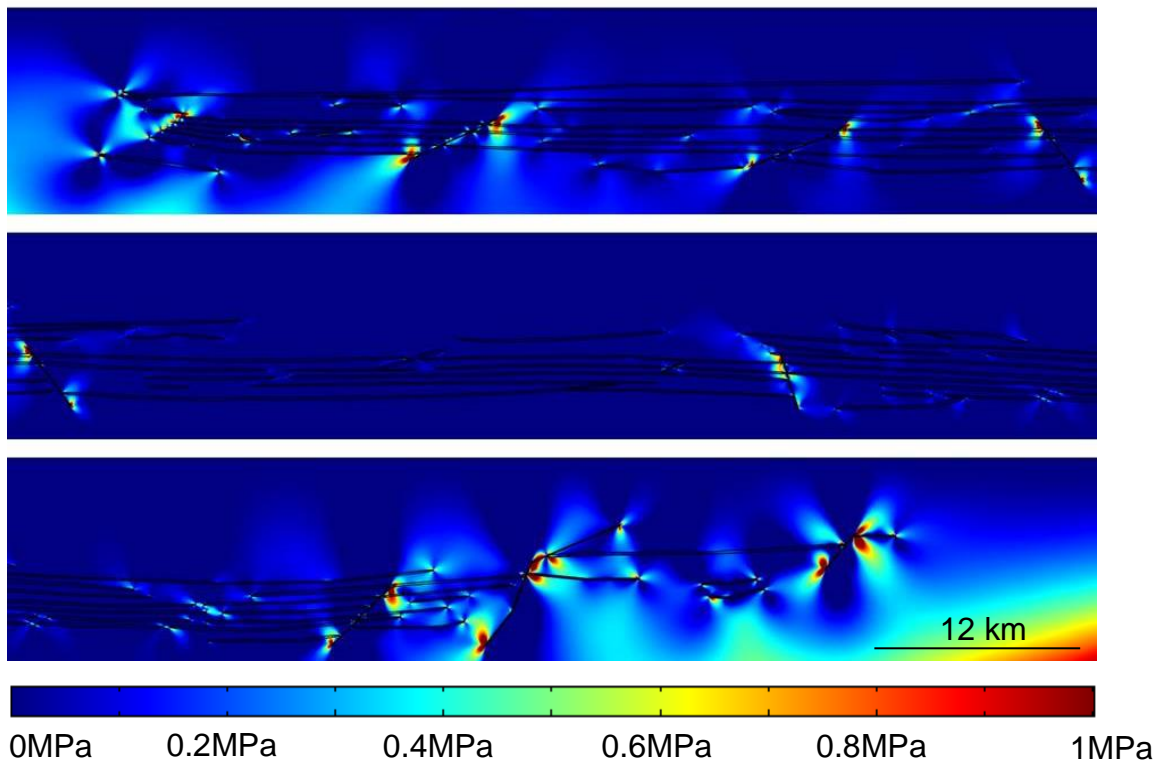
T = 46 Ma



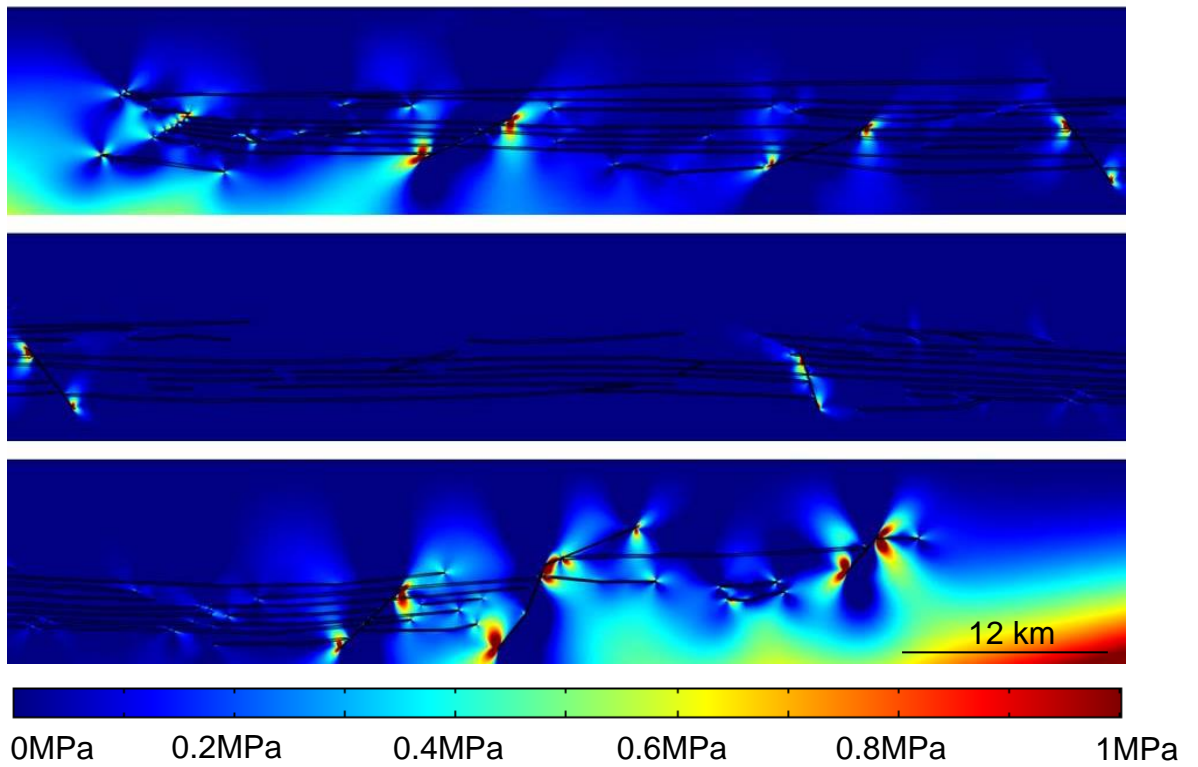
T = 36 Ma



T = 26 Ma



T = 16 Ma



T = 0Ma

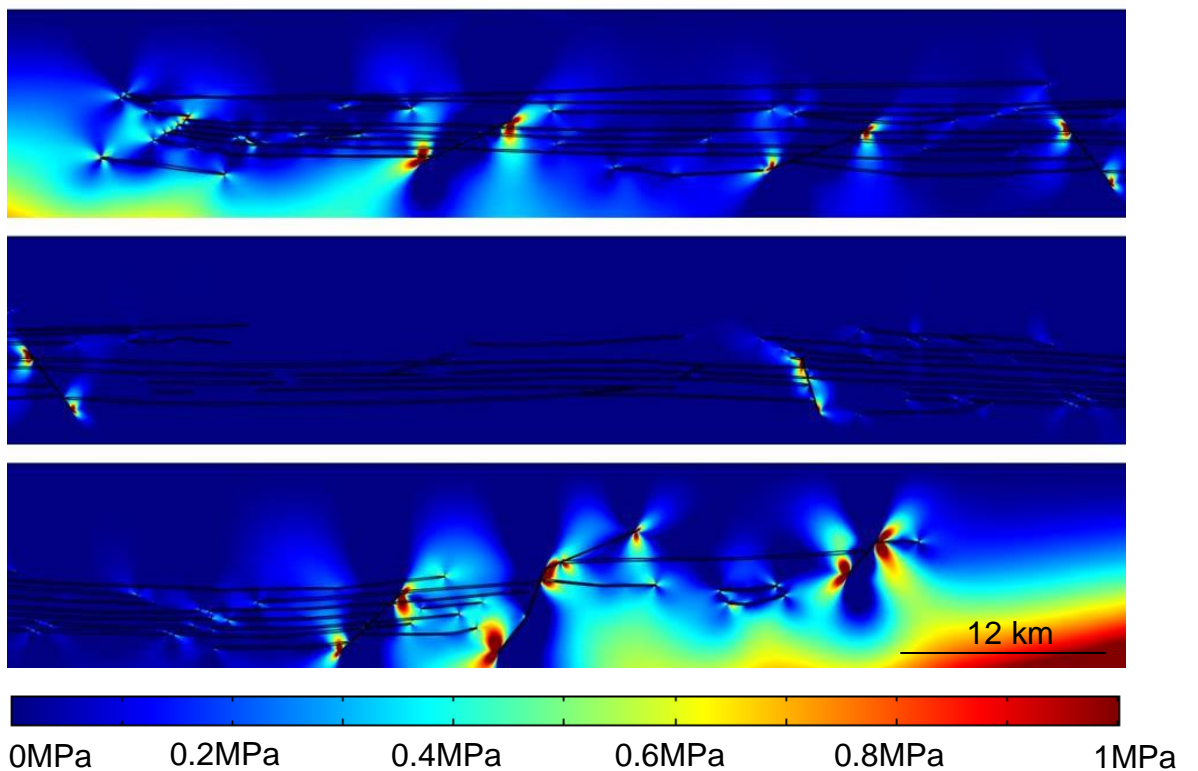


Figure 10.10: Line MNR05-7397. FEM models of tensile stresses represented by colour contours from a time sequence of 56 Ma to present. Model parameters described in Table 4.1 and model set-up illustrated in Figure 10.8. See text for model description.

form a fractured reservoir. Also, there is the possibility of fractured reservoirs forming in between the sills to the overlying sill because of induced stresses and will be discussed in later sections. Also, at 26 Ma to present, there is an increase in the stresses as a result of ridge push.

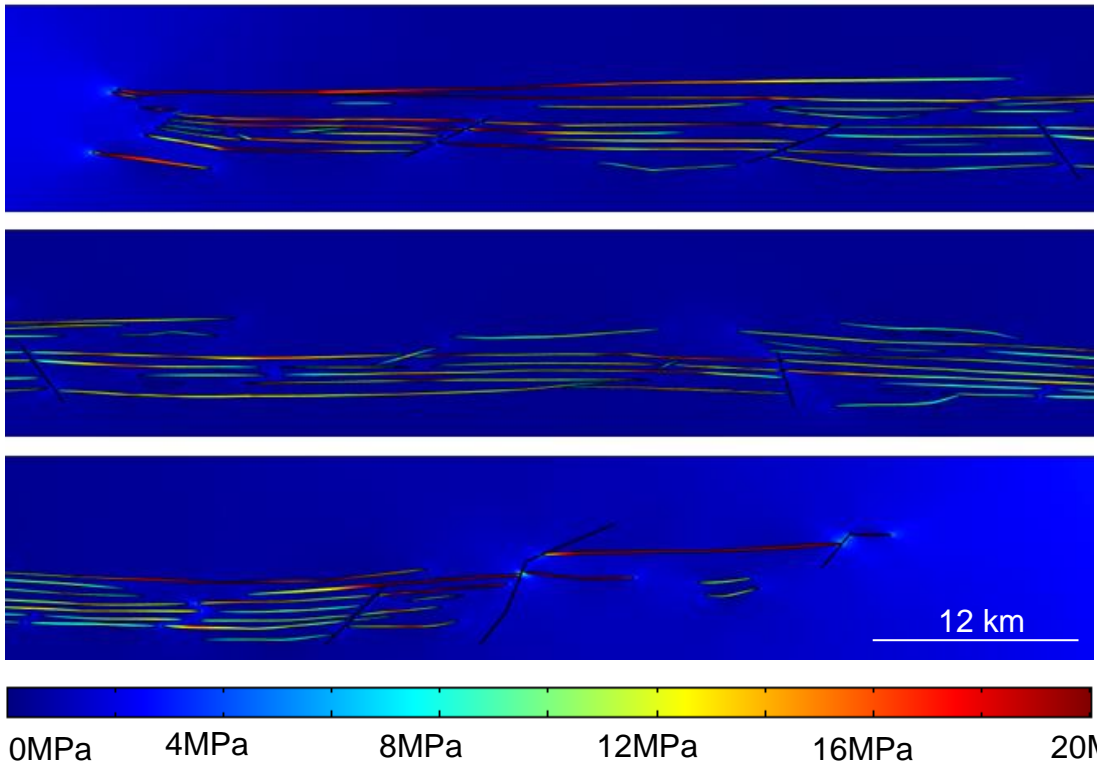
Figure 10.11 shows the concentration of shear stresses within the sills themselves. The largest shear stresses, >20 MPa, are generated in the first time frame when the sills are young. With the next ten million years, the shear stresses are relaxed to <10 MPa and yet again up until present, where the maximum shear stress is approximately 3 MPa. These shear stress concentrations represent the formation of shear fractures and possible small faults within the sills, where movement would be parallel to the fracture walls.

10.3.2 Line MNR06-7365

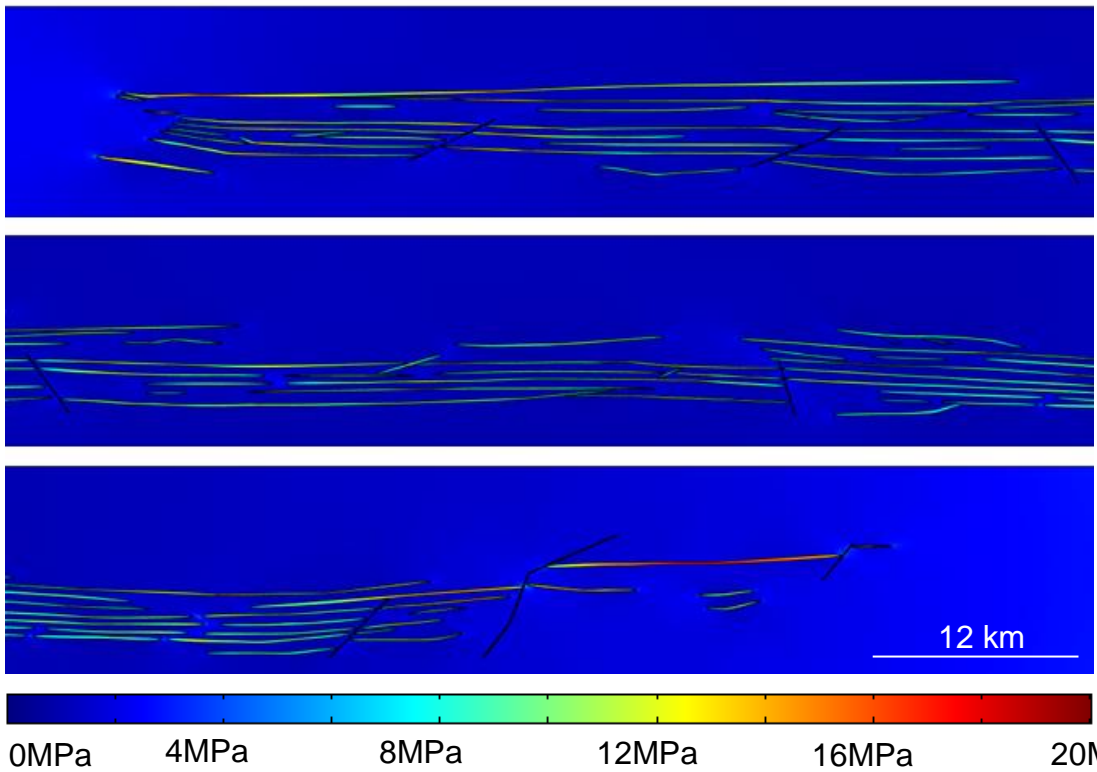
In comparison to MNR05-7397, the sills are far less extensive, but there are more interpreted faults present. General stress distributions were similar between the two lines. Figure 10.12 shows the distribution of tensile stresses from 56 Ma to present. In an extensive regime, in the first three time steps, the concentration of tensile stresses are within the sills, with the majority of the stresses <50 MPa. However, in the subsequent three time steps the tensile stresses are located mainly around the sills, and at 26 Ma within the shale host rock. These tensile stresses represent the formation of tension fractures either within the sill itself or in the host rock. Faults also have a small tensile stress concentration within them, for example $T = 16$ Ma, resulting in (1) increased permeability, and (2) possible fault reactivation.

Figure 10.13 shows the distribution of shear stresses, which is less than the distribution of tensile stresses. In an extensive regime ($T = 56-36$ Ma) the shear stresses are generally distributed in the sills themselves, with minimal shear stresses concentrated at the sill tips. At the start and near the end of this line, the shear stresses are significantly larger than in the middle of line. In a compressive regime ($T = 26-0$ Ma) shear stresses are concentrated also in the host rock and is especially high at 26 Ma (>2 MPa), when the tectonic regime reverses. The distribution of these shear stresses within the sills and host rock represent the reactivation of fractures, where fractures may link-up, increasing the permeability. These will be highlighted within the next sections.

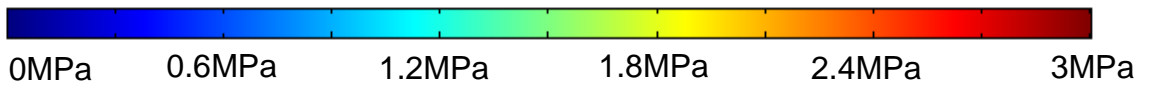
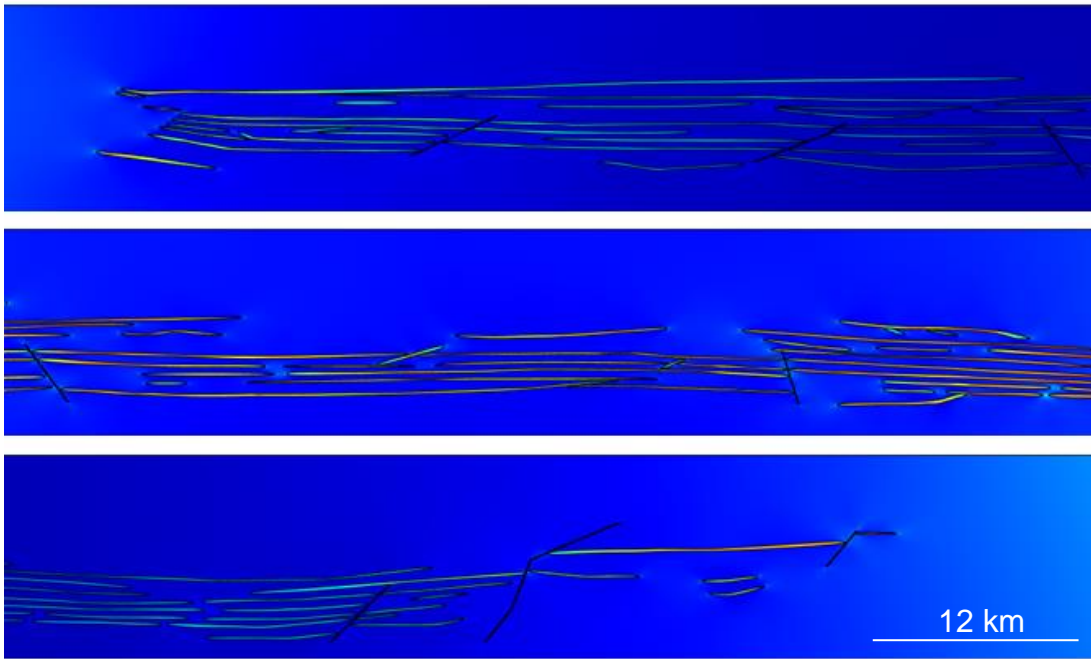
T=56Ma



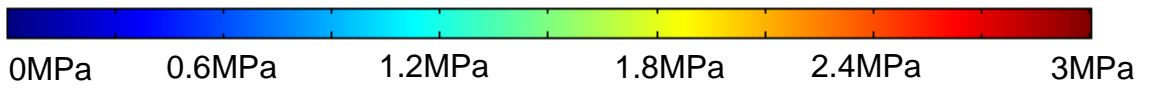
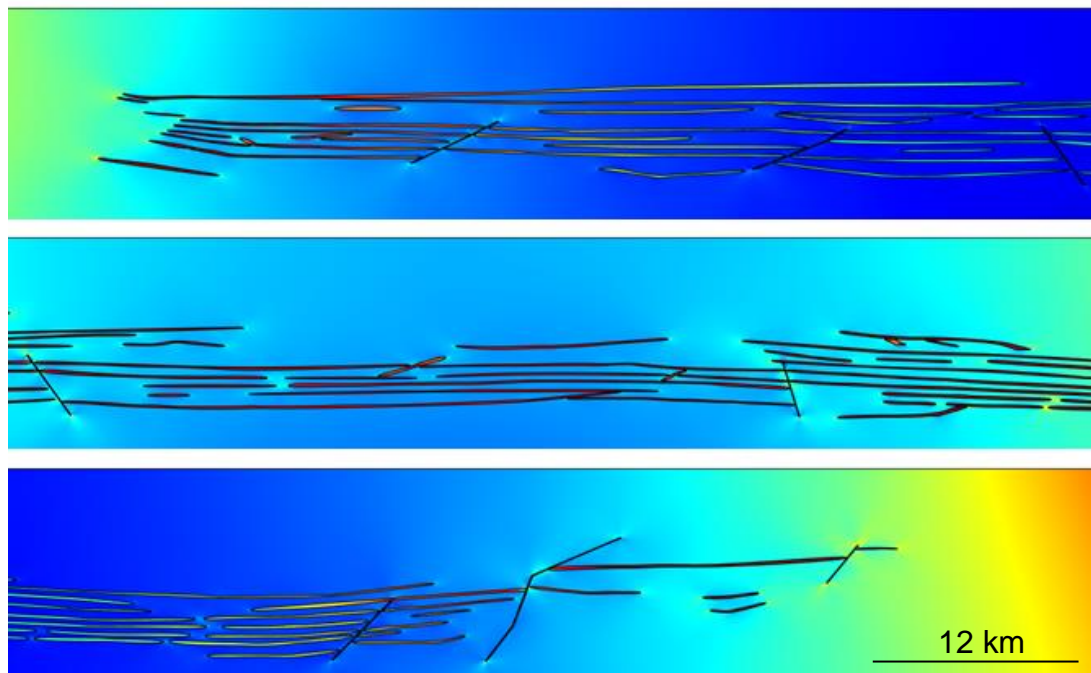
T=46Ma



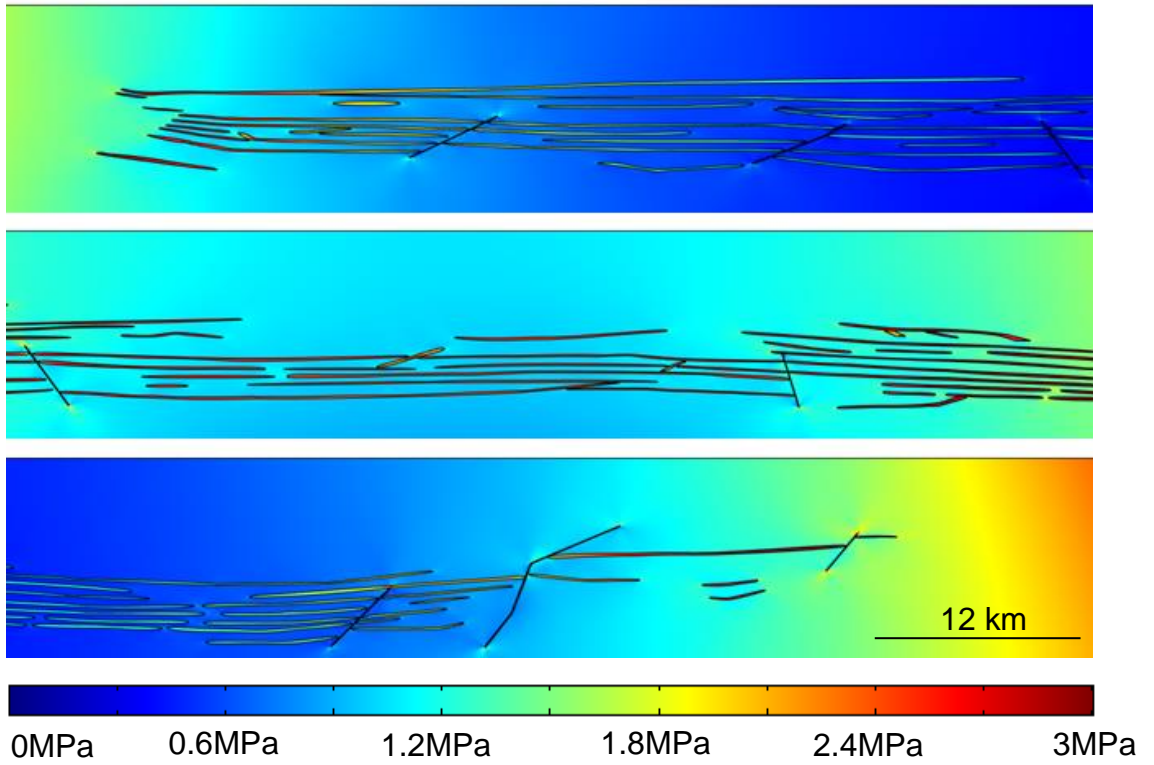
T=36Ma



T=26Ma



T=16Ma



T=0Ma

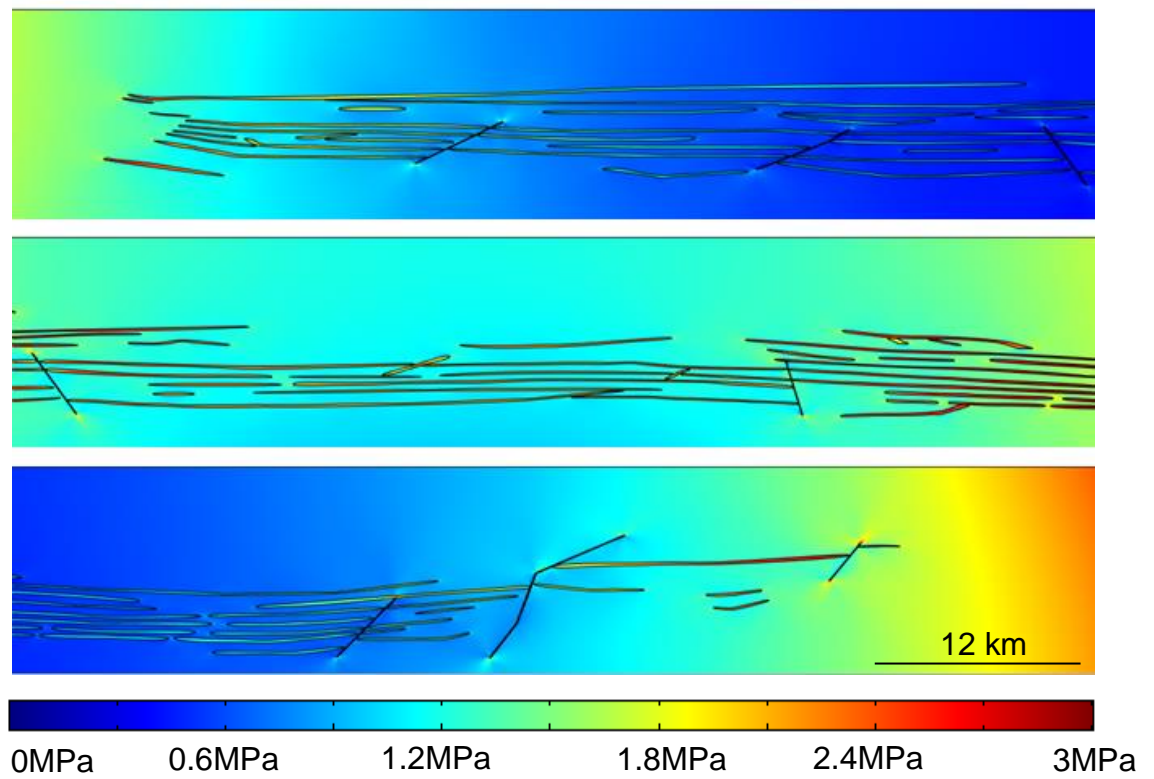
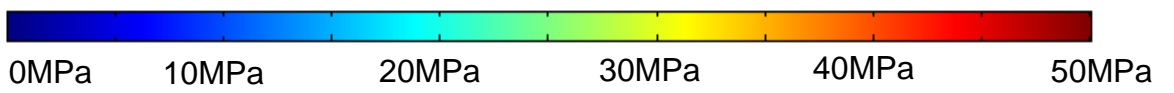
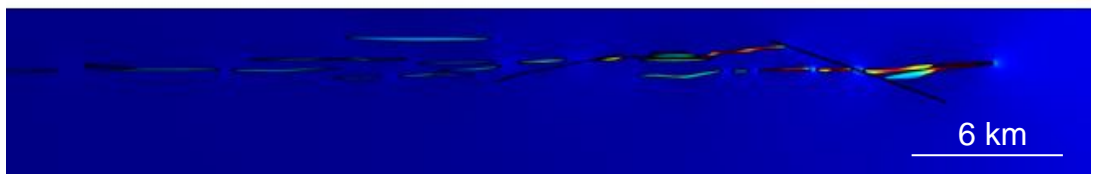
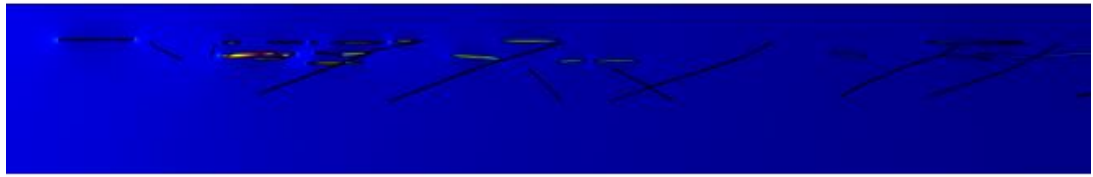
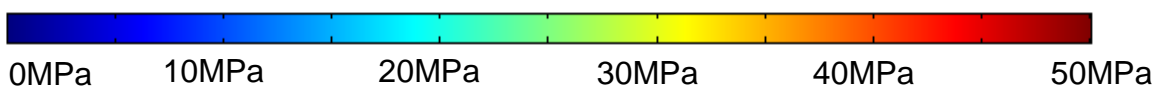
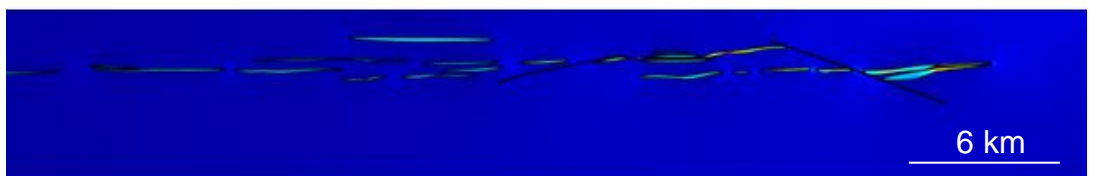
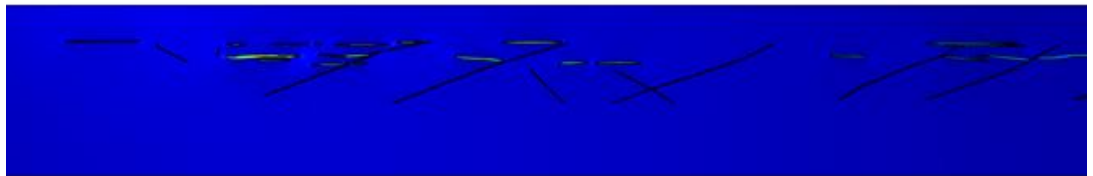


Figure 10.11: Line MNR05-7397. FEM models of shear stresses represented by colour contours from a time sequence of 56 Ma to present. Model parameters described in Table 4.1 and model set-up shown in Figure 10.8. See text for model description.

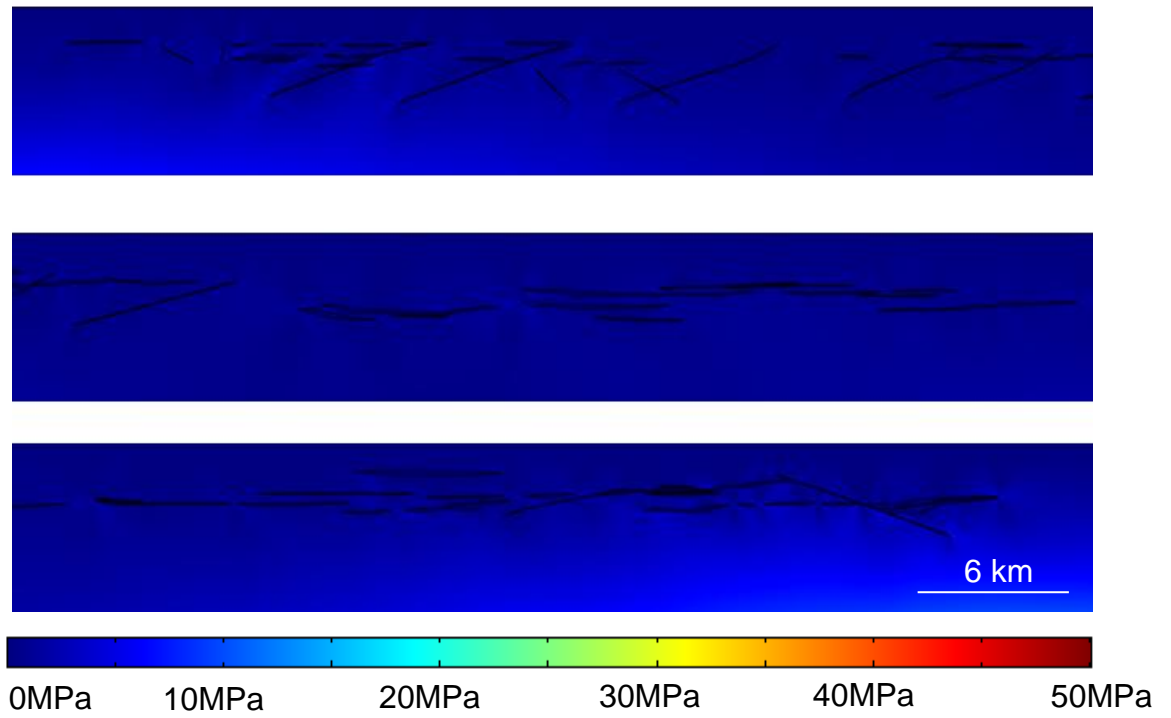
T=56Ma



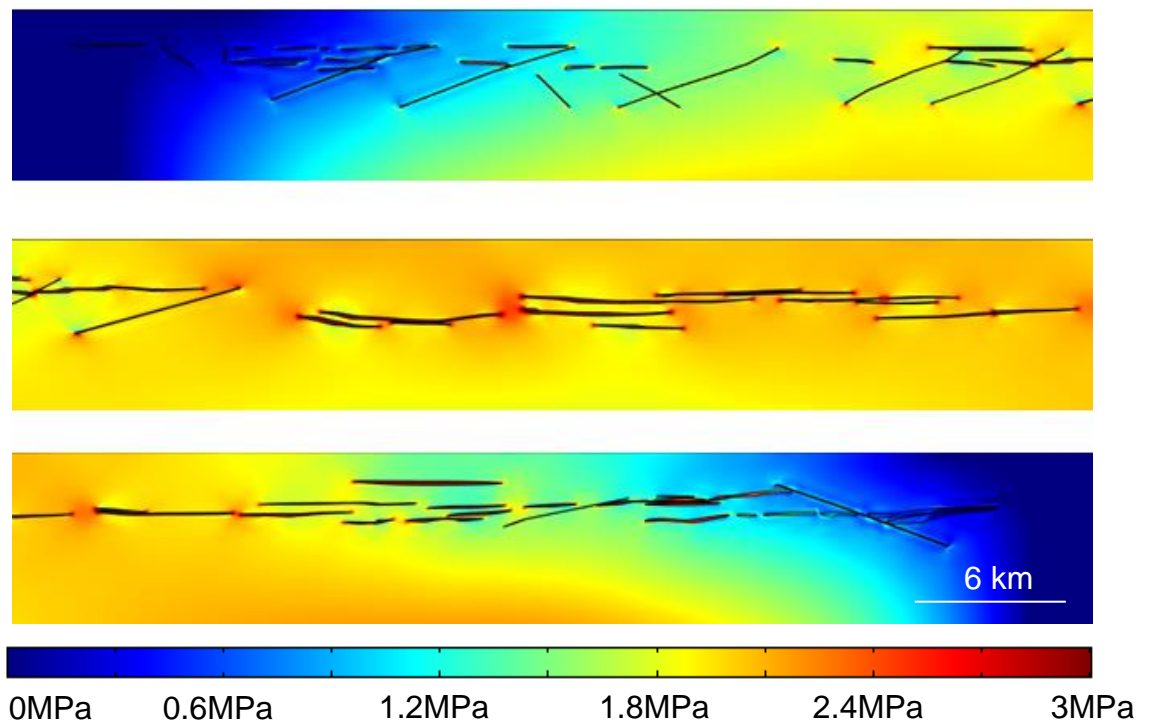
T=46Ma



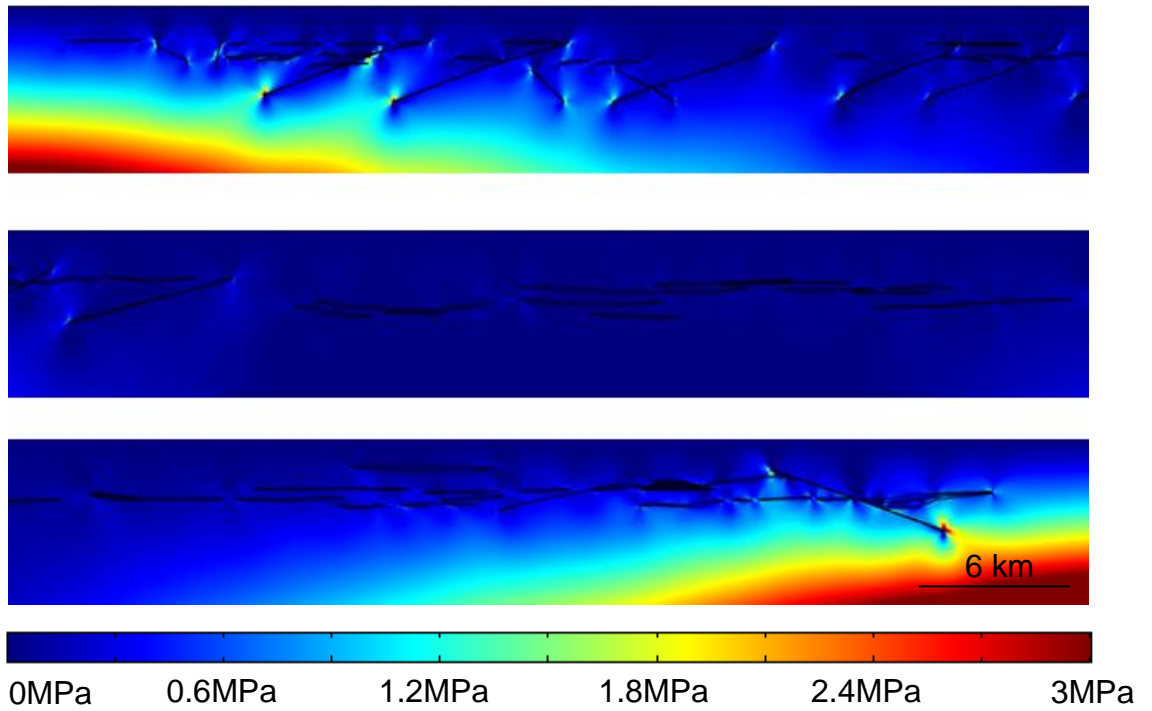
T=36Ma



T=26Ma



T=16Ma



T=0Ma

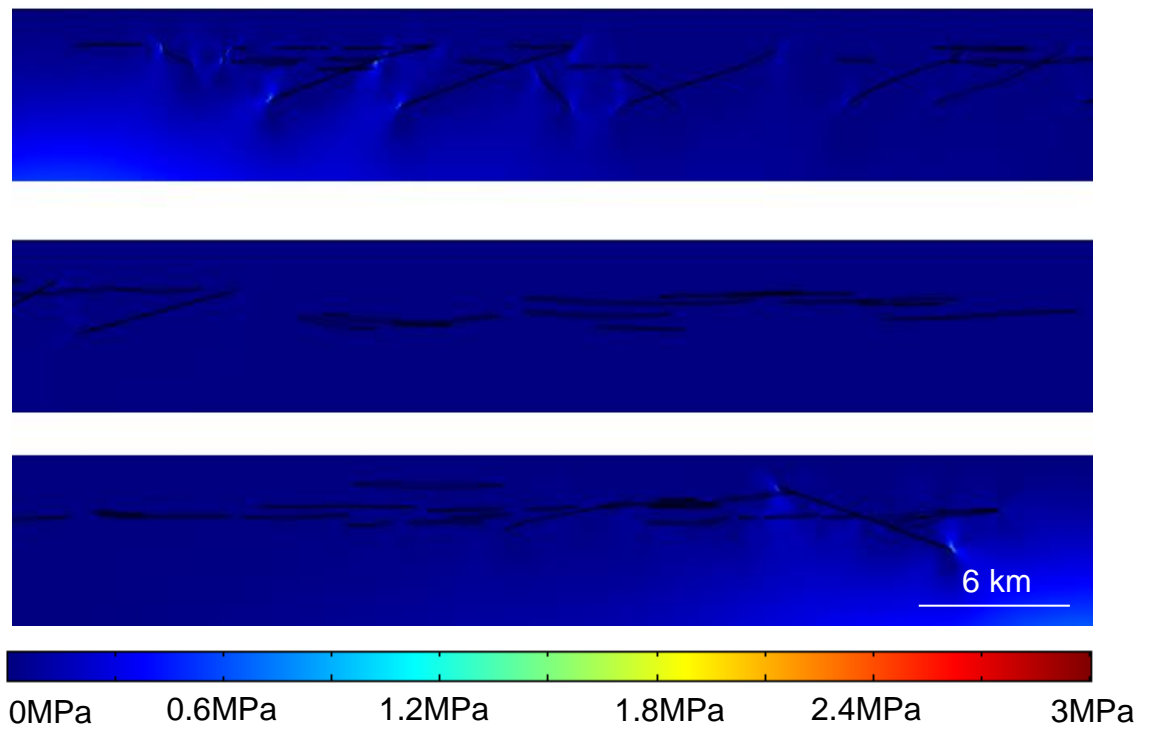
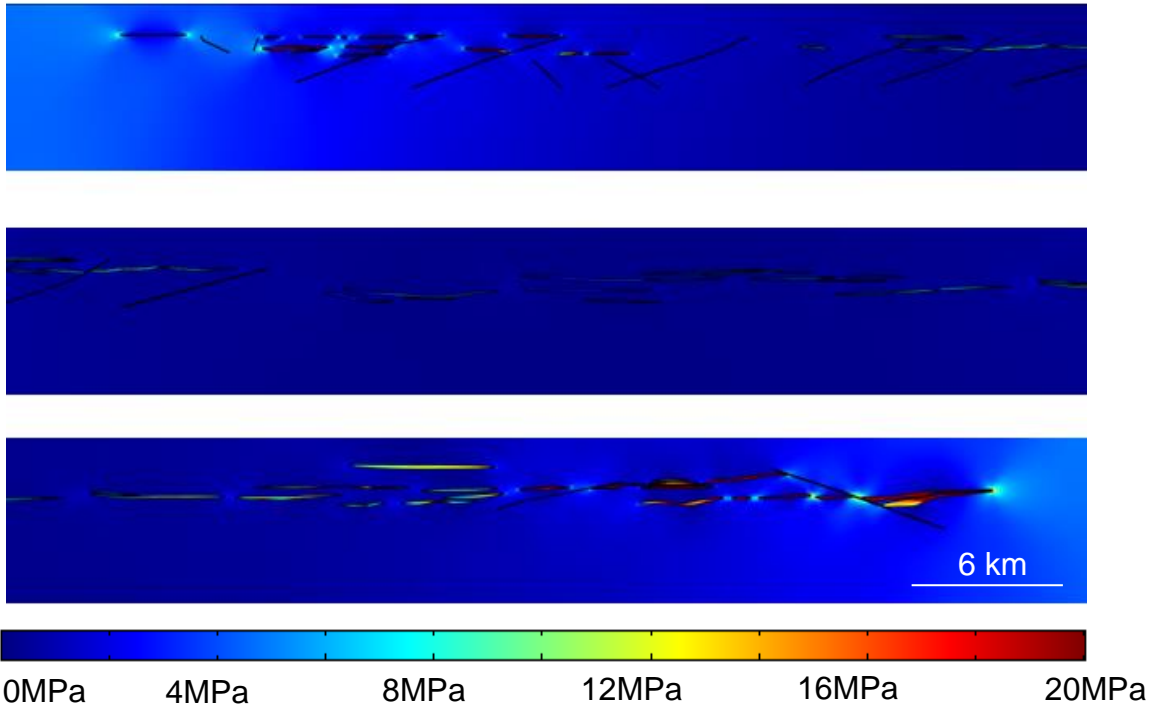
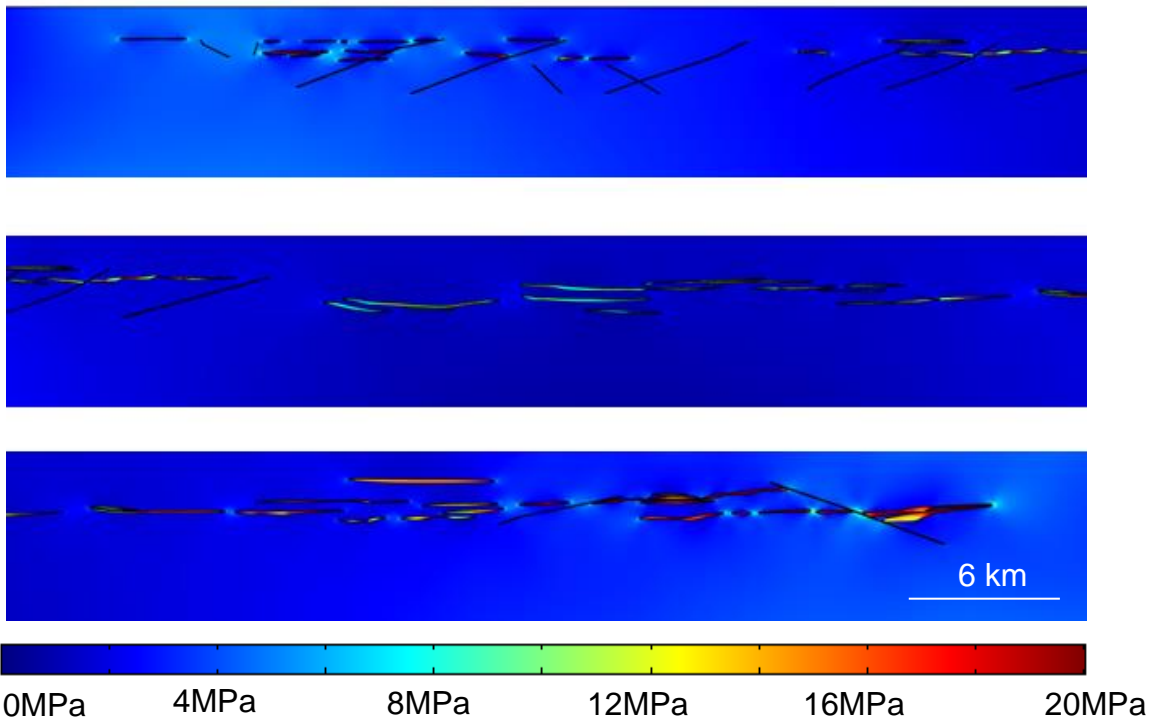


Figure 10.12: Line MNR06-7365. FEM models of tensile stresses represented by colour contours from a time sequence of 56 Ma to present. Model parameters described in Table 4.1 and model set-up illustrated in Figure 10.9. See text for model description.

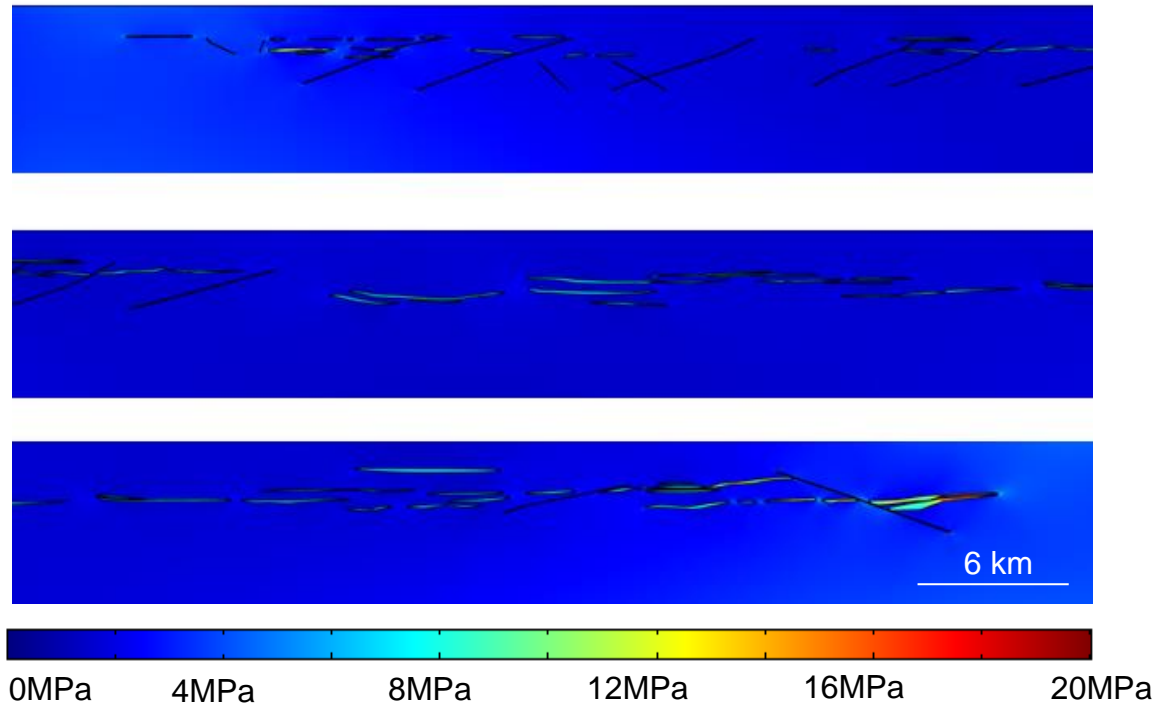
T=56Ma



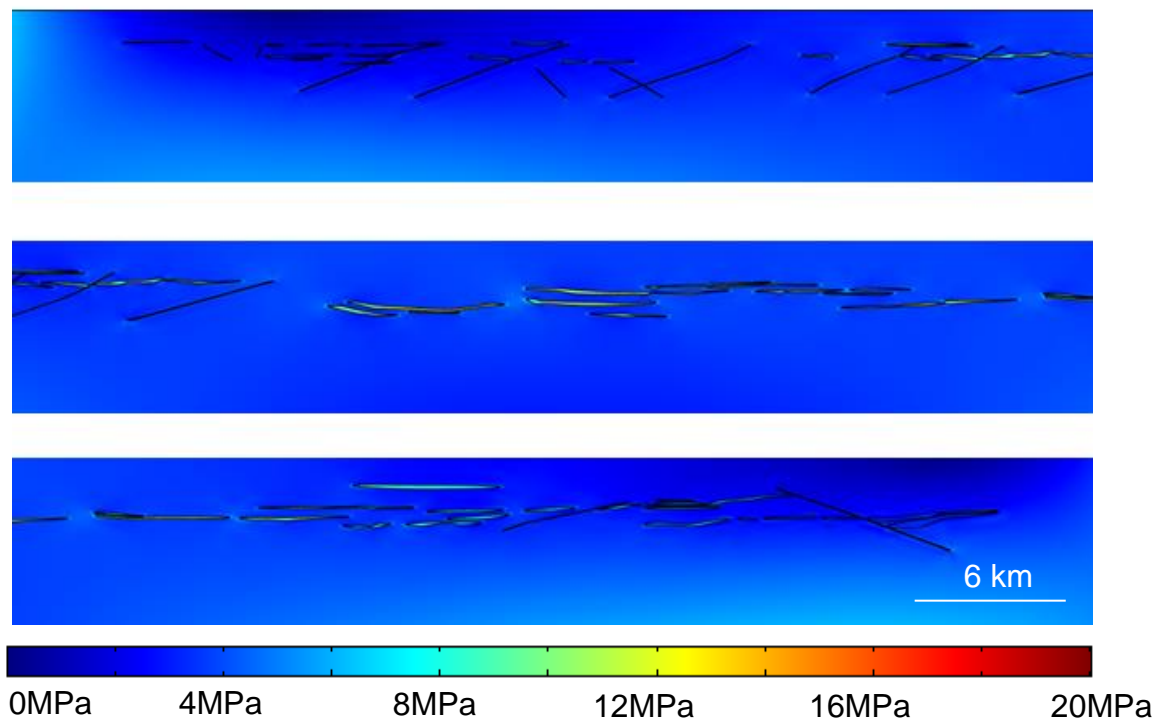
T=46Ma



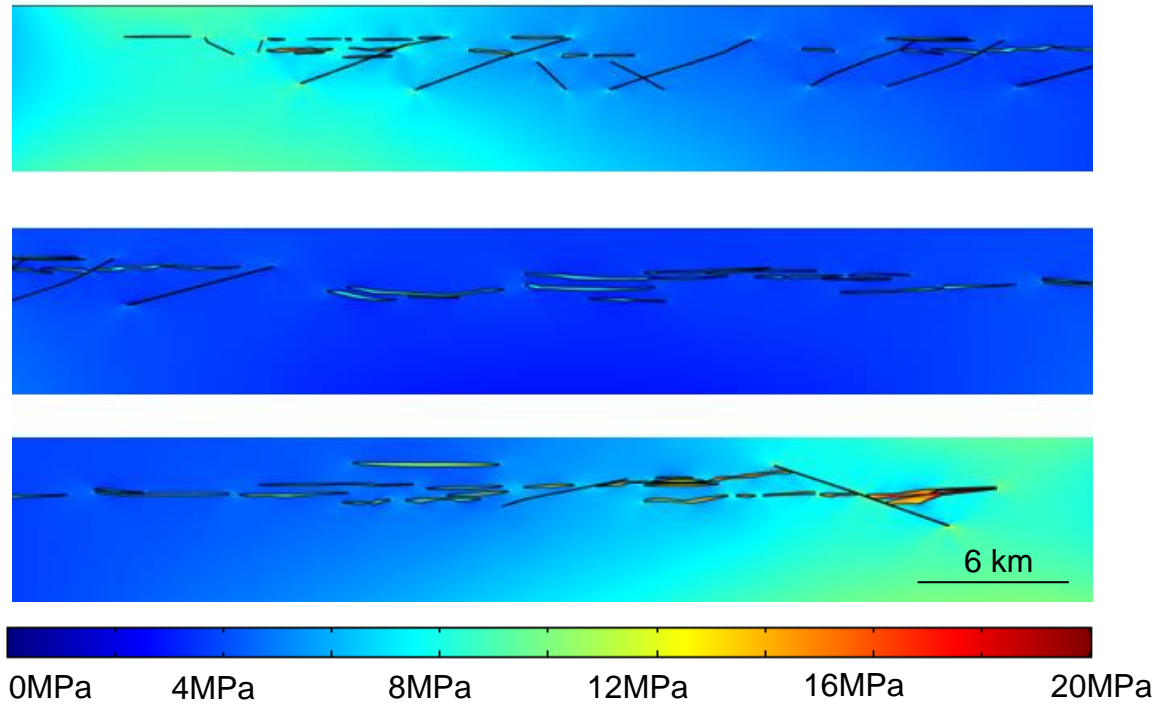
T=36Ma



T=26Ma



T=16Ma



T=0Ma

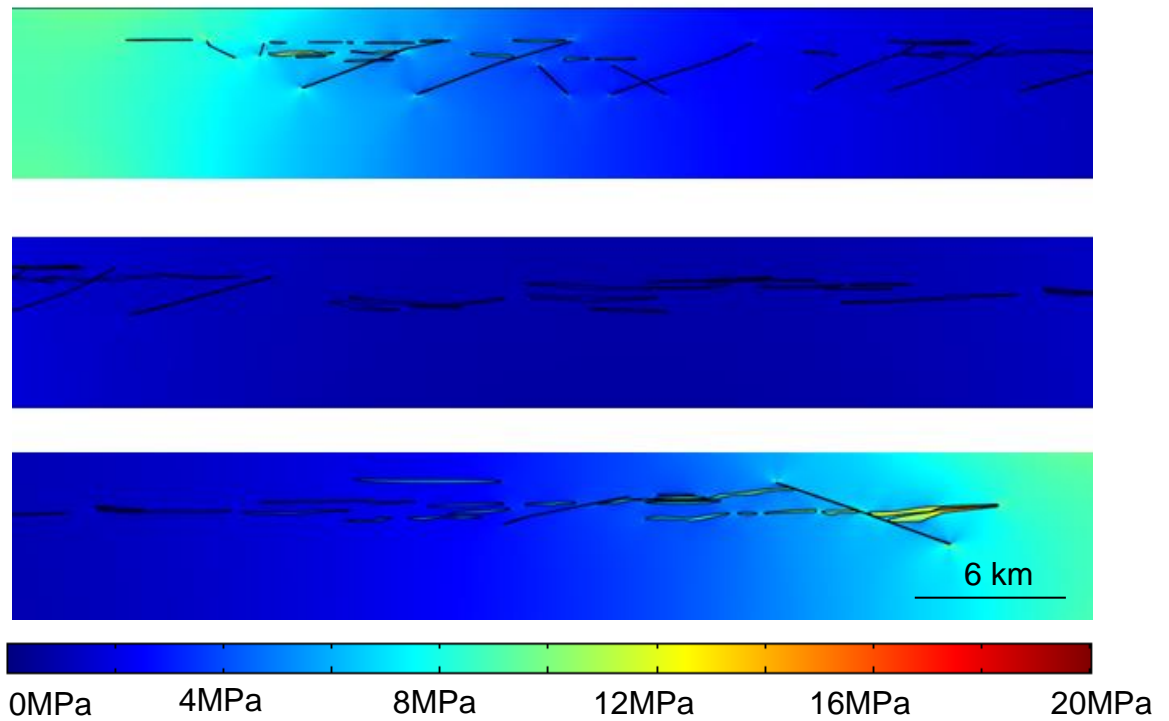


Figure 10.13: Line MNR06-7365. FEM models of shear stresses represented by colour contours from a time sequence of 56 Ma to present. Model parameters described in Table 4.1 and model set-up shown in Figure 10.9. See text for model description.

To summarise the interpretation of the numerical results, there are five scenarios that may occur due to the stress concentrations and are as follows: (1) tensile stresses at 56 Ma relate to first formation of tectonic fractures, (2) tensile stresses located in the sill in subsequent extension regime time steps relate to the formation of subsequent tension fractures, (3) tensile stresses located at the sill tips may represent fracture formation and reactivation of old fractures, (4) stresses located within faults could cause fault reactivation, (5) shear stresses represent the possible formation of shear fractures and small faults within the sill and the host rock and reactivation of old shear fractures. Overall, fracture formation and reactivation, whether an extension fracture or a shear fracture, would increase fracture interconnectivity and would result in a higher chance for transportation of hydrocarbons in the vicinity of the sills and associated faults.

10.4 Sills as seals for hydrocarbons

Figure 10.14 shows that when vertical migrating hydrocarbons meet the sill they are deflected at the low permeability margin until trapped at the contact, T-junction, between the sill and a secondary barrier. This secondary barrier may be a dip-slip or tight fault or near vertical intrusion. If the barrier is a fault and is reactivated by sill emplacement, its permeability will temporarily increase, but over time could still act as a trap via ‘healing’ and ‘sealing’ of the fault by geothermal fluids (Chapter 7).

Sills can act as traps by deforming the overburden and host rock. Hansen and Cartwright (2006a) present seismic images from the NE Rockall Basin, a sedimentary basin to the west of the UK, exhibiting the growth of forced folds above saucer-shaped sills, a potential trap for hydrocarbons. Their kinematic model is based upon works of Pollard and Johnson (1973) and Malthe-Sørensen *et al.* (2004). The earlier work of Pollard and Johnson (1973) was an experiment in laboratory conditions for the emplacement of saucer-shaped sills where the overburden was uplifted, possibly leading to dyke propagation towards the tips of the sill. Figure 10.15 from Hansen and Cartwright (2006a) shows that in stage one there is little deformation of the overburden. As the sill thickens over time, represented in stage two, a forced fold forms with steeply dipping limbs. This fold relates to the thickness and geometry of the sill, where the fold is located directly above the sill. As the sill transgresses into a saucer-shape in stage three, there is increased deformation of the

free surface, with gently dipping limbs as the sill thins at its tips. These forced folds or dome structures associated with saucer-shaped sills form a trap for hydrocarbons due to a four way dip closure (Hansen and Cartwright, 2006a; Polteau *et al.*, 2008a). If these folds are in a sandstone layer, there is a potential for a hydrocarbon reservoir. However, it is unknown how the stratigraphy of the folds could be altered by metamorphism and hydrothermal alteration, which is fundamental to understand as it has implications for hydrocarbon reservoir quality.

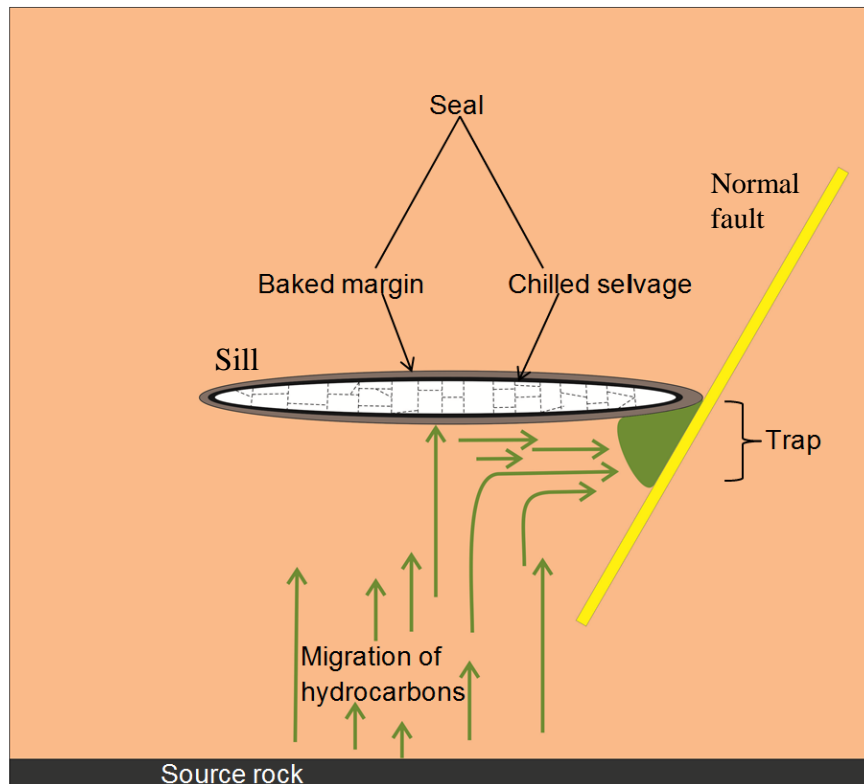


Figure 10.14: Schematic illustration of a sill as a seal and trap towards hydrocarbon accumulation. Here seal and trapping mechanism is at the junction between the sill and normal fault. The seal is the sill margins: the baked margin marked by the brown oval, and the chilled selvage marked by the black oval.

10.5 Fractured reservoirs associated with sill emplacement

For a sill to act as a fractured reservoir in its own right, the lower margin of the sill must be broken while the upper margin remains intact, so that the hydrocarbons are conserved within the sill and do not migrate out towards the surface, that is, the upper margin remains as a seal (Fig. 10.16). This depends on the geometry of sills

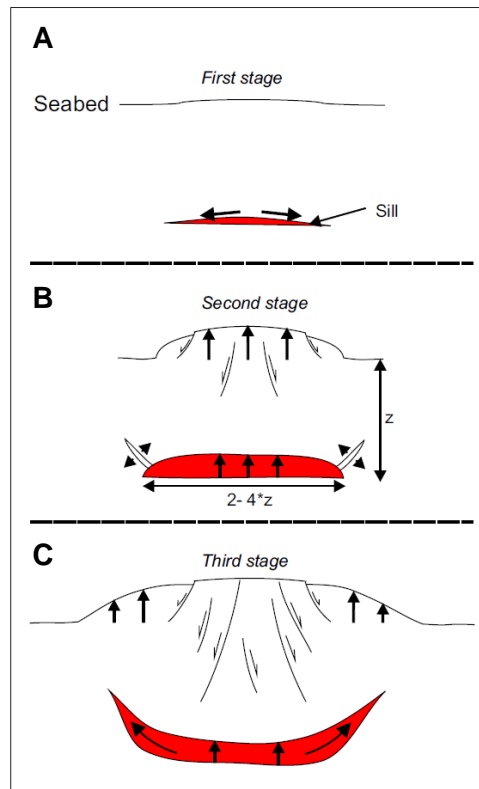


Figure 10.15: Kinematic model of forced fold above a saucer-shaped sill. See text for description of model (Hansen and Cartwright 2006a).

and also the loading. For example, a straight sill has a different stress concentration pattern to that of a concave sill for a given loading condition. The sill thickness is also an important factor, needing to be reasonably thick, as thick sills tend to have well developed fracture networks (e.g. Fig. 9.1C). For example, dimensions in the order of hundreds of metres in thickness and tens of kilometres in length, will have a potential yield for hydrocarbons of tens of cubic kilometres. Therefore, these thick sills have a higher probability to act as fractured reservoirs than thin sills (Fjeldskaar *et al.*, 2008; Wang *et al.*, 2011). We know thick sills worldwide, for example China and Argentina, are acting as fractured reservoirs for hydrocarbons today.

Fieldwork reveals the dominant fractures to have a vertical and sub-vertical orientation that are interconnected by horizontal and sub-horizontal fractures to produce good fracture interconnectivity (Chapter 9). With this interconnectivity the sills have a high storage capacity and permeability for hydrocarbons (and other crustal fluids) due to the dense fracture frequency. Conversely, for a fractured

reservoir to function within the host rock, there must be a high concentration of stresses, both normal and shear, within the reservoir unit. These local stresses are generated by the emplacement of the sills causing fracturing of the host rock and also reactivation of old fractures. Such a mechanism has been demonstrated by Gudmundsson and Løtveit (2012) who reveal a concentration of stresses in stiff layers, sometimes far above from the sill intrusion. These stiff layers may function as a potential fractured reservoir.

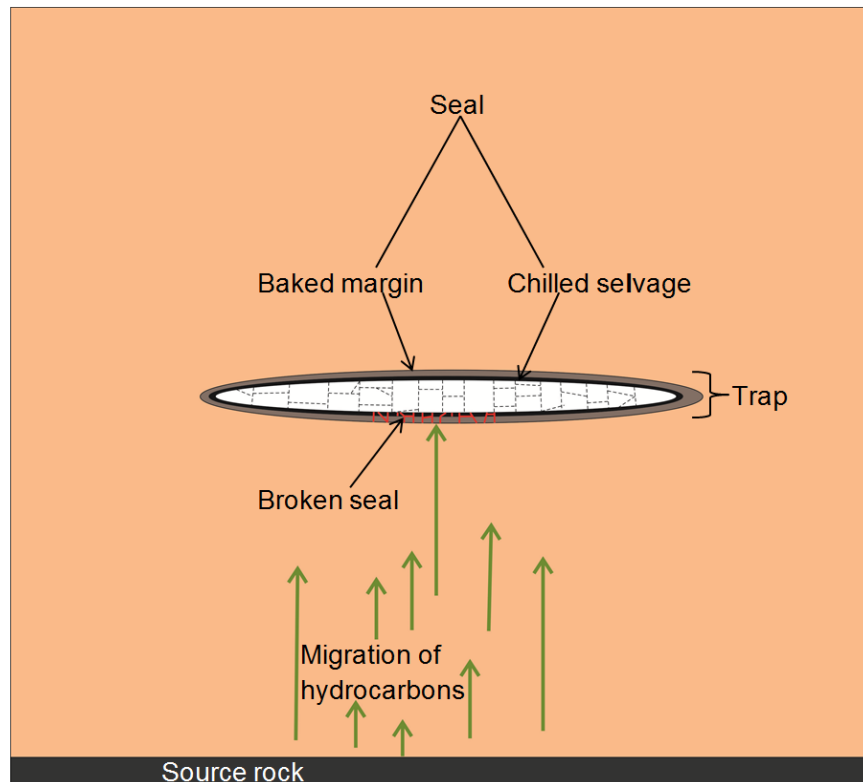


Figure 10.16: Schematic illustration of a sill functioning as a fractured reservoir. This is because the lower margin of the sill is broken (both baked margin marked by brown oval and chilled selvage marked by black oval), allowing hydrocarbons to migrate into the sill and accumulate providing the upper margin remains a seal.

Dykes can also be related to fractured reservoirs. This is especially true for thick dykes with a low permeability that have been deflected to form a symmetric or asymmetric sill. A reservoir would have the potential to form at the T-junction between the dyke and the sill because the dyke would function as a barrier to hydrocarbons, channelling them up along the contact following the hydraulic gradient. Such examples are provided in Schutter (2003a, b).

Numerical models for lines MNR05-7397 and MNR06-7365 illustrate how the stresses are generally distributed about the tips of the sills and associated faults. Numerous examples can be seen of stress concentration, both within and around the sills, together with sill-fault interaction. However, only a few key sites are picked here to identify the possible locations of fractured reservoirs (Figs. 10.17-10.23).

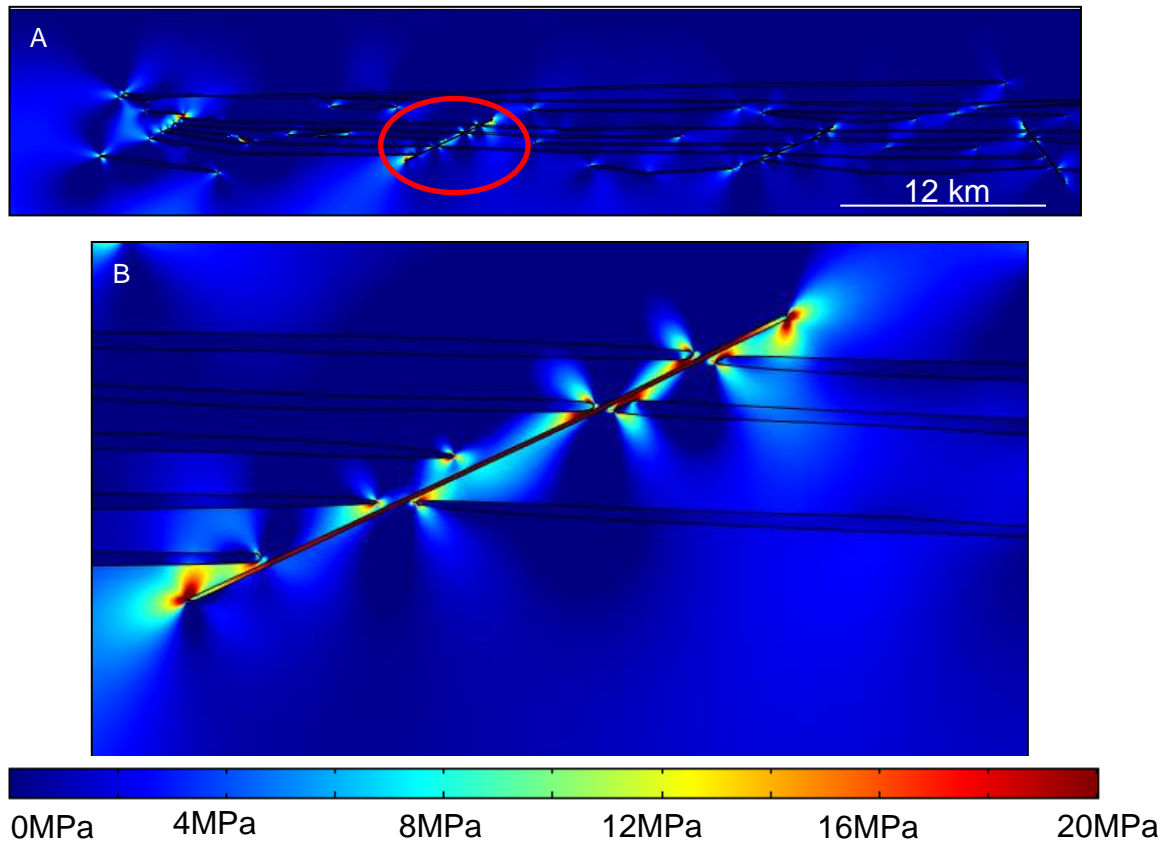


Figure 10.17: FEM model of tensile stress colour contours. (A) Overview of ~140-180 km of line MNR05-7397, 36 Ma. (B) Zoomed-in section of red circle in (A) to demonstrate tensile stress distribution. The sills are arrested at the fault and large tensile stresses are concentrated at the tips of the sills and also inside the fault itself. This illustrates that the permeability of the fault has increased and has the potential to act as a fractured reservoir, providing there is no fault reactivation.

Mechanisms of sill and fault interaction have been discussed in Chapter 7, but the application to the Vøring Margin is not covered. In general, when a sill is emplaced, hydrothermal fluids and gases are released from the tips of the sills forming hydrothermal vent complexes at the surface. These complexes are seen on seismic lines as eye structures at the palaeosurface and have been noted along the Vøring

Margin (Fig. 10.2; Svensen *et al.*, 2010). Hydrothermal fluids and gases can migrate into the fault due to its increased permeability, for example the outer sub-damage zone in Figure 7.8A. Over time the fault will become ‘healed’ and ‘sealed’ by these hydrothermal fluids via secondary mineralisation. Such a strong seal forming together with the sill could act as a trap for hydrocarbons for a period of thousands to millions of years. Fault permeability is identified, for example at 36 Ma on line MNR05-7397 (Fig. 10.17) and at 16 Ma on line MNR06-7397 (Fig. 10.18). With both of these examples, the sills are arrested at the faults, with large tensile stresses generated at the sill tips on meeting the fault. Also, there are large tensile stresses generated within the fault, representing an increased permeability and allowing the hydrocarbons to migrate along the fault. If these faults become ‘healed’ and ‘sealed’ over time then they may act as traps towards the migrating hydrocarbons. An example of a fault acting as a seal and trap mechanism towards the accumulation of hydrocarbons is seen in Figure 10.19.

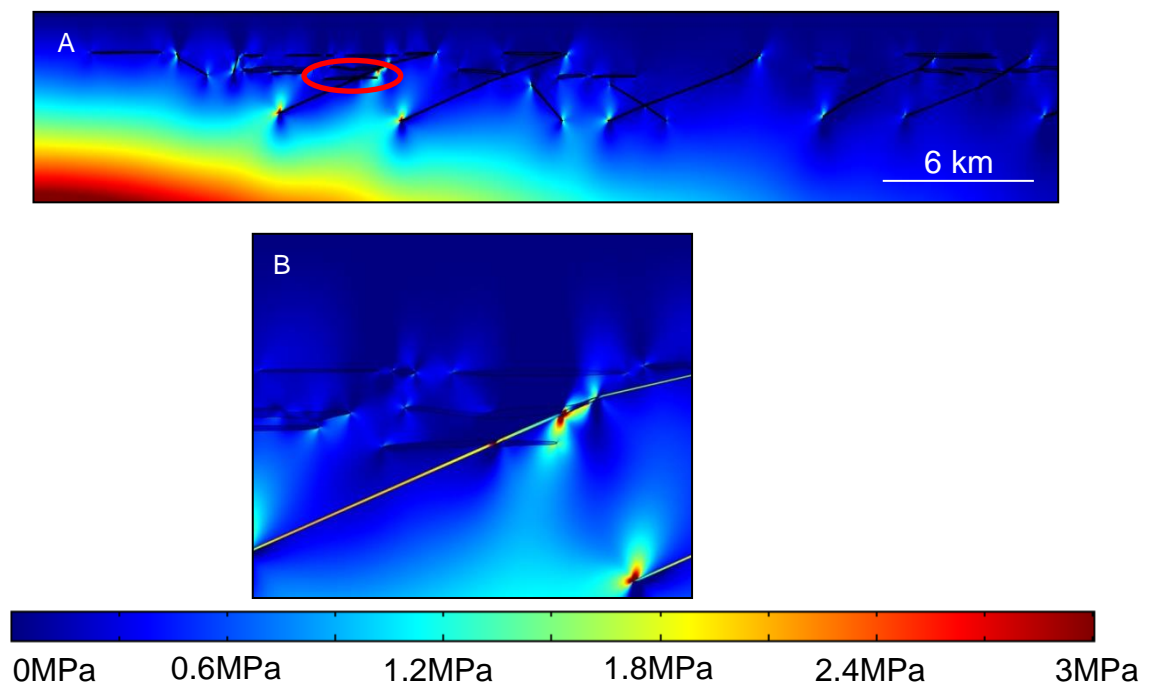


Figure 10.18: FEM model of tensile stress colour contours. (A) Overview of ~25-100 km of line MNR06-7365, 16 Ma. (B) Zoomed-in section of red circle in (A) to demonstrate tensile stress distribution within the fault.

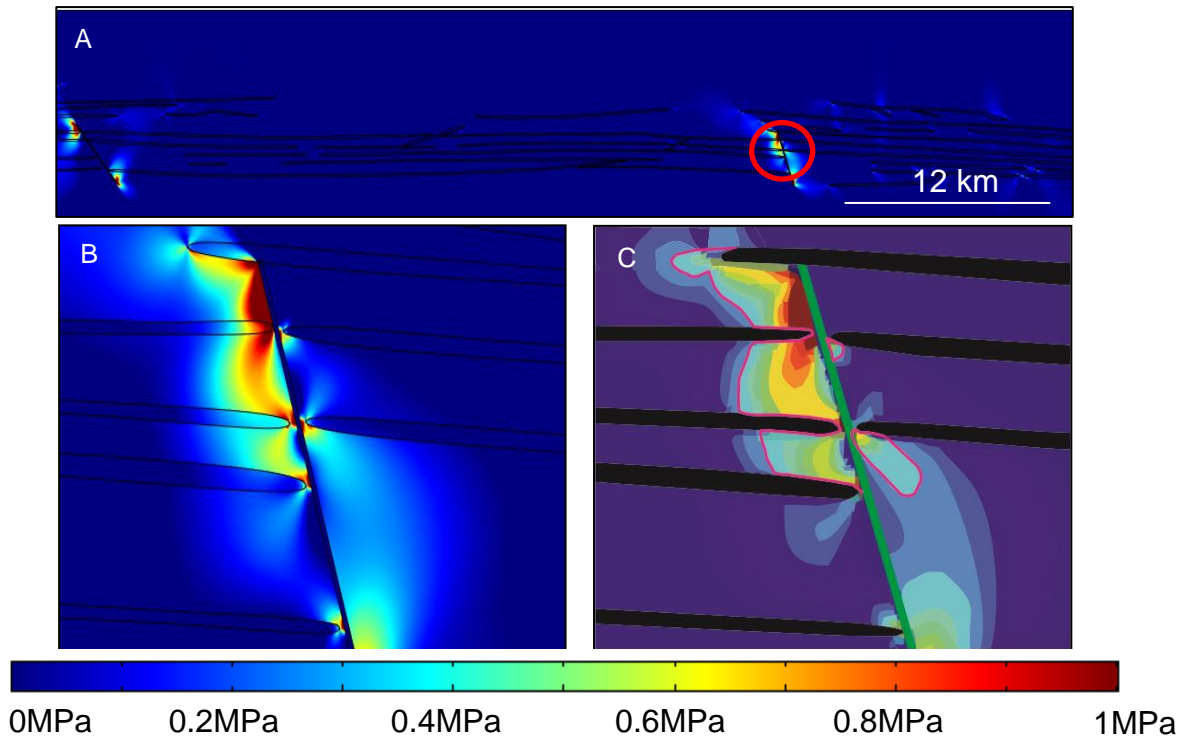


Figure 10.19: (A) FEM model of tensile stress contours from ~180-230 km from line MNR05-7397 at present. (B) Zoomed-in section of the red circle in (A) illustrating the tensile stress distribution around the sill tips. (C) Schematic illustration of (B) showing a possible region of hydrocarbon accumulation in pink, which is traced along a particular stress contour, thus maybe laterally more extensive.

In general, the sills themselves in a time-dependent framework did not function as fractured reservoirs. However, stresses generated by the emplacement of the sills may play a key role in fractured reservoirs forming in the host rock. This has been demonstrated in Figure 10.19, where the sill complex generates large tensile stresses between their tips and the steep dipping fault. The other main scenario is the sills interacting with each other, generating large stresses at their tips, whether it is tensile or shear stresses. These tip stresses represent an increased zone of fracture reactivation and formation within the host rock, where the fractures may link up between adjacent sill tips (Figs. 10.20-10.23). When fractures become reactivated or new ones are generated and grow, they begin to form interconnected fractures. This is because as fractures grow they generate their own stress field that overlaps with near-by fractures. Over time they become interconnected as a result of co-linear linkage and overall, increase the permeability of the host rock (Fig. 10.22C; Cartwright *et al.*, 1995; Barnett, 2011). These interconnected networks most likely

will be a combination of extension and shear fractures (shown in numerical results, e.g. Figure 15 in Gudmundsson *et al.* (2003)). Around these zones of fractures, hydrocarbons most likely will accumulate as highlighted in Figures 10.20, 10.21 and 10.23.

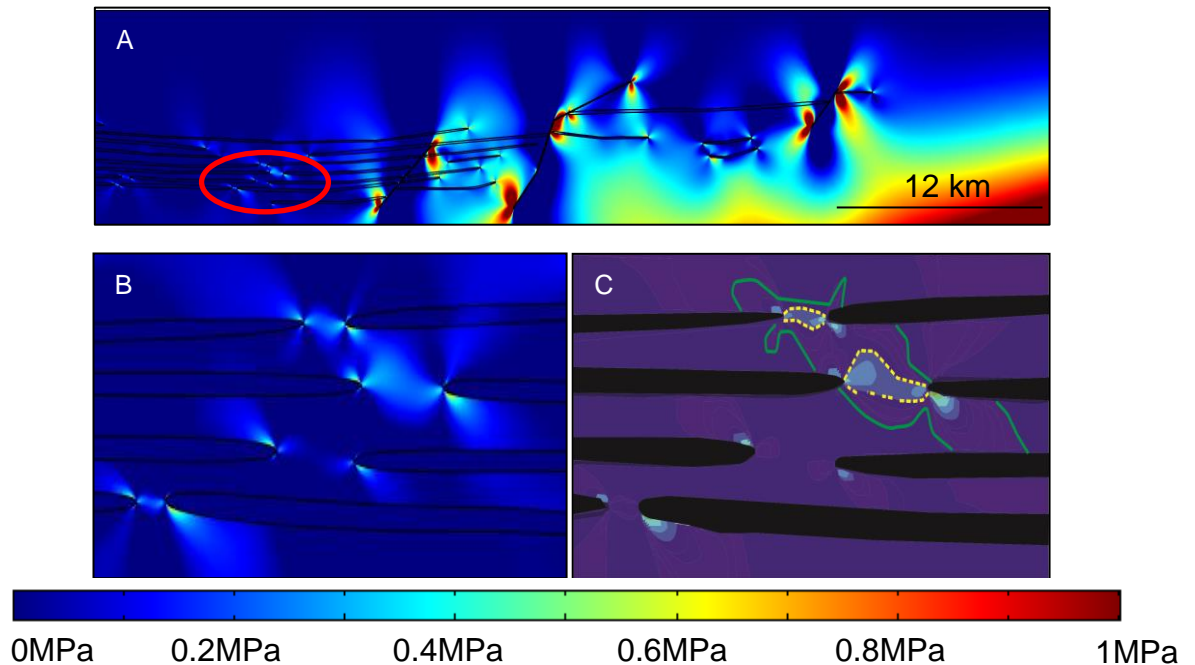


Figure 10.20: (A) FEM model representing tensile stress colour contours at present from ~230-265 km, line MNR05-7397. (B) Zoomed-in section of red circle in (A) showing tensile stress distribution around the sill tips. (C) Schematic illustration showing the possible migration of hydrocarbons towards the tips of the sills, where there is increased fracturing of the host rock (yellow dashed line following a high stress contour) and a possible fractured reservoir in the shale host rock, highlighted by the green zone (traced along a low stress contour- maybe more laterally extensive than shown here). Hydrocarbons would be trapped by the overlying sill seen in (A) above the red circle.

It is also important to note, as taken into account with the time-dependent modelling, that over time sedimentary rocks become stiffer. This variation is most likely due to diagenesis (e.g. pressure solution and cementation) and mechanical compaction of the layers. Such processes affect soft rocks, for example shales, which would have an effect on dyke arrest and sill emplacement in the Vøring Basin (Brenner and Gudmundsson, 2004). With respect to fractured reservoirs, the stiffness of the host rock may have an effect on fracture reactivation and thus permeability. However, for the petroleum industry it is the permeability of the sills and the host rock at the time

of hydrocarbon migration, rather than the present day permeability that is of interest. Moreover, the fracture apertures within the sills would most likely be narrower than those fractures in the shale host rock (process zone at the sill tips, for example), and therefore hydrocarbon migration would be more preferential in the soft shales.

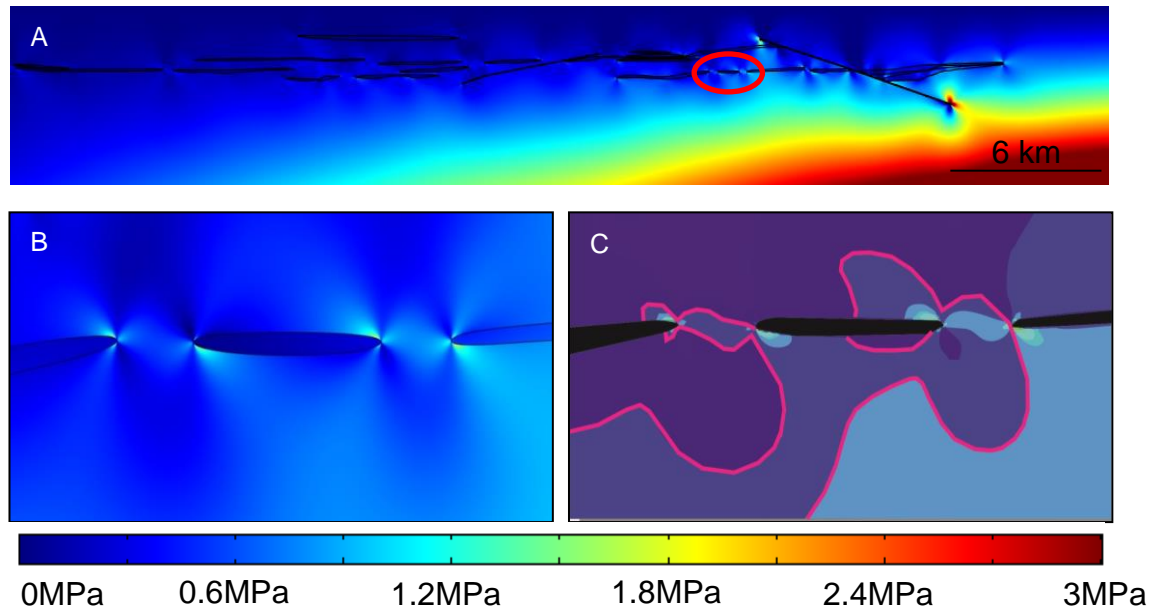


Figure 10.21: (A) FEM model representing tensile stress contours at present, ~230-265 km, line MNR06-7365. (B) Zoomed-in section of red circle in (A) to demonstrate tensile stress distribution around the sill tips. (C) Schematic illustration showing the possible migration of hydrocarbons towards the tips of the sills, where there is increased fracturing of the host rock, and a possible fractured reservoir in the shale host rock, highlighted by the pink zone (traced along a low stress contour- maybe more laterally extensive than shown here).

10.5.1 The Utgard sills

Well 6607/5-2 transects line MNR05-7397 at an easterly point giving a good overview of the sill composition and stratigraphy. The Utgard well transects three sills (Fig. 2.7; Svensen *et al.*, 2010), however only the geometry of the two lower, thicker sills could be modelled, as the upper sill was too thin to identify on seismic traces. These sills give a different perspective to numerical results so far, as here the anisotropy relating to the sandstone and shale layers could be modelled accurately.

Time-dependent modelling was undertaken with the same parameters and mesh as for those of MNR05-7397 and MNR06-7365 (Table 4.1), with the sandstone layer

becoming incrementally stiffer from 20-45 GPa (Gudmundsson, 2011a). Results (Fig.10.24) show that there are a concentration of tensile stresses within the sandstone body as it is stiffer than the shale unit, and also within the sills themselves. The possibility of three fractured reservoirs can be demonstrated here: (1) within the sandstone body, (2) under the upper sill, providing that the hydrocarbons are trapped by a secondary barrier, for example a dip-slip fault or dyke or inclined sheet, and (3) under the lower sill, which acts as a trap in its own right due to its concave downward geometry. The geometry of the upper sill (irregular concave, although not a 1:1 scale and exaggerated in the vertical dimension) suggests that it is terminated against a secondary barrier (perhaps a normal fault) because of its inclined nature. From the time series of models produced, although not shown, it is illustrated that there are no tensile stresses distributed around the sill margins, so rupture is unlikely. This stress concentration also holds true for the lower sill and is portrayed in Figure 10.24.

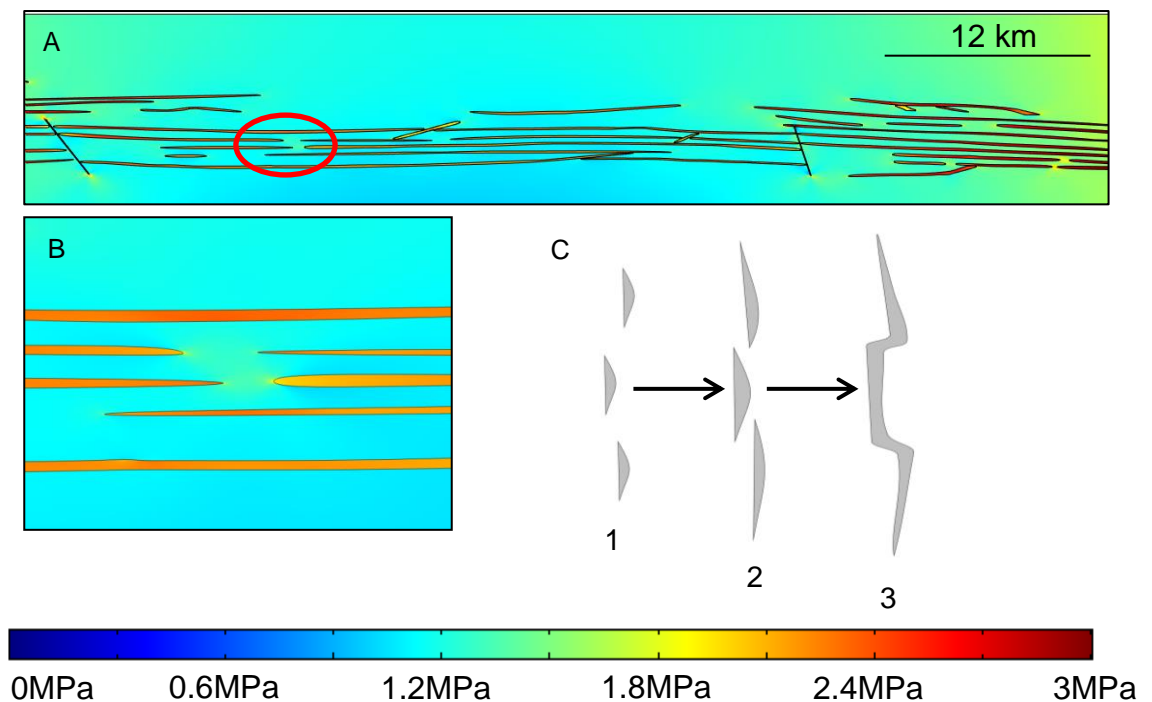


Figure 10.22: (A) FEM model representing shear stress contours at present from ~180-230 km, line MNR05-7397. (B) Zoomed-in section of red circle in (A) to demonstrate shear stress distribution around the sill tips, and the shear stress concentration within the sill indicating the formation of shear fractures. (C) Schematic illustration of fracture reactivation - as the fractures begin to interact with each other as they grow, they begin to join up via co-linear linkage.

Similar results are produced by Gudmundsson and Løtveit (2012), who demonstrate that in a homogeneous medium, where the sill is stiffer than the host rock, stresses are dissipated with an increasing distance from the sill. However, in a heterogeneous medium, where there are abrupt changes in layer stiffness, stress concentrations vary. They show that stresses induced by sill emplacement are concentrated within the stiffer layers, here the sandstone layer in the Utgard well. With such a scenario, fractured reservoirs may be formed in a stiff layer a large distance away from the sill intrusion itself.

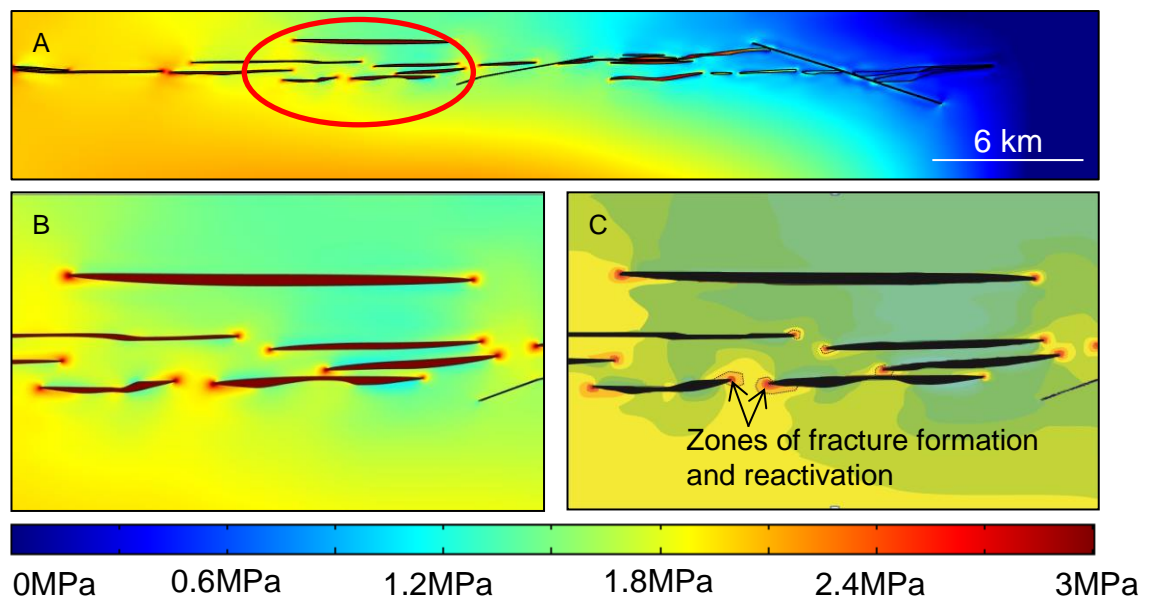


Figure 10.23: (A) FEM model representing tensile stress contours 26 Ma from ~170-215 km of line MNR06-7365. (B) Zoomed-in section of red circle in (A) to demonstrate tensile stress distribution around the sill tips, where the lower margins of the sill are not ruptured as no tensile stresses are concentrated here. However, stresses are concentrated within the sill itself increasing permeability owing to increased fracturing. (C) Schematic illustration showing the possible migration of hydrocarbons towards the tips of the sills where there is increased fracturing of the host rock (black dashed line following a high stress contour).

10.6 Conclusions

Factors that determine whether a sill will act as a fractured reservoir or as a seal or trap for hydrocarbons are dependent on several factors, but mainly the stress distribution around the sill itself. In general, sills concentrate stresses when emplaced within a soft host rock. For a fractured reservoir to form within the sill, the lower

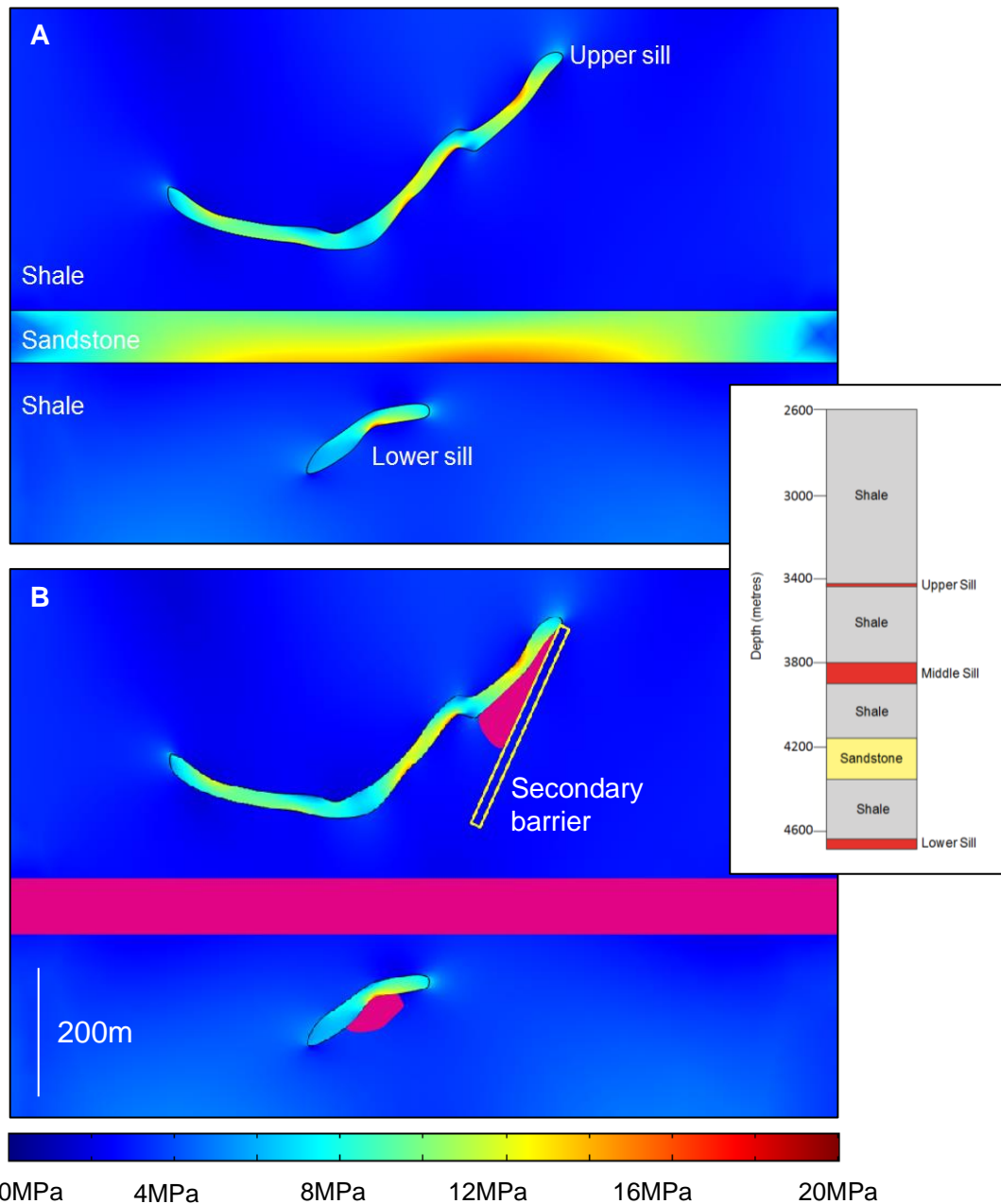


Figure 10.24: FEM model of tensile stresses in the Utgard sills (well 6607/5-2). (A) 46 Ma tensile stress concentration within the sills and also the sandstone layer. (B) Schematic illustration identifying three possible locations of hydrocarbon accumulation in pink: (1) between the upper sill and secondary barrier, (2) within the sandstone layer and (3) beneath the lower sill. Inset is the stratigraphic column (modified from Svensen *et al.*, 2010) where the thickness of the sandstone and sills were calculated.

margin must be ruptured while the upper margin remains intact as a seal, as to not allow the hydrocarbons to migrate towards the surface. By contrast, if the lower margin remains intact it forms a seal due to its low permeability and a fractured

reservoir may then form in the host rock. Stress concentration and distribution also depends on (1) the tectonic regime (loading conditions) subsequent to sill formation, and (2) on sill geometry; for example a concave up sill concentrates stresses at its lower margin under a given loading condition rather than its upper margin.

The quality of fractured sill reservoirs depends on the interconnectivity of the fractures within. An ideal fractured reservoir would have a well interconnected fracture pattern, increasing the permeability of the sill (or the host rock), and cover a large volume of the basin, holding tens of cubic kilometres of hydrocarbons (Fjeldskaar *et al.*, 2008; Wang *et al.*, 2011). Also, the depth of the sills, the degree of faulting and diagenesis of the host rock, as well as the individual thicknesses of the sills, also impacts reservoir quality.

Fractured reservoirs may also form in the host rock itself. Firstly, they may form at close proximity to the sills because of stress interaction between the sills and faults, causing fracture reactivation and growth of new fractures. Secondly, fractured reservoirs can also form in stiffer layers that may be a considerable distance from the sills themselves.

Chapter 11: Discussion

11.1 Limitations and assumptions

Analytical solutions have associated assumptions and limitations, which could restrict their application to more complicated scenarios in the real world. Such complicated scenarios can be better modelled using numerical solutions, as a wide range of parameters can be added to numerical models. Thus, numerical models can provide more accurate solutions, especially with respect to the heterogeneity of the upper crust in which igneous intrusions tend to be emplaced and their associated stress fields.

There are limitations to the models presented within this thesis because it is well known that sills have associated thermal effects as well as the mechanical effects that have been investigated. Thermal effects include the formation of chilled margins and the contact metamorphism of the host rock. Thus, convection within the sills and hydrothermal circulation of fluids around sills was not considered in the models. Also, the sills (and dykes) were modelled within an elastic medium, that is, the host rock was purely elastic, consequently deforming instantaneously. This may be a limitation as the formation of sills is a dynamic process that takes time. However, this was a reasonable assumption to make with shallow emplaced sills, as rocks at low temperatures and pressures behave linear elastically, obeying Hooke's law. In addition, simplified sill geometries limit the greater detail of the stress field produced. However, such geometries have not compromised results when comparing them to the mapped sills from the seismic lines, as overall stress patterns were similar.

With respect to modelling the Vøring Margin, the main limitation was that there was no heterogeneity in the models as lithological units were not interpreted on the original seismic data. To overcome this limitation, models were run to analyse potential fractured reservoirs in accordance with well data from the Utgard borehole 6607/5-2 (Svensen *et al.*, 2010) to better understand the effects of the heterogeneity of the crust and the associated stress distributions.

Further limitations and assumptions were associated with the fluid flow and particle tracing models. The main limitation was that two-dimensional fracture networks were represented, whilst in reality networks are three-dimensional. Also, the fracture walls were assumed to be smooth, parallel plates in the models, but in reality they exhibit small irregularities. Moreover, only fracture networks were considered for hydrocarbon (gas and oil) flow and not the matrix. For example, gas could be transported via the interconnectivity of vesicles. Finally, the particle tracing assumed that the impact of the individual fluid particles on the fluid flow was insignificant. This allowed first, simulation of the flow field and second, simulation of the movement of the fluid particles based on Newton's second law.

Although limitations and assumptions exist in the numerical models presented within this thesis, the results have not been compromised. I believe that this thesis provides new insights as to the emplacement of sills, their evolution into magma chambers, and also the possibility of sills acting as fractured hydrocarbon reservoirs in the Vøring Margin. The results can be correlated with field studies and analogue studies. Furthermore, results presented here have large implications in geological applications and in industry.

11.2 Emplacement of sills

The emplacement of sills has been detected by geophysical techniques, for example InSAR, GPS and seismic detection in active volcanoes such as during the 2010 eruption of Eyjafjallajökull in Iceland (Sigmundsson *et al.*, 2010; Gudmundsson *et al.*, 2012) and the 2011-12 eruption of El Hierro, Canary Islands (Becerril *et al.*, 2013; Martí *et al.*, 2013). In this thesis, the study of sill emplacement focuses partly on how their feeders propagate through a heterogeneous and anisotropic crust. There are three possible outcomes when a dyke meets a weak contact such as a scoria layer or shale horizon: (1) dyke arrest, (2) dyke propagation or (3) dyke deflection into a sill. These scenarios were modelled in Chapter 5 and were described by three mechanisms, these were Cook-Gordon debonding (or delamination), stress barriers and elastic mismatch. These three mechanisms tend to work simultaneously, but one may dominate in various scenarios. Figures 5.7 and 5.8 show that as a dyke or inclined sheet approaches a weak contact it begins to open up due to the large tensile stresses generated at the propagating dyke tip. The maximum opening of the contact

is where the dyke or inclined sheet intersects the weak contact, which primarily opens in the vertical direction followed by horizontal opening. With decreasing distance from this intersection the opening would also decrease. Thus, these weak contacts could be the principal control on the emplacement of sills. The ability for the weak contact to open up ahead of the propagating dyke or inclined sheet is known as Cook-Gordon debonding. These results are consistent with studies by Xu *et al.* (2003) and Zhang *et al.* (2007).

Figure 5.9 illustrates the deflection of a dyke into a sill because of a stress barrier. This stress barrier refers to the layer above the propagating dyke, which yields large compressive stresses in the horizontal plane that act perpendicular to the walls of the dyke, causing arrest or deflection. This barrier is related to the adjacent layers having differing mechanical properties, where the maximum principal compressive stress, σ_1 , is rotated 90° from being vertical (favouring dyke propagation) to becoming horizontal (favouring sill emplacement).

The varying mechanical properties of adjacent layers as modelled in Figures 5.6-5.9 are seen in the field where dykes are often seen to be deflected between soft pyroclastic layers and stiff lava piles, for example Iceland and Las Cañadas, Tenerife (Fig. 5.1B). This is known as elastic mismatch, which describes the contrast in Young's modulus of the adjacent layers and the material toughness of the weak contact. Although this concept has been developed within material science, for example by He and Hutchinson (1989), He *et al.* (1994) and Hutchinson (1996), it also holds large implications in Earth sciences, with respect to dykes becoming deflected into sills. These models are also supported by analogue models, for example Kavanagh *et al.* (2006), Maccaferri *et al.* (2010), and Menand (2011) who report similar results with respect to the emplacement of sills between layers with contrasting stiffnesses.

Sill formation may be favoured due to a level of neutral buoyancy (Francis, 1982; Corry, 1988; Ryan, 1993) or stress rotation (Roberts, 1970). The models presented in Chapter 5 favour the stress rotation hypothesis, where dykes are deflected into sills along lateral discontinuities or weak contacts a couple of kilometres below the surface.

Once emplaced, sills grow primarily from their tips, propagating laterally, indicated by high tip stresses as shown in Figures 6.5, 6.6 and 6.27. Although, lateral growth is preferential, sills sometimes have the ability to grow into an inclined sheet as shown in Figure 5.11, which illustrates the common stepped sill and/or saucer-shaped sill. Such geometries of stepped growth can be seen along the Whin Sill, where the sill generally follows bedding planes, but there are ‘steps’ through the stratigraphy (Fig. 6.32; Goulty, 2005).

The results produced in Chapters 5 and 6 further the knowledge of sill emplacement and propagation and are complemented by analogue studies by Xu *et al.* (2003), Rivalta *et al.* (2005), Wang and Xu (2006), Kavanagh *et al.* (2006), Menand (2008), Kavanagh *et al.* (2013), analytical studies by Gretener (1969), Gudmundsson (1990), Bunger and Cruden (2011) and numerical studies by Zhang *et al.* (2007), Maccaferri *et al.* (2010), Gudmundsson (2011b) and Maccaferri *et al.* (2011).

11.3 Shallow magma chambers

Figures 6.5 and 6.6 show the emplacement of the initial sill and its lateral growth, where high tip stresses denote an area for further growth. This zone of high tip stresses can be inferred as a process zone, where new fractures form and existing fractures are reactivated. Sill growth is extended in Figures 6.9, 6.13, 6.14, 6.16, 6.17 and 6.26 to show how the sill inflates vertically. In more detail, a small sill (sill radius is smaller than depth of emplacement) modelled in Figures 6.9, 6.13 and 6.14 is unable to displace the overlying crustal layers. Whereas, Figures 6.16, 6.17 and 6.26 reveal how a large sill (sill radius is larger than depth of emplacement) can inflate and deflect the overburden. Furthermore, models in Figures 6.23 and 6.24 illustrate that there is some downbending of the underlying layers. However, it is clear that deflection of the overlying layers is dominant and therefore, the initial sill may evolve into a shallow magma chamber or a laccolith. Thus, two steps can be interpreted for the formation of a shallow magma chamber: (1) lateral growth, and (2) vertical growth. For vertical growth to occur there must be a critical distance at which the sill is emplaced, this is described as the radius of the sill being equal to or larger than the depth of emplacement.

For a sill to evolve over time there must be input of magma into the system. Figure 6.33 proposes that the initial sill causes a change in the local stress field favourable to sill emplacement and deflection of subsequent dykes below the first sill. This suggests that a shallow magma chamber forms by the initial sill being underplated by subsequent sills, that is, top-down emplacement. Further models of sill complexes in Figures 6.35 and 6.36 show how the margins of the sills may rupture and magma may be transported between sills via interconnected fractures in the host rock. This indicates that sill complexes are critical for the transport of magma both laterally and vertically (Cartwright and Hansen, 2006). These model interpretations suggest that shallow magma chamber formation cannot be described as continuous and gradual through space and time, but rather as the amalgamation of smaller sills (or magma pulses) (Fig. 11.1). These results are consistent with field studies that document the amalgamation of igneous sheets. For example, the Henry Mountains, Utah (Horsman *et al.*, 2005, 2009) and the Torres del Paine Laccolith, Chile (Michel *et al.*, 2008; Baumgartner *et al.*, 2014), along with other studies by Hutton (1992), Barton *et al.* (1995), Wiebe and Collins (1998), de Saint-Blanquet *et al.* (2001), Rocchi *et al.* (2002), and Glazner *et al.* (2004). The Henry Mountains has three intrusions, 1) the Maiden Creek intrusion, which shows the stacking of two magma intrusions, (2) the Trachyte Mesa intrusion, which shows the formation of a large sill and inflation into the beginning of a laccolith and, (3) the Black Mesa intrusion, which shows the formation of a laccolith (Horsman *et al.*, 2005, 2009). Whereas, the Torres del Paine Laccolith has two complexes, the Paine Mafic Complex at the base, overlain by the Paine Granite of three sheeted intrusions, which is field evidence for the formation of top-down complexes (granitic laccolith) and bottom-up complexes (mafic complex) (Baumgartner *et al.*, 2014).

As sills lift the overburden, surface deformation occurs as shown in Figures 6.17 and 6.26, and due to the presence of weak contacts and other discontinuities the deflection of the overlying layers and deflection at the surface may be suppressed. Models for surface deformation are consistent with what has been observed at volcanoes, for example Campi Flegrei, Italy, where there has been uplift of 3 m since 1968 to 1984 (Woo and Kilburn, 2010), and Rabaul, Papua New Guinea, where there has been uplift of ~1.7 m between 1971-1984 (Geyer and Gottsmann, 2010). The models of surface deformation also have implications for predicting volcanic

eruptions, as this approach is commonly used to detect magma chamber inflation, deflation, and dyke propagation. This is because as the pressure within the shallow magma chamber increases by a few mega-pascals as new magma is injected from a deep seated magma reservoir, or when there is an increase in exsolved gases, the magma chamber will inflate. Inflation of the magma chamber generates ground deformation and seismic activity. Eventually, the chamber walls will fracture and propagation of a dyke or multiple dykes will be initiated towards the surface (McLeod and Tait, 1999), which also generates seismic activity as the host rock fractures (e.g. Bell and Kilburn, 2012).

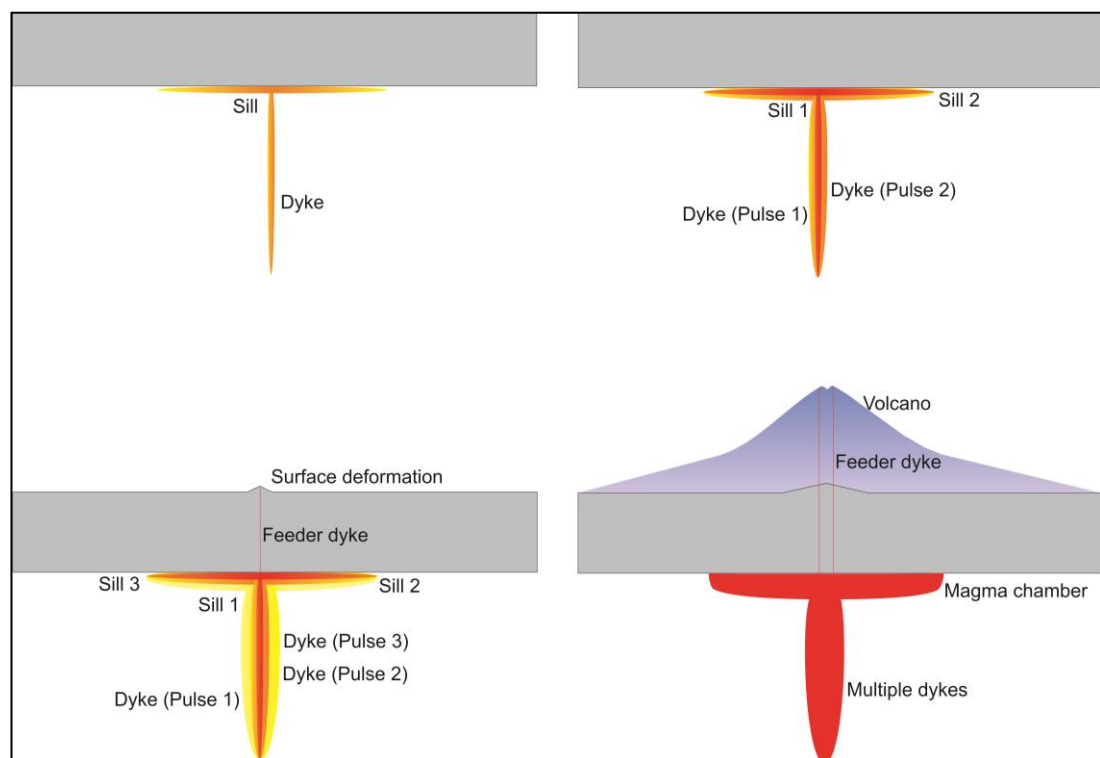


Figure 11.1: Schematic illustration showing the formation of a shallow magma chamber, where a complex forms from the top-down. The initial sill forms because of contrasting mechanical properties between adjacent layers (stress barrier and elastic mismatch). Subsequent dyke injections are deflected under the original sill due to an induced stress barrier. Providing that the initial sills remain at least partially molten as a result of a high magma injection rate, a magma chamber may form (modified from Gudmundsson, 2012a).

Field work and the literature (e.g. Pasquarè and Tibaldi, 2007) reveal the Stardalur sill cluster to be a laccolith built from several sill intrusions that contact each other (Fig. 11.2), similar to the Henry Mountains, Utah (Horsman et al., 2005, 2009). This finding is based on fracture measurements within the sills that at one end (westerly)

become rotated towards the feeder dyke (central depression; feeder to the west of field area in Figure 4.10). This sill emplacement was favoured because of mechanical layering of sediments, soft hyaloclastite and stiff lava, which affected the local stress field and the orientation of the maximum principal compressive stress. However, this laccolith most likely did not feed a volcanic eruption.

In order for a magma chamber to remain molten, the thermal input associated with the addition of new magma must be greater than that of thermal loss relating to a volcanic eruption or cooling and crystallisation of the chamber (Glazner *et al.*, 2004; Menand, 2011). Thus, shallow magma chambers are not associated with slow spreading ridges (Gudmundsson, 1990). Also, the magma inside the sill must remain molten, and therefore the evolution into a magma chamber depends on the magma supply rate. In the case of the Whin Sill, the injection rate of magma was not high enough for it to remain liquid, thus at least partial solidification took place within the sill, preventing the Whin Sill from evolving into a shallow magma chamber. This was firstly observed in the field as there was no layering within the intrusion, which is indicative of one pulse of magma (Figs. 6.28, 6.32; layering or pulses can be seen in the Slaufudalur pluton, SE Iceland, Figure 11.3). Secondly, calculations show that the period of solidification would have been relatively short, because the time it takes for magma to solidify is proportional to the square of the sill thickness (Jaeger, 1957). Thus, the Whin Sill did not act as a shallow magma chamber simply because there was not a high enough influx of magma into the system, and magma within the sill would have solidified. Eruption at the surface was unlikely too, as concluded by Francis (1982).

Volcano loading in Figure 6.8 shows where large tensile stresses are generated along the volcano flanks. This has implications for the location of volcanic eruptions, as the results reveal that eruption occurs away from the summit because of the stress field induced by the volcano loading. These numerical results are coherent with analogue models, for example Kervyn *et al.* (2009). Over time, a sill-like magma chamber may have lateral dimensions large enough to generate caldera collapse. This has been described by Gudmundsson (1988), where the excess pressure within an inflating chamber can generate caldera ring faults leading to eventual caldera collapse. However, the development of these ring faults depends on the mechanical layering of the crust as discussed by Kinvig *et al.* (2009).

11.4 Faulting

Predicting fault zone heterogeneity is important for hydrocarbon exploration both as reservoir capacity (exploration), and hydraulics (productivity). With respect to the transportation of hydrocarbons, faults can act as both traps and conduits as a result of their heterogeneity with regards to permeability and mechanical structure, both temporally and spatially. Figure 7.8 shows two normal faults, with one scenario showing non-reactivated faults (Fig. 7.8A) and the other scenario showing reactivated faults (Fig. 7.8B). The implications of these models is that it is critical for stresses not to build up along the fault, as this allows for fault reactivation, which can cause the associated seal to be breached and the trap to lose its integrity. In such a case, conduits form as a result of fault slip, where permeability increases, although short-lived, as hydrothermal fluids precipitate along the fractures – ‘self-sealing’ (Sibson, 19994; Aydin, 2000). Therefore, with respect to hydrocarbon exploration, faults can be a high risk factor.

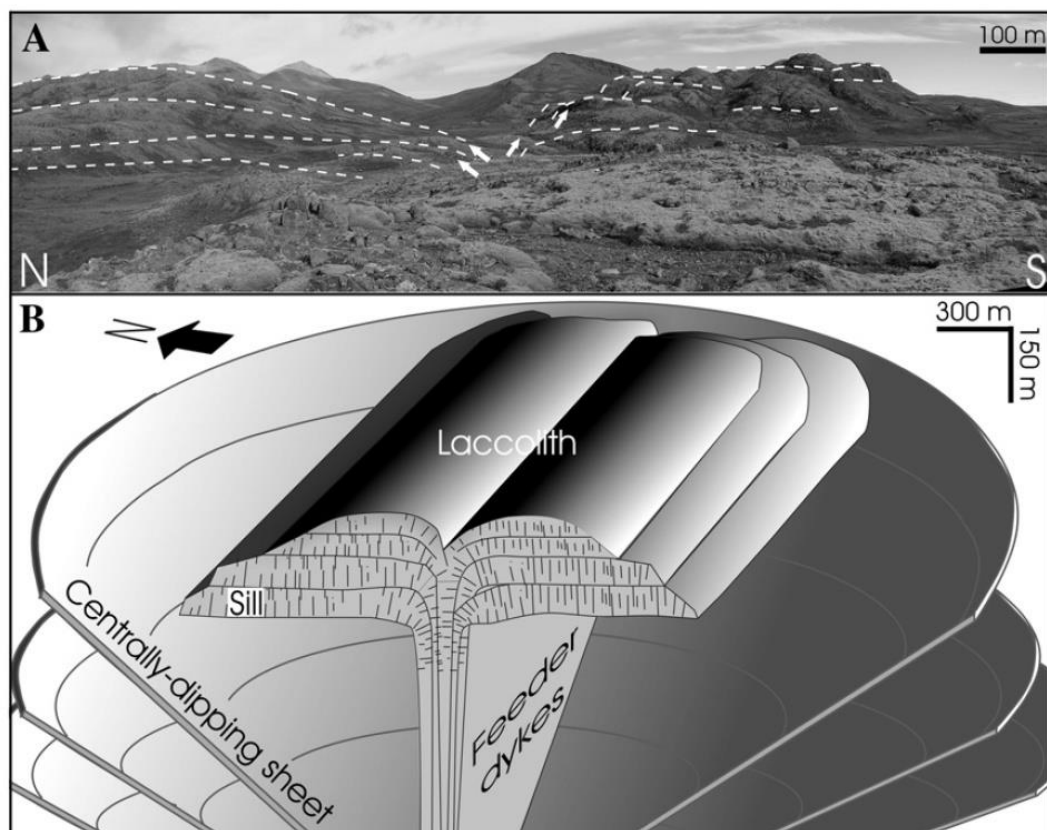


Figure 11.2: (A) Photograph illustrating the geometry of the Stardalur sills and how they are rotated towards the centre, where a possible feeder dyke may be located representing a laccolith geometry, which is schematically illustrated in (B) (Pasquarè and Tibaldi, 2007). Note that the right of the photograph is the field area in Figure 4.10.

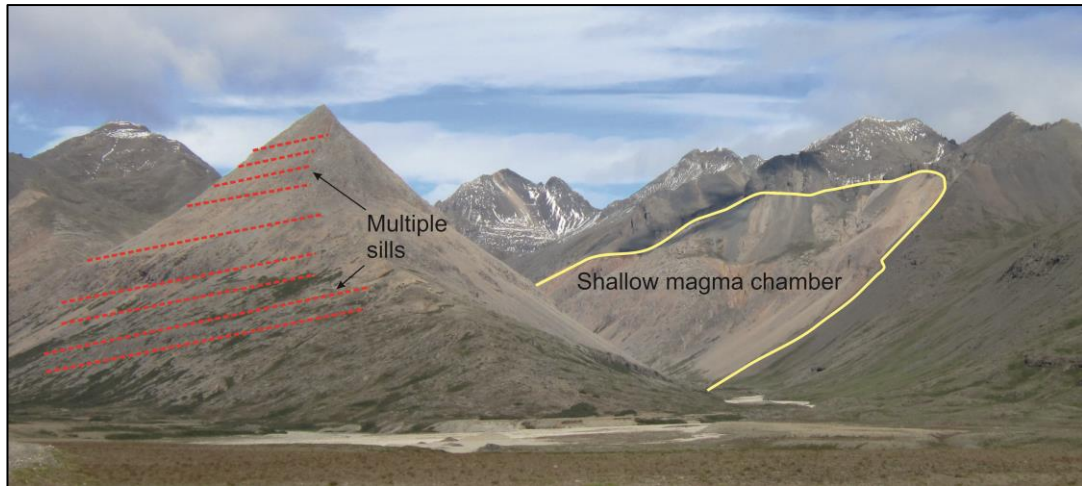


Figure 11.3: Slaufrudalur Pluton (yellow), SE Iceland, view NW. Multiple sills (red) where there is no host rock in between, showing many magma pulses. This peak, known as Bleikitundur is ~500 m.

Seismic line data of buried faults is still poorly understood as the heterogeneity of the fault cannot be determined. Thus, faults were modelled as one structural unit and fault heterogeneity was limited. Using this approach allowed for the interpretation of the overall permeability evolution, where examples in Chapter 10 show models of faults acting as barriers and conduits to flow. For example, Figures 10.17 and 10.18 show an increased permeability in the dip direction, allowing the hydrocarbons to migrate up along the fault to higher levels within the crust. Whereas, Figure 10.19 shows the fault to act as a trap and seal as there are no stresses generated within the fault itself. This indicates that the seal and trap mechanism does not rupture and the fault remains impermeable due to the presence of clay gouge and cementation. Although these results showing faults as barriers and conduits are robust, 3D seismic data can enhance our understanding of faults at depth, especially on how these faults grow and how fluid flows across a three-dimensional fault zone.

Figures 7.13, 7.14, 7.16 and 7.17 highlight the evolution of permeability within a fault zone, that is, a heterogeneous fault, which largely depends on the mechanical properties of the host rock and the fault, deformation of the fault plane, and local stress distribution. These models provide insight into fault permeability with various tectonic loading, showing that permeability evolution may enhance the efficiency of fluid flow migration paths.

11.5 *Sills as fractured reservoirs*

As sills propagate through cool crust, heat is lost to the surroundings, causing the magma to become more viscous and eventually solidify. Thus, the majority of sills do not evolve into magma chambers. However, if the sills are emplaced within a sedimentary basin they have the ability to act as another type of reservoir - a fractured reservoir for hydrocarbons.

11.5.1 Seals, traps and fractured reservoirs

Doming of the overlying strata as seen in Figures 6.17 and 6.26, can be identified on seismic lines interpreted as forced folding (Hansen and Cartwright, 2006a; Magee *et al.*, 2014). These forced folds indicate incremental growth of the sills, such as by minor magma injections (Magee *et al.*, 2014), and are of interest to the petroleum industry as they may act as traps. For example, NE Rockall Basin (Fig. 10.15; Hansen and Cartwright, 2006a) and along the NE Atlantic Margin (Magee *et al.*, 2014).

The numerical results in Figure 10.4 show a high concentration of tensile stresses along the upper margin of the sill and no stresses distributed along the lower margin of the sill. This suggests that the sill has the ability to act as a seal and trap mechanism to hydrocarbons because the lower margin of the sill remains intact. Thus, hydrocarbons can accumulate in the host rock, especially at T-junctions, such as a sill-dyke contact (Fig. 10.4) or sill-fault junction (Fig. 10.14). Contrastingly, Figure 10.5 shows a high concentration of tensile stresses along the lower margin of the sill and no tensile stresses along the upper margin. This suggests that the sill itself can act as a fractured reservoir, as the lower margin is ruptured due to the large tensile stress distribution, and the upper margin remains a seal. This scenario allows hydrocarbons to accumulate within the sill as portrayed in Figure 10.16. Thus, there are two types of fractured reservoirs that need to be considered: firstly, within the sill itself and secondly, in the host rock. The low permeability margins of sills and their strengths determine whether a sill will act as a conduit or barrier to hydrocarbon migration. With respect to the Vøring sills their geometries are more irregular (Fig. 10.6) than the concave sills modelled in Figures 10.4 and 10.5. Figure 10.6 illustrates that tensile stress distribution and the rupture of the sill margins depends on the sill

geometry. For example, a straight sill (similar to the lower sill in Figure 10.6) under a given loading condition will concentrate tensile stresses that are different to that of a concave sill (similar to the upper sill in Figure 10.6) under the same loading.

In the case of the Vøring Margin sills, there are several cases where high stresses concentrate in the shale host rock around the sill tips as shown in Figures 10.19-10.23. These areas may act as potential fractured reservoirs because there is an increase in fracture reactivation and formation of fracture clusters within the host rock due to zones of high tensile and shear stress. These fracture clusters may join up to form a fracture network at a sill-fault junction (Fig. 10.19) and between adjacent sills (Figs. 10.19-10.23). Thus, the concentration of stresses in the host rock has implications for the development of fractured reservoirs about sill tips in the Vøring Margin. Also, the numerical model of the Utgard sills in Figure 10.24 shows a high concentration of tensile stresses in the sandstone unit between the two sills. This highlights the possibility of hydrocarbon reservoirs forming in sandstone layers that potentially may be far above the sills. This result is consistent with work by Gudmundsson and Løtveit (2012). Moreover, although the sills themselves do not act as fractured reservoirs, there are examples where hydrocarbons are present in the host rock adjacent to sills, for example in the Bohai Bay Basin, China (Wang *et al.*, 2011).

Additionally, field studies show that dykes have chilled and baked margins (Fig. 10.1) comparable to those of a sill with an impermeable nature. When modelled (Fig. 10.4) there is no concentration of tensile stresses in the region of the dyke. Thus, the dyke margins will not rupture and a seal could form between the sill and dyke. Although the model in Figure 10.4 is simple, it gives reliable results for dykes to form traps and seals, and is consistent with field examples. For example, a dolerite dyke in the Solimões Basin, NW Brazil, acted as a seal to prevent horizontal hydrocarbon migration (Filho *et al.*, 2008).

This thesis has focused on sills, but laccoliths can also form hydrocarbon reservoirs, where results produced in Chapters 9 and 10 can be applied to larger and thicker intrusions. Like sills, laccoliths are intruded at a relatively shallow depth, approximately 1-3 km (Corry, 1988) at convergent plate margins and intraplate tectonic setting - sedimentary basins. Results produced within this thesis highlight

that the shape and thickness of the sills have an effect on the quality and volume of hydrocarbon reservoirs, and the same goes for laccoliths. As they are much thicker (dome-shaped) than sills, they can enhance hydrocarbon generation. This is because heat from the intruding magma will be conducted into the host rock much faster, as there is a greater volume of magma within the laccolith, than in the sills.

11.5.2 Fluid flow through sills

Field work in NE England and Iceland allowed for the analysis of sills and their associated fracture networks. The fractures present are primarily columnar joints, which form on self-organisation of shrinkage fractures owing to cooling of the magma (loss of heat and removal of water) to form ordered polygonal (ideally hexagonal) columns (Goehring and Morris, 2005). Once the initial columnar joints were formed, post tectonic events led to the formation of shear and extension fractures (initiated from point weaknesses, e.g. vesicles), otherwise known as tectonic fractures that traversed the initial columnar joints. These fractures formed well interconnected fracture networks as illustrated in Figures 9.16-9.20, where fracture networks were seen on a variety of scales. Such fracture networks are crucial for fluid flow through impermeable sills. Figures 9.21-9.28 are of particular interest with respect to the sills acting as potential fractured reservoirs. These figures show that the majority of flow, either water or crude oil, is through the fractures with the largest apertures, and through the vertical and sub-vertical fractures. Furthermore, fracture mapping (Figs. 9.16-9.20) and numerical results (Figs. 9.21-9.28) illustrate that fluid flow can occur on a variety of scales because of (1) fracture aperture variation, (2) fracture frequency and (3) fracture interconnectivity. This is best explained by flow channelling and the cubic law, where the volumetric flow rate is proportional to the cube of the aperture (de Dreuzy *et al.*, 2002; Klimczak *et al.*, 2010). Thus, it is crucial to understand fracture networks within sills in hydrocarbon environments as they have the ability to conduct fluids or become barriers. These results on flow channelling and the cubic law can be applied in the field of volcanology, for example to crater cones that form along fissures such as Laki, SE Iceland (Barnett, 2011). Power-laws of natural fractures also have implications in seismic hazards, tectonics, aquifers, hydrocarbon reservoirs and mineralization (Marrett *et al.*, 1999).

Numerical results in Figures 9.21-9.28 show that for fluid flow to occur along fractures they must be open, where the distribution of these open fractures is determined by the local stress field that controls their orientation (Figs. 9.3; 9.4). Furthermore, each set of fractures have unique geometries, interconnectivities, hydraulic properties and spacings between them. All of these factors could provide advantages and/or disadvantages to hydrocarbon migration and trapping depending on the environment (Barton *et al.*, 1995; Aydin, 2000; Faulkner *et al.*, 2010). In addition, the diameter of these open fractures allowed for the calculation of intrinsic permeability (Eq. 9.5) and porosity (Eq. 9.6). The Whin Sill has an intrinsic permeability of $0.59 \times 10^{-6} \text{ m}^2$ and porosity of 1.89%, whereas the Stardalur sill cluster has an intrinsic permeability of $0.62 \times 10^{-6} \text{ m}^2$ and porosity of 0.68%. These calculated intrinsic permeabilities are consistent with measured permeabilities of $<10 \times 10^{-6} \text{ m}^2$ (Huang *et al.*, 2009), and the calculated porosity values are in accordance to measured bulk porosity of typical fractured rocks of 0.1-1% (Gutmanis *et al.*, 2010). However, the effects of weathering may increase the porosity up to 10% (Gutmanis *et al.*, 2010). Also, these calculated values for the Whin Sill and Stardalur sill cluster do not take into account micro structures, for example vesicles and micro-fractures, which too have implications for fluid flow (Fig. 11.4).

11.6 Further work

While there are clear extensions of this research, there is a consistency between model results and field observations. Possible future extensions are as follows:

1. Future numerical studies of sill emplacement to couple firstly, solid mechanics and thermal modelling, and secondly, solid mechanics and fluid flow. To carry this out effectively, field studies should be used as a complimentary source of data input, for example solidified sills and eroded magma chambers as well as their host rocks.
2. To relate thermal modelling and stress modelling, preferably into a time-dependent framework, to estimate assimilation of the host rock into the magma - stoping.
3. In this thesis many of the models have only a few layers in order to show stress field patterns around dykes and sills. To extend this in the future,

models will be run to include varying host rock mechanics based upon findings in the field, for example the Whin Sill, to help better understand the emplacement mechanisms of shallow level sills.

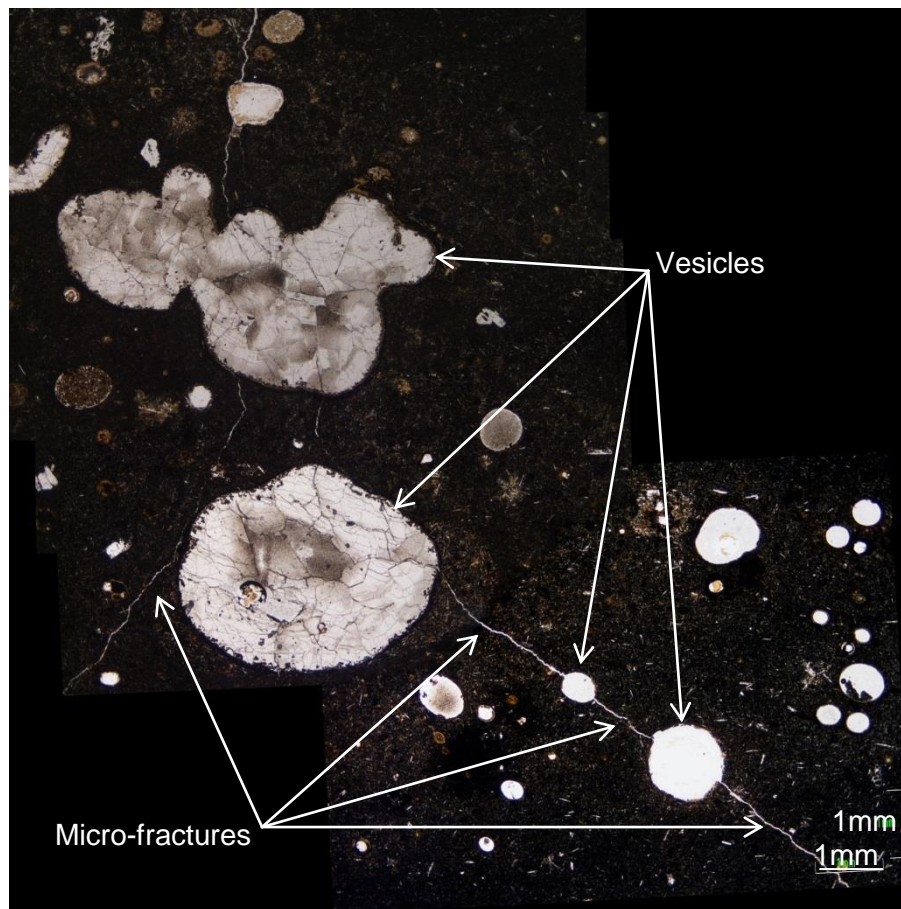


Figure 11.4: Thin section of Stiflisdalsvatn sill (grid reference: 64.26097N 021.328846W), with large circular vesicles interconnected by micro-fractures, showing implications for fluid flow paths. Scale in green, 1 mm.

4. In the majority of the models general loading conditions in extension and compression have been considered. However, in the future more comprehensive models can be made using more specific values.
5. The sills modelled in this thesis dominantly take a simple two-dimensional geometry, with some modelled in three-dimensions in Chapter 6. With respect to modelling hydrocarbon reservoirs, three-dimensional models of sills need to be considered to better understand all possibilities relating to sill margin rupture.
6. The fracture networks presented in this thesis are in two-dimensions. In the future, three-dimensional networks could be explored. A good location was

identified at Cow Green Reservoir, Northumberland, when undertaking fieldwork in the summer of 2013, and data has been collected for a three-dimensional fracture network.

7. In order to explore the heterogeneity of the upper crust further, the effects of fault propagation and orientation could be investigated. For example, flat and ramp geometries where stiff layers (e.g. sandstone) would accommodate a high angled fault while in a soft layer (e.g. shale), a low angled fault. Such fault geometries would most likely have an effect on permeability and fluid migration paths, and would therefore need to be modelled to see these effects.

Chapter 12: Conclusions

The main aim of this project was to study the sills in the Vøring Margin with a view to investigate their potential to be fractured reservoirs, seals and traps for hydrocarbons. This was done partly through analogies with sills exposed on land, such as England and Iceland. The main focus, however, has been on studying the mechanical interactions of the sills (modes of emplacement, stress fields, fracture networks (from the on-land analogies), permeabilities). Also, the volcanotectonic framework of sill emplacement and development has been studied, partly in relation to the potential of sills developing into shallow magma chambers, by using the field observations as well as numerical and analytical modelling. The main conclusions are as follows:

- Dykes are among the main building blocks of the Earth's upper crust, especially the oceanic crust. Numerical models illustrate that dykes may change the local stress field orientation and magnitude, so as to make it favourable for sill emplacement. Sill emplacement can be related to three principal mechanisms:
 1. Cook-Gordon debonding: opening of the contact
 2. Stress barriers: rotation of the local stress field
 3. Elastic mismatch: contrasting mechanical properties of the layers and material toughness of the contact
- Models support hypotheses that sills that have the ability to evolve into shallow magma chambers. Numerical models show that in order for magma chamber formation, the sill must have a radius that is larger than the depth at which the sill is emplaced. As the sill inflates, it deflects the overburden, and the underburden to some extent.
- Models show that graben subsidence favours deflection of dykes into sills because of an induced stress barrier. Fault zones themselves, may act as a trap towards crustal fluids if not reactivated. However, numerical models show that if reactivated, the fault permeability could temporarily increase in

the down-dip direction allowing for the escape of hydrocarbons towards the surface. Even if they are reactivated as a result of sill emplacement, the faults may still act as traps (along with the sills) because geothermal fluids generated by sill emplacement help to ‘heal’ and ‘seal’ the fault, reducing their overall permeability. In general, faults can act as conduits, barriers or a combination of both towards crustal fluid flow depending on their permeability structure.

- Fluid flow is along fracture networks within sills (and also along major faults). Field studies along the Whin Sill, NE England, and the Stardalur sill cluster, SW Iceland, allowed for analysis of such fracture networks, in terms of their fracture orientations, apertures, spacings and frequencies. Fracture orientations along with spacings and frequencies indicate a high degree of fracture interconnectivity and thus favourable paths for fluid migration. Fracture apertures show a power-law size distribution indicating the cubic law and effects of flow channelling, where flow is channelled along the few larger-aperture fractures. Furthermore, numerical models illustrate that fluid transport is most efficient where fractures have a suitable aperture and are favourably orientated. Thus, hydrocarbon transport through sills is primarily through fractures networks, which control the permeability (and porosity) of this relatively impermeable body.
- Sills have two low permeability margins, namely a chilled ‘glassy’ selvage and a baked margin as seen in the field, for example the Whin Sill. Numerical models show that tectonic loading subsequent to sill formation may cause these margins to become ruptured. For a sill to act as a fractured reservoir, the lower margin must be ruptured to allow the upward migrating hydrocarbons to accumulate within the sill, providing that the upper margin remains intact to form a seal. On the other hand, if the lower margin is not ruptured, hydrocarbons can accumulate in the host rock, as the sill may form a trap or a seal, especially in conjunction with a secondary barrier, for example dyke-sill contact and/or sill-fault contact.

References

- Abdelmalak, M.M., Mourgues, R., Galland, O., Bureau, D., 2012. Fracture mode analysis and related surface deformation during dyke intrusion: Results from 2D experimental modelling. *Earth and Planetary Science Letters*, **359-360**, 93-105.
- Aguilera, R., 1995. Naturally Fractured Reservoirs. Third edition. *PennWell*, 521pp.
- Agosta, F., 2008. Fluid flow properties of basin-bounding normal faults in platform carbonates, Fucino Basin, central Italy. In: Wibberly, C.A.J., Kurz, W., Imber, J., Holdsworth, R.E., Collettini, C., (eds) *The internal structure of fault zones: Implications for mechanical and fluid-flow properties*. Geological Society, London, Special Publications, **299**, 277-291.
- Amoruso, A., Crescentini, L., Berrino, G., 2008. Simultaneous inversion of deformation and gravity changes in a horizontally layered half-space: Evidences for magma intrusion during the 1982-1984 unrest a Campi Flegrei caldera (Italy). *Earth and Planetary Science Letters*, **272**, 181-188.
- Anderson, E. M., 1936. The dynamics of formation of cone sheets, ring dykes and cauldron subsidences. *Proceedings of the Royal Society of Edinburgh*, **56**, 128-163.
- Anderson, E.M., 1951. The dynamics of faulting and dyke formation with applications to Britain. Second edition. *Oliver and Boyd*, 206pp.
- Andrew R.E.B, 2008. *Volcanotectonic Evolution and Characteristic Volcanism of the Neovolcanic Zone of Iceland*. Ph.D. University of Göttingen, Germany, 130.
- Arnes, I., Svensen, H., Polteau, S., Planke, S., 2011. Contact metamorphic devolatilization of shales in the Karoo Basin, South Africa, and the effects of multiple sill intrusions. *Chemical Geology*, **281**, 181-194.
- Aydin, A., 2000. Fractures, faults, and hydrocarbon entrapment, migration and flow. *Marine and Petroleum Geology*, **17**, 797-814.

- Babiker, M., Gudmundsson, A., 2004. The effects of dykes and faults on groundwater flow in an arid land: the Red Sea Hills, Sudan. *Journal of Hydrogeology*, **297**, 256-273.
- Barnett, Z., 2011. *The mechanics of the 1783 Laki eruption, South Iceland*. MSci. Royal Holloway University of London, UK, 44.
- Barnett, Z. A., Gudmundsson, A., 2014. Numerical modelling of dykes deflected into sills to form a magma chamber. *Journal of Volcanology and Geothermal Research*, **281**, 1-11, doi: 10.1016/j.volgeores.2014.05.018.
- Barton, C.A., Zoback, M.D., Moos, D., 1995. Fluid flow along potentially active faults in crystalline rock. *Geology*, **23**, 683-686.
- Barton, M., Ghidotti, G., Holden, P., Goodwin, L., Heizler, M., 1995. Time-space evolution of a two-mica granite; the Birch Creek Pluton, CA, USA. In: Brown, M., Piccoli, P., (eds.) *The Origin of Granites and Related Rocks*. U. S. G. S. Circular, **1129**, 18-19.
- Baumgartner, L., Bodner, R., Leuthold, J., Muntener, O., Putlitz, B., Vennemann, T., 2014. The Torres del Paine intrusion as a model for a shallow magma chamber. *Geophysical Research Abstracts*, European Geoscience Union 2014, Vienna.
- Becerril, L., Galindo, I., Gudmundsson, A., Morales, J.M., 2013. Depth of origin of magma in eruptions. *Scientific Reports*, **3**, 1-6, doi: 10.1038/srep02762.
- Bédard, J.H., Naslund, H.R., Nabelek, P., Winpenny, A., Hryciuk, M., Macdonald, W., Hayes, B., Steigerwaldt, K., Hadlari, T., Rainbird, R., Dewing, K., Girard, É., 2012. Fault-mediated melt ascent in a Neoproterozoic continental flood basalt province, the Franklin Sills, Victoria Island, Canada. *Geological Society of America Bulletin*, **124**, 723-736, doi: 10.1130/B30450.1.
- Bell, A.F., Kilburn, C.R.J., 2012. Precursors to dyke-fed eruptions at basaltic volcanoes: insights from patterns of volcano-tectonic seismicity at Kilauea volcano, Hawaii. *Bulletin of Volcanology*, **74**, 325-339, doi: 10.1007/s00445-011-0519-3.

- Bell, B., Butcher, H., 2002. On the emplacement of sill complexes: evidence from the Faroe-Shetland Basin. *In: Jolley, D. W. & Bell, B.R. (eds) The North Atlantic Igneous Province: Stratigraphy, Tectonic, Volcanic and Magmatic Processes.* Geological Society, London, Special Publications, **197**, 307-329.
- Berner, U., Kus, J., Scheeder, G., Schneider, J., Schöner, R., Viereck-Götte, L., 2009. Influence of Jurassic sill intrusions on the organic matter of Upper Triassic lacustrine and fluvial sediments of North Victoria Land (Antarctica). *Geophysical Research Abstracts*, European Geoscience Union 2009, Vienna.
- Berkowitz, B., 1995. Analysis of fracture network connectivity using Percolation Theory. *Mathematical Geology*, **27**, 467-483.
- Berkowitz, B., Bour, O., Davy, P., Odling, N., 2000. Scaling of fracture connectivity in geological formations. *Geophysical Research Letters*, **27**, 2061-2064.
- Berndt, C., Skogly, O.P., Planke, S., Eldholm, O., 2000. High-velocity breakup-related sills in the Vøring Basin, off Norway. *Journal of Geophysical Research*, **105**, 28,443-28,454.
- Best, M.G., 2002. Igneous and metamorphic petrology. Second edition. *Wiley-Blackwell*, 752pp.
- Bianchi, R., Coradini, A., Federico, C., Giberti, G., Sartoris, G., Scandone, R., 1984. Modelling of surface ground deformations in the Phlegraean Fields volcanic area, Italy. *Bulletin of Volcanology*, **47**, 321-330.
- Bjørnseth, H.M., Grant, S.M., Hansen, E.K., Hossack, J.R., Roberts, D.G., Thompson, M., 1997. Structural evolution of the Vøring Basin, Norway, during the Late Cretaceous and Palaeogene. *Journal of the Geological Society*, **154**, 559-563.
- Blundell, S.J., Blundell, K.M., 2010. Concepts in thermal physics. Second edition. *Oxford University Press*, 493pp.
- Bonafede, M., Ferrari, C., 2009. Analytical models of deformation and residual gravity changes due to Mogi source in a viscoelastic medium. *Tectonophysics*, **471**, 4-13.

- Boncio, P., 2008. Deep-crust strike-slip earthquake faulting in southern Italy aided by high fluid pressure: insights from rheological analysis. *In: Wibberly, C.A.J., Kurz, W., Imber, J., Holdsworth, R.E., Collettini, C. (eds) The internal structure of fault zones: Implications for mechanical and fluid-flow properties.* Geological Society, London, Special Publications, **299**, 195-210.
- Bour, O., Davy, P., 1997. Connectivity of random fault networks following a power law fault length distribution. *Water Resources Research*, **33**, 1567-1583.
- Boutareaud, S., Wibberley, C.A.J., Fabbri, O., Shimamoto, T., 2008. Permeability structure and co-seismic thermal pressurization on fault branches: insights from the Usukidani fault, Japan. *In: Wibberly, C.A.J., Kurz, W., Imber, J., Holdsworth, R.E., Collettini, C. (eds) The internal structure of fault zones: Implications for mechanical and fluid-flow properties.* Geological Society, London, Special Publications, **299**, 341-361.
- Bradley, J., 1965. Intrusion of major dolerite sills. *Transactions of the Royal Society of New Zealand*, **3**, 27-55.
- Brebbia, C.A., Dominguez, J., 1992. Boundary elements: an introductory course. Second edition. *WIT Press*, 322pp.
- Brekke, H., 2000. The tectonic evolution of the Norwegian Sea Continental Margin with emphasis on the Vøring and Møre Basins. *Geological Society, London, Special Publications*, **167**, 327-378.
- Brenner, S.L., Gudmundsson, A., 2002. Permeability development during hydrofracture propagation in layered reservoirs. *Norges geologiske undersøkelse Bulletin*, **439**, 71-77.
- Brenner, S. L., 2003. *Field studies and models of hydrofractures in heterogeneous reservoirs.* Ph.D. University of Bergen, Norway, 36.
- Brenner, S.L., Gudmundsson, A., 2004. Arrest and aperture variation of hydrofractures in layered reservoirs. *In: Cosgrove, J.W, Engelder, T. (eds) The Initiation, Propagation and Arrest of Joints and Other Fractures.* Geological Society, London, Special Publications, **231**, 117-128.

- Bruhn, R.L., Parry, W.T., Yonkee, W.A., Tompson, T., 1994. Fracturing and hydrothermal alteration in normal fault zones. *Pure and Applied Geophysics*, **142**, 609-644.
- Bunger, A.P., Cruden, A.R., 2011. Modelling the growth of laccoliths and large mafic sills: Role of magma body forces. *Journal of Geophysical Research*, **116**, B02203, 1-18, doi: 10.1029/2010JB007648.
- Burchardt, S., 2008. New insights into the mechanics of sill emplacement provided by field observations of the Njardvik Sill, Northeast Iceland. *Journal of Volcanology and Geothermal Research*, **173**, 280-288.
- Caine, J.S., Evans, J.P., Forster, C.B., 1996. Fault zone architecture and permeability structure. *Geology*, **24**, 1025-1028.
- Cartwright, J.A., Trudgill, B.D., Mansfield, C.S., 1995. Fault growth by segment linkage: an explanation for scatter in maximum displacement and trace length data from the Canyonlands Grabens of SE Utah. *Journal of Structural Geology*, **17**, 1319-1326.
- Cartwright, J., Hansen, D.M., 2006. Magma transport through the crust via interconnected sill complexes. *Geology*, **34**, 929-932.
- Cathles, L.M., Erendi, A.H.J., Barrie, T., 1997. How long can a hydrothermal system be sustained by a single intrusive event? *Economic Geology*, **92**, 766-771.
- Chen, Z., Yan, H., Li, J., Zhang, G., Zhang, Z., Liu, B., 1999. Relationship between tertiary volcanic rocks and hydrocarbons in the Liaohe Basin, People's Republic of China. *The American Association of Petroleum Geologists*, **83**, 1004-1014.
- Cheng, A.H.-D., Cheng, D.T., 2005. Heritage and early history of the boundary element. *Engineering Analysis with Boundary Elements*, **29**, 268-302.
- Chevallier, L., Woodford, A., 1999. Morpho-tectonics and mechanism of emplacement of the dolerite rings and sills of the western Karoo, South Africa. *South African Journal of Geology*, **102**, 43-54.
- COMSOL, 2012. *COMSOL Multiphysics User's Guide*. USA, 1292pp.

- Cook, J., Gordon, J.E., 1964. A mechanism for the control of crack propagation in all-brittle systems. *Proceedings of the Royal Society of London*, **A282**, 508-520, doi: 10.1098/rspa.1964.0248.
- Corry, C.E., 1988. Laccoliths: mechanics of emplacement and growth. *Geological Society of America, Special Papers*, **220**, 1-110.
- Courant, R., 1943. Variational methods for the solution problems of equilibrium and vibrations. *Bulletin of American Mathematical Society*, **49**, 1-23.
- Cruden, A., McCaffrey, K., 2002. Different scaling laws for sills, laccoliths and plutons: Mechanical thresholds on roof lifting and floor depression. In: Breitzkreuz, C., Mock, A., Petford, N. (eds) *First International Workshop: Physical Geology of Subvolcanic Systems – Laccoliths, Sills and Dykes (LASI)*. Wissenschaftliche Mitteilung Institut für Geologie, Technische Universität Bergakademie Freiberg, **20/2012**, 15-17.
- Cruden, A., McCaffrey, K., 2006. Dimensional scaling relationships of tabular intrusions and their implications for a size, depth and compositionally dependent spectrum of emplacement processes in the crust. *Eos Transactions American Geophysical Union*, **87** (52), Fall Meeting Supplement, Abstract V12B-06.
- Cukur, D., Horozal, S., Kim, D.C., Lee, G.H., Han, H.C., Kang, M.H., 2010. The distribution and characteristics of igneous complexes in the northern East China Sea Shelf Basin and their implications for hydrocarbon potential. *Marine Geophysics Research*, **31**, 299-313.
- de Dreuzy, D., Davy, P., Bour, O., 2002. Hydraulic properties of two dimensional fracture networks following power law distributions of length and aperture. *Water Resources Research*, **38**, 12.1-12.9, doi:10.1029/2001WR001009.
- de Saint-Blanquat, M., Law, R. D., Bouchez, J.-L., Morgan, S. S., 2001. Internal structure and emplacement of the Papeuse Flat pluton: An integrated structural, petrographic, and magnetic susceptibility study. *Geological Society of America Bulletin*, **113**, 976-995.
- Deb, D., 2006. Finite Element Method, Concepts and Applications in Geomechanics. First edition. *PHI Learning Private Limited*, 269pp.

- DeGraff, J.M., Aydin, A., 1987. Surface morphology of columnar joints and its significance to mechanics and direction of joint growth. *Geological Society of America*, **99**, 605-617.
- Delpino, D.H., Bermudez, A.M., 2009. Petroleum systems including unconventional reservoirs in intrusive igneous rocks (sills and laccoliths). *The Leading Edge*, **28**, doi:10.1190/1.3167782.
- Dieterich, J.H., Decker, R.W., 1975. Finite element modelling of surface deformation associated with volcanism. *Journal of Geophysical Research*, **80**, 4094-4102, doi: 10.1029/JB080i029p04094.
- Doré, A.G., Lundin, E.R., 1996. Cenozoic compressional structures on the NE Atlantic margin: nature, origin and potential significance for hydrocarbon exploration. *Petroleum Geoscience*, **2**, 299-311.
- Doré, A.G., Lundin, E.R., Jensen, L.N., Birkeland, Ø., Eliassen, P.E., Fichler, C., 1999. Principal tectonic events in the evolution of the northwest European Atlantic margin. In: Fleet, A.J., Boldy, S.A.R. (eds) *Petroleum Geology of Northwest Europe: Proceedings of the 5th Conference*, 41-61.
- Duncan, R.A., Hooper, P.R., Rehacek, J., Marsh, J.S., Duncan, A.R., 1997. The timing and duration of the Karoo igneous event, southern Gondwana. *Journal of Geophysical Research*, **102**, 18127-18138.
- Dundurs, J., 1969. Edge-bonded dissimilar orthogonal wedges. *Journal of Applied Mechanics*, **36**, 650-652.
- Egbeni, S., McClay, K., Jian-kui Fu, J., Bruce, D., 2014. Influence of igneous sills on Paleocene turbidite deposition in the Faroe-Shetland Basin: a case study in Flett and Muckle sub-basin and its implication for hydrocarbon exploration. *Geological Society, London, Special Publications*, **397**, 33-57, doi: 10.1144/SP397.8.
- Eldhom, O., Tsikalas, F., Faleide, J.I., 2002. Continental margin off Norway 62-75°N: Palaeogene tectono-magmatic segmentation and sedimentation. *Geological Society, London, Special Publication*, **197**, 39-68.

- Evans, J.P., Forster, C.B., Goddard, J.V., 1997. Permeability of fault-related rocks, and implications for hydraulic structure of fault zones. *Journal of Structural Geology*, **19**, 1393-1404.
- Faleide, J.I., Tsikalas, F., Breivik, A.J., Mjelde, R., Ritzmann, O., Engen, Ø., Wilson, J., Eldholm, O., 2008. Structure and evolution of the continental margin off Norway and the Barents Sea. *Episodes*, **31**,82-91.
- Faulkner, D.R., Jackson, C.A.L., Lunn, R.J., Schlische, R.W., Shipton, Z.K., Wibberley, C.A.J., Withjack, M.O., 2010. A review of recent developments concerning the structure, mechanics and fluid flow properties of fault zones. *Journal of Structural Geology*, **32**, 1557-1575.
- Fejerskov, M., Linholm, C., 2000. Crustal stresses in and around Norway: an evaluation of stress generating mechanisms. In: Nøttvedt, A.(eds) *Dynamics of the Norwegian Margin*. Geological Society, London, Special Publications, **167**, 451-467.
- Fejerskov, M., Lindholm, C., Myrvang, A., Bungham, H., 2000. Crustal stresses in and around Norway: compilation of in-situ observations. . In: Nøttvedt, A.(eds) *Dynamics of the Norwegian Margin*. Geological Society, London, Special Publications, **167**, 441-449.
- Ferrill, D.A., Smart, K.J., Necsoiu, M., 2008. Displacement-length scaling for single-event fault ruptures: insights from Newberry Springs Fault Zone and implications for fault zone structure. In: Wibberly, C.A.J., Kurz, W., Imber, J., Holdsworth, R.E., Collettini, C. (eds) *The internal structure of fault zones: Implications for mechanical and fluid-flow properties*. Geological Society, London, Special Publications, **299**, 113-122.
- Fialko, Y., Kazhan, Y., Simons, M., 2001. Deformation due to a pressurized horizontal circular crack in an elastic half-space, with applications to volcano geodesy. *Geophysical Journal International*, **146**, 181-190.
- Filho, A.T., Pimentel, A.M., Antonioli, L., 2008. Magmatism and petroleum exploration in the Brazilian Paleozoic basins. *Marine and Petroleum Geology*, **25**, 143-151.

- Fischer, M.P., Gross, M.R., Engelder, T., Greenfield, R.J., 1995. Finite-element analysis of the stress distribution around a pressurized crack in a layered elastic medium: implications for the spacing of fluid-driven joints in bedded sedimentary rock. *Tectonophysics*, **247**, 49-64.
- Fjeldskaar, W., Helset, H.M., Johansen, H., Grunnaleite, I., Horstad, I., 2008. Thermal modelling of magmatic intrusions in the Gjallar Ridge, Norwegian Sea: implications for vitrinite reflectance and hydrocarbon maturation. *Basin Research*, **20**, 143-159, doi: 10.1111/j.1365-2117.2007.00347.x.
- Fjeldskaar, W., Grunnaleite, I., Zweigel, J., Mjelde, R., Faleide, J. I., Wilson, J., 2009. Modelled palaeo-temperature on Vøring, offshore mid Norway - The effect of the Lower Crustal Body. *Tectonophysics*, **474**, 544-558, doi: 10.1016/j.tecto.2009.04.036.
- Fossen, H., 2010. Structural Geology. First edition. *Cambridge University Press*, 480pp.
- Francis, E. H., 1982. Magma and sediment - I: emplacement mechanism of late Carboniferous tholeiite sills in the northern Britain. *Journal of the Geological Society of London*, **139**, 1-20.
- Fridleifsson, I.B., 1977. Distribution of large basaltic intrusions in the Icelandic crust and the nature of the layer 2 - layer 3 boundary. *Geological Society of America Bulletin*, **88**, 1689-1693.
- Galerne, C.Y., Neumann, E-R., Planke, S., 2008. Emplacement mechanisms of sill complexes: Information from the geochemical architecture of the Golden Valley Sill Complex, South Africa. *Journal of Volcanology and Geothermal Research*, **177**, 425-440.
- Galerne, C.Y., Galland, O., Neumann, E-R., Planke, S., 2011. 3D relationships between sills and their feeders: Evidences from the Golden Valley Sill Complex (Karoo Basin) and experimental modelling. *Volcanic and Magmatic Studies Group*, Annual Meeting 2011, Queens' College Cambridge.
- Galland, O., Planke, S., Neumann, E.R., Malthe-Sørensen, A., 2009. Experimental modelling of shallow magma emplacement: Application to saucer-shaped

- intrusions. *Earth and Planetary Science Letters*, **227**, 373-383, doi: 10.1016/j.pepi.2006.10.004.
- Galushkin, Y.I., 1997. Thermal effects of igneous intrusions on maturity of organic matter: A possible mechanism of intrusion. *Organic Geochemistry*, **26**, 645-658..
- Garcia, A.S., Thomas, D.N., Liss, D., Shaw, J., 2006. Low geomagnetic field intensity during the Kiaman superchron: Thellier and microwave results from the Great Whin Sill intrusive complex, northern United Kingdom. *Geophysical Research Letters*, **33**, 1-5, doi: 10.1029/2006GL026729.
- Gere, J.M., Goodno, B.J., 2012. Mechanics of materials. Eighth edition. *CENGARGE Learning Custom Publishing*, 1152pp.
- Gernigon, L., Ringenbach, J.C., Planke, S., Le Gall, B., Jonquet-Kolstø, H., 2003. Extension, crustal structure and magmatism at the outer Vøring Basin, Norwegian margin. *Journal of the Geological Society, London*, **160**, 197-208.
- Gernigon, L., Ringenbach, J.-C., Planke, S., Le Gall, B., 2004. Deep structures and breakup along volcanic rifted margins: insights from integrated studies along the outer Vøring Basin (Norway). *Marine and Petroleum Geology*, **21**, 363-372.
- Gernigon, L., Lucazeau, F., Brigaud, F., Ringenbach, J.-C., Planke, S., Le Gall, B., 2006. A moderate melting model for the Vøring margin (Norway) based on structural observations and a thermo-kinematical modelling: Implication for the meaning of the lower crustal bodies. *Tectonophysics*, **412**, 255-278.
- Geshi, N., Kusumoto, S., Gudmundsson, A., 2010. Geometric difference between non-feeder and feeder dikes. *Geology*, **38**, 195-198, doi: 10.1130/G30350.1.
- Geshi, N., Kusumoto, S., and Gudmundsson, A., 2012. Effects of mechanical layering of host rocks on dike growth and arrest. *Journal of Volcanology and Geothermal Research*, **223**, 74-82.
- Geyer, A., Gottsmann, J., 2010. The influence of mechanical stiffness on caldera deformation and implications for the 1971-1984 Rabaul uplift (Papua New Guinea). *Tectonophysics*, **483**, 399-412, doi: 10.1016/j.tecto.2009.10.029.

- Glazner, A.F., Bartley, J.M., Coleman, D.S., Gray, W., Taylor, R.Z., 2004. Are plutons assembled over millions of years by amalgamation from small magma chambers? *GSA Today*, **14**, 4-11.
- Goehring, L., Morris, S.W., 2005. Order and disorder in columnar joints. *Europhysics Letters*, **69**, 739-745, doi: 10.1209/epl/i2004-10408-x.
- Goodenough, K., 1999. The Shiant Isles site of special specific interest. Geological conservation review interest: Tertiary igneous. *Earth science management brief project*, 40pp.
- Goulty, N.R., Peirce, C., Flatman, T.D., Home, M., Richardson, J.H., 2000. Magnetic survey of the Holy Island Dyke on Holy Island, Northumberland. *Proceedings of the Yorkshire Geological Society*, **53**, 111-118.
- Goulty, N.R., 2005. Emplacement mechanism of the Great Whin and Midland Valley dolerite sills. *Journal of Geological Society, London*, **162**, 1047-1056.
- Goulty, N.R., Schofield, N., 2008. Implications of simple flexure theory for the formation of saucer-shaped sills. *Journal of Structural Geology*, **30**, 812-817.
- Gray, D.R., Janssen, C., Vapnik, Y., 1999. Deformation character and palaeo-fluid flow across a wrench fault within a Palaeozoic subduction-accretion system: Waratah Fault Zone, southeastern Australia. *Journal of Structural Geology*, **21**, 191-214.
- Gretener, P.E., 1969. On the mechanics of the intrusion of sills. *Canadian Journal of Earth Sciences*, **6**, 1415-1419.
- Griffith, A.A., 1920. The phenomena of rupture and flow in solids. *Philosophical Transactions of the Royal Society of London*, **A221**, 163-198.
- Grunnaleite, I., Fjeldskaar, W., Wilson, J., Faleide, J. I. and Zweigel, J., 2009. Effect of local variations of vertical and horizontal stresses on the Cenozoic structuring of the mid-Norwegian shelf. *Tectonophysics*, **470**, 267-283, doi: 10.1016/j.tecto.2009.01.005.
- Gudmundsson, A., 1984. Tectonic aspects of dykes in northwestern Iceland. *Jökull*, **34**, 81-96.

- Gudmundsson, A., 1988. Formation of collapse calderas. *Geology*, **16**, 808-810.
- Gudmundsson, A., 1990. Emplacement of dikes, sills and crustal magma chambers at divergent plate boundaries. *Tectonophysics*, **176**, 257-275.
- Gudmundsson, A., 1995. The geometry and growth of dykes. In: Baer, G., Heimann, A., (eds) *Physics and Chemistry of Dykes*. Balkema, Rotterdam, 23-34.
- Gudmundsson, A., 1999. Postglacial crustal doming, stresses and fracture formation with application to Norway. *Tectonophysics*, **307**, 407-419.
- Gudmundsson, A., Marinoni, L.B., Marti, J., 1999. Injection and arrest of dykes: implications for volcanic hazards. *Journal of Volcanology and Geothermal Research*, **88**, 1-13.
- Gudmundsson, A., 2000a. Dynamics of volcanic systems in Iceland: example of tectonism and volcanism at juxtaposed hot spot and mid-ocean ridge system. *Annual Review of Earth and Planetary Science*, **28**, 107-140.
- Gudmundsson, A., 2000b. Fracture dimensions, displacements and fluid transport. *Journal of Structural Geology*, **22**, 1221-1231.
- Gudmundsson, A., 2000c. Active fault zones and groundwater flow. *Geophysical Research Letters*, **27**, 2993-2996.
- Gudmundsson, A., 2001. Fluid overpressure and flow in fault zones: field measurements and models. *Tectonophysics*, **336**, 183-197.
- Gudmundsson, A., Brenner, S.L., 2001. How hydrofractures become arrested. *Terra Nova*, **13**, 456-462.
- Gudmundsson, A., Berg, S.S., Lyslo, K.B., Skurtveit, E., 2001. Fracture networks and fluid transport in active fault zones. *Journal of Structural Geology*, **23**, 343-353.
- Gudmundsson, A., 2002. Emplacement and arrest of sheets and dykes in central volcanoes. *Journal of Volcanology and Geothermal Research*, **116**, 279-298.

- Gudmundsson, A., Fjeldskaar, I., Brenner, S.J., 2002a. Propagation pathways and fluid transport of hydrofractures in jointed and layered rocks in geothermal fields. *Journal of Volcanology and Geothermal Research*, **116**, 257-278.
- Gudmundsson, A., Fjeldskaar, I., Gjesdal, O., 2002b. Fracture-generated permeability and groundwater yield in Norway. *Norges geologiske undersøkelse Bulletin*, **439**, 61-69.
- Gudmundsson, A., 2003. Surface stresses associated with arrested dykes in rift zones. *Bulletin of Volcanology*, **65**, 606– 619.
- Gudmundsson, A., Gjesdal, O., Brenner, S., Fjeldskaar, I., 2003. Effects of linking up of discontinuities on fracture growth and groundwater transport. *Hydrogeology Journal*, **11**, 84-99, doi: 10.1007/s10040-002-0238-0.
- Gudmundsson, A., 2004. Effects of Young's modulus on fault displacement. *Comptes Rendus Geoscience*, **336**, 85-92.
- Gudmundsson, A., Brenner, S.L., 2004. Local stresses, dyke arrest and surface deformation in volcanic edifices and rift zones. *Annals of Geophysics*, **47**, 1433-1454.
- Gudmundsson, A., Brenner, S.L., 2005. On the conditions of sheet injections and eruptions in stratovolcanoes. *Bulletin of Volcanology*, **67**, 768-782, doi: 10.1007/s00445-005-0433-7.
- Gudmundsson, A., Løtveit, I.F., 2005. Dyke emplacement in a layered and faulted rift zone. *Journal of Volcanology and Geothermal Research*, **144**, 311-327.
- Gudmundsson, A., 2006. How local stresses control magma-chamber ruptures, dyke injections, and eruptions in composite volcanoes. *Earth-Science Reviews*, **79**, 1-31.
- Gudmundsson, A., 2009. Toughness and failure of volcanic edifices. *Tectonophysics*, **471**, 27-35.
- Gudmundsson, A., Simmenes, T.H., Larsen, B., Philipp, S.L., 2010. Effects of internal structure and local stresses on fracture propagation, deflection, and arrest in fault zones. *Journal of Structural Geology*, **32**, 1643-1655.

- Gudmundsson, A., 2011a. *Rock Fractures in Geological Processes*. First edition. Cambridge University Press, 560pp.
- Gudmundsson, A., 2011b. Deflection of dykes into sills at discontinuities and magma-chamber formation. *Tectonophysics*, **500**, 50–64.
- Gudmundsson, A., 2012a. Magma chambers: Formation, local stresses, excess pressures, and compartments. *Journal of Volcanology and Geothermal Research*, **237**, 19-41.
- Gudmundsson, A., 2012b. Strength and strain energies of volcanic edifices: implications for eruptions, collapse calderas, and landslides. *Natural Hazards and Earth System Sciences*, **12**, 1-18.
- Gudmundsson, G., Løtveit, I.F., 2012. Sills as fractured hydrocarbon reservoirs: examples and models. *Geological Society, London, Special Publications*, **374**, doi: 10.1144/SP374.5.
- Gudmundsson, A., Kusumoto, S., Simmenes, T., Phillip, S., Larsen, B., Løtveit, I.F., 2012. Effects of overpressure variations on fracture apertures and fluid transport. *Tectonophysics*, **581**, 220-230.
- Gudmundsson, A., Mohajeri, N., 2013. Relations between the scaling exponents, entropies, and energies of fracture networks. *Bulletin de la Société Géologique de France*, **184**, 373-382.
- Gudmundsson, M.T., Thordarson, T., Hoskuldsson, A., Larsen, G., Bjornsson, H., Prata, F.J., Oddson, B., Magnusson, E., Hognadottir, T., Petersen, G.N., Hayward, C.L., Stevenson, J.A., Jonsdottir, J., 2012. Ash generation and distribution from the April-May 2010 eruption of Eyjafjallajökull, Iceland. *Scientific Reports*, **2**, 1-12, doi: 10.1038/srep00572.
- Gunn, B.M., 1966. Modal and element variation in Antarctic tholeiites. *Geochemica et Cosmochimica Acta*, **30**, 881-920.
- Gutmanis, J., Batchelor, T., colleagues at Geoscience Limited, 2010. Hydrocarbon production from fractured basement formations. Verison 9. *GeoScience Limited*, 40pp.

- Hancock, P.L., Skinner, B.J., 2000. The Oxford companion to the Earth. First edition. *Oxford University Press*, 1185pp.
- Hansen, D.M., Cartwright, J.A., Thomas, D., 2004. 3D seismic analysis of the geometry of igneous sills and sill junction relationships. *Geological Society, London, Memoirs*, **29**, 199-208, doi: 10.1144/GSL.MEM.2004.029.01.19.
- Hansen, D.M., Cartwright, J., 2006a. The three-dimensional geometry and growth of forced folds above saucer-shaped igneous sills. *Journal of Structural Geology*, **28**, 1520-1535.
- Hansen, D.M., Cartwright, J., 2006b. Saucer-shaped sill with lobate morphology revealed by 3D seismic data: implications for resolving a shallow-level sill emplacement mechanism. *Journal of the Geological Society, London*, **163**, 509-523.
- Hansen, J., Jerram, D.A., McCaffrey, K., Passey, S.R., 2011. Early Cenozoic saucer-shaped sills of the Faroe Islands: an example of intrusive styles in basaltic lava piles. *Journal of the Geological Society, London*, **168**, 159-178, doi: 10.1144/0016-76492010-012.
- Hardee, H.C., 1982. Incipient magma chamber formation as a result of repetitive intrusions. *Bulletin of Volcanology*, **45**, 41-49.
- Hartley, A., Schofield, N., 2010. Aspects of petroleum geology on the Isle of Skye: Sediments, maturity and complex reservoirs. *AAPG Aberdeen-Amsterdam-Lisbon student chapters joint fieldwork 2010 sponsors report*, Aberdeen, 11pp.
- Hatton, C.G., Main, I.G., Meredith, P.G., 1994. Non-universal scaling of fracture length and opening displacement. *Nature*, **367**, 160-162.
- Hawkes, L., Hawkes, H.K., 1933. The Sandfell laccolith and "dome of elevation". *Quarterly Journal of the Geological Society of London*, **89**, 379-400.
- He, M.Y., Hutchinson, J.W., 1989. Crack deflection at an interface between dissimilar elastic materials. *International Journal of Solids and Structures*, **25**, 1053-1067.

- He, M.Y., Evans, A.G., Hutchinson, J.W., 1994. Crack deflection at an interface between dissimilar elastic materials: role of residual stresses. *International Journal of Solids and Structures*, **31**, 3443-3455.
- Heidbach, O., Tingay, M., Barth, A., Reinecker, J., Kurfeß, D., Müller, B., 2010. Global crustal stress pattern based on the World Stress Map database release 2008. *Tectonophysics*, **482**, 3-15.
- Hicks, E.C., Bungum, H., Lindholm, C.D., 2000. Seismic activity, inferred crustal stresses and seismotectonics in the Rana region, Northern Norway. *Quaternary Science Reviews*, **19**, 1423-1436.
- Hillis, R.R., 1998. The influence of fracture stiffness and the *in situ* stress field on the closure of natural fractures. *Petroleum Geoscience*, **4**, 57-65.
- Hjelstuen, B.O., Eldholm, O., Skogseid, J., 1999. Cenozoic evolution of the northern Vøring Margin. *Geological Society of America Bulletin*, **111**, 1792-1807.
- Horsman, E., Tikoff, B., Morgan, S., 2005. Emplacement-related fabric and multiple sheets in the Maiden Creek sill, Henry Mountains, Utah, USA. *Journal of Structural Geology*, **27**, 1426-1444.
- Horsman, E., Morgan, S., de Saint-Blanquat, M., Habert, G., Nugent, A., Hunter, R.A., Tikoff, B., 2009. Emplacement and assembly of shallow intrusions from multiple magma pulses, Henry Mountains, Utah. *Earth and Environmental Science Transactions of the Royal Society of Edinburgh*, **100**, 117-132.
- Hrennikoff, A., 1941. Solution of problems of elasticity by the framework method. *Journal of Applied Mechanics*, **8**, 169-175.
- Huang, Y., Wang, P., Chen, S., 2009. Distribution and characteristics of volcanic reservoirs in China. *Global Geology*, **12**, 64-79, doi: 10.3969/j.issn.1673-9736.2009.02.002.
- Hubbert, M.K., 1937. Theory of scale models as applied to the study of geological structures. *Bulletin of the Geological Society of America*, **48**, 1459-1520.
- Hudson, J.A., Harrison, J.P., 1997. Engineering rock mechanics: An introduction to the principles. First edition. *Elsevier Science Ltd*, 456pp.

- Hughes, C.J., 1982. *Igneous Petrology*. Elsevier, 551 pp.
- Hutchinson, J.W., 1996. Stresses and failure modes in thin films and multilayers. Notes for a Dcamm Course. Lyngby: Technical University of Denmark, 1-45pp.
- Hutton, D. H. W., 1992. Granite sheeted complexes: evidence for diking ascent mechanism. *Transactions of the Royal Society of Edinburgh*, **83**, 377-382.
- Jaeger, J. C., 1957. The temperature in the neighbourhood of a cooling intrusive sheet. *American Journal of Science*, **255**, 306-318.
- Jaeger, J.C., Cook, N.G.W., 1979. *Fundamentals of Rock Mechanics*. Chapman and Hall, London, 593pp.
- Jaeger, J.C., Cook, N.G.W., Zimmerman, R., 2007. *Fundamentals of rock mechanics*. Fourth edition. Wiley-Blackwell, 488pp.
- Jahn, F., Cook, M., Graham, M., 2008. *Hydrocarbon exploration and production (Developments in Petroleum Science):55*. Second edition. Elsevier Science, 456pp.
- Jamtveit, B., Svensen, H., Podladchikov, Y.Y., Planke, S., 2004. Hydrothermal vent complexes associated with sill intrusions in sedimentary basins. *Geological Society, London, Special Publications*, **234**, 233-241.
- Jones, S.F., Wielens, H., Williamson, M-C., Zentilli, M., 2007. Impact of magmatism on petroleum systems in the Sverdrup Basin, Canadian Arctic Islands, Nunavut: A numerical modelling study. *Journal of Petroleum Geology*, **30(3)**, 237-256.
- Johnson, G.A.L., Dunham, K.C, 2001. Emplacement of the Great Whin Dolerite Complex and the Little Whin Sill in relation to the structure of northern England. *Proceedings of the Yorkshire Geological Society*, **53**, 177-186, doi: 10.1144/pygs.53.3.177.
- Kardar, M., 2007. *Statistical physics of particles*. First edition. Cambridge University Press, 330pp.

- Kavanagh, J.L., Menand, T., Sparks, R.S.J., 2006. An experimental investigation of sill formation and propagation in layered elastic media. *Earth and Planetary Science Letters*, **245**, 799–813.
- Kavanagh, J.L., Menand, T., Daniels, K.A., 2013. Gelatine as a crustal analogue: Determining elastic properties for modelling magmatic intrusions. *Tectonophysics*, **582**, 101-111.
- Kervyn, M., Ernst, G.G.J., van Wyk de Vries, B., Mathieu, L., Jacobs, P., 2009. Volcano load control on dyke propagation and vent distribution: Insights from analogue modelling. *Journal of Geophysical Research*, **114**, B03401, doi: 10.1029.2008JB005653.
- Kinvig, H.S., Geyer, A., Gottsmann, J., 2009. On the effect of crustal layering on ring-fault initiation and the formation of collapse calderas. *Journal of Volcanology and Geothermal Research*, **186**, 293-304, doi: 10.1016/j.jvolgeores.2009.07.007.
- Klimczak, C., Schultz, R.A., Parashar, R., Reeves, D.M., 2010. Cubic law with aperture-length correlation: implications for network scale fluid flow. *Hydrogeology Journal*, **18**, 851-862, doi: 10.1007/s10040-009-0572-6.
- Knipe, R.J., Jones, G., Fisher, Q.J., 1998. Faulting, fault sealing and fluid flow in hydrocarbon reservoirs: an introduction. In: Knipe, R.J., Jones, G., Fisher, Q.J. (eds) *Faulting, Fault Sealing and Fluid Flow in Hydrocarbon Reservoirs*. Geological Society, London, Special Publications, **147**, vii-xxi.
- Kühn, D., Dahm, T., 2008. Numerical modelling of dyke interaction and its influence on oceanic crust formation. *Tectonophysics*, **447**, 53-65.
- Kusumoto, S., Geshi, N., Gudmundsson, A., 2013. Aspect ratios and magma overpressures of non-feeder dikes observed in the Miyake-jima volcano (Japan), and fracture toughness of its upper part. *Geophysical Research Letters*, **40**, 1065-1068, doi:10.1002/grl.50284, 2013.
- Larsen, B., Grunnaleite, I., Gudmundsson, A., 2010. How fracture systems affect permeability development in shallow-water carbonate rocks: An example from the Gargano Peninsula, Italy. *Journal of Structural Geology*, **32**, 1212-1230.

- Leat, P.T., Luttinen, A.V., Storey, B.C., Millar, I.L., 2006. Sills of the Theron Mountains, Antarctica: evidence for long distance transport of mafic magmas during Gondwana break-up. *In: Hanski, E.; Mertanen, S.; Ramo, T.; Vuollo, J., (eds.) Dyke swarms: time markers of crustal evolution.* London, UK, Taylor and Francis, 183-199.
- Lee, C.K., Farmer, I., 1993. Fluid flow in discontinuous rocks. First edition. *Chapman & Hall*, 180pp.
- Lee, G.H., Kwon, Y.I., Yoon, C.S., Kim, H.J., Yoo, H.S., 2006. Igneous complexes in the eastern Northern Yellow Sea Basin and their implications for hydrocarbon systems. *Marine and Petroleum Geology*, **21**, 631-645.
- Lindholm, C.D., Bungum, H., Hicks, E., Villagran, M., 2000. Crustal stress and tectonics in Norwegian regions determined from earthquake focal mechanisms. *Geological Society, London, Special Publications*, **167**, 429-439, doi: 10.1144/GSL.SP.2000.167.01.17.
- Lister, J.R., Kerr, R.C., 1991. Fluid-mechanical models of crack propagation and their application to magma transport in dykes. *Journal of Geophysical Research*, **96**, 10049-10077.
- Liss, D., Owens, W.H., Hutton, D.H.W., 2004. New palaeomagnetic results from the Whin Sill complex: evidence for a multiple intrusion event and revised virtual geomagnetic poles for the late Carboniferous for the British Isles. *Journal of the Geological Society, London*, **161**, 927-938.
- Logan, D.L., 2011. A First Course in the Finite Element Method. Fifth edition. *Nelson Engineering*, 832pp.
- Long, J.C.S., Witherspoon, P.A., 1985. The relationship of the degree of interconnection to permeability in fracture networks. *Journal of Geophysical Research*, **90**, 3087-3098.
- Lundin, E.R., Doré, A.G., 1997. A tectonic model for the Norwegian passive margin with implications for the NE Atlantic: Early Cretaceous to break-up. *Journal of the Geological Society, London*, **154**, 545-550.

- Lunn, R.J., Shipton, Z.K., Bright, A.M., 2008. How can we improve estimates of bulk fault zone hydraulic properties? *In: Wibberly, C.A.J., Kurz, W., Imber, J., Holdsworth, R.E., Collettini, C., (eds) The internal structure of fault zones: Implications for mechanical and fluid-flow properties.* Geological Society, London, Special Publications, **299**, 231-237.
- Maccaferri, F., Bonafede, M., Rivalta, E., 2010. A numerical model of dyke propagation in layered elastic media. *Geophysical Journal International*, **180**, 1107-1123.
- Maccaferri, F., Bonafede, M., Rivalta, E., 2011. A quantitative study of the mechanisms governing dike propagation, dike arrest and sill formation. *Journal of Volcanology and Geothermal Research*, **208**, 39-50.
- Macdonald, K.C., 1982. Mid-ocean ridges: fine scale tectonic, volcanic and hydrothermal processes within the plate boundary zone. *Annual Reviews of Earth and Planetary Sciences*, **17**, 437-474.
- Mader, H.M., Manga, M., Koyaguchi, T., 2004. The role of laboratory experiments in volcanology. *Journal of Volcanology and Geothermal Research*, **129**, 1-5.
- Magee, C., Jackson, C.A-L., Schofield, N., 2013. The influence of normal fault geometry on igneous sill emplacement and morphology. *Geology*, **41**, 407-410, doi: 10.1130/G33824.1.
- Magee, C., Jackson, C. A-L., Schofield, N., 2014. Diachronous sub-volcanic intrusion along deep-water margins: insights from the Irish Rockall Basin. *Basin Research*, **26**, 85-105, doi: 10.1111/bre.12044.
- Malthe-Sørensen, A., Planke, S., Svensen, H., Jamtveit, B., 2004. Formation of saucer-shaped sills. *Geological Society, London, Special Publications*, **234**, 215-227.
- Marinoni, L.B., Gudmundsson, A., 2000. Dykes, faults and palaeostresses in the Teno and Anaga massifs of Tenerife (Canary Islands). *Journal of Volcanology and Geothermal Research*, **103**, 83-103.

- Martin, H.C., 1968. Finite element analysis of fluid flows. *Proceedings of the Second Conference on Matrix Methods in Structural Mechanics*, Wright-Patterson Air Force Base, Ohio, 517-535.
- Marrett, R., Ortega, O.J., Kelsey, C.M., 1999. Extent of power-law scaling for natural fractures in rock. *Geology*, **27**, 799-802.
- Martí, J., Pinel, V., Lopez, C., Geyer, A., Abella, R., Tarraga, M., Blanco, M.J., Castro, A., Rodriguez, C., 2013. Causes and mechanisms of the 2011-2012 El Hierro (Canary Islands) submarine eruption. *Journal of Geophysical Research*, **118**, 823-839, doi:10.1002/jgrb.50087.
- Masterlark, T., 2007. Magma intrusion and deformation predictions: sensitivities to the Mogi assumptions. *Journal of Geophysical Research*, **112**, doi: 10.1029/2006JB004860 (Article number B06419).
- McCaffrey, K., Petford, N., 1997. Are granitic plutons scale invariant? *Journal of the Geological Society*, **154**, 1-4, doi: 10.1144/gsjgs.154.1.0001.
- McCraig, A.M., 1989. Fluid flow through fault zones. *Nature*, **340**, 600.
- McKillup, S., Darby Dyar, M., 2010. Geostatistics explained: An introductory guide for Earth scientists. First edition. *Cambridge University Press*, 414pp.
- McLeod, P., Tait, S., 1999. The growth of dykes from magma chambers. *Journal of Volcanology and Geothermal Research*, **92**, 231-245.
- McHenry, D.A., 1943. Lattice anthology of the solution of plane stress problems. *Journal of Institution of Civil Engineering*, **21**, 59-82.
- McTigue, D., 1987. Elastic stress and deformation near a finite spherical magma body: Resolution of the point source paradox. *Journal of Geophysical Research*, **92**, 12,931-12,940.
- Menand, T., 2008. The mechanics and dynamics of sills in layered elastic rocks and their implications for the growth of laccoliths and other igneous complexes. *Earth and Science Planetary Letters*, **267**, 93-99.

- Menand, T., 2011. Physical controls and depth of emplacement of igneous bodies: A review. *Tectonophysics*, **500**, 11-19.
- Micarelli, L., Benedicto, A., Wibberley, C.A.J., 2006. Structural evolution and permeability of normal fault zones in highly porous carbonate rocks. *Journal of Structural Geology*, **28**, 1214-1227.
- Michel, J., Baumgartner, L., Putlitz, B., Schaltegger, U., Ovtcharova, M., 2008. Incremental growth of the Patagonian Torres del Paine laccolith over 90 k.y. *Geology*, **36**, 459-462, doi: 10.1130/G24546A.1.
- Middleton, G.V., Wilcock, P.R., 1994. Mechanics in the Earth and Environmental sciences. First edition. *Cambridge University Press*, 476pp.
- Meier, S., Bauer, J.F., Phillip, S.L., 2013. Characterization of fault zones in Triassic Muschelkalk limestones of the Upper Rhine Graben with regard to geothermal exploration. *Abstracts of the presentations of the Symposium, Rock Fractures in Geological Processes*, London, 70pp.
- Mjelde, R., Shimamura, H., Kanazawa, T., Kodaira, S., Raum, T., Shiobara, H., 2003. Crustal lineaments, distribution of lower crustal intrusives and structural evolution of the Vøring Margin, NE Atlantic; new insight from wide-angle seismic models. *Tectonophysics*, **369**, 199-218.
- Mjelde, R., Raum, T., Breivik, A., Shimamura, H., Murai, Y., Takanami, T., Faleide, J.I., 2005. Crustal structure of the Vøring Margin, NE Atlantic: a review of geological implications based on recent OBS data. *In: Doré, A.G., Vining, B.A., (eds) Petroleum Geology: North-West Europe and Global Perspectives- Proceedings of the 6th Petroleum Geology Conference*. Geological Society, London, 803-813.
- Mogi, K., 1958. Relations between eruptions of various volcanoes and the deformations of the ground surfaces around them. *Bulletin of the Earthquake Research Institute, University of Tokyo*, **36**, 99-134.
- Mohajeri, N., Gudmundsson, A., 2012. Entropies and scaling exponents of street and fracture networks. *Entropy*, **14**, 800-833, doi:10.3390/e14040800.

- Mohajeri, N., French, J., Batty, M., 2013. Evolution and entropy in the organization of urban street patterns. *Annals of GIS*, **19**, 1-16.
- Mudge, M.R., 1968. Depth control of some concordant intrusions. *Geological Society of America Bulletin*, **79**, 315-332.
- Müller, B., Zoback, M.L., Fuchs, K., Mastin, L., Gregersen, S., Pavoni, N., Stephansson, C., Ljunggren, C., 1992. Regional patterns of tectonic stress in Europe. *Journal of Geophysical research*, **97**, 11783-11803.
- Muller, J.R., Ito, S.J., Martel, S.J., 2001. Effects of volcano loading on dike propagation in an elastic half-space. *Journal of Geophysical Research*, **106**, 11101-11113.
- Newman, M. E. J., 2005. Power Laws, Pareto Distributions and Zipf's Law. *Contemporary Physics*, **46**, 323-351.
- Nichols, G., 1999. Sedimentology and stratigraphy. First edition. *Wiley-Blackwell*, 369pp.
- Odling, N.E., 1992. Network properties of a two-dimensional natural fracture pattern. *Pure and Applied Geophysics*, **138**, 95-114.
- Odling, N.E., 1997. Scaling and connectivity of joint systems in sandstones from western Norway. *Journal of Structural Geology*, **19**, 1257-1271.
- Odling, N.E., Gillespie, P., Bourguin, B., Castaing, C., Chilés, J-P., Christensen, N.P., Fillion, E., Genter, A., Olsen, C., Thrane, L., Trice, R., Aarseth, E., Walsh, J.J., Watterson, J., 1999. Variations in fracture system geometry and their implications for fluid flow in fractured hydrocarbon reservoirs. *Petroleum Geoscience*, **5**, 373-384.
- Oliveira, A.M. dos S., Brito, S.N.A de., 1998. Geologia de Engenharia. ABGE - Associação Brasileira de Geologia de Engenharia. ABGE. 8th ed. São Paulo. 587pp. (Not read).
- Ortega, O.J., Marrett, R.A., Laubach, S.E., 2006. A scale-independent approach to fracture intensity and average spacing measurement. *The American Association of Petroleum Geologists*, **90**, 193-208.

- Parnell, J., 2004. Titanium mobilization by hydrocarbon fluids related to sill intrusion in a sedimentary sequence, Scotland. *Ore Geology Reviews*, **24**, 155-167.
- Pasquarè, F., Tibaldi, A., 2007. Structure of a sheet-laccolith system revealing the interplay between tectonic and magma stresses at Stardalur Volcano, Iceland. *Journal of Volcanology and Geothermal Research*, **161**, 131-150.
- Peacock, D.C.P., Sanderson, D.J., 1992. Effects of layering and anisotropy on fault geometry. *Journal of the Geological Society*, **149**, 793-802, doi: 10.1144/gsjgs.149.5.0793.
- Pérez-Lopéz, R., Legrand, D., Garduño-Monhoy, V.H., Rodríguez-Pascua, M.A., Giner-Robles, J.L., 2011. Scaling laws of the size-distribution of monogenetic volcanoes within the Michoacán-Guanajuato Volcanic Field (Mexico). *Journal of Volcanology and Geothermal Research*, **201**, 65-72.
- Petford, N., 2003. Controls on primary porosity and permeability development in igneous rocks. In: Petford, N., McCaffrey, K.J.W., (eds) *Hydrocarbons in Crystalline Rocks*. Geological Society, London, Special Publications, **214**, 93-107.
- Petraske, A.K., Hodge, D.S., Shaw, R., 1978. Mechanics of emplacement of basic intrusions. *Tectonophysics*, **46**, 41-63.
- Pinel, C., Jaupart, C., 2004. Magma storage and horizontal dyke injection beneath a volcanic edifice. *Earth and Planetary Science Letters*, **221**, 245-262.
- Planke, S., Alvestad, E., Eldholm, O. 1999. Seismic Characteristics of Basaltic Extrusive and Intrusive Rocks. *The Leading Edge*, 19, 342-348.
- Planke, S., Svensen, H., Hovland, M., Banks, D.A., Jamtveit, B., 2003. Mud and fluid migration in active mud volcanoes in Azerbaijan. *Geo-Marine Letters*, **23**, 258-268.
- Planke, S., Rasmussen, T., Rey, S.S., Myklebust, R., 2005. Seismic characteristics and distribution of volcanic intrusions and hydrothermal vent complexes in the Vøring and Møre Basins. In: Doré, A.G., Vining, B.A., (eds) *Petroleum Geology*:

- North-West Europe and Global Perspectives-Proceedings of the 6th Petroleum Geology Conference*. Geological Society, London, 833-844.
- Pollard, D.D., Johnson, A.M., 1973. Mechanics of growth of some laccolithic intrusions in the Henry Mountains, Utah II: Bending and failure of overburden and sill formation. *Tectonophysics*, **18**, 311-354.
- Polteau, S., Mazzini, A., Galland, O., Planke, S., Malthé-Sørenssen, A., 2008a. Saucer-shaped intrusions: Occurrences, emplacement and implications. *Earth and Planetary Science Letters*, **266**, 195-204.
- Polteau, S., Ferré, E.C., Planke, S., Neumann, E.-R., Chevallier, L., 2008b. How are saucer-shaped sills emplaced? Constraints from the Golden Valley Sill, South Africa. *Journal of Geophysical Research*, **113**, B12104, doi: 10.1029/2008JB005620.
- Putz-Perrier, M.W., Sanderson, D.J., 2008. The distribution of faults and fractures and their importance in accommodating extensional strain at Kimmeridge Bay, Dorset, UK. In: Wibberley, C.A.J, Kurz, W., Imber, J., Holdsworth, R.E., Collettini, C., (eds) *the internal structure of fault zones: Implications for mechanical and fluid-flow properties*. Geological Society, London, Special Publications, **299**, 97-111.
- Rateau, R., Schofield, N., Smith, M., 2013. The potential role of igneous intrusions on hydrocarbon migration, West of Shetland. *Petroleum Geoscience*, **19**, 259-272, doi: 10.1144/petgeo2012-035.
- Ren, S., Faleide, J.I., Eldholm, O., Skogseid, J., Gradstein, F., 2003. Late Cretaceous-Paleocene tectonic development of the NW Vøring Basin. *Marine and Petroleum Geology*, **20**, 177-206.
- Rivalta, E., Böttinger, M., Dahm, T., 2005. Buoyancy-driven fracture ascent: Experiments in layered gelatine. *Journal of Volcanology and Geothermal Research*, **144**, 273-285.
- Roberts, J.L., 1970. The intrusion of magma into brittle rocks. In: Newhall, G., Rast, N., (eds.), *Mechanism of Igneous Intrusion. Journal of Geology Special Issue*, **2**, 287-338.

- Roberts, A.M., Lundin, E.R., Kuszniir, N.J., 1997. Subsidence of the Vøring Basin and the influence of the Atlantic continental margin. *Journal of the Geological Society*, **154**, 551-557.
- Rocchi, A., Westerman, S., Innocenti, F., Dini, A., Tonarini, S., 2002. Two-stage growth of laccoliths at Elba Island (Italy). *Geology*, **30**, 983-986.
- Rodriguez Monreal, F., Villar, Baudino, R., Delpino, D., Zencich, S., 2009. Modelling an atypical petroleum system: A case study of hydrocarbon generation, migration and accumulation related to igneous intrusions in the Neuquen Basin, Argentina. *Marine and Petroleum Geology*, **26**, 590-605.
- Ronchin, E., Masterlark, T., Martí Molist, J., Saunders, S., Tao, W., 2013. Solid modelling techniques to build 3D finite element models of volcanic systems: An example from the Rabaul Caldera system, Papua New Guinea. *Computers and Geosciences*, **52**, 325-333.
- Rubin, A.M., Pollard, D.D., 1988. Dike-induced faulting in rift zones of Iceland and Afar. *Geology*, **16**, 413-417.
- Rubin, A.M., 1995. Propagation of magma-filled cracks. *Annual Review of Earth and Planetary Sciences*, **23**, 287-336, doi: 10.1146/annurev.ea.23.050195.001443.
- Ryan, M.P., 1993. Neutral buoyancy and the structure of mid-ocean ridge magma reservoirs. *Journal of Geophysical Research*, **98**, 22,321-22,338, doi: 10.1029/93JB02394.
- Sanford, A.R., 1959. Analytical and experimental study of simple geologic structures. *Bulletin of the Geological Society of America*, **70**, 19-52.
- Schmincke, H-U., 2003. Volcanism. First edition. *Springer*, 324pp.
- Schofield, N.J., Brown, D.J., Magee, C., Stevenson, C.T., 2012. Sill morphology and comparison of brittle and non-brittle emplacement mechanisms. *Journal of the Geological Society, London*, **169**, 127-141, doi: 10.1144/0016-76492011-078.

- Schutter, S.R., 2003a. Hydrocarbon occurrence and exploration in and around igneous rocks. *Geological Society, London, Special Publications*, **214**, 7-33, doi: 10.1144/GSL.SP.2003.214.01.02.
- Schutter, S.R., 2003b. Occurrences of hydrocarbons in and around igneous rocks. *Geological Society, London, Special Publications*, **214**, 35-68, doi: 10.1144/GSL.SP.2003.214.01.03.
- Santha, J.P., 2006. Statistical mechanics: entropy, order parameters, and complexity. First edition. *Oxford University Press*, 374pp.
- Sibson, R., 1994. Crustal stress, faulting and fluid flow. *Geological Society, London, Special Publications*, **78**, 69-84, doi: 10.1144/GSL.SP.1994.078.01.07.
- Sibson, R.H., 2000. Fluid involvement in normal faulting. *Journal of Geodynamics*, **29**, 469-499.
- Sigmundsson, F., Hreinsdottir, S., Hooper, A., Arnadóttir, T., Pedersen, R., Roberts, M.J., Oskarsson, N., Aurlac, A., Decriem, J., Einarsson, P., Geirsson, H., Hensch, M., Ofeigsson, B.G., Sturkell, E., Sveinbjörnsson, H., Feigl, K., 2010. Intrusion triggering of the 2010 Eyjafjallajökull eruption. *Nature*, **468**, 426-430.
- Singh, S.C., Crawford, W.C., Carton, H., Seher, T., Combier, V., Cannat, M., Canales, J.P., Dusunur, D., Escartin, J., Miranda, J.M., 2006. Discovery of a magma chamber and faults beneath a Mid-Atlantic Ridge hydrothermal field. *Nature*, **442**, 1029-1032.
- Sinton, J.M., Detrick, R.S., 1992. Mid-ocean ridge chambers. *Journal of Geophysical Research*, **97**, 197-216.
- Skogseid, J., Pedersen, T., Eldholm, O., Larsen, B., 1992. Tectonism and magmatism during NE Atlantic continental break-up: the Vøring Margin. *Geological Society, London, Special Publications*, **68**, 305-320.
- Skogseid, J., 1994. Dimensions of the Late Cretaceous-Paleocene Northeast Atlantic rift derived from Cenozoic subsidence. *Tectonophysics*, **240**, 225-247.

- Skogseid, J., Planke, S., Faleide, J.I., Pedersen, T., Eldholm, O., Neverdal, F., 2000. NE Atlantic continental rifting and volcanic margin formation. *Geological Society, London, Special Publications*, **167**, 295-326.
- Smallwood, J.R., 2009. Back-stripped 3D seismic data: A new tool applied to testing sill emplacement models. *Petroleum Geoscience*, **15**, 259-268, doi: 10.1144/1354-079309-844.
- Sneddon, I.N., Lowengrub, M., 1969. Crack problems in the Classical Theory of Elasticity. First Edition. *Wiley*. 221pp.
- Storey, M., Duncan, R.A., Swisher III, C.C., 2007. Paleocene-Eocene thermal maximum and the opening of the Northeast Atlantic. *Science*, **316**, 587-589.
- Stuevold, L.M., Skogseid, J., Eldholm, O., 1992. Post-Cretaceous uplift events on the Vøring continental margin. *Geology*, **20**, 919-922.
- Svensen, H., Jamtveit, B., Planke, S., Pedersen, T., 2003. Seep carbonate formation controlled by hydrothermal vent complexes: a case study from the Vøring Basin, the Norwegian Sea. *Geo-Marine Letters*, **23**, 351-358.
- Svensen, H., Planke, S., Malthe-Sørensen, A., Jamtveit, B., Myklebust, R., Rasmussen, T., Rey, S. S., 2004. Release of methane from a volcanic basin as a mechanism for initial Eocene global warming. *Nature*, **429**, 542-545.
- Svensen, H., Planke, S., Corfu, F., 2010. Zircon dating ties NE Atlantic sill emplacement to initial Eocene global warming. *Journal of the Geological Society, London*, **167**, 433-436, doi: 10.1144/0016-76492009-125.
- Taisne, B., Jaupart, C., 2009. Dike propagation through layered rocks. *Journal of Geophysical Research*, **114**, B09203, doi: 10.1029/2008JB006228.
- Thomson, K., Hutton, D., 2004. Geometry and growth of sill complexes: insights using 3D seismic from the North Rockall Trough. *Bulletin of Volcanology*, **66**, 364-375, doi: 10.1007/s00445-003-0320-z.
- Thomson, K., 2007. Determining magma flow in sills, dykes and laccoliths and their implications for sill emplacement mechanisms. *Bulletin of Volcanology*, **70**, 183-201.










- Thordarson, T., Self, S., 1993. The Laki (Skaftár Fires) and Grímsvötn eruptions in 1783-1785. *Bulletin of Volcanology*, **55**, 233-263.
- Toramaru, A., Matsumoto, T., 2004. Columnar joint morphology and cooling rate: A starch-water mixture experiment. *Journal of Geophysical Research*, **109**, B02205, doi: 10.1029/2003JB002686.
- Transatti, E., Bonafede, M., Ferrari, C., Giunchi, C., Berrion, G., 2011. On deformation sources in volcanic areas: modelling the Campi Flegrei (Italy) 1982-84 unrest. *Journal of Volcanology and Geothermal Research*, **306**, 175-185.
- Twiss, R.J., Moores, E.M., 2007. Structural Geology. Second edition. *W.H Freeman*, 500pp.
- Upton, B. G. J., Rämö, O. T., Heaman, L. M., Blichert-Toft, J., Kalsbeek, F., Barry, T. L., Jepsen, H. F., 2005. The Mesoproterozoic Zig-Zag Dal basalts and associated intrusions of eastern North Greenland: mantle plume-lithosphere interaction. *Contributions to Mineralogy and Petrology*, **149**, 40-56.
- van Wijk, J.W., Cloetingh, S.A.P.L., 2002. Basin migration caused by slow lithospheric extension. *Earth and Planetary Science Letters*, **198**, 275-288.
- Vermilye, J.M., Scholz, C.H., 1995. Relation between vein length and aperture. *Journal of Structural Geology*, **17**, 423-434.
- Volkenstein, M.V., 2009. Entropy and information. First edition. *Birkhäuser*, 210pp.
- Wang, P., Xu, R., 2006. Dynamic interfacial debonding initiation induced by an incident crack. *International Journal of Solids and Structures*, **43**, 6535-6550.
- Wang, K., Lu, X., Chen, M., Ma, Y., Liu, K., Li, X., Hu, W., 2011. Numerical modelling of hydrocarbon generation of Tertiary source rocks intruded by doleritic sills in the Zhanhua depression, Bohai Bay Basin, China. *Basin Research*, **23**, 1-14, doi: 10.1111/j.1365-2117.2011.00518x.
- White, R.S., Smith, L.K., Roberts, A.W., Christie, P.A.F., Kusznir, N.J., iSIMM Team., 2008. Lower-crustal intrusion on the North Atlantic continental margin. *Nature*, **452**, 460-464, doi: 10.1038/nature06687.

- White, R.S., Drew, J., Martens, H.R., Key, J., Soosalu, H., Jakobsdóttir, S.S., 2011. Dynamics of dyke intrusion in the mid-crust of Iceland. *Earth and Planetary Science Letters*, **304**, 300-312.
- Wibberley, C.A.J., Yielding, G., Di Toro, G., 2008. Recent advances in the understanding of fault zone internal structure: a review. In: Wibberly, C.A.J., Kurz, W., Imber, J., Holdsworth, R.E., Colletini, C., (eds) *The internal structure of fault zones: Implications for mechanical and fluid-flow properties*. Geological Society, London, Special Publications, **299**, 5-33.
- Wiebe, R. A., Collins, W. J., 1998. Depositional features and stratigraphic sections in granitic plutons: Implications for the emplacement and crystallization of granitic magma. *Journal of Structural Geology*, **20**, 1273-1289.
- Wilson, E.L., Nickel, R.E., 1966. Application of the finite element method to heat conduction analysis. *Nuclear Engineering and Design*, **4**, 276-286.
- Woo, J.Y.L., Kilburn, C.R.J., 2010. Intrusion and deformation at Campi Flegrei, southern Italy: Sills, dikes, and regional extension. *Journal of Geophysical Research*, **115**, B12210, doi: 10.1029/2009JB006913.
- Xie, H., 1993. Fractals in rock mechanics. First edition. *Taylor and Francis*, 464pp.
- Xu, L.R., Huang, Y.Y., Rosakis, A.J., 2003. Dynamic crack deflection and penetration at interfaces in homogenous materials: experimental studies and model predictions. *Journal of Mechanics and Physics of Solids*, **51**, 461-486.
- Yang, Q., Tham, L.G., Swoboda, G., 2004. Relationship between refined Griffith criterion and power laws for cracking. *Mechanics Research Communications*, **31**, 429-434.
- Yang, X.-M., Davis, P., Dietrich, J.H., 1988. Deformation from inflation of a dipping finite prolate spheroid in an elastic half-space as a model for volcanic stressing. *Journal of Geophysical Research*, **93**, 4249-4257.
- Zhang, X., Jeffrey, R.G., Thiercelin, M., 2007. Deflection and propagation of fluid-driven fractures at frictional bedding interfaces: A numerical investigation. *Journal of Structural Geology*, **29**, 396-410.

- Zhang, Y., Schaub, P.M., Zhao, C., Ord, A., Hobbs, B.E., Barnicoat, A.C., 2008. Fault-related dilation, permeability enhancement, fluid flow and mineral precipitation patterns: numerical models. *In*: Wibberly, C.A.J., Kurz, W., Imber, J., Holdsworth, R.E., Collettini, C., (eds) *The internal structure of fault zones: Implications for mechanical and fluid-flow properties*. Geological Society, London, Special Publications, **299**, 277-291.
- Zhang, Y., Gartrell, A., Underschultz, J.R., Dewhurst, D.N., 2009. Numerical modelling of strain localisation and fluid flow during extensional fault reactivation: Implications for hydrocarbon preservation. *Journal of Structural Geology*, **31**, 315-327.
- Zhu, D., Jin, Z., Hu, W., Song, Y., Gao, X., 2007. Effect of igneous activity on hydrocarbon source rocks in Jiyang sub-basin, eastern China. *Journal of Petroleum Science and Engineering*, **59**, 309-320.
- Zienkiewicz, O.C., Watson, M., King, I.P., 1968. A numerical method of visco-elastic stress analysis. *International Journal of Mechanical Sciences*, **10**, 807-827.
- Zienkiewicz, O.C., 1977. The finite element method. First edition. *McGraw-Hill*, 787pp.
- Zoback, M.L., 1992. First - and second - order patterns of stress in the lithosphere: The world stress map project. *Journal of Geophysical Research*, **97**, 11703-11728.

Appendices

A. Simple solid mechanics model set-up in COMSOL

Pre-processing is primarily adding geometries that represent geological structures seen in the field or on seismic images. Figure A1 shows an eleven step guide to setting up the pre-processing part of the numerical model. First, the model is set-up using the **Model Wizard**. **1** we can select either a 2D or 3D **space dimension** and then click **Next** . **2 Add Physics** window under the **Structural Mechanics** module and selecting **Solid Mechanics** and then click **Next** . **3** A study type can be selected, here a **Stationary** study where time does not have an effect on the model, then click **Finish** . A geometry can now be drawn or imported. Under **4 Model 1 (mod1)** right click **5 Geometry** and select **6 Square** inputting desired geometries and **Layers** can be added too, to represent the heterogeneity of the Earth's crust, then click **Build All** . **7** draw an **Ellipse** by inputting desired geometries or **7' Import** a geometry with a DXF format, I used CorelDRAW X5. Next click **Build All** . Note it is important that elements (geometries) are not placed close to the edge of the model, as these will be later fixed, and therefore, will be affected as there is no displacement. The final stage to pre-processing is to take away any objects that are fractures. Right click **Geometry** and select **8 Boolean Operations** and **9** select **Difference**. **10** add the square by selecting it from the **Graphics** tab and clicking **Add to Selection**  to **Objects to add**, then click **Activate Selection**  and select the ellipses from the **Graphics** tab and **Add to Selection**  making sure you tick **Keep interior boundaries** and clicking **Build All** . The **Graphics** tab is now shown in **11** noting how the ellipses appear as holes (or cavities in 3D).

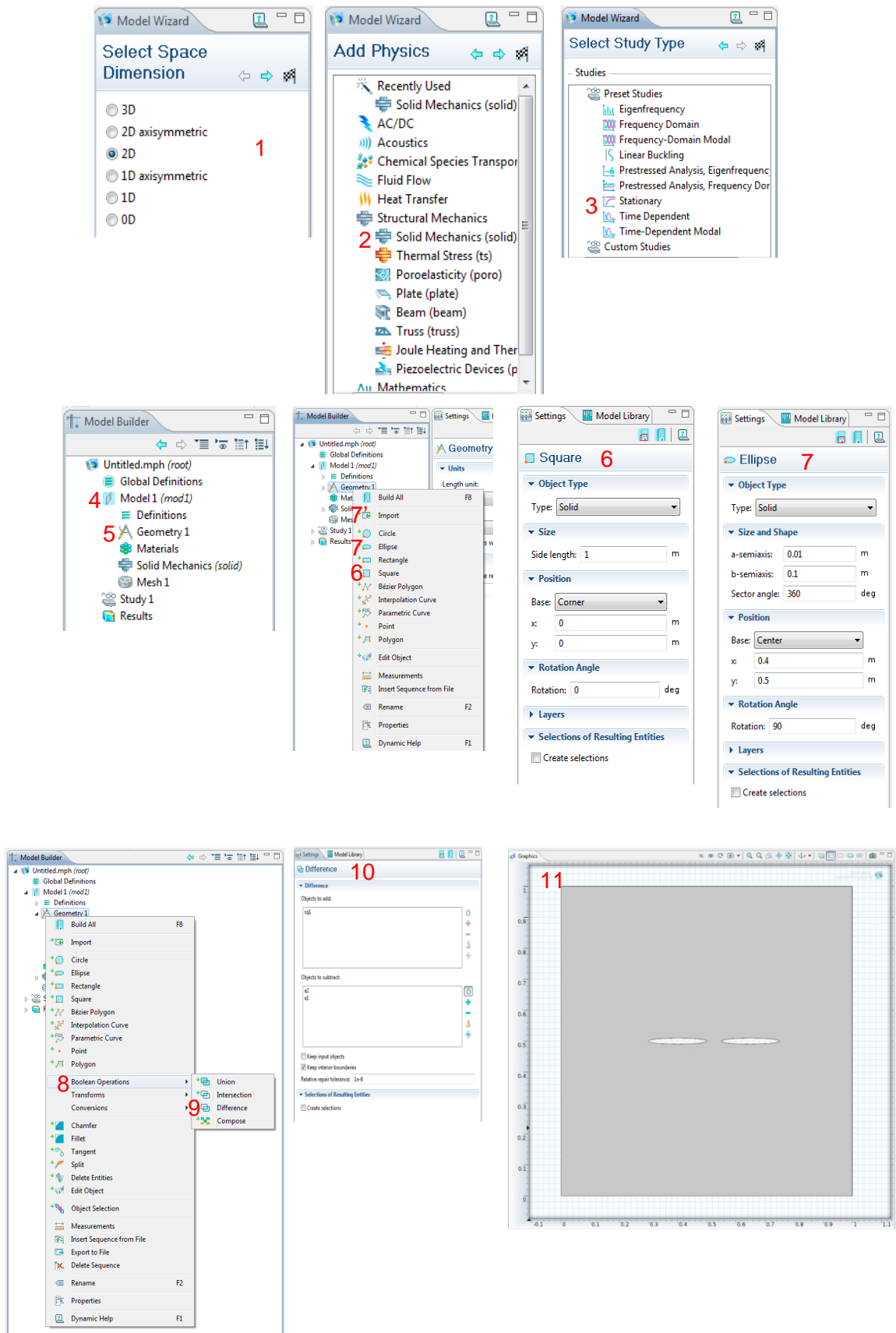




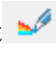


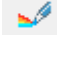


Figure A1: Step-by-step guide to pre-processing in COMSOL Multiphysics. Numbers in red represent the steps discussed above in the text.

Analysis allows for the input of geological parameters to the geological geometries, these include Young's modulus, Poisson's ratio, rock densities, loading and boundary conditions. Figure A2 shows six steps to setting up the analysis process for the numerical model. **12** by right clicking on **Solid Mechanics** under **Model 1 (mod1)** and selecting **Linear Elastic Material model**, mechanical properties can be inputted in **13**. For **Young's modulus**, **Poisson's ratio** and **density** we select **User defined** values (e.g. $E = 20e9$, $\nu = 0.25$, $\rho = 2500$) and also tick **Force linear strains**. Right click **Solid Mechanics** and select **Fixed Constraint**; this fastens the edges of the numerical model to avoid rigid body rotation and translation. **14** select the four sides of the square (to add a free surface do not add the upper boundary of the square) and **Add to Selection** . Right click **Solid Mechanics** and select **Boundary Load**. **15** select the boundaries of the geometries, here ellipses, and **Add to Selection** . Under the **Force** tab change the **Load Type** to **Pressure**, known in geology as overpressure and assign this as $10e6$. Another **Boundary Load** can be added from selecting it from **Solid Mechanics** and selecting the two boundaries of the square at which you want loading. Change the **Load Type** again to **Pressure**, here for external compression or extension, i.e. regional tectonics, and assign a value of $+ 5e6$ for extension or $-5e6$ for compression (note geology is opposite to engineering in which COMSOL Multiphysics operates). In more complicated models an internal spring may need to be added in the case of a fault plane, for example, or a weak contact. This can be done by selecting **Thin Elastic Layer** from the **Solid Mechanics** menu. The plane in which you want to add as an internal spring needs to be added, in the same way we did in steps 14 and 15, and changing the **Spring Type** under the **Spring** tab to **Spring constant per unit length** and assigning values for x and y. Finally a mesh can be added to the geometries with node points where the final solution for stress is calculated. This can be done by right clicking **Mesh 1**, under **Model 1 (mod1)** and selecting **16 Free Triangular** and finally clicking **Build All** . The **Graphics** tab is now shown in **17** showing the meshed study.

The final process in numerical modelling is post-processing where COMSOL Multiphysics produces a visualization of the model showing stress fields, deformations and 1D graphical results which allow for interpretation. Figure A3

shows the final steps in numerical modelling, where there are six steps to post-processing. 18 Right click **Study 1** and select 19 **Compute** this will then plot the results. By extending 20 **Results** and the 21 **Stress (solid)** and selecting 22 **Surface 1**, we can choose which stress analysis we would like to look at for our results. First, we analyse the shear stress, known as von Mises shear stress, this is done by clicking **Replace Expression**  and selecting **Solid Mechanics**, then **Stress** followed by 23 **von Mises stress**. As the units, we select **MPa**, and by extending the **Range** tab we can set the **Manual colour range** typically between 0-20MPa, but this can be altered to fit each model. Finally we click **Plot** . Next we can look at the normal stress and is selected the same as von Mises but instead we select **Principal Stresses** and then 24 **First Principal stress** (this is the minimum principal compressive stress, σ_3). The same parameters need to be set up in terms of units and ranges and relicking **Plot** . By extending **Surface 1** we can also add 25 **Deformation** which is set by default and the scale factor can be changed to suit your results. To add stress trajectories right click **Stress (solid)** and select 26 **Arrow Surface. Replace Expression**  and select **Solid Mechanics**, then **Stress** and **Principal stress directions** and select 27 **Principal stress direction 3** (this is σ_1 stress trajectories). By extending **Arrow Positioning** we can add many points (here choose atleast 100 in both x and y grid points). Extending **Colouring and Style** we can change the **Arrow type** to **Cone** and change the **Scale factor** to <0.1 . Finally click **Plot**  and results can be seen in the 28 **Graphics** tab, this gives us a visualization to be able to analyse and interpret.

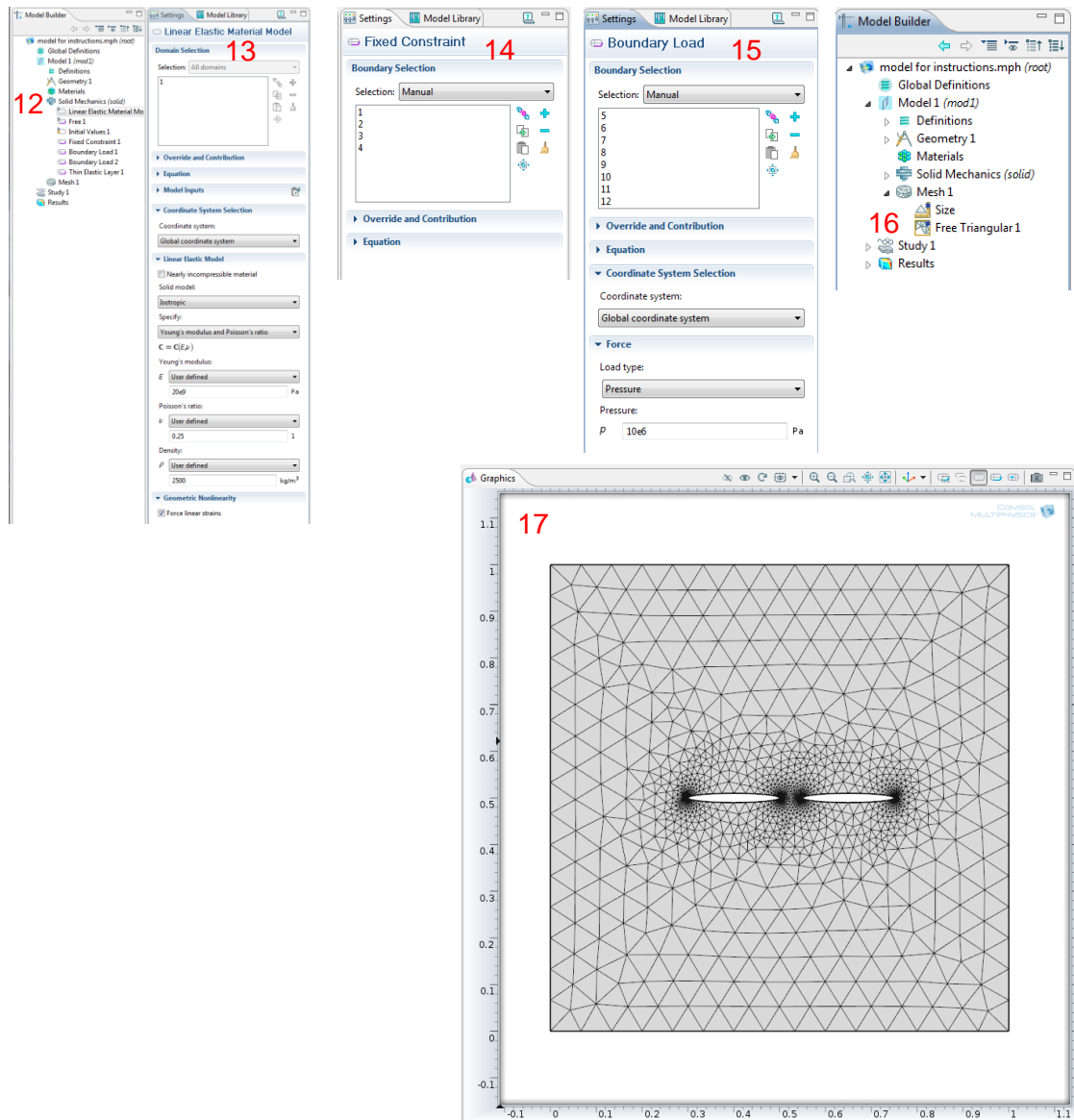


Figure A2: Step-by-step guide to analysis in COMSOL Multiphysics. Numbers in red represent the steps discussed above in the text.

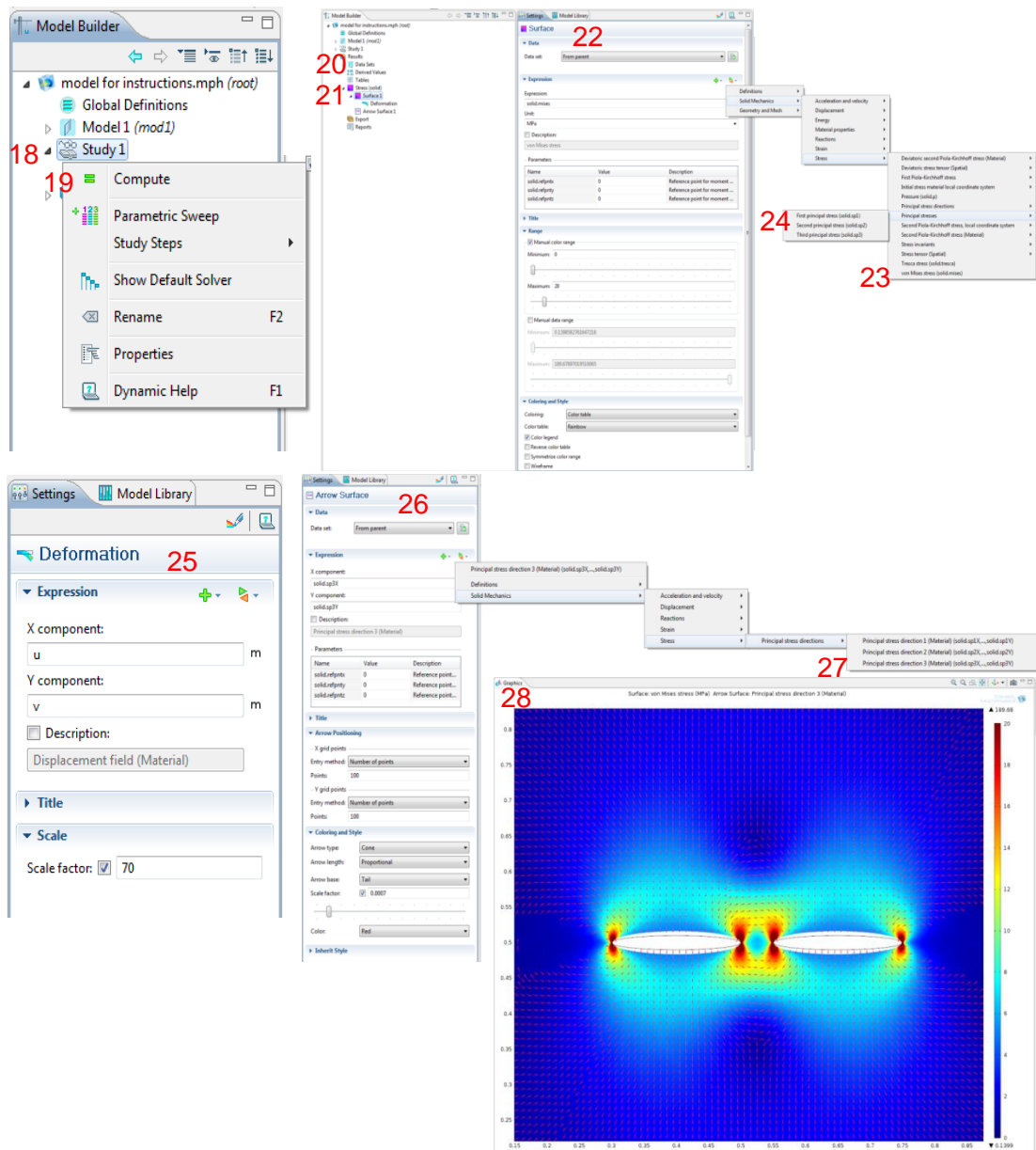


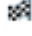










Figure A3: Step-by-step guide to post-processing in COMSOL Multiphysics. Numbers in red represent the steps discussed above in the text.

B. Fluid flow model set-up in COMSOL

Pre-processing is primarily adding geometries that represent fracture networks seen in the field. Figure B1 shows a six step guide to setting up the pre-processing part of the numerical model. First, the model is set-up using the **Model Wizard**. **1** select a **2D space dimension** and then click **Next** . **2** **Add Physics** under the **Fluid Flow** module and select **Single-Phase Flow** and then **Laminar Flow** and then click **Next** . **2'** A study type can be selected, here a **Stationary** study where time does not have an effect on the model, then click **Finish** . Repeat step **2**, but this time select **3 Particle Tracing for Fluid Flow**. **3'** A study type can be selected, here a **Time Dependent** study where time does have an effect on the model, then click **Finish** . A geometry can now be imported. Under **4 Model 1 (mod1)** right click **5 Geometry** and select **6 Import** a geometry with a DXF format, I used CorelDRAW X5. Next click **Build All** .

Analysis allows for the input of fluid flow parameters to the fracture network. Figures B2 and B3 shows nine steps to setting up the analysis process for the numerical model. **7** by right clicking on **Laminar Flow** under **Model 1 (mod1)** and selecting **Fluid Properties**, fluid properties can be inputted. For **Fluid Properties**, **7**, select **User defined** values (e.g. water $\rho = 1000$, $\mu = 1.5 \times 10^{-3}$). Right click **Laminar Flow** and select **Wall**, then set the **Boundary condition** to **No slip**, thus there is no fluid movement along the fracture walls. **8** select the walls of the fracture network that are fixed and **Add to Selection** . Right click **Laminar Flow** and select **Inlet**. **9** select the lower boundary of the fracture network as this is where the fluid will enter the network, then **Add to Selection** . Change the **Boundary condition** to **Pressure, no viscous stress** and add a value of 6 Pa. Right click **Laminar Flow** and select **Outlet**. **10** select the upper boundary of the fracture network as this is where the fluid will leave the network, then **Add to Selection** . Change the **Boundary condition** to **Pressure, no viscous stress** and add a value of 0 Pa. To add parameters to the particle tracing for fluid flow, right click **Particle Tracing for Fluid Flow** and select **Wall**. **11** select the walls of the fracture network that are fixed and **Add to Selection** , then set the **Wall conditions** to **Bounce**, this

reflects the particles from the fracture walls, thus conserving momentum. To add the fluid properties to each particle, right click **Particle Tracing for Fluid Flow** and select **Particle Properties**. 12 values for water particles are automatically selected. Next **Inlet** and **Outlet** are selected by right clicking on **Particle Tracing for Fluid Flow**, which are defined as that for laminar flow. 13 the **Initial position** of the particle can be selected to have a **Uniform distribution**, where the number of particles per release can be set, e.g. $N = 100$. Next set the outlet wall condition, 14, as **Freeze** to allow for visualization of the particles. Finally, a mesh can be added to the fracture network with node points where the final solution for velocity is calculated. This can be done by right clicking **Mesh 1**, 15, under **Model 1 (mod1)** and clicking **Build All** . The **Graphics** tab is now shown in 15 showing the meshed study.

The final process in numerical modelling is post-processing where COMSOL Multiphysics produces a visualization of the model showing velocity fields and pressures, which allow for interpretation. Figures B3 and B4 show the final steps in numerical modelling, where there are nine steps to post-processing. 16 right click **Study 1**, making sure that only **Laminar Flow** is ticked. 17 right click **Study 2**, making sure that only **Particle Tracing for Fluid Flow** is ticked. Next, 18 and 19, **Compute** this will then plot the results. Extend 20 **Results** and then 21 **Velocity** and select 22 **Surface**. As the units, select **m/s**, and then click **Plot** , the stationary results are displayed for surface velocity. The time dependent results are shown in 23 **Particle Trajectories** and selecting 24 **Particle Trajectories**, where an animation can be visualized of the velocity field in 22.

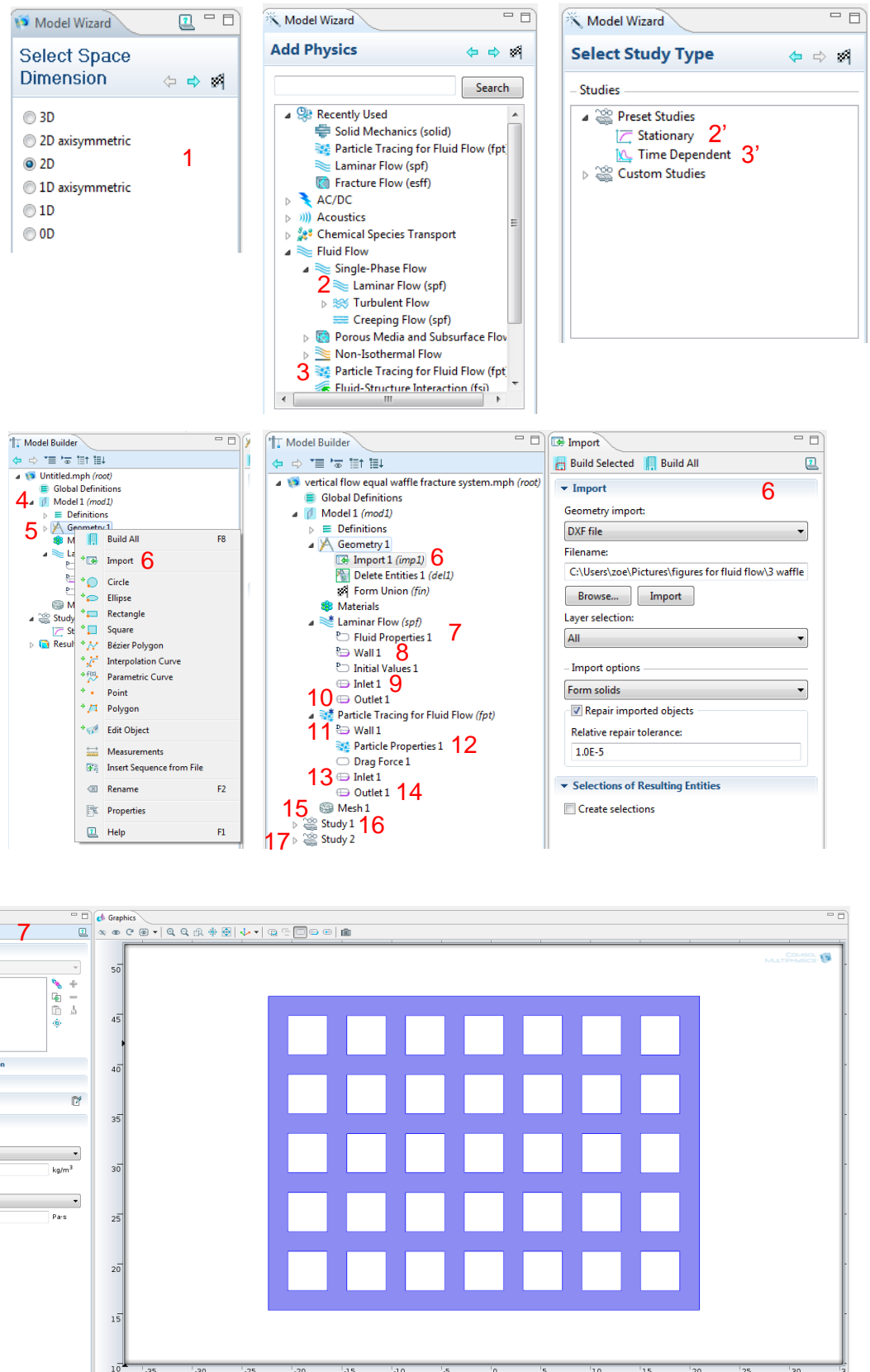


Figure B1: Step-by-step guide to fluid flow modelling in COMSOL Multiphysics. Numbers in red represent the steps discussed above in the text.

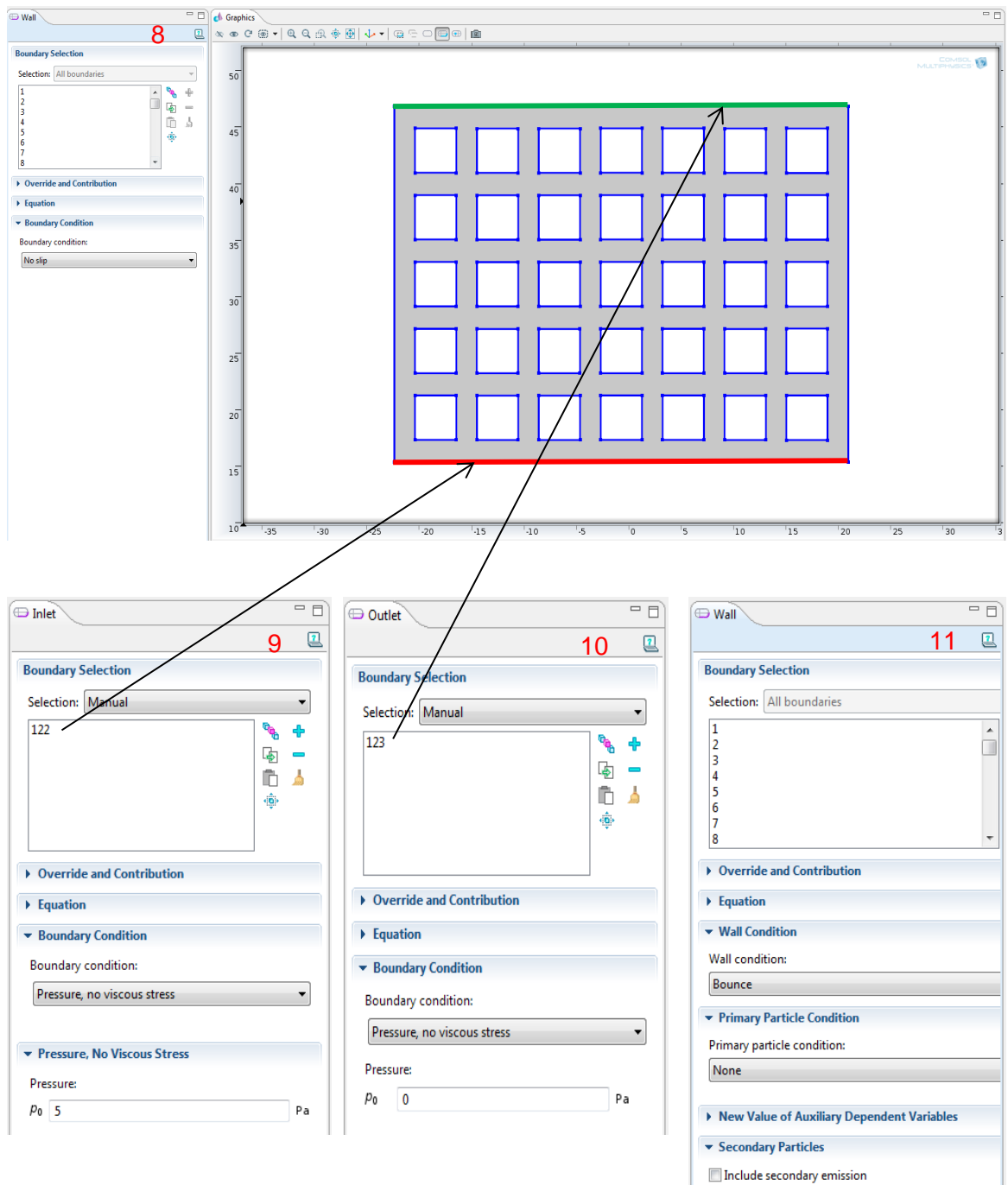


Figure B2: Step-by-step guide to fluid flow modelling in COMSOL Multiphysics. Numbers in red represent the steps discussed above in the text.

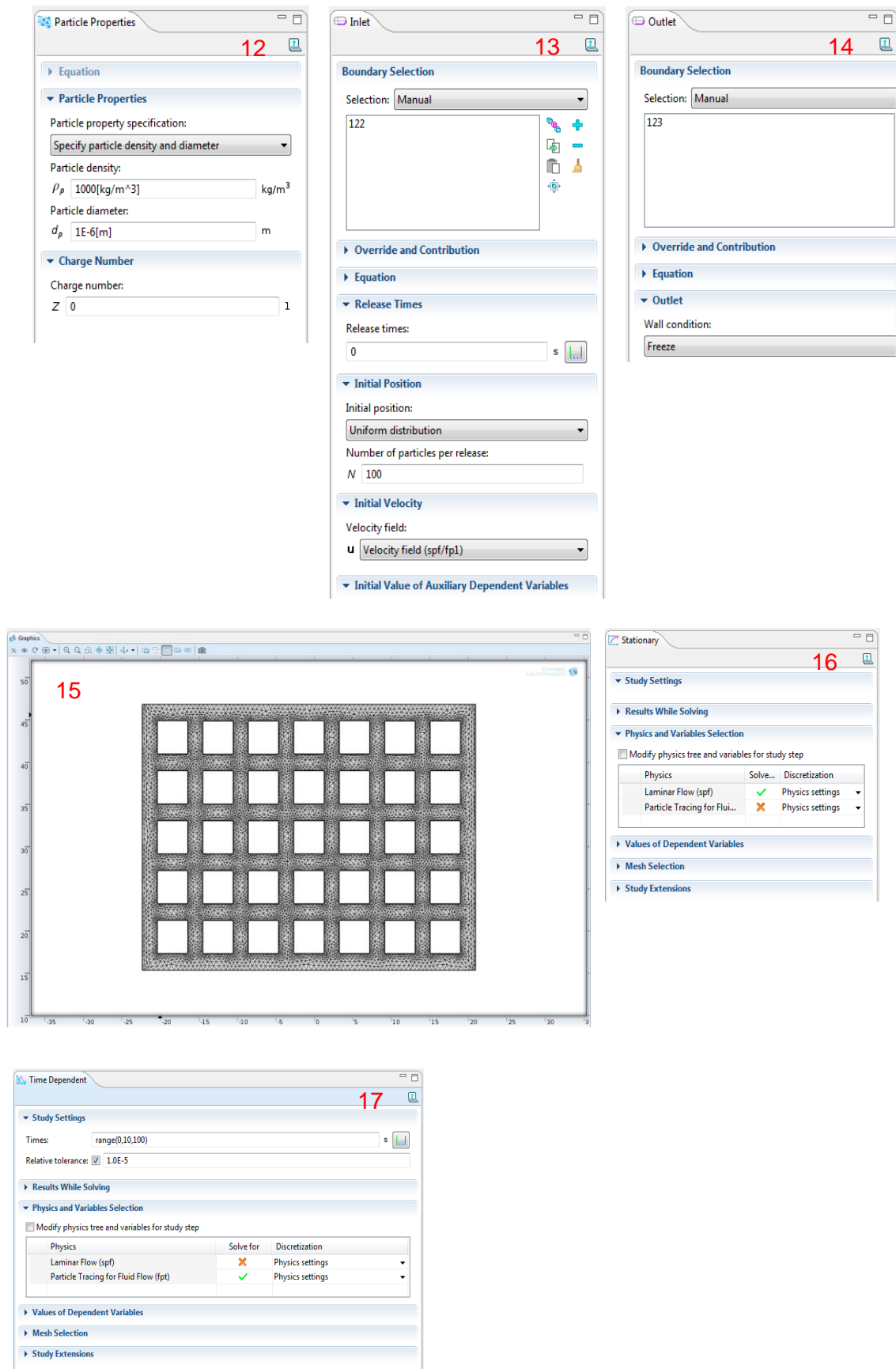


Figure B3: Step-by-step guide to fluid flow modelling in COMSOL Multiphysics. Numbers in red represent the steps discussed above in the text.

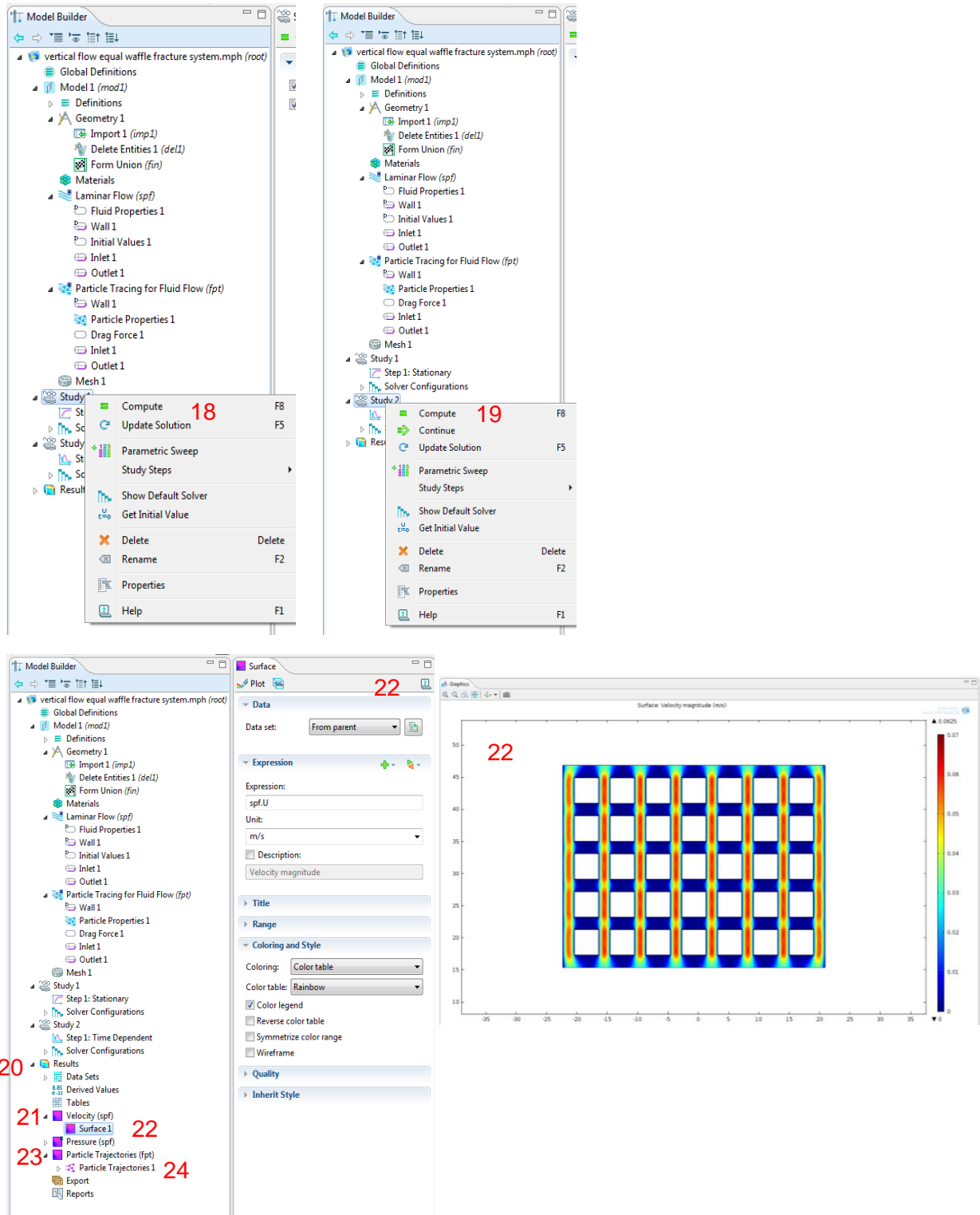


Figure B4: Step-by-step guide to fluid flow modelling in COMSOL Multiphysics. Numbers in red represent the steps discussed above in the text.

C. Seismic lines MNR05-7397 and MNR06-7365

Interpretation of sills and stratigraphic units provided by Tector AS, with a scale of 1:1 in km. The sill polygons in red have positions/geometries taken from seismic data. Only the top reflection of the sill is seen, so definition of the sill thickness is usually impossible.

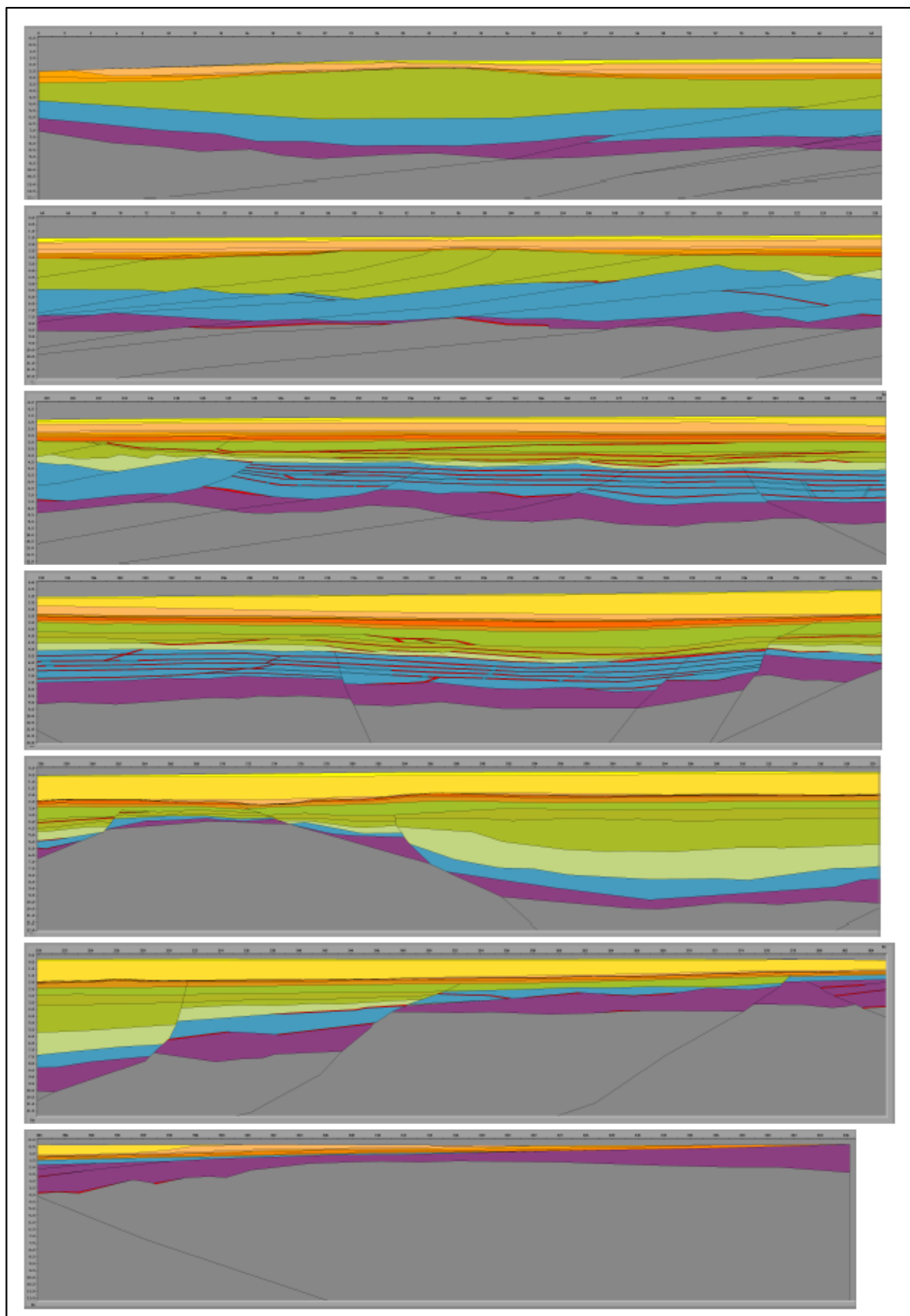


Figure C1: Line MNR05-7397 illustrating stratigraphic horizons and sills.

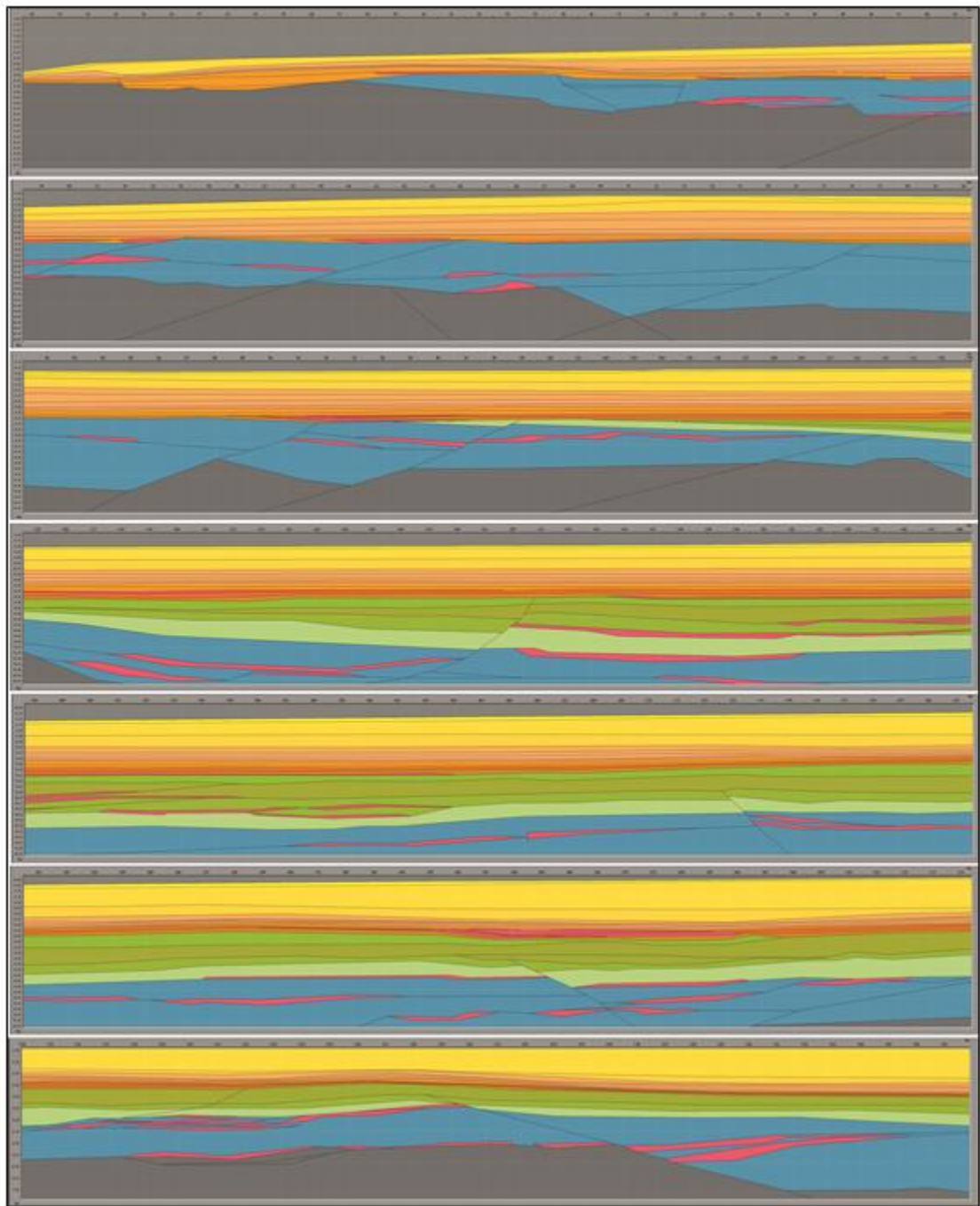


Figure C2: Line MNR06-7365 illustrating stratigraphic horizons and sills.

D. Barnett, Z. Gudmundsson, A., 2014. Numerical modelling of dykes deflected into sills to form a magma chamber

Journal of Volcanology and Geothermal Research 281 (2014) 1–11



Contents lists available at ScienceDirect

Journal of Volcanology and Geothermal Research

journal homepage: www.elsevier.com/locate/jvolgeores



Numerical modelling of dykes deflected into sills to form a magma chamber



Zoe A. Barnett*, Agust Gudmundsson

Department of Earth Sciences, Royal Holloway University of London, Egham, UK

ARTICLE INFO

Article history:

Received 2 March 2014

Accepted 24 May 2014

Available online 4 June 2014

Keywords:

Numerical models

Sills

Dykes

Magma chambers

Rock properties

Crustal stresses

ABSTRACT

Most shallow magma chambers are thought to evolve from sills. For this to happen, several conditions must be met. (1) There must be a discontinuity, normally a contact, that deflects a dyke (or an inclined sheet) into a sill. (2) The initial sill must have a considerable thickness, normally (depending on dyke injection rates) not less than some tens of metres. (3) The resulting sill must receive magma (through dykes) frequently enough so as to stay liquid and expand into a chamber. (4) The resulting magma chamber must remain at least partially molten and receive multiple magma injections over a given period of time to build up a volcano on the surface above. In this paper we present numerical models based upon field data and geophysical data as to how sills are emplaced and may subsequently evolve into shallow magma chambers. We suggest that most sills form when dykes meet contacts, particularly weak ones, which are unfavourable to dyke propagation. A contact may halt (arrest) a dyke altogether or, alternatively, deflect the dyke into the contact. The three main mechanisms for dyke deflection into a contact are (1) the Cook–Gordon debonding or delamination, (2) rotation of the principal stresses, generating a stress barrier, and (3) an elastic mismatch across a contact between adjacent layers. Elastic mismatch means that the layers have contrasting Young's moduli and varying material toughness. Once a sill is initiated, the developing magma chamber may take various forms. Many shallow magma chambers, however, tend to maintain a straight sill-like or somewhat flat (oblate) ellipsoidal geometry during their lifetimes. For a sill to evolve into a magma chamber there must be elastic-plastic deformation of the overburden and, to some extent, of the underburden. So long as the sill stays liquid, subsequent dyke injections become arrested on meeting the sill. Some magma chambers develop from sill complexes. For the sill complex to remain partially molten it must receive a constant replenishment of magma, implying a high dyke-injection rate. Alternatively, an initial comparatively thick sill may absorb much of the magma of the dykes that meet it and evolve into a single shallow magma chamber.

© 2014 Elsevier B.V. All rights reserved.

1. Introduction

Dykes and inclined sheets are easily identified in outcrops: they are subvertical (dykes) to steeply or gently dipping (sheets) planar intrusions that dissect the strata (commonly lava flows, pyroclastic layers, and sedimentary layers). Thus in contrast to sills, which are mostly concordant, dykes and inclined sheets are mostly discordant to bedding or any horizontal features (Fig. 1a). A dyke has normally a large length-thickness (or aspect) ratio, commonly 10^2 – 10^4 (Gudmundsson, 2011a). Dyke is thus a tabular intrusion with common strike and dip dimensions ranging from kilometres to tens of kilometres, while the longest dykes reach strike dimensions of thousand kilometres or more. The dip dimensions are necessarily limited by the depths to the source magma chambers or reservoirs. Dyke thicknesses are mostly in the range from tens of centimetres to tens of metres, while some dykes are as thin as

a few centimetres and the thickest ones many hundred metres (cf. Baer and Heimann, 1995).

Sills, on the other hand, are commonly a little harder to distinguish from their host rocks, particularly when hosted by a lava pile, as they are concordant (Fig. 1b) and in many ways similar to lava flows. However, there are several criteria which can be used to distinguish between the two. These include (e.g. Gudmundsson, 2011a):

1. sills normally have much better developed sets of columnar joints than lava flows;
2. sills have a chilled selvage on the upper and lower margins (the roof and floor), also known as glassy margins, whereas lava flows have chilled selvage (if at all) only at the lower margin;
3. sills have little or no scoria at their margins, whereas lava flows (particularly aa lava flows) have zones of scoria at their upper (commonly weathered) and lower margins;
4. vesicles are smaller, less angular, and less widely distributed in sills than in lava flows;

* Corresponding author.

E-mail address: Zoe.Barnett.2007@rhul.ac.uk (Z.A. Barnett).

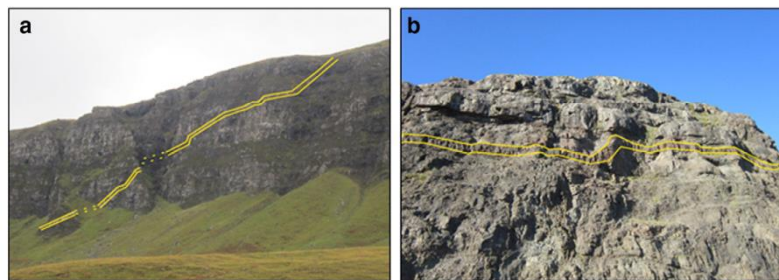


Fig. 1. a) View south, the inclined sheet is approximately 3 m thick and cuts through a basaltic lava pile on the Isle of Mull, Inner Hebrides, Scotland. b) View north, the sill is about 1 m thick and cut through a basaltic host rock, SE Iceland.

5. sills are commonly stepped (Fig. 1b), that is, change their elevation within the pile, and may increase their dips so as to become inclined sheets or dykes, neither of which applies to lava flows;
6. some lava flows gradually change into pillow lavas (others are formed directly as pillow lavas), which do not happen to sills.

Both dykes and sills are primarily fluid-driven extension fractures and, more specifically, hydrofractures. Hydrofractures propagate as a result of internal fluid overpressure (driving pressure, net pressure). Overpressure is the combined effect of the initial excess pressure in the magma chamber at the time of rupture (and dyke injection) and buoyancy. Excess pressure is the fluid pressure in a magma chamber in excess of the overburden pressure or lithostatic stress. When the chamber ruptures and injects a dyke (or an inclined sheet), the excess pressure is normally roughly equal to the in situ tensile strength of the host rock, or a few mega-pascals (Gudmundsson, 2011a). The buoyancy is due to the difference in the density between the fluid (here the magma) and the rock through which the fracture (here a dyke, an inclined sheet, or a sill) propagates. Since the fluid density can be higher, the same, or lower than the host-rock density, the buoyancy effect can be negative, neutral, or positive. Generally, many and probably most hydrofractures, even those subject to positive buoyancy effects, do not reach the surface but rather stall or become arrested or deflected along contacts at varying depths or stratigraphic levels within the crust (Menand, 2011; Gudmundsson, 2011b).

Sill emplacement has been studied in the field and also through geophysical measurements both as regards sill geometries as seen, for example, in seismic lines in sedimentary basins, as well as during active sill emplacement in volcanoes. Examples of direct field studies include those on the Midland Valley Sill and the Whin Sill in Britain (Francis, 1982), as well as those of sills in the Faroe Islands (Hansen et al., 2011), in the Karoo Basin, South Africa (Chevallier and Woodford, 1999; Malthes-Sørensen et al., 2004; Galerne et al., 2008; Polteau et al., 2008; Arnes et al., 2011; Galerne et al., 2011), in the Henry Mountains, Utah (Pollard and Johnson, 1973), and in the Theron Mountains and North Victoria Land, Antarctica (Leat et al., 2006; Berner et al., 2009). Seismic studies of sill geometries and depths in sedimentary basins include those of sills in the Vøring Basin and the Møre Basin, both offshore Norway (Planke et al., 2005; Hansen and Cartwright, 2006; Fjeldskaar et al., 2008), in the North Rockall Trough (Thomson and Hutton, 2004), in the eastern Northern Yellow Sea Basin and Bohai Bay Basin, both in China (Lee et al., 2006; Cukur et al., 2010; Wang et al., 2011) and in the Neuquén Basin in Argentina (Rossello et al., 2002). Sill emplacement (fed by dykes) has also been detected through geophysical (seismic and GPS/InSAR studies) in active volcanoes, such as for several years prior to the March 2010 eruption in Eyjafjallajökull

in Iceland (Sigmundsson et al., 2010; Gudmundsson et al., 2012). Another example is the sill (and dyke) emplacement during the 2011–12 eruption of (offshore) El Hierro, Canary Islands (Becerril et al., 2013; Marti et al., 2013).

Sill formation was initially explained through the concept 'level of neutral buoyancy' (Bradley, 1965; Francis, 1982; Corry, 1988), a mechanism also known as the hydrostatic hypothesis. This hypothesis suggests that when a magma-driven fracture, a dyke, meets a layer with the same density as that of the magma—namely, meets a level of neutral buoyancy—the dyke becomes deflected into a sill along that layer/level (or its contact with adjacent layers). Field and theoretical studies, however, show that this hypothesis is not tenable (Maccaferri et al., 2010, 2011; Gudmundsson, 2012a). More specifically, field studies such as of sill complexes in the Karoo Basin and 3D seismic data analysis (Cartwright and Hansen, 2006; Galerne et al., 2008; Menand, 2008; Galerne et al., 2011) and studies in Antarctica and elsewhere (Muirhead et al., 2011) indicate that neutral buoyancy is not a major controlling factor in the formation of sills. In sill complexes, the sills are stacked at different levels within the upper crust or in sedimentary basins (e.g., Planke et al., 2005; Muirhead et al., 2011), indicating that magma can travel vertically through many neutral-buoyancy layers as sill complexes form an interconnected network.

These results are in agreement with general results as to dyke and sill emplacement. The average rock density of the uppermost several hundred metres of a volcano-tectonically active rift zone anywhere in the world is typically around 2500 kg m^{-3} or less (Gudmundsson, 2012a). By contrast, basaltic magma commonly has densities of 2600 kg m^{-3} to 2750 kg m^{-3} (Murase and McBirney, 1973; Kilburn, 2000; Spera, 2000). It follows that to reach the surface, basaltic magma must normally propagate through crustal layers of densities that are less than that of the magma. This propagation happens everywhere in the world where basaltic volcanism takes place. Most of the basaltic dykes must pass through many 'neutral buoyancy' layers on their paths to the surface (Gudmundsson, 2012b). It follows that neither do dykes normally deflect into sills at levels of neutral buoyancy nor do neutral buoyancy layers/units halt or arrest the vertical propagation of the dykes.

The principal aim of this paper is to explore the conditions for sill emplacement at shallow depths. The focus is on the conditions for dyke deflection along a weak contact. Particular attention is given to the main mechanism of dyke deflection. A second aim is to analyse and explore the conditions that favour the development of an individual sill or a sill complex into a shallow magma chamber. Here the focus is on new numerical models with application to field examples from Iceland and Scotland. While applied to these particular areas, the mechanical results presented here are completely general and apply to sill emplacement and magma-chamber development in volcanic areas worldwide.

2. Numerical modelling of sill emplacement

Dykes are primarily extension fractures. This means that they form perpendicular to the minimum principal compressive stress which, for vertical dyke propagation, is horizontal. Most dykes do not reach the surface to feed a volcanic eruption but rather stall or stop at certain depths or stratigraphic levels in the crust—a process referred to as dyke arrest. One main reason for the commonly observed dyke arrest is the mechanical heterogeneity and anisotropy of the crust, in particular its layering.

Sills tend to be emplaced along contacts within layered host rocks. On meeting a contact between layers, the dyke may respond in one of three ways: (1) becoming arrested at the contact, (2) penetrating the contact, or (3) becoming deflected symmetrically or asymmetrically along the contact to form a sill (Gudmundsson, 2011b; Gudmundsson and Løtveit, 2012). Generally, a small or no difference in the stiffness (Young’s modulus) of the layers on either side of a contact favours dyke penetration, whereas a contrasting stiffness (particularly when the stiffer layer is above the contact, that is, closer to the surface) favours dyke arrest or deflection along the contact. This mechanism of dyke arrest/deflection is referred to as the elastic mismatch or material toughness mechanism and is a common reason for fracture deflection in industrial materials such as composite materials (He and Hutchinson, 1989; Sun and Jin, 2012). In addition to the elastic mismatch mechanism of fracture arrest or deflection, there are two other mechanisms that are important for fracture arrest/deflection in rocks. These are the Cook–Gordon debonding or delamination—also commonly observed in composite materials (Talreja and Singh, 2012)—and the stress barrier mechanism. All these mechanisms are discussed in detail below.

As an introduction to the discussion of the numerical results, the condition for a sill to form is normally that the vertical stress should

be the minimum principal compressive stress, σ_3 , and the maximum principal stress, σ_1 , horizontal (Anderson, 1951). This follows because sills are primarily extension fractures. In a rift zone, such a stress situation can, for example, be generated temporarily by dyke injections. The magmatic overpressure in the dykes may compress the layers (particularly the stiff ones) horizontally so as to, temporarily, modify the stress field and make σ_1 horizontal and σ_3 vertical, favouring sill emplacement (Gudmundsson, 1990). Another mechanism for flipping the normal stress field in a rift zone so that σ_1 becomes temporarily horizontal is through graben formation (or slip). Large slip on the graben faults increases the horizontal compressive stress in a direction perpendicular to the strike of the graben so that, following slip, this stress may for a while become σ_1 (Gudmundsson, 2011a). Some sills are fed by other sills, especially in sill complexes (Thomson and Hutton, 2004), although inclined sheets or dykes feeding sills (Fig. 2) is a much more common mechanism for sill formation, especially in rift zones and other regions undergoing extension.

The numerical models presented here were created using the finite element program ComsolMultiphysics 4.2. Briefly, the modelling procedure is as follows. Initially, pre-processing is carried out where geometries of the relevant geological structures are imported into the model. Here the modelled structures are, primarily, a vertical dyke and a weak (in tension and shear) contact between rock layers, along which the dyke may become deflected into a sill. This step is followed by adding suitable mechanical properties to the layers and the contact. The properties include Young’s modulus, Poisson’s ratio, and density, all of which are assigned to the host-rock layers. A thin elastic layer is then assigned to the contact, allowing it to open as a result of dyke-induced tensile stress, and a magmatic overpressure is assigned to the dyke. The next step is a meshing of the model, here using triangular elements, with the smallest element size (the highest element frequency)

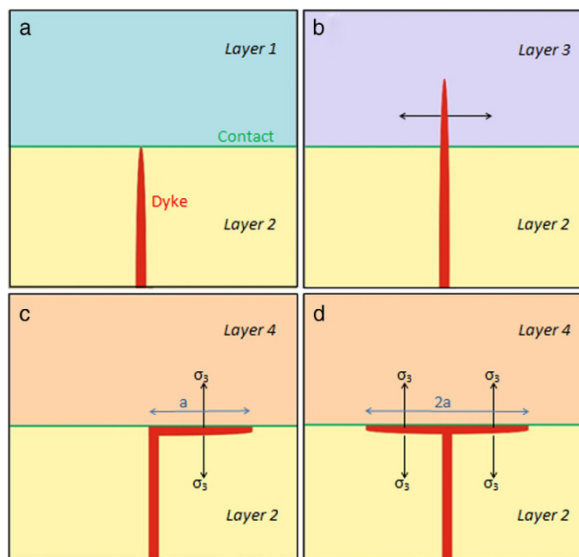


Fig. 2. When a dyke (red) meets a contact (green) the dyke can a) become arrested at the contact, b) penetrate the contact, c) deflect along the contact asymmetrically or d) deflect along the contact symmetrically. In cases c and d, the dyke forms a sill; here a represents the lateral dimension of the sill. Layers 1 and 4 are stiffer than layer 2, whereas layer 3 has the same stiffness as layer 2. σ_3 is the minimum principal compressive stress illustrating its direction to favour sill emplacement.

in the parts of the model that are of greatest interest, namely in the region between the dyke tip and the contact, and along the contact itself. The final step is to run the model, solving simultaneous equations to produce a solution (of stresses, strains, displacements, etc.). This is known as post-processing whereby the model can be visualised and the stress/displacement/strain variations throughout the model presented in terms of magnitude and/or direction (for the stress or displacement vectors, for example). Further details of the standard modelling procedure are given by Deb (2006).

Numerical models have been constructed to explore the ideas of the dyke–contact interaction shown in Fig. 2. The focus is on the conditions by which a dyke becomes arrested or deflected at a weak contact. The aim is, first, to explore the conditions whereby a weak contact will open up when a dyke propagates towards it and, second, to consider whether the dyke will be deflected along the open contact into a sill. The setup of the model is illustrated in Fig. 3. The dyke is modelled as a simple ellipse, a mode I crack (pure extension fracture, in this case a hydrofracture), emplaced in a host rock with a Young's modulus (stiffness) of 20 GPa. The dyke propagates towards a weak contact with a Young's modulus of 0.01 GPa with a more compliant or softer layer (Young's modulus 5 GPa) above the contact (cf. Gudmundsson, 2011a, b). In a composite volcano the weak contact is most likely to be scoria or a thin sedimentary (commonly soil) layer, whereas in sedimentary basins the contact would commonly be composed of shale or mudstone or siltstone. Although the crust is here modelled as layered (anisotropic), Poisson's ratio for all layers is the same, 0.25, which is a common value for many solid rocks (Gudmundsson, 2011a). The only loading is the dyke overpressure, that is, a magmatic driving pressure of 10 MPa, which is similar to that estimated from field data for many dykes (Kusumoto et al., 2013). The sides of the model are fastened to avoid rigid body rotation and/or translation.

The results show that the minimum compressive principal stress σ_3 , denoted by coloured contours (Fig. 4), tends to concentrate between the upper dyke tip and the weak contact. These stresses allow further propagation until the dyke reaches the contact. Dyke-induced tensile stresses concentrate at and below the contact, but do not penetrate into the layer above the contact. Thus, the weak contact suppresses the tensile stresses. Whether a dyke is asymmetrically or symmetrically deflected, that is, deflected in one or two directions along the contact (in a vertical section) depends on the angle that the dyke makes with the contact.

Fig. 4a–d illustrates the deformation induced by a dyke propagating towards a weak contact. In Fig. 4a the dyke is perpendicular to the

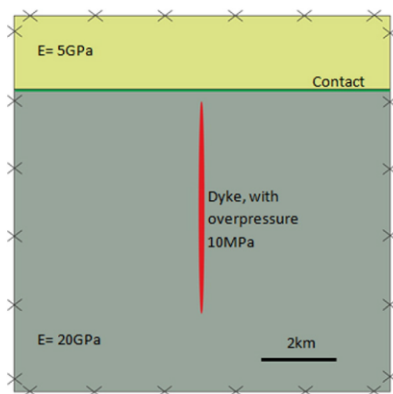


Fig. 3. Geometries and mechanical properties assigned to the models produced in Fig. 4.

contact. The contact opens symmetrically and the tensile stresses are distributed symmetrically around the tip of the dyke. On entering the contact, the dyke would either stall or become deflected symmetrically, that is, in both directions (double deflected) along the contact, as seen in a vertical cross section, to form a sill. By contrast, when the non-vertical dyke or an inclined sheet meets a weak contact at an acute angle, the tensile stress concentration is greater to the right of the dyke, and results in an asymmetric stress field and contact opening. If the dyke propagates along the contact, the deflection would tend to be in a single direction (singly deflected), so that the resulting sill would be asymmetric. Similar results have been obtained in analogue models, such as those by Kavangh et al. (2006), where gelatine is used as a crustal analogue to analyse sill formation, and are commonly observed in the field (e.g. Gudmundsson, 2011a, Fig. 10.5).

The trajectories of the maximum principal compressive stress, σ_1 , indicate the direction in which all extension fractures' propagation; here dykes, inclined sheets, and sills. For the boundary conditions set out in Fig. 4c and d, the σ_1 stress trajectories are perpendicular to the weak contact once it has opened and relaxed the tensile stress. Similarly, once an overpressured dyke is emplaced, the trajectories are perpendicular to the dyke and symmetrically distributed for a dyke approaching at 90° to a contact, whereas for the inclined sheet in Fig. 4b the trajectories indicate the main opening of the contact to the right of the inclined sheet.

Additional models were produced to illustrate the mechanism by which a stepped sill would form and propagate from one contact to another (Fig. 5). Here the dyke continues to propagate vertically until it reaches a weak contact where it is symmetrically deflected to form a sill. The sill then continues to propagate along the weak contact until a more favourable path is found, where the trajectories of σ_1 are inclined. On entering this local stress field, the sill changes into an inclined sheet (following the σ_1 trajectories) until it reaches the next weak layer above, where the inclined sheet turns into a horizontal (contact-parallel) asymmetric sill. This process can be repeated several times to form a step-like sill (Fig. 1b).

3. Sill emplacement mechanisms

When a dyke propagates towards a weak contact, the contact may open up and encourage the deflection of the dyke into a sill. The three principal mechanisms whereby a dyke can be transformed into a sill are (1) Cook–Gordon debonding (delamination), (2) stress barriers and (3) elastic mismatch. All these three mechanisms can theoretically give rise to sill emplacement. Since most magma chambers appear to evolve from sills (e.g. Gudmundsson, 2012a), these mechanisms provide the potential for understanding the initiation and evolution of shallow magma chambers.

3.1. Cook–Gordon debonding

Cook–Gordon debonding is a mechanism by which a weak contact opens up ahead of an approaching vertically propagating extension fracture, here a dyke (Figs. 4, 6). The tensile stress that forms ahead of a propagating dyke is ~20% of the tensile stress perpendicular to the vertically propagating dyke (Gudmundsson, 2011b; Gudmundsson and Løtveit, 2012). This is thus a possible, even a common, mechanism for the formation of sills, particularly at shallow depths in the Earth's crust. The tensile strength of the contact determines whether the dyke-induced tensile stress is large enough to open the contact ahead of the dyke tip. When the dyke eventually meets the open contact it may either become arrested if the overpressure is not large enough to overcome the tensile strength plus the vertical stress (which is minimum principal compressive stress, σ_3 , for sill formation). Alternatively, if the overpressure is larger than the tensile strength plus the minimum principal compressive stress, the dyke becomes deflected into a sill.

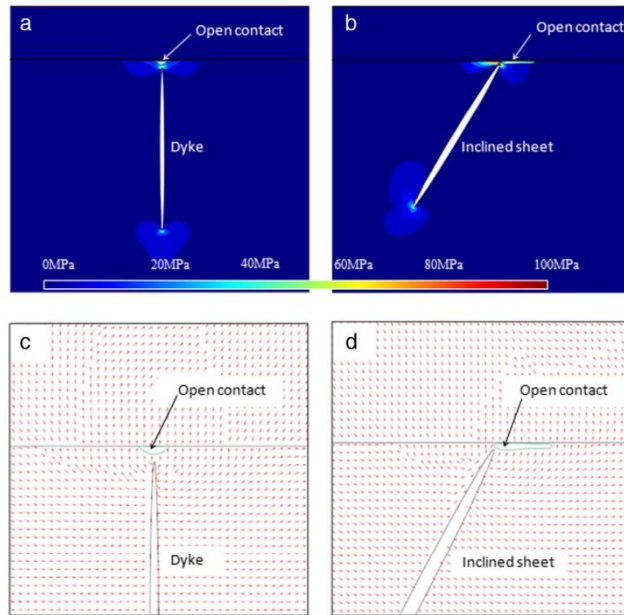


Fig. 4. FEM (finite element) models of dyke propagation towards a weak contact based on the boundary conditions in Fig. 3. a and b illustrate colour contours representing minimum principal compressive (maximum tensile) principal stress, σ_3 , where a maximum is reached at the tip of the dyke below the contact. c and d show the trajectories (ticks, directions) of the maximum compressive principal, σ_1 , represented by the red ticks where the weak contact opens up ahead of the propagating dyke.

3.2. Stress barriers

Stress barrier is simply a layer where the local stress field is unfavourable to the propagation of a fracture of a particular type and attitude that meets the layer. For a vertically propagating dyke, an extension fracture, a stress barrier is a layer where, for example, the maximum principal compressive stress σ_1 is horizontal and the minimum

principal compressive stress σ_3 is vertical. Such a local stress field would tend to arrest a vertically propagating dyke or, alternatively, deflect it along the contact between the stress barrier layer and the layer hosting the dyke (Gudmundsson, 2011b).

Stress barriers can develop in both stiff layers and soft layers. Commonly, a stiff layer becomes a stress barrier to vertical dyke propagation when the crustal segment hosting the layer has been subject to

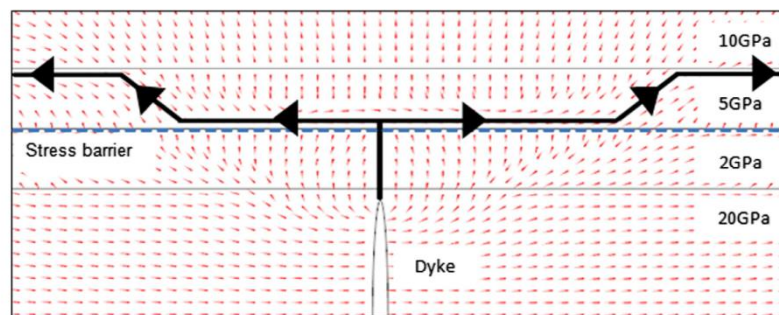


Fig. 5. FEM model of a layered crustal segment where both dyke and sill follow the maximum compressive principal stress (σ_1) trajectories represented by the red ticks. The black line shows the paths which the dyke and later the sill would follow as they reach different layers with varying stiffness.

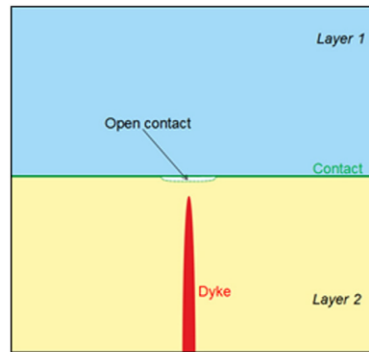


Fig. 6. Schematic illustration of Cook-Gordon debonding (delamination) mechanism showing how the contact opens ahead of the vertically propagating dyke, allowing the dyke to be deflected into a sill.

horizontal compressive stress. In a rift zone, such a compressive stress can, for example, be generated by the magmatic overpressure of earlier dykes. The magmatic overpressure can easily reach tens of megapascals (Geshi et al., 2010, 2012; Kusumoto et al., 2013), and much of the resulting horizontal compressive stress is taken up by the stiff layers. Therefore, the stiff layer may become subject to high horizontal compressive stresses, that is, become a barrier to the vertical propagation of dykes. Similar effects may be generated during normal faulting, particularly graben subsidence, where the vertical displacement may generate high horizontal compressive stresses in adjacent stiff layers (Gudmundsson, 2011a).

Stress barriers can also develop in compliant or soft layers. When there is an extension event, for example in a rift zone or in sedimentary basins, without earlier dyke injection, the stiff layers take on much of the relative tensile stress whereas the soft layers do not. As a consequence, relative tension in the stiff layers reduces their local horizontal compressive stress, which may become absolute tensile at shallow (a few hundred metres) depth in a rift zone. The soft layers, however, essentially maintain their horizontal compressive stress and thus, during extension events, may have higher horizontal compressive stresses than the stiff layers. Consequently, some of the soft layers may act as stress barriers to the vertical propagation of dykes (Gudmundsson and Brenner, 2001). This mechanism is illustrated in numerical models produced in Fig. 4c, d, and 5.

3.3. Elastic mismatch

This mechanism has until recently received little attention in the volcanotectonics literature, but is well known as a major mechanism for fracture arrest in the fracture mechanics and materials science literature (e.g. Freund and Suresh, 2003; Sun and Jin, 2012). Elastic mismatch occurs where there is a contrast in mechanical properties, that is, the material toughness and Young's modulus of adjacent layers on either side of a contact are very different. Consider the total energy release rate during fracture propagation, G_{total}

$$G_{total} = G_I + G_{II} + G_{III} \tag{1}$$

where G_I , G_{II} , and G_{III} are the energy release rates of mode I, mode II, and mode III cracks and given in Jm^{-2} (Gudmundsson, 2011a; Sun and Jin, 2012). Since dykes and sills are extension fractures, mode I cracks, their energy release rate is denoted by G_I . However, when a dyke

becomes deflected along a contact, its propagation is partly in a mixed mode, such as mode I and mode II, in which case, from Eq. (1), the total energy release rate is given by $G_{total} = G_I + (G_{II} \text{ or } G_{III})$ (He and Hutchinson, 1989; Sun and Jin, 2012).

On meeting a contact, a dyke may penetrate the contact (G_p) or deflect along the contact (G_d) depending on the energy release rate. For a dyke to penetrate the contact the following conditions must be satisfied

$$\frac{G_d}{G_p} < \frac{\Gamma_D(\Psi)}{\Gamma_L^I} \tag{2}$$

By contrast, a dyke to become deflected along the contact, the condition is

$$\frac{G_d}{G_p} \geq \frac{\Gamma_D(\Psi)}{\Gamma_L^I} \tag{3}$$

where Γ_D is the material toughness of the discontinuity or contact between layers, Γ_L^I is the material toughness of the layer above the contact, and Ψ is a measure of the relative proportion of mode I and mode II in the fracture propagation, that is, $\Psi = \tan^{-1}(K_{II}/K_I)$, where K_I is the stress intensity factor of a mode I crack, and K_{II} is the stress intensity factor of a mode II crack (He and Hutchinson, 1989; Sun and Jin, 2012). Thus, when $\Psi = 0^\circ$ then there is pure mode I propagation, and when $\Psi = 90^\circ$ there is pure mode II propagation.

Fig. 7, which is based on the results of He et al. (1994), shows that the curves for single and double deflected dykes are very similar. For practical purposes, the tendency for a dyke to form a sill through a double deflection or a single deflection may thus be regarded as essentially the same. More specifically, the results show that when the ratio G_d/G_p (on the vertical axis) is below the curves deflection of dyke into a sill along the contact between the layers is favoured (Fig. 7, c and d on the inset). When, however, this ratio is above the curves, dyke penetration through the contact and into the upper layer is favoured (Fig. 7, a and b on the inset). When the stiffnesses of the layers above and below the contact are equal, then the Dundurs parameter $\alpha = 0$ and deflection of a dyke into sill at the contact occur only if the material

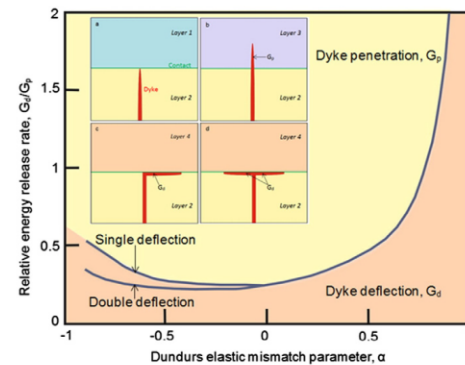


Fig. 7. Dundurs elastic mismatch parameter, α , versus the ratio of the energy release rates for dyke penetration of the contact G_p to dyke deflection along the contact G_d . The inset shows that when a dyke meets a contact there are three possible outcomes: arrest, penetration, or deflection all of which depend on whether the G_d/G_p ratio lies above or below the curve. If α is negative, the layer above the contact is softer than the layer hosting the dyke, and the dyke has a little tendency to deflection. When, however, α is positive then the layer above the contact is stiffer than the host layer, and the dyke has a strong tendency to deflection (single or double) along the contact (modified from He et al., 1994).

toughness of the contact is less than 26% of that of the layer above the contact. Such a low material toughness is rare. This is one reason why dykes tend to penetrate piles of mechanically similar layers, such as occurs in many basaltic edifices, rather than become deflected into sills.

When the Dundurs parameter α is less than zero ($\alpha < 0$), the layer above the contact is softer than the layer below the contact (and hosting the dyke). Deflection of a dyke along the contact then occurs only if the material toughness of the contact itself is comparatively low. It follows from the above considerations that these conditions are not very commonly met, so that, in this mechanism, deflection of a dyke into a sill along a contact is less likely when the layer above the contact is softer than the layer hosting the dyke. By contrast, as the value of the Dundurs parameter α increases ($\alpha > 0$), the layer above the contact becomes gradually stiffer in relation to the layer hosting the dyke, and the tendency for dyke deflection into a sill along the contact increases.

In this mechanism, the most favourable condition for dyke deflection into a sill is at a contact between a stiff lava flow or an intrusion (an earlier sill or sheet) above the contact and a soft pyroclastic or sedimentary layer below the contact. Such a deflection is often seen in the field, and the general results of these theoretical considerations are supported by experimental results from materials science (Kim et al., 2006) and analogue models in geology (Kavanagh et al., 2006). The results should, however, not be generalised too much. This is only one of the three principal mechanisms of dyke arrest or deflection at contacts. The other mechanisms—namely debonding/delamination and barriers play also an important role in dyke arrest and deflection, and are apparently commonly more important than the elastic mismatch mechanism. This is seen in the many cases where hydrofractures, not only dykes but also mineral veins, hosted by stiff layers become arrested at the contact with softer layers (cf. Gudmundsson, 2011a, b).

4. Shallow magma chamber formation

Sills show a great variation in size and geometry. Most sills range in thickness from a few metres to hundreds of metres. The lateral (strike) dimensions of sills range up to tens of kilometres and their areas may reach hundreds or thousands of square kilometres. The ratio between the lateral dimension and thickness of a sill (the aspect ratio) is commonly of the order of 10^{2-3} (Kavanagh et al., 2006; Hansen et al., 2011; Gudmundsson and Løtveit, 2012).

Sills' geometries can predominantly be classified into six groups (Fig. 8). The sills are then straight, either singly or doubly deflected (Fig. 8a, b), concave upwards (Fig. 8c), concave downwards (Fig. 8d), stepped-upwards (Fig. 8e) and stepped-downwards (Fig. 8f). Concave downwards and stepped-downwards sills are rarely observed. Concave-

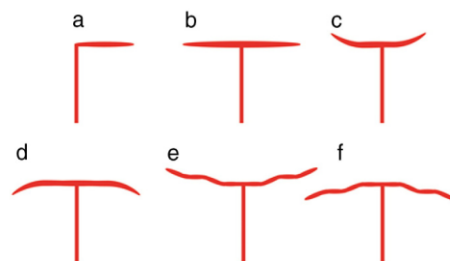


Fig. 8. Schematic illustration of sill geometries. a) singly deflected sill, b) doubly deflected sill, c) concave upwards sill, d) concave downwards sill, e) stepped upwards sill, and f) stepped downwards sill.

upwards and stepped-upwards sills are commonly referred to as saucer-shaped sills. Sills exhibit differing geometries primarily because of the different elastic responses of the host rock within which the sill is emplaced.

For a sill to evolve into a shallow magma chamber the associated dyke-injection rate must reach a certain minimum (depending on thickness of the initial sill, the host-rock temperature, and other factors) (Hardee, 1982; Gudmundsson, 1990). This minimum rate ensures that the initial sill does not solidify but remains partially molten. As indicated, the necessary dyke injection rate depends on the thickness of the initial sill; the thicker the initial sill, the longer it can stay partially liquid at a low dyke injection rate. Many magma chambers maintain their sill-like geometries throughout their lifetimes, and some are only a few tens of metres thick (Gudmundsson, 2012a), such as at fast-spreading ocean ridges (Macdonald, 1982). Other sills, however, develop into larger magma chambers through the accumulation of many sills as subsequent dykes are deflected into sills under or on top of the early sills to form a sill complex (Gudmundsson, 2012a). As sill grows the host rock above and below the sill becomes deformed. The deformation of the host rock, however, depends on the lateral dimension of the sill in relation to its depth below the surface. When its lateral dimensions are smaller than its depth below the free surface, the deformation of the host rock is primarily similar to that around an elastic crack in an infinite body. By contrast, when the lateral dimensions of the sill are much larger than the depth of the sill below the free surface, the sill may expand, partly through bending of the overburden (and to some extent the underburden), in which case flexural rigidity of the host rock affects the final thickness of the sill (Pollard and Johnson, 1973). Here we consider both small crack-like sills and larger sills where the bending of the host rock plays a role.

4.1. Small sills

The maximum deflection of the upper surface of the sill, w_{max} is given by (Sneddon and Lowengrub, 1969; Gudmundsson, 2011a)

$$w_{max} = \frac{4p_0(1-\nu^2)a}{\pi E} \tag{4}$$

where p_0 is the overpressure of the magma, a is the radius of the sill (assumed circular), ν is Poisson's ratio at 0.25, and E is Young's modulus of a homogeneous crust. As discussed, sills are normally emplaced at an interface or a contact between layers (Fig. 2). Consider the case when the adjacent layers both have a Young's modulus of 20 GPa and a Poisson's ratio of 0.25. For a sill with a radius of 2000 m and a magmatic overpressure of 10 MPa, emplaced at 4 km depth, it follows from Eq. (4) that the maximum deflection at the centre of the sill is 2.4 m. This analytical result is in agreement with the numerical results, for the same boundary conditions, presented in Fig. 9. Such a thin sill would solidify (in accordance with $t \approx 0.0825w^2$; where t is the time it takes for the sill to solidify, and w is the deflection or half the thickness of the sill) within a short period of time, about half a year (Jaeger, 1957), so it would not have the potential to act as a shallow magma chamber.

4.2. Large sills

When the radius of a sill is larger than its depth below the surface, the sill may bend the overburden. This bending may generate magma chambers of different shapes from a straight sill, in some cases laccoliths (Fig. 10; Pollard and Johnson, 1973). The maximum upward bending or deflection of such a sill w_{max} is given by (Ugural, 1981)

$$w_{max} = \frac{p_0 a^4}{64D} \left(\frac{5 + \nu}{1 + \nu} + \frac{4d^2}{(1 - \nu^2)a^2} \right) \tag{5}$$

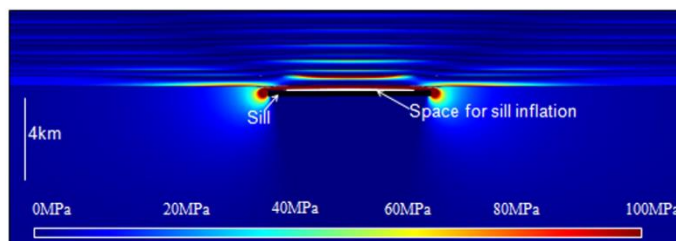


Fig. 9. FEM model of a sill emplaced 4 km below the surface, with colour contours indicating the magnitude of minimum compressive (maximum tensile) principal stress σ_3 . The sill is small and thin and would solidify quickly and thus have little chance of evolving into a magma chamber.

The symbols are the same as in Eq. (4) except that d is here the depth of the sill below the surface and D is the flexural rigidity, given by (Ugural, 1981)

$$D = \frac{ET_e^3}{12(1-\nu^2)} \quad (6)$$

where T_e is the effective thickness of the crustal segment. For the layered host rock presented in the numerical models here, the effective thickness T_e may be regarded as $T_e = 0.3d$ (Gudmundsson, 1990). This reduced thickness is because mechanical layers may slip along their interfaces/contacts which generally lowers the rigidity (Reddy, 2004). If a sill is emplaced at a boundary between two layers with different mechanical properties at a depth of 4 km, the effective thickness is thus 1.2 km. In the model in Fig. 11 Young's modulus is lower for the layers above the sill (the layers are softer or more compliant), alternating between 10 GPa and 30 GPa, while the layer hosting the sill has a higher Young's modulus of 40 GPa; all the layers have a Poisson's ratio of 0.25. The flexural rigidity can then be calculated from Eq. (6) for the layers above the sill as 1.54×10^{18} Nm. For ten layers forming the overburden the maximum deflection calculated from Eq. (5), when the magmatic overpressure is 10 MPa and the radius of the sill 2 km, is 90 m.

4.3. Magma chamber evolution

An expanding magma chamber needs to generate space for itself. This space is normally generated through elastic or elastic-plastic deformation of the host rock. For individual volcanotectonic events, the surface deformation associated with an inflating magma chamber has commonly been modelled using the nucleus-of-strain model



Fig. 10. View north, sill-laccolith microgabbro intrusion. The exposed thickness is approximately 15 m (person for scale), SW Iceland.

(Anderson, 1936; Mogi, 1958), commonly referred to as the 'Mogi model' in volcanology. This model has been developed by many including Bonafede and Ferrari (2009) who model a spherical source in a viscoelastic half space. The effect of host-rock layering on the various magma-chamber estimates using a 'Mogi model' has been considered by Masterlark (2007) who shows that the estimated depth to the magma chamber is significantly affected by the layering of the associated volcano.

Once a dyke has deflected into a sill, the local stress field becomes modified (Figs. 4c, 5). In particular, because the expansion of the sill is normally primarily related to upward deflection of the layer above the contact, the vertical stress in that layer may change from being the minimum principal compressive stress σ_3 , to being the maximum principal compressive stress σ_1 (Fig. 12). By contrast, below the sill the trajectories of σ_1 are inclined due to the combined effects of the sill and the feeder. Gradually, as more dykes are injected and partly absorbed by the sill, it grows into a larger magma chamber. This illustrates how a shallow magma chamber may develop from a sill (or sills) emplaced at a contact separating two rock layers with differing elastic properties.

5. Discussion

Geologists have been motivated in the past few decades to try to understand better the mechanics that controls dyke ascent through the Earth's crust. Until comparatively recently, the main attention was on dyke propagation (Lister and Kerr, 1991; Rubin, 1995), but sill emplacement is now receiving increasing attention (e.g. Pinel and Jaupart, 2004; Kavanagh et al., 2006; Menand, 2008; Gudmundsson, 2011b). The present paper focuses on the propagation of dykes through a heterogeneous, anisotropic crust where the dykes tend to be arrested or deflected primarily at weak contacts between mechanically dissimilar lithological units to form sills, some of which may evolve into shallow magma chambers. The mechanisms governing sill development have been widely studied through analogue (Xu et al., 2003; Rivalta et al., 2005; Kavanagh et al., 2006; Wang and Xu, 2006; Menand, 2008), analytical (Gretener, 1969; Gudmundsson, 1990; Bungler and Cruden, 2011) and numerical (Zhang et al., 2007; Maccaferri et al., 2010; Gudmundsson, 2011b; Maccaferri et al., 2011) modelling. Numerical models provide us with a more accurate solutions to problems as the heterogeneity and anisotropy of the crust can be taken into account providing us with more detailed results on the stress fields produced than analytical solutions. Therefore, when taking the layering of the upper crust into account numerical models can illustrate the sudden changes in mechanical properties and associated stress fields that can result in dyke deflection into sills through the mechanisms referred to as Cook-Gordon debonding, stress barriers, and elastic mismatch.

There are three principal mechanisms considered here by which a dyke may be deflected at a weak contact to form a sill which, eventually, may evolve into a magma chamber. These three mechanisms may often

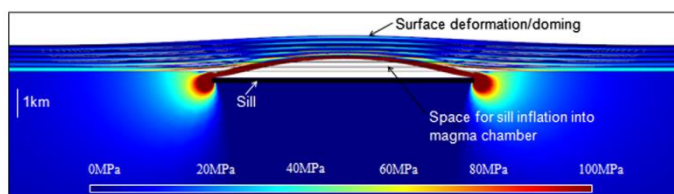


Fig. 11. FEM model of straight sill emplaced 1 km below the surface, with colour contours indicating the magnitude of minimum compressive (maximum tensile) principal stress σ_3 . The host rock has a Young's modulus of 40 GPa, with the softer layers above the sill alternating in stiffness between 10 GPa and 30 GPa. Large tensile stresses ~ 20 MPa are generated at the tips of the sill, allowing for further lateral propagation. The sill also induces large tensile stresses in the overlying strata and at the surface encouraging inflation of the sill, ground deformation (doming), and seismicity.

operate together, while for each case one may be the dominating mechanism. The first mechanism is Cook–Gordon debonding or delamination whereby the large tensile stresses generated by the propagating dyke (sheet) give the weak contact the ability to open up (debonding) ahead of the dyke (e.g. Wang and Xu, 2006). Many numerical models have been made from those presented in this study, which illustrate that the contact which opens up may have a variety of attitudes and

distances from the dyke tip. Our results (Figs. 4, 6) suggest that the contacts open up first vertically right above the dyke, as the dyke tip approaches, and then, in case a sill forms, vertically ahead of the sill tip. Similar opening of the contact has been described by Xu et al. (2003). The maximum opening of the contact occurs where the dyke eventually intersects it and from there decreases with an increasing distance from the intersection point (Figs. 4 and 6; Zhang et al., 2007). The opening of the weak contact suppresses the tensile stresses induced by the propagating dyke and then allows for the dyke to be either singly or doubly deflected into a sill, known in the fracture-mechanics literature as T-shaped fractures (Gudmundsson and Brenner, 2001). As a majority of sills are located along interfaces (Mudge, 1968; Gretener, 1969) such as weak contacts it suggest that contacts are a primary control on sill emplacement. As illustrated in Fig. 5 the magma within a sill can continue to flow laterally but it is also sometimes able to renew propagation in an inclined direction as a sheet (commonly) or as a dyke, giving rise to stepped geometries and saucer shaped sills (e.g. Gudmundsson and Lötveit, 2012).

The second mechanism is stress barriers. For a vertical dyke, this is a layer that has high horizontal compressive stresses acting perpendicular to the dyke and thus generally arresting or deflecting the dyke. More specifically, for a vertical dyke, the barrier occurs when there is rotation of the maximum principal compressive stress, σ_1 is rotated 90° from its original vertical orientation to a horizontal orientation. If, after rotation, σ_3 is also vertical and the magmatic pressure of the dyke is high enough to lift the overburden, then formation (deflection of the dyke into a sill along the contact) is encouraged. Commonly stress barriers are related to strong changes in the mechanical properties of the rocks across (commonly weak) contacts. Field studies (Gudmundsson, 2011a) show that dykes arrested through this mechanism commonly exhibit broad/blunt tips. This mechanism also operates for the formation of shallow magma chambers through sill amalgamation (Gudmundsson, 2011b).

The third mechanism is elastic mismatch, that is, stiffness (Young's modulus) contrasts across a weak contact/interface and is also related to the material toughness of the weak contact with respect to the adjacent layers. This mechanism has received much attention in materials science literature (He and Hutchinson, 1989; He et al., 1994; Hutchinson, 1996) but comparatively little in geological literature. However, this mechanism is important for understanding sill emplacement and shallow magma chamber formation. Analogue modelling tends to focus on stiffness contrasts (e.g. Kavanagh et al., 2006; Maccaferri et al., 2010; Menand, 2011), and experiments suggest that sills tend to form at interfaces between compliant (soft) and overlying stiffer layers. This is supported by field observations where dykes are seen to be commonly deflected along contacts between pyroclastic layers (soft) and stiff lava flows or intrusions on top of the lava flows.

Once a sill has formed, its growth into a magma chamber can be modelled in several ways. The theory of thin elastic plates has been used for over 30 years to model large sills and laccoliths, in particular where the horizontal dimensions of the intrusions are large in respect

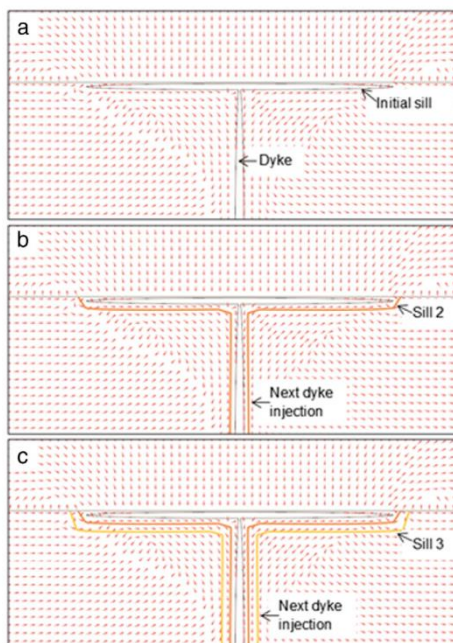


Fig. 12. FEM model of maximum compressive principal stress (σ_1) trajectories (red ticks) showing how the local stress field induced by the initial sill (a) can favour subsequent dyke injections (b and c) into sills to form an eventual shallow magma chamber. Here the first dyke is already deflected into a sill; the dyke and sill have an overpressure of 10 MPa. The layer in which the dyke is emplaced has a stiffness of 20 GPa, and the above layer has a stiffness of 5 GPa. The contact is modelled as a thin elastic layer. The model is fixed at all sides.

to their depths of emplacement. However, this theory is only an approximate and is perhaps not entirely successful in describing large sills and laccoliths in terms of their actual measured geometries (McCaffrey and Petford, 1997; Cruden and McCaffrey, 2006). More specifically, many sills and magma chambers in the field exhibit flat-topped geometries i.e. elliptical with a uniform thickness and not sort-of 'bell shaped' as is suggested by the thin elastic plate theory (Bunger and Cruden, 2011).

We believe that this paper provides insights into the geometric evolution of an initial sill into a magma chamber. These can be correlated with field studies. For example, field observations Henry Mountains, Utah (Pollard and Johnson, 1973; Horsman et al., 2009) and Iceland (Gudmundsson, 2012a) suggest that most shallow magma chambers (or laccoliths) are formed by many magmatic pulses via sheets and dykes. This has also been suggested by analogue models with gelatine by Rivalta et al. (2005), indicating that once a sill has been emplaced new dyke injections will increase the magmatic volume within the sill to form a chamber. This can be explained mechanically as a consequence of the initial sill forming a stress barrier arresting subsequent dykes (Fig. 12). The laccoliths of the Henry Mountains, Utah also suggest how shallow magma chamber may form. Pollard and Johnson (1973) suggest that bending of the overlying layers generates space for the growing intrusions as illustrated in Fig. 11. This is also supported by analytical models by Petraske et al. (1978) who conclude that a sill will initially grow laterally, and as magma is injected into the sill it will begin to deflect the overburden and the underburden to evolve into a magma chamber. The sheet and dyke injections must generally be frequent to keep the chamber liquid and growing (Gudmundsson, 1990; Glazner et al., 2004; Horsman et al., 2009).

There are limitations to the numerical models presented, in that we know sill emplacement has associated thermal effects in addition to the mechanical effects explored here. The thermal effects include contact metamorphism of the host rock and the formation of a chilled selvage along the margin of the sill. The thermal effects will be considered in a later publication.

6. Conclusions

Dykes, sills, and crustal magma chambers are fundamental building blocks for the accretion of the crust at divergent plate boundaries. Numerous examples in the field e.g. Iceland and Tenerife (Canary Islands), show that the majority of dykes never reach the surface to feed an eruption but are either arrested (Marinoni and Gudmundsson, 2000; White et al., 2011) or deflected into sills (e.g., Sigmundsson et al., 2010; Gudmundsson et al., 2012) may evolve into shallow magma chambers or laccoliths (Gudmundsson, 1990, 2011b; Menand, 2011). Based on numerical models and field studies presented here, several conclusions can be made on dyke deflection and the emplacement of sills and the formation of shallow magma chambers.

1. Most sills form when a dyke or dykes becomes deflected at an interface, in most cases a weak contact. The three principal mechanisms for dyke deflection are (1) Cook–Gordon debonding (delamination) where a contact opens up ahead of the nearby dyke tip, (2) stress barriers where the principal compressive stresses become rotated and unfavourable for vertical dyke propagation but favourable for sill emplacement, and (3) elastic mismatch where there are contrasting material properties of the layers on either side of a contact. The three mechanisms may function together during the emplacement sills, while one mechanism is likely to be the dominating one in each particular case.
2. Sills take a variety of forms including straight, concave, and stepped. Their final geometry is determined by mechanical (and stress) heterogeneities within the host rock.
3. Shallow magma chambers tend to evolve from straight, elliptical sills where there is a high dyke-injection rate so that the magma does not solidify before it receives new magma, supplied by the dykes.

4. Most sills that evolve into shallow magma chambers start as comparatively large sills, that is, the sill radius is larger than the depth below the surface. As the sill inflates the overburden (and underburden to some extent) becomes deflected creating space for the growing sill.
5. A high injection rate of new magma, through dykes, is needed into the sill in order for it to remain at least partially molten while growing into a shallow magma chamber.

Acknowledgements

This work forms part of the Tectonor project 'The effects of magmatic sill emplacement on the petroleum systems in the Vøring Margin' (VøMag). We thank E.ON E&P Norge, Repsol Exploration Norge and RWE DeaNorge for financial support and for permission to publish this work. We also thank Shigekazu Kusumoto and an anonymous reviewer for very helpful comments.

References

- Anderson, E.M., 1936. The dynamics of formation of cone sheets, ring dykes and cauldron subsidences. *Proc. R. Soc. Edinb.* 56, 128–163.
- Anderson, E.M., 1951. The Dynamics of Faulting and Dyke Formation with Applications to Britain. Oliver and Boyd, Edinburgh.
- Arnes, L., Svensen, H., Polteau, S., Planke, S., 2011. Contact metamorphic devolatilization of shales in the Karoo Basin, South Africa, and the effects of multiple sill intrusions. *Chem. Geol.* 281, 181–194.
- Baer, G., Heimann, A., 1995. *Physics and Chemistry of Dykes*. A A Balkema, Rotterdam, (339 pp.).
- Becerril, L., Galindo, I., Gudmundsson, A., Morales, J.M., 2013. Depth of origin of magma in eruptions. *Sci. Rep.* 3, 2762. <http://dx.doi.org/10.1038/srep02762> (Nature Publishing).
- Berner, U., Kus, J., Scheeder, G., Schneider, J., Schner, R., Viereck-Grote, L., 2009. Influence of Jurassic sill intrusions on the organic matter of Upper Triassic lacustrine and fluvial sediments of North Victoria Land (Antarctica). *Geophysical Research Abstracts*, European Geoscience Union 2009, Vienna.
- Bonafede, M., Ferrari, C., 2009. Analytical models of deformation and residual gravity changes due to a Mogi source in a viscoelastic medium. *Tectonophysics* 471, 4–13.
- Bradley, J., 1965. Intrusion of major dolerite sills. *Trans. R. Soc. N. Z.* 3, 27–55.
- Bunger, A.P., Cruden, A.R., 2011. Modelling the growth of laccoliths and large mafic sills: role of magma body forces. *J. Geophys. Res.* 116, B02203. <http://dx.doi.org/10.1029/2010JB007648>.
- Cartwright, J., Hansen, D.M., 2006. Magma transport through the crust via interconnected sill complexes. *Geology* 34, 929–932.
- Chevallier, L., Woodford, A., 1999. Morpho-tectonics and mechanism of emplacement of the dolerite rings and sills of the western Karoo, South Africa. *S. Afr. J. Geol.* 102, 43–54.
- Corry, C.E., 1988. Laccoliths: mechanics of emplacement and growth. *Geol. Soc. Am. Spec. Pap.* 220, 1–110.
- Cruden, A., McCaffrey, K., 2006. Dimensional scaling relationships of tabular intrusions and their implications for a size, depth and compositionally dependent spectrum of emplacement processes in the crust. *Field Meeting Supplement*, Abstract V12B-06. *Eos Transactions American Geophysical Union*, 87 (52).
- Cukur, D., Horozal, S., Kim, D.C., Lee, G.H., Han, H.C., Kang, M.H., 2010. The distribution and characteristics of igneous complexes in the northern East China Sea Shelf Basin and their implications for hydrocarbon potential. *Mar. Geophys. Res.* 31, 299–313.
- Deb, D., 2006. *Finite Element Method, Concepts and Applications in Geomechanics*. PHI Learning Private Limited, New Delhi.
- Fjeldskaar, W., Helset, H.M., Johansen, H., Grunnaleite, L., Horstad, L., 2008. Thermal modelling of magmatic intrusions in the Gjallar Ridge, Norwegian Sea: implications for vitrinite reflectance and hydrocarbon maturation. *Basin Res.* 20, 143–159. <http://dx.doi.org/10.1111/j.1365-2117.2007.00347.x>.
- Francis, E.H., 1982. Magma and sediment-l: emplacement mechanism of late Carboniferous tholeiite sills in the northern Britain. *J. Geol. Soc. Lond.* 139, 1–20.
- Freund, L.B., Suresh, S., 2003. *Thin Film Materials: Stress, Defect Formation and Surface Evolution*. Cambridge University Press, Cambridge.
- Galerne, C.Y., Neumann, E.-R., Planke, S., 2008. Emplacement mechanisms of sill complexes: information from the geochemical architecture of the Golden Valley Sill Complex, South Africa. *J. Volcanol. Geotherm. Res.* 177, 425–440.
- Galerne, C.Y., Galland, O., Neumann, E.-R., Planke, S., 2011. 3D relationships between sills and their feeders: evidences from the Golden Valley Sill Complex (Karoo Basin) and experimental modelling. *Volcanic and Magmatic Studies Group, Annual Meeting 2011*. Queens' College, Cambridge.
- Geshi, N., Kusumoto, S., Gudmundsson, A., 2010. Geometric difference between non-feeders and feeder dykes. *Geology* 38, 195–198.
- Geshi, N., Kusumoto, S., Gudmundsson, A., 2012. Effects of mechanical layering of host rocks on dike growth and arrest. *J. Volcanol. Geotherm. Res.* 223, 74–82.
- Glazner, A.F., Bartley, J.M., Coleman, D.S., Gray, W., Taylor, R.Z., 2004. Are plutons assembled over millions of years by amalgamation from small magma chambers? *GSA Today* 14, 4–11.
- Greener, P.E., 1969. On the mechanics of the intrusion of sills. *Can. J. Earth Sci.* 6, 1415–1419.

- Gudmundsson, A., 1990. Emplacement of dikes, sills and crustal magma chambers at divergent plate boundaries. *Tectonophysics* 176, 257–275.
- Gudmundsson, A., 2011a. Rock Fractures in Geological Processes. Cambridge University Press, Cambridge.
- Gudmundsson, A., 2011b. Deflection of dykes into sills at discontinuities and magma-chamber formation. *Tectonophysics* 500, 50–64.
- Gudmundsson, A., 2012a. Magma chambers: formation, local stresses, excess pressures, and compartments. *J. Volcanol. Geotherm. Res.* 237–238, 19–41.
- Gudmundsson, A., 2012b. Strength and strain energies of volcanic edifices: implications for eruptions, collapse calderas, and landslides. *Nat. Hazards Earth Syst. Sci.* 12, 1–18.
- Gudmundsson, A., Brenner, S.L., 2001. How hydrofractures become arrested. *Terra Nova* 13, 456–462.
- Gudmundsson, A., Løtveit, I.F., 2012. Sills as fractured hydrocarbon reservoirs: examples and models. *Geol. Soc. Lond., Spec. Publ.* 374. <http://dx.doi.org/10.1144/SP374.5>.
- Gudmundsson, M.T., Thordarson, T., Hoskuldsson, A., Larsen, G., Björnsson, H., Prata, F.J., Oddson, B., Magnússon, E., Hognadóttir, T., Petersen, G.N., Hayward, C.L., Stevenson, J.A., Jónsdóttir, J., 2012. Ash generation and distribution from the April–May 2010 eruption of Eyjafjallajökull, Iceland. *Sci. Rep.* 2, 572. <http://dx.doi.org/10.1038/srep00572>.
- Hansen, D.M., Cartwright, J., 2006. Saucer-shaped sill with lobate morphology revealed by 3D seismic data: implications for resolving a shallow-level sill emplacement mechanism. *J. Geol. Soc. Lond.* 163, 509–523.
- Hansen, J., Jerram, D.A., McCaffrey, K., Passey, S.R., 2011. Early Cenozoic saucer-shaped sills of the Faoe Islands: an example of intrusive styles in basaltic lava piles. *J. Geol. Soc. Lond.* 168, 159–178. <http://dx.doi.org/10.1144/0016-76492010-012>.
- Hardee, H.C., 1982. Incipient magma chamber formation as a result of repetitive intrusions. *Bull. Volcanol.* 45, 41–49.
- He, M.Y., Hutchinson, J.W., 1989. Crack deflection at an interface between dissimilar elastic materials. *Int. J. Solids Struct.* 25, 1053–1067.
- He, M.Y., Evans, A.G., Hutchinson, J.W., 1994. Crack deflection at an interface between dissimilar elastic materials: role of residual stresses. *Int. J. Solids Struct.* 31, 3443–3455.
- Horsman, E., Morgan, S., de Saint-Blanquat, M., Habert, G., Nugent, A., Hunter, R.A., Tikoff, B., 2009. Emplacement and assembly of shallow intrusions from multiple magma pulses, Henry Mountains, Utah. *Trans. R. Soc. Edinb. Earth Environ. Sci.* 100, 117–132.
- Hutchinson, J.W., 1996. Stresses and failure modes in thin films and multilayers. Notes for a Dcam Course/Technical University of Denmark. Lyngby, (1–45pp).
- Jaeger, J.C., 1957. The temperature in the neighbourhood of a cooling intrusive sheet. *Am. J. Sci.* 255, 306–318.
- Kavanagh, J.L., Menand, T., Sparks, R.S.J., 2006. An experimental investigation of sill formation and propagation in layered elastic media. *Earth Planet. Sci. Lett.* 245, 799–813.
- Kilburn, C.J., 2000. Lava flows and flow fields. In: Sigurdsson, H. (Ed.), *Encyclopedia of Volcanoes*. Academic Press, New York, pp. 291–305.
- Kim, J.W., Bhowmick, S., Hermann, L., Lawn, B.R., 2006. Transverse fracture of brittle bilayers: relevance to failure of all-ceramic dental crowns. *J. Biomed. Mater. Res.* 79B, 58–65.
- Kusumoto, S., Geshi, N., Gudmundsson, A., 2013. Aspect ratios and magma overpressures of non-feeder dikes observed in the Miyake-jima volcano (Japan), and fracture toughness of its upper part. *Geophys. Res. Lett.* 40 (1–5), 2013. <http://dx.doi.org/10.1002/grl.50284>.
- Leat, P.T., Luttinen, A.V., Storey, B.C., Millar, I.L., 2006. Sills of the Theron Mountains, Antarctica: evidence for long distance transport of mafic magmas during Gondwana break-up. In: Hanski, E., Mertanen, S., Ramo, T., Vuollo, J. (Eds.), *Dyke swarms: Time Markers of Crustal Evolution*. Taylor and Francis, London, pp. 183–199.
- Lee, G.H., Kwon, Y.I., Yoon, C.S., Kim, H.J., Yoo, H.S., 2006. Igneous complexes in the eastern Northern Yellow Sea Basin and their implications for hydrocarbon systems. *Mar. Pet. Geol.* 21, 631–645.
- Lister, J.R., Kerr, R.C., 1991. Fluid-mechanical models of crack propagation and their application to magma transport in dykes. *J. Geophys. Res.* 96, 10049–10077.
- Maccaferri, F., Bonafede, M., Rivalta, E., 2010. A numerical model of dyke propagation in layered elastic media. *Geophys. J. Int.* 180, 1107–1123.
- Maccaferri, F., Bonafede, M., Rivalta, E., 2011. A quantitative study of the mechanisms governing dike propagation, dike arrest and sill formation. *J. Volcanol. Geotherm. Res.* 208, 39–50.
- Macdonald, K.C., 1982. Mid-ocean ridges: fine scale tectonic, volcanic and hydrothermal processes within the plate boundary zone. *Annu. Rev. Earth Planet. Sci.* 17, 437–474.
- Malthe-Sørensen, A., Planke, S., Svendsen, H., Jamveit, B., 2004. Formation of saucer-shaped sills. *Geol. Soc. Lond., Spec. Publ.* 234, 215–227.
- Marinoni, L.B., Gudmundsson, A., 2000. Dykes, faults and palaeostresses in the Teno and Anaga massifs of Tenerife (Canary Islands). *J. Volcanol. Geotherm. Res.* 103, 83–103.
- Marti, J., Pinel, V., Lopez, C., Geyer, A., Abella, R., Tarraga, M., Blanco, M.J., Castro, A., Rodriguez, C., 2013. Causes and mechanisms of El Hierro submarine eruption (2011–2012) (Canary Islands). *J. Geophys. Res. Solid Earth* 118, 1–17. <http://dx.doi.org/10.1002/jgrb.50087>.
- Masterlark, T., 2007. Magma intrusion and deformation predictions: sensitivities to the Mogi assumptions. *J. Geophys. Res.* 112. <http://dx.doi.org/10.1029/2006JB004860> (Article number B06419).
- McCaffrey, K., Petford, N., 1997. Are granitic plutons scale invariant? *J. Geol. Soc.* 154, 1–4. <http://dx.doi.org/10.1144/gsjgs.154.1.0001>.
- Menand, T., 2008. The mechanics and dynamics of sills in layered elastic rocks and their implications for the growth of laccoliths and other igneous complexes. *Earth Sci. Planet. Lett.* 267, 93–99.
- Menand, T., 2011. Physical controls and depth of emplacement of igneous bodies: a review. *Tectonophysics* 500, 11–19.
- Mogi, K., 1958. Relations between eruptions of various volcanoes and the deformations of the ground surfaces around them. *Bull. Earthq. Res. Inst., Univ. Tokyo* 36, 99–134.
- Mudge, M.R., 1968. Depth control of some concordant intrusions. *Geol. Soc. Am. Bull.* 79, 315–332.
- Muirhead, J.D., Airoidi, G., Rowland, J.V., White, J.D.L., 2011. Interconnected sills and inclined sheet intrusions control shallow magma transport in the Ferrar large igneous province, Antarctica. *Geol. Soc. Am. Bull.* 124, 162–180. <http://dx.doi.org/10.1130/B30455.1>.
- Murase, T., McBirney, A.R., 1973. Properties of some common igneous rocks and their melts at high temperatures. *Geol. Soc. Am. Bull.* 84, 3563–3592.
- Petruske, A.K., Hodge, D.S., Shaw, R., 1978. Mechanics of emplacement of basic intrusions. *Tectonophysics* 46, 41–63.
- Pinel, C., Jaupart, C., 2004. Magma storage and horizontal dike injection beneath a volcanic edifice. *Earth Planet. Sci. Lett.* 221, 245–262.
- Planke, S., Rasmussen, T., Rey, S.S., Myklebust, R., 2005. Seismic characteristics and distribution of volcanic intrusions and hydrothermal vent complexes in the Vøring and Møre Basins. In: Doré, A.G., Vining, B.A. (Eds.), *Petroleum Geology: North-West Europe and Global Perspectives—Proceedings of the 6th Petroleum Geology Conference*. Geological Society, London, pp. 833–844.
- Pollard, D.D., Johnson, A.M., 1973. Mechanics of growth of some laccolithic intrusions in the Henry Mountains, Utah II: bending and failure of overburden and sill formation. *Tectonophysics* 18, 311–354.
- Polteau, S., Ferré, E.C., Planke, S., Neumann, E.-R., Chevallier, L., 2008. How are saucer-shaped sills emplaced? Constraints from the Golden Valley Sill, South Africa. *J. Geophys. Res.* 113, B12104. <http://dx.doi.org/10.1029/2008JB005620> (Article number B12104).
- Reddy, J.N., 2004. *Mechanics of Laminated Composite Plates and Shells*. CRC Press, New York, (856 pp.).
- Rivalta, E., Bttinger, M., Dahm, T., 2005. Buoyancy-driven fracture ascent: experiments in layered gelatine. *J. Volcanol. Geotherm. Res.* 144, 273–285.
- Rossello, E.A., Cobbold, P.R., Diraison, M., Arnaud, N., 2002. Aucmahuida (Neuquén Basin, Argentina): a Quaternary shield volcano on a hydrocarbon producing substrate. 5th International Symposium on Andean Geodynamics, Toulouse, Extended Abstracts, pp. 549–552.
- Rubin, A.M., 1995. Propagation of magma-filled cracks. *Annu. Rev. Earth Planet. Sci.* 23, 287–336. <http://dx.doi.org/10.1146/annurev.ea.23.050195.001443>.
- Sigmundsson, F., Hreinsdóttir, S., Hooper, A., Arnadóttir, T., Pedersen, R., Roberts, M.J., Óskarsson, N., Aurlac, A., Decriem, J., Einarsson, P., Geirsson, H., Hensch, M., Ófeigsson, B.G., Sturkell, E., Sveinbjörnsson, H., Feigl, K., 2010. Intrusion triggering of the 2010 Eyjafjallajökull eruption. *Nature* 468, 426–430.
- Sneddon, I.N., Lowengrub, M., 1969. *Crack Problems in the Classical Theory of Elasticity*. Wiley, New York.
- Spera, F.J., 2000. Physical properties of magmas. In: Sigurdsson, H. (Ed.), *Encyclopedia of Volcanoes*. Academic Press, New York, pp. 291–305.
- Sun, C.T., Jin, Z.H., 2012. *Fracture Mechanics*. Elsevier, Amsterdam.
- Talreja, R., Singh, C.V., 2012. *Damage and Failure of Composite Materials*. Cambridge University Press, Cambridge.
- K.Thomson, K., D.Hutton, D., 2004. Geometry and growth of sill complexes: insights using 3D seismic from the North Rockall Trough. *Bull. Volcanol.* 66, 364–375. <http://dx.doi.org/10.1007/s00445-003-0320-z>.
- Ugural, A.C., 1981. *Stresses in Plates and Shells*. McGraw-Hill, New York.
- P.Wang, P., R.Xu, R., 2006. Dynamic interfacial debonding initiation induced by an incident crack. *Int. J. Solids Struct.* 43, 6535–6550.
- Wang, K., Lu, X., Chen, M., Ma, Y., Liu, K., Li, X., Hu, W., 2011. Numerical modelling of hydrocarbon generation of Tertiary source rocks intruded by doleritic sills in the Zhanhua depression, Bohai Bay Basin, China. *Basin Res.* 23, 1–14. <http://dx.doi.org/10.1111/j.1365-2171.2011.00518x>.
- White, R.S., Drew, J., Martens, H.R., Key, J., Soosalu, H., Jakobsdóttir, S.S., 2011. Dynamics of dyke intrusion in the mid-crust of Iceland. *Earth Planet. Sci. Lett.* 304, 300–312.
- Xu, L.R., Huang, Y.Y., Rosakis, A.J., 2003. Dynamic crack deflection and penetration at interfaces in homogenous materials: experimental studies and model predictions. *J. Mech. Phys. Solids* 51, 461–486.
- Zhang, X., Jeffrey, R.G., Thiercelin, M., 2007. Deflection and propagation of fluid-driven fractures at frictional bedding interfaces: a numerical investigation. *J. Struct. Geol.* 29, 396–410.